

JOURNAL OF APPLIED PHYSICS

UNIVERSITY OF ILLINOIS
LIBRARY

NOV 22 1961

CHICAGO

Vol. 32, No. 11

November, 1961



Linear Arrays of Damage Due to Fission Fragments Passing through Platinum Foil.
See Page 2492.

Whatever radiation detector electronics system you employ

/insist on
HARSHAW SCINTILLATION CRYSTAL
radiation
detectors



NaI(Tl)
CsI(Tl)
LiI(Eu)
Li⁶I(Eu)
NaI_{PURE}
CsI_{PURE}
Anthracene
Plastic Phosphors

HARSHAW
Mounted NaI(Tl) Scintillation
CRYSTALS / *Standard line*
Matched window line
Integral line

THE HARSHAW CHEMICAL CO.
1945 E. 97TH STREET • CLEVELAND 6, OHIO

In This Issue

Special Issue on High-Polymer Physics

Method for Measuring Dynamic Mechanical Properties of Viscoelastic Liquids and Gels; the Gelation of Polyvinyl Chloride	Meyer H. Birnboim and John D. Ferry	2305
Isothermal Crystallization Kinetics of Polyethylene. III. Influence of the Sample Preparation	J. Rabesiaka and A. J. Kovacs	2314
Origins of Characteristic Bands in the Infrared Spectra of Isotactic Polystyrene and Isotactic Poly (Ring-d, Styrene)	T. Onishi and S. Krimm	2320
Non-Newtonian Viscosity of Polymers	Roger S. Porter and Julian F. Johnson	2326
Rate of Recrystallization of Polyethylene Single Crystals	W. O. Statton	2332
Hypothesis of Voids in Semicrystalline Polymers	Shiro Matsuoka	2334
Extension of the Eyring-Ree Theory of Non-Newtonian Flow	Joseph A. Faucher	2336
Molecular Motion in Disordered Regions of Solid Polyethylene	W. P. Slichter	2339
Light Scattering Study of the Annealing of Drawn Polyethylene	Marion B. Rhodes and Richard S. Stein	2344
Dielectric Loss in Poly-(Hexamethylene Adipamide) and Poly-(Hexamethylene Sebacadamide) at Low Temperatures	M. N. Stein, R. G. Lauttman, J. A. Sauer, and A. E. Woodward	2352
Growth of Crystals from Molten Crosslinked Oriented Polyethylene	Jane T. Judge and Richard S. Stein	2357
Swelling of Unfilled and Highly Filled Polymers	K. W. Bills, Jr., and F. S. Salcedo	2364

Regular Articles

Drift Velocity of a Charged Particle in an Inhomogeneous Magnetic Field	James Hurley	2368
Graphical Method for Determination of Mobility Ratio in the Semiconductors from Hall Effect Measurements Only	Krzysztof Pigoń	2369
Excess and Hump Current in Esaki Diodes	Richard S. Claassen	2372
Effects of Phosphor Powder Dispersion in Electroluminescent Lamps	W. A. Thornton	2379
Theory and Application of a Superposition Model of Internal Friction and Creep	J. Ross Macdonald	2385
New Derivation of the Vacuum Breakdown Equation Relating Breakdown Voltage and Electrode Separation	A. Maitland	2399
Excess Noise in Germanium and Gallium-Arsenide Esaki Diodes in the Negative Resistance Region	M. D. Montgomery	2408
Physical Behavior of Photographic Grains	G. Sprague	2410
Transparency of Glass and Certain Plastics under Shock Attack	H. Dean Mallory and William S. McEwan	2421
Determination of Field Strength for Field Evaporation and Ionization in the Field Ion Microscope	Erwin W. Müller and Russell D. Young	2425
X-Ray Measurement of Stacking Fault Widths in fcc Metals	B. E. Warren	2428
(110) Nickel Surface	L. H. Germer, A. U. MacRae, and C. D. Hartman	2432
Production of High Ion Densities in Helium by Means of High Explosives	G. E. Seay, L. B. Seely, Jr., and R. G. Fowler	2439
Magnetization Curve of an Infinite Cylinder	M. W. Muller and A. Wehlau	2448
Effects of Transition Metal Solutes on the Electrical Resistivity of Copper and Gold between 4° and 1200°K	C. A. Domenicali and E. L. Christenson	2450
Interrelation of Electronic Properties and Defect Equilibria in PbTe	E. Miller, K. Komarek, and I. Cadoff	2457
Determination of Certain Spectral Distributions of Soft X Rays by Theoretical Analysis of Absorption Experiments	Nancy A. Kerr	2465
Forbidden Reflections in Electron Diffraction Patterns of Evaporated Tin Films	Richard W. Vook	2474
Analysis of a Nonlinear First-Order System with a White Noise Input	T. K. Caughey and J. K. Dienes	2476
Study of Impact Cratering in Sand	F. L. Culp and H. L. Hooper	2480
Radiation from a Modulated Electron Beam with a Plasma Background	Philip Parzen	2484
Letters to the Editor:		
Damping Effects of Thin Surface Films	R. J. Huber, G. S. Baker, and P. Gibbs	2488
Electrical Control of the Critical Angle of Total Reflection	H. Nassenstein	2488
Preparation of Silicon Ribbons	E. S. Greiner, J. A. Gutowski, and W. C. Ellis	2489
Morphology and Growth Mechanism of Silicon Ribbons	R. S. Wagner and R. G. Treuting	2490
Backward Waves in Longitudinally Magnetized Ferrite Rods	G. H. B. Thompson	2491
Dislocation Etching Solution for Potassium Chloride and Other Alkali Halides	J. S. Cook	2492
Fission Fragment Damage to Platinum	E. Ruedl, P. Delavignette, and S. Amelinckx	2492
Transient Effects in Peltier Coolers	A. D. Reich, T. Arai, and J. R. Madigan	2493
New Magnetic Ternary Compound with a High Crystalline Anisotropy	J. H. Wernick, S. E. Haszko, and W. J. Romanow	2495

Books Reviewed	2495
Books Received	2497
Research Reports	2498
Announcements	2498
Index to Advertisers	xxviii

JOURNAL OF APPLIED PHYSICS

A journal of general physics and its applications to other sciences and to industry

Published by the
**American
Institute of Physics**

GOVERNING BOARD

Members

Ralph A. Sawyer, *Chairman*

James G. Baker
R. H. Bolt
Wallace R. Brode
Harvey Brooks
Dirk Brouwer
J. H. Elliott
Herbert A. Erf
N. S. Gingrich
S. A. Goudsmit
W. W. Havens, Jr.
W. V. Houston
Winston E. Kock
R. Bruce Lindsay
David L. MacAdam
H. Victor Neher
Leonard O. Olsen
C. J. Overbeck
Ray Pepinsky
S. L. Quimby
Ralph A. Sawyer
Francis W. Sears
Frederick Seitz
C. Guy Suits
Mary E. Wurga
William R. Willets

ADMINISTRATION

Elmer Hutchisson

Director

Wallace Waterfall
Secretary and Treasurer

Henry A. Barton
Administrative Consultant

W. C. Kelly
Director of Education

Eugene H. Kone
Director of Public Relations

Hugh C. Wolfe
Director of Publications

Kathryn Setze
Assistant Treasurer

James E. Mills
Supervisor, Editorial Department

Sistina Greco
Circulation Manager

Edward Tober
Manager, Production and Distribution

Theodore Vorburger
Advertising Manager

Emily Wolf
Manager, Special Services

Editor

J. H. Crawford, Jr.

Assistant Editor

Ethel McMillan

Editorial Board

J. E. Goldman

Herman A. Haus

Henry Hurwitz

J. L. Tuck

C. Lester Hogan

James A. Krumhansl

C. A. Wert

R. S. Rivlin

C. P. Slichter

THE JOURNAL OF APPLIED PHYSICS is devoted to general physics and its applications to other sciences, to engineering, and to industry. Previous to 1937, this journal was called PHYSICS.

The JOURNAL OF APPLIED PHYSICS welcomes articles of two distinct kinds: (1) Descriptions of new results in experimental or theoretical physics which are of general interest to physicists. The author should explain his contribution in such a way that a physicist or engineer in another field of specialization can appreciate its objectives and essential features. (2) Critical reviews of particular areas of physics or surveys of extensive investigations at a single laboratory. Authors contemplating writing such should correspond with the Editor before they begin writing.

The JOURNAL OF APPLIED PHYSICS welcomes Letters to the Editor which are short [approximately four (4) typewritten pages] communications without abstracts. Timeliness, brevity, and degree of current importance of the subject matter will be of primary concern in the publication of Letters. Letters should not be looked upon as partial publication or announcement of more comprehensive work, but rather self-contained presentations in themselves.

Manuscripts should be submitted to the Editor, J. H. Crawford, Jr., Solid State Division, Oak Ridge National Laboratory, Oak Ridge, Tennessee. Authors should read the "Information for Contributors," facing page 1 of the January issue, before writing articles or letters. The *Style Manual* of the American Institute of Physics is also helpful to writers preparing manuscripts for journals published by the American Institute of Physics. It can be obtained for \$1.00 from the American Institute of Physics, 335 East 45 Street, New York 17, New York.

Corrected proofs and all correspondence concerning papers in the process of publication should be addressed to the Supervisor, Editorial Department, American Institute of Physics, 335 East 45 Street, New York 17, New York.

Subscriptions, renewals, and orders for back numbers should be addressed to the American Institute of Physics, 335 East 45 Street, New York 17, New York.

Subscription Price

U.S. and
Canada

Elsewhere

To members of member organizations of the American Institute of Physics and Affiliated Societies ..
To all others

\$12.00

\$13.00

14.00

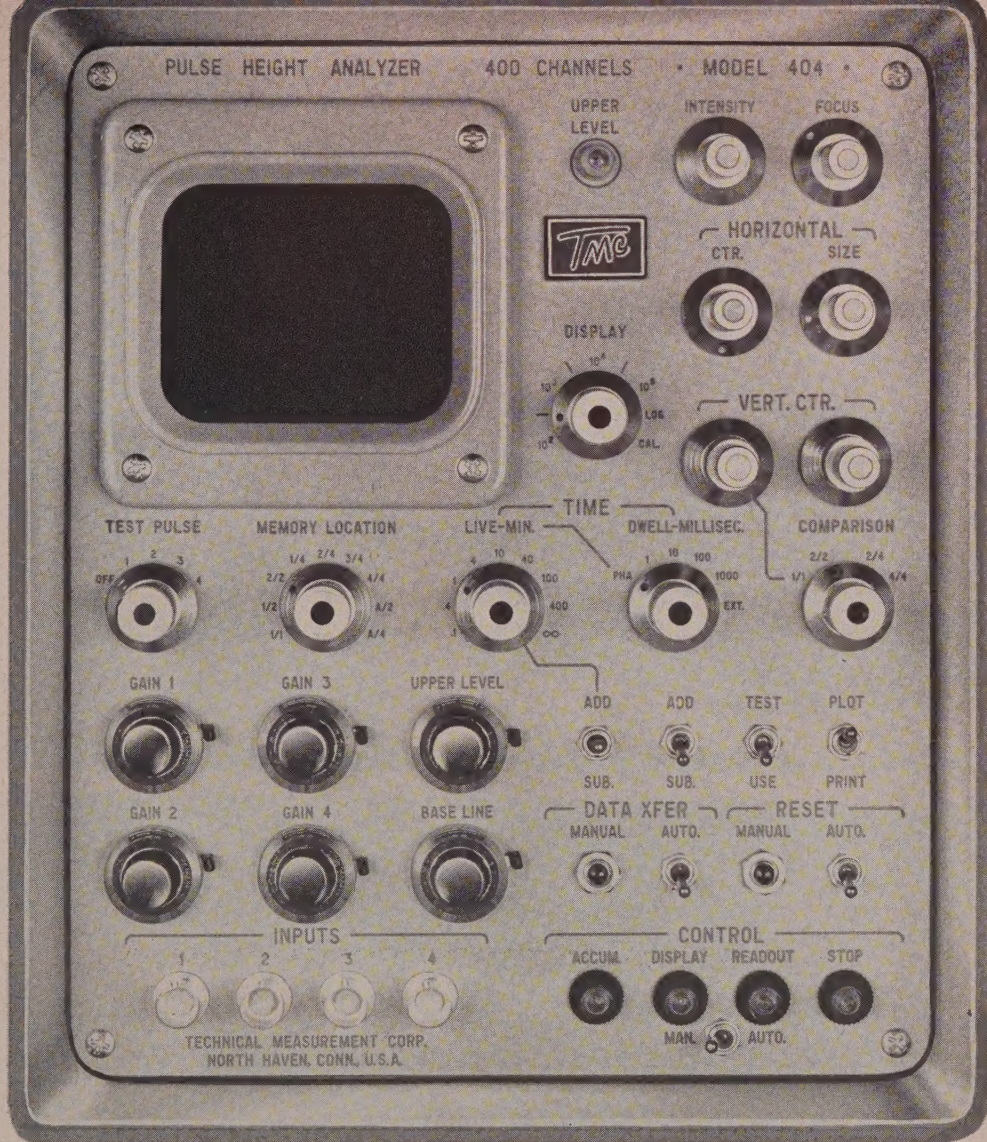
16.00

Back Number Prices

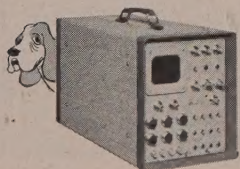
Yearly back number rate when complete year is available: \$17.00.
Single copies: \$1.75 each (exception: March, 1958—\$3.00 each).

Changes of address should be sent to the American Institute of Physics.

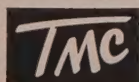
Advertising rates supplied on request. Orders, advertising copy, and cuts should be sent to the American Institute of Physics.



efficient 4-input, 400-channel pulse height analyzer is easy to use, has many "system" features, weighs 37 lbs., occupies one cubic foot, operates on 110 or 220 volts, 50 to 400 cycles AC.



Each input has its own linear amplifier and gain control. Information can be stored in four 100-channel groups, two 200-channel groups or one 400-channel group. Direct readout on TMC Model 500 Decimal Printer, X-Y or strip chart recorder, IBM computer typewriter or paper tape punch. Add these facts (and the moderate price of the instrument) to the versatility suggested by front panel photo — and you have the reason for the TMC 404's popularity. Write for Bulletin 400.



TECHNICAL MEASUREMENT CORPORATION
441 WASHINGTON AVENUE, NORTH HAVEN, CONN. — CE 9-2501

Physicists

The Hughes Research Laboratories offer an outstanding professional environment to Scientists and Engineers with an interest in basic and applied research. At these exceptional facilities you can realize maximum professional growth through programs including:

PLASMA PHYSICS

Thermionic energy conversion
Microwave plasma devices

SURFACE PHYSICS

Low work function surfaces
Thermionic electron emission
Thermionic ion emission

SOLID STATE PHYSICS RESEARCH

Microwave and millimeter wave magnetic resonance
Optical and infrared spectroscopy
Solid State masers
Semiconductor physics
Radiation Physics

ION PROPULSION

The facilities of the Hughes Research Laboratories are located in Malibu, California, overlooking the Pacific Ocean—immediately adjacent to major academic institutions—with programs of academic support and participation. These facilities were specifically designed for effective research efforts with private offices and complete research laboratories. In this uniquely creative atmosphere, Hughes scientists are continually adding to their record of accomplishments in electronics and physics research.

Your inquiry may be directed in strict confidence to: Mr. D. A. Bowdoin, Hughes Research Laboratories, Malibu, California.

All qualified applicants will receive consideration for employment without regard to race, creed, color or national origin.

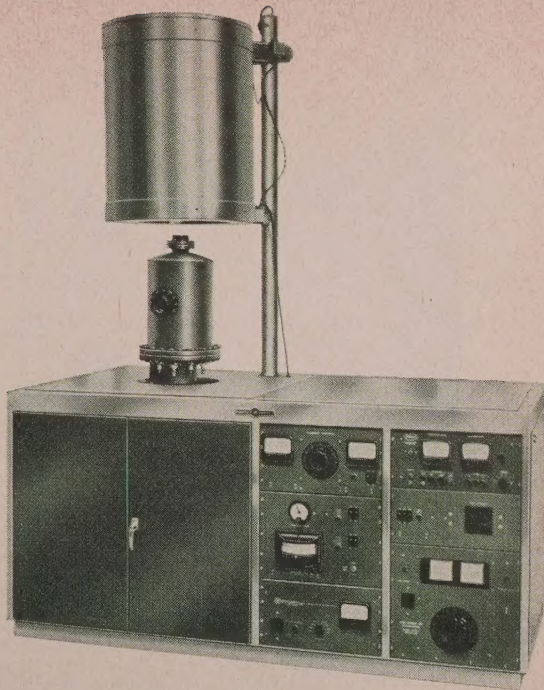
creating a new world with electronics

HUGHES

HUGHES AIRCRAFT COMPANY
RESEARCH LABORATORIES



off
the
shelf!



ULTRA-HIGH VACUUM SYSTEMS

Varian's new Ultra-High Vacuum System is now available as catalog-item equipment. Provides base pressures to 10^{-9} mm Hg or lower. Eliminates necessity for custom design of complex systems. A completely integrated system, ready-to-operate. Optional power and electronic accessories are available for special installation requirements. Applications: hyper-altitude simulation, vacuum evaporation, vacuum firing and brazing, etc.

Varian's revolutionary VacIon® pump is a major component. No necessity for liquid nitrogen traps or continuous mechanical pumping. VacIon pumps are all-electronic: pumpdown cycles are automatically fail-safe.

SYSTEM COMPONENTS: 400 Litre/second VacIon Pump ■ Ultra-High Vacuum Chamber ■ Instrumentation ■ Cabinet and Controls ■ Bakeout Oven ■ Roughing Manifold for Mechanical Pump or VacSorb® Pump

If your design or processing requirements demand integrated equipment producing extremely low pressures, Varian's Ultra-High Vacuum System may be just what you're looking for. For full technical data, write Vacuum Division.



VARIAN associates

PALO ALTO 36, CALIFORNIA

BOMAC LABORATORIES, INC.
VARIAN ASSOCIATES OF CANADA, LTD.
S-F-D LABORATORIES, INC.
SEMICON ASSOCIATES, INC.
SEMICON OF CALIFORNIA, INC.
VARIAN A. G. (SWITZERLAND)



NEW KEITHLEY AC AMPLIFIER

*can increase
scope sensitivity
1000 times!*

The Keithley Model 103 gives you the best attainable signal-to-noise ratio for source impedances from 3000 ohms to over 10 megohms. (The equivalent input noise resistance on the low noise position is only 3 k ohms.) Bandwidth of .1 cps to 100 kc covers a wide range of uses; eleven high and low frequency cuts permit restricted bandwidths for minimum noise.

Applications include Hall Effect studies, bridge null detection, and semi-conductor investigations, as well as such biophysical applications as recording nerve action potentials.

The usefulness of the Model 103 is enhanced by its versatility:

NOISE can be improved by changing input impedance with a "Normal" and "Low Noise" switch. Chart below indicates noise levels with input shorted, gain 1000x, 10 cps to indicated cutoff:

BANDWIDTH can be selected by using 11 high and low frequency cutoffs between .1 cps and 100 kc.

INPUT IMPEDANCE in the "Normal" mode is 10 megohms; in the "Low Noise" mode, 100 k ohms.

AMPLIFIER GAIN may be set at either 100 or 1000 and adjusted to precise values.

INPUT CONNECTIONS can be made single-ended or differential.

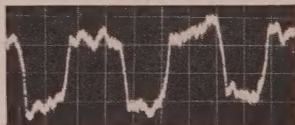
DIFFERENTIAL REJECTION is at least 80 db permitting increased signal-to-noise ratios in many applications.

POWER can be furnished by batteries or the Keithley Model 1031, a separate, solid state power supply with noise characteristics equivalent to battery operation.

PRICE: \$245.00. Rack-mounted: \$255.00

Frequency of high cutoff point	Maximum noise, microvolts RMS referred to input	
	Normal (10 meg impedance)	Low Noise (100 k impedance)
100 kc	3.0	1.9
30 kc	1.9	1.1
10 kc	1.4	0.8
3 kc	0.9	0.6
1 kc	0.7	0.4
300 cps	0.5	0.3
100 cps	0.4	0.25

This oscillograph shows a 2 kc square wave of 5 microvolts peak-to-peak amplitude at input with the amplifier in "Low Noise" position. Horizontal calibration equals 200 μ v per division; vertical equals 2 μ v per division. Low cut is 10 cps, high cut 1 kc. The unusually low noise levels in the 103 are achieved through the use of ceramic tubes in cascode circuitry.



send for complete specifications in latest engineering note...



KEITHLEY INSTRUMENTS

12415 EUCLID AVENUE

CLEVELAND 6, OHIO

electrometers • micro-microammeters • microvoltmeters • milliohmmeters

COMMUNICATION OF IDEAS

"Ideas must work through the brains and the arms of good and brave men, or they are no better than dreams."— EMERSON

Original painting by Emil Bisttram, Taos, New Mexico

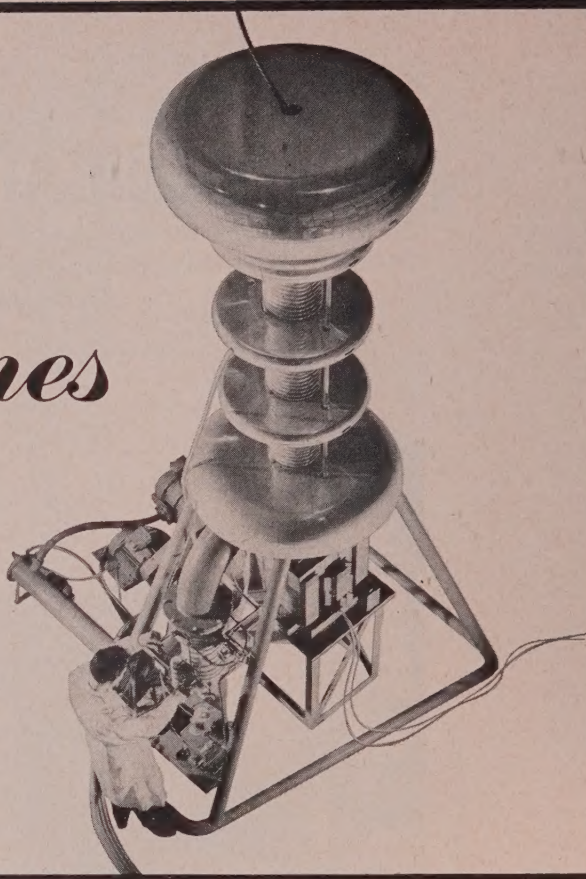


Qualified applicants are invited to send resumes to: Director of Personnel, Division 61-98

los alamos
scientific laboratory
OF THE UNIVERSITY OF CALIFORNIA
LOS ALAMOS, NEW MEXICO

All qualified applicants will receive consideration for employment without regard to race, creed, color, or national origin. U.S. citizenship required.

Sames



ELECTROSTATIC PARTICLE ACCELERATORS

These provide a wide range of particles and radiations: Electrons—Protons—Neutrons—Deuterons—X-Rays.

- Voltages to 600 KV, infinitely variable • Current to 4 ma • Stability to $\pm .01\%$ • Ion current (Protons or Deuterons) to 0.6 ma continuous • Electron beam current to 3 ma continuous • X-Rays to 1000 Roentgens/sec
- Beam diameters adjustable, 2 to 10 mm • Beam pulsing available, 10 to 200 μ s

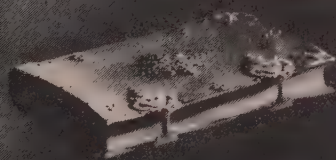
Maximum Safety: Low internal capacitance. Minimal short circuit currents. Remote adjustment and shut-down.

Sames

• Write for literature



Dept. 311, 30 Broad Street, New York 4, N.Y.



THE DIARY THAT IMPRISONED PROGRESS

Nearly two centuries ago, Karl Gauss, "Prince of Mathematicians," kept a diary which was destined to become one of the most significant documents in the history of mathematics.

In his diary Gauss jotted down the results of elaborate calculations that had led him to fundamental discoveries in mathematics. But he never published these discoveries, and many of them remained undisclosed during his lifetime.

It wasn't until almost 50 years after Gauss's death that his diary was found and published. Much time and talent, meanwhile, had been spent in duplicating Gauss's efforts. Mathematical progress had been needlessly slowed.

In contrast, today's scientists and engineers are alert to the importance of sharing their findings through publication. In fact, the number of definitive papers published

in a scientific or technological field has become a sure sign of the creative effort in that field.

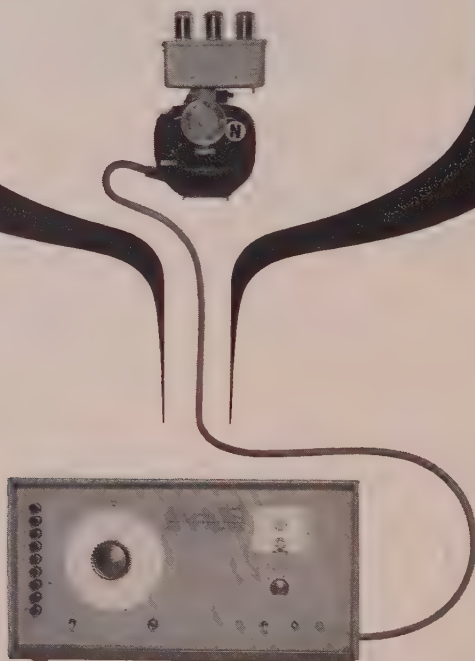
Bell Laboratories scientists and engineers publish more than 800 papers a year, reporting new observations and new thinking in the arts and sciences that serve communications. They have also authored more than 50 technical books, many of which have become standard works of reference. The steady stream of new information that comes out of Bell Laboratories again reflects the scope and depth of the creativity that works to improve Bell System communications.

BELL TELEPHONE LABORATORIES



World center of communications research and development

WHEN YOU NEED TO KNOW WHAT'S LEFT



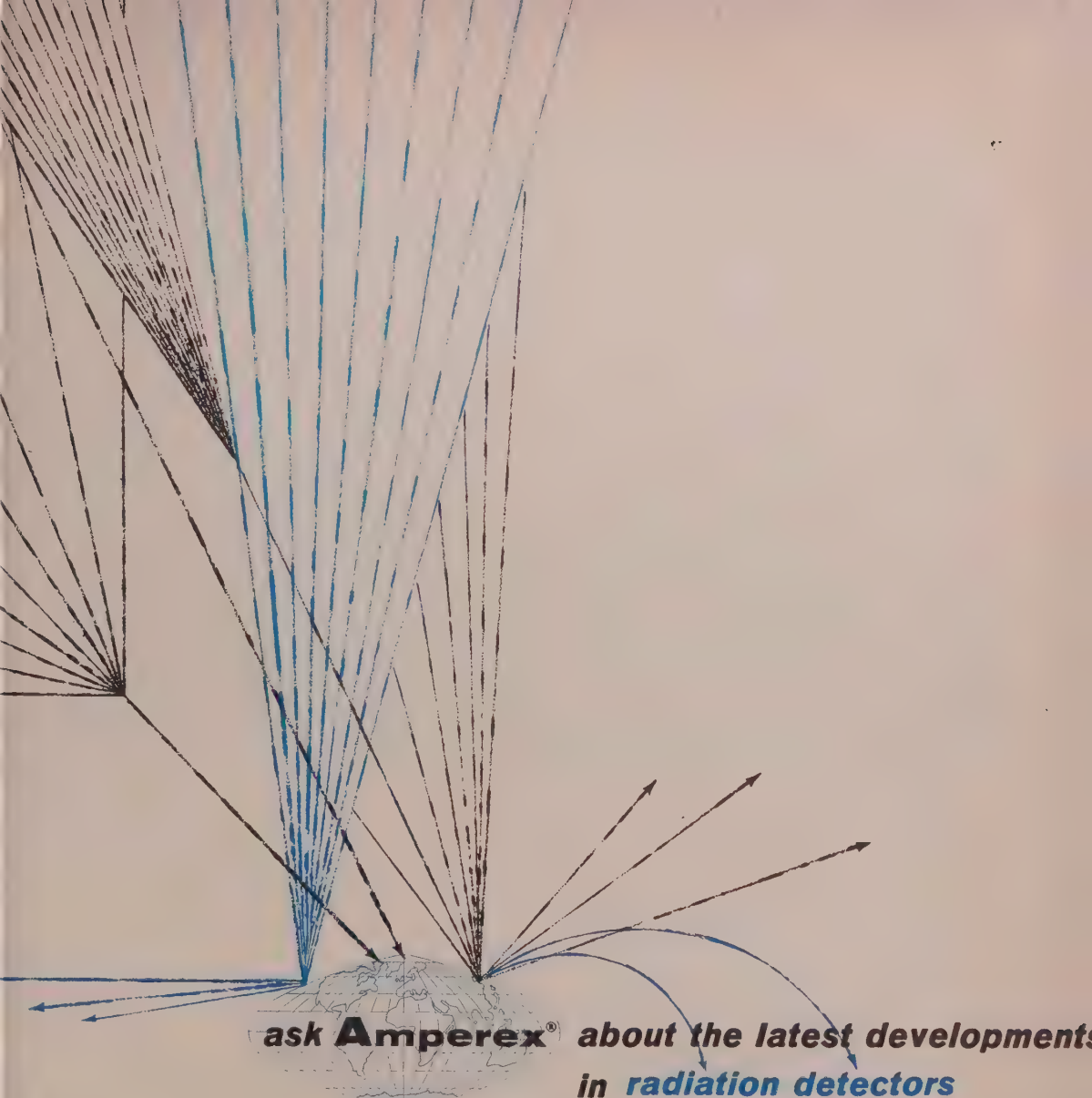
ask the new CEC Residual Gas Analyzer

It uses a Diatron 20 mass spectrometer tube... measures minute quantities of gas and vapors in vacuum systems over a mass range of m/e 2 to 80 with a resolving power that separates adjacent peaks up to mass 20... makes possible analyzing in the range of 10^{-4} to 10^{-9} mm Hg pressure! And it's bakeable to 450°C ... 150° hotter than any

comparable instrument! ☐ For full details on 26-212 Residual Gas Analyzer call your nearest CEC office or write for Bulletin CEC 1865.

Analytical & Control Division

CEC
CONSOLIDATED ELECTRODYNAMICS
PASADENA, CALIFORNIA • A SUBSIDIARY OF BELL & HOWELL



**ask Amperex® about the latest developments
in radiation detectors**

Continual Research and Development of unique and specialized components for nuclear applications...close contact with laboratory and field organizations...development of new and improved manufacturing techniques for maximum uniformity, reliability and economy—these are the factors that make Amperex the nuclear industry's unrivaled source for all types of radiation detectors, electron tubes and semiconductors as well as other specialized components.

neutron detectors

PROPORTIONAL COUNTERS: excellent pulse height resolution characteristics rugged construction utilizing ceramic-metal seals and heliarc welding techniques...stainless steel and aluminum modes. **FISSION COUNTERS:** excellent discrimination between neutron and alpha particles...all-aluminum construction utilizing heliarc welding...design versatility.

geiger tubes

Low operating voltage...infinite life, halogen quenched...but with the same plateau characteristics and detection efficiencies as short-lived organic quenched types. Plateau lengths of several hundred volts with slopes in the order of 2%/100V...large pulses...electrical and mechanical ruggedness...excellent reproducibility. Ideally suited for transistorized circuitry.

photomultipliers

Types 56 AVP and 58 AVP, already famed in high energy physics research. Unrivaled for time resolution characteristics...low transit time fluctuations...fast rise time...extreme uniformity...minimum guaranteed gain 10^6 . Unquestioned superiority for fast coincidence counting, Cerenkov radiation, etc. Other types for low noise and good energy resolution characteristics.

ask Amperex about flow and sealed proportional counters for alpha particles and low energy gamma and X-rays.

AMPEREX ELECTRONIC CORPORATION, Nuclear Products Department, 230 Duffy Avenue, Hicksville, L. I., N. Y.

OPTICS

Link's rapid diversification into geometric and physical optics has created interest areas which include improvements in metrology, automated electro-optical systems, photogrammetry, interferometry, and pattern and character recognition.

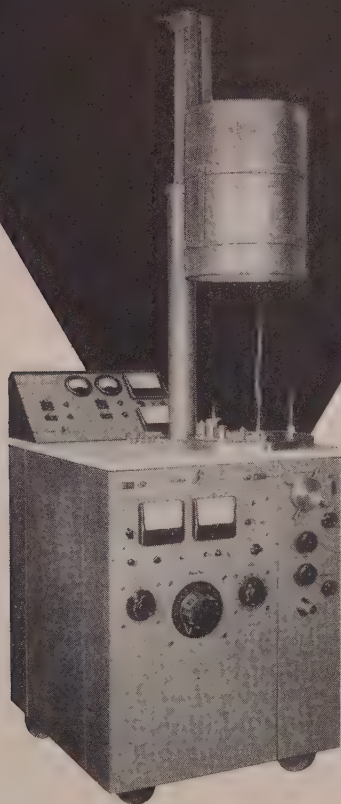
Men with a BS or MS in optics or physics who can contribute professionally in these fields of interest are needed. Basic development and design experience in interferometry or electro-optical equipments including projection and relaying lens systems is highly desirable.

Link offers stimulating assignments, the challenge of working with outstanding men in these fields, and unlimited opportunity for professional recognition and growth. Link is an equal-opportunity employer. Please send detailed résumé to Mr. James T. Gibbons.



**LINK DIVISION
GENERAL PRECISION, INC.**

Binghamton, New York



Outstanding | **IN EVERY RESPECT**

... a new series of precision evacuating systems and components, ideally designed to meet the requirements of varied research, manufacturing and test applications in Electronics, Metallurgy and allied fields. **KINGPIN** of the Vactronic 450 Line, the HVE-450, the most compact evaporator now available ... specially designed to provide clean, convenient and effective control of varied high vacuum operations. Included as standard equipment of the HVE-450 Evaporator are a complete Pumping Station plus a Base Plate, a Bell Jar and Guard, and a 1 KVA integral metered Power Supply with external switching facility.

Vactronic's complete line of high vacuum systems, individual components and accessories is representative of the highest standards in *Experienced Engineering ... Advanced Design ... Critical Construction.*

CVP-450
COLD TRAP



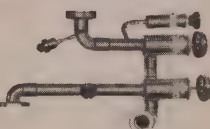
CBF-450
BAFFLE



HVP-450
OIL VAPOR
DIFFUSION PUMP



AVS-450
HIGH VACUUM
VALVE



RGH-450-NP
ROUGHING MANIFOLD



Vactronic LAB. EQUIPMENT, INC.
EAST NORTHPORT, LONG ISLAND, N. Y. Tel. (516) ANDrew 1-2660 Cable: LEL

Advanced High Vacuum Equipment For Industry's Varied Needs

Send for NEW Literature on The 450 Line.



Now 1×10^{-10} mm Hg

from

ILIKON CORPORATION

Modernize your laboratory with Cenco QUALITY EQUIPMENT



HOT PLATE MAGNETIC STIRRER

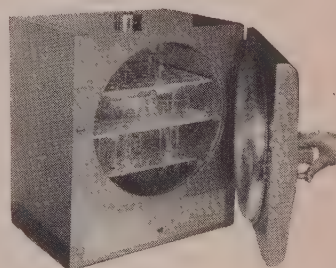
Combines an electric hot plate and magnetic stirrer which can operate independently or simultaneously. Variable speed stirring is powerful enough to stir 250 ml beaker of pure glycerin. Heat controlled thermostatically. Top plate is 7 3/4" of cast aluminum.

No. 16632.....\$64.50

CYLINDRICAL OVEN

An all-purpose, economical, three-shelfed oven for incubation, drying, sterilization or baking. Precise control of temperatures from 37° to 200°C, with variations as slight as 0.25° sensed by built-in thermostat. Chamber dimensions are 14 3/4" diameter, 11 1/2" depth. Specify either 115 or 230 volts.

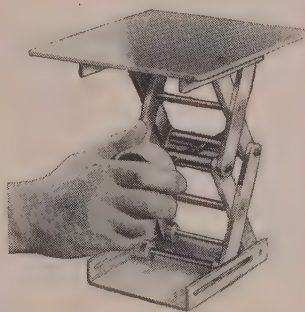
No. 95051.....\$201.75



CENCO-LERNER LAB JACK

This precise, utility support quickly adjusts through an elevation range of seven inches and will support 100 pounds. Particularly useful for supporting hot plates, oil baths, and for accurate positioning of ground glass joints. A removable auxiliary platform, eight inches square, increases work area. Comes with 17 3/4" support rod.

No. 19089.....\$38.75



For further information on Cenco's complete line of laboratory equipment, teaching aids and scientific apparatus, contact your nearest Cenco salesman, or write.



Quality
since 1889

CENTRAL SCIENTIFIC CO.

A Subsidiary of Cenco Instruments Corporation
1718-A Irving Park Road • Chicago 13, Illinois
Mountainside, N. J. Montreal Santa Clara
Somerville, Mass. Toronto Los Angeles
Birmingham, Ala. Ottawa Vancouver Houston
Cenco, S. A. Brda The Netherlands Tulsa



Ilikon's new metal ULTRAHIGH VACUUM CHAMBERS are the only complete systems available today that can reliably produce and maintain pressures as low as 1×10^{-10} mm Hg.

Designed specifically for advanced space simulation, vapor deposition and materials research applications. Literature on request.

ILIKON
NATICK INDUSTRIAL CENTRE
Natick, Mass. • Tel. CEdar 5-8220



SCIENTIFIC FOUNDATIONS of VACUUM TECHNIQUE

Second Edition

By the late SAUL DUSHMAN, formerly of the General Electric Research Laboratory, Schenectady; revised by members of the staff, J. M. LAFFERTY, Editor. Retaining the major theme of the first edition (i.e. a primary concern with the scientific foundations of vacuum technique), this book explores the bases of all the operations involved in the production and measurement of high and ultrahigh vacuum. It contains both practical information on the technology, and the background information necessary for a sound understanding of the applicability of modern techniques and future possibilities in the utilization of vacua. Extensive references to the original literature provide valuable guides for further study in each of the areas presented. Beyond a doubt the most comprehensive book on the subject presently available, the revision has included all the important progress made in high vacuum research during the twelve years since the original edition first appeared. 1961. Approx. 808 pages. Prob. \$17.50.

PROBABILITY and EXPERIMENTAL ERRORS in SCIENCE

By LYMAN G. PARRATT, Cornell University. After some comments on the various meanings of probability, the author uses the classical games of chance to provide a convenient framework for explaining basic principles. Once these are well established, he turns to their applications in more serious problems. 1961. 255 pages. \$7.25.*

The RARE EARTHS

Published under the Auspices of the American Society for Metals in Cooperation with the Office of Technical Information, United States Atomic Energy Commission.

Edited by F. H. SPEDDING, and A. H. DAANE, both of the Ames Laboratory of the U. S. Atomic Energy Commission. This book offers authoritative coverage of the rare earths, their separation, preparation of rare-earth metals, and properties of rare-earth metals and alloys. It also points out what needs to be accomplished in the immediate future. 1961. 641 pages. \$14.75.

Send for your examination copies today.

HANDBOOK of AUTOMATION, COMPUTATION, and CONTROL

Volume III—Systems and Components

Edited by EUGENE M. GRABBE, SIMON RAMO, and DEAN E. WOOLDRIDGE, all of Thompson Ramo Wooldridge, Inc. The final volume of the first complete handbook on all aspects of control, this book offers up-to-date, authoritative coverage of systems engineering design, component specifications, and design of important components. 1961. 1164 pages. \$19.75.

A Guide to FORTRAN Programming

By DANIEL D. McCracken, McCracken Associates, Inc. Describes problem solving through the use of a computer without presuming advanced knowledge of computer use. 1961. 88 pages. \$2.95.

ANALYSIS of NONLINEAR CONTROL SYSTEMS

By DUNSTAN GRAHAM, Princeton University and Systems Technology Inc.; and DUANE T. McRUER, Systems Technology, Inc. 1961. 482 pages. \$9.75.

BALLISTIC MISSILE and SPACE VEHICLE SYSTEMS

Edited by HOWARD S. SEIFERT, Stanford University; and KENNETH BROWN, John Wiley & Sons, Inc. 1961. 526 pages. \$12.00.

MICROWAVE FERRITES

By PETER J. B. CLARRICOATS, The Queens University, Belfast. 1961. 260 pages. \$8.00.

AN INTRODUCTION to the THEORY and PRACTICE of TRANSISTORS

By J. R. TILLMAN, and F. F. ROBERTS, both of The Post Office Engineering Station, London, England. 1961. 340 pages. \$8.00.

ITERATIVE ARRAYS of LOGICAL CIRCUITS

By FREDERICK C. HENNIE III, Massachusetts Institute of Technology. One of the M.I.T. Press Research Monographs. 1961. 242 pages. \$4.95.

The MECHANICS of INERTIAL POSITION and HEADING INDICATION

By WINSTON MARKEY, and JOHN HOVORKA, both of the Massachusetts Institute of Technology. 1961. 94 pages. \$3.95.

ELECTROMAGNETIC THEORY

By ERIK HALLÉN, Royal Institute of Technology, Stockholm. 1961. In Press.

AN INTRODUCTION to INFRARED SPECTROSCOPY

By WERNER BRÜGEL, Badische Anilin und Soda Fabrik, Ludwigshafen, Germany. 1961. In Press.

ABSORPTION SPECTROSCOPY

By ROBERT BAUMAN, Polytechnic Institute of Brooklyn. 1962. Approx. 568 pages. Prob. \$12.50.*

* Also available in a textbook edition for college adoption.

JOHN WILEY & SONS, Inc.,

440 Park Avenue South, New York 16, N. Y.

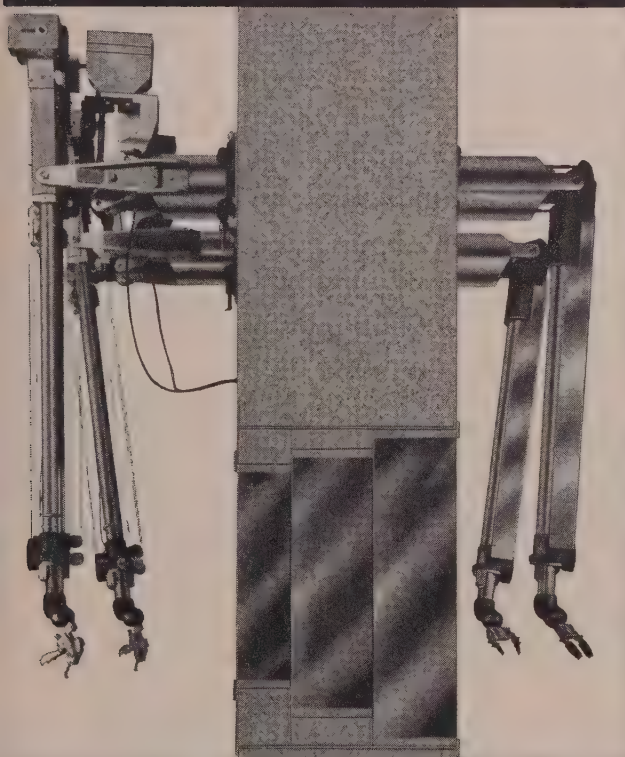
THE JOURNAL OF APPLIED PHYSICS NOVEMBER, 1961

AMAZING!

...the conservative word for

Central Research Laboratories

Model D rugged-duty Master-slave Manipulator



CAPABILITIES

Load capacities at tong tips with fully extended boom tube:

X motion—100 pounds

Y motion—100 pounds

Z motion—100 pounds

elevation rotation—50 pound feet

azimuth rotation—50 pound feet

twist-rotation—40 pound feet

gripping force and handling capacity—100 pounds

FEATURES—

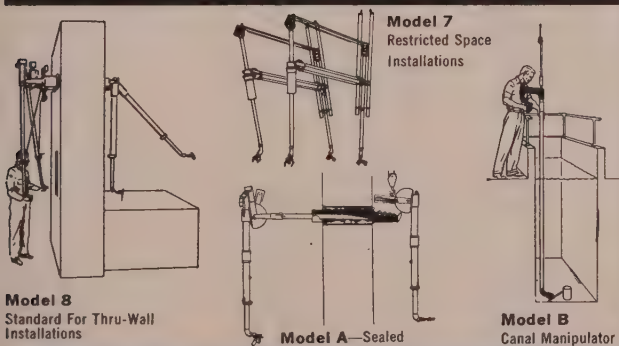
The Model D manipulator is a very rugged modification of the Model 8—a well-known and widely-used manipulator designed and first manufactured by Central Research.

Unique new features of the Model D include: a new wrist joint with sturdy stainless steel gears and a twofold increase in gear ratio; stainless steel boom and counterweight tubes; high-capacity boom-tube rollers; geared-up tape coupled azimuth rotation drive; center-supported pulley shafts; a mechanical, automatically shifting dual-ratio tong-squeeze drive; protected slave-end tapes.

INTERCHANGEABILITY

In general, the Model D is dimensionally interchangeable with a standard Model 8 manipulator with no alteration in mounting arrangement of existing or planned installations. The Model D offers greatly increased reliability and scope in rough-service hot-cell operations with no significant loss of dexterity for performing delicate operations.

COMPARE—THEN SPECIFY CENTRAL RESEARCH MANIPULATORS FOR EVERY NEED

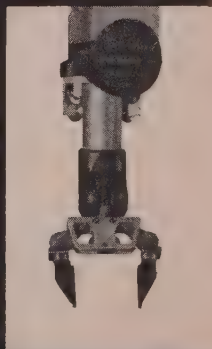
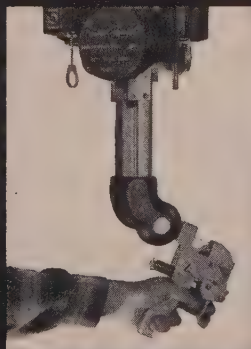


Model 8
Standard For Thru-Wall
Installations

Model 7
Restricted Space
Installations

Model A—Sealed

Model B
Canal Manipulator

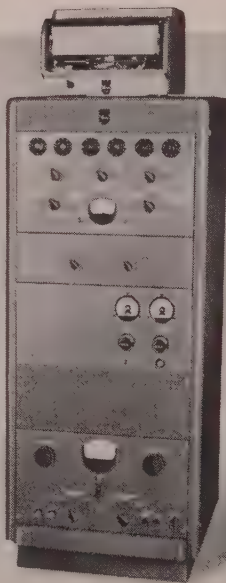
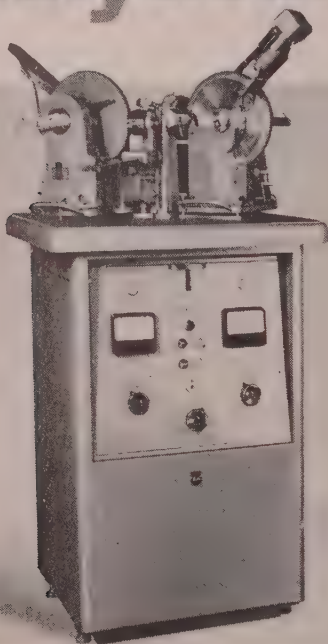


For further information write:

Central Research
laboratories, inc.

Red Wing, Minnesota, Dept. 316

There is a **BIG** Difference in **Norelco**[®] Analytical Instrumentation



Automatic recording of the fraction spectrum is achieved by the addition of a wide range goniometer and new electronic circuit panel to the basic diffraction unit.



Norelco high temperature, high vacuum diffractometer attachment is available for all diffractometers including competitors makes.

There have been obvious visual changes in the working tools of X-ray diffractometry and X-ray spectrography—a science which we at Philips Electronic Instruments know best. These Norelco product changes are based on years of experience accumulated in our own research and in the field. As a result, X-ray instrumentation for elemental analyses and structure determinations is greatly facilitated by ever widening investigative areas while producing data faster and easier.

But what about the physical differences? For one thing, the electronic circuit panel is top-to-bottom new with a linear/log scaler, and a double power supply with variable output for detectors operating on different voltages up to 3 KV. There is a time and fixed count operations feature also.

New high-intensity X-ray tubes can now be loaded double capacity—up to 2000 watts. Constant potential high tension transformers now lengthen tube life while providing greater precision in any given time. Any unit in operation can be updated because the constant potential feature is also available in kit form for an existing transformer in the field.

A new high-temperature furnace operates at temperatures over 2000°C with tantalum boats and even down to minus 185°C—in the cryogenic area. The furnace is adaptable to every Norelco wide-range goniometer made.

There you have a quick, boiled-down version of usual news... news you can put to work... updating new from Norelco for years of dependable, expandable, top quality performance.

* Incidentally, there are pronounced differences in all X-ray analytical instrumentation made by Philips. These differences are manifest in "know-how" and quality of apparatus, designed from-the-ground-up specifically for X-ray analytical work.

For more information and specifications on this remarkable Norelco instrument, write today on your letterhead to:

PHILIPS ELECTRONIC INSTRUMENTS

A Division of Philips Electronics and Pharmaceutical Industries Corp.

750 South Fulton Avenue, Mount Vernon, N. Y.

In Canada: Research & Control Instruments • Philips Electronics Industries Ltd. • 116 Vanderhoof Avenue • Leaside, Toronto 17, C





PROJECT TOMORROW...

The scientists and engineers at Amherst Laboratories are currently engaged in communications projects which are making vital contributions to our nation's defense efforts. The basic objective of this facility is the advancement of the state-of-the-art of communications and instrumentation systems, with emphasis on the role that microwave and millimeter wave technology will play in that advancement. Coupled with these on-going specific projects, is a freedom of investigation that allows no past premise to go unchallenged, allows no new avenues of inquiry to go unexplored. Together, they form what we like to call "Project Tomorrow"... a total dedication to the advancement of the science of communications.

MANAGEMENT AND STAFF OPPORTUNITIES exist for dedicated scientists and engineers with advanced degrees and creative desire. Physicists, Mathematicians and Electronic Engineers are invited to direct inquiries in complete confidence to Mr. H. L. Ackerman, Professional Employment,

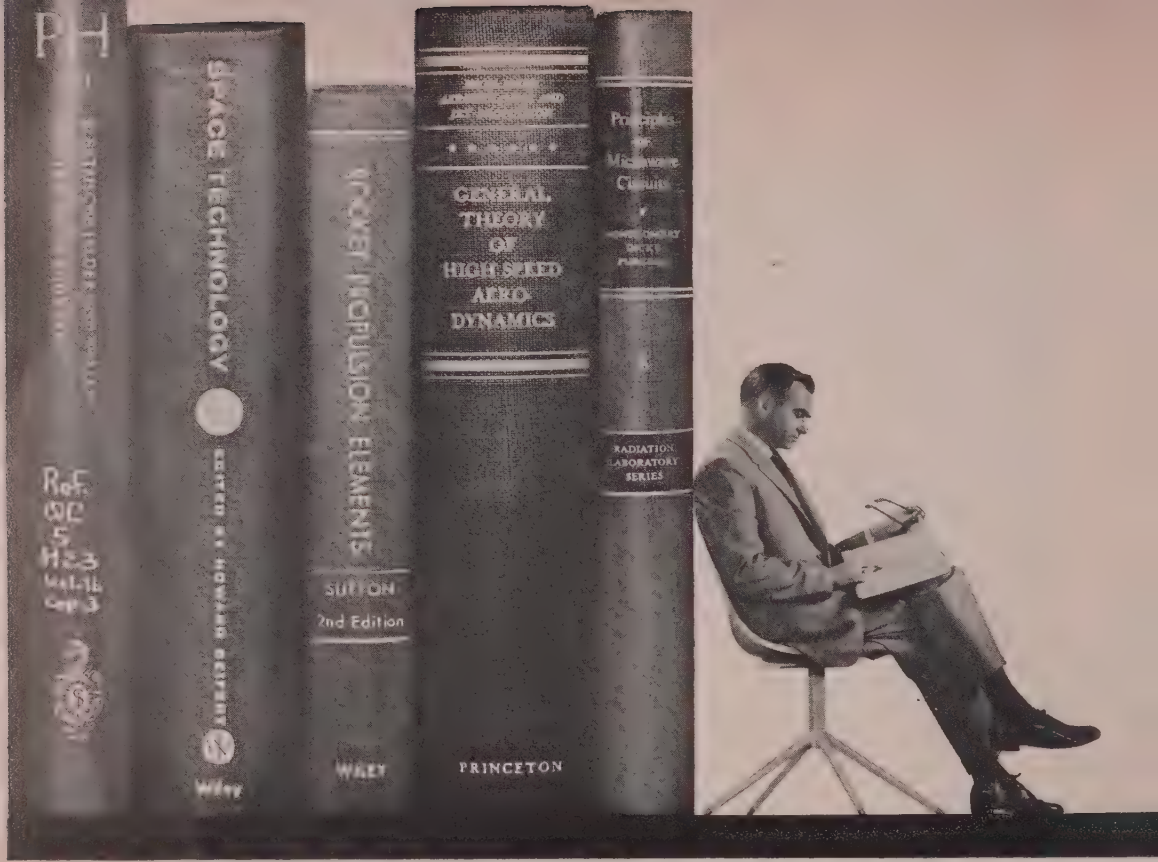
AMHERST LABORATORIES • 1183 WEHRLE DRIVE • WILLIAMSVILLE, NEW YORK
AN EQUAL OPPORTUNITY EMPLOYER

SYLVANIA ELECTRONIC SYSTEMS

Government Systems Management

for **GENERAL TELEPHONE & ELECTRONICS**





scientists and engineers in a unique role

The frontiers of space science and technology are being expanded at Aerospace Corporation. The scientists and engineers of this organization are the critical civilian link uniting government and the scientific-industrial team developing space systems and advanced ballistic missiles. In this mission Aerospace Corporation provides advanced systems analysis and planning, theoretical and experimental research, initial systems engineering, initial technical direction and general technical supervision. Included in the latter are integration and review of the engineering, development and test operations of industry to the extent necessary to assure achievement of system concept and objectives in an economical and timely manner. These people are privileged to view both the state-of-the-art and system development in their totality. Immediate assignments exist for those individuals highly skilled in these specialties and who are knowledgeable in inter-disciplinary problem solving. Men with advanced degrees are urged to contact Aerospace Corporation, Room 123, P.O. Box 95081, Los Angeles 45, California.

*Organized in the public interest and dedicated to providing objective leadership
in the advancement and application of space science and
technology for the United States Government.*

AEROSPACE CORPORATION



All qualified applicants will receive consideration for employment without regard to race, sex, religion, or ethnicity.

HIGH PURITY ELEMENTS

TH PLAINFIELD, N. J., Nov. 1 -- ASARCO
 TRAL RESEARCH LABORATORIES, USING SPECIAL
 INING AND ANALYTICAL TECHNIQUES, HAVE
 CEDED IN PURIFYING SELENIUM SO THAT NO
 KEL OR IRON CAN BE DETECTED AT 5 PARTS IN
 ,000,000. LEVELS OF OTHER IMPURITIES IN
 RCO HIGH PURITY ELEMENTS CAN AT TIMES
 MORE SPECIFICALLY LIMITED TO MEET
 TOMERS' SPECIAL REQUIREMENTS.

ASARCO HIGH PURITY ELEMENTS ANALYSES as of NOV. 1, 1961

Impurities sometimes found at maximum levels in parts per million
 (< denotes less than ppm indicated)

Element and Grade	Bi	Cu	Fe	As	Pb	Ag	Tl	Sn	Te	Au	Na	Cl	Cd
TIMONY A-60	<1	<1	<1	<2	<1								
SENIC A-60		<1											
SMUTH A-58		2	1		1	2						<1	
DMIUM A-60		<1	<1		1								
PPER A-58	No Impurities Detectable by Spectrographic Analysis												
LD A-59		<1	<1		<1	1							
DIUM A-58		<1			1		<1	1					
AD A-59	<1	<1	<1										
ENIUM A-58		<1		<1					1			<1	
VER A-59		<1	<1		<1								
LFUR A-58											1	1	
LLURIUM A-58		<1	<1										
ALLIUM A-60		1	1		<1	<1					2	<1	
NC A-59		<1	<1		<1								<1

ates element improved since last published analyses.



The analyses above are among pertinent data compiled by Asarco's
 Central Research Laboratories in an up-to-date catalogue now available
 to users of high purity elements. For a copy, write on your
 company letterhead to American Smelting and Refining Company,
 120 Broadway, New York 5, N. Y.

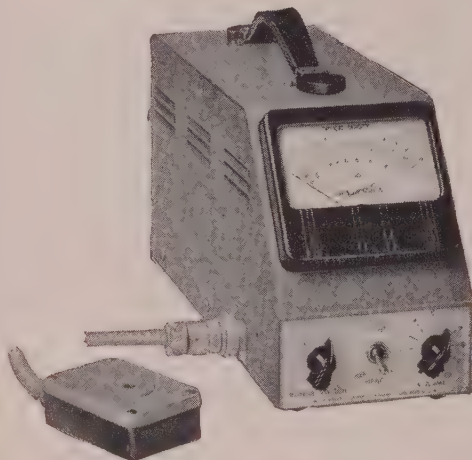
A Versatile Instrument for the Measurement of Reflectance and Transmittance

Welch

DENSICHRON

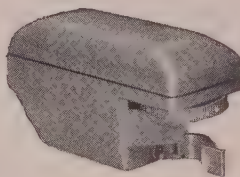
®

**ELECTRONIC
DENSITOMETER**



NO. 3830A DENSICHRON AND PROBE

- *Good Sensitivity*
- *High Stability*



REFLECTION
UNIT
NO. 3832A

—SPECIAL FEATURES—

Patented Magnetic Modulation
Simple to Use

Convenient Small Size—5" x 7 $\frac{1}{4}$ " x 13"

Light in Weight—only 11 $\frac{1}{2}$ pounds

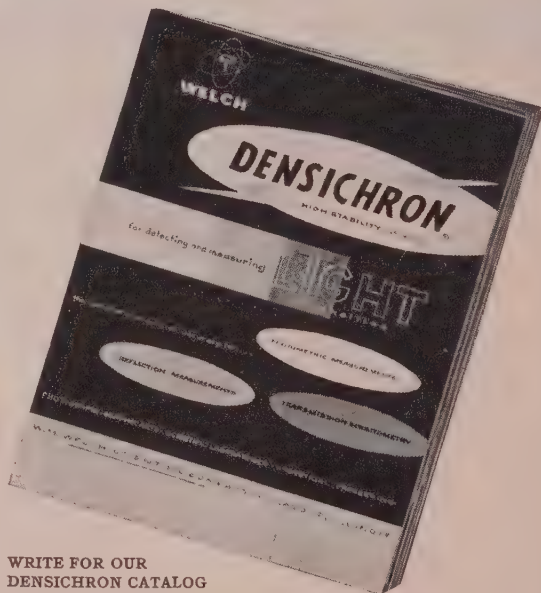
NO. 3830A. DENSICHRON WITH BLUE PROBE, including amplifier with logarithmic-scale meter, metal probe support, five different measuring apertures, a cone with $\frac{1}{4}$ inch aperture and a set of instructions. The amplifier operates on 115 volts, 60 cycle, A.C. only, except on special order.

Each \$270.00

No. 3830B. WITH RED PROBE. Each \$295.00

NO. 3832A. REFLECTION UNIT. When coupled to the Densichron amplifier this unit becomes a convenient reflectance meter. It has a self-contained light source, filter wheel and phototube, and includes optics for both small and large spot work, a calibrated gray scale, and three Carrara working standards.

Each \$200.00



WRITE FOR OUR
DENSICHRON CATALOG

THE WELCH SCIENTIFIC COMPANY

—ESTABLISHED 1880—

1515 SEDGWICK STREET, DEPT. C-1, CHICAGO 10, ILLINOIS, U.S.A.

Manufacturers of Scientific Instruments and Laboratory Apparatus

Journal of Applied Physics

Volume 32, Number 11

November, 1961

Special Issue on High-Polymer Physics

The following twelve papers were presented at the meeting of the Division of High-Polymer Physics of the American Physical Society at the U. S. Naval Postgraduate School, Monterey, California, March 21-23, 1961.

Method for Measuring Dynamic Mechanical Properties of Viscoelastic Liquids and Gels; the Gelation of Polyvinyl Chloride*

MEYER H. BIRNBOIM AND JOHN D. FERRY

Departments of Physics and Chemistry, University of Wisconsin, Madison, Wisconsin

An apparatus has been developed to determine the components of the complex shear modulus of viscoelastic liquids and dilute gels over a continuous frequency range from 0.01 to 5 cps by amplitude-phase shift measurements and from 2.5 to 400 cps by single coil transducer impedance measurements. The temperature range is from -40° to 150°C . The sample is deformed in very small strains with annular pumping geometry, as in the earlier apparatus of Smith, Ferry, and Schremp. Preliminary results on 2.29 and 3.00% solutions of polyvinyl chloride in di-2-ethyl hexyl phthalate provide the dynamic storage and loss moduli and the relaxation spectrum as they change during the process of gelation. The moduli of the ungelled solutions, at an early stage of the aggregation process, follow the Zimm theory rather closely, and the local effective viscosity derived therefrom lies between the solvent viscosity and the solution viscosity. The loss compliance of the aged gels is approximately represented by the Bueche theory for cross-linked networks. However, it is evident that the gels contain a large proportion of sol fraction (polymer species unattached to the network).

INTRODUCTION

ALTHOUGH a wide variety of experimental methods is available for measuring viscoelastic properties of soft and hard solids,¹ methods for studying viscoelastic liquids are more limited. To cover a wide frequency range in dilute polymer solutions, where the elastic component is small, more than one type of apparatus has been needed,²⁻³ and some of these are restricted to discrete frequencies.³⁻⁴ We now describe an apparatus in which a relatively dilute polymer solution can be studied over a continuous frequency range from 0.01 to 400 cps, and the transition from a viscoelastic liquid to a gelatinous solid can be followed in detail. A

relatively small quantity of the sample is needed. The application of the method is illustrated by measurements on the gelation of polyvinyl chloride in di-2-ethyl hexyl phthalate, at concentrations of 2.3 and 3.0% polymer.

DESCRIPTION OF APPARATUS

The prototype of the new apparatus was the transducer device of Smith, Ferry, and Schremp,⁵ in which a viscoelastic liquid was subjected to small oscillating deformations by a rod moving axially in a cylindrical container closed at one end (so-called annular pumping geometry), and the measurements were entirely electrical, based on changes in the impedance of a driving coil moving in a permanent magnetic field. In the present apparatus, impedance measurements somewhat similar to those of Smith, Ferry, and Schremp are used in a frequency range from 2.5 to 400 cps, and an alter-

* Part XXXV of a series on "Mechanical Properties of Substances of High Molecular Weight."

¹ J. D. Ferry, *Rheology* (Academic Press Inc., New York, 1958), edited by F. R. Eirich, Vol. II, Chap. 11.

² T. W. DeWitt, H. Markovitz, F. J. Padden, Jr., and L. J.apas, *J. Colloid Sci.* **10**, 174 (1955).

³ W. P. Mason, *Trans. Am. Soc. Mech. Engrs.* **69**, 359 (1947).

⁴ K. Sittel, P. E. Rouse, Jr., and E. D. Bailey, *J. Appl. Phys.* **25**, 112 (1954).

⁵ T. L. Smith, J. D. Ferry, and F. W. Schremp, *J. Appl. Phys.* **20**, 144 (1949).

native phase meter type of measurement is introduced to cover the range from 0.01 to 5.0 cps.

The basic equation for impedance measurements⁶ is

$$Z_M = (Bl)^2 / (Z - Z_0) \quad (1)$$

where Z_M is the mechanical impedance of the moving system (with real and imaginary components), B the magnetic field strength, l the length of wire in the driving coil, Z the electrical impedance of the coil in motion, and Z_0 the electrical impedance with the coil clamped motionless. Because it is difficult to achieve firm clamping, it has been customary^{5,7} to make measurements of Z under two or more sets of conditions with different mechanical or electrical modifications and eliminate Z_0 with simultaneous equations. However, the present apparatus provides sufficiently positive clamping to measure Z_0 directly. This is, of course, easier to accomplish when the mechanical impedance offered by the sample is small as it is for liquids.

The principal innovations in the new design, besides the provision of clamping, are: (a) improved sample geometry to minimize the dependence of the cell constant on the quantity of liquid and furnish an assortment of cells, (b) a mounting for the moving rod which maintains accurate centering, (c) precise temperature control by immersion of the entire apparatus in a liquid bath, and (d) improved structural stability.

Mechanical Construction and Hydrodynamic Relations

The mechanical part of the apparatus is shown in partial section in Fig. 1. The inner rod oscillates along its axis with a very small amplitude through a narrow annular gap whose upper end is defined by a cell section of much larger radius. Thus the quantity of liquid in the cell is not critical; it is normally about 1.0 cc. Cells with gaps from 0.024 to 0.150 in. have been used. The rod and cell are normally of stainless steel, but they also have been made of Kel-F for samples which cannot come in contact with metal. The cell holder, and the magnet and pole piece assembly which provides the magnetic field for the driving coil, are rigidly attached to a heavy central mounting plate for structural stability.

An exploded drawing of the moving system is shown in Fig. 2. The assembly is supported and accurately centered by spirally slotted flat springs of beryllium copper. The driving coil is wound with No. 34 copper wire on a phenolic resin cylinder and imbedded in epoxy resin cement; the cylinder is cemented to the aluminum coil frame. To the upper spring connecting rod is attached the core of a linear variable differential transformer, used for phase-shift mode measurements.

The mechanical impedance Z_M of such a system for

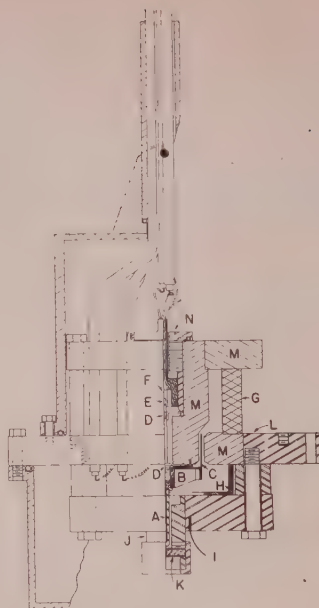


Fig. 1. Apparatus in quarter section with outer case shown in partial section. A, driving rod; B, coil mounting; C, aluminum; D, coil form and driving coil; E, beryllium copper slotted flat springs; F, core of differential transformer; G, transformer; H, Alnico V ring magnet; I, Teflon dust shield; J, thermocouple; K, sample cell; L, bottom cap of cell; M, central mounting plate (diam 8 in.); N, Armco iron pole pieces; O, nut and sleeve clamp for upper spring.

annular pumping geometry has been calculated by Markovitz,⁸ taking into account the inertia of the sample as a first approximation. It is

$$Z_M = f/v = AG''/\omega + i[\omega(M + \rho\beta A) - S_M \omega - AG'/\omega], \quad (2)$$

where

$$A = 2\pi L / [\ln \sigma - (\sigma^2 - 1)/(\sigma^2 + 1)], \quad (2a)$$

$$\beta = - (R_1^2/2) \{ 1/(\sigma^2 + 1) + \ln \sigma - (\sigma^2 - 1)^3 / [12(\sigma^2 + 1)^2] \times [\ln \sigma - (\sigma^2 - 1)/(\sigma^2 + 1)] \}, \quad (2b)$$

where $\sigma = R_2/R_1$, R_2 = radius of cell, R_1 = radius of driving rod, L = length of annular gap, Z_M = mechanical impedance, f = force, v = velocity (in phase with real component of force), G'' = loss shear modulus of sample ($=\omega\eta'$ where η' is the real component of dynamic viscosity of sample), ω = circular frequency of oscillation, M = mass of moving system, ρ = density of sample, S_M = elastance (spring constant) of spring mountings, and G' = storage shear modulus of sample. The term in β is adequate only if $\omega^2\rho\beta/|G^*|$ is small compared with 1, where $G^* = G' + iG''$, as is usually the case. From Eq. (2), after Z_M has been determined by either impedance or phase-shift measurements as described below, the frequency-dependent viscoelastic quantities G' and G'' can be calculated.

Cells with different values of R_2 provide a range of values of the basic cell constant A for samples of different consistencies. For a sample stiff enough to support its own weight, the bottom cap can be removed from the cell to convert from annular pumping to Pochettino

⁶ W. P. Mason, *Electromechanical Transducers and Wave Filters* (D. Van Nostrand Company, Inc., Princeton, New Jersey, 1942).

⁷ E. R. Fitzgerald and J. D. Ferry, *J. Colloid Sci.* **8**, 1 (1953).

⁸ H. Markovitz, *J. Appl. Phys.* **23**, 1070 (1952).

ometry⁹ with a marked decrease in the cell constant. Specifically, in the study of gelation, this change can be made after a gel has set *in situ* and become too stiff to give favorable values of Z_M with the original high value of A .

The value of A is calculated from the cell dimensions by Eq. (2a), and, for the cell used in the measurements reported here, is 4723 cm. This was confirmed by impedance measurements on a National Bureau of Standards calibrated oil, N-27, at two temperatures where the viscosities were 14.12 and 4.04 poises, respectively. The calculated values of $\eta' (=G''/\omega)$ from eq. (2) agreed within 0.2% and moreover were independent of frequency from 3 to 250 cps, indicating absence of apparatus resonances or other anomalies.

The constant β is also calculated from cell dimensions by Eq. (2b), and the value for the cell used here is 64×10^{-4} cm². This was confirmed by making impedance measurements with water in the cell, for which $\eta' = 1$ and $G' = 0$; thus in the imaginary part of Z_M the term $\rho\beta A$ can be distinguished here as an effective added mass. The experimental value of β determined in this way was about 20% smaller than that calculated, presenting satisfactory agreement since this difference presents only a 1% error in the sum $M + \rho\beta A$.

Further details of the design and hydrodynamics are given elsewhere.⁹ The determination of the other apparatus constants will be described below.

In an earlier stage of the design, a reservoir for excess sample was placed at the bottom of the cell below the annular gap. However, with this arrangement anomalies appeared which could be attributed to finite compression of the sample in the reservoir chamber; their nature and magnitude agreed with predictions based on a reasonable estimate for the compressibility.⁹ While such anomalies might in principle provide dynamic compressibility determinations, they represented an un-

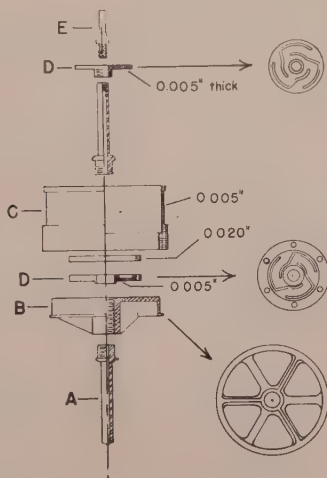


Fig. 2. Exploded view of moving system with units identified as in Fig. 1.

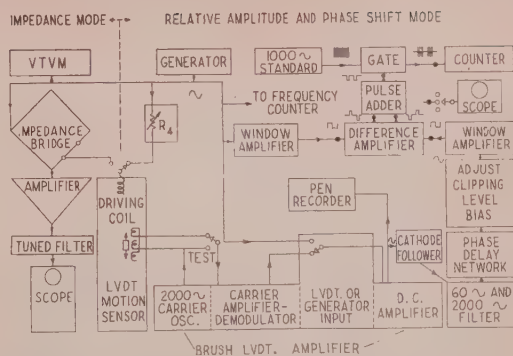


Fig. 3. Block diagram of electrical apparatus with the impedance measurement mode on the left and the phase shift mode on the right.

desirable complication for the present study, and the reservoir was therefore eliminated.

For temperature control, the apparatus is surrounded by a chromium-plated brass case, whose upper and lower sections are sealed to the central mounting plate by O-rings, as shown in partial section in Fig. 1; the case is immersed in a liquid bath. The connections are brought out through a standpipe which projects above the liquid level. The temperature of the sample is measured by a thermocouple in a well located close to the sample cell; the massive metal provides good thermal conductivity. The temperature can be controlled within 0.01°C between -40° and 150°. Cooling is accomplished by dry ice pockets. For improved mechanical isolation, the bath in which the apparatus is submerged rests on an inflated rubber inner tube.

Electrical Circuit and Operation: Impedance Measurement Mode

A block diagram of the electrical circuit is shown in Fig. 3. The driving coil is energized by a Hewlett-Packard low frequency function generator model 202A, or at higher frequencies by an audio oscillator model 200CR. The normal driving current is 0.1 ma, measured by a Ballantine vacuum tube voltmeter model 302B; in the impedance measurement mode, the voltmeter is connected across the impedance bridge of which the driving coil forms one arm. The bridge, similar to that described by Smith, Ferry, and Schremp,⁵ measures either positive or negative reactance in the coil arm, depending on the position of the variable capacitance. Above 20 cps the bridge input passes through an isolating transformer; below 20 cps the bridge output is taken through a balanced detector. The output is amplified by a Tektronix low-level preamplifier type 122, filtered by a General Radio vibration analyzer type 762B, and displayed on a Dumont oscilloscope type 304A (with long persistence screen) as a null detector.

To determine the components R_0 and X_0 of the clamped impedance Z_0 in Eq. (1), the cell is replaced by

⁹ M. H. Birnboim, Ph.D. thesis, University of Wisconsin, 1961.

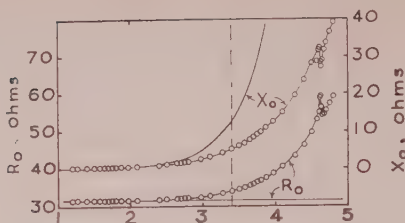


FIG. 4. Clamped resistance (R_0) and reactance (X_0) of driving coil at 130°C, plotted against $\log \omega$. Points, experimental; solid curves show idealized frequency dependence ($R_0 = \text{const}$, $X_0 = \omega L$). Vertical dashed line denotes upper limit of frequency range used for viscoelastic measurements.

a dummy cell with solid top, which is pushed against the coil mount to force the coil up 0.025 in. to a position against the pole piece; here it is locked by set screws. Impedance measurements over an extended frequency range provide curves such as those shown in Fig. 4. The adequacy of the clamping is evidenced by reproducibility of such curves and by the absence of resonances below 6800 cps. The departure from the theoretical curves for an idealized inductive resistance is due to eddy current losses in the iron core. The dashed line shows the high-frequency limit of actual measurements, 400 cps.

The values of R_0 and X_0 , especially the former, are of course temperature-dependent. When impedance measurements are to be made on a sample not too far from room temperature, they can be preceded or followed by a clamped impedance run at the identical temperature. The clamped values appear to be stable over a period of weeks. At higher or lower temperatures where this procedure is impractical, it has been found that the temperature and frequency dependence of R_0

and X_0 can be represented by empirical power series:

$$R_0 = (a_0 + k_0\theta) + (a_1 + k_1\theta)\nu + (a_2 + k_2\theta)\nu^2 + (a_3 + k_3\theta)\nu^3,$$

$$X_0 = \omega R_2 R_3 C_0,$$

$$1/C_0 = (b_0 + l_0\theta) + (b_1 + l_1\theta)\nu^{\frac{1}{2}} + (b_2 + l_2\theta)\nu^{\frac{1}{2}} + (b_3 + l_3\theta)\nu^{\frac{3}{2}}.$$

Here ν is frequency in cps; θ is Centigrade temperature; R_2 , R_3 , and C_0 refer to settings of the bridge arms; and a_0 , b_0 , the k 's, and the l 's are coefficients determined empirically by least-squares fitting of a large number of data with a high-speed computer.¹⁰ Over a temperature range from 28° to 119°C, values of R_0 calculated from Eq. (3) agreed within 0.01 ohm up to 400 cps with individual measurements representing the over-all precision of the method. The maximum deviation in R_0 was 0.05 ohm at 400 cps and less at lower frequencies, approximately proportional to $\nu^{\frac{1}{2}}$. This error is tolerable except in situations where $X - X_0$ is small; it is attributable to hysteresis effects associated with the iron core when the temperature is changed through a wide range and can be made smaller by more frequent calibrations.

The calibration of the transducer constant $(Bl)^2$ by Eq. (1) is as usual for such devices based on the inert mass M of the moving system.^{5,6} In specifying M from the added weights of the components in Fig. 2, one-half the weight of the deformable portions of the spring supports is taken, the uncertainty being insignificant. For impedance measurements with no sample in the cell, where G' , G'' , and ρ are all zero, combination of Eqs. (1) and (2) yields (where $Z = R + iX$)

$$-\omega(X - X_0) / [(R - R_0)^2 + (X - X_0)^2] = \omega^2 M / (Bl)^2 - S_M / (Bl)^2,$$

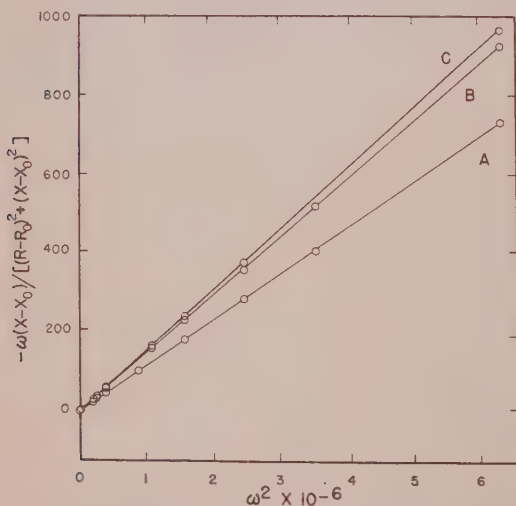


FIG. 5. Test plot for determining transducer constant $(Bl)^2$ using Eq. (6). A, with normal moving system, $M = 17.278$ g; B, with additional mass, $M = 21.864$ g; C, same as B with water in the cell.

so a plot of the experimentally measured quantity of the left against ω^2 gives a straight line whose slope is $M / (Bl)^2$ and from which $(Bl)^2$ is determined. An example is shown in Fig. 5; the precise linearity is further evidence of satisfactory operation and absence of resonances. Moreover, line B in Fig. 5 was obtained with an additional mass of about 4.6 g attached to the moving system, which displaced the equilibrium position of the driving coil downward about 0.005 in. in the magnetic field. The value of $(Bl)^2$ calculated from its slope agreed within experimental error with that from line A and many replicate determinations, showing that the transducer constant is insensitive to small displacements in the field. Line C in Fig. 5 was obtained with water in the cell, providing the confirmation of the term $\rho\beta A$ described in the preceding section.

Measurements of $(Bl)^2$ at different temperatures could be fitted to the empirical equation (units ohm

¹⁰ A Bendix G-15D, generously made available by the Theoretical Chemistry Laboratory of the Department of Chemistry.

(dyne sec cm^{-1})

$$(Bl)^2 = 1.474 \times 10^6 - 55.6\theta. \quad (7)$$

The spring constant S_M of Eqs. (2) and (6) was obtained by substituting impedance data at lower frequencies into Eq. (6) and averaging the results. Expressed as a function of temperature (units dyne cm^{-1}), these followed the empirical equation

$$S_M = 2.605 \times 10^6 - 1159\theta. \quad (8)$$

Electrical Circuit and Operation: Phase Meter Mode

The block diagram of the phase meter assembly is also included in Fig. 3, and the circuits are shown in detail in Fig. 6. The essential measurements are the ratio between maximum amplitudes of the driving force (f_0) and displacement (x_0) and the phase difference δ between them, from which the mechanical impedance can be obtained by the relation

$$Z_M = (f_0/\omega x_0)(\sin\delta - i \cos\delta) \quad (9)$$

and then converted to the desired quantities G' and G'' by Eq. (2).

The force amplitude is proportional to the current through the driving coil, which is measured by the voltage across the resistance R_4 (sufficiently greater than the impedance of the coil itself so the latter can be neglected by comparison). The displacement amplitude is measured by the output of the differential transformer, LVDT, which passes through a Brush type BL-520 carrier amplifier-demodulator. This signal and the voltage across R_4 and the driving coil are switched

in turn into the dc section of the Brush amplifier and registered alternately as sinusoidal traces on a Brush oscillograph pen recorder type BL-202 during steady-state operation. The value of R_4 is adjusted to bring the maximum recorder trace heights d_1 for the displacement and d_2 for the force signal to closely similar magnitudes. Then

$$f_0/x_0 = Cd_2/d_1R_4, \quad (10)$$

where C is a coefficient involving the product Bl for the driving coil, the electromechanical constant of the LVDT, and the gain of the carrier amplifier.

The coefficient C can be determined by measurements with no sample in the cell, where Eqs. (2) and (9) become

$$M/C - S_M/C\omega^2 = -(d_2/d_1\omega^2R_4) \cos\delta. \quad (11)$$

A plot on the right side of Eq. (11) against $1/\omega^2$ gives a straight line whose slope is S_M/C , and S_M has been obtained as given in Eq. (8). Because of some gain instability in the carrier amplifier, it is necessary at present to determine C at frequent intervals. In earlier measurements, C was obtained by comparison of G' and G'' by the impedance and phase meter modes in the overlapping frequency range of 2.5 to 5 cps.

For measurement of the phase angle δ the two sinusoidal signals corresponding to f and x are passed through window amplifiers with nominal clipping about zero voltage, and the resulting square waves are subtracted by a difference amplifier to yield an alternating positive-negative sequence of rectangular pulses. The average width of a consecutive pair times ω gives the phase difference δ_T between the two sine waves, including an electrical phase shift δ_2 which can be adjusted

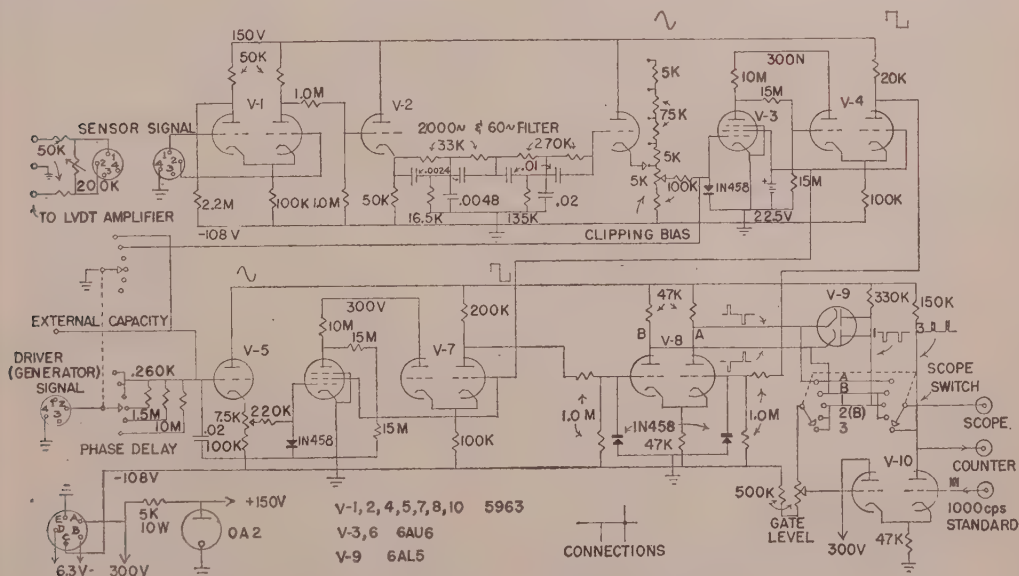


FIG. 6. Electrical circuit for phase meter measurements.

by a phase delay network in the path of the α signal. To achieve the required alternating pulses the clipping levels must be nearly equal and can be adjusted while monitoring on an oscilloscope (Dumont type 304A). The alternating pulse sequence is half-inverted to give a negative sequence which is used to pulse-modulate a 1000 cps carrier. This permits counting the summed duration of a given number of pulses on a Hewlett-Packard Electronic Counter type 5223. The electrical phase shift δ_2 is determined in the same manner by switching part of the generator output into the dc amplifier in place of the demodulated LVDT output. There remains another small electrical phase shift δ_1 from the carrier amplifier, which is calculated from the components of the latter to be 0.0016ω . In spite of some uncertainty, this calculated value is used since δ_1 is always a small correction. Finally, $\delta = \delta_T - \delta_1 - \delta_2$.

The calculations necessary to obtain G' and G'' from the apparatus readings in both impedance measurement and phase meter modes were programmed for the Bendix G-15D computer with the guidance of Dr. S. E. Lovell. Further details of the experimental procedures and calculations are given elsewhere.⁹

RESULTS ON POLYVINYL CHLORIDE SOLUTIONS

Materials

A sample of polyvinyl chloride (containing about 2.5% copolymerized vinyl acetate), lot VYNV-1524, was kindly furnished by Mr. A. T. Walter, Union Carbide Chemicals Company. A rough fractionation was made with tetrahydrofuran as solvent and water as precipitant, to separate and discard 10% with highest and 20% with lowest molecular weights. The remaining central fraction was dried in vacuo in the dark at 40°C. Its intrinsic viscosity in cyclohexanone at 25°C was 1.71 dl/g, corresponding to a molecular weight of 1.0×10^5 , according to the empirical equation given by Danusso, Moraglio, and Gazzera.^{11,12}

Di-ethyl hexyl phthalate was also obtained through the kindness of the Union Carbide Chemicals Company. Its density at 20°C was 0.986 g/cc, and its thermal expansion coefficient was $8.6 \times 10^{-4} \text{ deg}^{-1}$. Its viscosity was measured by the capillary method over the range from 2° to 70°C, using a viscosimeter calibrated with a Bureau of Standards oil. At 25°C the viscosity was 0.562 poise; taking this as a reference value, all the other data could be fitted closely to an equation of the WLF form¹³:

$$\log(\eta/\eta_0) = -3.36(T - T_0)/(128.3 + T - T_0), \quad (12)$$

where η and η_0 are the viscosities at temperatures T and $T_0 (= 298.2^\circ\text{K})$. Equation (12) was subsequently used

¹¹ F. Danusso, G. Moraglio, and S. Gazzera, *Chim. e ind.*, **36**, 883 (1954).

¹² We are greatly indebted to Dr. Stephen D. Morton for the fractionation and determination of intrinsic viscosity.

¹³ M. L. Williams, R. F. Landel, and J. D. Ferry, *J. Am. Chem. Soc.*, **77**, 3701 (1955).

for interpolation purposes. It may be mentioned that the viscosity of this solvent, about two orders of magnitude higher than those of common organic liquids, permits study of viscoelastic mechanisms whose frequency dispersion would otherwise fall outside the range of the present instrument.

Solutions were prepared by suspending the finely divided polymer in the solvent at room temperature and heating the slurry to 165°C. Exploratory studies of the steady flow viscosities of such solutions showed that gelation occurred at a concentration of 4.3% by weight after cooling to 70°C and at 2.6% after cooling to 62°C, while a 1.4% solution remained fluid at 25°C (compare the experiments of Walter).¹⁴ To study the viscoelastic properties during gelation, a hot solution of chosen concentration (either 2.29 or 3.00% by weight) was quickly cooled to either 25° or 40°C in the sample cell, and the apparatus was quickly assembled. Measurements were made repeatedly at constant temperature.

The densities of the solutions, needed for certain derived calculations, were estimated assuming that the volumes of solvent and polymer were additive; and their thermal expansion coefficients were assumed to be the same as that of the solvent.

Viscoelastic Measurements during Gelation

The time dependence of the storage and loss modulus during gelation of a 2.29% solution at 40°C is shown in Figs. 7 and 8. At the highest frequencies the changes with time are very slight; G' increases and G'' decreases very slowly. At the lowest frequencies, by contrast, G' is not detectable until the lapse of about 40 hr, even though rigidities as low as 10 dyne/cm² can be detected by this apparatus. Subsequently, it increases rather rapidly and becomes frequency-independent below 0.1 cps. At these lowest frequencies, G'' increases slowly and appears to pass through a shallow maximum.

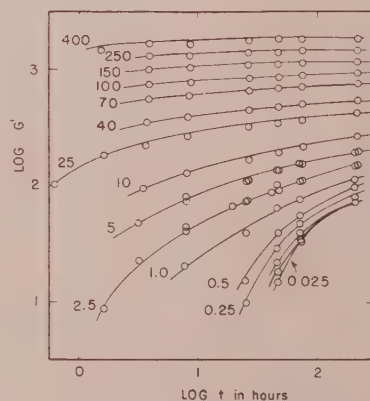


FIG. 7. Storage modulus (units dyne/cm²) of 2.29% solution of polyvinyl chloride plotted logarithmically against time at 40°C. Numbers denote frequency in cps.

¹⁴ A. T. Walter, *J. Polymer Sci.*, **13**, 207 (1954).

The difference between gelled and ungelled states is portrayed more clearly in Fig. 9. Interpolated values of G' and G'' at 2.5 hr (long before gelation) and at 220 hr (long after) are plotted logarithmically against radian frequency. The initial system represents a moderately dilute polymer solution below the concentration range in which most previous studies have been made; the final system is a cross-linked network as in more concentrated gels previously studied.¹⁵ At high frequencies the solution and gel are almost identical, as expected since moderately short-range configurational motions are scarcely affected by the cross-links.

Admittedly, there is some aggregation in the solution at the earliest times of measurement, as indicated by steady-flow viscosity measurements⁹ as well as the application of the Zimm theory to be discussed below. Moreover, even after 220 hr there must be a substantial proportion of "sol fraction" unattached to the gel network. The average molecular weight between cross-links calculated from the theory of rubberlike elasticity is $M_c = cRT/G_e$, where c is the polymer concentration in g/cc and G_e the pseudo-equilibrium modulus represented by the low-frequency limiting value of G' . The latter is 72 dyne/cm², corresponding to $M_c = 8 \times 10^5$, a meaninglessly large figure, since the average molecular weight before gelation is only 1.0×10^5 . No doubt the discrepancy arises primarily because c in the equation should refer to the concentration of network species, which is much less than the total polymer concentration in this system. A correction for loose ends of the form introduced by Flory¹⁶ must also be involved.

When gelation of a 2.29% solution occurs at 25°C the changes are much the same but occur earlier. From plots of G' and G'' for this system at 1.0 and 560 hr, similar

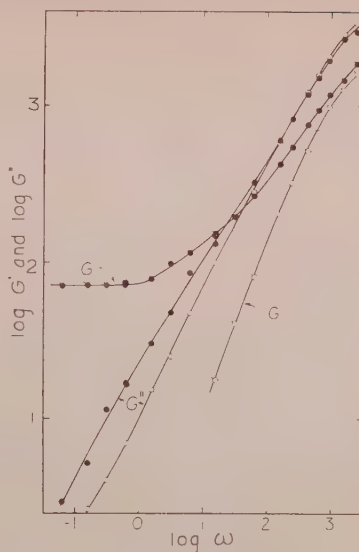


FIG. 9. Storage modulus (tagged circles) and loss modulus (untagged) interpolated from Figs. 7 and 8 at 2.5 hr (open circles) and at 220 hr (black), plotted logarithmically against radian frequency.

to those in Fig. 9, the relaxation spectrum H was calculated by the approximation methods of Ferry and Williams.¹⁷ The values from G' and from G'' were in excellent agreement,⁹ a feature which lends considerable confidence to the performance of the new apparatus. The mean values are plotted logarithmically in Fig. 10. At short times, again reflecting relatively short-range configurational motions, the spectra before and after gelation are identical. At long times gelation causes a moderate increase in H . The presence of the sol fraction makes these observations difficult to interpret. Similar curves for H were obtained for other systems.⁹

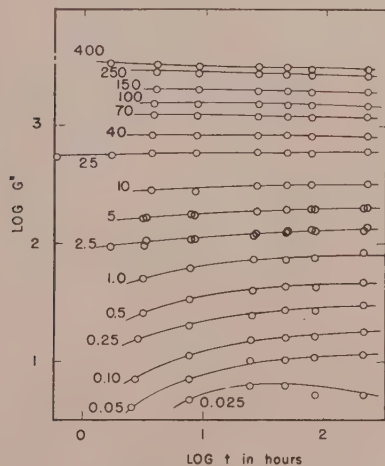


FIG. 8. Loss modulus plotted logarithmically against time as in Fig. 7.

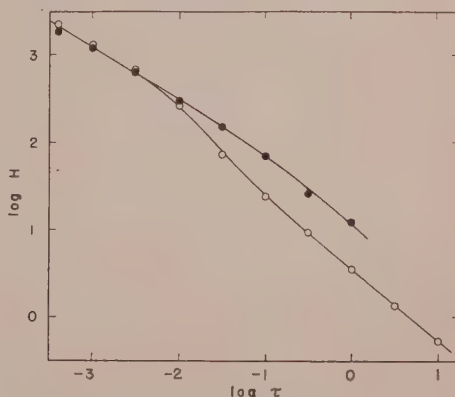


FIG. 10. Relaxation spectrum of 2.29% solution at 25°C. Open circles before gelation (elapsed time 1.0 hr); black circles after gelation (elapsed time 560 hr).

¹⁶ J. D. Ferry, D. J. Plazek, and G. E. Heckler, *J. chim. phys.* **55**, 152 (1958).

¹⁷ P. J. Flory, *Principles of Polymer Chemistry* (Cornell University Press, Ithaca, New York, 1954).

¹⁷ J. D. Ferry and M. L. Williams, *J. Colloid Sci.* **7**, 347 (1952).

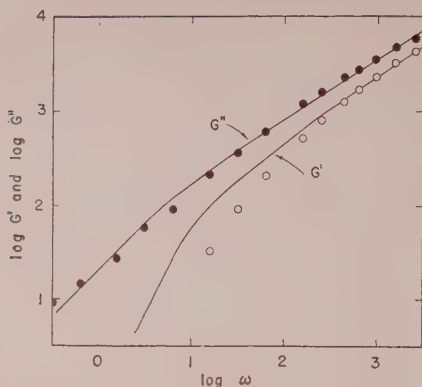


FIG. 11. Storage and loss moduli of 2.29% solution at 25°C before gelation (elapsed time 1 hr). Points, experimental; curves, Zimm theory with parameters M and η_s given in Table II.

The slope of H with logarithmic scales is -0.62 at short times instead of the -0.50 specified by the Rouse theory, so that friction coefficients cannot be calculated in the usual manner.¹⁸ Instead, the data for ungelled solutions are well described by the theory of Zimm,¹⁹ as shown in the next section; this theory predicts a slope of -0.67 for $\log H$ in the transition zone.²⁰

The quantity which changes most during gelation is G_s , the low-frequency limit of G' . Values for the 2.29% solution at 25°C are given in Table I. After 560 hr G_s is still increasing, as would be expected from the conclusion that a large part of the polymer is still unbound to the network.

Properties of the Ungelled Solutions; Theory of Zimm

While the Zimm theory¹⁹ should be best applicable to the viscoelastic properties of dilute polymer solutions,²¹ there have been no experimental data which conform closely to it. It is of considerable interest, therefore, that the frequency dependence of G' and G'' for 2.29%

TABLE I. Increase in G_s during gelation of 2.29% solution at 25°C.

Log elapsed time in hrs	Log G_s
1.02	1.10
1.22	1.66
1.40	1.79
1.70	2.00
2.00	2.17
2.16	2.22
2.75	2.44

¹⁸ J. D. Ferry, R. F. Landel, and M. L. Williams, *J. Appl. Phys.* **26**, 359 (1955).

¹⁹ B. H. Zimm, *J. Chem. Phys.* **24**, 269 (1956).

²⁰ J. D. Ferry, *Viscoelastic Properties of Polymers* (John Wiley & Sons, Inc., New York, 1961), p. 159.

²¹ R. Cerf, *Advances in Polymer Sci.* **1**, 382 (1959).

polyvinyl chloride solutions before gelation follows the Zimm theory quite well.

The equations of Zimm for G' and G'' were evaluated numerically by the Bendix computer by Dr. S. E. Lovell in reduced form. The reduced moduli, $G'_R = G'/cRT$ and $G''_R = G''M/cRT - \omega\eta_s M/cRT$, were obtained as functions of the reduced frequency $\omega_R = \omega\tau_1$. Here M is the molecular weight, η_s the solvent viscosity (in our system, the term in η_s can be ignored), and τ_1 the terminal Zimm relaxation time. Logarithmic plots of the reduced functions were then matched to experimental plots for the 2.29% solutions at 25° and 40°C with horizontal and vertical adjustments which specified the parameters M and τ_1 . The results are illustrated at 25°C in Fig. 11, showing quite good agreement. The derived parameters are listed in Table II.

In the Zimm theory, $\tau_1 = 0.200\eta_s a^2 Z^3/kT$, where η_s may be regarded as the effective local viscosity, a^2 is the mean square molecular length per monomer unit, Z the degree of polymerization, and k Boltzmann's constant. At higher frequencies G' and G'' depend on $\eta_s a^2$ only and are independent of M or Z . It follows that η_s can be obtained by matching the logarithmic plots as described above independently of any arbitrary shift, along a line of slope $2/3$, and it can be determined with considerably more precision than either M or τ_1 . Based on an assumed value of $a = 6 \times 10^{-8}$ cm in harmony with values for other polymers,¹⁶ η_s has been calculated and is listed in Table II together with the solvent viscosity η_s and the solution viscosity represented by the low-frequency limiting value of G''/ω . The effective local viscosity lies between the solvent and solution viscosities. It should be noted, however, that the value of a used is appropriate to a Θ -solvent and may be too small; a larger value for a would result in a smaller value for η_s .

The values of M in Table II are about 50 times too large, indicating no doubt that substantial aggregation had occurred by the time of these measurements, even though the gel point was not reached until many hours later. Since the aggregates must be branched, the Zimm theory is not strictly applicable and should be replaced by the modification of Zimm and Kilb,²² but this is impossible without knowledge of the pattern of aggregation. Nevertheless, the calculation of η_s should not be seriously affected by this complication.

TABLE II. Parameters obtained from Zimm theory for 2.29% polyvinyl chloride solutions.

Temp. of measurement	25°C	40°C
Elapsed time, hr	1.0	2.5
τ_1 , sec	0.065	0.046
M	4.0×10^6	6.7×10^6
η_s , poise	3.8	1.3
η_s , poise	0.56	0.26
lim G''/ω , poise	20	10

²² B. H. Zimm and R. W. Kilb, *J. Polymer Sci.* **37**, 19 (1959).

Properties of the Gels; Theory of Bueche

After a 2.29% gel had been aged at 25°C for 580 hr, its temperature was successively changed to 15.3°, 0.2°, 15.0°, and 40.0°C, with measurements at each temperature. The dispersion shifted to lower frequencies with decreasing temperature attributable to an increase in the local friction coefficient or effective viscosity, but this normal behavior was accompanied by changes in structure as evidenced by the changes in the pseudo-equilibrium modulus shown in Table III. Below 25°C the viscoelastic properties showed little change with elapsed time at a given temperature. The usual method of reduced variables²³ for describing temperature dependence was found to be inapplicable; apparent horizontal shifts of G' and G'' on the logarithmic frequency axis were not identical. This provides further evidence of changes in the nature of the structure with temperature.

Nevertheless, a comparison of the viscoelastic properties at different temperatures can be made with another type of corresponding-state plot. The most characteristic manifestation of a network structure among the various functions which can be used to describe viscoelasticity appears in the loss compliance, $J'' = G'' / (G'^2 + G''^2)$, as a rather broad maximum. The theories of Kirkwood²⁴ and Bueche²⁵ predict that the magnitude of J'' through this maximum should be proportional to the equilibrium compliance $J_e = 1/G_e$.

Logarithmic plots of J''/J_e were prepared and then replotted against $\log \omega/\omega_m$, where ω_m is the radian frequency corresponding to the maximum in J'' for each system. As shown in Fig. 12, such corresponding-state curves coincide rather closely despite the structural differences inferred above. Moreover, they agree moderately well with the Bueche theory reproduced by the dashed curve. The theory predicts a slightly sharper maximum, with $J''_m/J_e = 0.42$, as compared with the experimental value of 0.30.

Values of ω_m are also given in Table III. According to the Bueche theory ω_m should be inversely proportional

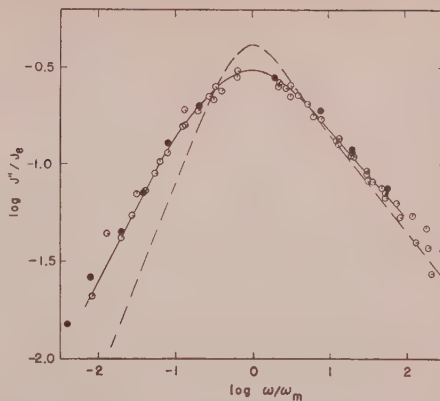


FIG. 12. Loss compliance of polyvinyl chloride gels plotted logarithmically in corresponding states. Open circles, 2.29%; pip up, 0.2°C; successive 45°C rotations clockwise, 15.3°, 25.1°, and 40.0°C. Black circles, 3.00% at 25.0°C. Dashed curve, Bueche theory.

to the local friction and hence in our system presumably to the solvent viscosity; however, it is at the same time inversely proportional to the square of the average spacing between cross-links, which is also changing with temperature. As discussed above, M_e cannot be calculated from G_e because of the presence of sol fraction. However, the ratios of ω_m at a standard temperature of 25°C, $\omega_{m,0}$, to ω_m at other temperatures can be compared with the corresponding solvent viscosity ratios η/η_0 . This comparison is made in the last two columns of Table III; the differences provide a measure of changes in M_e . Further analysis of data such as these will require consideration of the proportions of sol and gel fractions and their combined behavior.

CONCLUSIONS

The apparatus described here can be used for study of moderately dilute polymer solutions to define their viscoelastic properties in the transition and terminal zones, provided the solvents are sufficiently viscous. It can also provide new information on the process of gelation and the properties of dilute gels.

ACKNOWLEDGMENTS

This work was supported in part by the Research Committee of the Graduate School of the University of Wisconsin from funds supplied by the Wisconsin Alumni Research Foundation and in part by the Office of Naval Research. We are indebted to Mr. Robert W. Schmelzer for advice and painstaking work on construction of the apparatus and to Drs. Donald J. Plazek, Victor J. MacCosham, and Stuart E. Lovell for many helpful discussions.

TABLE III. Viscoelastic parameters for gels in chronological sequence.

Concn %	Temp °C	Elapsed time, hr ^a	$\log G_e$	$\log \omega_m$	$\log \omega_m/\omega_{m,0}$	$\log \eta/\eta_0$
2.29	25.1	335 ^b	2.44	1.08
2.29	15.3	18	2.56	0.90	0.18	0.27
2.29	0.2	24	2.78	0.71	0.37	0.78
2.29	25.0	9	2.45	1.08
2.29	40.0	48	2.52	1.69	-0.61	-0.34
3.00 ^c	25.0	2470	3.25	1.92

^a At temperature of measurement.

^b Time elapsed from moment of cooling from 165°C.

^c Measurements by Mr. R. B. DeMallie.

²³ J. D. Ferry, J. Am. Chem. Soc. **72**, 3746 (1950).

²⁴ J. G. Kirkwood, J. Chem. Phys. **14**, 51 (1946).

²⁵ F. Bueche, J. Chem. Phys. **22**, 603 (1954).

Isothermal Crystallization Kinetics of Polyethylene.

III. Influence of the Sample Preparation

J. RABESIAKA

Centre de Recherches sur les Macromolécules, Strasbourg, France

AND

A. J. KOVACS*

Department of Chemistry, University of Wisconsin, Madison, Wisconsin

Isothermal crystallization in bulk has been compared dilatometrically with linear polyethylene samples which have been molded in different ways, including melt orientation and sintering of precipitated powders from dilute solutions. These experiments show significant differences in the crystallization kinetics, which in some cases cannot be removed even by prolonged heating of the melt prior to crystallization. The data have been analyzed by an empirical expression in terms of nucleation and growth processes, according to the theoretical approach of Avrami. The results suggest that, in general, the melted polyethylene is not in a true thermodynamic equilibrium and includes some "quasi-indestructible" clusters, which act as heterogeneous nuclei in the crystallization process. The nature and the amount of these nuclei depend on the molding, melting, and mechanical history of the sample, so that the semicrystalline material may have a wide variety of structure.

INTRODUCTION

MEASUREMENT of volume contraction during isothermal crystallization is one of the useful methods for observing the time dependence of the organization process in crystallizing polymers.¹ Most of the available data concern the development of the semicrystalline structure from the undercooled melt, and the experimental results are explained in terms of Avrami's theory.² However, the agreement between this theoretical expression and the experimental data is often poor when the whole range of crystallization is considered. Since experiments are fairly reproducible with the same sample, it is generally assumed that the polymer is in a thermodynamic equilibrium above the limiting melting temperature, like an ordinary liquid, provided that thermal degradation is negligible.

During the past few years we have studied dilatometrically different crystallization kinetics for several linear and branched polyethylenes (PE). Some of these data are reported and discussed in the first two papers of this series.^{3,4} It has appeared during this investigation that the crystallization kinetics of the same polymer is very sensitive to the particular type of molding process. We will report here some of the characteristic data obtained in this field. The results suggest that a wide variety of semicrystalline structures may be obtained with the same PE which are related to the previous mechanical, molding, and melting history of the sample.

SAMPLE PREPARATION

Two fairly linear PE were used in a granulated form as starting materials. The M_1 was a "Marlex 50"

* Present address: Centre de Recherches sur les Macromolécules, Strasbourg, France.

¹ L. Mandelkern, *Chem. Rev.* **56**, 903 (1956).

² M. Avrami, *J. Chem. Phys.* **7**, 1103 (1939); **8**, 212 (1940); **9**, 177 (1941).

³ M. Gubler and A. J. Kovacs, *J. chim. phys.* (to be published).

⁴ M. Gubler, J. Rabesiaka, and A. J. Kovacs, *J. chim. phys.* (to be published).

polymer produced by Phillips Petroleum Company, and M_2 , called "Manolène," was prepared by the Manufacture Normande de Polyéthylène. These two products have very similar molecular characteristics, as can be seen from Table I, listing average molecular weights measured by light scattering,⁵ and CH_3/CH_2 ratio calculated from infrared spectroscopy.⁶ However, the densities of these polymers at 25°C (after quenching the melt) and at 150°C were slightly different. This difference may be attributed to some extent to various impurities imperfectly removed after the polymerization process.

Several samples were prepared from M_1 and M_2 in two different ways:

(1) The granulated polymer was compressed at 180°C between two polished metal plates under about 1000 kg/cm². The final thicknesses of the sheets obtained were defined by several wedges of chosen thickness (from 0.3 to 1 mm) disposed between the two plates. The uniaxial compression produces a random molecular orientation in the plane of the sheets. However, the effective pressure at the end of the molding is much less than the above nominal value supported by the wedges, so that this pressure could be removed and the sandwich quenched without appreciable modification of the sheet thickness.

TABLE I.

Sample	CH ₃		Density g/ml	
	10 ⁶ M_w	100 CH ₂	25°C	150°C
M_1	1.0	0.35	0.957	0.788
M_2	0.9	0.40	0.940	0.778
M_{2p} (91.6)	1.25	...	0.965	0.797

⁵ M. Gubler, C. Reiss, and H. Benoit, *J. chim. phys.* (to be published).

⁶ E. J. Slowinski, Jr., H. Walter, and R. L. Miller, *J. Polymer Sci.* **19**, 353 (1956).

These samples will be designated by a subscript f followed by the nominal thickness in mm (between brackets); for instance, $M_{2f}(0.3)$ means a sheet 0.3 mm thick obtained with M_2 .

(2) Solutions of about one percent of polymer were prepared from the granulated materials in boiling toluene. After complete dissolution they were rapidly cooled to some constant temperature T_p between 70° and 95°C. By increasing T_p , i.e., by decreasing supercooling, precipitation occurs more and more slowly. However, at high temperature a cold glass stirrer introduced into the undercooled solution may start the precipitation process much more rapidly, if the largest nuclei, formed on the stirrer, are still stable at T_p . Powders with $T_p > 90^\circ\text{C}$ were produced by this "seeding" technique.

Isothermal crystallization in dilute solutions was followed also dilatometrically and by light scattering measurements. Some of these data have been reported elsewhere⁷; the others will be published later.⁸

When the precipitation was nearly complete, the solution was filtered and rinsed with the solvent at T_p . All these successive operations were performed under nitrogen pressure to avoid oxidation. The wet powders were further washed at room temperature by methanol and dried under vacuum over several weeks.

The dry powder was then compressed at room temperature under about 1000 kg/cm², and the brittle cake was baked in vacuum at 150°C for half an hour. This sintering process, similar to that used for polytetrafluoroethylene, produced well-formed disks, about 1 mm thick, which were then investigated dilatometrically.

These samples will be designated by the subscript p and the temperature T_p (in brackets). One particular sintered sample $M_{2p}(95-70)$ of this type was obtained from a solution allowed to cool from 95° to 70°C in 24 hr.

The isothermal precipitation from dilute solution has a slight fractionating effect by removing the low MW fractions and the original impurities, as can be seen from Table I. Obviously the efficiency of the fractionation increases with T_p .

A drop of the polymer suspension before filtering was used for electron-microscopic examination. Depending on T_p , i.e., on the rate of precipitation, more or less perfect dendritic and pyramidal structures were observed as built up from diamond-shaped lamellae, similar to those reported by a number of authors.⁹⁻¹¹

EXPERIMENTAL TECHNIQUE

About one gram of each sample was introduced in the bulb of a dilatometer which was sealed and filled with pure mercury, as described in a previous paper.¹²

Several types of isothermal crystallization processes were investigated, but we will report here only some of the characteristic data obtained when crystallization was performed from the undercooled melt, i.e., when the samples were quenched from T_0 (about 170°C) to some constant temperature T between 120° and 132°C. The silicone oil baths, controlled by a mercury thermostat, were maintained at constant temperature with an accuracy of $\pm 0.02^\circ\text{C}$ during the whole duration of the experiment, which extended over about 100 hr.

The isothermal contraction induced by the crystallization was visually observed by a telescope, following the mercury level in the capillary as a function of time t measured from the moment when the dilatometer was immersed into the constant temperature bath. Thermal equilibrium was reached in less than 3 minutes. The actual volume v (per gram of PE) at t was compared with the volume of the undercooled melt v_l . The difference $v_l - v$ is expressed as mm³/g of polymer, or as crystallinity ratio: $x = (v_l - v)/(v_l - v_c)$. The specific volumes of the supercooled liquid v_l and that of the perfect crystal v_c were calculated from two relationships discussed in a previous paper.¹³ It must be recalled that the absolute values of x are somewhat questionable; however, in the temperature range investigated, they agree with an accuracy of one percent with those calculated in a more elaborate manner proposed by Swan.¹⁴

Two or more samples were investigated from each particular preparation. The data obtained by duplicate samples were quite similar in character, though often slightly different quantitatively.

RESULTS

Figure 1, obtained with sample $M_{2p}(91.6)$, shows the general behavior classically observed. Superposition of the crystallization isotherms may be obtained in a satisfactory manner when the curves are shifted along the $\log t$ axis, except for the range below 122°C. But in this latter case the crystallization process is so rapid that it can no longer be considered as isothermal. Superposition holds also when duplicate samples are used, but the time scales, compared by the "half-time" of crystallization $t_{0.5}$, are often slightly different for the same temperature.

Influence of the Melting Conditions

The time-scale, i.e., $t_{0.5}$, is also affected by the melting temperature T_0 and the duration of melting t_0 . With higher T_0 and longer t_0 the crystallization isotherm is slightly shifted towards increasing time scale. However, these effects are generally small, for instance at 126°C, for the polymer M_2 , $t_{0.5}$ changes from 1 to 1.2 hr when T_0 increases from 150 to 250°C ($t_0 = 15$ min), or when t_0 increases from 0.15 to 80 hrs (at 160°C). This effect

⁷ J. Rabesiaka, thesis, Fac. Sci. Strasbourg, France, 1960.

⁸ C. Reiss (private communication).

⁹ R. Jaccodine, *Nature* **176**, 305 (1955).

¹⁰ A. Keller, *Phil. Mag.* **2**, 1171 (1957).

¹¹ B. G. Rånby, F. F. Morehead, and N. H. Walter, *J. Polymer Sci.* **44**, 349 (1960).

¹² A. J. Kovacs, *Ricerca sci.* **25**, 668 (1955).

¹³ M. Gubler and A. J. Kovacs, *J. Polymer Sci.* **34**, 551 (1959).

¹⁴ P. R. Swan, *J. Polymer Sci.* **42**, 525 (1960).

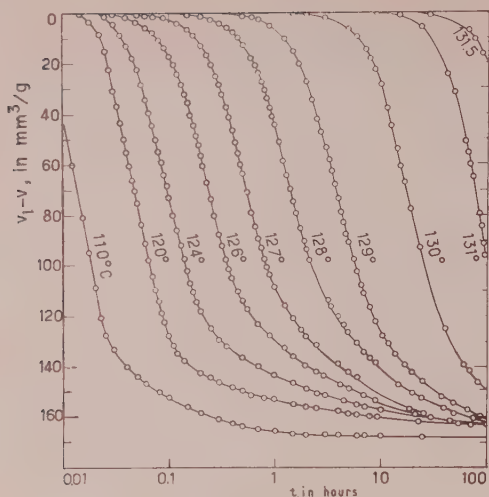


FIG. 1. Crystallization isotherms of sample $M_{2p}(91.6)$ at different (indicated) temperatures after quenching the melt from $T_0 = 175^\circ\text{C}$.

is even smaller for polymer M_1 , but more important for the M_p , and still more for the M_f samples. At the same time there is a slight increase of the inflexional tangent; $(\tilde{\beta}) = -(dx/d \ln t)_{\max}$, of the crystallization isotherms with increasing T_0 or t_0 .

The changes in $t_{0.5}$ and $(\tilde{\beta})$ are irreversible. If large values of $t_{0.5}$ and $(\tilde{\beta})$ are obtained after "severe" melting conditions, for instance at high T_0 and after a long duration of melting, a subsequent "light" melting at 150°C during 10 min will maintain the previous large values of these parameters. If this irreversible behavior had occurred from chemical degradation, the effect of identical melting conditions would be quite similar for M_2 and the M_{2f} samples, which is definitely not the case.

In fact these observations may be explained by assuming more or less heterogeneous nuclei in the melt, which can be removed to some extent when T_0 and t_0 are increased greatly. One can expect also that the effect of severe melting will be much larger when the initial concentration of the quasi-indestructible, heterogeneous nuclei is greater. This assumption is well supported by the above experimental evidence and also by the quantitative comparison of the different crystallization isotherms, which will be discussed later.

Influence of Preorientation

In Fig. 2 some M_{2f} samples are compared with the original M_2 polymer at 126°C . All these samples have been melted at 160°C several times so that there is no more macroscopic sign of the original sheets left; however, the shape of the crystallization isotherms varies in a continuous manner with the original thickness, i.e., with the amount of orientation induced by the

molding process. Both the inflexional tangent $\tilde{\beta} = (dx/d \ln t)_{\max}$ and the half-time $t_{0.5}$ are decreased with increasing preorientation, but the limiting value of x are only slightly affected. One can conclude on the basis of the above discussion that the orientation of the melt (at 180°C) results in an increase in the number of heterogeneous nuclei, which are quite stable during several light meltings. In fact, when severe melting conditions are used ($T_0 > 180^\circ\text{C}$), the difference between the M_{2f} samples and M_2 may completely vanish. This suggests that the stability of the nuclei originated by this molding process is limited below the temperature at which the initial orientation of the melt was performed.

Influence of the Sintering Process

In Fig. 3, polymers M_1 and M_2 are compared with two M_{2p} samples at 126°C . In this case not only the values of $\tilde{\beta}$ and $t_{0.5}$ are different but also the limiting crystallinity ratio $x_m = (v_l - v_m)/(v_l - v_c)$, where v_m is the specific volume at the end of the crystallization evaluated from a reasonable extrapolation.

Differences in x_m may occur from slightly different molecular weight distributions. If one assumes that the low MW fractions do not contribute to the crystallization at 126°C , one can explain that the $M_{2p}(91.6)$ sample, from which these fractions were removed, reaches higher crystallinity. On the other hand, samples $M_{2p}(95-70)$ and M_2 are quite close with respect to their x_m values; this is consistent with the much lower limit of T_p (70°C), for which presumably the fractionation effect is negligible.

The shape of isotherms with different x_m may better be compared when the "reduced" crystallinity ratio $z = x/x_m = (v_l - v)/(v_l - v_m)$ is plotted, rather than x , as a function of $\log t$. The parameter z has the further advantage of eliminating the somewhat uncertain

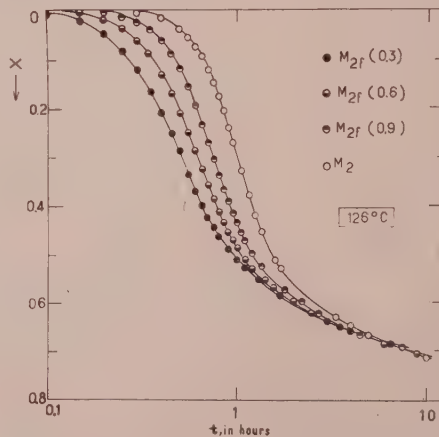


FIG. 2. Comparison of the crystallization isotherms of samples M_{2f} and M_2 at 126°C , ($T_0 = 160^\circ\text{C}$).

values of $(v_l - v_c)$, for it includes only the experimentally estimated value of v_m .

Crystallization isotherms of sample $M_{1p}(83)$ are fairly superposable to those of $M_{2p}(91.6)$, although the initial polymers M_1 and M_2 have different values of $\beta_z = \beta_z/x_m$. This means that the change in shape of the crystallization isotherms of a polymer is essentially related to the particular method of the sample preparation, rather than to the intrinsic properties of the starting product.

From the small β_z and $t_{0.5}$ values of the M_p samples one can conclude that the precipitation from dilute solution and the subsequent sintering increase, like the melt orientation, the number of quasi-indestructible nuclei. Furthermore, these nuclei are even more stable than in the preoriented M_{2f} samples, for severe melting conditions produce a much smaller effect on them.

Since the precipitated powder is composed mainly of diamond-shaped lamellar aggregates, it is reasonable to assume that the remaining nuclei in the melt have the same shape, and consequently they induce a similar growth in the bulk. In fact, steplike organizations of lamellae are commonly observed on free surfaces of bulk polyethylene.^{15,16}

DISCUSSION

Isothermal crystallization is mostly interpreted quantitatively in terms of Avrami's theory,² which has been simplified by Evans¹⁷ and Morgan¹⁸ and adapted to incomplete crystallization of polymers by Mandelkern.¹ The final expression, when formulated in terms of reduced crystallinity z , may be written

$$z = 1 - \exp(-Bt^n), \quad (1)$$

which contains only two parameters. B is the "time-scale parameter" related to $t_{0.5}$ and depends on the temperature of the experiment. The exponent n depends

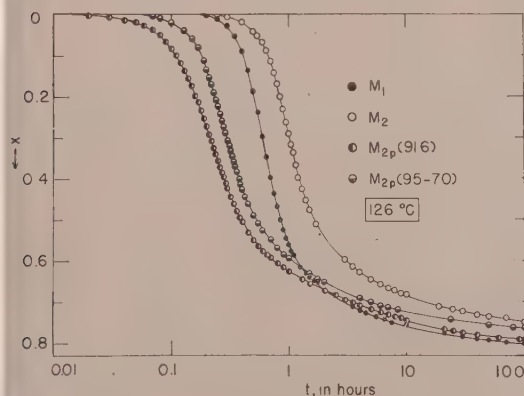


FIG. 3. Comparison of the crystallization isotherms of M_1 , M_2 , and two M_{2p} samples at 126°C ($T_0 = 175^\circ\text{C}$).

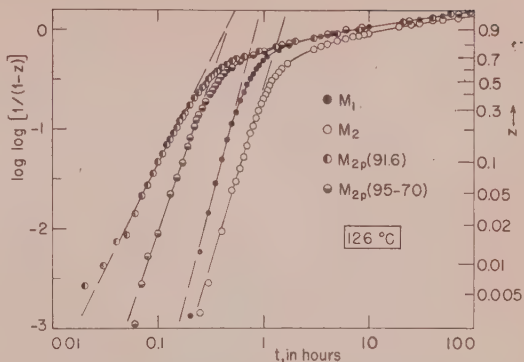


FIG. 4. Avrami's plot for isotherms of Fig. 3.

on the nature of the nuclei and the geometry of their growth,^{2,17,18} and it is related to β_z so that it may be considered as the "shape factor" of crystallization isotherms.

Figure 4 illustrates the comparison of the four curves shown in Fig. 3. According to expression (1), since

$$\log \log \frac{1}{1-z} = \log \frac{B}{2.303} + n \log t, \quad (2)$$

one may expect to obtain straight lines in Fig. 4 with a slope of n . In fact only the initial range of the crystallization process ($z < 0.3$) fits such a straight line, but when z is approaching 1 the exponent n (or alternatively, $\log B$) decreases rapidly to about one-tenth of its initial value. This discrepancy can be improved if one adopts for x_m a definitely smaller value than that of the one experimentally observed, i.e., if only some part of the rapid primary process is taken into consideration.

The only agreement in the literature between the theoretical expression (1) and experiments was obtained by such a procedure which assumes implicitly that two more or less overlapping processes are involved in the isothermal crystallization. Since the final stage of the process does not obey Avrami's treatment, one needs to introduce some additional parameter besides n and B .

We suggested in a previous paper³ that this final stage might be controlled by the rapidly decreasing mobility of the polymer segments for slipping one along the other, when some parts of the molecule are engaged in different, independent crystalline units. This decrease of mobility may result in an excessively high bulk viscosity comparable to that of supercooled liquids near the glass transition temperature. In that case, the volume contraction will no longer be controlled by the primary crystallization process but by the volume flow. This assumption is consistent with the genesis of voids and cracks in polymers of high crystallinity, which have been observed by several authors.^{19,20}

¹⁵ E. W. Fischer, Z. Naturforsch. **12a**, 753 (1957).

¹⁶ C. Sella and J. J. Trillat, Compt. rend. **248**, 410 (1959).

¹⁷ F. U. Evans, Trans. Faraday Soc. **41**, 365 (1945).

¹⁸ L. B. Morgan, Phil. Trans. Roy. Soc. London **A247**, 13 (1954).

¹⁹ F. J. Padden, Jr. and H. D. Keith, J. Appl. Phys. **30**, 1479 (1959).

²⁰ Shiro Matsuoka, Bull. Am. Phys. Soc. **116**, 171 (1961).

We attempted to find some empirical relationship which could describe the whole range of crystallization. Starting from the experimental fact that the crystallization isotherms of homopolymers are superposable when shifted along the $\log t$ axis¹ (allowing a slight temperature dependence of x_m , depending on the MW distribution), we can write, for the reduced crystalline ratio z ,

$$\beta_z = -\frac{dz}{dt} = \varphi(z) \quad (3)$$

From Avrami's expression we have

$$\begin{aligned} x_1 - z &= n(1-z) \ln \frac{1}{1-z} \\ &= n(1-z) \left(z + \frac{z^2}{2} + \cdots + \frac{z^j}{j} + \cdots \right) \end{aligned} \quad (4)$$

Assuming $\varphi(z)$ to be some incomplete polynomial of degree j ,

$$\varphi_j(z) = a_0 + a_1 z + a_2 z^2 + \cdots + a_j z^j, \quad (5)$$

one can calculate the coefficients a_i from j independent values of the experimentally measured β_z function. By using only the limiting conditions $\varphi(z)=0$, $z=0$, and $z=1$, we have a polynomial of second degree with $a_0=0$, $a_1=-a_2=K$, which can be written

$$\varphi_1(z) = K(1-z)z. \quad (6)$$

This expression is quite similar to expression (4) for small values of z , i.e., when Avrami's expression seems to be applicable. Consequently the constant K may be

interpreted as n . The integral form of $\varphi_1(z)$ leads to a expression

$$\Phi_1(z) \equiv \log \frac{z}{1-z} = K \log \frac{t}{t_{0.5}}, \quad (7)$$

which was originally proposed by Austin and Rickett²¹ for the isothermal transition of austenite into bainite and reported by Avrami²² as experimental evidence for his theoretical treatment. The same expression has also been theoretically established by Lin.²²

Equation (6) can be converted into the form

$$\beta_x = \beta_z x_1 = x_1 \varphi_1(z_1) = K \frac{x}{x_1} (x_1 - x), \quad (8)$$

(where x_1 is the limiting value of x for these kinetics) and compared with the values of β_x , calculated directly from the measured increase of x for small logarithmic intervals of time (rather than from the tangents of smoothed crystallization curves).

Figure 5 shows, for polymer M_1 , that the experimental points support fairly well the above parabolic expression in the range of $x < 0.6$. The full line of this figure was calculated from expression (8) with $K=3.8$ and $x_1=0.67$. Above this value of x there is a definite departure, which means that higher terms must be taken into consideration. Nevertheless, this simple expression describes the experimental behavior in a more extended range of x than did Avrami's formula. On the other hand, the value of x_1 to be used in the computation (which is here only a fraction of the limiting crystallinity ratio x_m) may be easily obtained from the abscissa of the vertical axis of the β_x parabola (Fig. 5), and so it involves a less arbitrary procedure than the estimation of x_m .

Another expression of (5) including third-order terms without any additional parameter may be written

$$\varphi_2(z) = K' z(1-z)^2, \quad (9)$$

in which K' may be compared to n for small values of z . The corresponding expression of β_x , shown by dashed lines in Fig. 4, with $K'=5.2$ and $x_m=0.83$, fits the experimental points fairly well over the whole range of measurements. However, this value of K' is too great to be interpreted in terms of Avrami's theory.

These empirical formulas and their consequences have been discussed in previous papers,^{3,4} and have been used with success for other types of isothermal crystallization than the one performed from the melt.

Whatever the case may be, it seems convenient to compare, for the different samples investigated, the values of n or K which govern the main part of the autocatalytic crystallization.

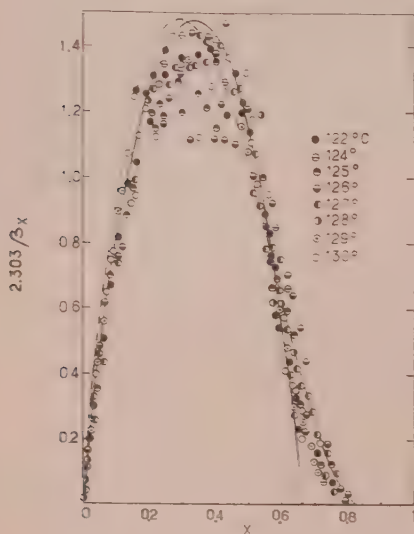


Fig. 5. Comparison of measured and calculated values of the slopes, $\beta_z = dz/d \ln t$, for crystallization isotherms of polymer M_1 . Solid line: $\beta_z = 3.8(x/0.67)(0.67-x)$; dashed lines: $\beta_z = 5.2 \times (x/0.69)(0.83-x)^2$.

²¹ J. B. Austin and R. L. Rickett, *Metals Technol.* (September, 1938) (from reference 2).

²² Tung-Po Lin (private communication).

The values of K may be calculated easily in three different manners⁴:

(a) from the value of $\tilde{\beta}_{z_1}$, when $\varphi_1(z_1)$ has its maximum ($z_1 = 0.5$), we have

$$\tilde{\beta}_{z_1} = \tilde{\beta}_x / x_1 = K/4; \quad (10)$$

(b) from the slope of straight lines obtained by plotting $\Phi_1(z_1)$ vs $\log t$ (Fig. 6),

$$d\Phi_1/d \log t = K; \quad (11)$$

(c) from the measure of the maximum rate of crystallization, $u_\gamma = (dz/dt)_{\max}$, and the time t_γ when this occurs. It can be shown from Eq. (6) that

$$u_\gamma t_\gamma = (K^2 - 1)/4K. \quad (12)$$

Table II shows the different values of K and n for some of the samples investigated at 126°C.

It can be seen that the values of K , calculated in two different manners, are fairly close to that of the Avrami's exponent. According to the theoretical meaning of n , one can now discuss the experimental data more accurately.

TABLE II.

Sample	x_1	K		x_m	n
		Eq. (10)	Eq. (11)		
M_1	0.67	3.8	3.9	0.83	4.0
M_2	0.62	3.6	3.7	0.78	3.6
M_{1p} (83)	0.67	2.1	2.2	0.83	...
M_{2p} (91.6)	0.66	2.2	2.3	0.82	2.1
M_{2f} (0.3)	0.60	2.8	...	0.76	...
M_{2p} (95-70)	0.63	2.8	2.9	0.79	3.0

Fractional values of n between 3 and 4, generally found for linear PE, are usually interpreted²³ in terms of tridimensional (spherulitic) growth from both heterogeneous ($n=3$) and homogeneous ($n=4$) nuclei. This should be the case of polymer M_2 . However, values less than 3 not yet reported to our knowledge for PE, which were definitely found for most of the M_{2p} samples, have to be explained by some sheetlike, two-dimensional growth from more or less heterogeneous nuclei. In fact, $n=3$ may be derived both from tridimensional or laminar growth, from, respectively, heterogeneous or homogeneous nuclei. Table II shows also that some of the samples investigated have n values very close to $4(M_1)$ and $2(M_{1p})$, though prepared from the same polymer. This result suggests that both tri- and bidimensional growth may occur in PE samples²⁴ from, respectively, pure homogeneous or heterogeneous nuclei. Therefore, intermediate values of between 2 and 4 may cover a wide variety of mixed

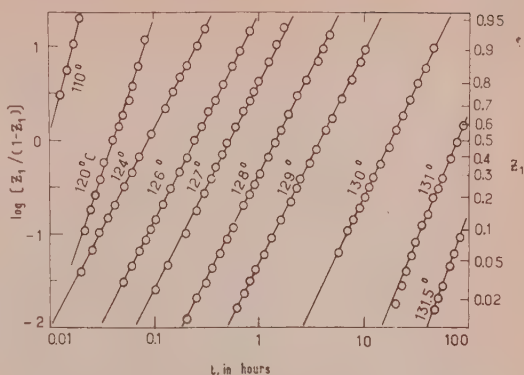


Fig. 6. Plot of $\log [z_1 / (1 - z_1)]$ versus $\log t$ for isotherms of sample M_{2p} (91.6); Fig. 1.

crystallization processes, which cannot be interpreted in an unequivocal manner without further information obtained with other methods of investigation.

Preliminary dilatometrical measurements of isothermal crystallization in dilute solutions (from 0.25 to 3% of polymer) show that,⁷ for a given concentration, the value of K may vary also from 4 to 2 when the temperature of crystallization is increased. This peculiar behavior will be discussed in a subsequent paper.

CONCLUSIONS

(1) The crystallization kinetics of linear polyethylene is very sensitive to the past molding and melting history of the sample.

(2) When the sample preparation involves orientation (of the melt) or folding of chain molecules¹⁰ a great many predetermined nuclei may be originated. Their destruction requires severe melting at high temperature for over a long period of time. This means clearly that the melted polymer is not necessarily in a true thermodynamic equilibrium, and it includes some organized clusters. The concentration, stability, and structure of these clusters depend mainly on the past history of the sample.

(3) These quasi-indestructible clusters, which behave as heterogeneous nuclei, must be quite different from the homogeneous nuclei which may occur during the crystallization process (whether isothermal or not). In fact the latter, if they exist at all, are easily removed above the melting temperature, as can be seen from the fair reproducibility of duplicate experiments after light melting.

(4) The crystallization process from the melt as detected by dilatometrical studies and interpreted from Avrami's theory involves, in general, tri- and bidimensional growth both from homogeneous and heterogeneous nuclei, so that the over-all structure may vary in wide limits. Some of these alternative structures may be favored by appropriate treatments of the sample.

²³ L. Mandelkern in *Growth and Perfection of Crystals* edited by H. Doremus, B. W. Roberts, and D. Turnbull (John Wiley & Sons, Inc., New York, 1958), p. 467.

²⁴ For some different crystallization techniques even $n \approx 1$ was found. See also reference 3.

(5) Except for a few ideal cases, dilatometric studies cannot give unequivocal information on the structure obtained. Nevertheless, this technique is extremely sensitive to any variation in the crystallization process.

ACKNOWLEDGMENTS

This work was partly supported by a grant from the National Science Foundation. We are much indebted to Professor J. D. Ferry for valuable discussions.

Origins of Characteristic Bands in the Infrared Spectra of Isotactic Polystyrene and Isotactic Poly (Ring- d_5 Styrene)

T. ONISHI AND S. KRIMM

Harrison M. Randall Laboratory of Physics, University of Michigan, Ann Arbor, Michigan

The origins of characteristic bands in the infrared spectrum of isotactic polystyrene have been studied with the aid of the spectrum of isotactic poly (ring- d_5 styrene). It is found that these bands can be classified into three types according to their experimental behavior upon crystallization of the specimen. Assignments show that the bands in any one group are associated with a specific kind of normal vibration, either of the chain or of the benzene ring. Analysis of one of these band types indicates that rotational disordering of the benzene rings may occur, and that crystallization of the polymer is probably correlated with the growth of regions which maintain statistical variability at the local chain level.

INTRODUCTION

A NUMBER of studies on the infrared spectrum of isotactic polystyrene, IPS, has been reported.¹⁻⁵ These indicate that certain characteristic band changes are associated with the transition from the atactic to the isotactic polymer, band changes which are presumably correlated with the appearance of a helical chain conformation in the stereoregular polymer. It appears further^{2,4} that the spectral changes are of a few distinct types, involving the appearance, frequency shift, or splitting of bands. Band assignment studies on polystyrene have been carried out,^{6,7} and have yielded preliminary information on the nature of the normal modes associated with the above bands. In order to use the infrared spectrum to investigate the physical changes which are associated with the introduction of configurational regularity in a polymer chain, it is clearly desirable to have a more detailed understanding of these band changes. To further this aim, we have undertaken the preparation of isotactic poly (ring- d_5 styrene), IPR d_5 S, and the analysis of its infrared spectrum.⁸ We discuss here the information which this study provides on the origins of the characteristic infrared bands of isotactic polystyrene.

EXPERIMENTAL

The isotactic polystyrene used in this study was a commercial sample. It was examined in the quenched state (heated to about 240°C and quenched in cold water) and in the crystalline state (obtained by heating at 180°C for 30 minutes). Oriented specimens were produced by stretching a film in hot water at 95°C over a period of several hours.

The isotactic poly (ring- d_5 styrene) was synthesized as follows. Acetic acid anhydride was added to a mixture of benzene- d_5 (99% deuterated) and anhydrous AlCl₃ in CS₂. The reaction mixture was poured into cold aqueous HCl, and acetophenone- d_5 was distilled from an ether extract. This was reduced to the methylphenyl carbinol- d_5 by reaction with LiAlH₄ in ether. The carbinol was dehydrated to styrene- d_5 using activated alumina as a catalyst in flowing N₂ at about 300°C. The resulting styrene- d_5 was examined in a mass spectrometer and found to consist of at least 95% of the ring deuterated species. The styrene- d_5 was polymerized with a Ziegler type catalyst,⁹ and the isotactic polymer obtained after a methyl ethyl ketone and *n*-heptane extraction. The melting point of the isotactic polymer was 220°C.

An x-ray diffraction pattern was obtained of a oriented sample of IPR d_5 S. It is shown in Fig. 1, together with the diffraction pattern of oriented IPS. The fiber axis repeat of the deuterated polymer was found to be 6.65 Å. Since this is the same as that of the ordinary polymer, and since the intensity distribution in the diffraction pattern is also essentially the same, we can assume that the structure of IPR d_5 S is the same as the threefold helical structure of IPS.¹⁰

¹ H. Tadokoro, N. Nishiyama, S. Nozakura, and S. Murahashi, *J. Polymer Sci.* **36**, 553 (1959); *Bull. Chem. Soc. Japan* **34**, 381 (1961).

² H. Tadokoro, S. Nozakura, T. Kitazawa, Y. Yasuhara, and S. Murahashi, *Bull. Chem. Soc. Japan* **32**, 313 (1959).

³ M. Takeda, K. Iimura, A. Yamada, and Y. Imamura, *Bull. Chem. Soc. Japan* **32**, 1151 (1959).

⁴ M. Takeda, K. Iimura, A. Yamada, and Y. Imamura, *Bull. Chem. Soc. Japan* **33**, 1219 (1960).

⁵ D. Morero, E. Mantica, F. Ciampelli, and D. Sianesi, *Nuovo cimento Suppl.* **15**, 122 (1960).

⁶ C. Y. Liang and S. Krimm, *J. Polymer Sci.* **27**, 241 (1958).

⁷ S. Krimm, *Fortschr. Hochpolym.-Forsch.* **2**, 51 (1960).

⁸ T. Onishi and S. Krimm (to be published).

⁹ C. G. Overberger and H. Mark, *J. Polymer Sci.* **35**, 381 (1959).

¹⁰ G. Natta, P. Corradini, and I. W. Bassi, *Nuovo cimento Suppl.* **15**, 68 (1960).

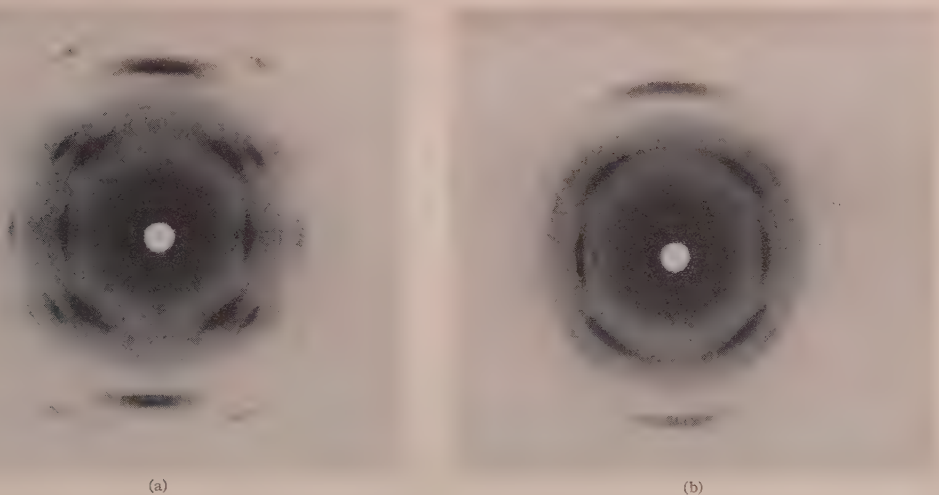


Fig. 1. X-ray diffraction patterns of oriented isotactic (a) polystyrene and (b) poly (ring-d₅ styrene).

Infrared spectra of quenched, crystallized, and oriented samples of IPS and IPRd₅S were obtained with Perkin-Elmer Model 21 spectrometer with NaCl and KBr prisms and a Perkin-Elmer Model 12 spectrometer with CsBr and CsI prisms, a AgCl polarizer being used for the dichroism studies. Spectra of quenched and crystallized polymers are compared in Fig. 2, and polarized spectra are shown in Fig. 3.

RESULTS

As can be seen from Fig. 2, several characteristic types of band changes occur in the infrared spectra of both

IPS and IPRd₅S when the quenched and crystallized samples are compared. Some of the differences are even more prominent when these spectra are compared with those of the atactic polymers. A classification of the various types of bands which change from the atactic through the crystalline isotactic polymer has been given.^{3,4} We have found that this particular classification, while setting out many of the important differences in band behavior, is not entirely satisfactory. Furthermore, we find that a somewhat different basis for classifying these bands is more revealing of their origin. We therefore define the following band classes:

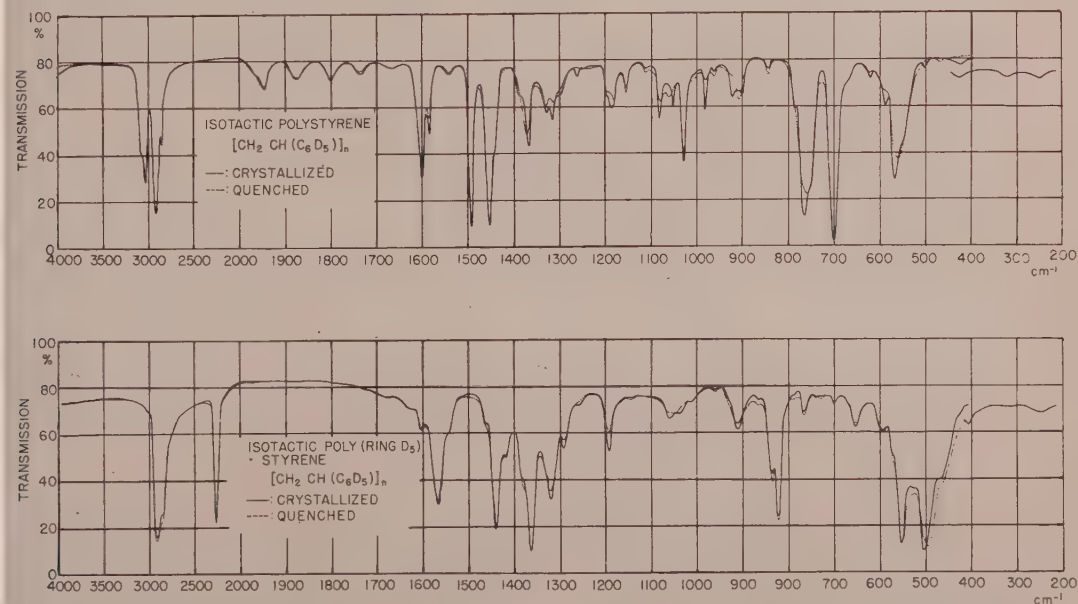


Fig. 2. Infrared spectra of unoriented crystallized and quenched isotactic (a) polystyrene and (b) poly (ring-d₅ styrene).

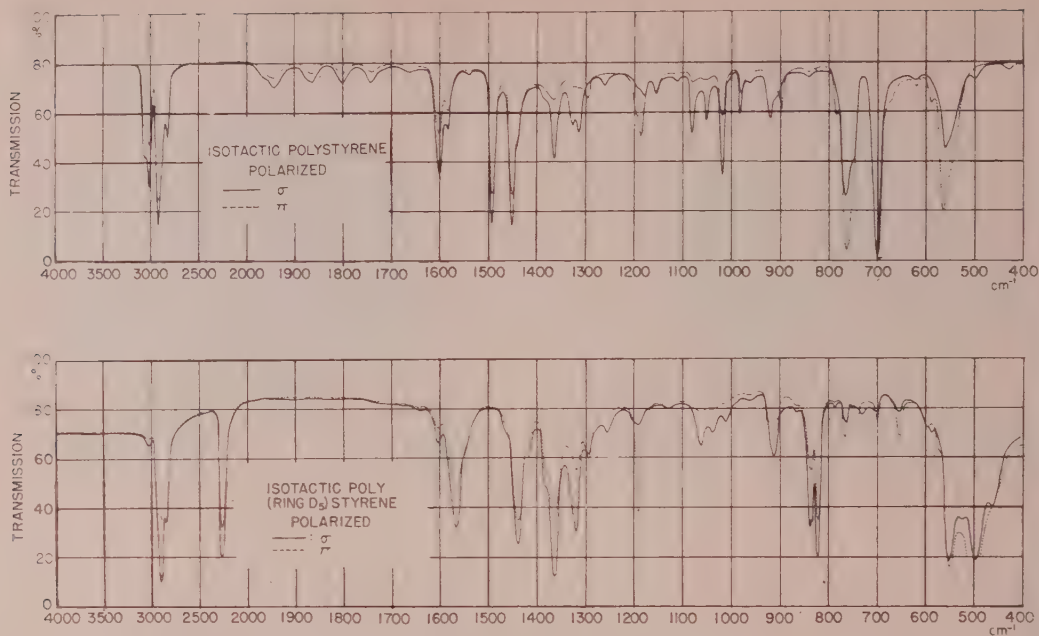


FIG. 3. Polarized infrared spectra of oriented isotactic (a) polystyrene and (b) poly (ring- d_3 styrene).

Type I. Bands which are weak or absent in atactic polystyrene, and which increase significantly in intensity in the crystalline stereoregular polymer, in some cases also accompanied by slight frequency shifts. These bands exhibit σ or π dichroism, with no detectable frequency separation between the σ and π components of a given band.

TABLE I. Band types and assignments for characteristic bands in isotactic polystyrene and isotactic poly (ring- d_3 styrene).

	IPS			IPRd ₃ S			Assignment ^a
	A ^a	Q	C	A	Q	C	
Type I	1373	1370	1365σ	1366 ^b	1365	1365σ	δ(CH)
	...	1298	1297π	1295	1291	1293π	γ ₁ (CH ₂)
	1260σ	...	1253	1265σ	ν(CC)E?
	1187π	1191π	ν(CC) _A
Type II	1312 ^d		1314σ			1061σ	
			...	1050		1037σ	ν' ₃ (B ₁)E
		1078	1082σ			839σ	
	1070			837			ν' _{18B} (B ₁)E
		1060	1051σ			835σ	
Type III			983σ			925π	ν ₆ (B ₂) _A
	982	982	982π	915	915	913σ	ν ₆ (B ₂) _E
			920σ			742π	ν' _{17B} (B ₂) _A
	906	906		735	735	730σ	ν' _{17B} (B ₂) _E
			897π			655π	ν' _{10B} (B ₂) _A
			766σ				
	757	758	764π	655	655	654σ	ν' _{10B} (B ₂) _E
			700σ			553σ	ν' ₁₁ (B ₂) _E
	700	700		549	553		
			699π			552π	ν' ₁₁ (B ₂) _A
			566π			501π	ν' ₄ (B ₂) _A
	542	558		486	496		
			562σ			496σ	ν' ₄ (B ₂) _E

^a A: atactic, Q: quenched isotactic, and C: crystalline isotactic.

^b Probably overlapped by a deuterated ring mode.

^c ν = stretching, δ = bending, and γ_2 = twisting.

^d At 1300 cm⁻¹ in IPTdS (Q), and 1303 cm⁻¹ and 1292 cm⁻¹ in IPTdS (C).

Type II. Bands which do not necessarily increase in intensity, but do split into two σ components upon crystallization. Their most important characteristic is that the frequency separation between the component increases with increasing crystallinity of the isotactic polymer.

Type III. Bands which may change slightly in intensity or frequency on crystallization, but whose main characteristic is a splitting into two components, one with σ dichroism and the other with π dichroism.

The frequency of the bands which fall into these classes are shown in Table I for various states of the two polymers. The assignments indicated in the table are discussed below in terms of approximate normal modes of the polymer chain, those of the benzene ring portion being shown in Fig. 4. The interesting result which emerges from the analysis of the above experimental classifications is that each type of band is associated with a specific group of normal vibrations of the molecule, type I being associated with vibrations of the CH₃ and CH₂ groups and probably also the chain skeleton; type II with the B₁ species hydrogen ring vibrations; and type III with the out-of-plane modes of the ring.

Type I Bands

Bands in this class, as we have noted, are characterized by a significant increase in intensity upon crystallization. As will be seen from Table I, they are present in both IPS and IPRd₃S, thus indicating that they may be correlated with the non-ring portion of the molecule. Assignments for these bands are aided by reference to

the assignments for polystyrene⁷ and some of its other deuterated analogues.^{1,11} Thus, the 1365 cm^{-1} σ band is readily assigned to the $\delta(\text{CH})$ mode, on the basis of its disappearance in isotactic poly- α_1 -styrene,¹¹ IPRd₅S, and its presence in IPRd₅S. We infer its presence in the latter polymer from the fact that the band at this position, which is expected to arise from the shifted ring vibration at 1452 cm^{-1} in IPS, is more intense in comparison with the 1440 and 1570 cm^{-1} bands than is the 1452 cm^{-1} band in comparison with the corresponding 1493 and 1601 cm^{-1} bands of IPS. In fact, in IPRd₅S there are two components to this band, one at 1365 cm^{-1} and the other at 1381 cm^{-1} . The π band at 1297 cm^{-1} is most reasonably assigned to $\gamma_t(\text{CH}_2)$ on the basis of its position (cf. this mode in polyethylene),⁷ its polarization, and its appearance in the spectra of IPRd₅S and IPRd₅S, but absence from the spectrum of isotactic poly- α,β,β -tri-deuterostyrene,¹ IPTdS. It probably shifts to 945 cm^{-1} in the spectrum of the latter polymer; the shift ratio of 1.37 further supports this assignment, in view of the shift ratios of 1.33, 1.33, and 1.36 for $\nu_s(\text{CH}_2)$, $\delta(\text{CH}_2)$, and $\nu_s(\text{CH}_2)$, respectively.¹² The origin of the σ band at 1260 cm^{-1} is not clear. It is present in IPS, IPRd₅S (at 1256 cm^{-1}), and in IPTdS (at 1250 cm^{-1}). It could quite possibly be one of the skeletal modes of the helix. The π band at 1187 cm^{-1} seems quite likely to be assignable to a skeletal vibration on the basis of normal vibration calculations for threefold helical

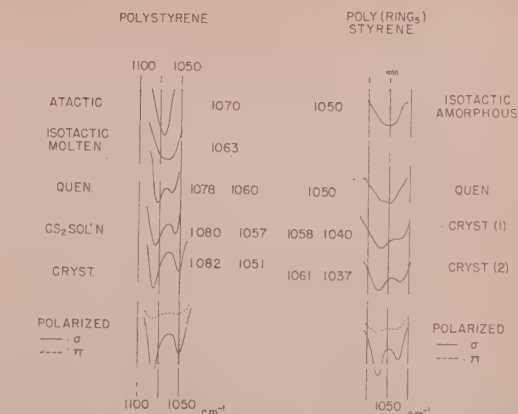


Fig. 5. Splitting in type II bands as a function of crystallinity for isotactic polystyrene and poly (ring- d_5 styrene)

vinyl polymers.¹³ Its presence in all of the deuterated species is consistent with this assignment. Its dichroism indicates that it belongs to the A symmetry species of the helical chain.⁷ The type I modes therefore are seen to be correlated with CH, CH₂, and skeletal vibrations.

2. Type II Bands

The prime example of a type II band is that at 1070 cm^{-1} in atactic polystyrene. This band is split in the isotactic polymer, even when in solution.⁴ As the extent of crystallization increases, the splitting increases up to a maximum of 31 cm^{-1} . Some of these changes are shown in Fig. 5, where it will be noted that both components show σ dichroism. Examination of the spectrum of IPRd₅S indicates that these bands have moved to about 837 cm^{-1} ; the latter, at 835 and 839 cm^{-1} in the crystalline polymer, also manifest increased splitting with crystallization. The frequency shift on deuteration is consistent with the assignment⁷ of these bands to the ring mode most closely related to $\nu_{18}(\text{B}_1)$. We have called this $\nu'_{18\text{B}}(\text{B}_1)_\text{E}$, where the subscript E indicates that it belongs to the E symmetry species of the helical chain.⁷ As will be seen from Fig. 5, the spectrum of IPRd₅S shows a group of bands of similar behavior near 1050 cm^{-1} . We believe that this group can be traced to bands near 1300 cm^{-1} in IPS. In IPTdS there is a band at 1300 cm^{-1} in the quenched material which begins to split into components at 1303 and 1292 cm^{-1} upon crystallization.¹ In IPS these bands are not as clearly defined, but it appears that the band at 1312 cm^{-1} , moving to 1314 cm^{-1} on crystallization, can be correlated with this group. The situation is complicated somewhat by the presence of the 1328 cm^{-1} band, which seems to correlate with the 1330 cm^{-1} band of IPTdS. Our interpretation is that these two bands are associated with the ν_8 and ν_{14} modes, found at 1350 and 1309 cm^{-1} ,

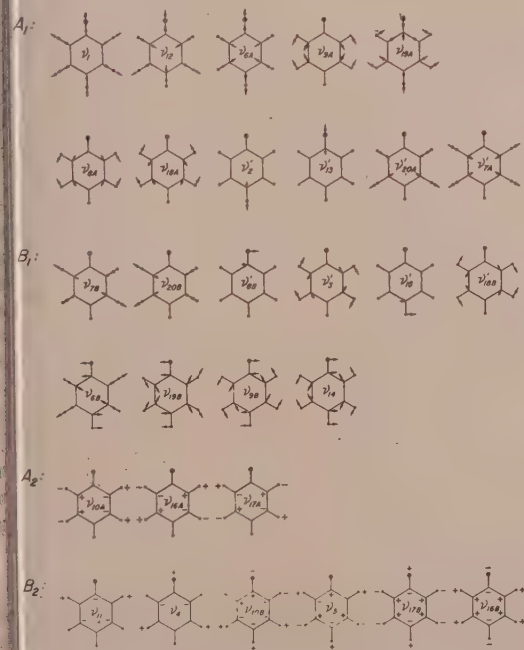


Fig. 4. Approximate normal modes of monosubstituted benzene.

¹¹ M. Kobayashi, Bull. Chem. Soc. Japan **33**, 1416 (1960).
¹² S. Krimm, J. Chem. Phys. **32**, 1780 (1960).

¹³ T. Onishi and S. Krimm, Symposium on Molecular Structure and Spectroscopy, Columbus, Ohio, June, 1961.

respectively, in benzene,¹⁴ and that whereas the ring deformation mode (ν_{14}) moves from 1330 cm^{-1} to 1320 cm^{-1} (in IPRd₅S), the hydrogen deformation mode (ν_8) moves from about 1300 cm^{-1} to 1050 cm^{-1} (in IPRd₅S). In IPS there may be some interaction between these various vibrations which results in a slight change in these frequencies, viz., to 1328 and 1312 cm^{-1} . The type II bands therefore arise from the B_1 species hydrogen ring modes and result in E species chain modes which split progressively on crystallization.

3. Type III Bands

The bands which are listed in Table I under type III all exhibit the characteristic of splitting into σ and π pairs upon crystallization. They have been assigned⁷ to out-of-plane ring modes, and the frequency shifts observed in going from IPS to IPRd₅S bear out these assignments. It should be observed that whether the modes indicated by a prime are as shown in Fig. 4 or are closer in form to the (unprimed) modes of benzene cannot be ascertained at present. The modes shown in Fig. 4 represent only a plausible approximation to the possible forms of monosubstituted benzene modes. The splitting of these bands indicates that for the B_2 ring modes the interaction between units along the helix is sufficiently large to give different frequencies for the A and the E chain modes. This was not observed to be true of the types I and II bands.

DISCUSSION

These results raise several questions about the underlying basis of the infrared spectral changes, to which only partially complete answers can be given at present. A detailed understanding will result only from a complete vibrational analysis of the polystyrene spectrum. We will attempt here to consider only the possible plausible bases for the observed effects.

Before doing this, it is necessary to consider the kinds of changes which might be expected in the infrared spectrum as a result of a change from an atactic to an ordered isotactic polymer. These can be of three kinds. First, there may be configurational isomer effects, such as *gauche* or *trans* configurations about neighboring bonds, which influence the local normal mode of a portion of the molecule. This could give rise to frequency shifts, intensity changes, or to the appearance of new bands. Second, the isotactic configuration could result in the formation of a regular chain structure, such as the threefold helix in the present case, whose symmetry then affects the spectrum. For example, the interactions between monomer units in one repeat of the helix can give rise to splittings in some of the normal frequencies and to the appearance of additional skeletal vibrations. It should be noted that this corresponds to a kind of one-dimensional crystallization and could quite con-

ceivably occur in solution or in a quenched polymer sample over short lengths of the chain. Third, if the increased one-dimensional order permits the growth of three-dimensionally ordered, or crystalline, regions, then interchain interactions may occur with effects somewhat similar to those for the one-dimensionally ordered case. The problem is to distinguish between these effects in the case of polystyrene.

The behavior of the type III bands upon crystallization is most readily understood in terms of the formation of helical chain segments. For such structures we expect that the normal vibrations will divide up into A species with transition moment parallel to the helix axis, and E species with transition moment perpendicular to the helix axis. If the interaction between units along the chain is large enough, the A and E chain modes corresponding to a given normal mode within one unit will occur at slightly different frequencies. This appears to happen for the out-of-plane type ring vibrations in polystyrene, although why it is observed for these modes and not any others is not completely clear. It probably implies that interaction for such essentially out-of-plane modes is greater between units in the chain than for the other types of normal vibrations of the monomer unit.

It is important to note in this connection that not all of the type III bands, although associated with out-of-plane ring modes, must be thought to be pure benzene ring modes. The evidence indicates that many of them are probably mixed in nature. For example, although the 700 and 757 cm^{-1} bands of IPS are well assigned to B_2 species ring modes, they nevertheless show different dichroic ratios. Measurements which we have made on thin oriented films, about 0.0002 in. thick, show that the parallel dichroism of the 757 cm^{-1} band is greater than that of the 700 cm^{-1} band by a factor of about 1.85 . Since the orientation distribution cannot produce such an effect in a single sample, it follows (unless the bands are composite, for which there is no evidence) that the transition moments of the two vibrations involved cannot be exactly parallel to each other. The mixed character of some of these out-of-plane vibrations may account for the fact that, although all B_2 ring modes should give rise to stronger π than σ absorption, this is not the case for two of the bands, viz., those at 982 and at 906 cm^{-1} .

In the case of the type I bands, in which significant intensity changes occur on crystallization, the origin of the changes is not in all cases clear. Of course, for the skeletal modes associated with the helical structure the enhanced intensity of such bands in the more highly crystalline material is understandable. The 1187 cm^{-1} band and possibly that at 1260 cm^{-1} appear to belong in this category. The origins of the intensity changes in the 1365 and 1297 cm^{-1} bands are less certain. These effects may arise from the altered form of the normal mode in the helical chain or from a general environmental effect involving coupling with other vibrations. There is no evidence to suggest that these bands are

¹⁴ S. Brodersen and A. Langseth, *Mat. Fys. Skr. Dan. Vid. Selsk.* **1**, 1 (1956).

associated with local isomeric forms of the groups involved.

The behavior of the type II bands is the most puzzling of all. The symmetry analysis⁷ would allow a progressive splitting of a band with, for instance, increasing helix length, but only into A and E modes, i.e., one π and one σ component, not into two σ bands. The latter might occur if another normal mode associated with the helix were to interact with the B_1 ring modes to which we assign these bands. However, both on the basis of the shift of the 1070 cm^{-1} doublet to a doublet at 837 cm^{-1} and the existence of two such groups of bands in different frequency regions, we are inclined to discount this explanation. Another possibility is that the splitting arises from interaction between neighboring chains. In the determination of the crystal structure¹⁰ it has been noted that a statistical variability in chain conformation and direction may occur such that neighboring chains are or are not related to each other by a center of symmetry. This would suggest the possibility of different frequencies resulting from the distinct interactions associated with these two locally different structures, perhaps accounting for the observed splitting. The difficulty with this explanation is that we are hard pressed to account for the large splitting (about 23 cm^{-1} at 1070 cm^{-1}) observed in CS_2 solutions of IPS,⁴ where we presume that side-to-side aggregation of helical regions is not extensive.

We wish to suggest what seems to be a plausible explanation of this splitting. The existence of degenerate E species helical chain modes is a consequence of the threefold screw (C_3) symmetry of the structure. If this symmetry were relaxed or destroyed, then the degeneracy of these modes would be removed. The result could be that a band associated with a given E species mode of the perfect helix would split into two σ components of slightly different frequency. The most likely mechanism for the relaxation of the perfect C_3 symmetry is the rotational disordering of the benzene ring about the bond connecting it to the chain. Steric considerations^{10,15} indicate that the favored position is such that the plane of the benzene ring bisects the CCC angle of

the chain at the carbon atom where it is attached. It is possible, however, that other orientations of this plane are permissible. In particular, in the statistically variable crystal structure¹⁰ in which a given chain can be surrounded by either of two types of chains, it is possible that two different orientations of the benzene ring about its local symmetry axis (the bond connecting it to the chain) could occur. This would destroy the C_3 symmetry for certain of the ring modes, thus leading to the splitting of the originally degenerate mode. It is interesting to note that the symmetry of the remaining portion of the chain is unaffected by this rotational disorder, so that we do not anticipate splittings for CH, CH_2 , and skeletal modes. Furthermore, the C_3 symmetry is essentially preserved for the A_1 species ring modes, whose transition moments are parallel to the symmetry axis of the benzene ring, so that we would not expect splittings to occur for these vibrations. The effect should be maximal for the B_1 species ring modes, where the transition moment is perpendicular to the symmetry axis of the ring. While this rotational disordering may be a maximum in the statistically variable crystal, it probably would also occur to some extent (perhaps smaller) in the isolated chain. We think that this could account for the observed splittings in the quenched polymer and in solution (cf. Fig. 5), the smaller magnitudes of the splittings in these cases being related to the smaller departure from extended C_3 symmetry in the helical portions of the chain. If this mechanism accounts for the progressive splittings in the type II bands, then it suggests that enhanced crystallization of the polymer is not associated with a growth of regions of specific space group symmetry (the $R\bar{3}c$ and $R3c$ symmetries allowed by the crystal structure),¹⁰ but rather the extension of regions which locally maintain the statistically variable chain structure.

ACKNOWLEDGMENTS

Support is gratefully acknowledged from the U. S. Public Health Service and the National Science Foundation. We are indebted to Dr. W. Burlant of the Ford Motor Company Scientific Laboratory for assistance in carrying out the polymerization of the ring-deuterated polystyrene.

¹⁵ C. W. Bunn and E. R. Howells, *J. Polymer Sci.* **18**, 307 (1955).

Non-Newtonian Viscosity of Polymers*

ROGER S. PORTER AND JULIAN F. JOHNSON
California Research Corporation, Richmond, California

The rheology of concentrated and bulk polymer systems has been investigated. Studies have been made on a low molecular weight series of several polymers using capillaries and a high shear concentric cylinder viscometer. The compositional and shear conditions for non-Newtonian flow have been closely defined. Limiting high and low shear viscosities and the path of non-Newtonian flow may be consistently correlated for concentrated systems of linear, flexible polymers. The minimum molecular weight for non-Newtonian flow is related to the transition at low shear in log viscosity vs log molecular weight correlations. For non-Newtonian systems, changes in apparent activation heat for viscous flow are reported as a function of shear. The conditions for laminar flow shear degradation of polymers are also given.

INTRODUCTION

THE non-Newtonian flow of high polymers in dilute solution is an established phenomenon. The observation of shear dependent viscosities has been generally limited, however, to polymers with molecular weights above 100 000.¹ In contrast, therefore, are interesting indications of non-Newtonian flow for certain polymers with molecular weights as low as 10 000.² Thus, this work is directed at evaluating the nature and dependence of non-Newtonian flow in low molecular-weight polymer systems.

INSTRUMENTAL

The principal viscometer used in these studies is diagrammed in Fig. 1. The basic design of this high-shear viscometer is due to Barber and co-workers.³ The test fluid is pumped between concentric steel cylinders where it is held by surface tension. The cylinders are nominally 1 in. in diameter and 2 in. in length. The inner cylinder is rotated by a flexible steel shaft which is connected to a variable gear train. Torques trans-

mitted through the test fluid are measured by transducer strain gauges that play against a torque arm attached to the outer cylinder. Both shear rate and shear stress are continuously recorded on the same chart in an electronic console.

The thickness of the test fluid may be varied down to 0.0002 cm by the choice among inner cylinders. Effective thicknesses are known to better than 10^{-5} cm by viscometer calibration with standard fluids. The use of thin films insures laminar flow and the minimum of temperature uncertainty. Temperature effects are also minimized by an important and unique double-thermostating arrangement. The thermostating fluid flows around the outer cylinder and washes against the inner wall of the inner cylinder. Test temperatures are measured at the outer cylinder by four thermocouples placed within $\frac{1}{16}$ in. of the shear volume. The same fluid element is sheared continuously, and all measurements are at equilibrium conditions relative to molecular relaxation times. Measurements are made in every case in order of both increasing and decreasing shear rate. Results on the systems reported here indicate an absence of heating effects, thixotropy, and molecular degradation, except where noted. The accuracy of measurements has been established by tests with Newtonian systems and with polymer solutions including API Oil 104, the most non-Newtonian viscosity standard currently available. Low shear reference viscosities were obtained on all test systems by use of crossarm capillary viscometers.⁴

RESULTS

In evaluating molecular flow, measurements have been made to high shear on a series of straight chain hydrocarbons.⁵ Results on *n*-alkanes up to C₃₂ and at shear rates to 0.8 million seconds⁻¹ are entirely Newtonian. Unrefuted literature data obtained with a jet viscometer indicate, perhaps incorrectly, non-Newtonian flow for these same and similar systems in this shear range.⁶ It is also predicted from rate process theory that compounds as low as *n*-pentane will show

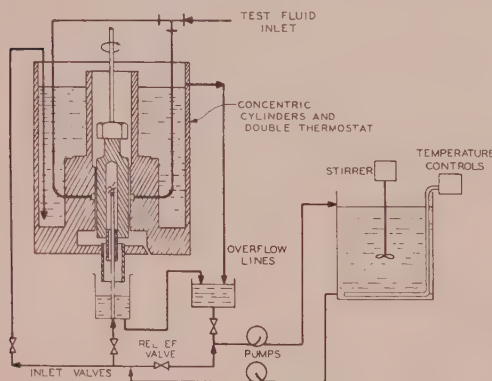


FIG. 1. High shear viscometer.

* Invited paper presentation, Am. Phys. Soc. meeting; Part VI of a series on "Flow properties of polymeric systems," Monterey, California, March 22, 1961.

¹ A. Peterlin and M. Copic, *J. Appl. Phys.* **27**, 434 (1956).

² R. S. Porter and J. F. Johnson, *J. Appl. Polymer Sci.* **3**, 200 (1960).

³ E. M. Barber, J. R. Muenger, and F. J. Villforth, Jr., *Anal. Chem.* **27**, 425 (1955).

⁴ J. F. Johnson, R. L. LeTourneau, and R. Matteson, *Anal. Chem.* **24**, 1505 (1952).

⁵ R. S. Porter and J. F. Johnson, *Wear* **4**, 32 (1961).

⁶ W. J. Morris and R. Schnurmann, *Nature* **167**, 317 (1951).

non-Newtonian flow at not much higher rates of shear.⁷ If non-Newtonian flow cannot be found at these low molecular weights (<450), where does it occur if one considers polyethylenes? In this evaluation, six conventional, commercial polyethylenes were tested. Some of these results are shown in Fig. 2. Shear measurements on the three lowest molecular weight polymers were entirely Newtonian to stresses $>5 \times 10^5$ dynes/cm². However, non-Newtonian flow was prominent at 8300 molecular weight and more pronounced at 18 000 molecular weight. These viscosity average molecular weights were derived from an equation by Ueberreiter for intrinsic viscosities in Decalin at 70°C.⁸ Viscosity-shear data in Fig. 2 pinpoint the molecular-weight transition range for non-Newtonian flow for conventional polyethylenes. These shear tests were all on systems of true liquids, i.e., in a region of constant coefficient of liquid expansion. Data indicate that non-Newtonian flow sets in abruptly with tenfold reversible viscosity changes with shear occurring above some critical polymer molecular weight. The results, therefore, invite evaluation by existing theories. A similarly

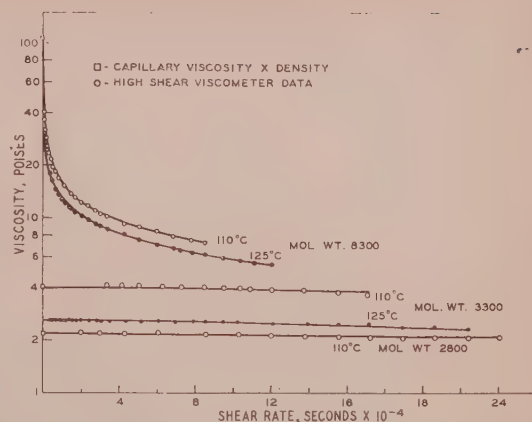


Fig. 2. Viscosity-shear effects for conventional polyethylenes.

TABLE I. Viscosities of polyethylenes dependence on shear comparison with theory of Bueche.

Molecular weight	Shear rate sec ⁻¹ × 10 ⁻⁴	Viscosity measured	Viscosity calculated
8300	0.5	20.6	29.5
8300	2.0	12.65	12.65 ^a
8300	8.0	7.52	4.84
3300	1.0	3.97	3.34
3300	18.0	3.97	1.50
2800	1.0	2.17	1.96
2800	24.0	2.17	1.02

^a Mathematically adjusted.

abrupt onset of non-Newtonian flow has also been observed here on increasing molecular weight in a series of polyethylene glycols and polyisobutenes in bulk and in concentrated solutions. Therefore, the discussion of theory which follows applies generally to these polymer systems as well.

Bondi has proposed a relationship based on rate theory which evaluates entropy changes accompanying molecular orientation.⁹ This expression gives a reasonably well-adjusted fit to the non-Newtonian data of 8300 molecular weight, but it predicts large viscosity changes with shear at lower molecular weights where results are entirely Newtonian. Another modification of the Eyring theory, which accounts for shear, has been derived by Grunberg and Nissan.⁷ The rate theory parameters in this equation were again adjusted to give the best fit to non-Newtonian data and the resulting form, compared with data for the lower molecu-

lar weight polymers. Just as in the case of the theory of Bondi, the equation of Grunberg and Nissan cannot account for the abrupt onset of non-Newtonian flow with increasing polymer molecular weight.

Ree and Eyring explain non-Newtonian flow by assuming a system made up of three types of flow units.¹⁰ The several parameters in this equation are calculated from experimental data. This equation will fit a variety of systems. However, there is no fundamental derivation of the parameters in the Ree-Eyring equation. In fact, the parameters are required to vary, in sometimes unpredictable fashion, in order to represent data.¹¹

Table I shows an evaluation of polyethylene data by the non-Newtonian theory of Bueche.¹²⁻¹³ This relationship for bulk polymers predicts a universal curve in terms of reduced viscosity vs shear rate times zero shear viscosity, all raised to the $\frac{2}{3}$ power. By adjusting Bueche's equation to non-Newtonian data at 12.65 poises (see Table I), a reasonable correlation with shear dependence is obtained. With the resultant equation, viscosities were calculated for the lower molecular weight polymers. The predicted non-Newtonian effects are again much larger than observed.

Pao and also Rouse have derived equations from viscoelastic theory which may be applied to steady-state non-Newtonian flow.¹⁴⁻¹⁶ These equations apply reasonably to some of these non-Newtonian data and notably may anticipate a lower molecular weight limit of applicability in terms of molecular relaxation times. In general, however, non-Newtonian theories either do not predict a lower molecular weight limit for non-Newtonian flow, which is prominently observed here

¹⁰ T. Ree and H. Eyring, *J. Appl. Phys.* **26**, 793, 800 (1955).

¹¹ F. H. Ree, T. Ree, and H. Eyring, *Ind. Eng. Chem.* **50**, 1036 (1958).

¹² F. Bueche, *J. Chem. Phys.* **22**, 603, 1570 (1954).

¹³ F. Bueche and S. W. Harding, *J. Polymer Sci.* **32**, 177 (1958).

¹⁴ Y. H. Pao, *J. Chem. Phys.* **25**, 1294 (1956).

¹⁵ Y. H. Pao, *J. Appl. Phys.* **28**, 591 (1957).

¹⁶ P. E. Rouse, Jr., *J. Chem. Phys.* **21**, 1272 (1953).

⁷ L. Grunberg and A. H. Nissan, *Nature* **156**, 241 (1945).

⁸ K. Ueberreiter and H. J. Orthmann, *Kolloid-Z.* **126**, 140 (1952).

⁹ A. Bondi, *J. Appl. Phys.* **16**, 539 (1945).

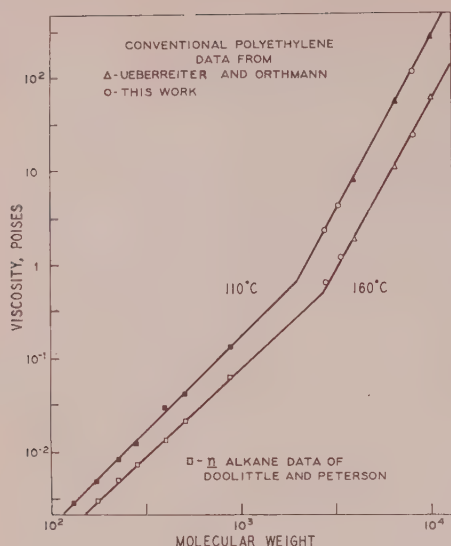


FIG. 3. Low-shear viscosity transition.

for several polymer types, or they do so only qualitatively and not in terms of steady-state flow.

In efforts to understand the nature of flow, a separate study of low-shear Newtonian viscosities for polyethylenes was developed. Figure 3 indicates some of these results in a plot of low-shear viscosity vs molecular weight for the polymers previously discussed. Figures 2 and 3 are similar to those previously published but contain additional data.^{2,17} Literature values for similar polymers are also given.¹⁷ The data at the higher molecular weights in Fig. 3 yield a power dependence of 3.4, in accord with results on many other polymers.¹⁸ Peticolas and also Tung indicate that high molecular weight linear and conventional polyethylenes also yield a 3.4 slope.¹⁹⁻²⁰ A salient point is that this slope commonly changes markedly to a lower value approaching one at lower molecular weights, represented in Fig. 3 by normal alkanes.²¹ For convenience, this marked change is commonly shown as an intersection of lines. Eyring and also Bueche have given credence to these empirical facts through their theoretical derivations.²²⁻²³ Bueche indicates that viscosity at low molecular weights is determined by simple frictional forces between molecules. The viscosity transition represents an abrupt appearance of a network

structure due to entangled or associated polymer chains. The high molecular weight region is then governed by a flow mechanism dependent on a slippage factor for intermolecular couplings. Experiment and theory thus strongly suggest a change in flow mechanism at the low-shear viscosity transition. Significantly then, there is a reasonable correspondence between this transition and the molecular weight conditions for non-Newtonian flow. This association can account for the abrupt onset and large magnitudes of non-Newtonian flow obtained at higher molecular weight for polyethylenes and other polymers. If the number or importance of these imagined entanglements becomes less with shear, then limiting high-shear viscosities should increase with molecular weight in a way similar to that for simple molecules. This would be approximated by extending the low slope of about one for low molecular weights into the non-Newtonian region. Limiting high-shear viscosities predicted in this way have been shown to be more satisfactory than those derived from the previously discussed theories.² It is probable, however, that certain theories will satisfy flow data, provided that minimum molecular weight conditions are defined. For example, Ferry, Landel, and Williams have modified the viscoelastic theory of Rouse to incorporate entanglement conditions.²⁴ This leads, in viscoelastic parlance, to a plateau region of lower dependence of complex shear modulus on frequency. This is clearly analogous, in steady-state flow, to the lower dependence of stress on shear rate, i.e., non-Newtonian flow, which has been found here for the same entanglement conditions.

Bagley and West have published an excellent brief article on polydimethylsiloxanes.²⁵ Using the coordinates in Fig. 3, they similarly find a sharp change in low-shear viscosity behavior, with the transition for polydimethylsiloxane being at about 29 000 in molecular weight. Bagley and West conclude that the conditions for the higher slope, which reaches 3.4 and above, are required for non-Newtonian flow. The higher slope also decreases regularly with increasing shear towards a lower slope at low molecular weights below the transition (see Fig. 3 for comparison). Polydimethylsiloxanes are apparently non-Newtonian only when chains are long enough to entangle, and this critical molecular weight is independent of shear rate.²⁵

With these similar results for polyethylenes and polydimethylsiloxanes, the flow of several other polymer types was investigated. One of these was polyisobutene, which has a carbon backbone but the same arrangement of pendant groups as polydimethylsiloxane. Previously developed studies on polyisobutene,²⁶ in agreement with Fox and Flory, indicate a low-shear viscosity transition at about 17 000 in molecular

¹⁷ R. S. Porter and J. F. Johnson, *J. Appl. Polymer Sci.* **3**, 194 (1960).

¹⁸ T. G. Fox and S. Loshaek, *J. Appl. Phys.* **26**, 1080 (1955).

¹⁹ W. L. Peticolas and J. M. Watkins, *J. Am. Chem. Soc.* **79**, 5083 (1957).

²⁰ L. H. Tung, *J. Polymer Sci.* **46**, 409 (1960).

²¹ A. K. Doolittle and R. H. Peterson, *J. Am. Chem. Soc.* **73**, 2145 (1951).

²² H. Eyring, T. Ree, and N. Hirai, *Proc. Natl. Acad. Sci. U. S. A.* **44**, 1213 (1958).

²³ F. Bueche, *J. Chem. Phys.* **20**, 1959 (1952).

²⁴ J. D. Ferry, R. F. Landel, and M. L. Williams, *J. Appl. Phys.* **26**, 359 (1955).

²⁵ E. B. Bagley and D. C. West, *J. Appl. Phys.* **29**, 1511 (1958).

²⁶ R. S. Porter and J. F. Johnson, *J. Polymer Sci.* **50**, 379 (1961).

weight.²⁷ For cetane and Tetralin solutions of polyisobutene, the viscosity transition is also found to occur near 17 000 for the product of polymer molecular weight and its volume concentration. Bulk and solution data above the transition are consistent with a 3.4 power dependence of viscosity on molecular weight.²⁶ Below the transition, the dependence approaches first power at higher temperatures, as predicted by Bueche, and indeed may be corrected to one by using the equation of Williams, Landel, and Ferry, which involves the change in glass transition temperature with molecular weight.^{18,28-30}

Viscosity shear tests to $>2 \times 10^5$ dynes/cm² gave entirely Newtonian results for six bulk polyisobutenes with molecular weights below 17 000 and also for higher molecular weight polyisobutenes in dilute solution. At slightly higher polyisobutene molecular weights and concentrations, however, pronounced non-Newtonian effects were easily induced.²⁵

From a great many shear tests on polyisobutenes, correlations of the type shown in Fig. 4 have been established.²⁶ Conventional capillary viscosities closely define limiting low-shear viscosities.⁴ The entirely reversible results obtained in the rotational viscometer describe an approximate high-shear limit. There is observed a regular change of viscosity-shear behavior with molecular weight with a minor effect for solvent. The solid lines in Fig. 4 represent limiting low-shear viscosities and the transitions. The vertical arrows represent the maximum reversible viscosity changes measurable to $>2 \times 10^5$ dynes/cm². Results thus indi-

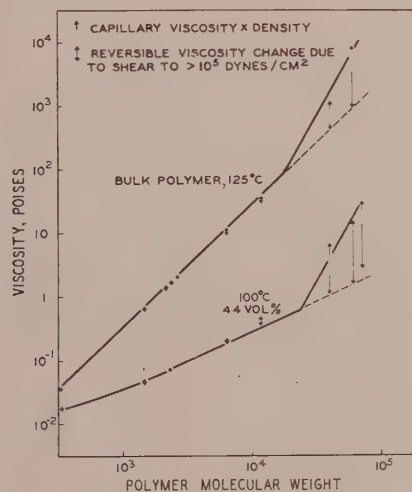


FIG. 4. Shear dependence of viscosity for polyisobutenes in cetane.

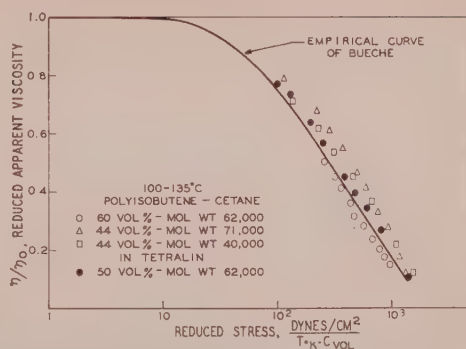


FIG. 5. Reduced variables for non-Newtonian flow high concentrations.

cate that high-shear viscosities may be approximated by a linear extension of the low molecular weight slope, which has a minimum value of one. Comparisons at a series of increasing shear rates show a regular decrease in the high molecular weight slope from 3.4 towards 1.

The evaluation of high-shear viscosity limits for higher molecular weight than those in Fig. 4 is of little significance because of laminar flow shear degradation of polyisobutene, which occurs both in bulk and in concentrated solutions. The stresses for degradation are sometimes only about a power of 10 higher than those required for the onset of non-Newtonian flow. The compositional requirements for shear degradation are always above the low-shear viscosity transition as concluded from these results and an abundance of literature data.^{26,31} Polymer degradation in laminar flow therefore may occur through extending forces on a network of entangled chains.

For treating non-Newtonian data on the stable polymer systems, the correlation shown in Fig. 5 has been successfully used. Figure 5 shows fractional viscosity losses vs a reduced shear stress. Various polyisobutenes overlap rather well with the empirical curve presented by Bueche, which, converted to these units, is shown as the solid line.³² This correlation has a form similar to that successfully used by Ferry and co-workers to interpret both viscoelastic and steady-state flow, except that no reference state is used here.³³ The maximum rate of viscosity change with shear is found to be somewhat greater for narrower polymer molecular weight distributions. The maximum slope of log viscosity vs log shear rate is near $-\frac{2}{3}$. This slope is in reasonable accord with the empirical-reduced variable curve of Bueche and is equivalent to that data reported to fit a power law function showing a third power dependence of shear stress on shear rate.³⁴

²⁷ T. G. Fox, Jr., and P. J. Flory, *J. Phys. & Colloid Chem.* **55**, 221 (1951).

²⁸ F. Bueche, *J. Appl. Phys.* **26**, 738 (1955).

²⁹ F. Bueche, *J. Chem. Phys.* **30**, 748 (1959).

³⁰ M. L. Williams, R. F. Landel, and J. D. Ferry, *J. Am. Chem. Soc.* **77**, 3701 (1955).

³¹ R. S. Porter and J. F. Johnson, *J. Phys. Chem.* **63**, 202 (1959).

³² F. Bueche, *J. Appl. Phys.* **30**, 1114 (1959).

³³ J. D. Ferry, *Viscoelastic Properties of Polymers* (John Wiley & Sons, Inc., New York, 1961).

³⁴ W. Philippoff and F. H. Gaskins, *J. Polymer Sci.* **21**, 205 (1956).

The general curve in Fig. 5 has been found to satisfy Tung's non-Newtonian data on polyethylenes, as well as some of the results obtained here on polyethylenes and polyethylene glycols.²⁰ Certain polystyrenes, polymethyl methacrylates, and rubber solutions also fit this curve just as they do Bueche's empirical correlation.³² The coordinates used here have the advantages of using actual shear stress and giving a closely linear region for non-Newtonian dependence, which extrapolates back to a common minimum stress for non-Newtonian flow. For bulk polymers at room temperature, this minimum is near 5×10^4 dynes/cm².

The general function given in Fig. 5 seems to describe excellently non-Newtonian flow for many linear, flexible polymers and for their concentrated solutions. It fails, however, at predictable compositional and shear conditions. Figure 6 shows deviations from this correlation as they occur for polyisobutenes of low concentration and molecular weight. These deviations coincide exactly with the molecular weight and concentration conditions for polymer entanglement. A successful reduced variable correlation has been previously reported for this low molecular weight and concentration state where polymer entanglements do not determine the flow process.³⁵

At low polyisobutene concentrations, the same correlation applies as used in Figs. 5 and 6, except that the concentration term vanishes.³⁵ Using this form, non-Newtonian data have been successfully superimposed for three polymer molecular weights, 40 000, 62 000, and 71 000, at three polymer concentrations from 10–50 volume percent, with two solvents, Tetralin and cetane, and at a series of temperatures from 20–135°C. The superposition of data for different molecular weights and solvents may be in part fortuitous as variations in molecular weight and solvent power were small.

The coordinate form used in Figs. 5 and 6 superimposes data at high polymer concentrations where re-

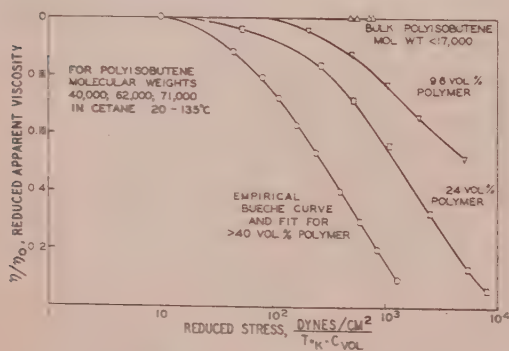


FIG. 6. Reduced variables for non-Newtonian flow transition range.

quired stresses for steady-state flow increase with the number of entanglements. At low concentrations, as long as polymer molecules are effectively separate, the concentration term is not required. Superposition on the general low concentration non-Newtonian curve is followed, except as the mechanism for non-Newtonian flow is approaching saturation.³⁵ The mechanism of non-Newtonian flow here is likely to be the traditional oscillation and deformation of individual molecules. Indeed, the shear dependence and the small fractional viscosity losses are of the magnitudes expected for non-Newtonian flow near intrinsic conditions.

The non-Newtonian flow of polymers is also indicated through viscosity-temperature coefficients. These lead to apparent heats of activation for viscous flow.³⁵ Low-shear flow activation heats increase regularly with increasing solution concentration of low molecular weight polymers. However, for higher molecular weight polymers it has been found here that a small plateau

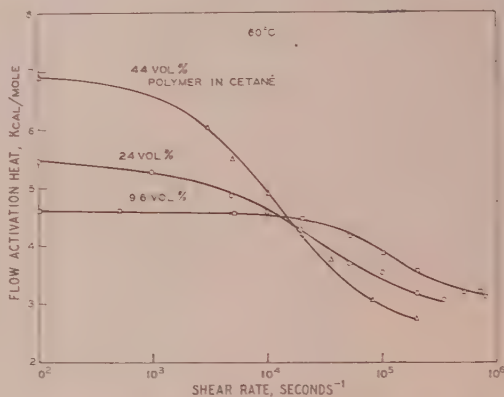


FIG. 7. Changes in flow activation heat with shear for 40 000 molecular weight polyisobutene in cetane.

exists in plots of flow activation energy against concentration for polyisobutenes. This plateau corresponds closely to concentrations sufficient for polymer network entanglement.^{18,26} This effect has been predicted by Hirai, who further concludes that the activation heat difference between the solvent and the plateau is a measure of formation energy of the state of the entangled polymer. Data on polyisobutenes in cetane indicate a formation energy of about 1 kcal, which is similar in magnitude to that found for other polymer systems.³⁶ This energy effect is a concomitance of the findings that the low-shear viscosity transition for these systems increases slightly with temperature.²⁶

Effects of shear on apparent activation heats for viscous flow are shown in Fig. 7. The low shear values increase markedly with concentration. At successively higher shear rates, however, activation heat decreases regularly for each system reflecting non-Newtonian

³⁵ R. S. Porter and J. F. Johnson, *J. Appl. Polymer Sci.* **3**, 107 (1960).

³⁶ H. Hirai, *J. Polymer Sci.* **39**, 435 (1959).

flow. At near 10^4 reciprocal seconds, these solutions have about the same activation heat as measured at constant shear rate. At high rates of shear all systems approach a limiting activation heat close to that of the solvent with a small effect for polymer. The changes are greater at higher polymer concentration. Activation heats for 60 volume percent polyisobutene in cetane change from over 9 at low shear to a limiting high shear value of 3.0–3.5 kcal. The activation heat for the solvent cetane is 3.5 at 60°C.

Activation heats for polyisobutene systems evaluated at constant stress are nearly constant. Only small fractional decreases in these activation heats are observed at the highest attainable stresses.³⁵ This conclusion appears to be true for a number of polymer systems. In accord, Bestul and Belcher have theoretically concluded that activation heats or energies at constant stress are always equal to or greater than those at constant rate. Quantitative predictions have also been made from rate theory as to how activation energies change with shear rate and stress.³⁷ This equation is only qualitatively correct for these polyisobutene data, although Ree and Eyring suggest that it may be adequately adjusted.^{10,11,35}

Figure 8 represents a summary of results obtained here on the flow behavior of flexible, linear polymers in bulk and concentrated solutions. The mechanism of flow for these systems is not sufficiently clear; polymer entanglements, associations, and/or the onset of chain flexibility with increasing polymer molecular weight may play a part. Experimentally, however, there is a clear association of the low-shear viscosity transition with non-Newtonian flow. The agreement is at least within a factor of two in molecular weight for polyethylene, polyethylene glycol, polydimethylsiloxane, and for polyisobutene and its solutions.^{2,25,26} In making these conclusions more definitive, a study of highly fractionated polymers is currently under way.

From present data some general conclusions are evident. For example, below the viscosity transition in Fig. 8 the slope depends on temperature but is independent of shear to extreme values. Conversely, above the transition the slope is independent of temperature but depends on shear. In the upper non-Newtonian

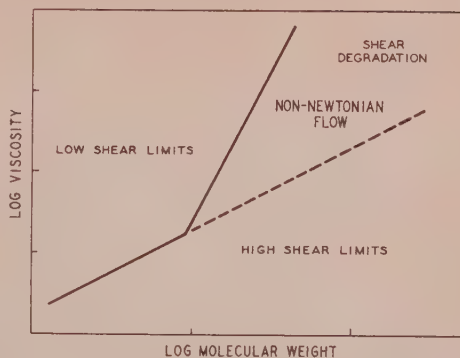


FIG. 8. Shear viscosities for systems of flexible, linear polymers.

region the slope decreases regularly from values near 3.4 toward 1 with increasing rates of shear. The total magnitude of reversible viscosity losses is thus defined by these limiting slopes. This correlation considers only the mechanism of non-Newtonian flow in concentrated polymer systems. The considerably smaller viscosity changes with shear at intrinsic conditions may not be included.

With increasing stress in polyisobutene, polyethylene glycol, and other polymer systems, laminar flow shear degradation has been encountered before reaching a high-shear Newtonian state.³¹ In the reversible viscosity range, data for many polymers and concentrated solutions are shown here to superimpose and to change, close to linearly, plots of percent viscosity loss vs stress over temperature and concentration. This general correlation indicates a common stress for activating non-Newtonian flow and implies a common flow mechanism. This correlation is equivalent to that presented by Bueche and is related to the reduced variables developed by Ferry.^{32–33} It is hoped that these results and correlations add definition to the nature of non-Newtonian flow. The conclusions, although new in part, are in accord with much experimentation and theory presented by others.

ACKNOWLEDGMENT

The authors wish to thank Mr. A. R. Bruzzone for assistance in the experimental work.

³⁷ A. B. Bestul and H. V. Belcher, *J. Appl. Phys.* **24**, 696 (1953).

Rate of Recrystallization of Polyethylene Single Crystals

W. O. STATTON

Textile Fibers Department, E. I. du Pont de Nemours and Company, Wilmington, Delaware

Platelet crystals of linear polyethylene recrystallize extremely rapidly when immersed in a bath of a hot liquid such as ethylene glycol, glycerine, or Woods metal. This recrystallization rate is much faster and to greater extent than when the heating medium is air. For example, heating in the liquids at 127°C causes the length of the chains between folds to increase 50% in 1 sec; the ultimate increase of 200% occurs in about 1 sec. No definite explanation is presently apparent for this much faster rate and greater extent in liquids. No evidence is found for reversibility when annealed crystals are reheated at a lower temperature.

It was shown in a previous communication¹ that when single crystal platelets of essentially linear polyethylene are heated in air at temperatures above 110°C they recrystallize with a greatly increased length for their fold period. The purpose of this communication is to report that the change occurs much more rapidly when the single crystals are heated in some media other than air.

The crystals used for the present experiments were from the same preparation as before, grown from a dilute solution of polyethylene in tetrachloroethylene, the crystals appearing at about 80°C as the hot solution was cooled. The crystals for the present study were concentrated by decantation, and the concentrated slurry was allowed to evaporate in a flat dish to form a dry, thin cake about 0.010 in. thick consisting of layered platelets. If residual solvent was present it was tightly associated, as there was no change in weight when several cakes were heated in vacuum at 100°C. The

recrystallization was followed by measuring the long period x-ray diffraction obtained at room temperature after the crystals were heated. The x-ray beam was sent parallel to the platelet surface. This long period corresponds to the platelet thickness and the length of the polymer chains between folds.

The earlier results, reproduced in Fig. 1, showed that equilibrium is slowly established in air at elevated temperatures; many hours were required for the final values to be attained. Similar data were recently reported by Fischer.² However, the present results, seen in Fig. 2, show that the recrystallization is extremely rapid if the crystals are immersed in hot ethylene glycol. The data indicate that the ultimate values of about 300 Å for the long period at 127°C is achieved in a matter of 10 sec. This corresponds to a 200% increase in the length of the segments between folds; a 50% change occurs in one sec. Wide-angle x-ray patterns showed that no change in orientation of the molecules was caused by the heating.

The scatter in the results can be attributed to several possible factors: imperfect control of the bath temperature, the existence of a gradient in the bath, error in timing the short intervals, or differences in cooling rate (the samples were rapidly cooled by lifting them from the bath with tweezers and placing them on a glass plate at room temperature). As shown in Fig. 1, there is a very steep dependence of the long period at these high temperatures, so that some scatter is not unexpected. It is emphasized that these experiments were

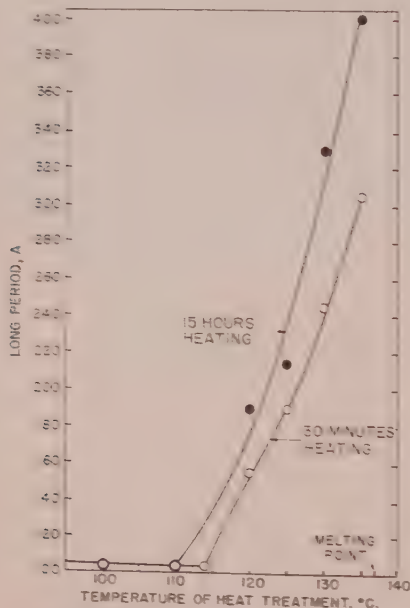
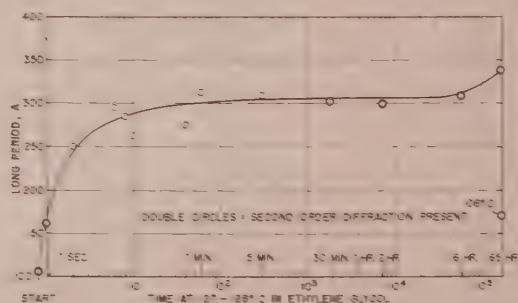


Fig. 1. Long period x-ray diffraction from layered aggregate of polyethylene crystals after annealing in air.



of an exploratory nature and need refinement before the results can be treated quantitatively. However, the inversion of the curve at the 65-hr point seems valid since a recording of the bath temperature showed no variation with time, and the results to be discussed below also indicate a similar effect.

Figure 3 shows results for similar heating in glycerin. The data can be interpreted as a repetition of the results with ethylene glycol with a final inversion at a shorter time. However, until more is known about this long-time effect, it may be just as valid to draw a line showing a gradual increase of long period with time, as shown. Either interpretation has puzzling aspects.

Isolated results are shown in Figs. 2 and 3 for treatments in baths at lower temperatures. These resulted in shorter long periods. This shows again that the extent of recrystallization is dependent upon temperature.

Since the results with ethylene glycol and glycerin are so different from the previous results in air, it was suspected that some type of plasticization occurs in the organic media which enables much more extensive molecular motion to occur at a given temperature. This suspicion was shown to be unfounded by experiments which substituted Woods metal for the organic liquids. This alloy (50 Bi, 25 Pb, 12.5 Sn, 12.5 Cd) has a melting point at about 70°C, so it was quite convenient for use as an immersion bath in the same manner. Figure 4 shows the results at four different temperatures. They indicate again that there is an extremely rapid change which occurs at the elevated temperatures. The values using Woods metal bath correspond closely to those using the organic liquids. In addition, it appears that disorder occurs after a certain time at a given temperature, as there were products, indicated in Fig. 4, which showed no long period diffraction. This disorder apparently occurs very soon at the highest temperature. However, order again developed in two experiments with longer heating of one hour. It is possible that the long period which developed at this high temperature is so large that it was beyond the 400-A resolution of this camera and that the reappearance of order is actually appearance of a second-order diffraction.³ This

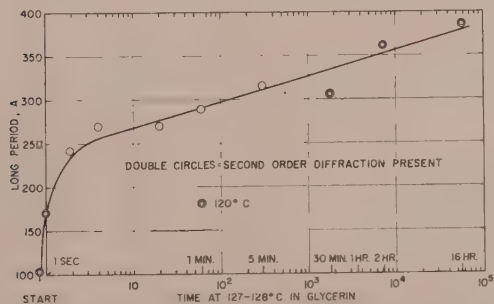


FIG. 3. Long period x-ray diffraction from layered aggregate of polyethylene crystals after immersion in glycerin.

³ L. Mandelkern, A. S. Posner, A. F. Diorio, and D. E. Roberts, *J. Appl. Phys.* 32, 1509 (1961).

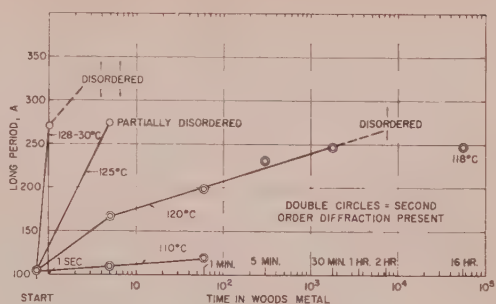


FIG. 4. Long period x-ray diffraction from layered aggregate of polyethylene crystals after immersion in Woods metal at different temperatures. Disorder judged by absence of sharp diffraction maxima within the limit of camera resolution, 400 Å.

puzzling behavior will need more study to be understood.

A summary of the results of heating in air and in liquids is shown in Fig. 5. It appears that heating in liquids causes not only a more rapid change, but it also causes the magnitude of the change to be greater also.

It is difficult at this time to propose a definite kinetic or thermodynamic reason for the great difference in recrystallization rate or extent in air versus liquid. No satisfactory explanation is apparent to the author on the basis of conventional mechanisms of diffusion or heat exchange from one medium to another. The data in liquids suggest a two-step mechanism having a fast initial change and a much slower final adjustment. It may be that in air this first fast step does not occur. This could explain the lower value of long period after an air recrystallization.

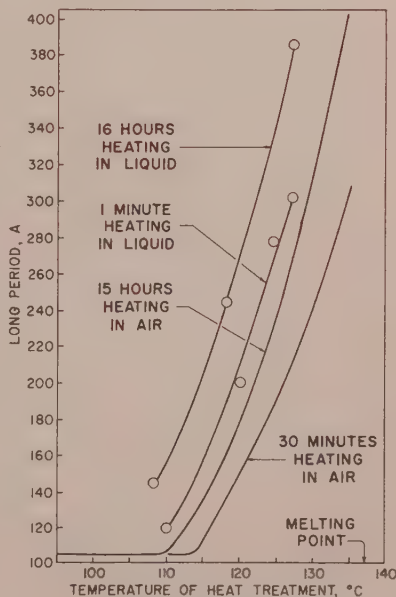


FIG. 5. Summary of long period spacings versus temperature of annealing, showing effect of heating medium and time of anneal.

It is important to note that the recrystallization either in air or in liquids is cooperative; all of the chains must refold to the same length in a given time at a certain temperature, since only a single value of the long period is observed in all of the products, and second orders are common. All of the results summarized in Fig. 5 for experiments both in air and in liquids indicate that time is a variable in addition to temperature in determining the fold length. This suggests that the recrystallization process is a melting of metastable crystals which are transformed into a more stable state. The nature of the new state would be dependent upon the time and temperature of treatment, but it is only an approach towards the ideal state which would have crystals with an infinite step height showing a true equilibrium melting point.²⁻⁵

* Mandelkern, Chem. Revs. 56, 903 (1956).

† Lauritzen and J. D. Hoffman, J. Research Natl. Bur. Stand., 64A, 73 (1960).

From a kinetic view, the data in Fig. 4 could be used to calculate rate constants if the experiments had been performed with sufficient precision. From a thermodynamic view, one might expect reversibility when the annealed crystals are reheated at a lower temperature. No such reversibility was found in one earlier experiment in air,¹ but has been reported recently using liquids.⁶ In the present study, several experiments showed no reversibility. For instance, one of the preparations, which had been heated for 65 hr in ethylene glycol at 128°C and had a long period of 330 Å, was reheated in ethylene glycol at 120°C for 65 hr; no decrease in long period was obtained. Other results for shorter times and at other temperatures similarly showed no change. It therefore must be concluded that this refolding is an irreversible effect.

* B. Rånby and H. Brumberger, Polymer 1, 399 (1960).

Hypothesis of Voids in Semicrystalline Polymers

SHIRO MATSUOKA

Bell Telephone Laboratories, Incorporated, Murray Hill, New Jersey

The expression $V = xV_c + (1-x)V_a$ for the specific volume of a semicrystalline polymer, is a highly successful approximation, here x is the degree of crystallinity, V_c is the specific volume for the crystalline regions, and V_a is the specific volume for the amorphous regions. In specimens for which x is near unity, however, this equation demands values for the parameters which are inconsistent with other experimental evaluations. We suggest that the discrepancy arises because of the presence of voids. Thus in addition to crystalline and amorphous regions we propose regions of zero density. The average volume of such voids is not known, but their existence can be inferred from the significant, permanent density enhancement which can be brought about by pressure-induced crystallization.

THE widely accepted expression for the specific volume of a semicrystalline polymer¹⁻³ is

$$V = xV_c + (1-x)V_a \quad (1)$$

where V is the over-all specific volume, V_c and V_a are the specific volumes for the crystalline and the amorphous domains, respectively, and x is the degree of crystallinity, or the mass fraction of the crystalline domains.

While there undoubtedly exists a substantial proportion of domains that cannot distinctly be classified either as crystalline or amorphous, the linear relationship between the over-all specific volume V and a properly defined degree of crystallinity x has often been observed to hold to a good approximation. Hence Eq. (1) as a two parameter (in V_c and V_a) empirical expression for V vs x has proved to conform to many experimental results well. It can be shown, however,

that in some cases the parameters V_c and V_a thus determined are not always very reasonable values. This is demonstrated in Table I, where various combinations of values for parameters for a typical compression-molded linear polyethylene (Marlex 50) at 23°C are shown. This polymer has been found to be about 90% crystalline by steady-state nuclear magnetic resonance,^{4,5} by calorimetry,⁶ and by x-ray diffraction.

TABLE I. Choice of parameters for Eq. (1) to hold for Marlex with the specific volume of 1.0417 (density of 0.960 g/cm³).

	Experimental			
x , crystallinity	0.900	0.900	0.75	0.900
V_c , specific volume of crystalline region	1.00	1.03	1.00	1.00
V_a , specific volume of amorphous region	1.42	1.17	1.17	1.17

¹ F. Bueche, J. Polymer Sci. 22, 115 (1956).

² F. Price, J. Chem. Phys. 19, 975 (1951).

³ E. Hunter and W. G. Daves, Trans. Faraday Soc. 41, 49 (1945).

⁴ W. P. Slichter and D. W. McCall, J. Polymer Sci. 25, 280 (1957).

⁵ R. L. Collins, J. Polymer Sci. 27, 75 (1958).

⁶ B. Wunderlich and M. Dole, J. Polymer Sci. 24, 201 (1957).

TABLE II. Amount of voids for Marlex 50 polyethylene following Eq. (2).

Condition of crystallization	Compression-molded	1 atm 132°C 40 days	870 atm 151°C 8 days
x , crystallinity	0.891	0.955	0.944
V , over-all specific volume	1.0363	1.0183	1.0101
V_v , voids, cm ³ /g	0.018	0.011	0.001

(The last-named based on measurements by the writer, using Aggarwal's method.⁷ The experimental value for the specific volume of a crystalline domain V_c was derived from the unitcell dimensions of polyethylene.⁸ For the specific volume of an amorphous domain V_a , the melt specific volume^{9,10} was extrapolated linearly to 23°C. This is a reasonable estimate since the thermal expansion coefficient of the polyethylene melt is nearly constant for a wide range of temperature. The entries in italics in Table I are the values which do not agree with the experimental quantities, which nevertheless have to be assigned if Eq. (1) is to hold. The magnitude of the discrepancies is seen from the following analysis: the figure 1.42 for V_a would obtain for the melt only at about 300°C; 1.03 would hold for V_c only at about 80°C; the 75% crystallinity is comparable to the value for a branched polyethylene whose density should be about 0.94 g/cm³ instead of 0.96 g/cm³.

In order to correct this difficulty, a hypothesis is proposed here that a semicrystalline polymer contains voids, or domain of zero density. We are not considering here free volume associated with the noncrystalline domains. The specific volume-crystallinity relationship may now be modified to the form

$$V = xV_c + (1-x)V_a + V_v, \quad (2)$$

where V_v is the volume of voids per gram of material, and all the other notations are the same as in Eq. (1).

In Table II the results of Eq. (2) as applied to the present samples of linear polyethylene are shown. Each value of crystallinity was calculated by measuring the amorphous fraction and subtracting it from 1. For the specific volume, the density was measured in a density gradient column. Variations in density and crystallinity among the three samples shown here are the result of different crystallization conditions. Crystallization at an elevated temperature for an extended period would obviously favor a better organized molecular arrangement. Subsequent slow cooling would produce a high crystallinity and a high density. Thus by crystallizing the present sample of linear polyethylene at 132°C

under 1 atm (or 5°C below the melting point) for 40 days and then cooling slowly to 23°C, the sample attained a density of 0.982 g/cm³ (0.960 g/cm³ for ordinary molding conditions).

An unusually high density can also be attained by pressure-induced crystallization.¹¹ A density of 0.990 g/cm³ is attained by crystallizing a sample at 151°C under 870 atmospheres (or 10°C below the melting point at this pressure)¹² for 8 days. In terms of the void hypothesis offered here, the high density in this sample is attributed primarily to a relatively small population of voids. This interpretation is borne out by a detailed study of Table II, for we see that the crystallinity of this sample is lower, and the density higher, than that of the previously mentioned sample crystallized at 132°C under 1 atm. The difference in the degrees of undercooling implies a difference in crystalline texture. Geil¹³ has observed that the lamellar thickness increases with the temperature of crystallization. In terms of Hoffman's model,¹⁴ the most dominant lamellar thickness is inversely proportional to the degree of undercooling, provided that the crystallization temperature is near the melting point; crystallization at 132°C, 1 atm would mean twice as great a thickness as in the case at 151°C, 870 atm. These observations suggest a possibility that two samples of the same linear polyethylene, with the same degree of crystallinity, could still have different densities, void contents, and crystalline textures.

In Table III, Eq. (2) is applied to various branched polyethylene specimens as well as the linear polyethylene sample, which were all compression-molded. While the noncrystalline volume varies considerably from the branched polymers to the linear polymer, V_v 's do not. This supports the viewpoint that the voids hypothesized here should be differentiated from thermodynamic quantities such as the free volume.

The existence of voids as the result of crystallization is consistent with the currently emerging view of polymer morphology. According to Keith and Padden,^{15,16} polymer spherulites grow in the form of

TABLE III. Amount of voids for polyethylene with various degrees of branching following Eq. (2).

CH ₃ /100C	3.3	1.8	0.85	0.3
V , over-all specific volume	1.0965	1.0929	1.0707	1.0363
x , crystallinity	0.569	0.607	0.699	0.891
V_v , voids, cm ³ /g	0.023	0.036	0.020	0.018
$(1-x)V_a$, amorphous volume, cm ³ /g	0.5043	0.460	0.352	0.053

¹¹ S. Matsuoka, J. Appl. Polymer Sci. **4**, 115 (1960).

¹² Data on the melting temperature vs pressure will be published in the immediate future.

¹³ P. H. Geil, J. Polymer Sci. **47**, 65 (1960).

¹⁴ J. D. Hoffman (private communication).

¹⁵ H. D. Keith and F. J. Padden, Jr., J. Polymer Sci. **39**, 123 (1959).

¹⁶ F. J. Padden, Jr. and H. D. Keith, J. Appl. Phys. **30**, 1479 (1959).

⁷ S. L. Aggarwal and G. P. Tilley, J. Polymer Sci. **18**, 17 (1955).

⁸ C. W. Bunn and T. C. Alcock, Trans. Faraday Soc. **71**, 317 (1945).

⁹ M. G. Gubler and A. J. Kovacs, J. Polymer Sci. **34**, 551 (1959).

¹⁰ S. Matsuoka and C. J. Aloisio, J. Appl. Polymer Sci. **4**, 116 (1960).

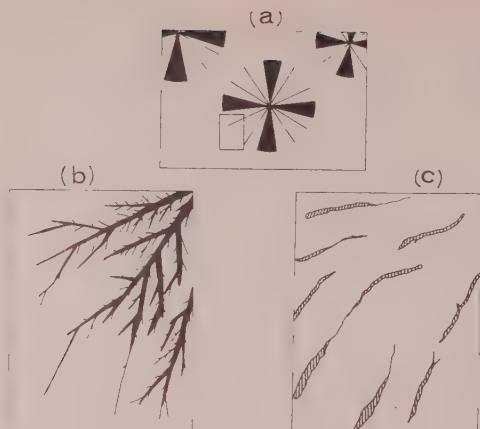


FIG. 1. Schematic drawings of Padden and Keith's observations^{14,15} of spherulite growth: (a) Growing spherulites under the polarized light. (b) The detail of the rectangular portion of the growing boundary indicated in (a). (c) Voids at completion of crystallization corresponding to the previous intervening portions between growing fibrils when the spherulite was growing.

radiating, branching fibrils or ribbons from the nucleus into the melt. The intervening melt between the discrete fibrils would crystallize at a later stage. Now, crystallization is accompanied by a considerable volume decrease. In order for the substance between the already crystalline fibrils to crystallize, either voids would have to form or additional liquid substance would have to flow in. In view of the high viscosity of polymer melts, it is reasonable to assume that the former case would be

more favored, unless some unusual crystallization conditions such as an extremely high pressure are imposed. The same authors have observed that under certain conditions cracks would indeed form in polypropylene crystallized between two glass plates. Schematic drawings in Fig. 1 represent these authors' observations of a growth boundary of a spherulite.

Thus, if the postulated voids actually exist in semicrystalline polymers, some methods of determining the crystallinity must be re-examined. For example, while the dilatometric method remains highly informative, we shall have to take into account that the specific volume measured below the melting point would involve voids. In light scattering studies we must consider that much of the scattering may occur at surfaces exposed to voids. These voids are to be distinguished from the free volume associated with liquids or noncrystalline solids, and their magnitude is not a thermodynamic quantity. Their size most likely would range from microvoids with the order of unit-cell dimensions to porosities and cleavages of much greater dimensions with nonrandom configurations. The size and shape distributions of these voids are closely related to the manners in which spherulites grow. Significance of presence of voids is apparent when physical phenomena such as fracture, dielectric breakdown, and permeation are being studied.

ACKNOWLEDGMENT

The author wishes to thank Dr. W. P. Slichter for various useful discussions.

Extension of the Eyring-Ree Theory of Non-Newtonian Flow

JOSEPH A. FAUCHER

Research Department, Union Carbide Chemicals Company, South Charleston, West Virginia

The Eyring-Ree theory of non-Newtonian flow is extended to the case of a continuous distribution of flow units. This results in an integral equation of the form

$$F(\dot{s}) = \int_0^\infty G(t) \operatorname{arc} \sinh(\dot{s}t) dt.$$

This equation can be solved by integral transform methods to yield the unknown distribution function $G(t)$ when the flow curve $F(\dot{s})$ is known as an analytic function. For the case of limited empirical data, approximation methods can be used to obtain $G(t)$. Experimental data are shown for polyethylene at two temperatures and the distribution functions calculated.

IN 1955 Eyring and Ree¹ proposed a theory of non-Newtonian flow based on the postulate of a small number of groups of flow units with appreciably different relaxation times. Although the theory has had some success in the flow of suspensions,² it seems to be less well adapted to molten polymers. In view of the continuous change in the size of molecules and segments

in most polymers, it seems more reasonable to expect a continuous distribution of flow units for this case. We have attempted, therefore, to extend the Eyring-Ree theory in this manner along the following lines.

The development begins with the basic flow equation [reference 1, Eq. (3)]

$$F(\dot{s}) = \sum_{n=1}^{\infty} \frac{X_n}{\alpha_n} \operatorname{arc} \sinh(\beta_n \dot{s}), \quad (1)$$

¹ H. Eyring and T. Ree, *J. Appl. Phys.* **26**, 793-800 (1955).

² S. H. Maron and P. E. Pierce, *J. Colloid. Sci.* **11**, 80-95 (1956); S. H. Maron and A. W. Sisko, *J. Colloid. Sci.* **12**, 99-107 (1957).

where F is the shearing force, \dot{s} is the shear rate, X_n the fractional area on the shear surface of the n th flow unit, α_n the ratio of shear volume to twice the kinetic energy of the n th flow unit, and β_n is proportional to the relaxation time of the n th unit. Actually, for simplicity we shall assume that β_n is identically the relaxation time. This assumption has no effect on the following argument, for the case where β_n is linearly proportional to relaxation time involves only a redefinition of the distribution function.

With a continuous distribution of relaxation times for the different flow units, the sum in Eq. (1) becomes an integral over all times

$$F(\dot{s}) = \int_0^\infty G(t) \operatorname{arc} \sinh(\dot{s}t) dt, \quad (2)$$

where $G(t)$ is the distribution of relaxation times. We thus have the problem of inverting the integral Eq. (2) for the unknown function $G(t)$, once we are given the form of the flow curve $F(\dot{s})$. The solution to this type of equation has been discussed in several places. Montroll³ derived a formal solution by Fourier transforms, but this method is apparently not applicable to our case since the arc sinh function has no Fourier transform. Titchmarsh⁴ performs the inversion by Mellin transforms to produce a solution of the type

$$G(t) = \int_0^\infty F(\dot{s}) K(t\dot{s}) d\dot{s}, \quad (3)$$

where $K(t\dot{s})$ is the so-called "solving kernel." However, we were unable to carry out the inverse Mellin transform leading to this function. Instead of a solution by such general means, we have found a particular method beginning with differentiation of Eq. (2)

$$F'(\dot{s}) = \int_0^\infty \frac{tG(t)dt}{[1+\dot{s}^2t^2]^2} = \frac{1}{\dot{s}} \int_0^\infty \frac{tG(t)dt}{[1/(\dot{s}^2+t^2)]^2}. \quad (4)$$

Noting that the denominator of the integrand is the Laplace transform of a zero-order Bessel function, we can write

$$\dot{s}F'(\dot{s}) = \int_0^\infty tG(t) \left[\int_0^\infty e^{-tz} J_0\left(\frac{x}{\dot{s}}\right) dx \right] dt \quad (5)$$

and reverse the order of integration

$$\dot{s}F'(\dot{s}) = \int_0^\infty J_0\left(\frac{x}{\dot{s}}\right) \left[\int_0^\infty tG(t) e^{-tz} dt \right] dx. \quad (6)$$

This step is legitimate provided that the integral

$$\int_0^\infty tG(t) e^{-tz} dt$$

converges. This condition will be satisfied by distribution functions of physical interest.

The integral in square brackets on the right side of Eq. (6) is the Laplace transform of $tG(t)$. Let $x\dot{p}(x)$ represent this transform, where $\dot{p}(x)$ is a function to be determined. Then,

$$\dot{s}F'(\dot{s}) = \int_0^\infty J_0\left(\frac{x}{\dot{s}}\right) x\dot{p}(x) dx \quad (7)$$

or

$$\frac{1}{y} F'\left(\frac{1}{y}\right) = \int_0^\infty x\dot{p}(x) J_0(xy) dx, \quad (8)$$

where $y = 1/\dot{s}$. The integral in Eq. (8) is simply the Hankel transform of $\dot{p}(x)$. The inversion for this transform can be performed at once,⁵ and gives

$$\dot{p}(x) = \int_0^\infty F'\left(\frac{1}{y}\right) J_0(xy) dy. \quad (9)$$

This is the required inversion of Eq. (2). If $F'(1/y)$ is some reasonable analytic function of y , then the integration in Eq. (9) can be performed explicitly and $\dot{p}(x)$ determined; $G(t)$ is then easily found by consulting tables of inverse Laplace transforms.

As an example, we shall calculate the distribution of relaxation times for a flow curve of the form

$$F(\dot{s}) = a\dot{s}^b, \quad \text{where } 0 < b < 1. \quad (10)$$

This power law has been frequently used by investigators in the past, although it has the evident disadvantage of predicting an infinite viscosity at zero shear rate. From Eq. (10) we have

$$F'(\dot{s}) = ab\dot{s}^{b-1} \quad (11)$$

or

$$F'(1/y) = aby^{1-b}. \quad (12)$$

Putting this into Eq. (9) we obtain

$$\dot{p}(x) = ab \int_0^\infty y^{1-b} J_0(xy) dy. \quad (13)$$

Hence

$$\dot{p}(x) = 2^{1-b} ab x^{b-2} \Gamma(1-b/2) / \Gamma(b/2) \quad (14)$$

and

$$x\dot{p}(x) = 2^{1-b} ab x^{b-1} \Gamma(1-b/2) / \Gamma(b/2) = \mathcal{L}\{tG(t)\}, \quad (15)$$

with the usual Laplace transform notation. The inverse transform is easily found where

$$G(t) = \frac{ab 2^{1-b} \Gamma[1-(b/2)] t^{-b-1}}{\Gamma(b/2) \Gamma(1-b)} = \frac{2ab \pi^{1/2} t^{-b-1}}{\Gamma(1/2-b) \Gamma(b/2)}, \quad (16)$$

making use of the Γ -function duplication formula. A check on the mathematics is provided by substituting $G(t)$ from Eq. (16) into Eq. (2) which indeed yields the result of Eq. (10).

³ E. W. Montroll, J. Chem. Phys. **10**, 228-9 (1942).

⁴ E. C. Titchmarsh, *Introduction to the Theory of Fourier Integrals* (Oxford University Press, New York, 1948), 2nd ed, Chap. 8.

⁵ C. J. Tranter, *Integral Transforms in Mathematical Physics* (Methuen and Company, Ltd., London, England, 1956), pp. 11-12.

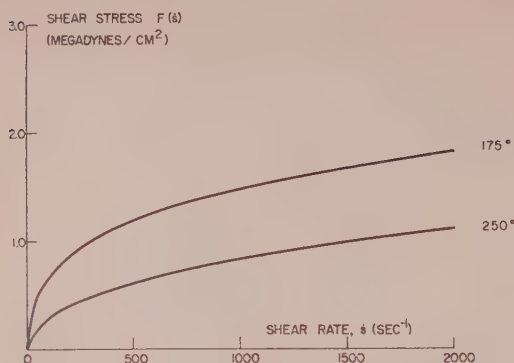


FIG. 1. Flow curves for high pressure polyethylene.

It is interesting to observe that the physically impossible flow curve of Eq. (10) leads to a physically impossible distribution of relaxation times, Eq. (16), in which the magnitude of the distribution function increases beyond all bounds as t approaches zero.

In actual practice, of course, the flow curve $F(\dot{s})$ is determined empirically for a limited range of \dot{s} and is not readily fitted by an analytic function. In such cases one has to resort to approximation procedures. We begin with Eq. (4), writing it in the form

$$F'(\dot{s}) = \int_0^{1/\dot{s}} \frac{tG(t)dt}{[1+\dot{s}^2t^2]^{\frac{1}{2}}} + \int_{1/\dot{s}}^{\infty} \frac{tG(t)dt}{[1+\dot{s}^2t^2]^{\frac{1}{2}}} \quad (17)$$

For small \dot{s} (say less than 1) the first integral is the main contribution.

$$F'(\dot{s}) \approx \int_0^{1/\dot{s}} \frac{tG(t)dt}{[1+\dot{s}^2t^2]^{\frac{1}{2}}} \approx \int_0^{1/\dot{s}} tG(t)dt, \quad (18)$$

since $\sqrt{1+\dot{s}^2t^2}$ is of order unity in this range. Differentiate both sides with respect to $1/\dot{s}$ to get

$$G(t) = 1/\dot{s} \approx -\dot{s}^3 dF/d\dot{s}^2. \quad (19)$$

For large \dot{s} (greater than 1) the second integral makes the major contribution, and we have

$$F'(\dot{s}) \approx \int_{1/\dot{s}}^{\infty} \frac{tG(t)dt}{[1+\dot{s}^2t^2]^{\frac{1}{2}}} \approx \frac{1}{\dot{s}} \int_{1/\dot{s}}^{\infty} G(t)dt, \quad (20)$$

since $[1+\dot{s}^2t^2]^{\frac{1}{2}} \approx \dot{s}t$ in this range. From this equation we can, by differentiation, arrive at

$$G(t) = 1/\dot{s} \approx \dot{s}^3 (d^2F/d\dot{s}^2) + \dot{s}^2 (dF/d\dot{s}). \quad (21)$$

Actually, neither of the formulas, for Eqs. (19) or (21), is very satisfactory. The first involves the second derivative of an empirical function, and the second is usually the difference of two large numbers. Nevertheless, it is of some interest to calculate the distribution function for a specific polymer melt. We have determined, by capillary extrusion, the flow curve $F(\dot{s})$ for

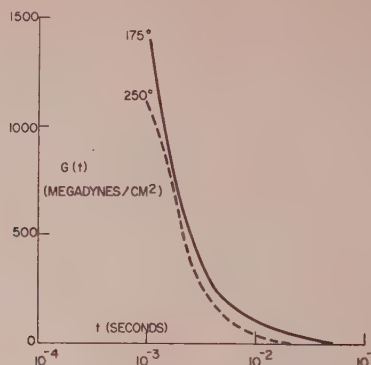


FIG. 2. Relaxation distributions for high pressure polyethylene.

a low-density, high-pressure polyethylene at 175° and 250°C. The usual corrections for entrance effect were made as well as the "Rabinowitch correction" to get the true shear rate at the wall.⁶ The two curves are shown in Fig. 1. From these data, first and second derivative curves were obtained by graphical differentiation and the distribution functions calculated by the approximations above. The functions thus found are shown in Fig. 2. Although the approximations are quite rough, nevertheless, the time scale (10^{-3} to 10^{-1} sec) is certainly of a reasonable order of magnitude. Also, the distribution for 250°C falls at shorter times than that for 175°C as expected. The values of $G(t)$ for t less than 10^{-3} seconds cannot be obtained from our data since shear rates much greater than 1000 sec^{-1} are required.

In conclusion we should like to point out that the description of non-Newtonian flow in terms of the distribution of relaxation times leads to some new insight into the mathematical formulation of the flow curve $F(\dot{s})$. Any physically reasonable distribution function generates, by means of Eq. (2), a stress function which has qualitatively the correct shape for pseudoplastic flow. Hence we can find new possible analytic functions to fit empirical data.

As an example, consider the distribution te^{-bt} which gives

$$F(\dot{s}) = \frac{1}{b^2} \left\{ \frac{\pi}{2} \left[H_0\left(\frac{b}{\dot{s}}\right) - Y_0\left(\frac{b}{\dot{s}}\right) \right] + \frac{\pi b}{2 \dot{s}} \left[H_1\left(\frac{b}{\dot{s}}\right) - Y_1\left(\frac{b}{\dot{s}}\right) \right] - \frac{b}{\dot{s}} \right\}, \quad (22)$$

where the H 's are Struve functions and the Y 's are Bessel functions of the second kind. Although the functions in Eq. (22) may appear rather complex, they are easy to work with numerically, being tabulated in Watson's treatise.⁷

⁶ See, for example, T. Alfrey, *Mechanical Behavior of High Polymers*. (Interscience Publishers, Inc., New York, 1948), pp. 41-42.

⁷ G. N. Watson, *A Treatise on the Theory of Bessel Functions* (Cambridge University Press, New York, 1958), 2nd ed., p. 666.

Molecular Motion in Disordered Regions of Solid Polyethylene

W. P. SLICHTER

Bell Telephone Laboratories, Murray Hill, New Jersey

Proton magnetic resonance studies have been made to compare the molecular motions ascribable to the disordered regions of solution-grown and melt-grown specimens of solid polyethylene. Studies have been made of both the spin-lattice and spin-spin relaxations. Restricted motion attributable to defect regions develops in solution-grown crystals as the temperature is raised, but the number of protons in motion changes reversibly with heating and cooling, provided the maximum temperature is below $\sim 100^\circ\text{C}$. With higher temperatures the motion is greater in abundance and broader in frequency distribution. The increase is permanent despite annealing. Segmental motion attributed to molecules within the crystal is seen in solution-grown crystals in the interval 50 – 100°C , but occurs to a much smaller degree in melt-grown and heat-treated samples. A model for the observed behavior is proposed.

INTRODUCTION

THE discovery that single crystals of polyethylene and other polymers can be grown from dilute solution has stimulated great interest in the nature and properties of these structures. The interest arises not only for the solution-grown structures themselves, but also for their significance to the study of polymers crystallized from the melt. The aspect of solution-grown crystals that has received the greatest attention is their morphology. Rather little has been said about the nature of chain motions in these substances. Indeed, chain motion in bulk polymers is principally ascribed to what has traditionally been termed the "amorphous" portion. This paper reports some proton magnetic resonance measurements that were undertaken to study motion in solution-grown crystals of linear polyethylene and to compare such samples with polyethylene crystallized from the melt.

EXPERIMENTAL

Proportion of Mobile Segments

Previous studies¹⁻³ on solution-grown crystals of polyethylene have shown that a substantial fraction of the chain segments exhibit thermal motion at room temperature after the sample has been heated to temperatures in the range 100 – 135°C . The proportion of protons exhibiting this motion, the "mobile fraction,"² increases as the temperature of heat treatment approaches the melting point of bulk polyethylene. This behavior has been associated² with the thickening of polyethylene single crystals under similar heat treatment, as seen in low-angle x-ray diffraction.⁴ The segmental mobility has been ascribed to the influence of lattice disorder, thought to be produced by the heat treatment.

Earlier studies¹⁻³ dealt with room-temperature measurements of mobility following heating. Figure 1

shows the development of the mobile fraction as measured at *elevated temperatures*. Two samples are described, both consisting of linear polyethylene (Phillips Marlex 6000 series, type 50) crystallized at 80°C from 0.1% solution in xylene.⁵ The data in Fig. 1 were collected over a period of several days, with the ascending values taken in sequence of increasing temperature. Thus, the heating rate was effectively a few degrees an hour. Similarly, the descending points were taken in sequence of decreasing temperature. One sample (circles) had not previously been heated to elevated temperature. During the course of heating the mobile fraction became progressively greater (open circles). However, the trend was reversible; return to a lower temperature brought about a mobile fraction comparable to that encountered previously, provided the maximum temperature was not too high. However, when the maximum temperature exceeded 115 – 120°C , a return to lower temperatures yielded values of the mobile fraction that lay well above those measured for the previously unheated material. This phenomenon is shown in Fig. 1 (filled circles).

The second sample described in Fig. 1 (triangles) had been heated following crystallization to a fairly high temperature, 132°C . The temperatures for the NMR measurements lay below this figure. It is seen that the values for the mobile fraction during heating (open triangles) and those measured during cooling (filled triangles) follow essentially the same course.

It is appropriate to report in passing how the mobile fraction in melt-grown polyethylene depends on the conditions of crystallization. Mandelkern⁶ has crystallized a series of samples from the melt at selected temperatures over various intervals of time. Figure 2 shows the variation of the mobile fraction with time and temperature of crystallization, measured by NMR at room temperature. Also shown are data for two samples

⁵ As in the previous study,² the crystallizations were carried out from 1-liter batches of solution. Crystallization occurred overnight. The resulting crystals were filtered off fairly rapidly and were then heated gently (65 – 70°C) for several days in a vacuum oven. Certain of the subsequent heat treatments were performed in the sample holder of the spectrometer, in which case the temperature uncertainty was about $\pm 1^\circ\text{C}$. In other cases the heat treatment took place before the NMR measurements, and then the temperature uncertainty for the preparation was $\pm 0.05^\circ\text{C}$.

⁶ L. Mandelkern (to be published).

¹ A. Peterlin, F. Krasovec, E. Pirkmajer, and I. Levstek, *Macromol. Chem.* **37**, 231 (1960).

² W. P. Slichter, *J. Appl. Phys.* **31**, 1865 (1960).

³ A. Peterlin and E. Pirkmajer, *J. Polymer Sci.* **46**, 185 (1960).

⁴ W. O. Statton and P. H. Geil, *J. Appl. Polymer Sci.* **3**, 357 (1960).

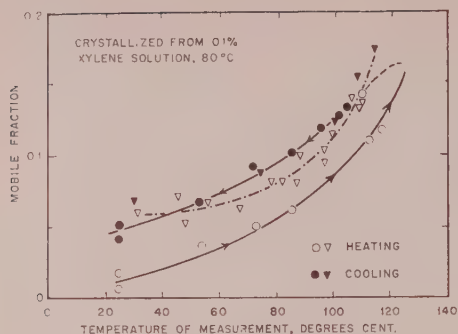


FIG. 1. Variation of the mobile fraction with temperature: (a) linear polyethylene crystallized from 0.1% xylene solution at 80°C (circles); (b) same, following heat treatment at 132°C (triangles).

that Mandelkern crystallized from the melt at 0°C and subsequently annealed for 93 days at the temperatures indicated. It is seen that the proportion of chain segments having mobility is strongly influenced by the conditions of crystallization and is capable of being brought to quite small values.

Scale of Motion

The scale of the motion responsible for what has been called the mobile fraction requires identification. NMR studies such as these are responsive to two relaxation processes, the spin-lattice and spin-spin processes, characterized by time constants T_1 and T_2 , respectively.⁷ These parameters are invoked to identify characteristic frequencies of molecular motion and to deduce, in a rudimentary fashion, the distributions of these frequencies. The quantity T_2 , which is inversely proportional to the linewidth, begins to undergo change with rising temperature when the thermal motions reach frequencies of the order of 10^4 or 10^5 cps and amplitudes of the order of lattice dimensions. The quantity T_1 is shown theoretically⁸ to depend in an explicit way on the Brownian rotation in simple liquids and to exhibit a minimum when the thermal motion attains a frequency close to the frequency of the nuclear resonance, i.e., about 10^7 – 10^8 cps. It is hardly to be expected that theories developed to describe idealized behavior in simple liquids will also pertain in any detail to polymer solids. Still, the existence of a minimum in T_1 graphed as a function of the temperature may be presumed to identify a characteristic frequency of thermal motion.

Powles⁷ has remarked on the importance of measuring both T_1 and T_2 in polymers. The NMR studies on solid polymers to date have mainly dealt with T_2 (usually

reported in terms of the linewidth). Experimental complications have largely militated against T_1 measurements. With semicrystalline polymers, in particular, there exists the additional complication of distinguishing between the components of the resonance arising from the crystalline and amorphous portions of the solid.⁹ Thus, T_1 studies with semicrystalline polymers have been sparse.^{10,11} In the following, both T_1 and T_2 are reported for solution-grown and bulk polyethylene. The T_1 measurements were made by a saturation method.⁸ Although it would be more gratifying to measure T_1 directly by a transient technique,¹² only the saturation method was applicable to these samples with the apparatus at hand. The scale of T_1 's in these materials was set by making saturation studies on a sample of dilute CuSO_4 solution, for which T_1 was found directly in another apparatus using transient methods.

Linewidth Measurements

Figure 3 shows the temperature dependence of the NMR linewidth for the broad ("crystalline") component of the absorption. Four kinds of material are represented: (a) linear polyethylene crystallized from 0.02% xylene solution at 70°C, collected by filtration, and air-dried for five days at room temperature; (b) same, except dried in vacuum oven at 70°C for seven days; (c) same as (a), except subsequently heated at 132°C for one day; (d) crystallized in bulk at uncertain temperature, and annealed at 132°C for eight days.

It is seen that sample (a) experiences a narrowing of the resonance not far above room temperature (open circles), until a temperature is reached in the vicinity of 125°C. The maximum temperature attained is in some doubt, but did not exceed 128°C. Some transformation

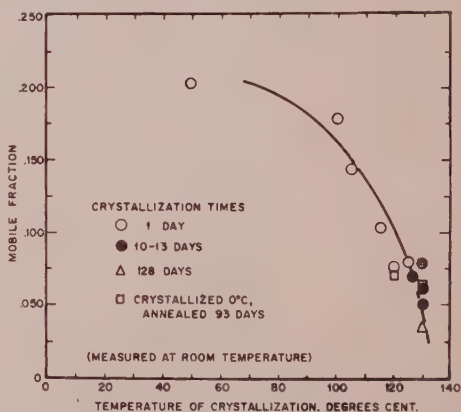


FIG. 2. Variation of mobile fraction with time and temperature of crystallization from the melt. (Samples prepared by Dr. L. Mandelkern, National Bureau of Standards.)

⁹ W. P. Slichter and D. W. McCall, *J. Polymer Sci.* **25**, 230 (1957).

¹⁰ C. W. Wilson, III, and G. E. Pake, *J. Chem. Phys.* **27**, 115 (1957).

¹¹ I. M. Ward, *Trans. Faraday Soc.* **56**, 648 (1960).

¹² H. Y. Carr and E. M. Purcell, *Phys. Rev.* **94**, 630 (1954).

⁷ For a discussion of these terms, the reader is referred to the review by J. G. Powles, *Polymer* **1**, 219 (1960); see also G. E. Pake, *Solid State Physics* (Academic Press, Inc., New York, 1956), Vol. 2, pp. 12–19.

⁸ N. Bloembergen, E. M. Purcell, and R. V. Pound, *Phys. Rev.* **73**, 679 (1948).

evidently occurred, for the linewidths measured with descending temperature (filled circles) lie well above those encountered during heating. Indeed, the linewidths during the cooling are comparable to those experienced with sample (c), which had received a preliminary heat treatment at 132°C (shown by triangles). In turn, this trend is also comparable to the temperature dependence of the linewidth for sample (d), the melt-grown specimen (data shown by squares).

It appears that the solution-grown material behaves singularly, unless it has experienced elevated temperatures. That is, molecular motion affects the broad component of the NMR line for the solution-grown polymer at comparatively low temperatures. The possibility suggests itself that this mobility may result from a residue of the solvent which disappears only when the temperature is fairly high. Sample (b), shown in Fig. 3 by crosses, was prepared to test this possibility. This sample was given moderate heating under vacuum, with the hope of removing residual solvent. The temperature dependence of the linewidth is seen to be similar to that of sample (a), which had not received this additional treatment. This result implies either that the solvent is too tenacious to be removed by such measures, or else that the greater segmental mobility is in fact a property of samples grown from solution. Under the circumstances, the latter alternative seems the more likely of the two.

It should be noted at this juncture that we have not undertaken to identify the broad component exclusively with the well-ordered regions of the samples, or to say that the narrow component wholly represents the disordered regions. Such a division would imply a morphological model consisting of two distinct phases and would overlook the possibility of a range of order and a corresponding range in segmental mobility. We do not offer a morphological interpretation at this point, but the important observation remains that there is a marked difference between the solution-grown and melt-grown samples with respect to the temperature dependence of the broad linewidth.

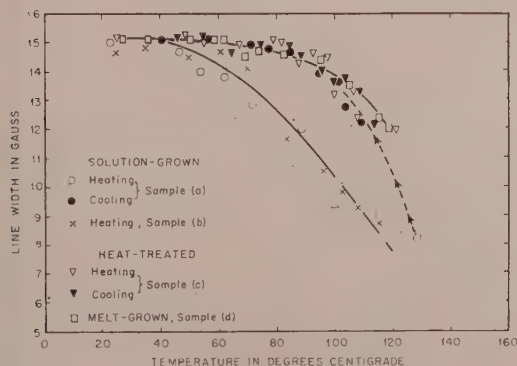


FIG. 3. Temperature dependence of the linewidth in the broad component of the NMR absorption.

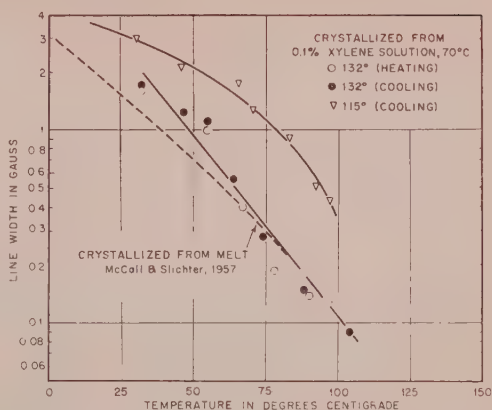


FIG. 4. Temperature dependence of the linewidth in the narrow component of the NMR absorption.

Figure 4 shows the temperature dependence of the linewidth for the narrow component of the resonance envelope, the portion previously^{10,13,14} ascribed to the "amorphous" regions of the solid. The graph shows data for two samples: (a) linear polyethylene crystallized at 70°C from 0.1% xylene solution, heated to 115°C and measured at descending temperatures; (b) similar material, but heat-treated at 132°C and measured with both ascending and descending temperatures. Also indicated (dashed line) is the behavior for melt-grown polyethylene.¹³ Not shown are the values found for the solution-grown polymer before reaching temperatures in the vicinity of 115°C. These values were so small that they were evidently fixed by the inhomogeneity of the laboratory magnet.

It is seen that heat treatment of the solution-grown material at 132°C produced about the same temperature variation of the narrow component as is observed in the bulk material. When the heat treatment is less drastic (115°C), the scale of motion in the mobile segments is less vigorous, as evidenced by the greater linewidth. However, the *broadening* of the narrow component of the resonance, experienced when the solution-grown material is first heated to the vicinity of 115°C, points to a change in the nature of the motions involved.

T_1 Measurements

Figure 5 shows the temperature dependence of the spin-lattice relaxation time T_1 for three samples: (a) polyethylene crystallized from 0.1% xylene solution at 70°C; (b) same, heated at 132°C for 24 hours; (c) polyethylene crystallized from the melt at uncertain temperature, and then annealed at 132°C for eight days. Since it is commonly supposed that thermal motions obey the Arrhenius relation, the values of T_1 are plotted

¹³ D. W. McCall and W. P. Slichter, J. Polymer Sci. **26**, 171 (1957).

¹⁴ R. C. Rempel, A. E. Weaver, R. H. Sands, and R. L. Miller, J. Appl. Phys. **28**, 1082 (1957).

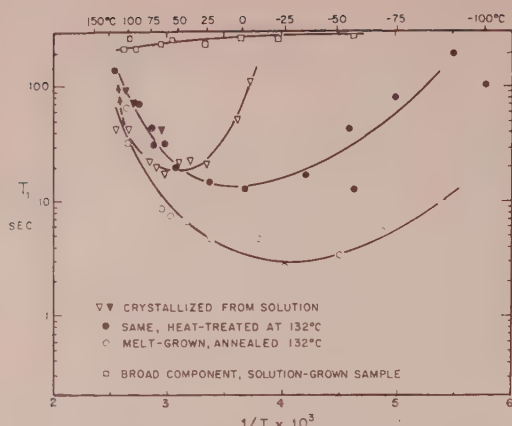


FIG. 5. Variation of the spin-lattice relaxation time T_1 with the reciprocal of the absolute temperature. (Data for narrow component of resonance, except as indicated otherwise).

against the reciprocal of the absolute temperature. The abscissa then represents the correlation time for molecular motions on some logarithmic scale. The data in Fig. 5 pertain chiefly to the mobile component in the resonance envelope. However, data for the broad component in the unheated sample of the solution-grown crystals is also plotted. T_1 for the broad component in each of the other samples was similar, being essentially constant over the range studied.¹⁵ In these studies $T_2 \ll T_1$, in contrast to the theory for simple liquids,⁸ which has $T_2 \cong T_1$ at higher temperatures. The maximum T_2 observable by the method used here was of the order of 10^{-8} sec, limited by the inhomogeneity of the magnet.

It should be emphasized that the existence of a minimum in the T_1 curve implies rather large amplitude in molecular motion occurring over all directions in space. This conclusion follows from the theory for simple liquids⁸ and from the analysis (cf. Pake⁷) that shows the vibrations of simple crystalline lattices to be inadequate to yield short T_1 's. Therefore, the existence of T_1 minima in Fig. 5 is evidence for substantial motion. Conversely, the absence of a T_1 minimum in the broad components of the samples studied here is in keeping with the interpretation that the corresponding motions are relatively restricted. It is therefore not surprising that T_1 for the broad component was similar for each of these samples.

The values of T_1 reported in Fig. 5 at the higher temperatures lie well above those reported by McCall, Douglass, and Anderson¹⁶ for similar polymers in the melt. The latter values are of the order of 0.2–0.3 sec and were obtained by transient methods rather than saturation studies. The data on molten polyethylene

show T_1 to decrease with decreasing temperature, without attaining a minimum at the lowest temperature studied (120°C). Possibly the differences between the data on molten polyethylene and those reported here arise from ambiguities which have already been implied as inherent in the saturation method. However, in comparing the results from the melt studies with those in Fig. 5, it must be remembered that the thermal histories of the specimens were very different, and therefore the lack of an overlap in the two sets of T_1 data is not surprising.

It is seen in Fig. 5 that T_1 for the mobile regions of the solution-grown sample shows a relatively sharp minimum near 50°C (open triangles). However, when the temperature reaches $\sim 120^\circ\text{C}$ and then descends, the T_1 curve follows a different course, leading to a broader and lower minimum occurring at a lower temperature (filled triangles). The temperature dependence of T_1 then resembles that of a similar sample that had been heat-treated at 132°C prior to measurement (filled circles). A still broader curve, with a lower minimum, is exhibited by the melt-grown sample.

By extension from the interpretation for simple liquids we may reach several qualitative conclusions. First, the existence of a T_1 minimum within the mobile component of the resonance identifies a characteristic correlation frequency of the order of the Larmor frequency (here, 3×10^7 cps). This characteristic motion is found at about 50°C for the solution-grown crystals prior to heat treatment, somewhat below 0°C after heat treatment, and still lower for the melt-grown material. The magnitude of T_1 at the minimum decreases in the same order, i.e., the molecular motions are increasingly effective in causing the spin-lattice relaxation. Concurrently, the T_1 minimum becomes progressively broader in this same order, a trend that is ascribable formally to an increasing span in the distribution of molecular relaxation times.^{16,17} The theoretical interpretation that describes this behavior also predicts that the broadening of the curve is accompanied by a lifting of the minimum.^{16,17} The present observation that the T_1 curve becomes deeper while it broadens may be taken as evidence that the motions are not only wider in frequency distribution but also greater in amplitude.

DISCUSSION

These observations include a number of features that call for explanation: (1) the existence in the solution-grown crystals, prior to extreme heating, of motion that evidently is associated with disordered regions ("amorphous" regions in previous terminology), and that is restricted in its frequency spectrum compared to the motions seen in bulk samples; the existence of motion associated with the crystalline lattice that is large relative to that in bulk samples; (2) the development of

¹⁶ D. W. McCall has suggested (private communication) that the spin-lattice relaxation in the ordered regions may occur by diffusion of nuclear spin to the disordered regions, where the relaxation process occurs relatively efficiently (cf. G. E. Pake⁷).

¹⁷ J. G. Powles and K. Luszczynski, *Physica* **25**, 455 (1959).

more intense motion, characterized by a wider frequency distribution, in the disordered regions of these crystals when the temperature is high enough, and the concurrent decrease in the motion associated with the crystalline lattice; (3) reversibility of the properties described in (1) with change in temperature over a modest temperature range; the irreversible change to the properties in (2) when the temperature is high enough. The following interpretation seems to form a self-consistent picture. However, it must be emphasized that this scheme is to be regarded merely as a model.

First, with reference to the solution-grown crystals, it is plausible that the concentrations and rates employed in growing these crystals from solution produced structures that were by no means ideal in their order. We postulate that inefficiency in the growth process leaves numerous small-scale imperfections in the chain packing even though allowing the familiar, folded structure. The chain segments directly around these imperfections experience less constraint than they would in a well-ordered lattice, and therefore they display a degree of motion, rotational and translational, that produces a narrow resonance envelope and a minimum in the T_1 curve. It should be emphasized again that the frequencies of thermal motion necessary to produce these effects in NMR spectroscopy are very small in terms of lattice vibrations, such as those active in the infrared. The significant criterion here is that the amplitudes of motion have to be large, for otherwise they will not produce the observed reduction in the spin-spin coupling or the observed T_1 minimum. In particular, to achieve the narrow lines shown in Fig. 4, the spin couplings responsible for the broadening at lower temperatures must be averaged out to a large extent. This means that the proton-proton vectors concerned must take on all directions in space in the time scale involved (i.e., a scale short compared with 10^{-8} sec, though not necessarily approaching the scale of infrared vibrations, $\sim 10^{-13}$ sec).

From these requirements we infer that the regions of disorder have to be large compared with the cross-sectional dimensions of the molecule, and it is reasonable to suppose that they include voids whose volume corresponds to several CH_2 groups. On the other hand, the T_1 data suggest that the spectrum of motions is narrower and possesses less amplitude than in the disordered regions of the heat-treated and bulk materials. From this, we infer that the disordered regions in the solution-grown crystals are comparatively small, so that they give rise to relatively sharply defined motions.

The unusual narrowing of the broad component in the solution-grown crystals (Fig. 3) points to motion that is appreciable for a crystalline solid. Indeed, the linewidth falls to half its low-temperature value, a transformation that corresponds to rotation of all the chain segments about their long axes.^{13,18} Again, we

recall that this behavior requires rotations at the rate of only $\sim 10^5$ cps, so that the conclusion is not at all incompatible with the picture of a static lattice that comes from other types of measurement, e.g., x-ray diffraction. The important aspect is the contrast between these crystals and those belonging to heat-treated or bulk specimens, which display much less motion. It is suggested that the disorder discussed in the preceding paragraphs has the further consequence of lowering the constraints to chain rotation in the nominally ordered parts of the solution-grown crystals.

We then suggest that heating to higher temperatures, in the vicinity of 110–125°C, causes these motions to become sufficient in amplitude that they permit longitudinal adjustment of the chain segments within the lattice. The consequence will be for the structure to seek a more favorable array, in which most of the segments are packed over long sequences with a well-ordered structure, and in which the imperfections tend to coalesce into larger regions of disorder. This process constitutes an annealing for the comparatively well-ordered portions of the solution-grown crystals and results in greater constraint to chain motion, as seen in the broadening of the corresponding part of the NMR envelope (Fig. 3). The coalesced regions of imperfections are now more voluminous, however, and display a wider spectrum of frequencies, with motions of greater amplitude.

The motions that produce the annealing process postulated here evidently have still further effects as the temperature is raised, for it is clear from the work of Statton and Geil⁴ that a recrystallization process occurs above 115°C. This change in morphology evidently produces fairly extensive regions in which the constraints to chain motion are small.

The chief elements in the foregoing model are: (1) that small-scale disorder inherently occurs abundantly in polyethylene crystals as they are commonly grown from solution, and (2) that chain segments are capable of considerable mobility at temperatures below the melting point of the bulk polymer. The concept of imperfections calls for devising studies of samples that may be presumed to differ only in their structural regularity.

ACKNOWLEDGMENTS

I am grateful to Dr. L. Mandelkern, National Bureau of Standards, for supplying samples of polyethylene from his experiments. It is a pleasure to acknowledge the contribution to this work from discussions with Dr. Mandelkern, with Professor A. E. Woodward and Dr. A. Odajima, Pennsylvania State University, and with Dr. H. D. Keith, Dr. S. Matsuoka, and Dr. D. W. McCall, Bell Telephone Laboratories. I am also grateful to Dr. P. H. Geil and Dr. W. O. Statton, E. I. duPont de Nemours and Company, for their valuable comments on the manuscript.

¹⁸ E. R. Andrew, J. Chem. Phys. **18**, 607 (1950).

Light Scattering Study of the Annealing of Drawn Polyethylene*

MARION B. RHODES AND RICHARD S. STEIN

Department of Chemistry, University of Massachusetts, Amherst, Massachusetts

Low-angle light-scattering patterns are obtained for stretched polyethylene films which are annealed both with and without the constraint of constant length. The effects of stretching temperature, annealing temperature, temperature of measurement, and degree of elongation are studied. Morphological changes in superstructure are found which parallel changes in crystal orientation.

INTRODUCTION

THE low-angle photographic light-scattering patterns from polyethylene films have been shown to result from the variation in orientation of the polarizability ellipsoid accompanying the optical anisotropy of close-packed spherulites.¹ The pattern has been shown to depend upon the size of the spherulite and the difference between its radial and tangential polarizability.

All samples studied were a medium density (0.93) experimental Monsanto polyethylene. Films were prepared by placing moulding pellets between sheets of aluminum foil on the platens of a Carver press, heating to 146°C, and applying about 5000 lb pressure for about 45 min. The press was then allowed to cool at its natural rate by shutting off power to the heaters.

Samples were stretched in a hand stretching jig at an approximately uniform rate of about 50% per minute. Elongations were measured for the samples held at constant length in the elongated state, but were measured

after the contraction took place (before annealing) for the unconstrained samples.

The change in the scattering pattern upon drawing the polyethylene films has been reported.¹ For example, Fig. 1 shows the change in the H_V scattering pattern (vertical polarization of the incident light with horizontal orientation of the analyzing polaroid in the scattered beam). The four-leaf clover-type pattern characteristic of anisotropic spherulite scattering decreases in intensity and approaches a horizontal streak. It has been pointed out that this is related to the change from spherulitic to fibrillar morphology upon stretching.

Polarization studies in the stretched state indicate that the scattering elements are most polarizable approximately in the stretching direction and are most elongated in this direction. A more detailed examination of the scattering patterns, especially at intermediate elongations (25–200%), indicates that the principal polarizability direction does not lie exactly in the

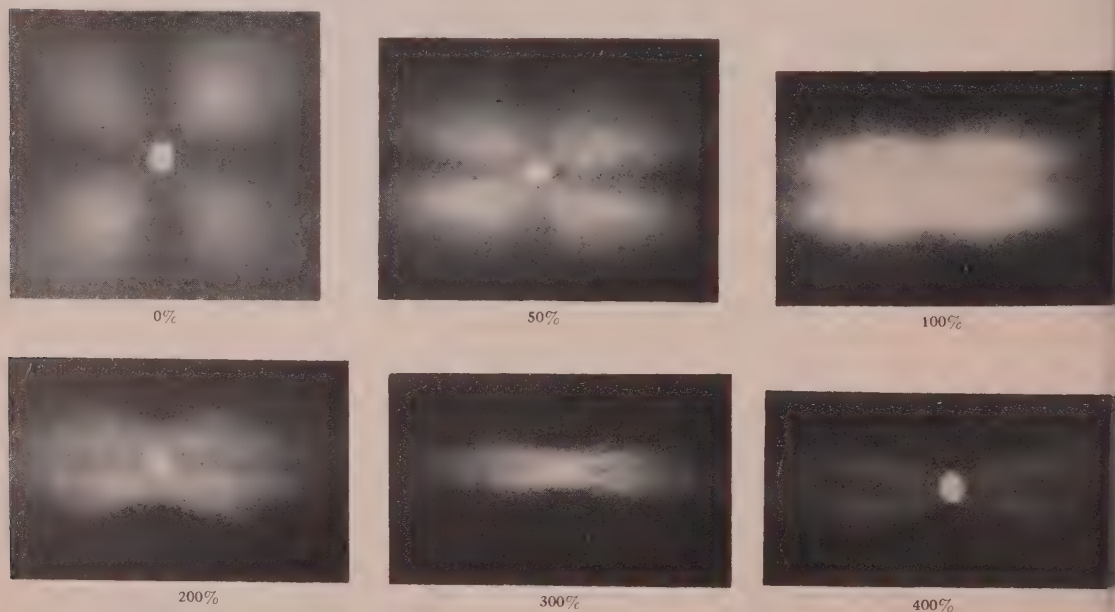


FIG. 1. The change in the H_V scattering pattern for polyethylene with percentage elongation. The stretching direction is vertical. (For notation and experimental arrangement, see reference 1.)

* Supported in part by a contract with the Office of Naval Research and grants from the Petroleum Research Fund, the Plastic Corporation, and the Fabric Research Laboratories, plus assistance from Monsanto Chemical Company.

¹ R. S. Stein and M. B. Rhodes, *J. Appl. Phys.* **31**, 1873 (1960).

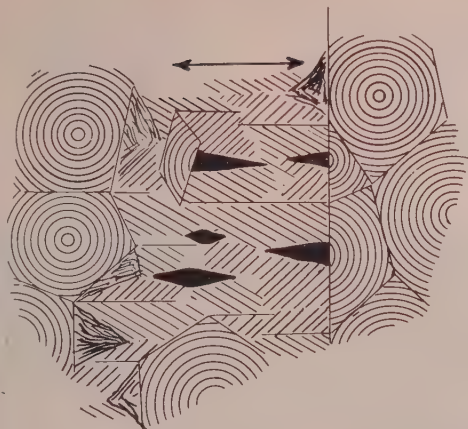


Fig. 2. A postulated structure of partially elongated polyethylene sample having a fibrillar and spherulitic phase coexistent.

stretching direction but at a small angle to it. This postulate is necessary in order to account for the cusps at a small angle to the horizontal scan in Fig. 1 and in the other polarization cases which have been reported. An example of a possible type of morphology for an elongated sample that might account for the scattering patterns is given in Fig. 2.

Photomicrograph structures of this type have been observed in drawn polyethylene.^{2,3} A more detailed examination of the structures which might lead to the observed patterns is in progress using the optical-diffraction technique. The lines on the figure represent positions of extinction and are seen when the sample is viewed between crossed circular polarizers. The usual Maltese cross pattern in the spherulites is seen with crossed plane polarizers. They probably result from periodicity of orientation of crystallites in the drawn regions as well as in the spherulites.

This orientation of the principal polarizability direction at a preferred angle to the stretching direction was also inferred from studies of scattering at higher angles.^{4,5} In order to account for the variation of the intensity of scattering of polarized light with elongation, it was necessary to assume that the angle α between the principal polarizability direction and the stretching direction changed from a random distribution in an unoriented sample to a preferred value of about 40° at about 25% elongation. With further stretching the preferred average value of α decreased, but the distribution of values about this average remained narrow (Fig. 3).

This preferred orientation of the scattering aggregate is analogous to the observed, preferred orientation of

the c -crystal axis observed by x-ray diffraction.^{6,7} It is probably also related to the observation that the modulus of a stretched polyethylene film is least at an angle to the stretching direction.⁸ It may be a consequence of the deformation of the polyethylene occurring most easily by a shear mechanism, with the direction of maximum shear occurring at 45° to the direction of applied force combined with an easy mechanism of crystal shear in this direction. It has been observed that this initial orientation is accompanied by the a axis of the crystal orienting perpendicularly to the stretching direction more rapidly than the b axis.

Closer examination of the H_V patterns in the vicinity of 200% extension proves interesting. It is apparent in Fig. 4 that the change in orientation is not uniform but appears to undergo an abrupt transition in this region. Several 200% photographs are included since the change at this elongation is sufficiently abrupt that it is difficult to obtain reproducible patterns. One sees from Fig. 1 that the angle between the maxima and the vertical in the four-leaf clover pattern increases from 45° to about 80° . With further elongation there is no increase in this angle but a more or less abrupt transition to a pattern consisting of two horizontal parallel lines. A region of coexistence of the two patterns exists. With further elongation the low elongation pattern disappears, the horizontal lines become sharper, and their intensity decreases. The discontinuous morphological change occurring upon drawing closely corresponds to the mechanism proposed by Richard and Gaube.⁸

The behavior is suggestive of the three regions of orientation previously deduced from x-ray diffraction studies.⁹ It would seem as though the first region corresponds to a reversible deformation of the spherulites with maintenance of their structure, while the second

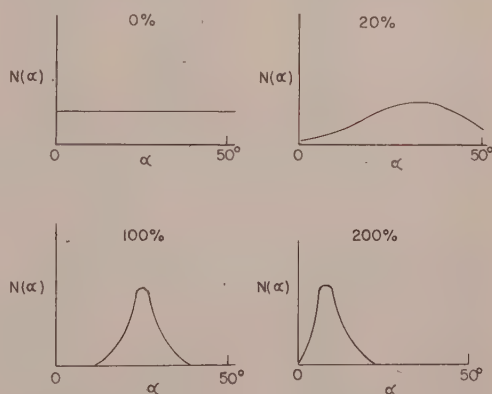


Fig. 3. The variation of the angle α between the c axis and the stretching direction with elongation.

² A. J. Foglia (private communication).

³ R. Ullman (private communication).

⁴ F. H. Norris and R. S. Stein, *J. Polymer Sci.* **27**, 87 (1958).

⁵ R. S. Stein, J. J. Keane, F. H. Norris, F. A. Bettelheim, and P. R. Wilson, *Ann. N. Y. Acad. Sci.* **83**, 37 (1959).

⁶ R. A. Horsley and H. A. Nancarrow, *Brit. J. Appl. Phys.* **2**, 345 (1951).

⁷ A. Keller, *J. Polymer Sci.* **15**, 31 (1955).

⁸ K. Richard and E. Gaube, *Kunststoffe* **6**, 262 (1956).

⁹ R. S. Stein and F. H. Norris, *J. Polymer Sci.* **21**, 381 (1956).

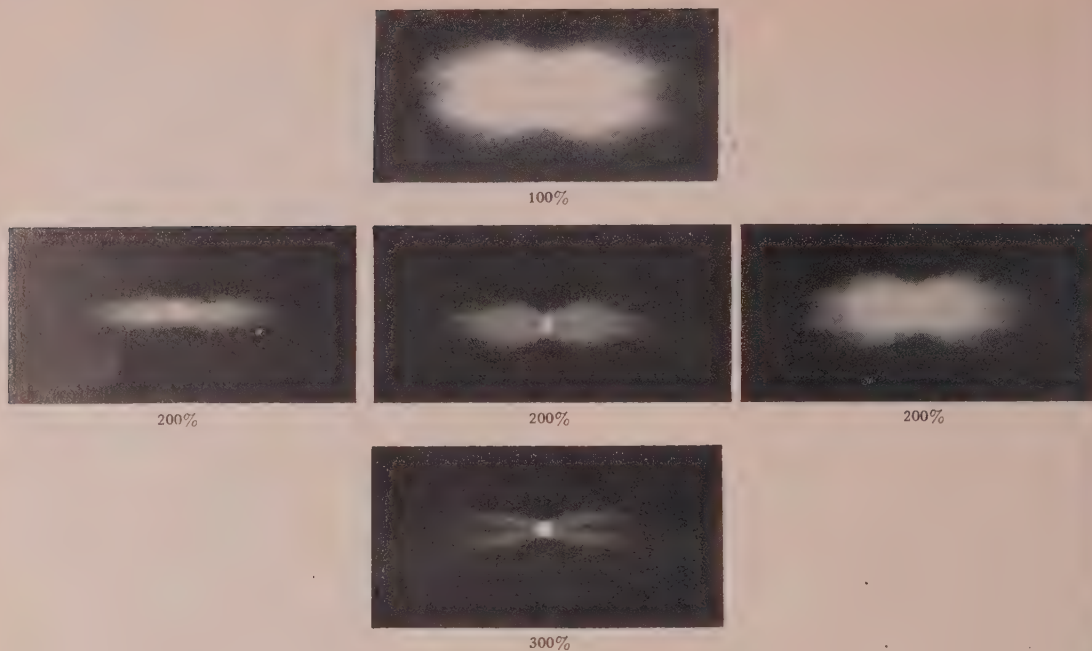


FIG. 4. Some H_V pictures in the vicinity of 200% elongation.

is related to an irreversible destruction of the spherulite with a discontinuous transformation to fiber-like structures. With further elongation, the orientation of the structures and their repeat distance both increase.

EFFECT OF SWELLING STRETCHED SAMPLES

If the scattering from stretched polyethylene is interpreted in terms of the refractive index heterogeneity associated with a bundle of oriented parallel anisotropic fibrils, the question of what is between these fibrils becomes paramount. Two possibilities are (a) voids and (b) amorphous material. In both cases, the scattering should be affected appreciably by introducing a swelling solvent having a refractive index different from that of the polymer. This was done for two polyethylene samples which were stretched 50%, held at that elongation, and swollen for 240 hr with trichlorobenzene ($n=1.5671$) and heptane ($n=1.3879$). The "before and after" light scattering patterns are presented in Fig. 5. The V_V polarization was used because this is most sensitive to scattering due to density fluctuations as well as orientation fluctuations.

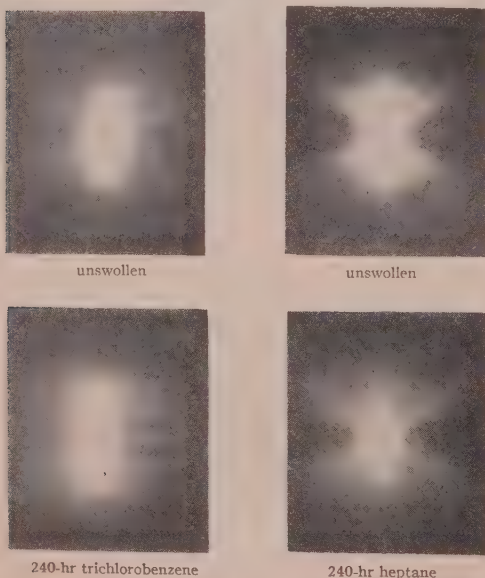


FIG. 5. V_V scattering patterns for unswollen polyethylene samples which were stretched (vertically), held at 50% elongation, and then swollen for 240 hr in (a) trichlorobenzene and (b) heptane.

It is apparent that there is negligible effect on swelling, in agreement with previous observations in the high-angle scattering region and in the case of scattering from portions of single polyethylene oxide spherulites. The most reasonable interpretation of this observation is that the refractive index heterogeneity at the fibril boundary is a result of an orientation rather than a density discontinuity. Thus a fibril axis would be defined (at least from a light scattering point of view) as the locus of a set of crystals with highly correlated orientation. The fibril is distinguished from neighboring fibrils in that orientations of crystals in these would differ from those in it in a discontinuous way. (Orientational angle

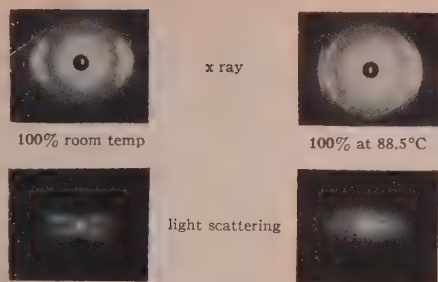


FIG. 6. The x-ray diffraction and H_V light scattering patterns for a polyethylene sample stretched 100% at (a) room temperature and (b) 88.5°C.

would be clustered about a different average value.) From the point of view of considerations of mechanical properties, it would be necessary to introduce other requirements to define a fibril (such as connectivity between crystals by molecular chains).

EFFECT OF TEMPERATURE OF STRETCHING

It was pointed out that the splitting of the low-elongation scattering pattern into cusps was indicative of a preferential orientation of principal polarizability directions at a small angle to the stretching direction. A comparison with the x-ray diffraction pattern is made in Fig. 6 in the left-hand pair of patterns. The splittings of the 110 reflection (the most intense one) is apparent. One finds, upon stretching at higher temperatures, that the splitting of the 110 reflection is lost, indicating a uniform distribution of orientations of the c axes about the stretching direction, rather than preferred orientation at a fixed angle to the stretching direction. As can be seen in the right-hand photographs in Fig. 6, the splitting of the light scattering pattern is also lost for the sample stretched at 88.5°C. Thus, there is also diffuseness of orientation of the macroscopic structures for orientation at the higher temperatures.

EFFECT OF ANNEALING AT CONSTANT LENGTH

It has been reported that, upon heating stretched polyethylene film to a temperature somewhat below the melting point, there is a reorganization of the crystal orientation with a change from the previously described type of orientation produced by drawing at room temperature (with the c -axis at a small angle to the stretching direction) to a state characterized by the x-ray diffraction pattern shown in Fig. 7.^{6,7,10,11} The 200 reflection has moved from the equator to the meridian. An analysis of this state shows that it is characterized by the b axis being oriented perpendicular to the stretching direction, with some preference of the orientation of the a axis along the stretching direction.

Corresponding H_V light scattering patterns were obtained at 99°C for a sample stretched 500% at 30°C and heated to 107°C at constant length (Fig. 8). It was then cooled to 30°C. One observes that, under these conditions, some disorientation occurs which is accompanied by a loss of diffuseness of the scattering pattern, indicating a more narrow distribution of orientations at a greater angle to the stretching direction. There is no appreciable difference between the scattering pattern obtained at 99°C and that obtained on cooling back to room temperature, indicating no appreciable regrowth of crystalline material on recoiling to 30°C.

A proposed interpretation of both the light scattering and x-ray patterns is that the drawing at room temperature produces strained crystalline structure. Other evidence for this comes from x-ray diffraction data showing an appreciable increase in the width of diffraction peaks on stretching.¹² It appears that the melting point of these strained crystals is lowered below that of normal crystals (115–117°C) so that, upon heating to 99°C, strained crystals are melted out and replaced by less strained ones having a better defined distribution of orientations. Further evidence for this comes from studies of heat-shrunk samples described in the next section:

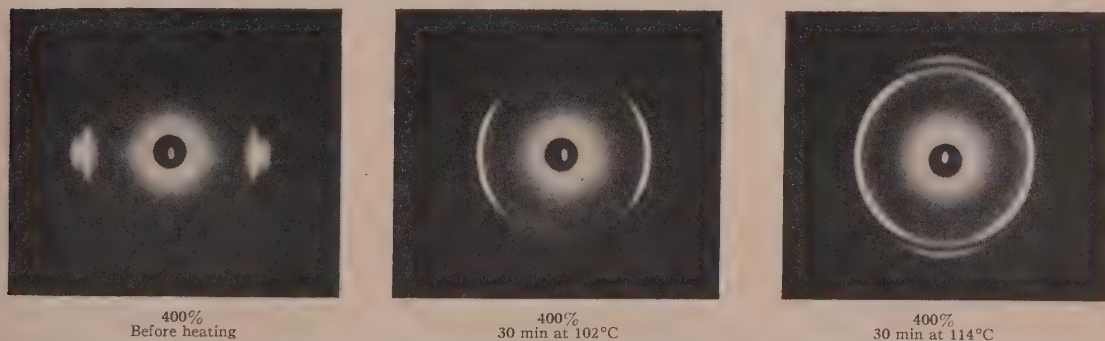


FIG. 7. The variation of the x-ray diffraction patterns for a polyethylene film (not constrained to constant length) drawn 400% at room temperature and then annealed.

¹⁰ A. Brown, J. Appl. Phys. 20, 552 (1949).

¹¹ S. Krimm, J. Appl. Phys. 23, 287 (1952).

¹² S. Krimm and A. V. Tobolsky, J. Polymer Sci. 7, 57 (1951).

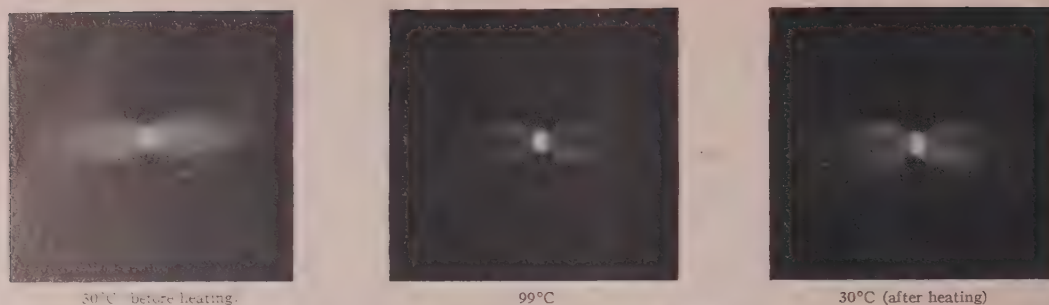


Fig. 8. H_V light scattering patterns for a polyethylene sample stretched 500% at 30°C heated to 107°C at constant length. Pictures were taken during the heating cycle at 99°C and again after recooling to 30°C.

EFFECT OF ANNEALING WITH SHRINKAGE

In Fig. 9 a series of H_V light-scattering photographs is presented for a sample which was stretched 400% at 30°C and then heated for 30 min in an air thermostat at the indicated temperature without constraint on length. The samples were then cooled to room temperature and the scattering pictures were taken. It is apparent that changes on annealing are observable at an annealing temperature of 75°C. With successively higher annealing temperatures, two changes become more pronounced. (1) There is an intensification and spreading out of the horizontal streaks, characteristic of the fibrillar scattering of the drawn samples into a pair of lobes. This is interpreted as resulting from disorientation, with an increase in the average angle between the

principal polarizability direction and the vertical. As has been pointed out, H_V scattering should be zero if the principal polarizability direction is along the polarizer or analyzer direction and should be a maximum when it makes an angle of 45° to the polarizer or analyzer. Consequently, disorientation should result in an increase in scattered intensity at an angle perpendicular to the direction of the maximum extension of the spacial distribution of dipoles. (2) A superimposed second pattern develops which is of the four-leaf clover type and similar to that obtained with the unstretched film. It is postulated that this results from the spherically symmetrical structure growing from the deformed crystals, which have melted at the annealing temperature and have regrown in an undeformed state upon



Fig. 9. The effect of annealing temperature on H_V scattering patterns for polyethylene samples stretched at room temperature, annealed for 30 min without constraint on length, and then cooled to room temperature. The elongation of the sample was 400% (measured after release of tension but before annealing).

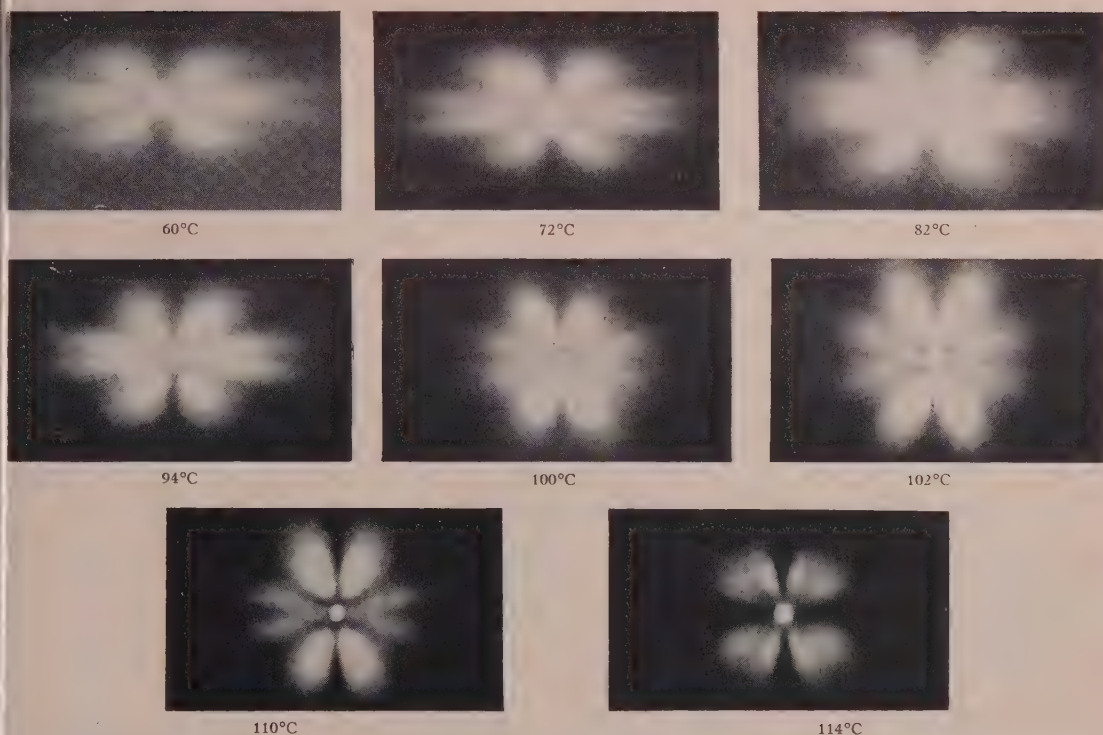


FIG. 10. The effect of annealing temperature on H_V scattering patterns for polyethylene samples stretched at room temperature, annealed for 30 min without constraint on length, and then cooled to room temperature. The elongation of the sample was 200% (measured after release of tension but before annealing).

cooling back down to room temperature. At about 100°C one notices a decrease in the angle between the lobes of the four-leaf clover pattern and the vertical direction to an angle less than 45°. This would indicate a departure from spherical symmetry of the distribution of principal axes, with a tendency toward orientation of the optic axes in directions perpendicular to the original stretching direction. The angle decreases further up to the 114°C annealing temperature.

This observation parallels the x-ray observation that recrystallization occurs with a tendency toward orientation of the c axis (which has maximum polarizability) perpendicular to the stretching direction.¹³

Between about 102° and 110°C there is little change in the angular spread of fibril component of the patterns, indicating that no additional disorientation is occurring. However, there is an increase in the ratio of the intensity of the clover-leaf pattern to that of the fibril component. At 114°C the fibril component has completely disappeared, and the clover-leaf pattern has decreased in size. Remembering the reciprocal relationship between the size of the scattering pattern and that of the scattering object, this would signify that the deformed spherical aggregate of relaxed crystals becomes larger

at this temperature which is very close to the melting point.

The effect of annealing temperature for a sample stretched 200% is given in Fig. 10. It is seen that changes occur at a lower temperature and may be seen to begin at 60°C. The fibril-type pattern is less pronounced in this series, and reversion to the spherical type pattern appears to occur more easily. It seems reasonable that the stability of the fibril phase is greater at the higher elongation.

The changes in V_V patterns on annealing with shrinkage are illustrated in Fig. 11 where patterns before and after annealing are given for polarization parallel to and perpendicular to the stretching direction. The pattern from the spherically symmetrical phase which develops upon annealing differs from the V_V spherulite pattern shown in Fig. 11. Thus, the structure which develops upon annealing a stretched sample at a temperature below the melting point differs from that of an unstretched polymer. In fact, x-ray patterns and birefringence indicate that orientation remains under those conditions, so that the spherical symmetry of superstructure is accompanied by anisotropic arrangement of the individual crystals.

Some pictures taken at the high temperature are given in Fig. 12. A sample stretched 500% at room tem-

¹³ T. T. Li, R. J. Lungis, and R. S. Stein, *J. Polymer Sci.* **20**, 199 (1956).

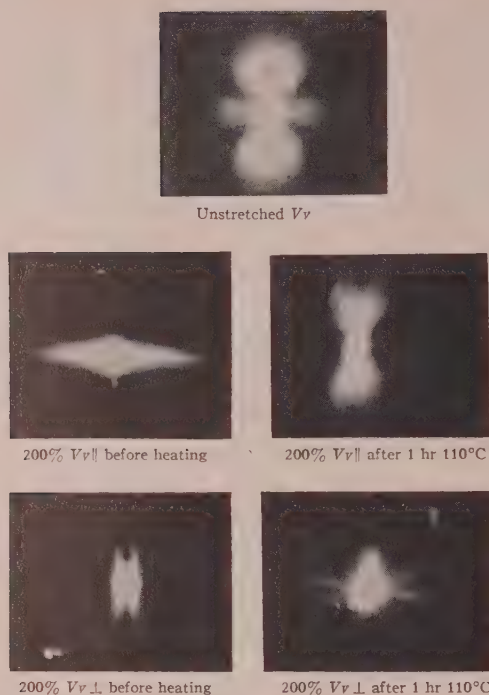


FIG. 11. The effect of annealing on V_V scattering patterns for polyethylene samples stretched at room temperature (unheated) and for samples then annealed at 110°C for 1 hr with shrinkage and then recoiled. The final elongation was approximately 50%.

perature was annealed for 1 hour at 102°C , then cooled to 30°C , and reheated. Photographs were taken at 30° , 90° , and 106°C . The 90°C pattern is not appreciably different in shape from the 30°C pattern, except that it is lower in intensity as a result of melting of crystals in both fibrillar and spherical arrangement. However, upon heating further to 106°C , the fibril contribution decreases more in intensity than the clover-leaf spherical contribution. The relative loss in intensity of this component persists upon cooling back to room temperature (Fig. 9), in support of the postulated mechanism of

melting of the deformed crystals and regrowth in a spherically symmetrical state.

The effect of elongation upon the change with annealing is shown in Fig. 13. An interesting observation is that the perpendicular orientation of the annealed structure (as indicated by the angular contraction of the clover-leaf pattern) is greater for the 200% elongated sample than for the 300%. In fact, for the 100% elongated sample the clover-leaf appears to have degenerated to a vertical streak (indicating fibril-like orientation of the annealed crystals in a direction perpendicular to the original stretching direction)! The apparent clover-leaf component in the 100% picture appears to arise from the relaxed fibril-like structure, as the angle that this makes with the vertical increases beyond 45°C with increasing elongation.

A more detailed study of the vertical streak occurring at 100% elongation and its variation with temperature is given in Fig. 14. It is seen to persist up to at least 114°C . Careful examination, especially at the higher temperatures, reveals banding within this streak, possibly characteristic of a lateral order of this perpendicularly oriented structure.

A more complete series showing the variation of the annealed pattern with elongation is given in Fig. 15. One sees that at 70% elongation the annealed pattern is identical with the unstretched pattern. It is likely that, at these low elongations below the yield point, spherulites are deformed without being disrupted to form fibrils, and that annealing merely returns the spherulite to the undeformed state. It appears that the perpendicularly oriented annealed structure arises from the melting and recrystallization of the deformed fibrillar material. The greater tendency for perpendicular orientation of the annealed crystals at low elongations corresponds to observations made on the orientation of crystals grown from oriented amorphous polyethylene.¹⁴ It is found (by x-ray diffraction and birefringence studies) that increasing degrees of a -axis orientation of these crystals occur with elongations up to 200%, but that increasing amounts of c -axis orientation occur with higher elongations.

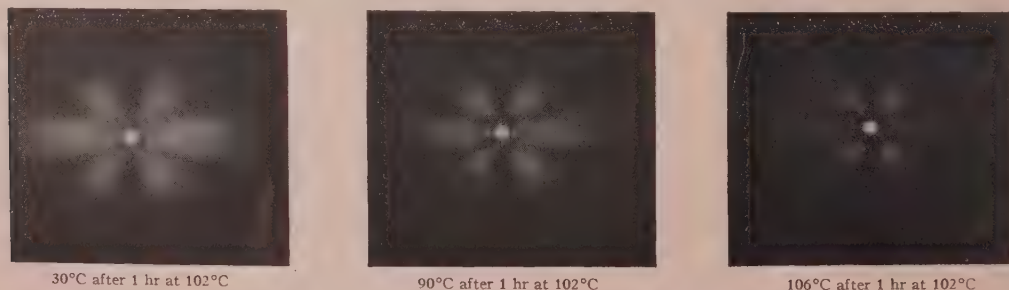


FIG. 12. The effect of reheating on H_V scattering patterns for annealed 500% stretched polyethylene film.

¹⁴ J. Judge and R. S. Stein, *J. Appl. Phys.* **32**, 2357 (1961).

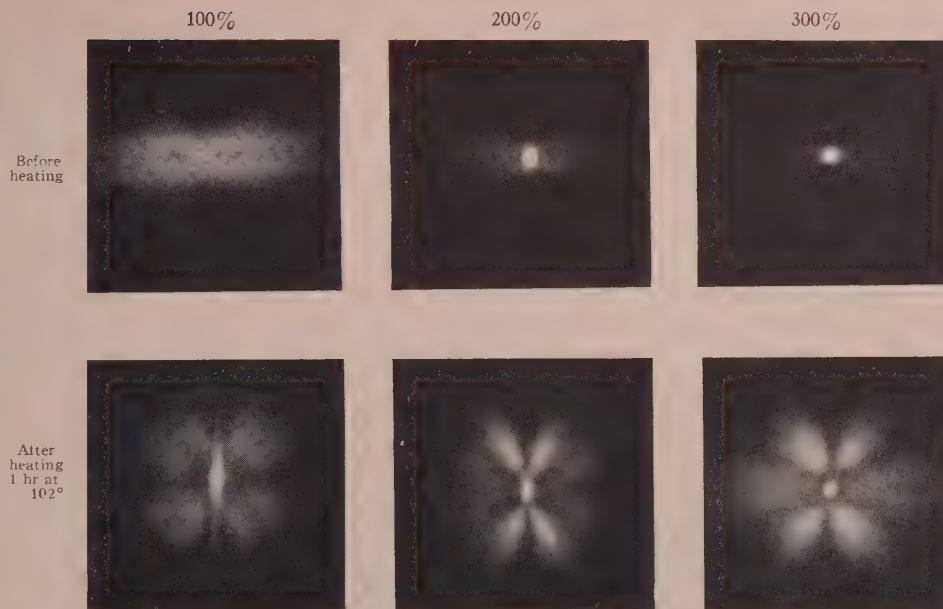


FIG. 13. The effect of percentage elongation on the change in the H_V scattering pattern produced by annealing a sample at 102°C for one hour with shrinkage.

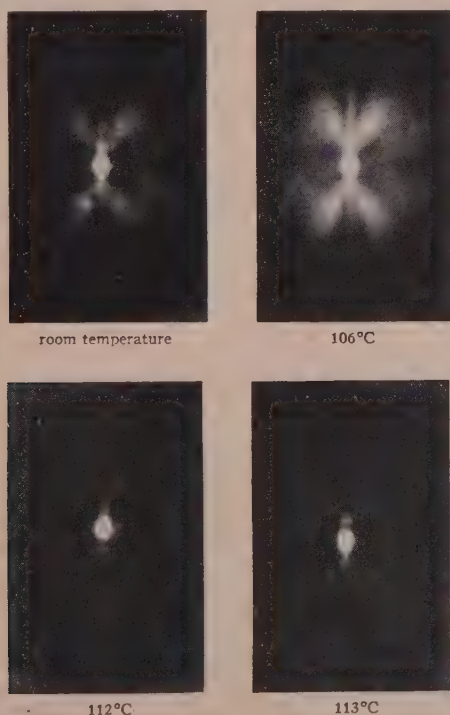


FIG. 14. The variation of the scattering pattern with reheating for a sample elongated at room temperature and annealed at 102°C with shrinkage for 30 minutes. The elongation before annealing was 100%.

Recent electron microscopic studies of heat-shrunk samples have revealed the presence of banded and/or helical structures, having a repeat distance corresponding to the position of the scattering maxima. The significance of these structures is being investigated.

CONCLUSIONS

Changes in morphology of structures having sizes up to several microns occur upon annealing, as revealed by the low-angle, photographic light scattering technique. These parallel previously observed changes in the

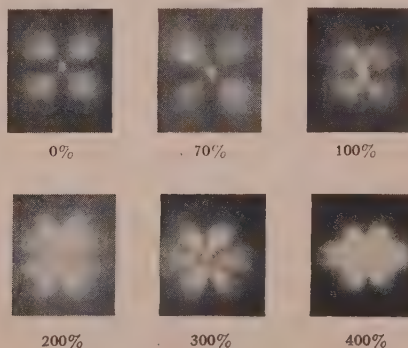


FIG. 15. The effect of a more extended variation of percentage elongation on the change in the H_V scattering pattern, produced by annealing a sample stretched at room temperature and annealed at 102°C for one hour with shrinkage.

orientation of the individual crystals. Thus, it appears that the explanation of these orientational changes must also be compatible with the accompanying change in the texture of the superstructure.

The scattering patterns for heat-shrunk samples prove the coexistence of two phases, one having fibrillar

symmetry and the other spherical symmetry. The scale of these two phases has not yet been established.

The results are consistent with an annealing mechanism which involves melting of deformed fibrillar crystals and recrystallization in a spherically symmetrical phase.⁵

Dielectric Loss in Poly-(Hexamethylene Adipamide) and Poly-(Hexamethylene Sebacamide) at Low Temperatures*

M. N. STEIN AND R. G. LAUTTMAN

U. S. Army Signal Research and Development Laboratory, Fort Monmouth, New Jersey

AND

J. A. SAUER AND A. E. WOODWARD

Department of Physics, The Pennsylvania State University, University Park, Pennsylvania

The dielectric behavior of samples of nylon 6-6 and nylon 6-10 has been studied in the temperature region from -160° to 60°C at frequencies of 0.1 to 100 kc/sec. The effects of thermal history, electron irradiation, and post irradiation annealing on the two dielectric loss peaks found in this frequency-temperature range have been explored. Electron irradiation of nylon 6-6 and 6-10 and thermal quenching of nylon 6-6 lowers the γ peak (-70°C at 1 kc/sec for 66 nylon) and raises the β peak ($+15^{\circ}\text{C}$ for 66 nylon at 1 kc/sec). Post irradiation annealing of nylon 6-6 or 6-10 irradiated to low doses (25 to 100 mrad) removes the effect of the irradiation on the dielectric behavior, but on irradiation to high dosages (900–1000 mrad) the dielectric loss values in the region of the β maximum at 0.1 and 1.0 kc/sec are greatly reduced. The frequency shifts of the dielectric loss maxima for all samples give activation energies in kcal/mole which fall in the 8–15 range for the β maximum and 9–19 for the γ maximum. These absorption peaks and the effect of various variables on them are discussed in terms of the molecular structure and possible molecular motions responsible for their occurrence.

INTRODUCTION

IN previous publications from these laboratories, measurements of dynamic mechanical properties in the temperature region from 77° to $500\text{--}530^{\circ}\text{K}$ have been reported for nylon 6-6¹⁻³ poly-(hexamethylene adipamide), nylon 6-10,¹⁻³ poly-(hexamethylene sebacamide), and irradiated nylon 6-6.^{1,2} In addition, some proton magnetic resonance measurements from 77° to $400\text{--}420^{\circ}\text{K}$ for 6-6 and 6-10 nylons have been described.^{4,5} It was found that 6-6 and 6-10 nylon specimens containing 1–2% water exhibited two mechanical loss peaks below room temperature, one at about 160°K (γ process) and the other around $240\text{--}250^{\circ}\text{K}$ (the β process), in agreement with an earlier investigation.⁶ For nylon 6-6 both peaks were found to be markedly

dependent on the water content, the γ peak increasing in height and the β peak decreasing in height with decreasing percent water.^{2,3} High energy irradiation of vacuum dried samples was found to bring about similar changes to those caused by the addition of water. It was concluded^{1,6} that both of these relaxation processes were due to the onset of a particular type of segmental motion in the amorphous region of the polymer. The γ process was believed to involve cooperative movement of methylene groups only.⁶ It was suggested that in the β process the moving units include amide groups not bonded to other amide groups but including any small molecules, such as water, associated with these groups.⁶ An alternate explanation is that the moving unit is the water molecule alone.⁷

In order to obtain more information about the molecular processes which are responsible for the γ and β peaks, an investigation of the dielectric properties of 6-6 and 6-10 nylons at temperatures as low as 120°K was carried out. Prior to the inception of this investigation the only published dielectric measurements on the polyamides were those of Baker and Yager⁸ for 6-10 nylon which were confined to the temperature region

* Supported in part by the National Science Foundation and the U. S. Atomic Energy Commission.

¹ A. E. Woodward, J. A. Sauer, C. W. Deeley, and D. E. Kline, *J. Colloid Sci.* **12**, 363 (1957).

² C. W. Deeley, A. E. Woodward, and J. A. Sauer, *J. Appl. Phys.* **28**, 1124 (1957).

³ A. E. Woodward, J. M. Crissman, and J. A. Sauer, *J. Polymer Sci.* **44**, 23 (1960).

⁴ R. E. Glick, R. P. Gupta, J. A. Sauer, and A. E. Woodward, *J. Polymer Sci.* **42**, 271 (1960).

⁵ A. E. Woodward, R. E. Glick, J. A. Sauer, and R. P. Gupta, *J. Polymer Sci.* **45**, 367 (1960).

⁶ K. Schmieder and K. Wolf, *Kolloid-Z.* **134**, 149 (1953).

⁷ K. H. Illers, *Macromol. Chem.* **38**, 168 (1960).

⁸ W. O. Baker and W. A. Yager, *J. Am. Chem. Soc.* **64**, 217 (1942).

above 25°C. While the present investigation was being pursued, Boyd⁹ reported the presence of a β dielectric loss peak for 6-6 nylon and some effects of water thereon. After the present investigation was completed, the results of Curtis¹⁰ showing the presence of both γ and β dielectric loss processes became available. Therefore, part of the present investigation involving measurements on samples vacuum dried at elevated temperatures parallels the work of Boyd⁹ and Curtis¹⁰; it is found that the present results confirm those of the previous investigators. In addition, the effects of electron irradiation, post irradiation annealing, and thermal quenching have been investigated. These data are presented and discussed in terms of possible operative molecular mechanisms.

EXPERIMENTAL

Apparatus

Measurements of the dielectric constant and dielectric loss were made utilizing a General Radio 716-C capacitance bridge in conjunction with a balanced guard circuit. The samples used were in the form of three-inch-diameter disks of thin film about 0.004 to 0.005 in. in thickness. The dielectric cell, similar to that of Fitzgerald and Miller,¹¹ was kept evacuated during all measurements. A Hewlett-Packard 200-C oscillator provided the input to the bridge circuit, the frequency being calibrated to an accuracy of 1 part in 10 000 with a Berkeley model 2000 scaler. The detector circuit consisted of the amplifier of a Hewlett-Packard model 400-C vacuum tube voltmeter filtered by a simple r-c 60 cycle filter and observed on a Tektronix 510 oscilloscope.

The capacitance could be determined to $\pm 0.2 \mu\mu\text{f}$, giving an over-all precision of 0.05%, while repeated measurements at different times were reproducible within $\pm 0.5\%$. Measurements of the dissipation factor were reproducible to within $\pm 2\%$.

All measurements were carried out with the dielectric cell placed in a shielded thermostatically controlled test cabinet which could be cooled either with air circulated through an auxiliary dry ice compartment or by use of liquid nitrogen in the test cabinet. Heating was accomplished by elements inside the cabinet. The temperature inside the cabinet was controlled to $\pm 0.2^\circ\text{C}$ and was measured by two copper-constantan thermocouples, one located on the outside of the cell and one imbedded in a hole in the guard electrode with the thermocouple tip being within 0.05 in. of the top surface of the sample. The potential difference was measured with a Rubicon potentiometer and simultaneously recorded with a Brown Electronik recording potentiometer, the accuracy of the measurement being $\pm 0.1^\circ\text{C}$. Prior to

taking measurements at any given temperature, a fifteen minute interval was allowed to elapse after the desired cell temperature was reached. If this was not done, the data obtained in an increasing temperature run did not agree with that obtained in a decreasing temperature run on the same sample.

Measurements of ϵ' and ϵ'' were made in the -160° to $+60^\circ\text{C}$ temperature range at four frequencies: 0.1, 1.0, 10, and 100 kc/sec, except for the nylon 6-10 sample No. 4 which was only studied at 1 kc/sec. Due to the difficulties of making precise measurements of sample thickness, the absolute values of ϵ' and ϵ'' may be in error by $\pm 6\%$. However, the data given in the following section expressed in terms of $\tan \delta = \epsilon''/\epsilon'$ is probably accurate, as indicated above, to $\pm 2\%$.

Preliminary measurements of dielectric constant and dielectric loss were also made on samples of poly-(vinyl chloride), polytrifluoromonochloroethylene, and poly-(ethylene terephthalate). In all cases, the data were found to be in approximate agreement with that reported previously.¹²⁻¹⁴

Samples

Nylon 6-6 and 6-10 were obtained in film form of thickness 4.5 mils from Polychemicals Department, E. I. du Pont de Nemours and Company, Inc. Densities of samples heated at 120°C under vacuum to constant weight were found to be 1.134 and 1.079 g/cc at 25°C , respectively; using the data of Starkweather and Moynihan,¹⁵ crystallinities of 46% for nylon 6-6 and 37% for nylon 6-10 were calculated.

Nylon 6-6 sample No. 9 and nylon 6-10 sample No. 1 were heated at 90°C to constant weight (~ 48 hr) under a vacuum of at least one micron and were stored under vacuum at room temperature prior to measurement, the transfer from the vacuum chamber to the dielectric cell taking about one minute or less. Subsequent tests indicated that nylon 6-6 samples given such a thermal treatment still contain about 0.5% volatile material, presumably water (see below). Nylon 6-6 samples Nos. 16, 15, 14 and nylon 6-10 samples Nos. 2 and 4 given the same drying treatment as the above specimens were subsequently irradiated with 2-Mev electrons in a Van de Graaff accelerator to dosages of 25, 100, 900, and 100 and 1000 megarad, respectively. The irradiations were carried out while the samples were in an evacuated aluminum cell which was kept at a temperature $\leq 27^\circ\text{C}$ by water cooling. The electron beam intensity was determined by probing the field with a Faraday cup and measuring the current with a vibrating reed electrometer. The current density of the beam thus determined

¹² S. G. Turley, doctoral dissertation, Pennsylvania State University, University Park, August 1957.

¹³ G. P. Mikhailov and B. I. Sazhin, Soviet Phys.—JETP **1**, 1670 (1956).

¹⁴ W. Reddish, Trans. Faraday Soc. **46**, 459 (1950).

¹⁵ H. W. Starkweather, Jr., and R. E. Moynihan, J. Polymer Sci. **22**, 363 (1956).

⁹ R. H. Boyd, J. Chem. Phys. **30**, 1276 (1959).

¹⁰ A. J. Curtis, J. Chem. Phys. **34**, 1849 (1961); J. Research Natl. Bur. Standards **65A**, 185 (1961).

¹¹ E. R. Fitzgerald and R. F. Miller, J. Colloid Sci. **8**, 148 (1953).

was converted to megaread units on the basis that one megaread $\equiv 10^8$ ergs/g. The dosage variation over the entire sample area was found to be $<10\%$.

Two nylon 6-6 samples, Nos. 29 and 30, were heated under vacuum at 250°C to constant weight. Sample No. 29 was then thermally quenched from 250°C by immersing the vacuum desiccation cell containing the sample in an acetone dry ice slurry; the cell was then allowed to warm to room temperature before the sample was transferred to the dielectric cell. Sample No. 30 was slowly cooled from 250°C , placed in the dielectric cell, and annealed at 80°C prior to the measurements.

Following various cooling and heating runs below room temperature, the irradiated samples and the quenched specimen (No. 29) were given an annealing treatment in the dielectric cell by heating to 80°C while measurements were being made. A second set of dielectric measurements was then made over the whole temperature range by decreasing the temperature gradually from 80° to about -150°C . A second annealing treatment was carried out on sample No. 29 in the cell at 110°C and measurements again made. The initial cooling and heating runs made below room temperature gave the same results, indicating that no annealing of the specimens occurred at room temperature. After annealing at 80°C , however, both irradiated and quenched polyamide specimens exhibited markedly different dielectric behavior.

In a separate set of measurements it was found that the percentage weight loss, which occurs on heating as received nylon 6-6 specimens at various temperatures under vacuum to constant weight, was essentially the same in the 70° to 160°C temperature region but increased for temperatures from 160° to 250°C .

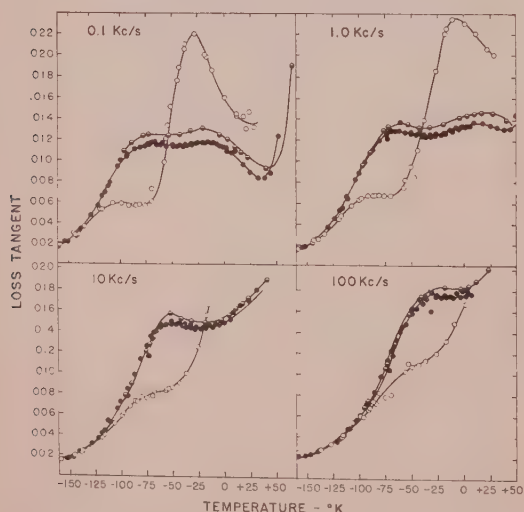


Fig. 1. Dielectric loss tangent vs. temperature at 0.1, 1.0, 10, and 100 kc/sec for nylon 6-6 sample No. 9 (\bullet), irradiated (25 mrad) nylon 6-6 sample No. 16 (\circ), and post irradiated annealed sample No. 16 (\bullet).

RESULTS

In Fig. 1 the dielectric loss tangent is plotted as a function of temperature at 0.1, 1.0, 10 and 100 kc/sec for nylon 6-6 samples No. 9 (unirradiated) and No. 16 (irradiated to 25 mrad). At 0.1 kc/sec two maxima at temperatures of about -15° (β) and -70°C (γ) are apparent for the unirradiated specimen. An increase of frequency to 1.0 kc/sec causes a shift of these maxima to higher temperatures. At a frequency of 10 kc/sec the β maximum has shifted into the temperature region of the large higher temperature loss peak (α) investigated by other workers.^{8-10,16} However, the γ maximum is distinguishable even at 100 kc/sec. The apparent effect of the 25 mrad electron irradiation is to cause an approximate twofold increase in the magnitude of the β maximum and an approximate twofold decrease in the magnitude of the γ maximum at 0.1 kc/sec. These maxima are also found to occur about 10° to 25°C lower in temperature. Upon post irradiation annealing at 80°C , however, the values of $\tan \delta$ in the vicinity of the γ maximum increase and in the vicinity of the β maximum decrease, giving a loss tangent curve in the -95° to $+25^\circ\text{C}$ range which is similar in shape to that for the unirradiated specimen but shifted upward on the $\tan \delta$ scale by about 10% . Similar effects are noted for the β and γ maxima at 1 kc/sec and the γ process at 10 and 100 kc/sec.

Irradiation dosages of 100 mrad and 900 mrad were also found to lower the level of the γ maximum and raise that of the β maxima, but the changes are much smaller, being of the order of 15% for the 100 mrad and 25% for the 900 mrad sample at 0.1 kc/sec. Runs were made on both of these specimens at the four frequencies.

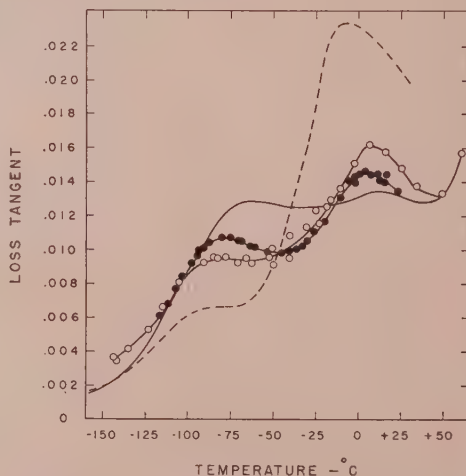


Fig. 2. Effect of electron irradiation on the dielectric loss tangent at 1 kc/sec of nylon 6-6. Unirradiated (—), 25 mrad (---), 100 mrad (\bullet), and 900 mrad (\circ).

¹⁶ D. W. McCall and E. W. Anderson, J. Chem. Phys. 32, 23 (1960).

but only the data obtained at 1.0 kc/sec are given in Fig. 2. For comparative purposes the $\tan \delta$ curves, taken from Fig. 1, for the unirradiated and 25 mrad samples are included. The effect of annealing the 100 and 900 mrad samples is to raise the γ maximum and lower the β maximum, the same effect found for the 25 mrad sample (see Figs. 2 and 3). The effect of this annealing treatment on the height of the β maximum is quite different for the 100 mrad and 900 mrad samples, with the former being reduced by 10%, while for the latter the reduction is about 45% with only a slight indication that a β maximum still exists (Fig. 3); at the three dosages used the γ maximum for the post-annealed samples is somewhat greater than that for the unirradiated one.

It was found that nylon 6-10 also shows two low temperature loss peaks, although both are not distinguishable at the same frequencies. At 0.1 kc/sec the γ maximum appears only as a broad satellite on the left-hand side of the β maximum, while at 1.0 kc/sec the γ maximum is clearly apparent, since the β maximum has shifted into the α' region and is no longer visible as a separate peak. As can be seen in Fig. 4, electron irradiation to dosages of 100 and 1000 mrad leads to noticeable reductions ($\sim 20\%$ and $\sim 30\%$, respectively) in the γ maximum and to the appearance of a β maximum at 1 kc/sec. Annealing of the irradiated samples leads to increases of the γ maximum back to the level of the unirradiated sample and decreases in $\tan \delta$ in the vicinity of the β maximum.

In Fig. 5 the loss tangent vs temperature is shown at 1 kc/sec for two nylon 66 samples with different thermal histories (Nos. 29 and 30) along with the $\tan \delta$ curve for sample No. 9 taken from Fig. 1. Annealing at 250°C (No. 30) is found to reduce significantly $\tan \delta$ values in the vicinity of the β peak and to lead to lower values of loss over the whole temperature range, as compared to the specimens annealed at 90°C (No. 9). Quenching from 250°C (No. 29) increases the β peak and decreases the γ maxima. Upon subsequent annealing of the quenched sample No. 29, however, the loss tangent becomes similar to that of sample No. 30. The same type

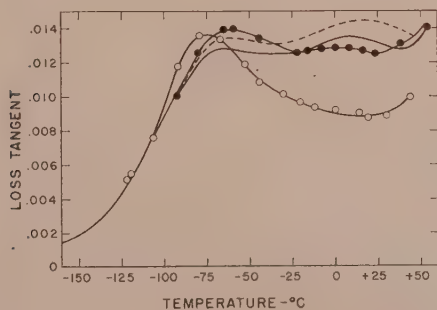


FIG. 3. Effect of post irradiation annealing on the dielectric loss tangent at 1 kc/sec of nylon 6-6, unirradiated (—), 25 mrad (---), 100 mrad (●), and 900 mrad (○).

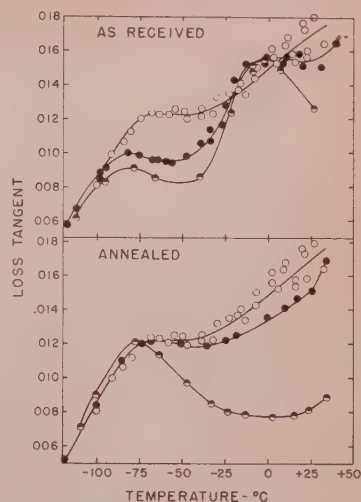


FIG. 4. Effect of electron irradiation and post-irradiation annealing on the dielectric loss tangent at 1 kc/sec of nylon 6-10. Unirradiated (○), 100 mrad (●), 1000 mrad (●).

of changes are observed when the loss tangent is measured at 0.1 kc/sec.

From the data obtained in this investigation, activation energies have been determined from the slope of the straight line drawn through the points on a plot of log frequency vs the reciprocal temperature of the loss tangent maximum and are given in Table I; post-annealed samples are marked with a letter (a). Also listed are the frequencies at which the γ and β maxima were apparent in the data.

It can be seen that the activation energy for the γ maximum of nylon 6-6 samples irradiated to 25 mrad (No. 16) and 100 mrad (No. 15) and of the nylon 6-10 sample irradiated to 100 mrad (No. 2) increases upon post-irradiation annealing. With the exception of nylon 6-6 sample No. 9, the γ maximum for the unirradiated

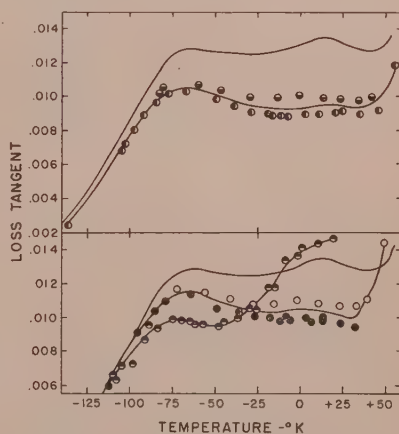


FIG. 5. Effect of thermal history on the dielectric loss tangent at 1 kc/sec of nylon 6-6, sample No. 9, 90°C anneal (—), sample No. 30, 250°C anneal (●), same sample after heating to 80°C (●), sample No. 29, quenched from 250°C (●), same sample, 80°C anneal (●), and same sample, 110°C anneal (○).

TABLE I. Activation energies for β and γ dielectric loss maxima for nylon 6-6 and nylon 6-10.

Sample	Act. energy kcal/mole		Max obs freq. kc/sec	
	γ	β	γ	β
Nylon 6-6 No. 9	19 \pm 3	11	0.1, 1.0, 10, 100	0.1, 1.0
Nylon 6-6 No. 14	12 \pm 2	13	0.1, 1.0, 10, 100	0.1, 1.0, 10
Nylon 6-6 No. 14(a)	13 \pm 2	...	0.1, 1.0, 10, 100	...
Nylon 6-6 No. 15	11	14	0.1, 1.0, 10, 100	0.1, 1.0
Nylon 6-6 No. 15(a)	17 \pm 1	...	0.1, 1.0, 10, 100	0.1, 1.0
Nylon 6-6 No. 16	9 \pm 1	12	0.1, 1.0, 10, 100	0.1, 1.0
Nylon 6-6 No. 16(a)	15 \pm 2	8	0.1, 1.0, 10, 100	0.1, 1.0
Nylon 6-6 No. 29	10 \pm 3	11	0.1, 1.0, 10, 100	0.1, 1.0
Nylon 6-6 No. 29(a)	13 \pm 1	...	0.1, (?), 1.0, 10, 100	0.1 (?)
Nylon 6-6 No. 30	12 \pm 1	...	0.1, (?), 1.0, 10, 100	0.1, (?), 1.0, (?)
Nylon 6-10 No. 1	13 \pm 1	...	0.1, (?), 1.0, 10, 100	0.1
Nylon 6-10 No. 2	12	15	0.1, 1.0, 10, 100	0.1, 1.0
Nylon 6-10 No. 2(a)	18 \pm 3	...	0.1, 1.0, 10, 100	0.1
Nylon 6-10 No. 4	1	1
Nylon 6-10 No. 4(a)	1	...

nylon 6-6 and 6-10 specimens have values around 12-13 kcal/mole. Since all but one of the activation energies for the β peak were obtained using data at two frequencies only one decade apart, they are considered approximate and of the order of 10 kcal/mole.

Complete data for all samples of nylon 6-6 and nylon 6-10, including plots of the real and imaginary parts of the dielectric constant vs temperature, have been given elsewhere.¹⁷

DISCUSSION

The results of this investigation concerning the existence and the temperature and frequency locations of the γ and β dielectric loss maxima are in good agreement with those of Curtis.¹⁰ He reported an activation energy for the γ maxima of 13 kcal/mole, in agreement with most of the values listed in Table I.

The similarities between the dielectric loss processes and those found in dynamic mechanical data have already been discussed by Curtis¹⁰ who also points out that since a γ maximum is found in the dielectric loss, the hypothesis that it is due to segmental motion of CH_2 groups between amide functions in the amorphous regions must be modified somewhat to include at least small oscillations of the polar components of the repeat units.

There at present appear to be three interpretations of the β dielectric and dynamic mechanical loss maxima. One^{1,2,9,18} postulates that it is the result of configurational changes in the amorphous regions of chain segments containing amide groups that are not rigidly hydrogen bonded to other neighboring amide groups although they may be bonded to other small molecules, such as water. A second is that it is due to configurational changes of a water-amide complex,¹⁰ and the third interpretation is that it is associated with configurational changes of the water molecules alone.⁷ It is difficult to see why motion, presumably rotational in

nature, of small amounts of water (<1%) should cause such a sizeable mechanical loss maximum. More important is that the present results concerning the effects of thermal quenching and electron irradiation are inconsistent with this explanation, if it is assumed that water has not been introduced during the treatments. Under no conditions should thermal quenching of a dry sample yield an increased β maximum if this maximum depends upon the presence of water. In addition, it has been found from both dynamic mechanical³ and dielectric¹⁰ measurements that essentially dry samples of nylon 6-10 have sizeable β maxima. Therefore, it appears that the first explanation^{1,2} is a better one. However, in light of the comments of Illers,⁷ it may not be necessary that the amide group be completely free of hydrogen bonds to other amide groups but rather that it be only weakly bound.

Although infrared studies^{19,20} appear to indicate that there are few unassociated amide groups even in the melt, it is known from x-ray evidence²¹ that rotationally disordered states, in which neighboring chains are oriented independently, can and do exist in the polyamides. From x-ray diffraction studies of nylon 6 Sandeman and Keller²¹ have shown the existence of such a disordered phase even at room temperature. They found that the proportion of this phase increased on quenching and decreased on annealing at high temperatures. They also stated that x-ray studies of nylon 6-6 and 6-10 indicated that this phase was also present but to a lesser extent.

The nonrigidly bonded amide groups whose configurational motions are considered to lead to both the dielectric and the mechanical β loss peaks may well be associated with such a disordered phase. If so, one would expect that quenching would increase the height of the β peak, and careful annealing would reduce it; this is precisely what has been found. Addition of water

¹⁷ M. N. Stein, doctoral dissertation, Pennsylvania State University, University Park, 1960.

¹⁸ T. Kawaguchi, J. Appl. Polymer Sci. 2, 56 (1959).

¹⁹ C. G. Cannon, Spectrochim. Acta 16, 302 (1960).

²⁰ D. S. Trifan and I. F. Terenzi, J. Polymer Sci. 28, 443 (1958).

²¹ I. Sandeman and A. Keller, J. Polymer Sci. 19, 401 (1956).

should increase it and careful drying should reduce it, and this too is found. Irradiation to low dosages (~ 25 mrad) raises the height of the β peak and in general appears to have the same effect as quenching; again these effects are largely removed by annealing. Hence one may postulate that low dose electron irradiation, perhaps through the breaking of hydrogen bonds by ionization or perhaps through the agency of a thermal spike mechanism,²² also leads to an increase in the rotationally disordered phase.

Upon irradiation to higher doses, an additional process enters. It is known^{1,2} that nylon crosslinks on irradiation, and that the amount of crosslinking increases with irradiation dose. Crosslinking would be expected to exert a restrictive effect on configurational movement of chain segments by bringing neighboring chains into closer proximity. The decrease that is found to occur in the β loss peak for the 900 and 1000 mrad samples after annealing at 80°C could possibly be due to the crosslinking that takes place when some of the free radicals present on the irradiated polymer chains are given increased mobility. Since all irradiated samples were kept under vacuum after irradiation, it is not surprising that some free radicals should still be present in the polymer at the time of testing a week or so later.

²² G. J. Dienes and G. H. Vineyard, *Radiation Effects in Solids* (Interscience Publishers, Inc., New York, 1957).

The decrease of the γ maximum which accompanies an increase in the β maximum upon quenching or upon electron irradiation was also noted in the dynamic mechanical data when small amounts of water were added^{3,7} or when samples were irradiated in a nuclear reactor.²

The lowering of the γ maximum with increasing water content has been explained as either due to hindrance by the water molecules to CH_2 motion² or to an ordering of these units in the amorphous regions upon rupture of the H bonds between amide groups by the water.^{3,23} The results of the present investigation are more in accord with the second hypothesis as the γ peak is decreased both by irradiation of samples with low water contents (nylon 6-6 and 6-10) and by quenching of an essentially dry sample (nylon 6-6).

In conclusion, it is found that the existence of the γ and β dielectric loss maxima and the effects thereon of irradiation and thermal history are consistent with the explanations given for similar maxima in the dynamic mechanical loss,¹⁻³ if some modifications are made in the mechanism suggested for the γ maximum. However, further investigation of the influence of irradiation, of thermal history, and of small amounts of water on these two loss maxima are necessary before any final conclusions can be reached.

²³ H. W. Starkweather, Jr., *J. Appl. Polymer Sci.* **2**, 129 (1959).

Growth of Crystals from Molten Crosslinked Oriented Polyethylene*†

JANE T. JUDGE AND RICHARD S. STEIN

Department of Chemistry, University of Massachusetts, Amherst, Massachusetts

The growth of crystals from the melt in oriented, crosslinked polyethylene was studied by x-ray diffraction and birefringence as a function of orientation. It was found that for samples elongated more than about 200%, the crystals grow with their c axes parallel to the stretching direction. At elongations less than 200%, there is a rather abrupt transition to a mode of growth in which the b axis is perpendicular to the stretching direction with a tendency for the a axis to be aligned parallel to this direction. An interpretation is made in terms of the folded-chain concept of crystal structure.

INTRODUCTION

THE a -axis orientation of crystals grown from oriented, crosslinked, melted polyethylene has been previously reported.¹ In this paper, conditions leading to this type of orientation are defined, and the resulting state of orientation is characterized by x-ray

diffraction and birefringence. The effects of polymer type and degree of orientation are also examined.

EXPERIMENTAL

Two types of samples were studied. These were a Phillips Marlex 50 linear polyethylene film² and a Monsanto experimental medium density ($\rho=0.93$) branched polyethylene.³ Films of branched polyethylene were pressed between polished plates lined with sheets of aluminum foil on a Carver press at a pressure of about

* Taken in part from a Ph.D. thesis by Miss Judge at the University of Massachusetts, Amherst, Massachusetts (1961).

† Supported in part by a contract from the Office of Naval Research and in part by grants from the Petroleum Research Fund, the Plax Corporation, the Fabric Research Labs, and assistance from Monsanto Chemical Company.

¹ T. T. Li, R. J. Volungis, and R. S. Stein, *J. Polymer Sci.* **20**, 199 (1956).

² Supplied through the courtesy of Phillips Petroleum Company.

³ Supplied by Monsanto Chemical Company, Plastics Division, Texas City, Texas.

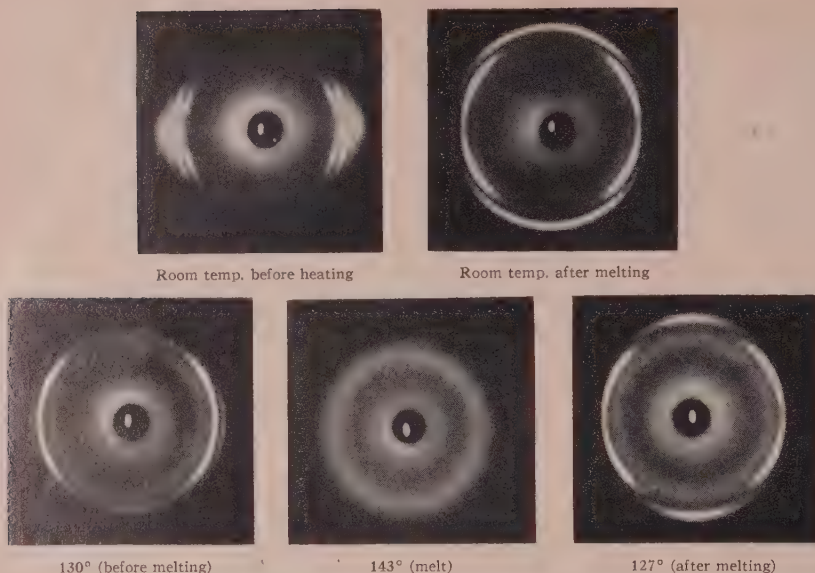


FIG. 1. X-ray diffraction photographs for a crosslinked linear polyethylene sample stretched 100% and subjected to a heating cycle at constant length.

1500 psi and a temperature of 150°C. They were allowed to cool slowly in the press. Subsequent examination of birefringence and x-ray diffraction indicated negligible residual orientation. The films studied averaged 10–15 mils in thickness. The films, still sandwiched between aluminum foil, were irradiated by 800 kv (peak) electron radiation to an average dosage of about 30 mrad.⁴ They were then annealed in the Carver press under about 1500 psi pressure at 150°C for 15 minutes and then cooled over several hours. Such annealed films showed less tendency to break when subsequently heated in the stretched state (possibly because of a decrease in trapped radical content). The aluminum foil served to retard oxidation during annealing.

The aluminum foil was removed and strips about 5 cm × 3 cm were cut from the annealed samples. These were slowly stretched in a hand stretching jig described previously.⁵ Elongations were measured from distances between ink lines ruled on the sample. While under tension, a section of the sample was clamped between brass rings and then removed from the stretching jig.

As sample breakage resulting from oxidation occurred at the higher temperature, it was necessary to work in an inert atmosphere. The samples (clamped between brass rings) were placed in an aluminum vacuum oven. This was capable of being heated by resistance wires placed around its periphery. A thermocouple mounted close to the sample monitored its temperature. The Mylar windows permitted passage of light and x-rays for structural studies. Metal covers with vacuum ports were placed over these windows during evacuation to prevent their breakage by air pressure differential. In practice, the oven was evacuated to 50 μ and then filled

with nitrogen. Evacuation and refilling with nitrogen were repeated prior to heating.

The x-ray diffraction photographs and birefringence measurements were taken initially and at critical stages during heating and cooling. In order to characterize more completely its orientation, a more detailed radial and azimuthal x-ray diffractometer scan was carried out on the oriented films prior to the heat treatment and again after returning the sample to room temperature. This was done using crystal filtered $\text{CuK}\alpha$ radiation with an automatic diffractometer of our design.⁶

In a normal run, branched samples would be heated to 130°C, and linear samples would be heated to about 160°C, and then gradually cooled to room temperature at a rate of approximately 65°C per hour. Some thickening was observed during heat treatment, indicating that some viscous flow (possibly of some incompletely cross-linked component) may have occurred.

In studies of samples cooled at constant load, the annealed samples were placed in an evacuable glass tube with a weight hung from their end. These were then heated and cooled while under vacuum. Birefringence measurements were made on them while in the tube. Changes in length were followed using a cathetometer.⁷

X-RAY DIFFRACTION CHANGES DURING HEATING AND COOLING

The x-ray diffraction photographs for a 100% stretched linear polyethylene sample at various stages of heat treatment at constant length are presented in

⁶ D. G. LeGrand, D. Keedy, and R. S. Stein, ONR Technical Report No. 26 under contract, National Research project, University of Massachusetts, Amherst, Massachusetts, December 2 (1960).

⁷ R. J. Volungis, M.S. thesis, University of Massachusetts, Amherst, Massachusetts (1955).

⁴ Supplied through the courtesy of General Electric Company, Pittsfield, Massachusetts.

⁵ R. S. Stein and F. H. Norris, *J. Polymer Sci.* **21**, 381 (1956).

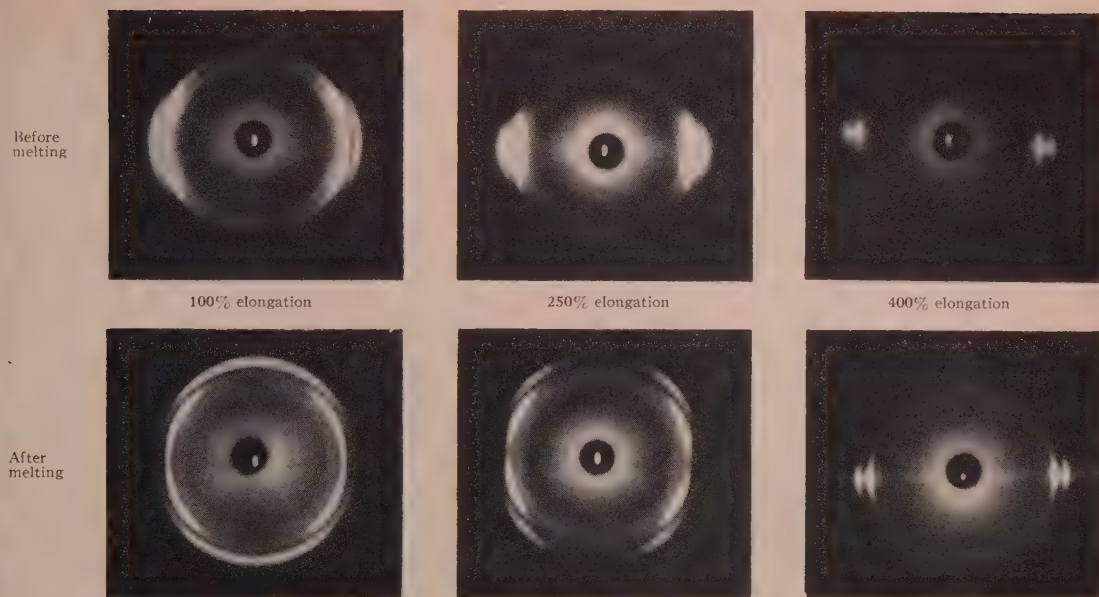


FIG. 2. X-ray diffraction photographs for a crosslinked, branched polyethylene sample stretched differing amounts and heated and cooled at constant length.

Fig. 1. The original sample exhibits a typical c -axis oriented pattern. At 130°C , slightly below the melting point, the increased amorphous scattering is apparent, as is the partial disorientation of the residual crystalline material. At 143°C , above the melting point, only the amorphous halo remains, with no trace of orientation present. Upon recooling to 127°C , the growth of a -axis oriented crystalline material is seen. This increases in amount without appreciable change in orientation as the sample is cooled back to room temperature. The x-ray patterns for samples cooled at constant load are similar.¹

The effect of elongation is shown in the series of x-ray photographs of Fig. 2, in which the room temperature x-ray diffraction photographs are shown for three different samples of branched crosslinked polyethylene before and after heating through the melting point and recooling. In the unheated samples, the successively greater degree of c -axis orientation with increasing elongation is seen. However, the change in resultant orientation upon undergoing a heating cycle is striking. The 100% sample, as pointed out in the previous section, gives an a -axis type pattern. The 400% elongated sample, however, recrystallizes to give a c -axis oriented pattern, not differing appreciably from that of the unheated sample. At 250% elongation, an intermediate type of pattern is obtained. These intermediate patterns can only be obtained over a relatively narrow range of elongations, perhaps 25% wide, in the vicinity of 250%. At all elongations lower than this, a -axis type patterns are obtained, while at higher elongations, c -axis patterns result.

CHARACTERIZATION OF THE a -AXIS STATE

In order to characterize better the a -axis state of orientation, a quantitative diffractometer analysis was made. From radial diffractometer scans, the 200 and 020 components of diffraction were resolved. The variation of these with azimuthal scattering angle was determined. For example, a typical azimuthal variation of the integrated 200 intensity for an a -axis and c -axis oriented sample is presented in Fig. 3, in which it is apparent that the 200 reflection is most intense on the meridian for

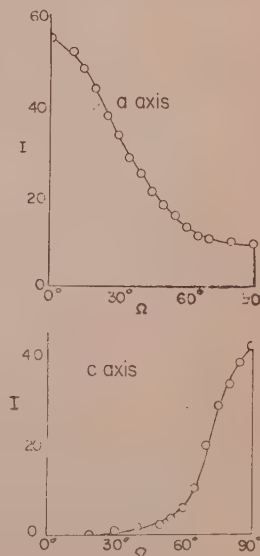
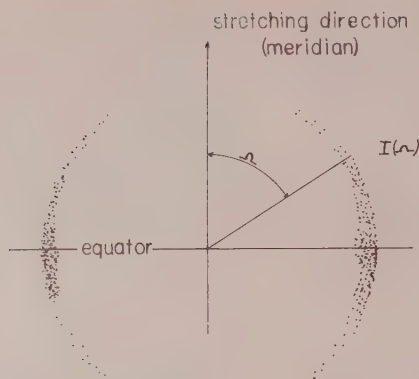


FIG. 3. The azimuthal variation of the 200 intensity reflection for a typical a -axis and c -axis oriented sample.

FIG. 4. The definition of the polar angle, Ω .

the a -axis case, but on the equator for the c -axis case. From a scan such as this, the value of $\cos^2\alpha$ (where α is the angle between the stretching direction and the a axis) may be obtained from

$$\langle \cos^2\alpha \rangle = \frac{\int_0^{\pi/2} I_{200}(\Omega) \cos^2\Omega \sin\Omega d\Omega}{\int_0^{\pi/2} I_{200}(\Omega) \sin\Omega d\Omega}, \quad (1)$$

where Ω is the polar angle between the 200 reflection and the meridian (Fig. 4). A similar average for the b -axis $\cos^2\beta$ was obtained using the 020 reflection.

Orientation functions for these axes were calculated using⁸

$$f_\alpha = (3\langle \cos^2\alpha \rangle - 1)/2 \quad (2)$$

$$f_\beta = (3\langle \cos^2\beta \rangle - 1)/2. \quad (3)$$

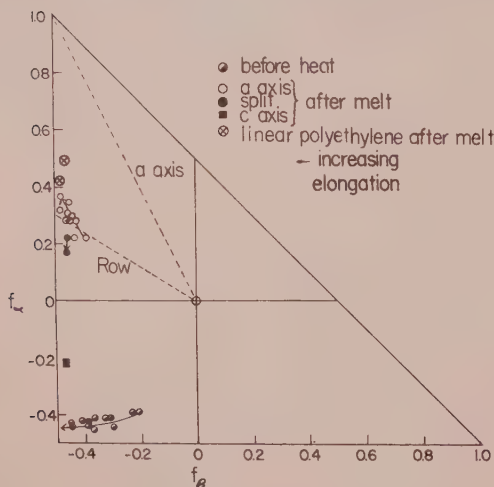


FIG. 5. The orientation state of sample before and after heat treatment.

As has been pointed out,⁸ these functions vary from $-\frac{1}{2}$ to $+1$ depending on whether the axis is oriented perpendicular to or parallel to the stretching direction, and is zero for random orientation. In a plot of f_α against f_β all points must lie within a right triangle (because of the restriction of the axes being perpendicular). Such a plot for samples before and after heating is given in Fig. 5.

The apices of the triangle correspond to perfect orientation of the respective crystal axes parallel to the stretching direction. The right-angled apex corresponding to $f_\alpha = f_\beta = -\frac{1}{2}$ is the state where both the a and b axes are perpendicular to the stretching direction, and the c axis is parallel to it. Upon elongating, the sample tends to approach this state.

For the samples heat-treated at high elongation where c -axis orientation is preserved, the point representing the orientational state of the sample moves upward on the diagram, corresponding to some loss of orientation of the a axis without appreciable change in the b . Samples heat-treated at low elongation retain the perpendicular b axis orientation, but the value of f_α changes discretely from a negative value to a positive one in the range of f_α of 0.3–0.4.

There has been some discussion whether this state of orientation is a -axis or row orientation.^{9–11} The a -axis orientation might be defined as a state of preferred orientation of the a axis, with respect to the stretching direction with random orientation of the b and c axes about the a . That is, $f_\beta = f_c$ (where f_c is the orientation function for the c axis).

Since⁸

$$f_\alpha + f_\beta + f_c = 0, \quad (4)$$

$$f_\alpha = -2f_\beta. \quad (5)$$

This corresponds to the dotted line labeled " a " in Fig. (5).

Row orientation, on the other hand, is a state where the b axis tends to be perpendicular to the stretching direction, and there is random orientation of the a and c axes about it. Then $f_\alpha = f_c$ and

$$f_\alpha = -\frac{1}{2}f_\beta. \quad (6)$$

The line corresponding to this relationship is labeled "Row" in Fig. (5).

It is noted that the measured points for the heat-treated, low-elongation samples are between these two limiting lines, being somewhat closer to the row case. Thus, the state of orientation is one in which the b axis is strongly oriented perpendicular to the stretching direction, with some tendency for the a axis to be oriented parallel to the stretching direction.

⁸ R. S. Stein, J. Polymer Sci. **31**, 327, 335 (1958).

⁹ A. Keller, J. Polymer Sci. **15**, 31 (1955).

¹⁰ A. Keller and I. Sandeman, J. Polymer Sci. **15**, 133 (1955).

¹¹ S. L. Aggarwal and O. J. Sweeting, Chem. Revs. **57**, 60 (1957).

BIREFRINGENCE CHANGES

The birefringence of the branched polyethylene is plotted against elongation before and after heat treatment at constant length in Fig. (6). The differing behavior at high and low elongations is quite apparent. The low birefringence values result from *a*-axis orientation, while the higher values result from *c*-axis orientation. The transition between the two occurs over a fairly narrow range of elongation.

The crystalline contribution to the birefringence may be calculated from the equation⁸

$$\Delta_c = -X_c(0.061f_a + 0.056)f_b, \quad (7)$$

where X_c is the degree of crystallinity, and the constants are related to the principal refractive indices of the crystal. The points calculated with this equation from the orientation functions obtained from the x-ray scans are included in Fig. (6). The crystalline birefringence is seen to account for most of the observed birefringence.

The changes in birefringence with temperature for typical *c*- and *a*-axis orientation cases are presented in Figs. 7 and 8. The initial birefringence and the decrease upon heating are quite similar for the two samples. However, for the sample elongated 200%, most of the birefringence returns upon cooling, whereas with the 100% elongated sample, the birefringence decreases to a very low value.

Details of the cooling curve at low elongations are presented in Fig. 9. The initial birefringence decreases with decreasing temperature and then increases slightly with further cooling. The initial decrease in birefringence

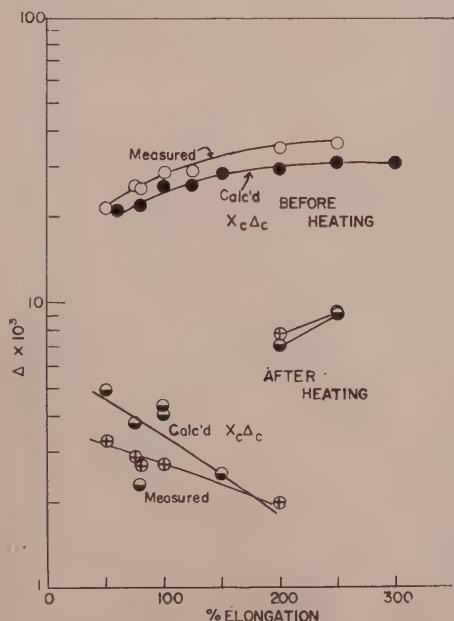


Fig. 6. The variation of birefringence with elongation for branched polyethylene before and after heat treatment at constant length.

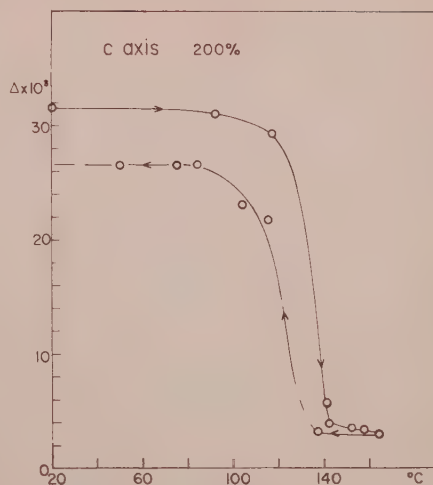


Fig. 7. The variation of birefringence with temperature for a sample of branched polyethylene elongated 200% and heated and cooled at constant length.

is greater with increasing elongation up to 200% where the transition to *c*-axis orientation occurs. Thus, it appears that the *a*-axis orientation of the first crystals which grow from the oriented melt is greater than that of those which grow at lower temperatures. This is also apparent from the x-ray studies (Fig. 1).

A comparison of birefringence changes during cooling at constant length and at constant load is presented in Fig. (10). The *a*-axis orientation occurs in both cases, but the initial decrease in birefringence is greater in the constant length experiment. The length changes occurring during the cooling at constant load are plotted in Fig. (11). As the crosslinked sample is cooled, there is an increase in length with decrease in temperature down to about the melting point. The length increases some-

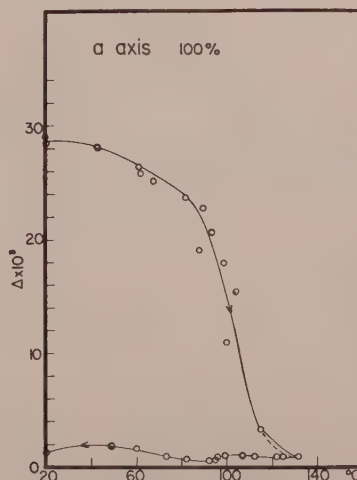


Fig. 8. The variation of birefringence with temperature for a sample of branched polyethylene elongated 100% and heated and cooled at constant length.

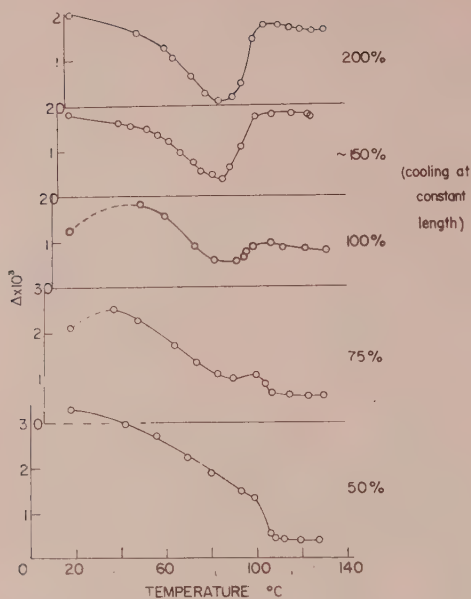


Fig. 9. The variation of birefringence with temperature for samples of branched polyethylene cooled from the melt at several elongations.

what more than might be expected from considerations of the kinetic theory of rubber elasticity, increasing by about 10% for a 3% decrease in absolute temperature. The length is a maximum at about 138°C, after which

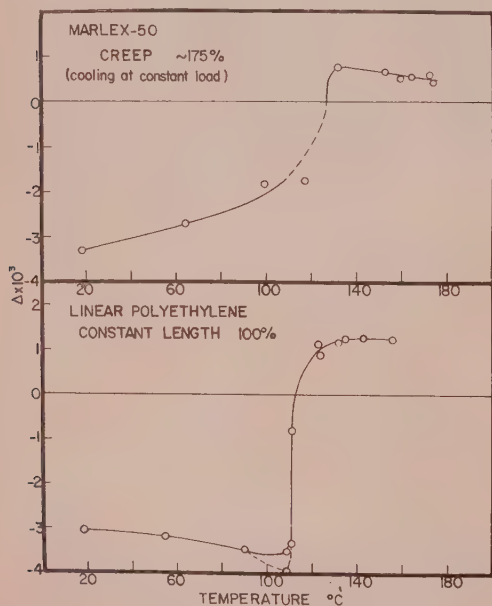


Fig. 10. A comparison of birefringence changes during cooling linear polyethylene samples from the melt at constant load and at constant length.

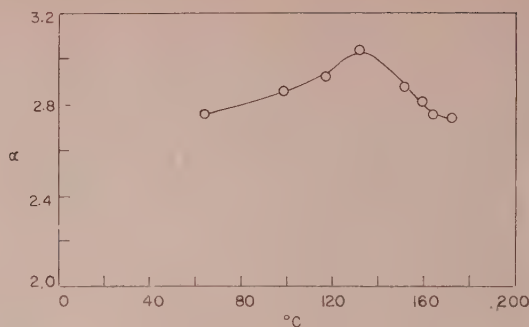


Fig. 11. The change in length accompanying the cooling of a linear polyethylene sample from the melt at constant load. Length is expressed in terms of the elongation ratio α (length/initial length).

it decreases upon further cooling and has shrunk by about 15% at room temperature. This behavior is to be contrasted with that observed when oriented rubber is crystallized, where a spontaneous elongation occurs. The decrease in length upon cooling polyethylene is a consequence of crystal growth where the chain orientation is perpendicular to the stretching direction.

INTERPRETATIONS

Several interpretations of row or a -axis orientation have been advanced. One of these⁹ proposes that nucleation tends to occur along "cracks, edges, and flow lines" produced during extension. Because of steric interference, degenerate spherulites grow cylindrically rather than spherically from such row nuclei. Since the b axis tends to orient in a radial direction in a polyethylene spherulite, it would be perpendicular to the cylinder axis, and hence perpendicular to the stretching direction.

On the basis of this explanation, it is difficult to understand the transition from a - to c -axis orientation with increasing elongation. It would seem that the strain-induced nucleation would be more prevalent at high elongation, under which conditions one might expect to find enhanced row orientation. Also, the mechanism would be kinetically controlled and would depend upon such factors as rate, temperature of stretching, annealing temperature, and time, all of which should affect the density of heterogeneities, producing row-like nuclei. In practice, this was not found to be the case. The final orientation state appeared to depend primarily on the degree of orientation of the melt and was not affected appreciably by repeated remelting and cooling.

A second explanation, involving the orientational changes accompanying the contraction occurring upon annealing, has been proposed.¹² Again, it would seem that the extent of such contractions should be greater

¹² D. R. Holmes, R. G. Miller, R. P. Palmer, and C. W. Bunn, *Nature* **171**, 1104 (1953).

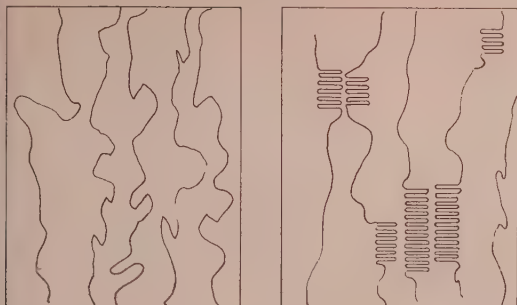


Fig. 12. A possible mechanism for intramolecular crystallization of an oriented chain.

for the sample initially extended a greater amount. Also, the observation that *a*-axis type orientation occurs both in constant length and constant load experiments seems to contradict this explanation.

A hydrodynamic explanation has been proposed by Aggerwal and Sweeting,¹¹ in which the longer dimension of the crystallites (assumed to be those of the *a* axis) orients in the flow gradient of extrusion. This explanation cannot apply to our experiments carried out under conditions of constant length.

An alternative explanation is proposed by us. It is known that polyethylene crystals having folded chains¹³ grow from solutions. Many workers believe that chain folding may also occur with polymer crystals grown from the melt.^{14,15} If a chain from which such a crystal grows is oriented, then it would appear possible that the chain may fold to produce a perpendicularly oriented crystal as indicated in Fig. 12. This "intramolecular crystallization" would produce a contraction in a constant load experiment, as is actually observed. In a constant length experiment, the force on the sample would increase. The occurrence of this is indicated by the fact that the samples often exhibit a tensile break upon cooling.

This increase of force represents an increase in free energy which causes a lowering of the melting point of such crystals. The higher the elongation the greater this effect. Thus, it would seem reasonable that this crystal

¹³ P. H. Till, Jr., J. Polymer Sci. **24**, 301 (1957); A. Keller, Phil. Mag. **2**, 1171 (1957); E. W. Fischer, Z. Naturforsch. **12a**, 753 (1957).

¹⁴ P. Geil, J. Polymer Sci. **47**, 65 (1960).

¹⁵ J. Hoffman, paper presented at American Physical Society meeting, Monterey, California, March (1961).

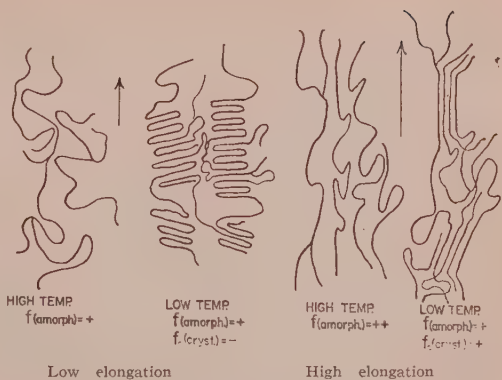


Fig. 13. A comparison of proposed intramolecular and intermolecular crystallization mechanism at low and high elongation. The elongation direction is vertical.

form might become unstable with respect to another form of lower free energy upon elongation. Such an alternate form might be a "bundle" or "intermolecular" crystallite involving the ordering of a number of adjacent chains aligned parallel to the stretching direction (*c*-axis orientation). This is the usual form of crystallization occurring, for example, when a rubber crystallizes on stretching. Since growth of these crystals involves straightening out and lengthening of the chains, elongation produces a lowering of their free energy. A comparison of proposed types of crystallization occurring at high and low elongations is given in Fig. 13.

Thus, the transition from *a*- to *c*-axis orientation may be explained on the basis of a transition of crystal morphology from intra- to intermolecular growth. If this occurs, then it would also follow that folded chain crystals predominate in samples crystallized in the usual unoriented state. This would give rise to samples in which the local orientation of the crystals tends to be perpendicular to the local orientation of the amorphous material.

Other evidence for such crossed local orientation of amorphous and crystalline material comes from (1) lower birefringence of spherulites than expected from the orientation of their constituent crystals,¹⁶ and (2) the initial negative amorphous orientation observed on stretching polyethylene.¹⁷

¹⁶ A. Keller, J. Polymer Sci. **17**, 351 (1955).

¹⁷ D. G. LeGrand, Ph.D. thesis, University of Massachusetts, Amherst, Massachusetts (1959).

The Swelling of Unfilled and Highly Filled Polymers

K. W. BILLS, JR., AND F. S. SALCEDO

Aerojet-General Corporation, Chemical Division, Azusa, California

The swelling of elastomers in solvents is a useful method for determining the effective crosslinking of the polymeric structure. However, it is now shown that this method may be applied satisfactorily to highly filled polymers. A unique method has been devised for the accurate measurement of the swelling ratio of the gel phase of the filled polymers. The method is based on the observation that the binder-filler bond, for most filler particles, releases on swelling. The binder around the particle swells, leaving a hollow pocket which becomes filled with solvent. Corrections for this "waste" solvent lead to the equations from which the swelling of the polymer can be calculated. Experimental verification is given for several filled systems.

INTRODUCTION

CHEMICAL crosslinking of the polymeric binder is possibly the most significant factor affecting the mechanical behavior of highly filled elastomers. A more complete knowledge of the state of crosslinking in the polymeric binder should provide a valuable advance to filled polymer technology, especially if the necessary investigations can be made in the presence of the filler material. In an unfilled polymer this property is easily determined through the conventional method of swelling the material to equilibrium in a solvent medium. However, no previously known method was available for evaluating the results of swelling measurements of highly filled polymers or elastomers. In this paper we report some new concepts of the swelling process which have been applied successfully to highly filled systems. The objective of this paper is to describe these concepts and the testing methods.

BACKGROUND

Theory

Swelling measurements on polymers may be used to yield a parameter called the effective crosslink density (the number of effective crosslinking sites per unit volume of the polymer). The equation relating crosslink density ν_e/V_0 and the volume fraction of the polymer in the swollen gel v_2 is given by Flory,¹

$$-\left[\ln(1-v_2) + v_2 + \chi v_2^2\right] = V_1 \frac{\nu_e}{V_0} \left[(v_2 v_0^2)^{1/3} - 2v_2/f\right], \quad (1)$$

where χ is a dimensionless quantity which characterizes the interaction between solvent and polymer molecules, V_1 is the molar volume of the solvent, f is the functionality of the crosslinking agent, ν_e/V_0 is the moles of effective network chains per unit volume, and v_0 is the volume fraction of the network polymer present in the original polymer sample.² The equilibrium swelling ratio q which is defined as the ratio of volume of the swollen network V to that of the unswollen network V_0 can be expressed as

$$q = V/V_0 = 1/v_2. \quad (2)$$

¹ P. J. Flory, *J. Chem. Phys.* **18**, 108 (1950).

² The value v_0 is important only for those polymer systems containing plasticizers or non-network polymers, which are extractable by the solvent during the swelling process.

In order to calculate ν_e/V_0 from swelling measurements it is also necessary to make an independent determination of the interaction parameter χ . The value of χ is obtained through the application of any one of several procedures. The most widely applied method is the measurement of vapor pressures of solutions of the linear polymer in a given solvent.

Restrictions on the Use of the Fundamental Equation

The assumptions and approximations involved in the derivation of the fundamental theory of swelling introduce certain restrictions on its applications. Fortunately, the limits imposed are reasonable and permit the testing of most of the elastomeric binder systems employed in highly filled elastomers. The following assumptions of the fundamental relation are stated or implied: (1) nearly identical molecular geometries are required for the solvent and polymer segments (this requires the proper selection of a solvent); (2) specific interactions between neighboring components are neglected in the interaction parameter; (3) the polymer must approximate isotropic elastic behavior; and (4) the polymer must have a permanent network structure and must not chemically rearrange or flow (i.e., it must possess an equilibrium retractive force to reach equilibrium swelling).

DEVELOPMENT OF SWELLING RELATION FOR FILLED POLYMERS

General Observations on the Problem

In the past, application of the fundamental relation [Eq. (1)] to filled polymers has lead to erroneous and contradictory results. The reasons for these errors are numerous and for the most part are associated with the interaction effects between the filler and the binder. For example, the filler may chemically affect the interaction parameter χ between the solvent and the polymer. In addition, the filler-polymer bond may remain firmly intact, or it may break on swelling. In the second case, the effect of the bond is to limit greatly the extent of swelling, giving a false impression of a high crosslink density for the binder. In the third case, an equally important problem arises when the filler-

binder bond is released at the interface as a result of swelling. A hole or cavity is formed around the particle which fills with solvent. This quantity of entrapped solvent is rather large and would lead to erroneous conclusions if it were assumed that it has been taken up by the binder.

In addition to the problem areas given above, the polymeric binder in a highly filled polymer frequently consists of two phases: (1) a crosslinked network structure called the gel, and (2) a linear polymer fraction called the sol fraction, which includes the plasticizer. In many systems the sol fraction is frequently large and must be taken into account. Fortunately, a correction for this sol fraction is possible since it is largely removed by the solvent during the swelling process. The results presented below take account of these problems.

Development of the Theory

In the derivation of a relation which may be applied to filled polymers, certain assumptions and limitations are made regarding the testing conditions and the behavior of the material in swelling. These conditions are imposed in order to take account of the major problem areas given above. These conditions are: (1) 100% bond release is to be achieved through a proper selection of solvents; (2) the sol fraction is assumed to be entirely extracted into the solvent medium; (3) the removal of the sol fraction does not alter the density of the gel phase nor the interaction parameter χ ; and (4) Eq. (1) and its associated restrictions apply to the swelling behavior of the binder network. Experience on real systems has shown these restrictions to be entirely acceptable. The first restriction of 100% bond release must be verified experimentally on the filled system, while conditions (2), (3), and (4) can be verified on the binder.

Filler-Binder Bond Release

The first of these restrictions has been met with several rubbery binders (polyurethans, GRS, and polyisobutylene) containing a variety of fillers (glass, NH_4ClO_4 , NaCl, aluminum, and tin). For example, the photomicrograph presented in Fig. 1 shows a glass bead in a polyurethan binder. The halo-like ring around the bead is the swollen boundary of the binder, which was originally (before swelling) in intimate contact with the glass sphere. Note the uniform (isotropic) enlargement of the halo. Isotropic enlargement was also found for a variety of shapes and types of particles.

The effect of filler packing on the swelling process was also tested. Isotropic enlargement of the binder about the particles was observed. Examples of these effects are shown in Figs. 2 and 3 for highly filled systems containing sodium chloride crystals and glass beads. A high magnification (600 diam) of a single glass sphere (Fig. 4) in a highly filled polyurethan

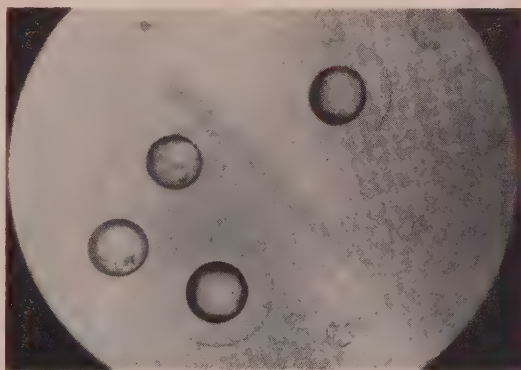


FIG. 1. Glass spheres in swollen polyurethan rubber.

binder shows that the swelling about the filler particle is unaffected by the close packing.

The halo-like pattern defines the swollen boundary of the binder which gives a measure of the final volume. The space contained between these boundaries was found to be filled with solvent which does not enter into the swelling of the gel. A measure of the "waste" solvent taken up in these holes should provide a means for correcting the swelling ratios to yield the desired values of v_2 .

General Swelling Ratio

The geometric behavior of a filled polymer specimen in swelling is directly related to the swelling ratio of its binder system. Furthermore, the observed behavior of total filler-polymer bond release (with a cavity about the particle) demonstrates that the particle does not interfere with the binder swelling behavior.

Direct physical measurements of the over-all length of a sample before and after swelling (l_0 and l , respectively) gives a measure of the gross geometric change, or geometric swelling ratio Q (which is equal to q under the condition of no sol fraction)

$$Q = (l/l_0)^3. \quad (3)$$

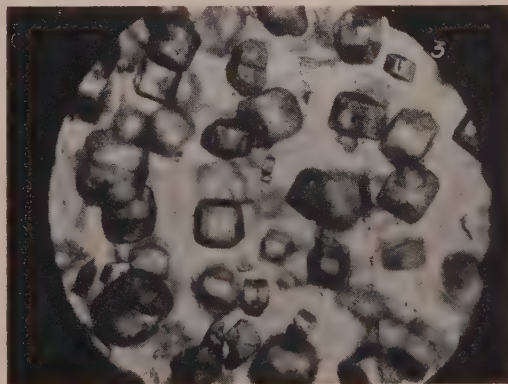


FIG. 2. Sodium chloride in swollen polyurethan rubber.

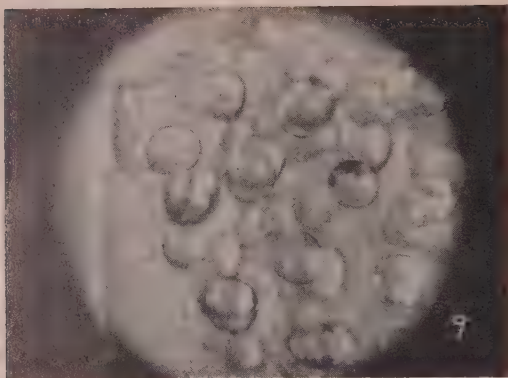


FIG. 3. Glass spheres in swollen polyurethane rubber initially at 52 volume percent solids.

Similarly, the geometric swelling ratio of the cavity formed around a particle (as shown in Fig. 1) would be expected, on the basis of isotropic and homogeneous swelling behavior, to obey the relation

$$Q = V_H / V_b \quad (4)$$

where V_H is the volume of the swollen hole around the particle (including the particle) and V_b is the original volume of the particle. A typical result is shown below for glass beads in two polyurethane rubbers swollen in dioxan at 80°F. These values are the result of direct measurements on the binder and on the glass beads.

Binder	$Q = V_H / V_b$	$Q = (l/l_0)^3$
Polyurethane rubber No. 1	6.64	6.65
Polyurethane rubber No. 2	5.80	5.65

In synopsis it can be said that the gross geometric swelling ratio of a filled rubber is independent of the filler content, providing 100% binder-filler bond release is obtained. For filled binder systems with a negligible amount of extractable material (sol fraction) the value of Q is equal to q . Therefore, a direct physical measurement of l/l_0 or of the original and final volumes of the specimen will yield the swelling ratio q , and no corrections for the filler content are required.

The swelling relation which takes account of the sol fraction is based on the assumptions and testing conditions indicated above. For a swollen polymer without fillers the following relation holds:

$$v_2 = (V_0 - V_E) / (V_0 + V_S - V_E) \quad (5)$$

where v_2 = volume fraction of gel in the swollen gel phase only, V_0 = initial volume of binder (including sol fraction), V_E = volume of extractable polymer (sol), and V_S = volume of solvent in the gel phase after swelling. This relation gives the ratio of the corrected original volume to the final volume of the specimen. An equivalent relation is expected to hold for the filled polymer and is determined from the following considerations.

Consider a single particle in the swollen medium

which follows the behavior shown here. The geometric swelling ratio is related to the volume of the swollen hole of diameter d and the initial volume of the particle of diameter d_0 (see Fig. 5). Expressed mathematically,

$$Q = (d/d_0)^3 \quad (6)$$

However, upon the loss of the sol fraction the equilibrium resting state of the unswollen polymer is of a smaller volume than that of the original specimen. Hence, the original polymer boundary must be corrected to a hypothetically smaller value than that for the given particle size. The corrected relation gives the true swelling ratio q of the residual polymer

$$q = (d/d_0 - \epsilon)^3 \quad (7)$$

The final volume of the hole is directly proportional to the final volume of the over-all specimen. Thus,

$$d^3 = K(V_F + V_{ST} - V_E) \quad (8)$$

where K = a proportionality factor equal to $6/\pi$ times the ratio of the over-all specimen volume to that of the given hole, V_F = original volume of the filled polymer specimen, and V_{ST} = total volume of solvent taken up by the specimen.

The corrected volume of the given particle is directly proportional to the initial extracted volume of the specimen

$$(d_0 - \epsilon)^3 = K(V_F - V_E) \quad (9)$$

The constant K may be shown to apply as a direct result of the uniform isotropic swelling behavior of the polymer.

Inserting the relations (7), (8), and (9) into Eq. (2) yields the desired relation

$$v_2 = \frac{V_F - V_E}{V_F + V_{ST} - V_E} \quad (10)$$

The volume fraction of the network polymer in the

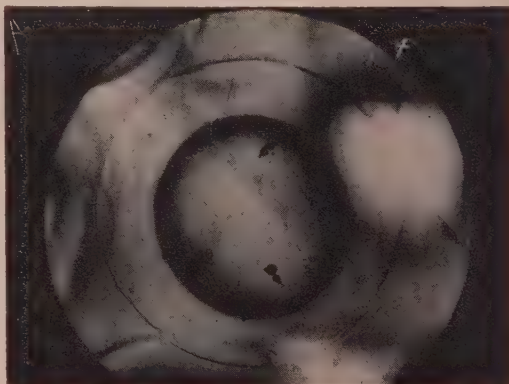


FIG. 4. A single glass sphere in swollen polyurethane rubber initially at 52 volume percent solids.

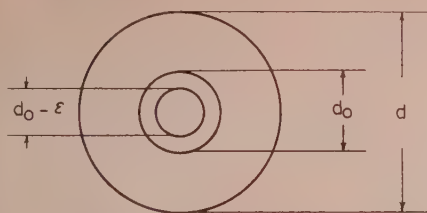


FIG. 5. Schematic representation of the swollen polymer boundary (d) about a filler particle (d_0).

TABLE I. Effect of fillers upon the volume fraction of gel obtained in swelling measurements of filled polyurethan rubbers in dioxane.

Batch no.	Type solids	Solids volume %	v_2	Remarks
1	Glass	0	0.143	polyurethan rubber No. I
2	NH_4ClO_4	52	0.147	
3	NaCl	55	0.134	
4	Aluminum	0	0.153	polyurethan rubber No. II
5	Glass	20	0.155	
6	Glass	0	0.133	
7	Glass	20	0.130	
8	Glass	50	0.133	
		61	0.136	

original rubber binder v_0 is given by

$$v_0 = \frac{v_b V_F - V_E}{v_b V_F} = 1 - \frac{V_E}{v_b V_F} \quad (11)$$

where v_b = volume fraction of polymer in the original, filled rubber specimen.

The volume fractions v_2 and v_0 as determined by Eqs. (10) and (11) can be substituted into Eq. (1) which yields the value of the crosslink density.

Equation (10) indicates that the swelling ratio of the gel, $1/v_2$, is equal to the swelling ratio of the highly filled polymer. Hence, the ratio is independent of the concentration of the filler, as observed previously.

Experimental Verification of Calculation Procedures

Equation (10) provides a means of calculating v_2 in terms of easily measured parameters of the filled sample before and after swelling in a solvent. The verification of this relation was performed experimentally on several filled systems. To eliminate contamination effects by the fillers, special methods were devised, as shown below. Typical of the swelling ratio measurements on filled polymers were those made on samples of two polyurethan binders containing various concentrations of fillers (prepared from 150 g batches of binder). After the fillers were mixed into the polymer they were cast into tall containers and allowed to settle before the fuel was cured. Thus the top portion of the specimen became essentially filler-free, while the bottom of the casting was highly filled. It was believed that by this method the contamination of the binder by filler impurities should be essentially the same in both regions. A section at the bottom of the casting, where the filler was concentrated, was taken for the

swelling measurement, while an adjacent sample was analyzed for density and volume of solids. Similar samples of the binder were taken from the upper portion of the casting from which the filler had settled.

The assumption is made that the swelling of the binder, with and without the filler, would be the same as a result of this treatment. This assumption appears to be justified by the experimental results of Table I. Here the volume fraction of swollen gel v_2 (i.e., the reciprocal of the equilibrium swelling ratio q) obtained on swelling the binder samples is shown.

The results show that in all cases v_2 for the treated binder and for the filled binder are the same. Glass beads, sodium chloride, aluminum, and ammonium perchlorate fillers gave approximately the same results.

Equation (10) appears to be adequately verified for the polymer systems reviewed. However, it should be pointed out that these results may not be applied to a system where the polymer-filler bond does not release in swelling. In addition, the determination of χ for the filled polymer system must be made before the value of the crosslink density of the gel can be calculated.

ACKNOWLEDGMENTS

The authors wish to acknowledge the patience and experimental skills of Mr. R. A. Smith who performed a large portion of this experimentation. In addition, the advice and technical support of Dr. K. H. Sweeny and Dr. E. Mishuck are gratefully acknowledged.

This work was supported by the Bureau of Naval Weapons, Special Projects Office.

Regular Articles

Drift Velocity of a Charged Particle in an Inhomogeneous Magnetic Field

JAMES HURLEY

New York University, New York, New York

(Received May 17, 1961)

Alfvén and Spitzer have obtained an expression for the drift velocity of a charged particle in an inhomogeneous magnetic field. The result is correct to first order in the ratio of the drift velocity to the particle velocity. We have presented here a class of fields for which the drift velocity may be calculated exactly.

ANALYSIS

At the present time, the problem of the drift motion of a charged particle in an inhomogeneous magnetic field is treated by considering the inhomogeneity as a perturbation. In a uniform field the particle will revolve in a circle. A uniform inhomogeneity causes the particle to spiral so that the mean velocity of its center of curvature (guiding center approximation) is a drift in a direction perpendicular to both the field and the component of the gradient perpendicular to the field. The magnitude of this drift has been determined by Alfvén¹ and Spitzer² to be

$$v_D = mc v_0^2 \mathbf{B} \times \nabla B / 2eB^3.$$

This is a good approximation so long as the drift velocity is small compared to the particle velocity. For electrons this condition is almost always satisfied. However, it may not be satisfied for the high-energy component of protons in the Van Allen belts.

We shall present here a class of magnetic fields for which the drift velocity may be calculated exactly. In a recent article, Seymour³ calculated exactly the drift motion in a magnetic field of constant gradient, i.e., $B_x=0$, $B_y=0$, and $B_z=\lambda Bx$. We shall begin by considering the more general case $B_x=0$, $B_y=0$, and $B_z=B(x)$. The vector potential for such a field is $A_x=0$, $A_y=A(x)$, and $A_z=0$ with $B=dA/dx$. The drift will be along the y axis so that the drift velocity is

$$v_D = \int v_y dt / \int dt,$$

where the integration is over one cycle. The generalized integral of momentum gives⁴

$$v_y = -eA/mc + b,$$

where b is a constant chosen to satisfy the initial conditions. Also, since the kinetic energy is a constant,

$$v_x^2 + v_y^2 = v_0^2.$$

¹ H. Alfvén, *Cosmical Electrodynamics* (Clarendon Press, Oxford, England, 1950).

² L. Spitzer, *Astrophys. J.* **116**, 299 (1952).

³ P. W. Seymour, *Australian J. Phys.* **13**, 309 (1960).

⁴ Since the speed of a particle in a magnetic field is constant the results may be made relativistic by setting $m = m_0 / (1 - v_0^2/c^2)^{1/2}$.

We may therefore set $v_x = v_0 \cos \theta$ and $v_y = v_0 \sin \theta$. For simplicity, we shall assume that θ ranges from 0 to 2π as the particle describes one cycle. This is equivalent to assuming that the field does not change sign along the path of the particle. (Seymour has considered such a complication for the case $B = \lambda x$.) We may now evaluate the drift velocity implicitly.

$$v_0 = \frac{\int v_y / v_x dx}{\int 1 / v_x dx} = \frac{\int_0^{2\pi} \tan \theta dx / d\theta d\theta}{\int_0^{2\pi} 1 / \cos \theta dx / d\theta d\theta}.$$

Now

$$v_0 \sin \theta = -eA/mc + b \quad (1)$$

and

$$v_0 \cos \theta = -eB/mcdx/d\theta,$$

so that

$$v_D = v_0 \frac{\int_0^{2\pi} \sin \theta / B d\theta}{\int_0^{2\pi} 1 / B d\theta}.$$

We may express x as a function of θ using Eq. (1) so that B is a known function of θ and the integrals may be evaluated.

We can calculate the drift velocity in a similar way

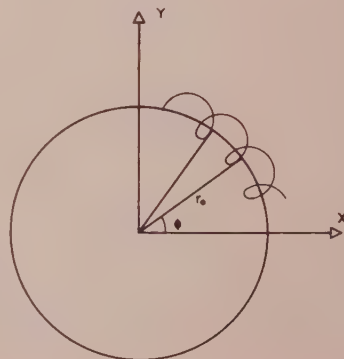


FIG. 1. Drift motion of a charged particle in an axial field.

or fields with axial symmetry, i.e., $B_r=0$, $B_\phi=0$ and $B_z=B(r)$, so that $A_r=0$, $A_\phi=A_0$, and $A_z=0$. The analysis may also be applied to a particle moving in the equatorial plane of a dipole since the above conditions on the field are satisfied in the plane. The path of the particle has been sketched in Fig. 1. In Fig. 1, r_0 is the distance from the center of symmetry of the field to a point on the path where $v_\phi=0$. We define the drift velocity by

$$v_D = r_0 \int d\phi / \int dt,$$

where the integrals are taken over one cycle. The momentum integral is

$$v_\phi = -eA/mc + b/r, \quad (2)$$

and the energy integral

$$v_r^2 + v_\phi^2 = v_0^2.$$

We again set

$$v_\phi = v_0 \sin\theta$$

$$v_r = v_0 \cos\theta$$

so that

$$v_D = \frac{\int_0^{2\pi} r_0/r v_\phi/v_r dr/d\theta d\theta}{\int_0^{2\pi} 1/v_r dr/d\theta d\theta} = v_0 \frac{\int_0^{2\pi} r_0/r \tan\theta dr/d\theta d\theta}{\int_0^{2\pi} 1/\cos\theta dr/d\theta d\theta}.$$

From Eqs. (2) and (3) we may determine r as a function of θ and so may evaluate the integrals. For example, let $B=A_0/r$ and $A=A_0$, then

$$v_D = -v_0/k[1 - (1-k^2)^{1/2}](1-k^2),$$

where

$$k = mc v_0 / e A_0.$$

For $k \ll 1$,

$$v_D \simeq -mc v_0^2 / 2e A_0,$$

which is the Alfvén-Spitzer result.

A Graphical Method for Determination of Mobility Ratio in the Semiconductors from Hall Effect Measurements Only

KRZYSZTOF PIGOŃ

Department of Physical Chemistry, Institute of Technology, Wrocław, Poland

(Received April 24, 1961)

A method is presented for the approximate estimation of mobility ratio $b = \mu_n/\mu_p$ from the Hall constant measurements taken in the vicinity of the intrinsic region and in this region itself. It is based on the discussion of a formula giving the Hall constant of a nondegenerate semiconductor at the exhaustion. Examples of these determinations are given; the results obtained show reasonable agreement with others' estimations.

THE usual method of estimation of the mobility ratio b is based on the measurements of the thermoelectric force α at various temperatures in the intrinsic range. These measurements have to be very accurate, however, particularly in the case of high b values where an error in the estimation of the slope of α vs $1/T$ line can seriously affect the results. This makes it necessary to take the measurements over a rather wide range of temperatures, far above the intrinsic region. These requirements cannot always be fulfilled, especially in the case of impure materials.

A method is presented below, by which an approximate estimation of mobility ratio seems to be possible, using measurements of the Hall constant (R) only.

Let us consider a nondegenerate semiconductor with completely ionized impurity centers of donor and acceptor types, whose densities are N_D and N_A , respectively. In the case when b is temperature independent (as is usually assumed) the Hall constant may be

expressed by a formula¹:

$$R = -\frac{A}{en_i} \frac{b-1}{b+1} \left\{ \frac{b^2+1}{b^2-1} \frac{N_D-N_A}{2n_i} + \left[\left(\frac{N_D-N_A}{2n_i} \right)^2 + 1 \right]^{1/2} \cdot \left\{ \frac{b-1}{b+1} \frac{N_D-N_A}{2n_i} + \left[\left(\frac{N_D-N_A}{2n_i} \right)^2 + 1 \right]^{1/2} \right\}^{-2} \right\}, \quad (1)$$

where A is the scattering factor, n_i is the density of intrinsic carriers ($n_i^2 = np$), and b is the mobility ratio μ_n/μ_p .

Denoting the last term in Eq. (1) by $\varphi(\eta, b)$, where η stands for $(N_D - N_A)/2n_i$, we have, after a simple

¹ G. Busch, U. Winkler, *Ergeb. exakt. Naturwiss.* **29**, 145 (1956).

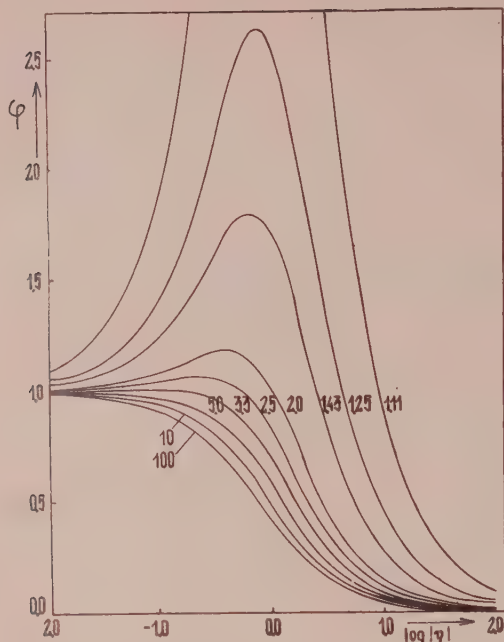


FIG. 1. φ -functions for n -type semiconductors and for values of b as denoted in the graph. For anomalous p -semiconductors one should take the reciprocal values of b .

rearrangement,

$$-R \cdot (en_i/A)(b+1)/(b-1) = \varphi(\eta, b). \quad (2)$$

As the "intrinsic" Hall constant amounts to $R_i = -(A/en_i)(b-1)/(b+1)$, Eq. (2) may be rewritten in a short form:

$$R/R_i = \varphi(\eta, b). \quad (3)$$

The right-hand expression can be numerically evaluated for various values of η and b and drawn as one-parameter family of curves vs $\log|\eta|$. These graphs are presented in the Fig. 1 for $\eta > 0$ (n -type semiconductor) and in Fig. 2 for $\eta < 0$ (p -type semiconductor), b being > 1 in both cases.

It is noticeable that the curve for a given b and η is identical with that for $-\eta$ and $1/b$. Thus the graphs presented in the Figs. 1 and 2 are also valid for the anomalous semiconductors with $b < 1$, the only difference being that Fig. 1 now represents the case $\eta < 0$ and Fig. 2 the case $\eta > 0$.

A second diagram based on the experimental results is now drawn; it gives the relationship $\log(RT^3)$ vs $1/T$. One of its usual forms is shown in Fig. 3.

The straight line obtained by extrapolation of the high-temperature portion of the experimental curve allows the calculation of R_i at various temperatures. The distances between the curve and this straight line give directly the logarithm of the ratio R/R_i at various temperatures (and thus at various n_i). Now a number of these ratios together with the corresponding values of R_i is taken (R_i stands for n_i which cannot be evalu-

ated without knowing b . These quantities are, however, proportional to each other and no complications from this procedure arise, as the logarithms of n_i are what we are actually interested in.) Next we put on millimeter tracing paper points representing pairs of quantities (R/R_i as ordinates, $\log R_i$ as abscissas) using the same scale as for the $\varphi(\log|\eta|)$ diagram. Then we place the tracing paper over this diagram with the abscissa axes covering each other. The tracing paper is then moved horizontally to obtain the best fit of experimental points to one of the curves. When this is done, we have directly found the right value of b .²

Two examples are given below as a proof of the ability of this method for estimation of b . They are based on the Hall effect measurements presented in a paper by Winkler³ for a p - Mg_2Sn sample (originally denoted as 3202a) and a n - Mg_2Ge sample (denoted as 2149). The values of R/R_i recalculated from original Winkler graphs together with the best fitting curves $\varphi(\log|\eta|)$ are shown in Figs. 4 and 5.

In both cases the values of b estimated by us agree exactly with those given by Winkler and based on the measurements of the thermoelectric power in the intrinsic region. ($b=1.4$ for Mg_2Sn and $b=5.0$ for Mg_2Ge .)

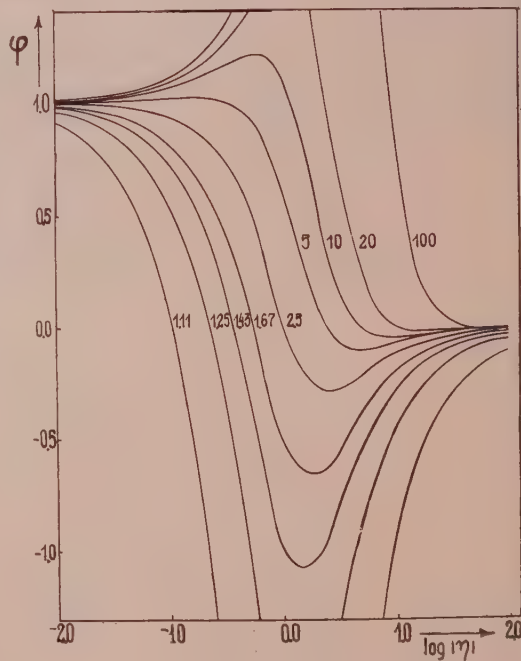


FIG. 2. φ -functions for a p -type semiconductor and for values of b as denoted in the graph. For an anomalous n -semiconductor one should take the reciprocal values of b .

² Editor's note: Because of column-width requirements, preservation of the appropriate scale factors in the figures was not possible. It is therefore suggested that the users of the numerical results of this analysis use a photographic expansion of these figures to an appropriate scale.

³ U. Winkler, *Helv. Phys. Acta* 28, 633 (1955).

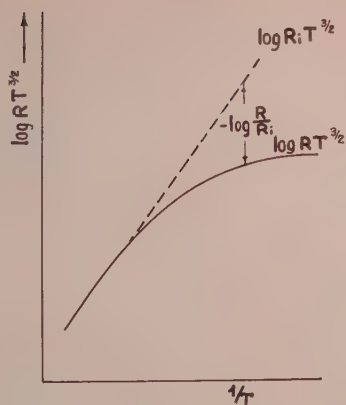


FIG. 3. Estimation of quotients R/R_i from experimental data.

Similarly, by this method we have found $b=80$ for a p -InAs sample from the paper of Folberth and co-workers.⁴

As follows from the shape of the curves presented in Figs. 1 and 2, the measurements of Hall effect in n -type samples are suitable for the evaluation of b when its value is close to 1. For the semiconductors with high values of b , the use of p -type samples is recommended.

It seems that despite various restrictions made in the derivation of Eq. (1), the method presented above can be useful for approximate estimation of b when no measurements or only inaccurate measurements of the thermoelectric force exist for a given semiconductor. It should be noticed that these restrictions are, for the most part, valid also in the "thermoelectric" method of the evaluation of b . The most critical assumption in our case seems to be assuming the constancy of A in Eq. (1). In the "thermoelectric" method the tempera-

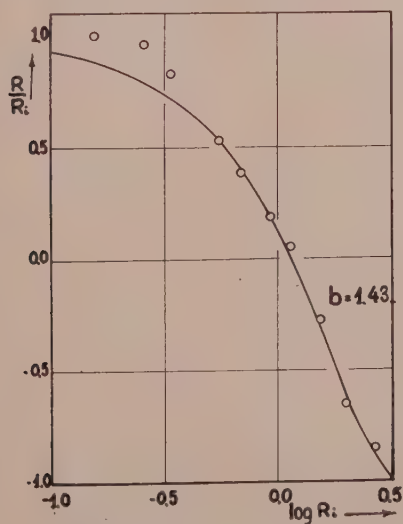


FIG. 4. Values of R/R_i for Mg_2Sn recalculated from Winkler's data (O), together with the best fitting curve $\varphi(\log|\eta|)$ (—).

⁴ O. G. Folberth, O. Madelung, and H. Weiss, Z. Naturforsch. 9a, 954 (1954).

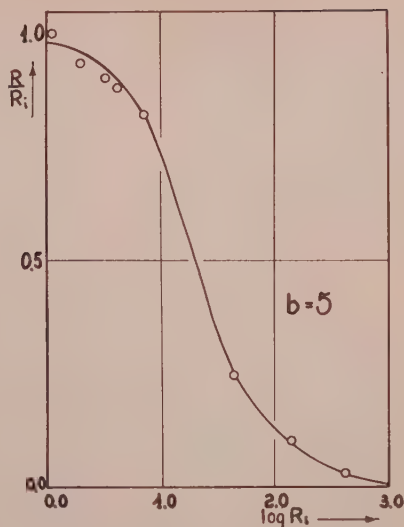


FIG. 5. Values of R/R_i for Mg_2Ge recalculated from Winkler's data (O), together with the best fitting curve $\varphi(\log|\eta|)$ (—).

ture is usually high enough to secure the predominance of the thermal scattering; here, however, the Conwell-Weiskopf mechanism of carrier scattering can also contribute to A . Because the relative participations of both mechanisms change with temperature, the value of A is also temperature-dependent. In this case it is not possible to make the experimental points overlap the curves in Figs. 1 or 2; this overlapping occurs for different samples at distinctly different values of b . This gives, however, immediately the information that the method is useless for the particular case, and may prevent one from making an erroneous determination of b .

Apart from the estimation of the mobility ratio, the method presented here allows one to determine in a simple manner the density of uncompensated impurities $N_D - N_A$. After the fitting of the two graphs as described above we have only to note the value of $\log R_{i,0}$ corresponding to $\log|\eta|=0$. We have then:

$$N_D - N_A = 2(A/e)(b-1)/(b+1)(1/R_{i,0}). \quad (4)$$

This procedure gives more nearly correct values of $N_D - N_A$ than the determination from the horizontal portion of the $R(T)$ curve in the extrinsic region.

Finally, the graphs presented in Figs. 1 and 2 also give interesting information about the shape of the diagram $\log R$ vs $1/T$ in the vicinity of intrinsic region first discussed by Madelung and Weiss⁵ and by Hunter.⁶

More extended description of this method together with the tables of φ -functions should be shortly published in *Zeszyty Naukowe Politechniki Wrocławskiej*.

ACKNOWLEDGMENTS

The author is obliged to Mrs. Krusińska and Mr. Różycka for their kind help in numerical calculations.

⁵ O. Madelung and H. Weiss, Z. Naturforsch. 9a, 527 (1954).

⁶ L. P. Hunter, Phys. Rev. 94, 1157 (1954).

Excess and Hump Current in Esaki Diodes*

RICHARD S. CLAASSEN

Sandia Laboratory, Albuquerque, New Mexico

(Received May 29, 1961)

The origin of the excess and hump current in Esaki diodes is described in terms of discrete defect energy levels in the forbidden band. The hump current results from equal-energy transitions of electrons which originate in a defect level in the n side and tunnel to the valence band on the p side. Impurity conduction is required for appreciable hump currents. The position of the hump locates the defect level if the Fermi level is known for the n side. The excess current is explained in terms of energy dissipating transitions in which electrons start from a defect location within the junction, tunnel to a virtual state in a localized defect in the p region, and drop to the valence band by impact recombination. A crude derivation by the WKB method relates the logarithm of the excess current to the bias voltage where the proportionality factor contains the square root of the effective mass of the electron. From current-voltage curves for diodes fabricated from germanium, silicon, and gallium arsenide, the effective electron masses are estimated as 0.01, 0.1, and 0.05 m , respectively. Defect levels in germanium are estimated at 0.06 and 0.24 eV below the conduction band; levels in silicon are located at 0.04 and 0.42 eV; and in gallium arsenide 0.12 and 0.5 eV below the conduction band. The simultaneous existence of two defect levels can give rise to two distinct slopes of the $\log I$ vs V curve which have been observed in silicon and gallium arsenide diodes following irradiation with 2 MeV electrons.

I. INTRODUCTION

ESAKI has described an interesting and useful phenomenon due to tunneling in narrow p - n junctions.^{1,2} For sufficiently abrupt junctions in heavily doped semiconductor materials, it is possible to obtain a negative resistance region in the characteristic I - V curve. Esaki has explained the negative resistance in terms of band-to-band tunneling at equal energies for the electron in the initial and final state. This type of tunneling current ceases when the "bands are uncrossed," that is, when sufficient bias is applied to raise all conduction electrons to an energy higher than the empty states in the valence band on the opposite side of the junction. At relatively high applied voltage or bias, the diode will conduct current by the normal diode injection mechanism. In between these two regions, Esaki observed a current in excess of that accounted for by either of the above mechanisms and he has called this the "excess current." This region is also referred to as the "valley" current. In any event, it is the magnitude of this current which reduces the peak-to-valley ratio, a figure of merit for tunnel diode applications.

Esaki observed that the excess current varied approximately as the exponential power of the applied voltage. Chynoweth *et al.*,³ have proposed a mechanism in which the carriers tunnel by way of energy states having a continuous distribution within the forbidden gap. Esaki has also observed, in both germanium² and in silicon,⁴ that there may be some structure

to the excess current. He has labeled this the "hump of excess current." Structure in the excess current range has also been observed by Longo⁵ in germanium following electron irradiation and by Sah⁶ in silicon diodes doped with metal.

It is the purpose of this paper to suggest a mechanism for the excess and hump current in terms of discrete defect levels in the forbidden band gap similar to those defect levels associated with radiation damage or crystal deformation.

In Sec. II, the hump current is examined and with its aid the Fermi levels and prominent defect levels are developed for diode samples fabricated from germanium, silicon, and gallium arsenide. In Sec. III, a mechanism is proposed to explain the excess current in terms of tunneling from localized defect levels, and the values in Sec. II are used to compute the effective mass for the tunneling electron. Section IV deals specifically with diodes in which two defect levels contribute distinctly to hump and excess current.

II. THE HUMP CURRENT

Esaki has observed hump current in diodes as constructed of germanium and silicon, as may be seen in Figs. 2 and 4 which are reproduced from his work.^{2,4} With the aid of electron radiation, we have observed humps in diodes made from germanium, silicon, and gallium arsenide.⁷ In most cases the hump current seems to be a small addition to other currents. Figure 1, however, shows the characteristic curves of a germanium diode where the hump caused by electron radiation becomes so large as to cause a new negative resistance region at a bias voltage considerably higher than the normal Esaki negative resistance region. This negative resistance associated with the hump current

* This work performed under the auspices of the U. S. Atomic Energy Commission.

¹ L. Esaki, Phys. Rev. **109**, 602 (1958).

² L. Esaki in *Solid State Physics in Electronics and Telecommunications*, edited by M. Desirant and J. L. Michiels (Academic Press, Inc., New York, 1960), Vol. I, p. 514.

³ A. G. Chynoweth, W. L. Feldman, and R. A. Logan, Phys. Rev. **121**, 684 (1961).

⁴ L. Esaki and Y. Miyahara, Solid State Electronics **1**, 13 (1960).

⁵ T. A. Longo, Bull. Am. Phys. Soc. **5**, 160 (1960).

⁶ C. T. Sah, Bull. Am. Phys. Soc. **5**, 507 (1960).

⁷ R. S. Claassen, Bull. Am. Phys. Soc. **5**, 406 (1960).

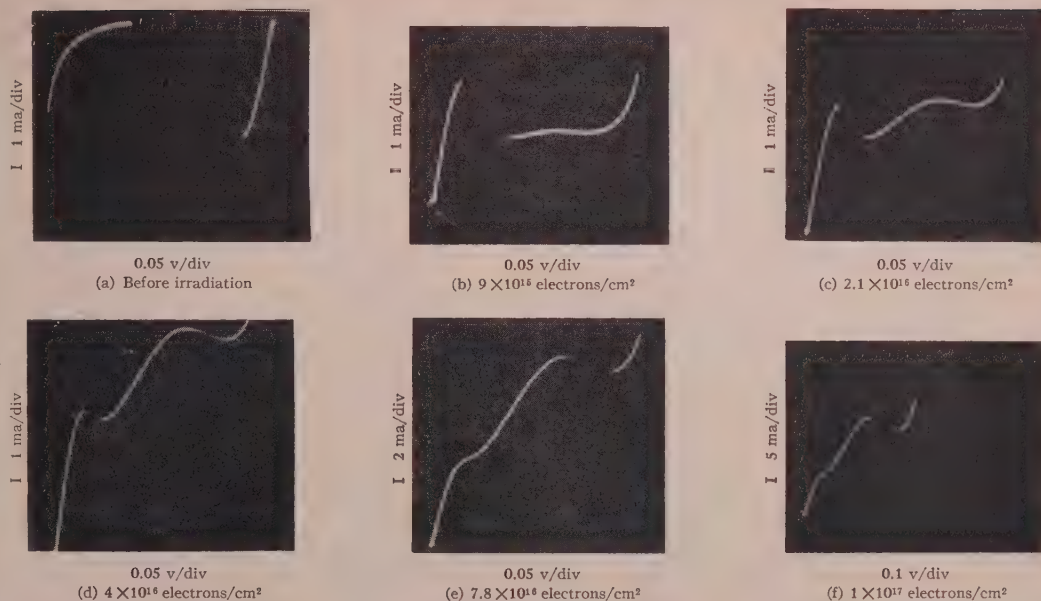


FIG. 1. The current vs voltage traces for a germanium diode showing the development of a hump due to electron irradiation. Electrons of 2-Mev energy impinge directly on junction area. The diode was continuously cooled to a temperature estimated as 230°K.

is a strong indication that the hump current is carried by a process very similar to the normal Esaki diode current.

By close analogy to Esaki's analysis, the hump current is due to equi-energy transitions from a defect level in the forbidden gap on the n side to a vacant state in the valence band on the p side. The hump current will start at such a bias that the defect level is just opposite the Fermi level on the p side, that is,

$$\zeta_C + \epsilon_d = eV_F,$$

where ζ_C is the Fermi level in the n side, taken positive upward from the conduction band edge, ϵ_d is the depth of the defect level measured down from the conduction band edge, V_F is the applied voltage, and e is the electronic charge. This is an approximation assuming that kT is small compared to the other quantities involved. The hump current will cease at a bias voltage such that

$$eV_F = \zeta_C + \epsilon_d + \zeta_V,$$

where ζ_V is the Fermi level on the p side taken positive down from the valence band. Thus, the width of the hump in volts gives the depth of the Fermi level on the p side.

Hump current might also occur by the process of electrons from the conduction band tunneling to empty states in defect levels in the forbidden band on the p side. This process would produce a hump of voltage width equal to the Fermi level on the n side. Since the junctions studied are unsymmetrical in Fermi levels, it is possible to identify the hump with transitions to the valence band.

The hump current is not always seen in combination with the excess current. In fact, in most diodes tested, damage by electron irradiation has been necessary to produce a hump. Although both currents are probably due to the same defect level, the appearance of one without the other is explained in the following way. For sufficiently low concentrations of defects, each defect acts as an independent center of attraction holding an electron in a bound state. As will be described in the next section, this still allows a mechanism for the excess current. For the hump current, however, this means that the number of electrons available for tunneling to the valence band is limited to the number of defect centers in a very narrow layer at the edge of the junction. Now, as the density of defects is increased, the defects begin to interact, the wave functions overlap, and finally, at sufficiently high concentrations, defect or impurity conduction is established.⁸⁻¹⁰

With impurity conduction, a defect band is established which makes all electrons associated with the defect on the n side available for tunneling. For the situation on the n side of a tunnel diode, the defects will all be filled since they are far below the Fermi level and impurity conduction should be negligible for low concentration. For antimony-doped n -type germanium and gallium-doped p -type germanium, Fritzche classifies low concentration as $< 2 \times 10^{16} \text{ cm}^{-3}$, where conduction associated with impurity centers takes place by an electron jumping or tunneling from an occupied to an unoccupied defect level. Impurity conduction

⁸ H. Fritzche, Phys. Rev. **99**, 406 (1955).

⁹ H. Fritzche, J. Phys. Chem. Solids **6**, 69 (1958).

¹⁰ H. Fritzche, Phys. Rev. **113**, 999 (1959).

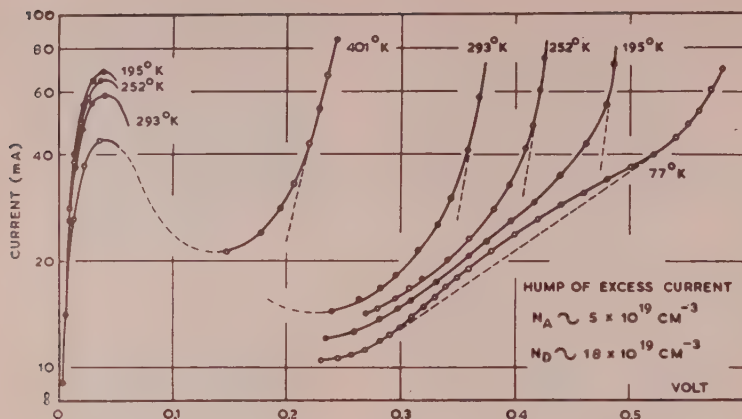


Fig. 2. The current-voltage curve for a germanium p - n junction. From L. Esaki, reference 2.

occurs at impurity concentration above $2 \times 10^{17} \text{ cm}^{-3}$. For defect levels whose energy is considerably further down in the gap than gallium in germanium, one might expect different concentration ranges appropriate to the two types of conduction. For lack of better information, however, a value of 10^{17} cm^{-3} is assumed for the onset of impurity conduction and therefore hump current. The hump in Fig. 1 begins to appear at 9×10^{15} electrons/cm². Using the defect production rate quoted by MacKay and Klontz¹¹ of 2 cm^{-1} for 1.1-Mev electrons on n -type germanium, and assuming one defect per electron removed, gives a defect density of $\sim 2 \times 10^{16} \text{ cm}^{-3}$, which is in fair agreement with the estimate above.

In Fig. 2, which is reproduced from Esaki's article on germanium p - n junctions,² the hump current at 77°K is seen to start at about 0.3 v and stop at about 0.51 v. To calculate the Fermi levels we use the concentration values given by Esaki as $N_A = 5 \times 10^{19} \text{ cm}^{-3}$ and $N_D = 1.8 \times 10^{19} \text{ cm}^{-3}$ and assume that all donors and acceptors are ionized at these concentrations. For the case of very strong degeneracy and the Fermi level ζ much greater than kT ,^{12,13}

$$\zeta = - \left(\frac{3}{2} \right)^{\frac{1}{3}} \frac{h^2}{m_e} n^{\frac{2}{3}},$$

or

$$\zeta = 37 \times 10^{-16} n^{\frac{2}{3}} / G \text{ (in ev)}, \quad (1)$$

where h is Planck's constant, m_e is the effective mass of the charge carrier, G is the ratio m_0/m_e , and n is the density of carriers. Using the effective mass ratios of 0.412 and 0.216 for electrons and holes, respectively, as given in Hannay,¹⁴ the values of $\zeta_c = 0.062 \text{ ev}$ and $\zeta_v = 0.23 \text{ ev}$ are obtained. This gives a value for the defect level of

$$\epsilon_d = 0.30 - 0.06 = 0.24 \text{ ev}.$$

This level may be due to deformation or dislocation which takes place during the alloying process. Newman¹⁵ has observed a characteristic recombination radiation from deformed germanium p - n junctions. The wavelength of the radiation is independent of the doping impurities and indicates a level 0.2 ev below the conduction band (or above the valence band). Precisely the same band was observed in alloyed p - n junctions. This was true for both indium alloyed to n -type germanium and for an indium-arsenic dot alloyed to p -type germanium.

The calculated Fermi level ζ_v , of 0.23 ev is in agreement with the observed hump width of 0.21 v.

The diode of Fig. 1 showed no indication of a hump before irradiation. After 2×10^{16} electrons/cm², the hump current started at 0.15 v and stopped at 0.37 v. Although the doping level of this diode is unknown, an approximation to the Fermi level can be made by assuming that the peak current occurs at a bias which is 80% of the Fermi level on the n side.¹⁶ This gives an estimate of 0.09 ev for ζ_c and 0.06 ev for the defect level. By a similar analysis, two other similar diodes showed irradiation induced humps from a defect level at about 0.06 ev. These diodes were fabricated from arsenic-doped germanium alloyed with an indium-gallium dot.¹⁷ From the hump width, ζ_v is estimated as 0.22 ev.

In silicon there are two humps. The first is clearly visible in Fig. 3, which is a copy of the recorder trace for a silicon diode following 3×10^{17} electrons/cm² irradiation. The hump starts at about 0.14 v and stops at about 0.42 v. The junction was fabricated from a wafer of arsenic-doped silicon of approximately 6×10^{-4} ohm cm resistance and an alloy dot of aluminum with boron.¹⁸ From the location of the current peak at

¹⁵ R. Newman, Phys. Rev. **105**, 1715 (1957).

¹⁶ I. A. Lesk, N. Holonyak, Jr., J. S. Davidsohn, and W. Aarons, 1959 IRE, Wescon Convention Record, Part 3-EC-4441.

¹⁷ These diodes were furnished through the courtesy of Stanley Brown, Hughes Semiconductor Products, Newport Beach, California.

¹⁸ Information supplied by H. Weinstein, Hoffman Electronics Corporation, Santa Barbara, California.

¹¹ J. W. MacKay and E. E. Klontz, J. Appl. Phys. **30**, 1269 (1959).

¹² E. Spence, *Electronic Semiconductors* (McGraw-Hill Book Company, Inc., New York, 1958).

¹³ J. S. Blakemoore, Electrical Communications **29**, 131 (1952).

¹⁴ N. B. Hannay, *Semiconductors* (Reinhold Publishing Corporation, New York, 1959).

²⁴ L. W. Aukerman, E. M. Baroddy, R. D. Graft, and T. S. Shilliday, *Theoretical and Experimental Studies Concerning Radiation Damage in Selected Compound Semiconductors*, Thirteenth Interim Rept. (December 30, 1960).

²¹ D. E. Hill, Phys. Rev. **114**, 1414 (1959).

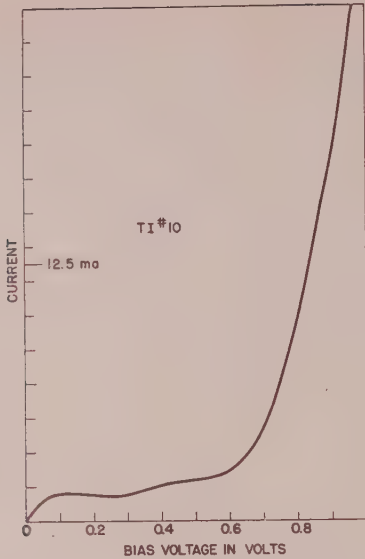


FIG. 5. The current-voltage trace for a GaAs diode following 3.2×10^{18} 2-Mev electrons/cm². The diode was immersed in liquid nitrogen during measurement.

The structure of these humps indicates discrete energy levels. The values of ζ_C , ζ_V , ϵ_{d1} , ϵ_{d2} as determined in this section are used in the next section in analyzing excess current and are summarized in Table I.

III. EXCESS CURRENT

Figure 7 is a schematic representation of an abrupt junction with forward voltage applied. The commonly used linear approximation is made to facilitate calculations. Energy is plotted on the vertical and distance perpendicular to the junction plane on the horizontal. The normal gap is ϵ ; ζ_C , ζ_V , and ϵ_d are as already defined. The junction width is W . As an approximation,

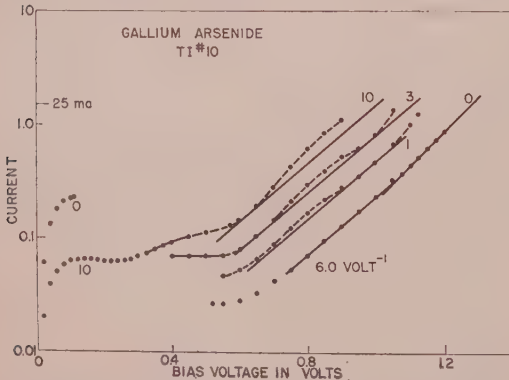


FIG. 6. The current-voltage traces for a GaAs diode immersed in liquid nitrogen. Curves 0, 1, 3, and 10 were taken following 2-Mev electron irradiation of 0, 0.25, 0.74, and 3.2×10^{18} electrons/cm².

the Fermi level is taken as a straight line connecting the level on the two sides. Use of the quasi-Fermi level,^{24a} which extends into the transition region at a level equal to the Fermi level on the n side, would lead to results similar to those presented below but the more complicated expressions are probably not warranted in this simple model. The value W_1 is the distance from the p side to the intersection of the Fermi level with the defect level. We define

$$(\epsilon + \zeta_C + \zeta_V)/e \equiv V_D, \quad (2)$$

the diffusion, or built-in voltage. The junction width W varies with the total voltage across the junction

$$W = W_0(V_D - V_F)^{\frac{1}{2}}, \quad (3)$$

where W_0 is the width at unit voltage and is given¹² by

$$W_0 = \left(\frac{K}{2\pi e} \frac{N_D + N_A}{N_D N_A} \right)^{\frac{1}{2}}, \quad (4)$$

where K is the dielectric constant, e the charge of the

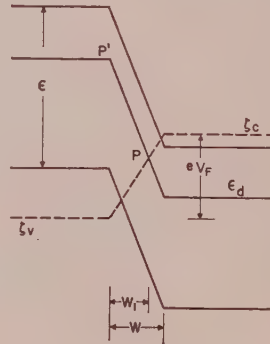


FIG. 7. Schematic representation of an abrupt p - n junction with forward bias V_F applied. Energy is plotted vertically, and distance perpendicular to the junction plane horizontally. The magnitudes are scaled to a typical germanium tunnel diode.

electron, N_D and N_A the density of donors and acceptors on the two sides of the junction.

From Fig. 7, it is evident that the sum of the vertical distance from ζ_V to P and from P to P' must equal $\epsilon - \epsilon_d + \zeta_V$. Since the slope of the potential lines is $e(V_D - V_F)/W$,

$$\frac{W_1}{W} e V_F + \frac{W_1}{W} e (V_D - V_F) = \epsilon - \epsilon_d + \zeta_V.$$

Therefore,

$$W_1 = (\epsilon - \epsilon_d + \zeta_V) W / (e V_D). \quad (5)$$

Note that the ratio W_1/W is independent of applied voltage although the thickness W varies according to (3).

Electrons located at point P on Fig. 7 may tunnel to the p side through a virtual state located at a level ϵ_d below the conduction band on the valence side (P'). For low levels of excess current, where the concentra-

^{24a} See, for example, W. Shockley, *Electrons and Holes in Semiconductors* (D. Van Nostrand Company, Inc., Princeton, New Jersey, 1950), p. 308.

tion of defects is low, the associated states are bound and there is no associated crystal momentum. The transition from the intermediate virtual state to the valence band probably takes place by radiationless impact recombination.^{25,26} In this process, an electron localized in a defect level is dropped to the valence band with the excess energy being carried away by a hole which, in turn, rapidly loses its energy through scattering in the valence band. Since the probability of impact recombination varies as the concentration of holes,²⁶ the transition should be very rapid for the heavily-doped material used in tunnel diodes.

Note that the process invoked for the excess current is not an equi-energy transition as occurs in band-to-band tunneling or in hump current. The fact that the electron must go to a virtual, intermediate bound state argues for a start from a localized defect state as described above. The electrons in the conduction band have, in general, nonzero momenta and therefore can-

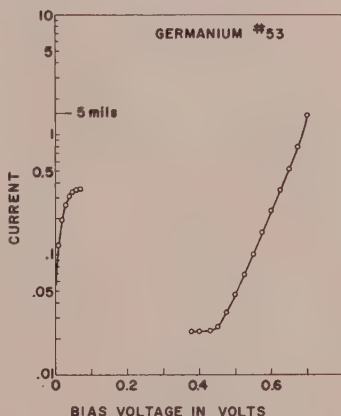


FIG. 8. A replot of the current-voltage trace for a germanium diode immersed in liquid nitrogen; no irradiation.

not go to a localized state without a phonon interaction which makes the transition unlikely.

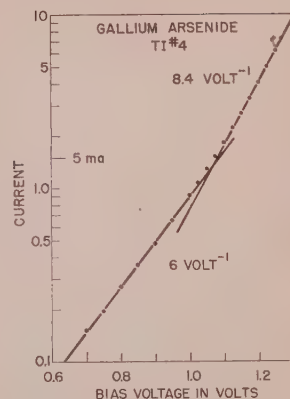
We assume that the excess current is controlled by the probability of tunneling through the potential barrier from P to P' . The potential barrier has a slope $e(V_D - V_F)/W$ and a width W_1 for a transition from P . We treat the electron in the periodic potential field of the crystal as equivalent to an electron of effective mass m_e in a uniform field region. Then using the WKB approximation, we calculate the probability T_p , of penetrating the potential barrier:

$$T_p = C \exp \left[-\frac{4}{3} \frac{(2m_e)^{1/2}}{\hbar} \left(\frac{e}{W} \right)^{1/2} (V_D - V_F)^{1/2} W_1^{1/2} \right]. \quad (6)$$

Use of (3) and (5) gives

$$T_p = C \exp \left[-\frac{4}{3} \frac{(2m_e)^{1/2}}{\hbar} e^{1/2} W_0 \left(\frac{\epsilon - \epsilon_d + \zeta v}{e V_D} \right)^{1/2} (V_D - V_F)^{1/2} \right], \quad (7)$$

FIG. 9. A replot of the current-voltage trace for a GaAs diode following 3×10^{17} 2-Mev electrons/cm². Sample immersed in liquid nitrogen.



where C is a constant. The current in the excess region will be given by

$$I_x = AD_x T_p, \quad (8)$$

where D_x is the density of defect centers and A is a constant containing the area of the junction and the previous constant C .

Substituting the numbers in (8) and letting

$$(\epsilon - \epsilon_d + \zeta v / e V_D)^{1/2} = R \quad (9)$$

gives

$$I_x = AD_x \{ \exp[-6.85 \times 10^7 G^3 W_0 R (V_D - V_F)] \}, \quad (10)$$

where $G = m_e/m$, W_0 is in cm, and $(V_D - V_F)$ is in volts.

In the voltage range where excess current only is important, a plot of $\ln I$ vs V_F should give a straight line of slope

$$S = 6.85 \times 10^7 G^3 W_0 R. \quad (11)$$

Figure 8 is plot of current vs applied voltage for a germanium diode. At 77°K, where the normal diode injection current is suppressed, it is apparent that a straight line is obtained.

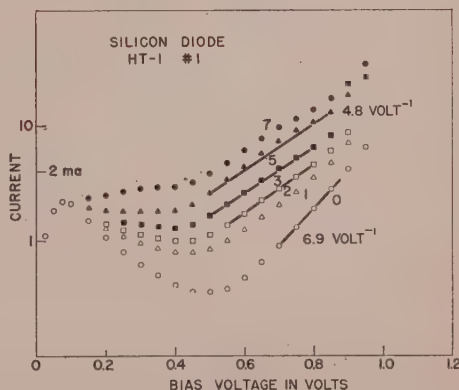


FIG. 10. A replot of the current-voltage traces for a silicon diode immersed in liquid nitrogen. Curves 0, 1, 2, 3, 5, and 7 were taken following 2-Mev electron irradiation of 0, 0.44, 0.8, 1.2, 1.9 and 3.0×10^{17} electrons/cm².

²⁵ N. Sclar and E. Burstein, Phys. Rev. **98**, 1757 (1955).

²⁶ L. Bess, Phys. Rev. **105**, 1469 (1957).

Since the doping level in this diode is unknown, we refer to Esaki's work^{2,4} for a quantitative comparison.

From Fig. 2 we obtain a slope of 5.4 v^{-1} for the curve at 77°K (ignoring the hump). For this junction $N_A = 5 \times 10^{19} \text{ cm}^{-3}$, $N_D = 1.8 \times 10^{19} \text{ cm}^{-3}$. From (4),

$$W_0 = 1.15 \times 10^{-6} \text{ cm at unit voltage.}$$

This value compares favorably with the width for this doping level as indicated by Esaki's capacity measurement.

The Fermi levels as estimated in Sec. II are $\zeta_C = 0.06$ and $\zeta_V = 0.23 \text{ ev}$. For ϵ_d , a value of 0.24 ev is again used and ϵ is taken as 0.751 ev at 77°K .²⁷

When these values are used, $R = 0.61$, and substitution in Eq. (11) gives $m_e = 0.013 m$. This value may be compared to $0.02 m$ quoted by Hall for the reduced effective mass in band-to-band tunneling²³ or the transverse effective mass $m_t = 0.082$.²³

For a quantitative check with silicon diodes we refer to the data in Fig. 4. The $\log I$ vs voltage plot is for a silicon diode fabricated by alloying aluminum-boron to a silicon wafer of $1.1 \times 10^{20} \text{ cm}^{-3}$ phosphorus concentrations.

From Sec. II, we take $\zeta_C = 0.07$, $\zeta_V = 0.3 \text{ ev}$, and $\epsilon_d = 0.48$. The band gap is taken as $\epsilon = 1.17$ for 77°K ¹⁴ giving $R = 0.52$. To calculate the junction width, n_a is calculated from $\zeta_V = 0.3$, using (1) and an effective hole mass of 0.458 .¹⁴ The assumption that all acceptors are ionized then gives $N_A = 2.3 \times 10^{20} \text{ cm}^{-3}$, which is in reasonable agreement with the solubility data for boron in silicon as given by Trumbore.²⁸ This value with $N_D = 1.1 \times 10^{20} \text{ cm}^{-3}$ gives $W_0 = 4.5 \times 10^{-7} \text{ cm}$. The slope of the $\ln I$ vs V curve at 77°K , 5 v^{-1} , with the above values yields $G = 0.10$. This may be compared with the transverse effective mass for electrons in silicon of $0.19 m$.²³

Figure 6 is a replot of the recorder traces taken, following increasing levels of electron irradiation for the GaAs junction TI 10. With the exception of the upper line of run 0, the straight lines have been drawn parallel and have a slope of 6.0 v^{-1} . For computation of the effective mass through Eq. (11), the quantities

developed in Sec. II are used, namely, $N_A = 10^{19}$, $N_D = 5 \times 10^{19}$, $\zeta_C = 0.11$, $\zeta_V = 0.5$, $\epsilon_d = 0.12$, $\epsilon_d = 0.52$. For the band gap at 77°K , $\epsilon = 1.50 \text{ ev}$ is used.¹⁴ Then $R_1 = 0.81$, $R_2 = 0.54$. With a dielectric constant for GaAs of 11.1 ,¹⁴ $W_0 = 5.7 \times 10^{-7} \text{ cm}$. For the lower slope of Fig. 4, the lower defect level is appropriate and $6.0 = 5.685 \times 10^7 \times 5.7 \times 10^{-7} \times 0.54 \times G^{\frac{1}{2}}$, so $G = 0.053$. This value may be compared with 0.078 for the conduction electrons.²³

IV. MULTIPLE DEFECT LEVELS

It is apparent that more than one defect level may play an important role in a given tunnel diode. If the same effective mass is appropriate to the several defect levels, then the slopes pertinent to each defect should be proportional to the factor

$$R = \left(\frac{\epsilon - \epsilon_d + \zeta_V}{\epsilon + \zeta_V + \zeta_C} \right)^{\frac{1}{2}}.$$

More conveniently, $S_1/S_2 = R_1/R_2$. Figure 9 is a replot of the recording on sample TI 4 after 3×10^{17} electrons/cm² bombardment. Two distinct slopes of 6.0 and 8.4 v^{-1} are clearly seen, giving a ratio of 1.4 . Using the values of R_1 and R_2 computed for TI 10 gives the ratio $R_1/R_2 = 1.5$, in fair agreement.

For silicon the two levels from Sec. II are used, namely, $\epsilon_d = 0.04$ and $\epsilon_d = 0.42$. Again taking $\epsilon = 1.17$, $\zeta_C = 0.10$, $\zeta_V = 0.28 \text{ ev}$, and the ratio is $R_1/R_2 = 1.6$. Figure 10 has an initial slope of 6.9 and a final slope of 4.8 v^{-1} following 3×10^{17} electrons/cm² bombardment. The ratio is 1.44 , which is in fair agreement with 1.6 .

Two distinct slopes have not been observed in germanium diodes. Many diodes do not exhibit any straight line portion of the $\ln I$ vs V plot. This could be due to several closely spaced defect levels playing a role in the excess current.

ACKNOWLEDGMENTS

The author is indebted to H. H. Sander for obtaining the major part of the data used in this analysis, to A. G. Chynoweth, W. L. Feldman, and R. A. Logan for the opportunity to study and discuss their paper prior to publication, and to L. Esaki for permission to reproduce Figs. 2 and 4 from his work.

¹ L. Esaki, *Phys. Rev.* **108**, 1051 (1957).

² L. Esaki, *Rev. Mod. Phys.* **35**, 36 (1960).

³ E. Herman, *Proc. Inst. Radio Engrs.* **43**, 1703 (1955).

⁴ E. A. Trumbore, *Bell System Tech. J.* **39**, 205 (1960).

Effects of Phosphor Powder Dispersion in Electroluminescent Lamps

W. A. THORNTON

Research Department, Westinghouse Electric Corporation, Bloomfield, New Jersey

(Received May 27, 1960)

The statistical distribution of phosphor crystals in the solid dielectric material of a practical electroluminescent lamp influences the observed characteristics of the lamp. Calculation on the basis of a very simple model shows that maximum efficiency is favored by high phosphor concentration, fine particles, and thick phosphor layers; the slope and intercept of the usual brightness voltage plots are affected by the same variables. Measurements on electroluminescent lamps with these variations are in substantial agreement with the predictions.

INTRODUCTION

ELECTROLUMINESCENCE depends strongly, in both light emission and power absorption, upon the magnitude of the average field experienced by the luminescent material.¹ In a typical electroluminescent lamp,¹ which is normally a thin layer of phosphor-dielectric mixture sandwiched between two large area electrodes, the dispersion of phosphor powder in solid dielectric material leads to wide variation in the average field experienced by each phosphor particle. In a column along a normal to the plane parallel electrodes the proportion of phosphor may vary from point to point over the area of the lamp from zero to nearly one hundred percent. Since the dielectric constants of phosphor and embedding material are generally different, the average field experienced by each particle will depend upon the fraction of the total interelectrode distance occupied by phosphor along the normal at that particular point. Therefore, the light emission and power absorption contribution by each particle varies widely depending upon the placement of neighboring particles. These statistical effects have apparently not been considered to date.

Some effects due to this dispersion of phosphor particles in a medium of different dielectric constant have been calculated statistically using a very simple model. The results based on this model serve to explain the following experimental observations: (a) the slope and intercept, represented by V_0 and L_0 in the usual equation

$$L = L_0 \exp[-(V_0/V)^{1/2}] \quad (1)$$

relating electroluminescence light emission L to applied voltage V , were shown by Lehmann² and Goldberg³ to increase with decreasing mean particle diameter, (b) Lehmann² showed that peak efficiency increases and moves toward higher voltage with decreasing mean particle diameter, and (c) experimental data given in the present paper show that peak efficiency decreases and moves toward higher voltage with decreasing volume fraction of phosphor in the phosphor-dielectric

layer. The agreement between calculation and experiment in these three cases is obtained by using a much oversimplified model assuming identical phosphor particles, randomly dispersed at points of a cubic lattice. It appears not to be necessary to call on electrical or emissive differences among particles of different sizes to explain the experimental observations.

METHOD OF CALCULATION

In the simple model on which calculations were made, the phosphor layer is considered to be a random distribution of identical phosphor particles dispersed in a solid dielectric medium. The layer is divided into columns (Fig. 1) perpendicular to the plane parallel electrodes, each column consisting of n possible phosphor particle positions; the particles are taken to be cubes of side $1/n$, and each position in the column is completely occupied either by one phosphor particle or by the dielectric material. It is further assumed that there is no field interaction or fringe effects between adjacent columns. The probability W of finding x phosphor particles in a column of n positions, if the over-all volume fraction of phosphor in the entire layer is f , is given by Newton's relation^{4,5}

$$W = \frac{n!}{x!(n-x)!} f^x (1-f)^{n-x}. \quad (2)$$

Hence, the probability of finding a proportion x/n of phosphor in a given column depends on the gross phosphor concentration, described by parameter f , and upon the particle size relative to the lamp thickness or electrode spacing, described by parameter n . The volume fraction of dielectric material is $(1-f)$.

The probability W as a function of x/n is shown in Fig. 1 for three values of n . The volume fraction f of phosphor is taken to be 0.33, a typical value for electroluminescent lamps. Actually, nW is plotted in Fig. 1 to equalize the areas under the curves. Smooth curves are drawn merely for convenience; the probability W is, of course, not defined for other than integral values of x .

⁴ H. Margenau and G. M. Murphy, *The Mathematics of Physics and Chemistry* (D. Van Nostrand Company, New York, 1948), p. 422 *et seq.*

⁵ This relation was applied to a similar geometrical situation in a paper by R. Gerson and T. C. Marshall, *J. Appl. Phys.* **30**, 1650 (1959).

¹ G. Destriau and H. F. Ivey, *Proc. Inst. Radio Engrs.* **43**, 1911 (1955). For a general discussion of the electrical properties of electroluminescent materials, see this review paper.

² W. Lehmann, *J. Electrochem. Soc.* **105**, 585 (1958).

³ P. Goldberg, *J. Electrochem. Soc.* **106**, 34 (1959).

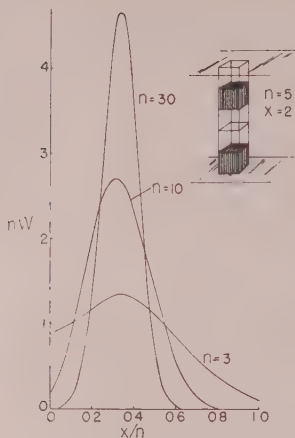


FIG. 1. The probability W of finding x phosphor particles in a column of n positions as a function of x/n for $n=3, 10, 30$. nW is plotted to equalize areas; phosphor volume fraction $f=0.33$.

It is apparent from Fig. 1 that W is more sharply defined for large n (small particle size, for example). This means that the average electric field experienced by the phosphor particles is more sharply defined for large n . For small n (large particles or thin layers), the probability is appreciable that a particular column contain either no particles, or that every position be filled by phosphor. The dependence of the probability W on f is shown in Fig. 2. Here, fW is plotted as a function of x/f to equalize areas and peak positions, and $n=10$. It is seen that the proportion of phosphor in a column is more sharply defined at high phosphor concentrations than at low. The characteristics of Figs. 1 and 2 are later shown to be of practical importance.

For large values of n ($n > 10$), Eq. (2) is inconvenient and can be approximated by Gauss' error law⁴

$$W = [2\pi n f (1-f)]^{-1/2} \exp[-(x-nf)^2/2nf(1-f)]. \quad (3)$$

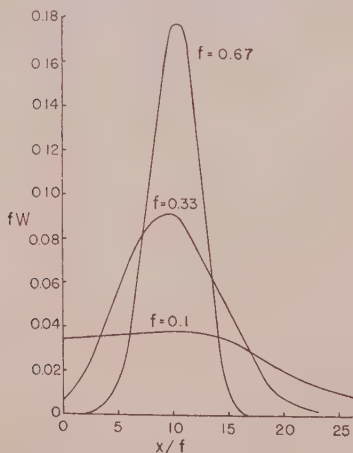


FIG. 2. The probability W of finding x phosphor particles in a column of n positions as a function of x , for phosphor volume fraction $f=0.1, 0.33, 0.67$. fW is plotted against x/f to equalize areas and peak positions; $n=10$.

At $n=10$, Eq. (3) is accurate to 10% where $W > 0.01$ and to 30% at smaller values of W . Equation (3) was used in this paper to calculate W for $n=30$ only.

Although Figs. 1 and 2 give a qualitative idea of the practical implications of phosphor powder dispersion in a real electroluminescent lamp, these effects can be more quantitatively described by further calculation. Suppose a certain voltage V is applied to the plane parallel electrodes bounding the phosphor dielectric layer under discussion. The light output per particle $l(x)$ and the power absorption per particle $p(x)$ depend only upon the number x of identical particles found in that particular column of n positions. If unit area of the lamp is taken to be a square of side equal to the electrode spacing, the light output per unit area is

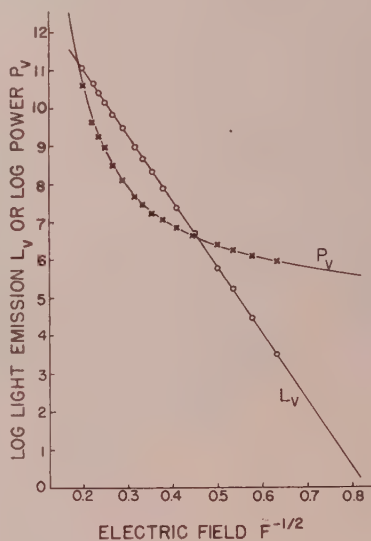


FIG. 3. Light emission L_v and power absorption P_v vs. field strength F from which the calculations were made. The plotted data are taken from an electroluminescent ZnS film and the curves extrapolated; the curves are typical of electroluminescent phosphor powders as well. Arbitrary units.

given by

$$L = n^2 \sum_{x=0}^n x W l(x), \quad (4)$$

and the power absorption per unit area by

$$P = n^2 \sum_{x=0}^n x W p(x). \quad (5)$$

Relations between L_v , the light output per unit volume of phosphor, P_v , the power absorption per unit volume of phosphor and F , the electric field in that volume, are now needed. Equation (1) is generally observed for a wide variety of electroluminescent

phosphor powders,^{2,3,6,7} single crystals,⁸ and films.⁹⁻¹¹ The P_v - F relation can be obtained from efficiency data^{2,12} which are also well known. For concreteness, the relations¹³ used in this paper are experimental curves (Fig. 3) from data on electroluminescent ZnS films since the behavior of these films is similar to that of powder phosphors, and, in addition, the films represent the ideal case $f=1$.¹⁴ The experimental curves given in Fig. 3 are reasonably extrapolated to allow calculation at voltages higher and lower than the range experimentally covered.

It remains to determine the relation between the electric field F experienced by the dispersed phosphor particles and V , x/n , and the complex dielectric constants K_p of the phosphor and K_d of the dielectric material. It is assumed that $K_p=10.0$, $K_d=3.33$, and that no power absorption takes place in the dielectric material. If in each column the voltage division between phosphor and dielectric material is dependent on their respective capacitance, then

$$\frac{V_p}{V} = \frac{(x/n)K_d}{K_p + (x/n)(K_d - K_p)} \quad (6)$$

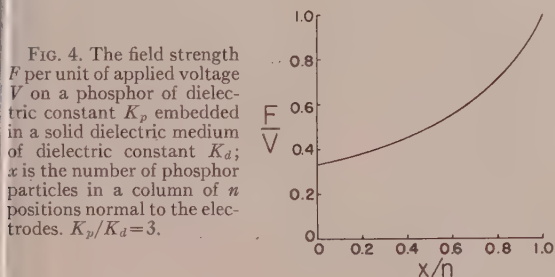


FIG. 4. The field strength F per unit of applied voltage V on a phosphor of dielectric constant K_p embedded in a solid dielectric medium of dielectric constant K_d ; x is the number of phosphor particles in a column of n positions normal to the electrodes. $K_p/K_d=3$.

where V_p is the total voltage across all of the phosphor particles present in the column. Taking the electrode spacing as unit distance,

$$F = \frac{VK_d}{K_p + (x/n)(K_d - K_p)} \quad (7)$$

The quantity F/V from Eq. (7) is plotted as a function

⁶ W. Lehmann, J. Electrochem. Soc. **107**, 20 (1960).

⁷ P. Zalm, G. Diemer, and H. A. Klasens, Philips Research Rept. **10**, 205 (1955).

⁸ G. F. Alfrey and J. B. Taylor, Proc. Phys. Soc. (London) **67**, 775 (1955).

⁹ F. A. Schwartz and R. E. Freund, Phys. Rev. **98**, 1134 (1955).

¹⁰ W. A. Thornton, J. Appl. Phys. **30**, 123 (1959).

¹¹ W. A. Thornton, Phys. Rev. **116**, 893 (1959).

¹² W. Lehmann, Illum. Eng. **51**, 684 (1956).

¹³ The analytical form of these relations is not important here. Further calculation is based entirely on the experimental curves of Fig. 3 and reference is made only to the slopes and intercepts of the approximately straight plots.

¹⁴ The thin film case corresponds to $f=n=1$ and $L=L_v$.

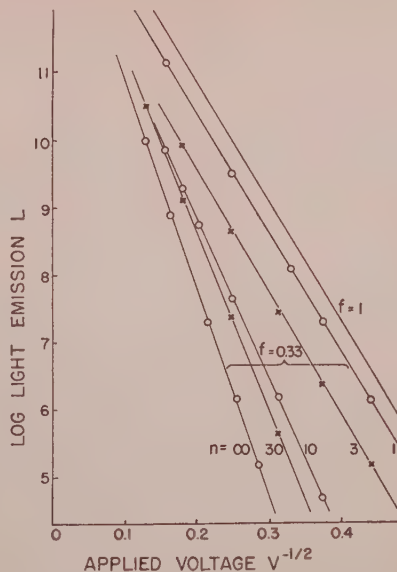


FIG. 5. The calculated dependence of light emission on voltage for various values of n ; $f=0.33$ (particle size $=1/n$).

of x/n in Fig. 4.¹⁵ Note that the electric field on the phosphor particles can vary by a factor of three in such a lamp; according to Fig. 3 this variation can cause very large differences in light emission and power absorption and, since these are not proportional, in efficiency also.

Finally, since the light output per particle $l=L_v n^{-3}$, and similarly $p=P_v n^{-3}$, Eq. (4) can be rewritten as

$$L = - \sum_{n=1}^{\infty} x W L_v \quad (8)$$

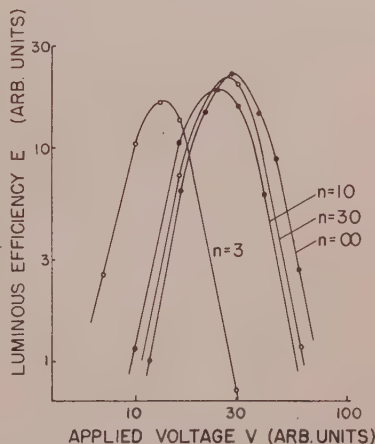


FIG. 6. The calculated dependence of efficiency on voltage for various values of n ; $f=0.33$ (particle size $=1/n$).

¹⁵ The Maxwell-Wagner formula for the field in a uniform suspension of phosphor spheres (see, for example, reference 1.) leads to a curve of the same shape as Eq. (7); it requires, in addition to spherical particles, a sparse enough distribution that no interparticle interaction occurs.

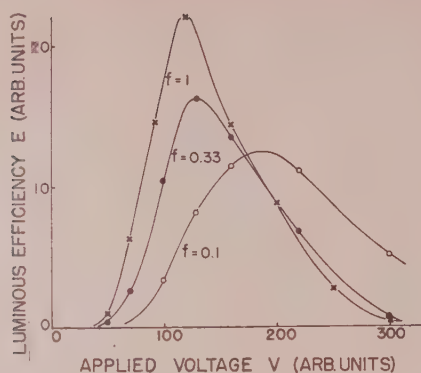


FIG. 7. The calculated dependence of efficiency on voltage for various values of phosphor volume fraction f ; $n=3$.

and the efficiency is given by

$$E = \sum_{x=1}^n xWL_v / \sum_{x=1}^n xWP_v. \quad (9)$$

The procedure for calculating L and E as functions of applied voltage V for given values of n and f is as follows. The probability W and product xW are calculated for all values of x/n from Eq. (2) or (3). For a given V , F is calculated for all values of x/n from Eq. (7); corresponding values of L_v and P_v are taken from the curves of Fig. 3. The products xWL_v and xWP_v are formed for each x/n and the summations made. This yields one point on the L vs V curve, for example.

RESULTS OF CALCULATIONS

The calculated dependence of light emission on voltage for $n=1, 3, 10, 30$, and ∞ ($f=\frac{1}{3}$) is shown in Fig. 5; n is the number of possible particle positions and so is proportional to layer thickness or inversely proportional to particle size. The calculated points are plotted and delineate essentially straight lines which increase in parameters L_0 and V_0 [Eq. (1)] with increasing n . The calculated dependence of efficiency on voltage for some values¹⁶ of n is shown in Fig. 6; the peak efficiency increases and moves toward higher voltage with increasing n . The calculated dependence of efficiency on voltage for $f=1, 0.33$ and 0.1 ($n=3$) is shown in Fig. 7; peak efficiency decreases and moves toward higher voltage with decreasing values of phosphor volume fraction f .

EXPERIMENTAL RESULTS

Phosphor-dielectric layers were made by a special technique in order to approach random spatial distri-

bution of the particles as closely as possible. Three requirements are: first, the electrode spacing should be uniform and equal in all lamps; second, all particles should remain in suspension and randomly distributed; third, the phosphor volume fraction f must be constant. Sprayed layers are difficult to make uniform in thickness and random in particle distribution since agglomeration cannot be avoided; furthermore, coarse particles tend to settle out before being deposited and f is altered. Oil dielectric cells do not maintain completely random distribution. Therefore, suspensions of several water-settled fractions, differing in mean particle diameter, of a standard green ZnS:Cu, Cl phosphor in a highly viscous epoxy resin¹⁷ were clamped between conducting glass plates, flat to a few fringes over the cell dimension, with a 0.005-in. Teflon spacer. The resin plus activator set in a few minutes. A phosphor resin weight ratio of two was used, corresponding to $f=0.5$.

The experimental dependence of light emission on voltage is shown in Fig. 8. In agreement with the calculated dependence of Fig. 5, the parameters L_0 and V_0 increase with decreasing mean particle diameter (increasing n).¹⁸ This result was also obtained experimentally by Lehmann² and Goldberg³ earlier using oil as the dielectric material, even though presumably particle dispersion was less random in their cases than here. Note that in Fig. 8 the light emission from the coarser particles is always greater than that from the finer particles; one of these lamps broke down at the highest voltage reached (500 v), so presumably the crossover region near 900 v could not have been approached.

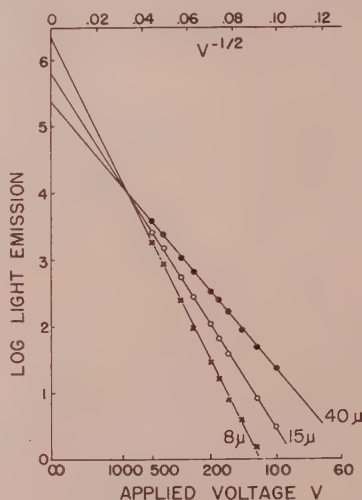


FIG. 8. The experimental dependence of light emission on voltage for phosphor fractions of various mean particle diameters. Layer thickness 0.005 in.; 400 cps.

¹⁷ C-3, Armstrong Products Company, Warsaw, Indiana.

¹⁸ No relation between the parameter n and mean particle diameter is assumed except that as one increases the other decreases.

¹⁶ The condition $n=1$ is a discontinuity (allowing no variation in field strength) and so is not a member of the family of curves in Fig. 6; the curve for $n=1$ has the same shape and peak value as that for $n=\infty$ but is positioned at lower voltage.

Although not shown in Fig. 5, the values of L_0 obtained by extrapolating the straight lines do not agree with the calculated ones. The curves of Fig. 5 must of course intercept at the same point (L_0) at $V = \infty$ since the layers of varying n contain the same volume of phosphor per unit area and the particles have been assumed to be identical in all respects except their dimensions. Calculation shows that the curves of Fig. 5 do, in fact, converge to an L_0 point about equal to that of the $n=30$ curve as extrapolated in Fig. 5; this means that the curve for $n=3$, for example, is concave upward at very high voltages. Plots for very coarse particles at very high voltage (outside the usually accessible range of voltage) therefore should be concave upward. This has been observed, as shown in Fig. 9, on a single phosphor particle fifty microns in diameter between tantalum electrodes with castor oil dielectric. The curve was run and repeated at 10 000 cps and similar curvature noted at 1000 and 100 cps. The single particle and close electrode spacing, of course, corresponds to small n , the predicted requirement. Similar voltage brightness plots for smaller single particles are either completely straight, in agreement with the calculations, or are concave downward at highest voltages (hooked) as is often the case with phosphor layers, including films.¹⁰

Due to the small area (one-half cm²) of the epoxy lamps, their impedance was too high for efficiency measurements to be made; large area lamps of the same type in which random dispersion is attempted have not yet been made. The calculated dependence of peak efficiency on n (particle size) of Fig. 6, however, is in qualitative agreement with Lehmann's data² reproduced in Fig. 10.

An experimental determination of the dependence of efficiency on voltage for various volume fractions (parameter f) of phosphor was made. These measurements were made on sprayed lamps, using polyvinyl chloride-acetate as the dielectric material, with careful

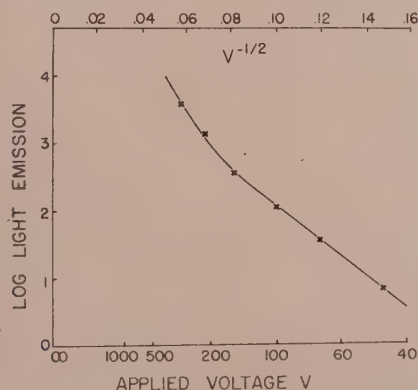


FIG. 9. The observed brightness voltage characteristic of a single coarse phosphor particle. Diameter of particle 50 μ , electrode spacing about the same, dielectric castor oil, 10 000 cps.

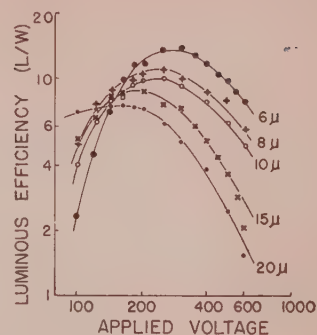


FIG. 10. The experimental dependence of efficiency on voltage for varying mean particle size. Castor oil dielectric. (Data from Lehmann.²)

attention paid to maintaining constant thickness while varying phosphor concentration. The results are shown in Fig. 11 where phosphor concentration is given in terms of phosphor-to-plastic weight ratio; approximate corresponding values of f are 0.6, 0.4, 0.25, 0.1, respectively. The calculated curves of Fig. 7 are indistinguishable from those of Fig. 11 even though power absorption in the dielectric in the practical case is expected to have some effect. The dashed curve of Fig. 11 represents data obtained with an oil dielectric cell and suggests that the "bridging"¹⁹ of phosphor particles, free to move under the influence of the applied voltage, leads to behavior characteristic of high phosphor concentration (high peak efficiency) whatever the actual phosphor volume fraction in the oil cell.

DISCUSSION

The main features of the calculated curves of Figs. 5-7 are simply explained. In Fig. 5 small n leads to relatively high brightness at low applied voltage because the probability of columns almost completely occupied by phosphor particles, ($x/n=1$, Fig. 1), is relatively high; the field strength in this phosphor is, therefore, relatively high and contributes strongly to the total light emission. This is, however, true at any voltage (although most marked at low voltage where dL/dV is greater), and therefore a hypothetical lamp of small n always will be brighter than one of large n (see Fig. 8). The curve for $n = \infty$ in Fig. 5 represents the case in which each phosphor particle experiences the same field strength since W is zero for all but $x/n=f$. This is therefore equivalent to a lamp with two layers, one a uniform phosphor layer such as a film and the other a layer of dielectric material. In fact, every electroluminescent lamp of $f=\frac{1}{2}$ would follow the $n = \infty$ curve of Fig. 5 except for the statistical probability of phosphor aggregation with the associated higher fields and thus greater emission from these aggregates; the smaller n , the greater the probability of electric field variation from the mean, and the greater the departure from the $n = \infty$ curve.

¹⁰ W. Lehmann, J. Electrochem. Soc. 103, 24 (1956).

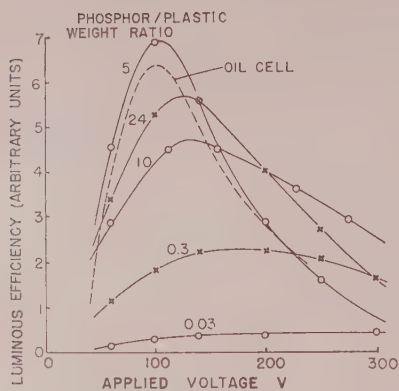


FIG. 11. The experimental dependence of efficiency on voltage for various values of phosphor plastic weight ratio. Corresponding values of phosphor volume fraction f are: 0.6, 0.4, 0.25, 0.1 and 0.01, respectively. Dashed curve: oil dielectric cell, 400 cps.

Peak efficiency is observed at the applied voltage at which the greatest percentage of the particles are experiencing the optimum electric field. This voltage is lower for small n than for large n (Fig. 6) for the reason discussed previously, that at small n proportionately more particles experience higher than average fields. Peak efficiency is higher in magnitude for large n (Fig. 6) because proportionately more particles experience the optimum electric field; the narrower the distribution in Fig. 1 the more well defined the optimum field and the higher the observed peak efficiency. Similarly, peak efficiency is higher in magnitude for large f (Fig. 7) since the distribution is narrower (Fig. 2) in that case. The voltage for peak efficiency increases for small f (Fig. 7) because the dielectric material takes a progressively larger fraction of the applied voltage. In other words, the probability of aggregation (large x/n , high field) decreases with decreasing f , as shown in Fig. 12 which is to be compared to Fig. 1. In Fig. 7 at high voltage, large f leads to lower efficiency than small f because at this voltage the electric field in the phosphor, when f is large, is too high, on the average, for maximum efficiency.

The luminous efficiency of electroluminescence, measured in lumens output per watt of input power to the lamp, has been thought to depend only on the physical characteristics of the phosphor or of the solid dielectric material. Electroluminescent phosphors have been gradually improved until, recently, efficiencies approaching 20 lu/w have been measured under ideal laboratory conditions; the highest published values of electroluminescence efficiency have been measured in a type of laboratory cell in which the dielectric is oil.² Such efficiencies are not usually achieved in practical electroluminescent lamps, partly because operating frequency and electric field strength are, in general, different from those which lead to peak efficiency; practical electroluminescent lamps are operated as near

breakdown as feasible for maximum brightness, and this voltage is often far higher than that at which peak efficiency occurs. Peak efficiencies of actual lamps (as distinguished from efficiencies measured under operating conditions) are, according to these calculations, predicted to be lower than measured peak efficiencies in laboratory cells with oil dielectric but containing the same phosphor. This discrepancy, if it exists, might be attributed entirely to power absorption in the solid dielectric material of the actual lamp. One purpose of this paper is to present evidence that such lower, observed efficiencies in practical lamps can be partly due to the statistical distribution or dispersion of the phosphor crystals in the dielectric matrix, and not to characteristics of the phosphor or dielectric.

The phosphor-dielectric layer in actual lamps differs from the ideal case on which the calculations were based in at least three ways.

(a) In the range of normal phosphor concentrations, microscopic examination immediately shows that voids and clumps ($x/n=0$ or $x/n=1$) are much more frequent than in a random distribution. This further smears out the distribution in magnitude of electric field and accentuates the behavior due to the fact that the electric field is not well defined. In commercial lamps particle size is as large as possible to achieve good maintenance²⁰ and thickness is as small as possible for maximum brightness at a given voltage. Therefore n is already small, and the voids and aggregations further reduce the observed peak efficiency.

(b) Electroluminescent phosphor powders are usually broad distributions in particle size⁶ rather than identical in dimension as assumed for simplicity in the calculations. However, since brightness and power absorption are field dependent, rather than voltage dependent, a distribution of particle diameters about a mean, as is always the case, should not greatly affect the analytical results here.

(c) Finally, it was assumed here that the idealized phosphor particles changed only in dimension, with

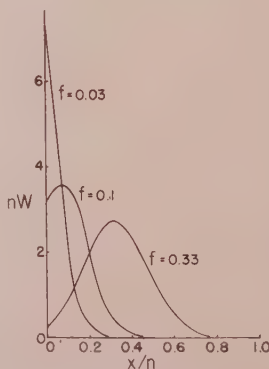


FIG. 12. The probability W of finding x phosphor particles in a column of n positions as a function of x/n for volume fraction $f=0.03, 0.1, 0.33$; $n=10$; nW is plotted to equalize areas.

²⁰ W. A. Thornton, J. Electrochem. Soc. **107**, 895 (1960).

change in n , for example, and not in any electrical or emissive properties. Coarse and fine particles from the same lot do vary somewhat in activation as shown by the fact that their emission color often changes systematically with the mean particle size of the fraction separated.²⁰

The calculations in this paper indicate, however, that it may be sufficient to consider only effects due to phosphor particle dispersion in the dielectric material

to explain variations in brightness, the parameters L_0 and V_0 , and efficiency, with particle size.

ACKNOWLEDGMENTS

I wish to thank W. Lehmann for supplying Fig. 10, R. M. Potemski for experimental assistance, and H. F. Ivey for pointing out that Newton's relation might be applicable to the problem and also for his continued interest and encouragement.

Theory and Application of a Superposition Model of Internal Friction and Creep*

J. ROSS MACDONALD

Texas Instruments Inc., Dallas 22, Texas

(Received May 15, 1961)

Energy dissipation in solids is important in both transient and steady-state measurements. The results of such measurements can be associated with a distribution of relaxation times provided the material is linear. In the present work, general relations are derived for the attenuation factor, phase factor, and specific dissipation function $1/Q$ pertaining to transmission of small amplitude stress waves in a material describable by a distribution of relaxation times. Next, a specific, physically realizable relaxation time distribution is used to obtain a creep function and to relate transient creep and frequency response measurements. Curves of $1/Q$ vs frequency are calculated with a digital computer and show a region approximately proportional to frequency at sufficiently low relative frequencies, a region of virtual frequency independence, and a final region proportional to inverse frequency at high relative frequency. The relation of the present work to other treatments of creep and internal friction is discussed, and the applicability is examined of the analytic and numeric results to creep measurements on metals and rocks, to low-frequency wave transmission in the earth, to other damping results for the earth as a whole, and to higher-frequency wave transmission and vibration results for geophysical and other solids. Good agreement between theory and experiment is found for frequency regions where adequate data are available, indicating that all the damping phenomena considered may be well described by a linear theory in the range of very small strain.

INTRODUCTION

WHEN a solid is set in motion, some of the elastic energy of the material is dissipated as heat. The various means by which such energy loss occurs are collectively known as internal friction.¹ The presence and magnitude of internal friction can be inferred from the results of two different but related kinds of experiments which involve, respectively, the transient and the steady-state response of the material. When a very small constant mechanical stress is suddenly applied to a solid, there results an "instantaneous" strain followed by a retarded deformation whose rate continuously decreases. The "instantaneous" strain, which is actually transmitted with the speed of sound in the medium,

is the usual Hooke's law linear response. The remaining response, which is termed transient creep and which occurs particularly at temperatures low compared to the melting point and at low strain amplitudes, is characteristic of viscoelastic behavior. Internal friction can also often be determined from a transient experiment in which the sample is initially set vibrating and the logarithmic decrement of its amplitude decay is determined. This method is not very convenient when a wide range of frequencies must be covered. Alternatively, energy loss occurs when a steady-state stress wave is transmitted through the sample, and the magnitude of such loss can be related to the attenuation factor of the waves.¹

The transient and steady-state responses of a system are intimately associated when the system is linear and either can be calculated when the other is known.² It is often useful, however, to make measurements of both kinds on the same material since they usually cover different time spans. For the study of materials exhibiting short relaxation times, steady-state measurements with periods less than one second are appropriate.

* A part of the present work, consisting mainly of the figures and some of the mathematical results but none of the present analysis, discussion, and interpretation was presented jointly by C. Lomnitz and the author at the 1960 Helsinki meeting of the International Geophysical Union.

¹ H. Kolsky, *Stress Waves in Solids* (Clarendon Press, Oxford, England, 1953). This reference gives a good introduction to internal friction and the various ways it can be measured. A summary of modern methods of measuring dynamic elastic properties is also given by K. W. Hillier, *Stress Wave Propagation in Materials*, edited by N. Davids (Interscience Publishers, Inc., New York, 1960), p. 183.

² J. R. Macdonald and M. K. Brachman, *Revs. Modern Phys.* **28**, 393 (1956).

On the other hand, creep measurements can extend for a week or greater and are useful when a material with long relaxation times must be investigated.

In the present work, we shall consider the interrelation of transient creep and steady-state measurements for a viscoelastic solid exhibiting a distribution of relaxation times. This distribution will be selected, in so far as possible, to make the resulting theoretical creep and wave-attenuation functions agree with experimental results. The entire treatment is based on the validity of the principle of superposition and hence on the linear behavior of the material. The theory is therefore applicable only for small strains and small wave amplitudes. Brinkman and Schwarzl³ and Knopoff and MacDonald⁴ have given nonlinear theories of energy loss in solids. Although all materials are of course nonlinear, it is reasonable to expect that at sufficiently small strains nonlinear behavior can be neglected and that only linear response need be considered. It will be shown in this work that energy dissipation in such a limiting linear system can explain considerable experimental creep and wave attenuation results, and that therefore nonlinear effects need not be invoked to describe such results.

In the next section, some possible creep functions which imply a distribution of relaxation times will be considered. Then, in the following section, general relations between transient and steady-state response functions will be presented and a specific, physically realizable creep function obtained. Finally, quantitative predictions of the theoretical work obtained from a digital computer calculation will be discussed and compared with various experimental data on solids.

THE CREEP FUNCTION

The response of a linear mechanical system to a suddenly applied stress was formulated as an empirical law by Boltzmann.⁵ The result is an instance of the real convolution⁶ or superposition integral well known⁷ to mathematicians before its use by Boltzmann. For a linear viscoelastic material subjected to a stress $\sigma(t)$ suddenly applied at $t=0$, the resulting strain is

$$\epsilon(t) = M^{-1} \left[\sigma(t) + \int_0^t \sigma(\tau) A(t-\tau) d\tau \right], \quad (1)$$

where M is the appropriate elastic modulus, and the lower limit is here given as 0— to include the effects of any impulse functions centered at $t=0$ contained

in $\sigma(t)$. This limit can be extended to $-\infty$ if desired.² The quantity $A(t)$ is a memory or rate-of-creep function and its appearance in the part of the response associated with creep shows that the over-all behavior of the material at a given time greater than zero is influenced by past states of the system. The strain resulting from a constant stress applied at $t=0$, $\sigma(t) = \sigma_0 u(t)$, is thus

$$\epsilon(t) = \sigma_0 M^{-1} [u(t) + \psi(t)], \quad (2)$$

where

$$\psi(t) \equiv \int_0^t A(x) dx \quad (3)$$

and $u(t)$ is the unit step function defined so that $u(0-) = 0$ and $u(t > 0) = 1$. The quantity $\psi(t)$ is usually called the creep function.

A number of authors^{2,8-16} have treated the relationships between such defining functions as $\psi(t)$ or $A(t)$ and other response or describing functions of the pertinent linear system. Such relations apply formally to the description of either viscoelastic or dielectric behavior. For the viscoelastic body, the useful application of theoretical results to the analysis of experimental data depends upon a felicitous choice of $\psi(t)$. Many explicit functions have been proposed, with forms of the power law¹⁷⁻¹⁹ and logarithmic law^{5,19-22} being found particularly useful. Some time ago, creep applications of the modified logarithmic law

$$\psi(t) = q \ln[1 + (t/\tau_0)], \quad (4)$$

where q and τ_0 are constant, were discussed by Lyons.²² More recently, Lomnitz²³ independently suggested this expression and showed that it could be used to describe his experimental results for creep in igneous rocks under shear stress. Unfortunately, measurements were not extended to times such that (t/τ_0) was of the order of or less than unity; thus, a complete comparison between (4) and experiment was impossible and no distinction could be made between (4) and simple $\ln t$ dependence. The latter dependence clearly cannot hold in the limit

² V. Volterra, *Ann. Ecole norm. super.* **24**, 401 (1907).

³ B. Derjaguine, *Beitr. angew. Geophys.* **4**, 452 (1934).

¹⁰ C. Zener, *Elasticity and Anelasticity of Metals* (University of Chicago Press, Chicago, Illinois, 1948).

¹¹ B. Gross, *Mathematical Structure of the Theories of Viscoelasticity* (Hermann & Cie, Paris, France, 1953).

¹² E. R. Love, *Australian J. Phys.* **9**, 1 (1956).

¹³ J. Schrama, "On the phenomenological theory of linear relaxation processes," dissertation (Leiden, 1957).

¹⁴ H. König and J. Meixner, *Math. Nachr.* **19**, 265 (1958).

¹⁵ D. R. Bland, *The Theory of Linear Viscoelasticity* (Pergamon Press, New York, 1960).

¹⁶ S. C. Hunter, *Progress in Solid Mechanics* edited by I. N. Sneddon and R. Hill (Interscience Publishers, Inc., New York, 1960), Vol. I, p. 3.

¹⁷ E. N. daC. Andrade, *Proc. Roy. Soc. (London)* **A84**, 1 (1910).

¹⁸ B. Gross, *J. Appl. Phys.* **18**, 212 (1947).

¹⁹ B. J. Rigby, *Brit. J. Appl. Phys.* **11**, 281 (1960).

²⁰ F. Phillips, *Phil. Mag.* **9**, 513 (1904).

²¹ D. T. Griggs, *J. Geol.* **47**, 225 (1939).

²² W. J. Lyons, *J. Appl. Phys.* **17**, 472 (1946).

²³ C. Lomnitz, *J. Geol.* **64**, 473 (1956).

³ H. C. Brinkman and F. Schwarzl, *Discussions Faraday Soc.* **23**, 11 (1957).

⁴ L. Knopoff and G. J. F. MacDonald, *J. Geophys. Research* **65**, 2191 (1960).

⁵ L. Boltzmann, *Pogg. Ann. Phys. Lpz.* **7**, 624 (1876); *Sitzber. K. Akad. Wiss. Wien, Math.-Naturwiss. Classe* **70**, 275 (1874).

⁶ I. I. Hirschmann and D. V. Widder, *The Convolution Transform* (Princeton University Press, Princeton, New Jersey, 1955).

⁷ M. F. Gardner and J. L. Barnes, *Transients in Linear Systems* (John Wiley & Sons, Inc., New York, 1942), pp. 364-365.

of short times. Later, Lomnitz²⁴ showed theoretically that (4) led to approximate frequency independence of the specific dissipation, or internal friction factor $1/Q$, in good agreement with many observations on the attenuation of stress waves in solids. Earlier, Bennewitz²⁵ carried out calculations of the steady-state response with a creep function of the form (4).

Jeffreys^{26,27} has recently proposed a simple generalization of (4),

$$\psi(t) = q\nu^{-1} \{1 + (t/\tau_0)\}^{\nu-1}, \quad (5)$$

where ν is a constant which will here be restricted to the range $0 \leq \nu < 1$. Some physical interpretation of the parameters of (5) will be given later. Equation (5) reduces to the logarithmic form (4) in the limit $\nu \rightarrow 0$. A creep function of the form of (5) but with $\nu \leq 0$ has also been used to describe the behavior of polymeric materials and has been derived theoretically from consideration of the microscopic processes which may occur during elongation under stress.^{19,28} The $A(t)$ function corresponding to (5) is

$$A(t) = (q/\tau_0) [1 + (t/\tau_0)]^{\nu-1}. \quad (6)$$

An expression of this form was first proposed by Voglis²⁹ to describe the dielectric analogue of viscoelastic creep—the time dependence of the charging and discharge currents of dielectrics. Further dielectric applications of equations related to (6), including the case $\nu < 0$, will be discussed elsewhere by the author.

The form (5) is a generalization of both the simple power law and the logarithmic form and has the advantage over the former that it leads to a finite rather than infinite initial rate of creep. Unfortunately, both (4) and (5) imply infinite final strain for constant applied stress. Ways of modifying (5) to achieve a form which predicts a finite final strain and thus allows it to describe a physically realizable linear solid have been discussed by the author.³⁰ The consequences of one such modification of (5) will be considered in some detail in the present work. The expression (5) is picked as a starting point both because of its considerable generality and because, as will be shown, its physically realizable modification can explain an appreciable amount of transient and steady-state data.

SYSTEM ANALYSIS

In this section we shall present the equations which connect a given creep function with other functions and observables of the described system. In particular, general relationships will be derived between the phase and attenuation factors of a stress wave in a solid and the sinusoidal energy storage and loss factors of the material. Then, Eq. (5) will be modified to make it apply to a physically realizable linear system, and pertinent measurable quantities will be derived and evaluated.

Equation (1) shows that $A(t)$ is the impulse response of $\epsilon(t)$ for the creeping part of the system, since if $\sigma(t)$ is taken as $\sigma_1 \delta(t)$, where $\delta(t)$ is the Dirac delta function, (1) leads to

$$\epsilon(t) = (\sigma_1/M) [\delta(t) + A(t)]. \quad (7)$$

On differentiating (1), one obtains

$$\frac{d\epsilon}{dt} = \frac{1}{M} \left[\frac{d\sigma}{dt} + \sigma(0-)A(t) + \int_{0-}^t \frac{d\sigma(\tau)}{d\tau} A(t-\tau) d\tau \right]. \quad (8)$$

This equation indicates that $A(t)$ is also the creep contribution to the step-function response of $d\epsilon/dt$; for if $\sigma(t) = \sigma_0 u_0(t)$, then

$$d\epsilon/dt = (\sigma_0/M) [\delta(t) + A(t)]. \quad (9)$$

In both (7) and (9), the $\delta(t)$ term represents the elastic or Hookean part of the response and the $A(t)$ term the viscoelastic part which is associated with creep.

If now a sinusoidally varying stress is applied to the system, the work per unit volume done in a cycle of period t_0 is

$$\Delta W = \int_0^{t_0} \sigma(t) \frac{d\epsilon(t)}{dt} dt. \quad (10)$$

Equations (8) and (10) now allow us to identify $A(t) = d\psi/dt$ with the indicial admittance² of the system, and we shall use the $A(t)$ and $\psi(t)$ notation and the notation of reference 2 hereafter.

The Laplace transform of $A(t)$ defines the network function

$$Q(p) \equiv \mathcal{L}[A(t)] = \int_{0-}^{\infty} A(t) e^{-pt} dt, \quad (11)$$

where p is a complex frequency variable. For $A(t)$ functions without singularities at the origin, $Q(0) = \psi(\infty)$, where $(\sigma_0/M)\psi(\infty)$ is the final strain arising from creep when a step function of stress is applied at $t=0$. For sinusoidal excitation of the form $\sigma(t) = \sigma_0 e^{i\omega t}$, the real part of the complex frequency variable p may be taken arbitrarily small and the network function $Q(p)$ (not to be confused with the quality factor appearing in the specific dissipation $1/Q$) may be separated into real and imaginary parts,

$$Q(p) \rightarrow Q(i\omega) \equiv J(\omega) - iH(\omega). \quad (12)$$

²⁴ C. Lomnitz, J. Appl. Phys. **28**, 201 (1957). The square-root signs in Eqs. (27), (28), (33), and (36) are incorrect and should be eliminated. Their elimination makes only a small difference in the $1/Qq$ curves shown, however. This error is corrected in the present work.

²⁵ K. Bennewitz, Phys. Z. **25**, 417 (1924).

²⁶ H. Jeffreys, Geophys. J. **1**, 92 (1958).

²⁷ H. Jeffreys, Monthly Notices Roy. Astron. Soc. **118**, 14 (1958).

²⁸ H. Burte and G. Halsey, Textile Research J. **17**, 465 (1947).

²⁹ G. M. Voglis, Z. Phys. **109**, 52 (1938).

³⁰ J. R. Macdonald, J. Appl. Phys. **30**, 453 (1959). In this reference the present $\psi(t)$ was denoted $\phi(t)$. The notation has been changed in the present work to agree with that of the majority of recent authors on viscoelastic relations.

The dynamic or complex compliance relating $\epsilon(i\omega t)$ and $\sigma(i\omega t)$ is then $M^{-1}[1+Q(i\omega)]$.

For sinusoidal applied stress, we may follow the procedure of Collins and Lee³¹ to obtain the following one-dimensional equation for displacement $U(x,t)$ for plane waves incident on an isotropic material describable by superposition,

$$V_e^2 \frac{\partial^2 U}{\partial x^2} = \frac{\partial^2 U}{\partial t^2} + \frac{\partial^2 U}{\partial t^2} \star A, \quad (13)$$

where the star denotes the convolution transform,^{2,6,7} the relations $\epsilon = \partial U / \partial x$, Eq. (1), and $\partial \sigma / \partial x = \rho \partial^2 U / \partial t^2$ have been used; ρ is the material density, and $V_e = (M/\rho)^{1/2}$ is the elastic (zero dissipation) phase velocity.

On taking the Laplace transform of (13) with respect to t , one finds

$$\frac{d^2 u}{dx^2} = \frac{p^2 [1+Q(p)] u}{V_e^2} \equiv \gamma^2(p) u, \quad (14)$$

where $u(x) = \mathcal{L}[U(x,t)]$. For given initial conditions and a physically realizable form of $Q(p)$, Eq. (13) can, in principle, be solved for $U(x,t)$. Here, we are primarily interested in the x dependence of the plane wave in the material. From (14), this dependence for decaying waves will be of the form

$$u(x) = u_0 e^{-\gamma x} \equiv u_0 e^{-ikx} \equiv u_0 e^{-(\alpha + i\beta)x}, \quad (15)$$

where k is the wave number and $\gamma(i\omega) = \alpha + i\beta$ is the transmission factor. Here α is the attenuation factor, and the phase factor is $\beta = \omega/V$, where V is the phase velocity.

Equations (12) and (14) lead to

$$\alpha(\omega) + i\beta(\omega) = (i\omega/V_e) [1+J(\omega) - iH(\omega)]^{1/2}. \quad (16)$$

On separating real and imaginary parts, one finds the general relations³²

$$\alpha^2 = \frac{1}{2} \left(\frac{\omega}{V_e} \right)^2 [1+J(\omega)] \left\{ \left[1 + \left(\frac{H(\omega)}{1+J(\omega)} \right)^2 \right]^{1/2} - 1 \right\}, \quad (17)$$

$$\beta^2 = \frac{1}{2} \left(\frac{\omega}{V_e} \right)^2 [1+J(\omega)] \left\{ \left[1 + \left(\frac{H(\omega)}{1+J(\omega)} \right)^2 \right]^{1/2} + 1 \right\}. \quad (18)$$

In the zero dissipation case, $J(\omega)$ and $H(\omega)$ are zero, and (18) yields $\beta = \omega/V_e$, the correct result for this case. Note that Eq. (18), together with the definition of β , allows one to calculate the phase velocity V when creep and loss are present and described by the functions $J(\omega)$ and $H(\omega)$.

Either by analogy with the dielectric case or by

using Eqs. (8) and (10) directly, one can show³³ that the energy dissipation per cycle in the system for sinusoidal driving stress is proportional to $H(\omega)$ and the maximum stored energy is similarly proportional to $[1+J(\omega)]$. Since the specific dissipation factor is the ratio of energy dissipated in a cycle to the maximum energy stored during a cycle, it may be written as

$$1/Q \equiv H(\omega)/[1+J(\omega)], \quad (19)$$

allowing (17) and (18) to be rewritten in terms of $J(\omega)$ and $(1/Q)^2$. Then these equations may be combined to yield the exact result

$$\frac{1}{Q} = \frac{2\alpha/\beta}{1 - (\alpha/\beta)^2}, \quad (20)$$

which reduces to the usual approximate form, $1/Q \cong 2\alpha/\beta$, in the small-dissipation case. Note that $1/Q$ is independent of stress amplitude as expected for a linear system.

When the functional form of $\psi(t)$ or $A(t)$ is known, one can obtain $J(\omega)$ and $H(\omega)$ by carrying out Fourier cosine and sine transforms² of $A(t)$. In order, however, to obtain equations which are most convenient for computation and which represent a physically realizable system, we shall work with a distribution of relaxation times function $G_1(\tau)$. Actually, this function here describes a distribution of retardation times,^{11,13,32} but this distinction, a matter of nomenclature, will not be stressed herein. In the present case, it will prove convenient to use the variable $z \equiv \tau_0/\tau$, where τ_0 is a fixed relaxation time such as that occurring in Eq. (5). When $G(z) \equiv G_1(\tau)$ is known, the following quantities may be calculated from² it²:

$$Q(p) = \tau_0 \int_0^\infty \frac{z^{-1} G(z) dz}{z + (p\tau_0)}, \quad (21)$$

$$J(W) = \tau_0 \int_0^\infty \frac{G(z) dz}{z^2 + W^2}, \quad (22)$$

$$H(W) = W\tau_0 \int_0^\infty \frac{z^{-1} G(z) dz}{z^2 + W^2}, \quad (23)$$

$$A(T) = \int_0^\infty z^{-1} G(z) e^{-Tz} dz, \quad (24)$$

$$\begin{aligned} \psi(T) &= \tau_0 \int_0^T A(x) dx \\ &= \tau_0 \int_0^T \int_0^\infty z^{-1} G(z) e^{-xz} dz dx \\ &= \tau_0 \int_0^\infty z^{-2} G(z) \{1 - e^{-Tz}\} dz, \end{aligned} \quad (25)$$

³³ B. Gross, J. Appl. Phys. 19, 257 (1947).

³¹ F. Collins and C. C. Lee, Geophysics 21, 16 (1956).

³² Some time after the derivation of (17) and (18) in 1958 it was found that equivalent expressions had been published by T. Alfrey, Jr. and E. F. Gurnee, *Rheology*, edited by F. R. Eirich (Academic Press, Inc., New York, 1956), Vol. 1, p. 387.

on interchanging the order of integration in (25) and integrating with respect to x . In these equations, $W \equiv \omega\tau_0$ and $T \equiv t/\tau_0$. To avoid introducing new symbols, we have not distinguished between such functions as $J(\omega) \equiv J(W/\tau_0)$ and $J(W)$ in Eqs. (22)–(25) and throughout the remainder of the paper. If $A(T)$ is known, $G(z)$ itself can be readily obtained on inversion of (24), yielding

$$z^{-1}G(z) = \mathcal{L}^{-1}[A(T)], \quad (26)$$

where \mathcal{L}^{-1} is the inverse Laplace transform operator, here involving the variable T instead of the usual p .

The $A(T)$ function corresponding to Eq. 6 is

$$A(T) = q\tau_0^{-1}[1+T]^{-\nu-1}. \quad (27)$$

The associated $G(z)$ is, from (26),

$$G(z) = (q/\tau_0)z^{1-\nu}e^{-a(z/a)^2}/\Gamma(1-\nu). \quad (28)$$

An equivalent form was first given by Voglis.²⁹ This result, in turn, leads to

$$Q(p) = q(p\tau_0)^{-\nu}e^{p\tau_0}\Gamma(\nu, p\tau_0), \quad (\nu < 1), \quad (29)$$

which involves the incomplete gamma function,³⁴ a fact first mentioned by Jeffreys.²⁷ Equations (22) and (23) yield

$$J(W) = \frac{q}{\Gamma(1-\nu)} \int_0^\infty \frac{z^{1-\nu}e^{-z}dz}{z^2+W^2}, \quad (30)$$

$$H(W) = \frac{qW}{\Gamma(1-\nu)} \int_0^\infty \frac{z^{-\nu}e^{-z}dz}{z^2+W^2}. \quad (31)$$

The last two integrals may be expressed in terms of Lommel functions of a single variable,³⁵

$$J(W) = q|W|^{1-\nu}(1-\nu)S_{\nu-1,1}(|W|), \quad (30')$$

$$H(W) = q|W|^{1-\nu}(\text{sgn} W)S_{\nu-1,1}(|W|), \quad (31')$$

but these functions are not sufficiently well tabulated to be useful over the entire ranges of W and ν of interest. For large W , they lead to $J(W) \rightarrow q(1-\nu)/W^2$ and $H(W) \rightarrow q/W$.

A more important difficulty is that the $G_1(\tau)$ corresponding to (28) cannot be normalized when $\nu \geq 0$. It is easy to prove that

$$J(0) = Q(0) = \psi(\infty) = \int_0^\infty G_1(\tau)d\tau, \quad (32)$$

but (30) shows that $J(0) = \infty$, consistent with $\psi(\infty) = \infty$ from (5). This failure of normalization means that (27) and (28) do not describe a physically realizable relaxation system. In fact, $\psi(\infty) = \infty$ implies an infinite

number or concentration of relaxation times, an impossible requirement for a finite piece of matter.

In previous work,³⁰ various modifications of $G_1(\tau)$ or $A(t)$ were suggested which would lead to a physically realizable system without appreciable alteration of $\psi(t)$ in the main region of times usually accessible to observation. The lack of convergence of (32) in the present case arises from too slow a decay of the density of relaxation times at long τ 's or short z values. As discussed previously, normalization can be achieved if an increase in the decay rate of $G_1(\tau)$ is made for long τ 's exceeding a specific value which may be called τ_∞ . Such an increase will result in a smaller density of relaxation times for $\tau > \tau_\infty$ than predicted by (28) and can lead to finite final strain. Dealing again with the z variable, convergence is assured if we take, for example,

$$\left. \begin{aligned} G(z) &= (q/\tau_0)a^{1-\nu}e^{-a(z/a)^2}/\Gamma(1-\nu), & 0 \leq z \leq a, \\ G(z) &= (q/\tau_0)z^{1-\nu}e^{-z}/\Gamma(1-\nu), & z \geq a, \end{aligned} \right\} \quad (33)$$

where $a \equiv \tau_0/\tau_\infty$ and will usually be very small compared to unity. For $z \leq a$, the initial slope of $G(z)$ on a log-log plot is two instead of the value $(1-\nu)$ which follows from (28). Any value greater than one could have been used to ensure convergence of (32). Were experimental creep data available for such long times that the actual distribution of very long relaxation times could be inferred, a different slope than the value here used or a different form of the distribution function in this region might prove preferable. One possibility would be to set $G(z) = 0$ for $z \leq a$. In the absence of such data, the present initial slope of two is a reasonable choice. Other alternatives will be discussed in a later paper dealing with dielectric phenomena.

On substituting Eq. (33) in (24), one can obtain the modified rate-of-creep function,

$$A(T) = \frac{q}{\tau_0\Gamma(1-\nu)} \left[\frac{\Gamma(1-\nu, a+aT)}{(1+T)^{1-\nu}} + a^{1-\nu}e^{-a(aT)^{-2}} \{1 - (1+aT)e^{-aT}\} \right]. \quad (34)$$

When $a \ll 1$, (34) reduces to (27) to good approximation as long as $aT \ll 1$.

It is easiest to obtain $\psi(T)$ from (33) and (25), yielding

$$\psi(T) = -\frac{q}{\Gamma(1-\nu)} \left[\Gamma(-\nu, a) - \frac{\Gamma(-\nu, a+aT)}{(1+T)^\nu} - a^{-\nu}e^{-a} \{1 + (aT)^{-1}(1-e^{-aT})\} \right]. \quad (35)$$

From this expression it follows that $\psi(0) = 0$ as it should and that

$$\psi(\infty) = -\frac{q}{\Gamma(1-\nu)} [\Gamma(-\nu, a) + a^{-\nu}e^{-a}]. \quad (36)$$

³⁴ A. Erdélyi, W. Magnus, F. Oberhettinger, and F. G. Tricomi, *Higher Transcendental Functions* (McGraw-Hill Book Company, Inc., New York, 1953), Vol. 2, pp. 133–143.

³⁵ G. N. Watson, *Theory of Bessel Functions* (Cambridge University Press, New York, 1944), 2nd edition, pp. 345–352.

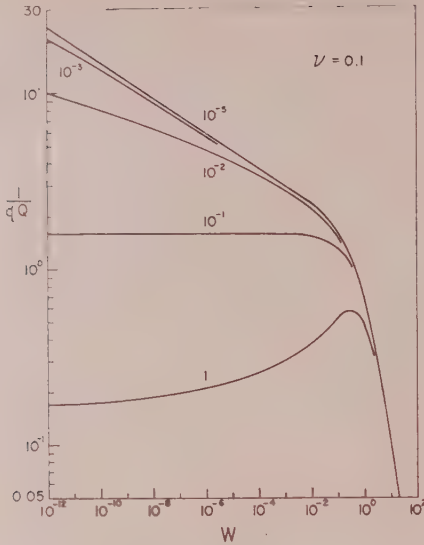


FIG. 1. $1/qQ$ vs normalized frequency W for $\nu=0.1$, $a=0$, and various q values.

Thus, the final strain is finite and positive for $a>0$ as it must be for final mechanical stability. For $a\ll 1$, series expansion of the incomplete gamma function leads to

$$\psi(\infty) \cong \begin{cases} q(1-\gamma-\ln a), & \nu=0, \\ -\frac{q}{\Gamma(1-\nu)} \left[a^{-\nu} \left(1+\nu^{-1} + \frac{a}{1-\nu} \right) - \frac{\Gamma(1-\nu)}{\nu} \right], & 0<\nu<1, \end{cases} \quad (37)$$

where γ is Euler's constant. In the earlier note³⁰ some of the terms appearing in (37) were inadvertently omitted.

The $J(W)$ and $H(W)$ functions corresponding to (34) are

$$J(W) = \frac{q}{\Gamma(1-\nu)} \left[a^{-\nu} e^{-a} \left\{ 1 - \frac{|W|}{|a|} \tan^{-1} \frac{|a|}{|W|} \right\} + \int_a^\infty \frac{z^{1-\nu} e^{-z} dz}{z^2 + W^2} \right], \quad (38)$$

$$H(W) = \frac{q}{\Gamma(1-\nu)} \left[a^{-\nu} e^{-a} (W/a) \ln \{ 1 + (a/W)^2 \}^{\frac{1}{2}} + W \int_a^\infty \frac{z^{-\nu} e^{-z} dz}{z^2 + W^2} \right]. \quad (39)$$

These equations are in a form appropriate for computation with a digital computer and may be used in (19) to yield the dependence of $1/Q$ on W .

When $a \rightarrow 0$, Eqs. (38) and (39) reduce to (30) and (31). In addition, the main contribution to $J(W)$ and

$H(W)$ arises from the integral terms when $100a < W$; the other terms are important when W is of the same order of magnitude or smaller than a . One principal region of interest of W will be $W \ll 1$. For $a \ll W \ll 1$, the main contributions to the integrals in (38) and (39) will occur for z near W , and we can thus set e^{-z} to unity and a to zero in this case to good approximation. The resulting integrals may be treated as Mellin transforms, leading to

$$\left. \begin{aligned} J(W) &\cong q\Gamma(\nu) \cos(\pi\nu/2) W^{-\nu}, & 0 < \nu < 2, \\ H(W) &\cong q\Gamma(\nu) \sin(\pi\nu/2) W^{-\nu}, & -1 < \nu < 1. \end{aligned} \right\} \quad (40)$$

Two cases must now be introduced depending on the magnitude of $J(W)$, which of course depends on $\psi(\infty)$ through (36) as well as on W and ν . Equations (19) and (40) lead to

$$\left. \begin{aligned} 1/Q &\cong H(W) \cong q\Gamma(\nu) \sin(\pi\nu/2) W^{-\nu}, & (J(W) \ll 1), \\ & & 0 < \nu < 1, \\ 1/Q &\cong H(W) \cong J(W) \cong \tan(\pi\nu/2), & (J(W) \gg 1). \end{aligned} \right\} \quad (41)$$

Note that a $1/Q$ much less than unity, necessary for agreement with experiment, is possible with $J(W) \ll 1$ for any value of ν in the range $0 < \nu < 1$ but that $1/Q \ll 1$ requires $\nu \ll 1$ when $J(W) \gg 1$. Whenever $\nu \ll 1$, (41) shows that $1/Q$ will be either completely frequency independent or virtually so.

In the singular case $\nu=0$, one can obtain approximate values of $J(W)$ and $H(W)$ when $a \ll W$ by setting $a=0$ in (38) and (39) and treating the integrals as Laplace

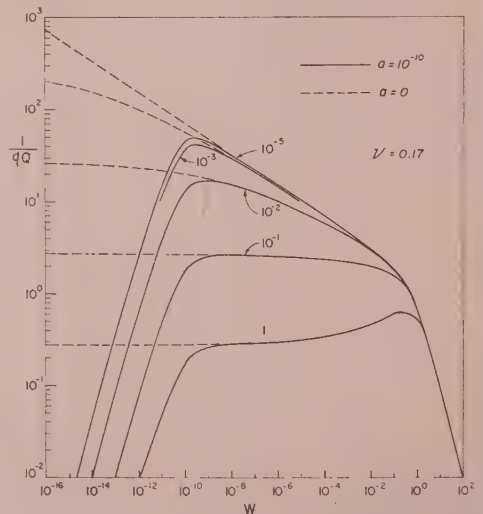


FIG. 2. $1/qQ$ vs normalized frequency W for $\nu=0.17$, $a=10^{-10}$ and zero, and various q values.

transforms. The results of such a procedure are^{2,34}

$$\left. \begin{aligned} J(W) &\cong q[\cos Wci|W| - \sin|W|si|W|], \\ H(W) &\cong -q \operatorname{sgn} W[\sin|W|ci|W| + \cos Wsi|W|]. \end{aligned} \right\} \nu=0, \quad (42)$$

When $W \ll 1$, these results become, approximately,

$$\left. \begin{aligned} J(W) &\cong q[\tfrac{1}{2}\pi|W| - \gamma - \ln|W|], \\ H(W) &\cong q \operatorname{sgn} W[\tfrac{1}{2}\pi + |W|\{\gamma + \ln|W|\}]. \end{aligned} \right\} \begin{aligned} a \ll W \ll 1, \\ \nu=0, \end{aligned} \quad (43)$$

$H(W)$ will usually dominate in the expression for $1/Q$ in the present case and will eventually lead to a slow decrease in $1/Q$ as W decreases.²⁴

Values of the quantity $1/Qq$ versus W have been calculated from (38) and (39) with a digital computer for various values of a , ν , and q . Some of the results of such calculations are presented in Figs. 1-4. Those figures which do not have a value of a shown on them were computed with $a \ll W$, equivalent to $a=0$. The parameters shown on the curves of Figs. 1-3 are values of q , while those shown on Fig. 4 are ν values. In Fig. 2, the effect of taking $a=10^{-10}$ has been shown and compared with the results obtained with $a \ll W$ ($a=0$). In general, the curves will begin their left-hand decays for W values near $W=a$, as illustrated in Fig. 2. Since this decaying region is generally far below the low-frequency region accessible to observation, only a single instance of such decay has been shown.

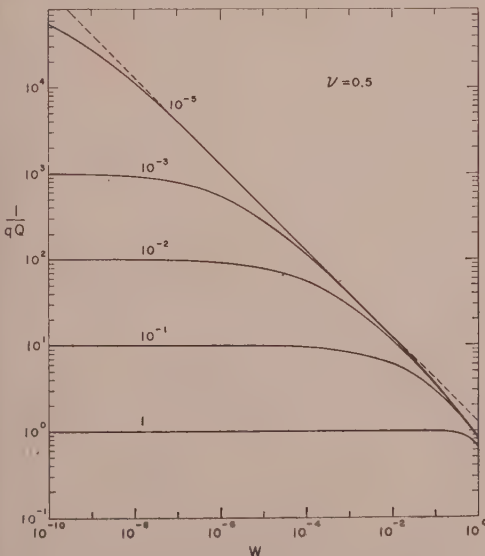


FIG. 3. $1/qQ$ vs normalized frequency W for $\nu=0.5$, $a=0$, and various q values.

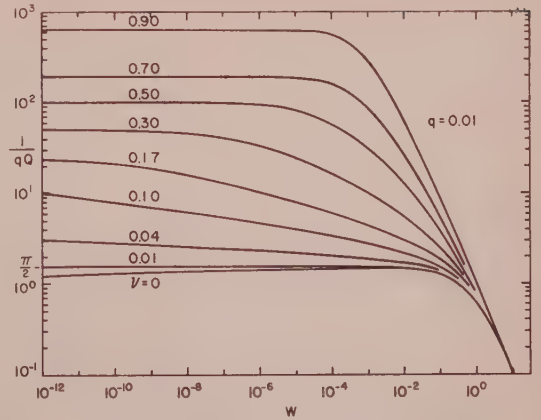


FIG. 4. $1/qQ$ vs normalized frequency W for various ν values, $a=0$, and $q=0.01$.

The level regions where $1/Qq$ is independent of frequency should be especially noted in Figs. 1-4. The values of $1/Qq$ in these regions are consistent with the predictions of Eq. (41) when pertinent. The attenuation and phase factors which follow from (40) when $(1/Q)^2 \ll 1$ and $\nu > 0$ are approximately

$$\left. \begin{aligned} \alpha &\cong q\Gamma(\nu) \sin(\pi\nu/2) W^{1-\nu}/2V_e\tau_0, \\ \beta &\cong W/V_e\tau_0, \end{aligned} \right\} \begin{aligned} 0 < \nu < 1, \\ a \ll W \ll 1, \end{aligned} \quad (44)$$

for $J(W) \ll 1$, and

$$\left. \begin{aligned} \alpha &\cong [q\Gamma(\nu) \sin(\pi\nu/2) \tan(\pi\nu/2)]^{1/2} W^{1-\nu/2}/2V_e\tau_0, \\ \beta &\cong [q\Gamma(\nu) \cos(\pi\nu/2)]^{1/2} W^{1-\nu/2}/V_e\tau_0, \end{aligned} \right\} \begin{aligned} 0 < \nu < 1, \\ a \ll W \ll 1, \end{aligned} \quad (45)$$

for $J(W) \gg 1$. Since $\nu \ll 1$ is the only condition which results in regions where $1/Q$ is both frequency independent and much less than unity, the usual experimental results, both (44) and (45) show that α will be closely proportional to frequency in the constant $1/Q$ region of interest.

When $a \ll 1 \ll W$ and $0 \leq \nu < 1$, expansion of the Lommel-function relations (30') and (31') show that for $(1/Q)^2 \ll 1$,

$$\left. \begin{aligned} 1/Q &\cong q/W, \\ \alpha &\cong W/2\tau_0 V_e Q = q/2\tau_0 V_e, \\ \beta &\cong W/\tau_0 V_e. \end{aligned} \right\} \begin{aligned} 0 \leq \nu < 1, \\ a \ll 1 \ll W, \end{aligned} \quad (46)$$

In this region where $1/Q$ decreases as W^{-1} , the attenuation factor is frequency independent and determined by the properties q , τ_0 , and V_e of the material in question. The frequency dependence of $1/Q$ in the region $W \leq a$

depends somewhat on details of the distribution of relaxation times for $\tau \geq \tau_\infty$. For the present distribution function, $1/Q$ is approximately proportional to W for $W \ll a$ and $(1/Q)^2 \ll 1$.

DISCUSSION

In the following discussion, we shall consider various data to which the present results may apply and shall present a brief summary of work by various authors which is pertinent to the microscopic interpretation of the parameters q , ν , and τ_0 . In order to establish firmly the applicability of the present distribution-of-relaxation-times model to the analysis of experimental data, it is necessary to have available either $1/Q$ vs frequency measurements in a range that extends from $W \sim 10$ down to perhaps 10^{-5} or less or to have small-strain creep data in the range of times near τ_0 . Data of either type will allow τ_0 to be quite accurately determined if the present results are applicable and should permit reasonable estimates to be made of q and ν as well.

In the usual wave transmission measurements of $1/Q$, the maximum strains produced in the material by a stress wave are of the order of 10^{-5} or less. The specific dissipation factor $1/Q$ is usually found to be independent of strain amplitude in this range for polycrystalline metals³⁶ and the response of the material may be considered linear. In some metallic single crystals,³⁷ however, linearity is not reached until the strain amplitude is less than 10^{-7} . On the other hand, most creep measurements involve maximum strains which considerably exceed 10^{-5} . The present theory can, therefore, only be applied to creep experiments in the range of strains for which it has been established that linear response is obtained. As Eq. (2) indicates, this requires that the total strain at a given time after the application of a constant stress σ_0 be proportional to this stress. Furthermore, direct comparison between $1/Q$ results obtained from wave transmission measurements and those obtained for the same material by the application of linear analysis of the present type to creep experiments should only be made if it is certain that the linear range of strains is not exceeded in either type of measurement.

Creep measurements are usually made with either tensile or shear stress applied, while a large number of different kinds of waves such as Rayleigh, shear, and compressional waves may be produced by earthquakes or used for internal friction measurements in solids. Ideally, distinctions should be made between these different phenomena since they will each have specific $1/Q$ functions associated with them.³⁸ It would obviously be wrong to compare directly $1/Q$ values derived from creep measurements under shear with those obtained

from measurements on the same material using compressional waves.

Creep and Internal Friction

Because of the restriction to the linear stress-strain region, viscous or steady-state creep³⁷ is excluded from present consideration. Even in measurements of transient creep it appears that the linear stress-strain region is often exceeded. For generality, some transient creep results will be mentioned herein, however, for which no test of linearity was made and the linear region may be exceeded. When $(t/\tau_0) \gg 1$ and logarithmic time response of creep is found, Eqs. (6) and (9) may be simplified to show that $(d\epsilon/dt)$ should be a linear function of the applied stress σ_0 . Lomnitz²³ has indeed found such linearity for at least the early part of his creep tests on rocks under shear stress. We may thus be assured that the response of the materials was linear over at least part of his total strain range, which extended from about 3×10^{-6} to about 1.5×10^{-4} rad.

Another restriction on creep in the linear region is that it be recoverable or reversible. On removal of the applied stress, the material should creep back toward its original shape, reaching it in the limit of long times. Lomnitz²³ measured such recovery, and it appears likely from his results that most or all of the strain was reversible. Kê³⁹ has carried out measurements on internal friction and creep in polycrystalline aluminum and finds that the results are mutually consistent, the creep is recoverable, and the material behaves as a viscoelastic solid. He interprets his results on the basis of grain boundary slip and keeps the total shear strain in creep less than 2×10^{-5} , essentially within the range that Mason³⁶ found the internal friction of polycrystalline aluminum to be amplitude independent.

Two review articles^{37,40} and a book⁴¹ have recently appeared which discuss transient creep in metals in some detail. It appears, particularly from the work of Wyatt,⁴² that logarithmic creep predominates for polycrystalline metals at relatively low temperatures while Andrade power-law creep,¹⁷ described by $\epsilon(t) \propto t^{\frac{1}{2}}$, yields a better fit to the data at higher temperatures and larger strains. In the present analysis, the basic expression for $\psi(t)$ given in (5) or that in (35) grades almost continuously from the logarithmic form for $\nu=0$ to the Andrade form for $\nu=\frac{1}{2}$. Note, however, that $\nu=\frac{1}{2}$ does not yield exactly the Andrade power law function since the latter predicts an infinite initial rate of creep while (9) and (34) lead to $\sigma_0 q/M\tau_0$ for the initial rate. It is well known that creep increases rapidly as the temperature is raised, and insofar as a generalized power law can describe the creep results on

³⁹ T. S. Kê, *Phys. Rev.* **71**, 533 (1947).

⁴⁰ A. H. Sully, *Progress in Metal Physics*, edited by B. Chalmers and R. King (Pergamon Press, New York, 1956), Vol. 6, p. 135.

⁴¹ H. G. Van Bueren, *Imperfections in Crystals* (North-Holland Publishing Company, Amsterdam, 1960).

⁴² O. Wyatt, *Proc. Phys. Soc. (London)* **B66**, 459 (1953).

³⁶ W. P. Mason, *J. Acoust. Soc. Am.* **28**, 1197 (1956).

³⁷ J. Fleeman and G. J. Dienes, *Rheology*, edited by F. R. Eirich (Academic Press, Inc., New York, 1956), Vol. 1, p. 201.

³⁸ J. R. Macdonald, *Geophys. J.* **2**, 132 (1959).

metals, it appears that ν must be taken temperature dependent, increasing with temperature from a value near or equal to zero which is appropriate at temperatures low compared to the melting point of the material.

The results of Wyatt⁴² indicate that in the usual range of temperatures the quantity here denoted $\sigma_0 q/M$ is approximately proportional to absolute temperature. Transient creep still appears at temperatures near absolute zero, however, and the absence of much temperature dependence of q/M in this range indicates that the observed creep is not associated with a thermally activated process.^{43,44} Glen⁴³ has suggested that the actual process involves quantum mechanical tunneling of dislocations through energy barriers which impede their motion and Mott⁴⁵ has given this suggestion a theoretical treatment.

Thus far, although it has been shown that experimental creep results for the linear region of strains may be associated with a distribution of relaxation times (actually retardation times), nothing has been said about microscopic processes which might lead to such a distribution. Because of the complexity of the effects observed, only a qualitative discussion is warranted at this time. Since some discussion of this matter for rubbers and polymers has been given,^{19,46} the present discussion will be restricted to other materials such as metals and rocks.

Although the results of steady-state internal friction measurements and creep experiments on the same material at the same temperature should be interrelated in the linear range as shown herein and as found experimentally by Kê,⁴⁹ separate theories of internal friction and transient creep have been developed in the last few years. This is at least in part because the creep theories are usually intended to apply at higher strains than the theories of internal friction. In the range to which the present results apply, the same time-independent distribution-of-relaxation-times function should be involved in both effects.

All creep theories which have been applied in the temperature range appreciably above absolute zero where tunneling effects are apparently no longer of importance have made use of Becker's⁴⁷ idea that thermal fluctuations are necessary to produce flow.⁴⁸ The widespread applicability of the logarithmic and power laws of creep to such diverse materials as fibers, polymers, metals, and rocks suggests, as Cottrell⁴⁸ has pointed out, that there are general features involved in creep common to all or most solids. A number of thermal activation theories of creep which include the

combined action of stress and thermal vibrations have been proposed.^{19,28,42,48-53} These theories generally involve energy barriers separating distinct states of the system and transitions between such states of such entities as molecules, molecular groups, flow units, and dislocations or dislocation loops. Several of these creep theories lead to simple or modified logarithmic or power laws.

The dislocation model of internal friction due to Koehler⁵⁴ and Granato and Lücke^{55,56} treats viscous damping of dislocation lengths or loops which are anchored at pinning points and vibrate under applied stress. Similarly, dislocation theories of creep in metals, associated with the work of Orowan,^{49,51} Cottrell,⁴⁸ and Mott^{50,52} involve the movement and trapping by obstacles of dislocations already present or generated in the material. The obstacles may be other dislocations, foreign atoms, Peierls's hills, nodes of the dislocation network, etc.,⁵⁶ and dislocations may be released from them by thermal vibrations and stress. It is clear that even ignoring grain boundary motion effects there are more than sufficient different interactions and processes likely to occur in a real material to account for a distribution of relaxation times. For example, there may be, among others, a distribution of dislocation loop lengths,^{54,55} of activation energies or energy levels between different states, of pinning strength, and of different surroundings of different dislocation loops.

In Mott's latest theory,⁵² which can lead to logarithmic time dependence, the slowing down of creep with time is ascribed to the increasing difficulty of release of dislocations from obstacles as work hardening progresses. This is a partly irreversible process and so cannot be completely related to the reversible linear processes associated with the very small strains considered in the present work. Consequently, Mott's theory, in common with most of the other thermal-activation theories already cited, does not lead to a linear stress-strain relation. Creep slows down on the present model because there is a lower and lower density of relaxing units which have relaxation times of the order of the time of measurement as this increases beyond $t \sim \tau_0$. Although the linear, reversible character of the present theory requires that the distribution of relaxation times appropriate at a given temperature be a time-independent property of the material, this

⁴⁹ E. Orowan, J. West Scot. Iron Steel Inst. **54**, 45 (1946-47).

⁵⁰ N. F. Mott and F. R. N. Nabarro, *Report of Conference on Strength of Solids* (Physical Society, London, 1948), p. 1.

⁵¹ E. Orowan, *Imperfections in Nearly Perfect Crystals*, edited by W. Shockley et al. (John Wiley & Sons, Inc., New York, 1952), p. 191.

⁵² N. F. Mott, Phil. Mag. **44**, 742 (1953).

⁵³ A. J. Kennedy, J. Mech. and Phys. Solids **1**, 172 (1953).

⁵⁴ J. S. Koehler, *Imperfections in Nearly Perfect Crystals*, edited by W. Shockley et al. (John Wiley & Sons, Inc., New York, 1952), p. 197.

⁵⁵ A. Granato and K. Lücke, J. Appl. Phys. **27**, 583, 789 (1956).

⁵⁶ K. Lücke and A. Granato, *Dislocations and Mechanical Properties of Crystals*, edited by J. Fisher et al. (John Wiley & Sons, Inc., New York, 1957), p. 425.

⁴³ J. W. Glen, Phil. Mag. **1**, 400 (1956).

⁴⁴ H. M. Rosenberg, *Progress in Metal Physics*, edited by B. Chalmers and R. King (Pergamon Press, New York, 1958), Vol. 7, p. 339.

⁴⁵ N. F. Mott, Phil. Mag. **1**, 568 (1956).

⁴⁶ Reference 32, pp. 408-413.

⁴⁷ R. Becker, Phys. Z. **26**, 919 (1925); Z. tech. Physik **7**, 547 (1926).

⁴⁸ A. H. Cottrell, J. Mech. and Phys. Solids **1**, 53 (1952).

does not preclude application of the present results to creep measurements on a previously work-hardened material; it merely restricts the theory to such small deformations that additional work hardening or similar irreversible changes are unimportant during creep or during the transmission of a stress wave.

Both the theories of Mott⁵² and of Wyatt⁴² lead to direct dependence on absolute temperature of the quantity equivalent to the present $\sigma_0 q/M$, in approximate agreement with Wyatt's experimental results. Note that Eq. (36) shows that q is connected with the value of $\psi(\infty)$, an intrinsic property of the material at a given temperature, since $\psi(\infty)$ is itself dependent on the relaxation time distribution.

Although Mott's work-hardening theory is not closely applicable to the present model, it is worth mentioning that it yields an analytic expression for a time constant such as the τ_0 which appears, for example, in (4). Mott⁵² has shown that reasonable values for the microscopic parameters determining τ_0 lead to a value for it in order of magnitude agreement with the figure of 1 sec found experimentally by Davis and Thompson⁵⁷ for a precipitation-hardened Cu-Ag alloy at room temperature. As we shall see in the next part, the figure of $\tau_0 \sim 1$ sec is also in fair agreement with the τ_0 obtained by fitting the present theory to $1/Q$ results associated with long-period phenomena.

The magnitude of τ_0 is a critical factor in the present theory because it determines the frequency range where $1/Q$ changes from being roughly constant to decreasing as ω^{-1} . It also determines the time at which the creep rate first deviates from its initial value and becomes time dependent. Unfortunately, most creep measurements have not been carried out to sufficiently short times or analyzed properly to give good values of τ_0 . Lomnitz's measurements for creep in rock²³ start at about 30 sec after the application of shear stress, yet he derives a value of τ_0 (his a^{-1}) of about 10^{-3} sec. Since his results are well fitted in the range of measurement by simple logarithmic time dependence, a value of τ_0 far less than the shortest time of measurement cannot be extracted from them. It can only be concluded from his work that τ_0 for rocks is less than 30 sec. Wyatt's creep measurements on pure metals⁴² begin at about 2 sec and allow us to infer that τ_0 is likely to be less than this for such materials.

Whenever creep measurements for $t \ll \tau_\infty$ can be fitted by a form like Eq. (2) with the expression (5) used for $\psi(t)$, τ_0 can probably be obtained most accurately by analyzing $d\epsilon/dt$ results. For $t > 0$ we may write

$$d\epsilon/dt = (\sigma_0 q/M\tau_0)[1 + (t/\tau_0)]^{\nu-1}. \quad (47)$$

Let us denote by B the quantity $(\sigma_0 q/M\tau_0)^{1/(\nu-1)}$. Then (47) may be rewritten as

$$(d\epsilon/dt)^{1/(\nu-1)} = B + (B/\tau_0)t. \quad (47')$$

If now the quantity on the left is plotted versus t for various values of ν near and including zero, one such

value of ν should lead to the best straight line, from which τ_0 , ν , and B can be obtained. A somewhat similar procedure was used by Davis and Thompson⁵⁷ to obtain the value of τ_0 already quoted, although they did not fit their data to a modified logarithmic form like that in Eq. (4). Further discussion will be given later of the quantities ν , q , and τ_0 which appear in the present work.

The time constant τ_∞ cannot be determined directly unless the data can be extended to the region $W \leq a$ or $t \geq \tau_\infty$. We have found no data pertaining to sufficiently long times or low frequencies that these conditions are reached. In addition, without data in this region to allow more precise definition of the form of the relaxation spectrum at these long relaxation times, the present specific modification of the distribution-of-relaxation-times function is somewhat speculative. Nevertheless, some such modification is necessary to make the theory describe a physically realizable system. If the present distribution of relaxation times is accepted in lieu of better information, τ_∞ is well defined theoretically and an estimate of its magnitude can be obtained from the ratio of final to initial strain predicted by the present theory when all the parameters involved are well known. Jeffreys²⁶ has somewhat arbitrarily taken a value of 1.1 for this ratio for the earth and states that there is good evidence that it is less than 1.6. The present results yield

$$\epsilon(\infty)/\epsilon(0) = 1 + \psi(\infty), \quad (48)$$

where $\psi(\infty)$ is given by (36) or (37). If we take the approximate values $\nu=0$, $q=10^{-2}$, and $\tau_0=8.5$ sec, which are found in the next part, and use 1.1 for the above ratio, τ_∞ is about 1.4 days, manifestly too short. However, for the value $q=10^{-2}$ used here, τ_∞ increases by e^{10} for each 0.1 increase in $\epsilon(\infty)/\epsilon(0)$ when $\nu=0$. Therefore, if this ratio is taken to be 1.4, τ_∞ is about 4×10^{10} yr, a sufficiently long time. The quantity τ_∞ decreases as ν increases. For $\epsilon(\infty)/\epsilon(0)=1.1$, one finds $\tau_\infty \sim 0.3$ day for $\nu=0.01$ and 2.1 hr for $\nu=0.04$. When the ratio is 1.4, $\tau_\infty \sim 2.3 \times 10^7$ yr and 1.3×10^8 yr for $\nu=0.01$ and 0.04, respectively. The $a^{-\nu}e^{-a}$ term in (36), which arises from taking $G(\tau) > 0$ for $0 < z \leq a$, has only a relatively small effect on the above values. Because of the strong dependence of τ_∞ on the uncertain quantities $\epsilon(\infty)/\epsilon(0)$, q , and ν , we can only conclude that within their present limits of uncertainty they can indeed lead to a large enough τ_∞ value to have escaped direct observation.

Long-Period Phenomena

Transient creep is a time-domain phenomenon concerned with strain and its rate of change. We shall now pass on to small-amplitude frequency-domain measurements associated with vibration, oscillation,

⁵⁷ M. Davis and N. Thompson, Proc. Phys. Soc. (London) **B63**, 847 (1950).

and wave motion. Disagreement between results obtained by transient and frequency response methods on the same material may indicate that the range of linearity has been exceeded. Such a conclusion is only justified, however, provided that the time span in the transient measurements is consonant with the range of periods in the frequency response measurements. The geophysical results discussed in this section are roughly consonant in this way only with usual creep measurements.

In Fig. 5, $1/Q$ values primarily pertaining to wave phenomena in the earth are plotted vs angular frequency. Data for body waves have been indicated with an open symbol while a solid symbol or line has been used for data pertaining to surface and mantle waves. When Q is large, Eq. (20) shows that $1/Q$ and the attenuation factor α are related by

$$1/Q = \alpha t_0 V / \pi, \quad (49)$$

where t_0 is the period and V the phase velocity of the waves. The logarithmic decrement δ is given approximately by π/Q and the time lag, or time of retardation, by $1/\omega Q$. The data shown on Fig. 5 have been obtained from a variety of sources,⁵⁸⁻⁶⁹ and it is surprising that they are as consistent as indicated. For convenience, the type of phenomenon considered has been listed after each of references 58 through 69. For the data shown as horizontal lines, $1/Q$ was roughly constant over the limits indicated. The S-wave point which includes an arrow represents a lower limit. The extremes of the vertical lines indicate points obtained from measurements associated with two different earthquakes.

In the region where $1/Q$ decreases as ω^{-1} , Eq. (49) indicates that αV is constant. Since Q is high in this region, dispersion of the velocity will be negligible and α will be essentially frequency independent, in agreement with Eq. (46). There is sufficient data on Fig. 5 to allow theoretical curves to be fitted approximately. The results of such fitting are indicated by the solid lines. The values used for the theoretical lines were $q = 10^{-2}$ and $\tau_0 = 8.5$ sec. Since the beginning of a bend

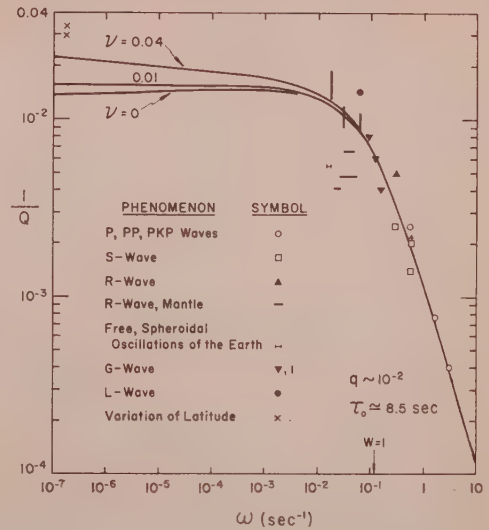


FIG. 5. $1/Q$ vs angular frequency ω for $\nu=0, 0.01$, and 0.04 ; $\alpha=0$; $\tau_0=8.5$ sec; and $q=0.01$. A variety of experimental points are also shown.

can be observed in the data for longer periods, the estimate for τ_0 is probably accurate to within 50% or less.

The absence of much data at very long periods makes the determination of q , and even more so ν , very uncertain. A damping value for the semi-diurnal earth tides has not been plotted because of scatter arising from the effects of ocean loading. Data obtained from mid-continental stations suggests⁷⁰ that the appropriate $1/Q$ with such loading minimized may be as low as 5×10^{-3} . The two values of $1/Q$ obtained from the 14-month variation of latitude of the earth are quite uncertain^{68,70} and represent over-all system values which include interface dissipation, especially that at the boundary between the core and the mantle and that between the mantle and the oceans.⁷⁰ Without these dissipations, the over-all value of $1/Q$ might be 5×10^{-3} or smaller. A small negative value of ν would lead to a curve falling below that for $\nu=0$ in Fig. 5 and might be more appropriate in this case.

It will be noted from Fig. 5 that the $1/Q$ values for the body waves which travel in both core and mantle are consistently lower than those that are restricted to the mantle and surface alone. At least part of such a difference might arise from the higher Q to be expected for material under high pressure in the core. In addition, the uncertain and varying effects of scattering arising from inhomogeneities along the paths of the various waves involved in Fig. 5 have not been estimated and corrected for. Further, no account has been taken of the fact that the $1/Q$ values for Rayleigh, shear, and compressional waves of the same period traveling in the same medium are in general different but related.³⁸

⁷⁰ G. J. F. MacDonald (private communication).

⁵⁸ B. Gutenberg, Bull. Seismol. Soc. Am. 48, 269 (1958). P, PP, PKP, S waves.

⁵⁹ F. Press, Science 124, 1204 (1956). S waves.

⁶⁰ B. Gutenberg, Bull. Seismol. Soc. Am. 35, 3 (1945). Rayleigh waves.

⁶¹ M. Ewing and F. Press, Bull. Seismol. Soc. Am. 44, 127 (1954). Mantle Rayleigh waves.

⁶² M. Ewing and F. Press, Bull. Seismol. Soc. Am. 44, 471 (1954). Mantle Rayleigh waves.

⁶³ H. Benioff, F. Press, and S. Smith, J. Geophys. Research 66, 605 (1961). Free, spheroidal oscillations of the earth.

⁶⁴ M. Bath, Geofis. pura e appl. 41, 91 (1958). Mantle Rayleigh waves.

⁶⁵ Y. Satō, Bull. Seismol. Soc. Am. 48, 231 (1958). Gutenberg waves (mantle Love waves).

⁶⁶ B. Gutenberg, Phys. Z. 25, 377 (1924). Love waves.

⁶⁷ H. Jeffreys, The Earth (Cambridge University Press, Cambridge, England, 1959), 4th ed., p. 255.

⁶⁸ W. H. Munk and G. J. F. MacDonald, The Rotation of the Earth (Cambridge University Press, Cambridge, England, 1960). Variation of latitude.

⁶⁹ P. Felgett, work in progress: quoted in reference 68. Variation of latitude.

Here, the situation is complicated by unequal periods for the waves and, in view of the uncertainty of the data and even uncertainty in the applicability of the present theory to the raw data presented, it has not been felt worthwhile to try to take the above effect into account.

It is a hazardous extrapolation to expect the present theory to describe loss in the core, mantle, and crust simultaneously in a very accurate fashion.⁷¹ Therefore, the theoretical fitting shown in Fig. 5 can only be expected to give order of magnitude values. It is suggestive, however, that the present τ_0 value is reasonably consistent with the results of creep measurements on metals and rocks already mentioned. If sufficient accurate wave transmission data for the earth were available, especially at long periods, it might be preferable to analyze it into two (or more) dispersion regions, a high- Q one pertaining to the average core, and a lower- Q , perhaps half as large, for the average mantle. The present theoretical results could be applied separately to these regions with different values of τ_0 , q , and possibly ν for each. An over-all response could then be obtained by addition of $1/Q$ values for the separate regions.

The present rough curve fitting and previously considered creep data both suggest that the most likely value of ν for rocks and metals in the small strain range is near zero and is almost certainly less than 0.05. Jeffreys²⁷ has derived an approximate value of $\nu=0.17$ using (5) and assuming, on the basis of Lomnitz's erroneous value $\tau_0^{-1}=10^8$, that $W \ll 1$ for seismic waves. The data and curve fitting of Fig. 5 show that this assumption is unwarranted. Furthermore, Fig. 2 indicates that the combination of a sufficiently high Q to agree with experiment and an appreciable region of frequency independence of $1/Q$ is unrealizable for ν as large as 0.17.

Short-Period Phenomena

Acoustic, seismological, and vibrational determinations of energy loss in solids are generally carried out under conditions which involve very small strains. Therefore, the present linear theory should be particularly applicable to the analysis of such amplitude-independent measurements. A variety of measurements have recently been summarized by Knopoff and MacDonald⁷² who conclude that $1/Q$ for inorganic, non-ferromagnetic materials is very nearly frequency-independent over the range from 10^{-2} to 10^7 cps, a conclusion in some apparent disagreement at the lower end with the data of Fig. 5. No single material has been measured at all frequencies of this entire range, however. The magnitude of $1/Q$ usually found is of the order of 10^{-2} to 10^{-3} , although it may be even smaller.

Other internal friction data discussed in an article by Niblett and Wilks,⁷³ which also includes a discussion of mechanisms leading to internal friction, show some frequency dependence of $1/Q$ (or logarithmic decrement) over small frequency ranges, but the majority of data leads to very weak or absent frequency dependence over a wide frequency range. Kolsky⁷⁴ has presented data on several non-metallic materials which also show negligible frequency dependence.

Measurements on a number of solids over a limited frequency range indicate that the attenuation factor is rather closely proportional to frequency. Equation (49) cannot be used to establish the frequency independence of $1/Q$ from such results unless the phase velocity is shown to be frequency-independent. Equations (44) and (45) of the present theory indicate that for $a \ll W \ll 1$ and $0 < \nu \ll 1$, the frequency dependence of α will be very difficult to distinguish experimentally from direct proportionality. Alternatively, when $\nu=0$ and Q is large, Eqs. (17) and (43) indicate that α is given quite closely for $a \ll W \ll 1$ by

$$\alpha \cong (W/2\tau_0 V_s) H(W) [1 + J(W)]^{-1}. \quad (50)$$

Here, α may increase slightly more rapidly than direct frequency proportionality over an appreciable range, but the deviation will be difficult to detect experimentally.

Of especial interest are stress attenuation results obtained on granite and other surface rocks. The measurements of Bruckshaw and Mahanta⁷⁵ indicate that $1/Q$ is frequency independent for several such materials from 40–120 cps. Others^{72, 76–78} have found evidence of such frequency independence up to 10 Mcps and down to lower seismic frequencies. These results seem difficult to reconcile with those of Fig. 5 at first. It should be noted, however, that except for recent results on Solenhofen limestone⁷⁹ there are no accurate $1/Q$ data available for rocks in the frequency region from about 1 cps to 20 or 30 cps. The above discrepancy may be reconciled in one of two ways. First, the decrease in $1/Q$ shown at the right in Fig. 5 may not arise primarily from the present loss mechanism but may appear because of the increase in Q with increasing pressure and even from a possible decrease in scattering effects at shorter wavelengths. Thus, the short-period body waves which penetrate deeper into

⁷³ D. H. Niblett and J. Wilks, *Advances in Phys.* **9**, 1 (1960).

⁷⁴ H. Kolsky, *Stress Wave Propagation in Materials*, edited by N. Davids (Interscience Publishers, Inc., New York, 1960), p. 59.

⁷⁵ J. Mc. Bruckshaw and P. C. Mahanta, *Petroleum* **17**, 14 (1954).

⁷⁶ F. Birch and D. Bancroft, *Bull. Seismol. Soc. Am.* **28**, 243 (1938).

⁷⁷ Ye. V. Karus and I. P. Passechnik, *Akad. Nauk S.S.S.R., Izvest. Ser. Geofiz.* **6**, 514 (1954).

⁷⁸ L. Peselnick and I. Zietz, *Geophysics* **24**, 285 (1959).

⁷⁹ L. Peselnick and W. F. Outerbridge, *J. Geophys. Research* **66**, 581 (1961).

⁷¹ B. Gutenberg, *Physics of the Earth's Interior* (Academic Press, Inc., New York, 1959), p. 191.

⁷² L. Knopoff and G. J. F. MacDonald, *Revs. Modern Phys.* **30**, 1178 (1958).

the earth would have most of their path lengths in high- Q core material. In this case, the hypothesis of frequency-independence of $1/Q$ for many materials at constant pressure and temperature over the range from 10^{-2} or 10^{-1} to 10^7 cps may be accepted, although even so the lower end of the range seems somewhat difficult to reconcile with creep results.

Secondly, if pressure and scattering effects are actually unimportant and the present model is assumed to apply to the lower frequencies such as those covered by Fig. 5 with $\tau_0 \sim 10$ sec, new loss mechanisms will begin to be important at higher frequencies. Somewhere in the region of 1 to 20 cps, the $1/Q$ decrease shown in Fig. 5 would then cease and either $1/Q$ would remain constant at a new lower value or it would, more likely, increase up to 10^{-3} to 10^{-2} again and then remain constant to very high frequencies. In either case, this new dispersion region might again be well described by a linear loss mechanism of the present type with values of τ_∞ and τ_0 different from those applicable to the lower dispersion region, and values of q and ν either the same or different. It is known that $1/Q$ is considerably less in single crystals than in polycrystalline aggregates of the same material. It is possible that the higher-frequency dispersion region begins to become important in polycrystalline material when the wavelength is short enough that the boundaries between individual grains and crystallites can begin to play an important role in energy dissipation.³⁹ Under these conditions, one would naturally expect a distribution of relaxation times. At the longer wavelengths of Fig. 5, grain-boundary effects and degree of compaction might be expected to be less important. Knopoff and MacDonald⁴ have considered various models for acoustic loss in solids and conclude that microscopic scattering effects will not become important until very high frequencies are reached. The very recent results of Peselnick and Outerbridge⁷⁹ on internal friction in Solenhofen limestone indicate a nearly constant $1/Q$ from about 4 cps up to the limit of acoustic frequencies or above. For this material at least it is therefore likely that there is only one dispersion region rather than two separate ones with a transition region in the 1–10 cps frequency range.

If the hypothesis of separate upper and lower dispersion regions is accepted, the present analysis can also explain the experimental constancy of $1/Q$ to very high frequencies and the nearly direct proportionality of α to frequency. In the region from perhaps $\omega = 10^2$ to 10^8 , $1/Q$ remains at least roughly constant and of the order of 10^{-3} to 10^{-2} . When $\nu = 0$, Eqs. (19) and (43) show that $1/Q \sim \pi q/2$, thus setting limits on q . Alternatively, if $0 < \nu < 1$, Eq. (41) requires $\nu \ll 1$ for essentially frequency independent $1/Q$ coupled with a sufficiently large value of Q . If $W = a$ at $\omega \approx 10^2$, the τ_∞ for this dispersion region will be 10^{-2} sec. Further, if $W = 1$ at $\omega \approx 10^8$, τ_0 will be 10^{-8} sec. These results are predicated on sufficient separation of the low- and high-

frequency dispersion regions that they can be represented by two essentially nonoverlapping distributions of relaxation times. If overlapping is considerable, a single relaxation distribution function must be used which covers both dispersion regions, and the distinction between the τ_0 for the lower region and the τ_∞ for the upper region will become blurred or disappear. If the decrease in $1/Q$ shown in Fig. 5 is largely a pressure or boundary-layer artifact associated with mantle and core wave paths, the distinction disappears completely and small amplitude loss in a given material such as a metal or rock should be describable by the present theory using a τ_∞ between 10^2 and 10^9 yr and a τ_0 of 10^{-8} sec or less, a remarkably wide range of times and wide distribution of relaxation times.

The usual theory of amplitude-independent internal friction losses⁵⁴⁻⁵⁶ leads to an expression for $1/Q$ which is proportional to the mean length of a vibrating dislocation loop raised to the fourth power and directly proportional to frequency for frequencies appreciably below 100–1000 Mcps. As the foregoing discussion indicates, such frequency dependence is in poor agreement with most experiments. Wilks⁸⁰ has recently suggested, however, that the L^4 term may be an inverse function of frequency. Such dependence of L will make the over-all frequency dependence of $1/Q$ less strong and may even lead to a decrease in internal friction at high frequencies. Wilks' argument is that the effective length of a loop will decrease with frequency for frequencies appreciably greater than the inverse of the average time required for the unpinning of a dislocation from an impurity atom. Although Wilks relates this time to an activation energy which may depend on the nature of the impurity and the distance to adjacent pinning points, he does not explicitly consider a distribution of times and activation energies. A distribution of activation energies is certainly likely and can lead to a distribution of relaxation times and, equivalently, a dependence of effective loop length on frequency.

The problem of explaining a dissipation factor which is nearly independent of frequency over many decades also arises in the field of dielectrics. A number of authors have attacked the dielectric problem by also considering a distribution of activation energies.⁸¹⁻⁸³ For example, one may often write

$$\tau = \tau_a \exp(E/kT), \quad (51)$$

where E is an effective activation energy for the process and may be discontinuously or continuously distributed over a finite range from E_1 to E_2 .

If $K(E)dE$ is the density of relaxation times having activation energies in the range dE , then $K(E)dE = G_1(\tau)d\tau$. Since $K(E)$ should be a temperature-

⁸⁰ J. Wilks, *Phil. Mag.* **4**, 1379 (1959).

⁸¹ M. Gevers and F. K. Du Pré, *Trans. Faraday Soc.* **A42**, 47 (1946).

⁸² C. G. Garton, *Trans. Faraday Soc.* **A42**, 56 (1956).

⁸³ H. Fröhlich, *Theory of Dielectrics* (Clarendon Press, Oxford, England, 1958), 2nd ed., pp. 92–98.

independent, time-invariant property of the system, $G_1(\tau)(d\tau/dE)$ should also be temperature independent.⁸⁴ This requirement imposes restrictions on the form of a distribution-of-relaxation-times function which can be used to describe an activated process. In the present case when $G(z)$ is given by Eqs. (28) or (33), these restrictions cannot be met exactly, primarily because of the presence of the e^{-z} term. Note that the $G(z)$ of Eq. (33) is still physically realizable, however, when the distribution of relaxation times considered does not arise solely from a distribution of activation energies. The actual distribution function of Eq. (28) multiplied by z^{-1} is, in fact, of the form of a Poisson distribution, a distribution commonly met in nature. For example, such a distribution (with $\nu < 0$ and integral) has been found to describe the size statistics of polycrystalline aggregates under some conditions.⁸⁵

If the activation energy range extends from E_1 to E_2 , the smallest and largest relaxation times are $\tau_s = \tau_a \exp(E_1/kT)$ and $\tau_l = \tau_a \exp(E_2/kT)$. If τ_l is identified with the present τ_∞ , then the minimum value of z is a and $G(z)=0$ for $z < a$, a possibility already mentioned. The quantity τ_s may be set equal to τ_0 without appreciably changing the transient or frequency response results already considered in the range of primary interest. Then the maximum value of z is unity. One will still find a wide frequency region where $1/Q$ will be constant and $1/Q$ will still decrease as W^{-1} for $W \gg 1$. Note that even if the intrinsic vibration time τ_a is very small, the time $\tau_s = \tau_0$ may be made a second or longer by taking E_1 , the minimum height of a potential barrier, sufficiently large. If E_1 is taken zero or proportional to temperature, τ_0 will be temperature independent.

When τ is given by Eq. (51) and $G(z)$ is expressed by (28) in the range $a \leq z \leq 1$ and is zero outside this range, it turns out that the resulting $K(E)$ may be made very nearly temperature independent when $\nu \ll 1$ by taking ν and q both proportional to absolute temperature, results in at least qualitative agreement with experiment. The temperature dependence of the e^{-z} term which appears in $K(E)$ cannot be removed by the above choices but such dependence will be quite small for the present choice of $\tau_0 = \tau_s$. Distribution functions

which are entirely consistent with thermally activated processes having a distribution of activation energies and which can be related to both dielectric and internal friction behavior will be discussed elsewhere.⁸⁴

The present theory is linear in that superposition applies, and it involves a linear dependence of strain on stress at a given time even though the creep function itself may be a nonlinear function of time, such as that in Eq. (5). Knopoff and MacDonald⁷² have stated, however, that no model of dissipation in solids which is based on a linear stress-strain relation can account for the frequency independence of $1/Q$ observed for many materials. This conclusion is based on an approximate treatment of a lumped-parameter model of a linear solid. It has led them, as already mentioned, to propose a nonlinear theory which leads to such constancy of $1/Q$ in the range where $1/Q$ is amplitude independent. The present work, based on a continuously distributed model, shows that a linear theory can also lead to a $1/Q$ which is virtually frequency independent over a wide range of frequencies.

Two of the particular virtues of the present approach are that Q increases at each end of the constant $1/Q$ range. Such increase causes the effects of a given dispersion mechanism to be of importance in a limited, but possibly very wide, frequency range only. Outside this range, other dispersion mechanisms may come into play which themselves may possibly be describable by a theory of the present type with different material constants. Most other theories^{55,72,74} lead to Q 's which decrease indefinitely at high frequencies and often at low frequencies as well, precluding the simple superposition of similar solutions to cover several different dispersion regions in the same material.

ACKNOWLEDGMENTS

The author is indebted to Dr. C. Lomnitz for originally drawing the function of Eq. (6) to his attention several years ago. He also wishes to thank Dr. Lomnitz for appreciable correspondence and comments on some of the present work and for supplying a number of references, especially the majority of those from which the data of Fig. 5 came. Finally, the valuable comments and suggestions of Dr. N. Einspruch, Dr. F. Gilbert, Dr. G. J. F. MacDonald, and Professor C. W. Horton are much appreciated.

⁸⁴ J. R. Macdonald (submitted to J. Chem. Phys.).

⁸⁵ P. J. Gellings, Appl. Sci. Research **A10**, 165 (1961).

New Derivation of the Vacuum Breakdown Equation Relating Breakdown Voltage and Electrode Separation

A. MAITLAND*

Research Department, Associated Electrical Industries (Manchester) Limited, Trafford Park, Manchester, England

An analysis of the published measurements of breakdown voltage for various gap lengths for uniform and approximately uniform fields shows that the results may be represented by the breakdown equation $V = Cx^\alpha$ and that the values of α lie in the range 0.1 to 1.1 with a mode of 0.7. A theory is developed which leads both to a breakdown equation of the same form and to a general expression to account for the range of values of α . This expression is confirmed for gaps up to 0.075 cm by direct experiment. The development is based on the postulate that an electron beam is emitted from the cathode, diverges, and bombards the anode to cause breakdown when a critical power flux is reached. The factor C is shown to include the critical power flux and to be related to both field and electrode separation. In support of the theory, the radii of craters produced on the anode are measured and shown to be related to the radius of an electron beam at the anode. Calculation shows the current carried by the beam to be of the order of 10^{-4} amp. Values of the critical power flux obtained from the equation $V = Cx^\alpha$ and from anode crater data, respectively, agree within a factor of 1.5 and are of the order of 10^8 w cm $^{-2}$. To explain the observed phenomena, a multiple electron beam system is proposed.

I. INTRODUCTION

A RELATIONSHIP between breakdown voltage and gap length for plane electrodes in vacuum was first deduced by Cranberg¹ on the basis of his well-known "clump" theory of breakdown initiation. This relationship is $V = Cx^{0.5}$ where C is a constant. For the purpose of the discussion to follow, the equation will be written in the form $V = Cx^\alpha$. In support of his equation, Cranberg presented a summary of some previous results which were interpreted as giving the value 0.5 for α , a value which has come to be generally accepted.

A more detailed analysis of the available experimental results obtained with uniform and approximately uniform macroscopic fields has been made² and the summary³⁻¹³ is presented in Fig. 1. In most cases, the data used in constructing the histogram were published in the form of curves and the necessary values were estimated from the plotted experimental points. The values of α were calculated by the method of least

squares where four or more experimental values were given. In many cases, it was found that the points followed a curve rather than a straight line, in which case the values of α between consecutive pairs of experimental values were taken. In other cases, two straight lines could be drawn through the plotted points, each covering a definite range of gaps.

The values of α have been taken to one decimal place and, for the purpose of Fig. 1, the total number of experimental points used in determining the respective values of α has been considered to be the number of times each value of α occurred. Inspection of Fig. 1 shows a weakness in the Cranberg equation in that the single value of 0.5 for α is, at best, a rough approximation.

A second weakness in the equation lies in the obscurity of the physical nature of the constant C .

However, in spite of these weaknesses in the equation produced, "clump" theory has been the only one which has yielded an equation expressing breakdown voltage in terms of gap length. Other theories of the initiation of breakdown in vacuum suffer from the disadvantage that they have not yielded equations of the known ex-

* Present address: C. A. Parsons and Company Limited, Nuclear Research Centre, Newcastle-upon-Tyne, 6, England.

¹ L. Cranberg, J. Appl. Phys. **23**, 518 (1952).

² Material supplementary to this article has been deposited as Document number 6820 with the ADI Auxiliary Publications Project, Photoduplication Service, Library of Congress, Washington 25, D.C. A copy may be secured by citing the Document number and by remitting \$2.50 for photoprints, or \$1.75 for 35-mm microfilm. Advance payment is required. Make checks or money orders payable to: Chief, Photoduplication Service, Library of Congress.

³ A. S. Denholm, Can. J. Phys. **36**, 476 (1958).

⁴ J. G. Trump and R. J. van de Graaff, J. Appl. Phys. **18**, 327 (1947).

⁵ W. S. Boyle, P. Kisliuk, and L. H. Germer, J. Appl. Phys. **26**, 720 (1955).

⁶ P. Kisliuk, J. Appl. Phys. **25**, 897 (1954).

⁷ P. H. Gleichauf, J. Appl. Phys. **22**, 766 (1951).

⁸ H. W. Anderson, Trans. Am. Inst. Elec. Engrs. **54**, 1315 (1935).

⁹ J. E. Jennings, A. C. Schwager, and H. C. Ross, Elec. Eng. **75**, 350 (1956).

¹⁰ W. W. Chupp and H. G. Heard, UCRL-1962, 1954.

¹¹ J. L. McKibben and R. K. Beauchamp, AECD-2039.

¹² I. N. Slivkov, J. Tech. Phys. (U.S.S.R.) **27**, 2081 (1957).

¹³ N. B. Rozanova and B. L. Granovskii, J. Tech. Phys. (U.S.S.R.) **26**, 489 (1956).

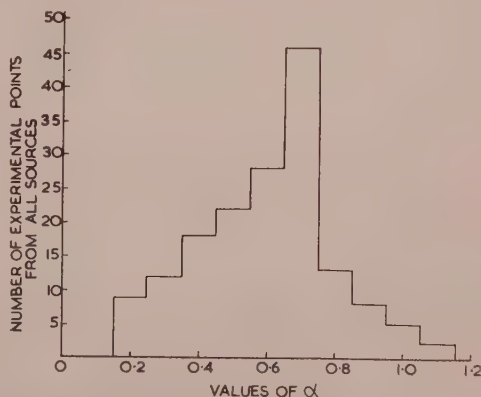


Fig. 1. Distribution of values of α obtained from publications relating to plane or near-plane geometry.

perimental form. One such theory, which is otherwise quite adequate in accounting for much of the observed breakdown phenomena, is that based on the emission from the cathode of an electron beam which bombards the anode and leads to breakdown in the vapor produced. This concept is well known and has been considered by several investigators, some of whom are enumerated below.¹⁴⁻²² In relation to the development to be described herein, the works of Denholm,²³ and of Boyle *et al.*⁵ are perhaps the most significant.

In the present paper the above concept is developed into a new breakdown equation which is of the form $V = Cx^\alpha$, in agreement with experiment. Thus, the disadvantage alluded to above, from which this theory of breakdown initiation has hitherto suffered, has been removed. Moreover, the new equation is free from the two weaknesses associated with the equation as developed on the basis of "clump" theory. In the new equation the full physical significance of the constant C becomes quite clear and a general equation for α is presented.

II. THEORETICAL CONSIDERATIONS

A. Development of Breakdown Equation

It is postulated that an electron beam issuing from a site at the cathode diverges due to the mutual repulsion of the electrons and finally impinges on the anode to cause vaporization of anode material and subsequent breakdown in the vapor when the power flux at the bombarded anode site reaches a critical value. To calculate the critical value it is essential first to investigate the divergence of the electron beam in order to find the value of the beam radius when it strikes the anode.

Assume that the electrodes are plane surfaces parallel to each other and consider n electrons per second emitted from a site of radius r to form an electron beam. Assume also that the electrons have no initial velocity component in a direction parallel to the plane of the emitting site and let v be their velocity at any instant in a direction normal to this plane. Let the x axis be normal to the plane of the electrodes and y the radius of the beam at a distance x along the axis. Let $R = y/r$.

An analysis which follows that of Watson²⁴ arrives at the equation in emu

$$x = \left[\frac{m_0 r^2}{4\pi e^2} \right]^{1/2} \left[1 - \frac{v^2}{c^2} \right]^{-1/2} \frac{v^{3/2}}{c} F(R),$$

where m_0 is the rest mass of an electron, e the electronic charge, and c the ratio of the electromagnetic to the electrostatic unit of charge.

$$F(R) = \int_1^R \frac{dR}{(\log_e R)^{3/2}}.$$

Using the initial current density J of the beam,

$$x = \left[\frac{m_0}{4\pi e J} \right]^{1/2} \left[1 - \frac{v^2}{c^2} \right]^{-1/2} \frac{v^{3/2}}{c} F(R). \quad (1)$$

For a potential difference V , by neglecting higher orders than the second, we obtain

$$x(1 + AV) = B(V^{1/2}, J^{1/2})F(R),$$

where

$$A = 3e/16m_0c^2 \approx 3.7 \times 10^{-15},$$

$$B = (e/2m_0\pi^2c^4)^{1/2} \approx 1.0 \times 10^{-9}.$$

Inspection shows that V does not significantly influence the value of $(1 + AV)$ until V is about 300 kv. When $V < 300$ kv, $AV < 10^{-1}$. Neglecting AV , the equation becomes

$$x = \frac{BV^{1/2}}{J^{1/2}} F(R). \quad (2)$$

Values of R in the ranges 10-100 and 100-500 respectively, have been calculated² and show that a close approximation to the form of $F(R)$ is given by

$$F(R) = \beta R + \gamma, \quad (3)$$

where β and γ are constants. Watson²⁴ gives graphs which show that for values of R in the range 2-10, $F(R)$ is approximately equal to R .

The approximate values of the constants β and γ over the three ranges are

$$\begin{array}{lll} \beta_{2-10} = 1 & \beta_{10-100} = 0.51 & \beta_{100-500} = 0.43 \\ \gamma_{2-10} = 0 & \gamma_{10-100} = 4.68 & \gamma_{100-500} = 13.29. \end{array} \quad (4)$$

From (2) and (3)

$$x = (BV^{1/2}/J^{1/2})(\beta R + \gamma).$$

Putting

$$R = y/r$$

$$[y + (\gamma/\beta)r]V^{1/2} = (rJ^{1/2}/B\beta). \quad (5)$$

Experimental evidence supporting the application of this equation to the initiation of breakdown in vacuum is presented below. The equation represents the spreading of the electron beam which bombards the anode.

So far, the following basic assumption has been made: that a beam of electrons is emitted from the cathode under the simplifying conditions described. The second basic assumption is that breakdown is certain when the power flux at the bombarded anode site reaches a certain critical value, E . The actual form and value of the breakdown probability function are unknown, so the assumption that breakdown is certain represents a

¹⁴ A. W. Hull and E. E. Burger, Phys. Rev. **21**, 1121A (1928).

¹⁵ L. B. Snoddy, Phys. Rev. **37**, 1678A (1931).

¹⁶ J. W. Beams, Phys. Rev. **44**, 803 (1933).

¹⁷ A. J. Ahearn, Phys. Rev. **50**, 238 (1936).

¹⁸ J. A. Chiles, J. Appl. Phys. **8**, 622 (1937).

¹⁹ K. Hashimoto, J. Phys. Soc. Japan **2**, 71 (1947).

²⁰ R. C. Mason, Phys. Rev. **52**, 126 (1937).

²¹ H. G. Heard, UCRL-2251, 1953.

²² O. E. Myers and W. A. Raatz, U. S. Atomic Energy Commission LRL-158 (1955).

²³ A. S. Denholm, Ph.D. thesis, University of Glasgow, 1954.

²⁴ E. E. Watson, Phil. Mag. **3**, 849 (1927).

first approximation. It is emphasized that E is not necessarily a constant for a given material and surface conditions, but may be a function of gap and field. If the current carried by the beam when breakdown is initiated at minimum voltage V is $J\pi r^2$ and the area of the bombarded site is πy^2 , then

$$y^2 = VJr^2/E. \quad (6)$$

Applying (5) to the conditions of minimum breakdown voltage expressed by (6),

$$V = \left(\frac{E}{B^2\beta^2} \right)^{0.4} x^{0.8} \left(1 - \frac{\gamma BV^{\frac{1}{2}}}{J^{\frac{1}{2}}x} \right)^{0.8}, \quad (7)$$

which may be expressed in an alternative form for values of $R > 100$

$$V = \left(\frac{E}{B^2\beta^2} \right)^{0.4} x^{0.8} \left(1 - 0.8 \frac{\gamma}{\beta R} \right). \quad (8)$$

Substitution of known values in this equation shows that

$$(0.8\gamma/\beta R) \ll 1$$

and so Eq. (8) may be written as

$$V = (E/D)^{0.4} x^{0.8} \quad (9)$$

to a close approximation, where $D = B^2\beta^2$.

B. General Expression for α

It has been pointed out that E is not necessarily a constant. It remains now to discuss the implications of this notion. Electrons arriving at the anode either deliver power of sufficient flux to produce evaporation of anode material which subsequently leads to the establishment of a discharge channel in the inter-electrode space; or, the bombarding electrons produce a sufficient number of secondary particles to cause a breakdown to develop. In this latter case some such criterion as that expressed in the papers by Van de Graaff *et al.*^{4,26} may be operative, but determinations of the values of the coefficients^{4,26-32} reveal them to be 2-3 orders of magnitude too small. In view of the small values of the coefficients, only the first possibility of evaporation of anode material is considered here.

The electron beam bombarding the anode surface is a surface source heating a volume of metal. For a given power flux, as the beam radius increases, the power

entering the metal increases as the square of the radius, but the volume to be heated increases as the cube. Thus, from this elementary consideration, a greater power flux is necessary at the greater beam radii if the anode surface is to be brought to the temperature at which a discharge develops. The same qualitative result may be obtained by using the formulas of Zingerman³³ or that presented by Boyle *et al.*⁵ To obtain a quantitative result from the formulas would involve making detailed assumptions about the conditions necessary for the development of the discharge which are not justifiable at present.

However, on the basis of the above consideration, it is proposed that $E = pf(y)$, where p is the critical power flux for unit radius of the bombarded site, and $f(y)$ is a function of y . Since y is related to x through (5), it then follows by neglecting $\gamma r/\beta$ that $E = LF_1(x)$, where L is the critical power flux for unit gap and $F_1(x)$ is a function of x .

The subsequent ionization of the vapor in the vicinity of the anode may be expected to be dependent upon the field, X , at the anode and, since the number of atoms available for ionization is related to E , it is proposed that $E = MF_2(X)$, where M is the critical power flux for unit field, and $F_2(X)$ is a function of X .

Evidence is presented in Figs. 10 and 11 to show that the forms of the functions $F_1(x)$ and $F_2(X)$ are such that, approximately

$$E = Lx^{\phi_1}, \quad (10)$$

and

$$E = MX^{\theta_1}. \quad (11)$$

Combining (10) and (11)

$$E = PX^{\theta}x^{\phi}, \quad (12)$$

where $\theta = \theta_1/2$, $\phi = \phi_1/2$, and $P = (LM)^{\frac{1}{2}}$. Remembering that for uniform field $X = V/x$, Eqs. (9) and (12) give an equation which shows that

$$\alpha = 0.4(2 + \phi - \theta)/(1 - 0.4\theta), \quad (13)$$

which implies that the factors influencing the value of α are the field and the gap, and suggests one possible cause for the numerous different values of α found by the various investigators and presented in Fig. 1 and in the tabular summary of reference 2.

III. APPARATUS AND PROCEDURE

A. Apparatus

The vacuum envelope was made of standard glass components manufactured by Quickfit Visible Flow, Ltd. O-rings were used and the system was evacuated by a conventional oil diffusion pump backed by a rotary pump. Liquid nitrogen trapping was used.

The circuit is shown in Fig. 2. The pulse forming network (PFN) had a characteristic impedance of 100 ohm and delivered a 4.5- μ sec pulse. The voltage to

²⁵ L. C. van Atta, R. J. van de Graaff, and H. A. Barton, *Phys. Rev.* **43**, 158 (1933).

²⁶ A. I. Bennett, *J. Appl. Phys.* **28**, 1251 (1957).

²⁷ E. W. Webster, R. J. van de Graaff and J. G. Trump, *J. Appl. Phys.* **23**, 264 (1952).

²⁸ H. C. Bourne, *J. Appl. Phys.* **26**, 625 (1955).

²⁹ H. C. Bourne, R. W. Cloud, and J. G. Trump, *J. Appl. Phys.* **26**, 596 (1955).

³⁰ I. Filosofo and A. Rostagni, *Phys. Rev.* **75**, 1269 (1949).

³¹ B. Aarset, R. W. Cloud, and J. G. Trump, *J. Appl. Phys.* **25**, 1365 (1954).

³² A. G. Hill, W. W. Buechner, J. S. Clark, and J. B. Fisk, *Phys. Rev.* **55**, 463 (1939).

³³ A. S. Zingerman, *J. Tech. Phys. (U.S.S.R.)* **26**, 2008 (1956).

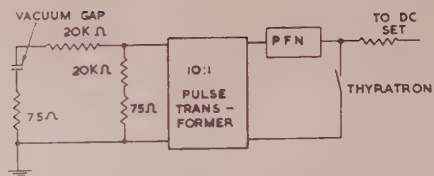


Fig. 2. Circuit used for the investigations.

which the PFN was charged could be set with an accuracy of $\pm 1.0\%$ at 5 kv and $\pm 0.1\%$ at 18 kv by adjusting the Variac input from a mains stabilizer, having $\pm 1\%$ stability, to a dc set having 0.2% ripple. The final pulse voltage to be delivered by the 10:1 pulse transformer was thus set with an accuracy of $\pm 2\%$. However, the absolute values of the final pulse voltages quoted in this report are $\pm 5\%$, due to the uncertainty of the pulse transformer ratio. The errors quoted represent extreme values.

The electrodes studied were shaped to Bruce's profile with plane surfaces approximately 1.5 cm in diameter. The molybdenum electrodes had plane surfaces 1.5 cm in diameter and had rounded edges. The electrode spacing could be set to any value from 0-1 cm with an accuracy of ± 0.0005 cm, the movement being made through a Wilson seal. The electrode separation was set at the desired value immediately before the study to be made.

B. Procedure Adopted in the Study of Anode Erosion

Before every experiment, the copper electrodes were polished with $\frac{1}{4}\text{-}\mu$ diamond paste on microcloth to remove all visible traces of the previous experiment. They were then immediately washed with water, then acetone, and installed in the vacuum system. It was necessary to etch the molybdenum electrodes with alkaline potassium ferricyanide solution prior to polishing them with the diamond paste.

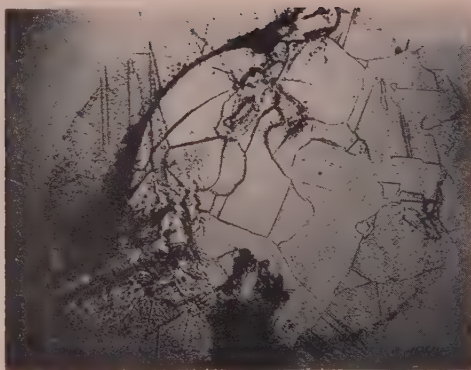


Fig. 4. Gross spot showing crystal structure and evidence that more than one discharge (possibly four) has occurred at the site. Copper (vacuum cast) anode.

When the pressure was about 5×10^{-6} mm Hg, the electrode separation was set and voltage pulses were applied to the electrodes at 1-kv increments in sequences of 10 pulses at each voltage until 10 pulses produced 10 breakdowns. The number of breakdowns occurring in each sequence was recorded and from these a mean breakdown voltage was calculated. This procedure was considered necessary to ensure that a suitably large number of discharges took place under approximately minimum breakdown conditions.

Having subjected the electrodes to the discharges, they were removed and examined with a Vickers projection microscope at various magnifications up to 600 \times . No erosion was visible on the cathode, but some fine particles of material transferred from the anode were sometimes visible. Examination of the anode revealed that each discharge had produced a separate "gross" spot. Fig. 3 shows two separate spots. Occasionally there was evidence that two or more discharges had occurred at the same site (Figs. 4 and 6). Each gross spot was made up of individual shallow craters, as seen in Figs. 5 and 7, which covered the entire area occupied

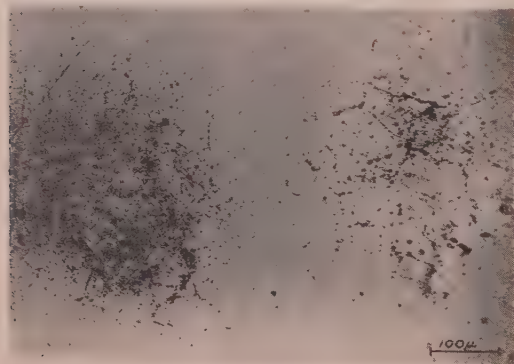


Fig. 3. Two gross spots formed on a copper (hard drawn) anode. Each spot is caused by one discharge of maximum duration 4.5 μ sec.



Fig. 5. Part of a gross spot produced by a single discharge showing shallow craters and erosion of crystal edges. Copper (vacuum cast) anode.

by the gross spot. Also present in the fine detail of the gross spot were deep craters which seemed to have formed at crystal boundaries and at sites which were probably impurity centers, as shown in Figs. 6 and 7. This tendency was more marked in the case of hard drawn copper, as may be seen by comparing Figs. 5 and 6. For comparison, Fig. 8 shows the virgin surface of the anode. One region of each gross spot was photographed at a magnification of 600 for subsequent measurement.

Figures 5 and 7 are typical of the photographs which were used in making measurements of the shallow crater radii. Five shallow craters on each photograph were randomly selected; each shallow crater was measured across its diameter from center to center of the defining rim. The mean radius y_m , corresponding to each gap used, was calculated from about 50–100 readings.

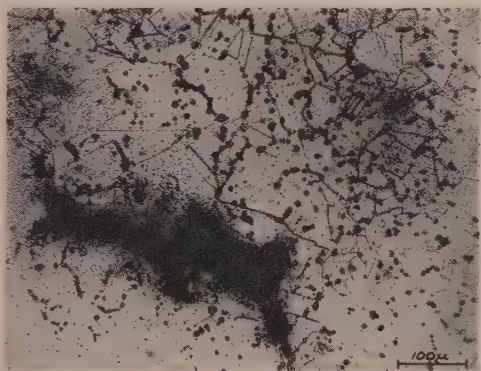


FIG. 6. Fine structure of gross spot produced by a single discharge showing craters at probable impurity centers and crystal edges. The large black patch is the site of a second discharge. Copper (hard drawn) anode.

The shallow craters rather than the deep craters were chosen because of the general uncertainty concerning the formation of the deep craters.

IV. RESULTS OF ANODE EROSION STUDIES

A. Verification of the Equation for a Divergent Electron Beam

Equation (5) was developed from the basic assumption that a beam of electrons is emitted from the cathode, diverges, and bombards the anode; this form of equation is thus fundamental to the establishment of Eq. (9). It was, therefore, desirable to find a method of assessing the validity of (5) in the particular circumstances of breakdown in vacuum. The method described in Sec. III. B is founded upon two assumptions. The first is that the electron beam is responsible for the vaporation of anode material which produces each one of the large number of shallow craters (Figs. 3 and 4) resulting from a single discharge. The second is that the

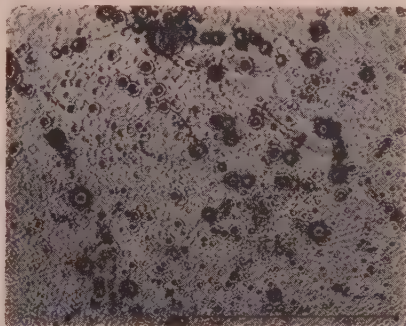


FIG. 7. Part of the gross spot of Fig. 6 showing deep craters formed at probable impurity centers or crystal edges and the background of shallow craters. Copper (hard drawn) anode.

radius of a shallow crater is directly related to the radius y of the beam at impact. Equation (5) may now be expressed in a form applicable to the measurements to be described. Let y_r = real mean radius of the base of the electron beam at the anode; y_m = mean radius of the base of the electron beam at the anode as given by measurements of shallow crater radii; ρ = difference between the two radii; and

$$y_r = (y_m - \rho). \quad (14)$$

The experiment is not sufficiently sensitive to justify anything more refined than this expression.

From Eq. (5)

$$y_m V^{\frac{1}{2}} = (r J^{\frac{1}{2}} / B \beta) x + [\rho - (\gamma / \beta) r] V^{\frac{1}{2}}. \quad (15)$$

Figure 9 shows the results plotted in the form of Eq. (15). Within the limitations of the experiment, the results for each material shown in Fig. 9 may each be represented by a straight line as predicted by Eq. (15). Let

$$a = r J^{\frac{1}{2}} / B \beta \quad (16)$$

and

$$b = (\rho - \gamma r / \beta) V^{\frac{1}{2}}. \quad (17)$$

A typical value for a is 5×10^6 emu.

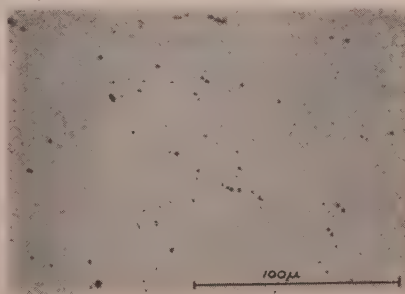


FIG. 8. Plain copper (hard drawn) surface showing distribution of impurity centers and "pinholes."

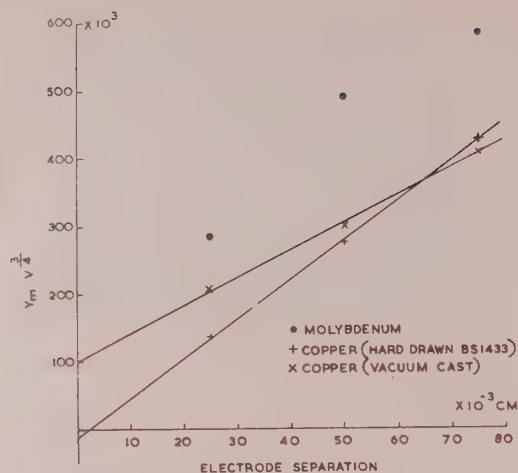


FIG. 9. Experimental verification of Eq. (15). Y_m = mean radius (cm) of shallow craters appearing on anode; V_m = mean breakdown voltage (emu potential).

B. Estimation of Current Carried by Electron Beam at Breakdown

The experimental results in Fig. 9 show that a [Eq. (16)] is approximately constant over the range of values investigated. B and β have also been shown to be approximately constant. This indicates that $rJ^{1/2}$ is approximately constant. Now, since the electron current necessary to initiate breakdown is $I = \pi r^2 J$, it follows that a constant value for a implies a critical current necessary to initiate breakdown. Measurement of a thus yields values of this critical current. The respective values of a given by the graphs of Fig. 9 give the following values for the current I carried by the electron beam at breakdown: 2×10^{-4} amp for hard drawn copper, 1×10^{-4} amp for vacuum cast copper, and values in the range 0.7×10^{-4} to 4.0×10^{-4} amp for molybdenum. The currents are seen to be of the same order of magnitude as that of the prebreakdown currents measured by Denholm,²³ Clifford,³⁴ Mansfield and Fortescue,³⁵ Boyle *et al.*,⁵ and others.

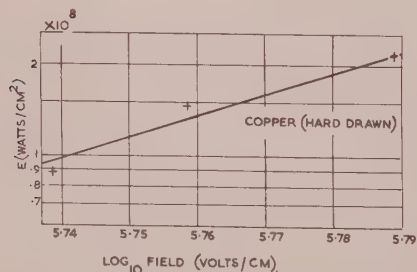


FIG. 10. Relationship between critical power flux and macroscopic field (gap not constant).

It is known from the work of Dyke *et al.*³⁶ that the current density at the point cathode of a field emission microscope at breakdown is of the order of 10^8 amp/cm². If this value is used in (16), an estimate of the probable lower limit of d , the diameter of the cathode site from which the beam is emitted, is obtained. For the specimens studied, d is of the order of 10^{-6} cm. Since the electrodes were polished with $\frac{1}{4}$ - μ diamond paste, the probable maximum value of d is of the order of 10^{-5} cm.

These values, together with the measurements of the anode shallow craters, show that the electron beam diameter at the anode is such that the value of R is probably about 200.

C. Estimation of Real Radius of Electron Beam at Anode

The values of b enable ρ to be calculated from (17). The value of r was obtained from $(y_m - \rho)/R = r$ in which $R = 200$. The values of ρ were then used in (14) to give values of y_r . A typical value of y_r is 1×10^{-4} cm. A fraction of the value of ρ might be expected to arise in the method of making the measurements of the erosion marks, since the technique involved measuring shallow crater diameters from the middle of the surrounding rim. Both the measured rim thickness and the values of ρ were of the order of 10^{-5} cm.

D. Values of Critical Power Flux

Values of E may now be arrived at from two different directions. From one direction, measurements of breakdown voltage appropriate to various gap lengths give data which, when used in Eq. (9), enable E to be calculated for each gap investigated; from the other direction, measurements of the shallow craters formed on the anode surface also lead to values of E for each gap investigated. This latter route is through the value of a which enables I to be calculated for use in the equation.

$$E = VI/\pi y_r^2, \quad (18)$$

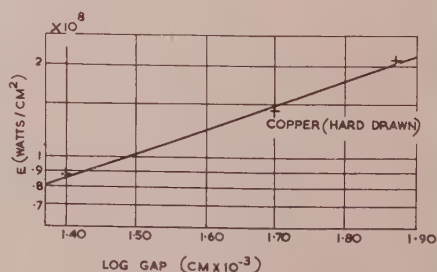


FIG. 11. Relationship between critical power flux and gap (field not constant).

³⁴ D. S. Clifford, Ph.D. thesis, University of London, 1952.

³⁵ W. K. Mansfield and R. L. Fortescue, Brit. J. Appl. Phys. 8, 73 (1957).

³⁶ W. P. Dyke, J. K. Trolan, E. E. Martin, and J. P. Barbour, Phys. Rev. 91, 1043 (1953).

where V is the mean voltage which initiates breakdown. The values of E derived from Eqs. (9) and (18) are of the order 10^8 w cm $^{-2}$ and agree within a factor of 1.5. This agreement is evidence supporting the validity of the concepts which led to the development of the two equations, and which relate them.

Analysis² of the results of previous investigators give values of the order of 10^8 w cm $^{-2}$ for E .

E. Verification of the General Expression for α

The values of E derived independently of Eq. (9) provided a means of testing the validity of Eqs. (10) and (11) and their application to give Eq. (13), the general expression for α . Approximate values for θ_1 and θ_2 for copper (hard drawn) were derived from Figs. 10 and 11, respectively, to give the values of α shown in Table I. The other values of α were each derived from two experimental points.

It can be seen that the general expression for α gives values which agree well with those calculated from the $\log V - \log x$ graphs of the experimental results.

F. Critical Power Flux and Values of α in Relation to Breakdown Probability

Figure 12 shows a typical result of breakdown studies in which, at each gap setting, 10 pulses were applied at each voltage increment, the increments being 1 kv. The minimum voltage at which a breakdown occurred during a sequence of 10 pulses was recorded together with the voltage at which 10 pulses caused 10 discharges.

The results represent voltages for which the breakdown probability is approximately 0.1 and 1, respectively. The values of α are $\alpha_{0.1}=0.754$ and $\alpha_{0.1}=0.797$; the values of E , $E_{0.1}=0.99 \times 10^8$ w cm $^{-2}$ and $E_{0.1}=0.74 \times 10^8$ w cm $^{-2}$. These values were calculated by the method of least squares and are typical of a large number of results from similar experiments with various materials. These results show that a choice of breakdown criteria based on probability does not alter the form of the breakdown equation obtained and does not alter the value of α , though the value obtained for E is altered, as would be expected.

TABLE I. Experimental verification of the general expression for α .

Specimen	Experimental points used (cm)	ϕ	θ	α exptl.	α from Eq. (13)
Copper (hard drawn)	0.025-0.050-0.075 Figs. 10 and 11	0.39	3.28	1.10	1.13
Copper (vacuum cast)	0.025-0.050 0.050-0.075	0.12 -0.10	-0.95 0.53	0.88 0.81	0.89 0.70
Molybdenum	0.025-0.050 0.050-0.075	0.22 -0.24	-12.9 0.56	0.98 0.59	0.99 0.62

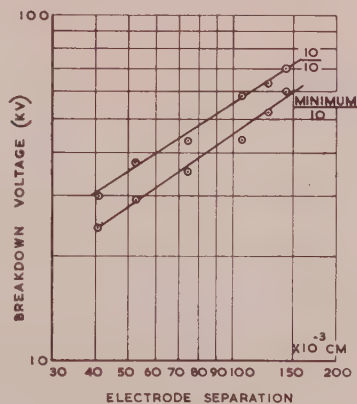


Fig. 12. Influence of breakdown probability on values of α and E .

G. Number of Shallow Craters Formed per Discharge

A Vickers microscope was used to measure the diameter of each gross spot photographed. To measure the diameter, the reference points were taken as the estimated midpoints of the peripheral regions of each spot. From each photograph, a mean value for y_m was obtained from five shallow craters chosen at random.

From these measurements the following information was obtained for use in the arguments developed in the discussion. The diameters of the gross spots were found to increase with the diameters of the shallow craters. From the diameters the number n of shallow craters forming each gross spot was obtained. The ratio n (max)/ n (min) varied between 1.8 and 3.8 with a mean of 2.5. The number of shallow craters constituting a gross spot is shown in Fig. 13 to be a function of the voltage applied.

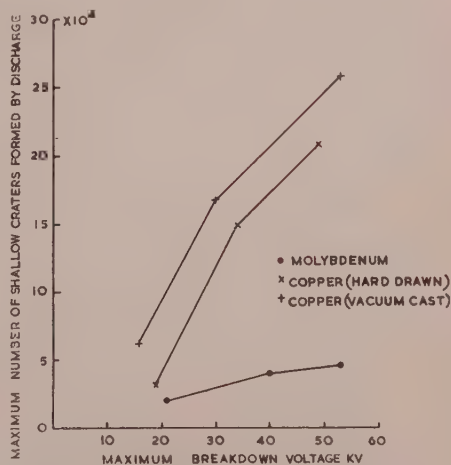


Fig. 13. Influence of voltage on number of shallow craters produced by a discharge.

V. DISCUSSION

In deriving Eq. (9), the following basic assumptions were made: A beam of electrons is emitted from the cathode under certain simplifying conditions to produce vaporization of anode material, thus forming a crater and initiating breakdown when the power flux at the bombarded anode site reaches a certain critical value E .

The verification of Eq. (15), as presented in Fig. 9, indicates that the assumptions made concerning the shallow craters are probably correct. The close agreement of the experimental results with the form of Eq. (15), together with the accuracy of the predictions made by using the measured values of a and b , provide strong evidence in support of the application to breakdown in vacuum of the concepts which led to Eq. (9) and justifies the use of (5) in developing Eq. (9). The question now arises as to whether the electron beam is present only in the initial stages of the discharge, or whether it persists throughout the discharge.

Figures 5-7 are typical of the structure of gross erosion marks, Figs. 3 and 4, caused by a single discharge. Inspection of the photographs shows that the areas displayed are covered with the shallow craters, and in fact the whole area of a gross erosion mark, with the exception of the peripheral regions, is made up of these shallow craters. The appearance of the shallow craters is such that they each seem to be formed individually; some may be seen to overlap. The number of shallow craters constituting a gross spot is about 10^5 .

To explain the formation of such large numbers of separate shallow craters, three possibilities arise; that the craters are formed consecutively, simultaneously, or by a process in which simultaneous and consecutive formation are combined. The first possibility implies that the craters are formed by a single electron beam. The second and third possibilities imply that the craters are produced by a multiple beam system.

The maximum duration of the main discharge current of the order of 1 amp, passed when the main discharge channel has been established, is 4.5 μsec . If the shallow craters are formed consecutively, and throughout the discharge period, their frequency of formation is of the order of 10^{10} sec^{-1} . The frequency 10^{10} sec^{-1} is such that 10^{-10} sec is available to vaporize the anode material and thus form a shallow crater. When this formative time is calculated from the maximum power available in the beam to vaporize a hemispherical volume of material, neglecting heat losses by conduction and radiation, the time required is 10^{-10} to 10^{-9} sec . The maximum power available was calculated from the current carried by the beam (10^{-4} amp, Sec. IV.B) and the voltage accelerating the beam when breakdown is initiated, i.e., the breakdown voltage. This point is referred to again below. Thus, consideration of the maximum power available for the vaporization of anode material precludes higher frequencies than those of the order of $10^{-10} \text{ sec}^{-1}$ and therefore indicates that if only

one electron beam forms the shallow craters, it is present throughout the discharge, and the discharge must last 4.5 μsec . The consequences of this deduction show that the consecutive formation of the shallow craters by a single electron beam is improbable. These consequences will now be discussed.

The estimate of the formative time of the shallow craters to agree with the deduced frequency of formation was based on the maximum power available. Since it has been shown that the beam must necessarily be present throughout a 4.5 μsec discharge, and since considerations of the dimensions of the shallow crater indicate that the beam is accelerated by a voltage equal to the breakdown voltage, this voltage must accelerate the beam for the duration of the discharge. This deduction does not agree with the voltage measured across the discharge.

If the shallow craters are formed consecutively by a single electron beam existing for the duration of the discharge, the number of shallow craters formed by each discharge should be closely related to the duration of each discharge. The discharge duration has been observed to vary from a fraction of a microsecond to 4.5 μsec , giving a possible scatter of at least a factor of 1 between the possible minimum number and the possible maximum number of shallow craters formed in each gross spot. Throughout the experiments the greatest value found for this factor was 3.8 and the mean value was 2.5. These values are too small to be explained in terms of variation in discharge duration. The range of voltages used to produce the gross spots could account for the scatter observed in each case, since Fig. 1 shows that the number of shallow craters formed is a function of the voltage applied.

Thus, from the argument and evidence presented above, the hypothesis of a single electron beam forming shallow craters consecutively is untenable.

The possibility of simultaneous formation of the craters will now be considered. If each crater is formed by an electron beam, then, in the extreme case, of the order of 10^4 electron beams exist simultaneously. It is suggested that the small amount of scatter present in the number of shallow craters produced, and the general consistency of the features of this scatter, is evidence supporting the hypothesis of a multiple beam system. It is suggested that when the prebreakdown current carried by one electron beam reaches a value such that a critical current density at the site of emission at the cathode is exceeded, a spontaneous, catastrophic division of the emitting site takes place so that a multiple beam system is established, each beam carrying a current, the value of which is dictated by the requirement that the critical density at the site of emission is not exceeded. If the value of the current is taken as 10^{-4} amp (Sec. IV.B) and 10^4 beams exist simultaneously, the current carried by the system is 1 amp. The voltage accelerating the electron beams has been taken as that

of the breakdown voltage. It remains now to show that the electrode system can maintain the breakdown voltage while delivering a current of 1 amp for sufficient time to enable each beam to form a shallow crater. Consider the copper (hard drawn) specimen for which $I = 2 \times 10^{-4}$ amp (Sec. IV.B), $V = 53$ kv (maximum breakdown voltage), and $n = 25.9 \times 10^4$. The beam system carries a current of 52 amp and has an impedance of approximately 10^3 ohm. The capacity of the electrodes alone has a minimum value of one picofarad and so the period over which the beam system may be accelerated by voltages greater than 90% of the full breakdown voltage is of the order of 10^{-10} sec. Thus, even in this extreme case, the electrode capacity charged to the breakdown voltage is sufficient to maintain the voltage and current of the multiple beam system for a period long enough to form shallow craters. The bombardment of the anode by a multiple system of electron beams probably lasts for a period of 10^{-8} to 10^{-10} sec at the start of the discharge, depending upon the number of beams constituting the system. An estimate of the possible number of beams may be deduced from the results of Boyle *et al.*⁵ who observed prebreakdown currents up to a maximum of the order of 10 ma using 1- μ sec pulses. Currents of this order could be due to a multiple system consisting of 100 beams, each beam carrying 10^{-4} amp.

Additional evidence favoring the existence of a multiple beam system producing vaporization for a fraction of the discharge period is supplied by the work of Snoddy,¹⁵ who obtained streak photographs of impulsive breakdown between copper electrodes. The photographs showed that luminosity started at the anode 1 to 2×10^{-7} sec before that at the cathode and lasted from 1 to 4×10^{-7} sec only, while the luminosity at the cathode lasted throughout the discharge. The anode did not remain luminous unless the current was very large. Chiles¹⁸ obtained photographs which showed that luminosity at the anode appeared 1 to 4×10^{-8} sec before it appeared at the cathode. The photographs also showed that the luminosity at the cathode persisted for a longer period than that at the anode and confirmed the results of Snoddy.

It is suggested that once a vapor cloud has been established at the anode by the electron beams the discharge mechanism changes. The vapor produced by the electron bombardment is at high pressure and therefore the electrons lose energy by collision and are scattered before impinging on the anode surface, thus terminating the production of the shallow craters which are characteristic of the beam bombardment. Each cloud of metal vapor is subjected to bombardment by a high-energy electron beam. It is suggested that this bombardment of the vapor produces ionization and electron

avalanches in the vapor as the cloud migrates across the gap, away from the anode, under the influence of the field and diffusion processes. The short duration of luminosity at the anode lends support to these views.

The critical power flux E at which the electron beams bombarding the anode lead to vaporization and breakdown is a parameter which is intimately related to conditions at the anode surface, such as surface micrography, gas content, chemical composition, and presence of adsorbed and chemisorbed films; it was shown in Sec. IV.F that the value obtained in a given experiment is dependent on the breakdown criterion selected.

It has been shown in Figs. 10 and 11 that other conditions which may influence the value of E are electrode separation and field. These may or may not influence E independently of each other; the experiments do not resolve this question. Furthermore, the form of the functions introduced, while agreeing fairly well with experiment, are clearly only crude approximations. Further investigation, both theoretical and experimental, into the true form of the functions is necessary so that an accurate expression for α may be determined. It is suggested that one of the criteria which should be used in assessing the validity and usefulness of any theory purporting to summarize vacuum breakdown phenomena is that the theory should hold within its structure an explanation of the different values of α .

The measurements of E provide information about the surface of an electrode in relation to electrical breakdown and so may be used in studying the effects of conditioning processes. The existing information relating to conditioning is in the form of the higher breakdown voltages which the conditioning processes give.

Throughout the present investigation attention has been focused on the anode phenomena although it is realized that anode events, on the basis of the theory presented, constitute the second stage of the breakdown process, the first stage being the emission of electrons from the cathode. In formulating a complete breakdown theory, the first events which occur at the cathode must obviously be considered, but it is the conditions existing at the anode which determine whether the emission from the cathode leads to the development of a discharge.

ACKNOWLEDGMENTS

The author wishes to thank Sir Willis Jackson, F.R.S., Director of Research and Education, Associated Electrical Industries (Manchester) Ltd., for permission to publish, and to express his appreciation to Dr. K. Phillips, Dr. E. Kuffel, Mr. E. W. Durham, and Mr. A. Watson for many stimulating discussions.

Excess Noise in Germanium and Gallium-Arsenide Esaki Diodes in the Negative Resistance Region

M. D. MONTGOMERY

U. S. Naval Research Laboratory, Washington, D. C.

(Received May 1, 1961; in final form, June 12, 1961)

Low-frequency noise measurements have been made throughout the entire useful bias range of germanium and GaAs Esaki diodes. Evidence is presented in agreement with Esaki and Yajima that a near square-law relationship exists between the mean-square, short-circuit noise current and excess current for bias voltages beyond the valley voltage in germanium diodes. Attempts to find a like relationship in GaAs were not conclusive. Measurements of the noise within the negative-resistance regions of the diodes showed a nearly continuous exponential relationship between excess noise and bias for the germanium units and a similar plot was obtained for the GaAs diodes, except a well-defined peak in the noise current was found at about 0.2 v forward bias. The evidence that the results indicate a rather continuous distribution of allowed states in the forbidden band of the germanium samples and a possible localized maximum in these states in the GaAs samples is discussed.

A STRONG relationship between excess noise ($1/f$ noise) and excess current¹ has been measured in germanium Esaki diodes.² A number of investigations have been made to determine the source of this current which is in excess of the normal injection and tunneling currents.³⁻⁵ The purpose of this paper is to describe experiments measuring the bias dependence of excess

noise in Esaki junctions at low forward biases for both germanium and GaAs diodes.

Measurements of excess noise in the negative-resistance region are drastically reduced in sensitivity because the low source resistance necessary for dc biasing shunts a large fraction of the diode noise voltage. The measurements reported here were made by using a transistorized, wide-band preamplifier with a very good noise figure at low source impedances and by averaging the output noise power for periods of several minutes at the detector.

All the noise data which are graphically presented here were taken at a frequency of 1 kc, but in each case the noise power was measured vs frequency and found to be very nearly $1/f$ in character down to the lowest frequency measured (30 cps), and up to well above 1 kc.

The results of the noise measurements on the germanium diodes are shown in Fig. 1. These diodes were fabricated with a base material of 0.0009 ohm-cm arsenic-doped germanium alloyed with a dot of $\text{In}_{1/2}\%$ Ga. This author's measurements of the excess noise plotted in Fig. 2 for bias voltages greater than the

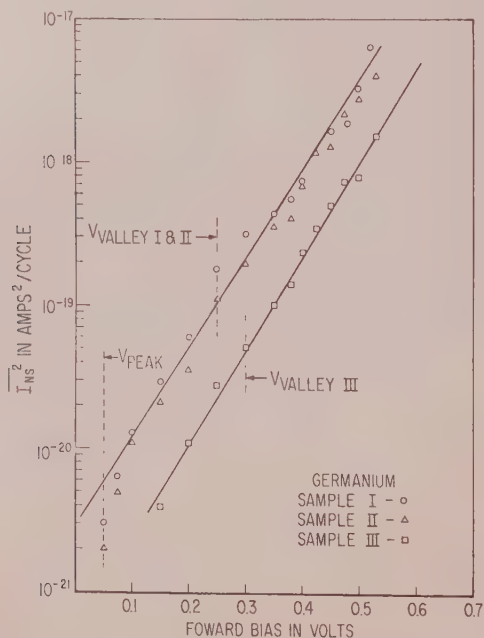


FIG. 1. Semilogarithmic plots of the observed short-circuit noise current in three germanium Esaki diodes. The peak and valley points from the I-V characteristics are indicated by markings labeled V_{peak} and V_{valley} .

¹ T. Yajima and L. Esaki, J. Phys. Soc. Japan **13**, 1281 (1958).

² L. Esaki, Phys. Rev. **109**, 603 (1958).

³ S. L. Miller, M. I. Nathan, and A. G. Smith, Phys. Rev. Letters **4**, 60 (1960).

⁴ R. A. Logan and A. G. Chynoweth, Bull. Am. Phys. Soc. **5**, 160 (1960).

⁵ R. S. Claussen, Bull. Am. Phys. Soc. **5**, 406 (1960).

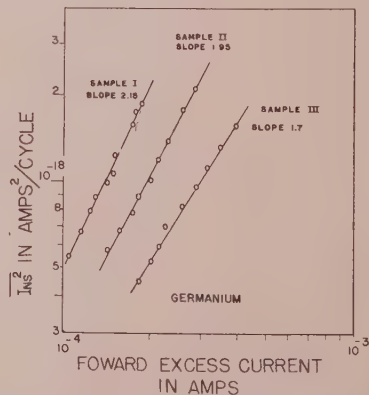


FIG. 2. Log-log plots of the observed short-circuit noise current vs excess current in the three germanium Esaki diodes whose noise characteristics appear in Fig. 1.

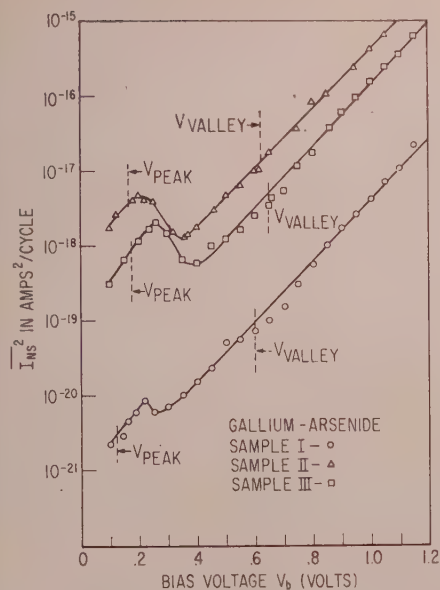


Fig. 3. Semilogarithmic plots of the observed short-circuit noise current in three gallium-arsenide Esaki diodes. The peak and valley points from the I-V characteristics are labeled.

valley voltage seem to agree with those of Esaki¹ in that a near square-law relationship between the excess current and mean-square noise current is observed. All measurements were made at room temperature. The valley current in samples I and II was of the order of $0.4 I_p$ (peak current), while that of sample III was about $0.2 I_p$ ($I_p \approx 1$ ma). It is seen from Fig. 1 that the noise power is nearly exponential with bias, but there is some tendency for the noise power to deviate from exponential in the same general way in each sample at the lower bias values. It must be pointed out that the low bias values are the least accurate.

The results of the measurements on the GaAs samples are presented in Fig. 3. These diodes were G.E. type J61-10 units. The p -type substrate crystals were Cd doped by diffusion to a level of about 6×10^{19} atoms/cm³ and alloyed with tin doped with sulfur. The doping on the n side is estimated at 4×10^{18} atoms/cm³. The I-V characteristics of the units are quite similar, but the magnitudes of the noise characteristics are quite different. In fact, little if any correlation was found between the magnitude of the valley current and the level of the observed noise characteristic in either GaAs or germanium. The seeming correlation in the chosen germanium samples is probably coincidental. It was difficult to find a strong power-law relationship between the mean-square short-circuit noise current and excess current in the GaAs diodes, because the exponential thermal-injection current (proportional to $\exp \alpha V_b$) extended relatively further into the valley current region at room temperature than did the germanium samples. As can be seen from Fig. 4, the

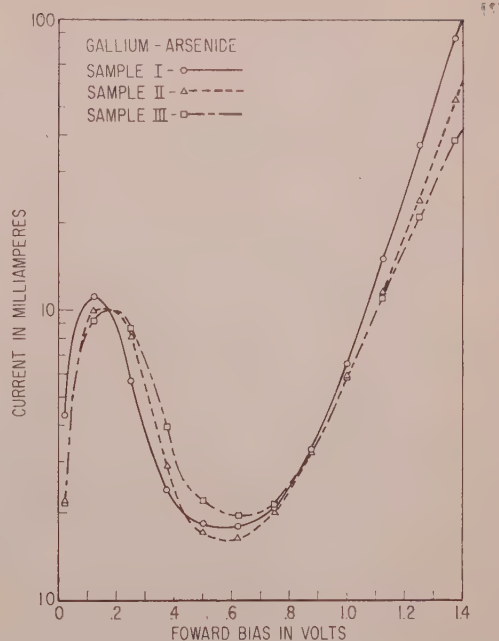


Fig. 4. Semilogarithmic plots of the forward characteristics of the gallium-arsenide Esaki diodes whose noise characteristics are shown in Fig. 3.

exponential coefficient α is only about 6 instead of 40 (q/kT), as predicted by simple theory and as was observed for the germanium samples. The excess current vs bias was, however, close to exponential over a short region of bias from 0.65 to 0.8 v, becoming flatter than exponential at both ends. The spreading resistance was about 2 ohms. The peaks in the noise characteristics at about 0.22-v forward bias were found in all samples and are discussed below.

An excess current model has been proposed by Chynoweth, Feldman, and Logan,⁶ who believe that this current is due to an internal field emission from allowed energy states in the forbidden band of the semiconductor. Following their notation, the excess current is then given by

$$I_x = AD_x P_x,$$

where D_x is the density of occupied energy levels and P_x is the tunneling probability. If we assume that for some reason or other there is a time variation in D_x , the occupancy of D_x , or in the electric potential near D_x , of the form to produce a $1/f$ spectrum as first proposed by Esaki and Yajima,¹ we then can say that the current tunneling from these levels is "tagged" by the excess noise it produces. If we now further assume that all levels (D_x) are equally noisy, i.e., that the magnitude of the time variations in D_x do not depend on energy, we may say that a known and useful

⁶ A. G. Chynoweth, W. L. Feldmann, and R. A. Logan, Phys. Rev. **121**, 684 (1961).

relation exists between the excess current and the short circuit mean-square noise measured in this experiment. This is the power-law (power ≈ 2) relationship observed for germanium outside the negative-resistance region of the diode (plotted in Fig. 1), and there is no reason to believe that this behavior will be different within it. We will assume that this is also the case for GaAs.

The results of this experiment then indicate in the case of the germanium samples that the tunneling current from forbidden band energy levels continues to be exponential in the region where it is masked by the ordinary band-to-band tunneling current. These results seem to support the results obtained by Chynoweth *et al.* (in the case of silicon); that is, they indicate a rather continuous distribution of gap states across the so called forbidden band. These diodes showed no current peaks in their I-V characteristics other than the expected band-to-band tunneling current peak at either room temperature or 78°K.

As can be seen in Fig. 3, the noise characteristics of the GaAs samples are also very nearly exponential for all forward biases except near 0.22 v. Figure 4 indicates no "extra" current peaks and none were noted at 78°K, but it is quite probable that any peak near 0.22 v would be obscured by the ordinary tunneling current. The peaks noted in the noise characteristics cannot be explained by contact or other noise dependent on total current flow because the voltage at which they occur does not correspond to the voltage (V_p) at which the peak Esaki current occurs. The bias at which these peaks occur seems to also agree with that of one of the current peaks observed by Holonyak, Jr.⁷ It would seem, in the light of the theory of Chynoweth *et al.*, that this peak in excess noise could originate from a rather localized maximum in D_x located very close to the conduction or valence band edges. The exact reason for the formation of a localized group of "noisy" states at this energy is not known at present.

⁷ N. Holonyak, Jr. (private communication).

Physical Behavior of Photographic Grains

G. SPRAGUE

Physics Department, Cornell University, Ithaca, New York

(Received May 1960; and in final form, July 13, 1961)

A quantitative treatment of the photographic process is carried out, modeled on the Gurney Mott theory. This is extended by taking account of the distribution of photolytic silver during and after the exposure. Applications of the theory are made to some simple types of sensitizing. The most important physical parameter of a photographic grain seems to be the number of electron traps.

INTRODUCTION

THE development of photography as a practical process has inspired a great number of investigations into the precise nature of the changes caused by light in the silver halide grains of a photographic emulsion. The complexity of the physical processes involved, together with the commercial advantages of restricted knowledge, have together defeated any final explanation of the phenomena involved. The present article is an attempt to give a quantitative explanation of the physics of a photographic grain in terms of its electronic and ionic properties. Pre-quantum-mechanical treatments of the photographic process were generally based upon the behavior of grains, sensitivity specks, the latent and sublatent image, and other concepts primarily relating to the development and the action of gelatine, rather than relating to the physical processes in the grains prior to development. An attempt will be made to adhere to the conventional terminology of solid-state physics, although tentative identifications of the earlier concepts will be pointed out when they seem relevant.

The important steps in bringing a grain of a photographic emulsion (which will be called a grain) into the condition such that it will become developed seem to be as follows.

- (1) The exposing agent causes the production of one or more electron-hole pairs, perhaps with an intermediate exciton phase.^{1,2}
- (2) The electron-hole pairs are either separately trapped or else recombine, the latter process being unlikely in a commercial product.³
- (3) The trapped electrons are neutralized by interstitial silver ions, forming what will be referred to as silver atom, although it may well be a rather complex arrangement of ion, electron, and lattice impurities or defects.^{4,5}
- (4) The silver atoms either capture further conduct

¹ R. E. Peierls, *Ann. Phys.* **13**, 905 (1932).

² C. F. Goodeve and J. H. Kitchener, *Trans. Faraday Soc.* **34**, 902 (1938).

³ J. Eggert and W. Noddack, *Z. Physik* **58**, 861 (1929).

⁴ R. W. Gurney and N. F. Mott, *Proc. Roy. Soc. (London)* **164A**, 151 (1938).

⁵ J. W. Mitchell, *Repts. Progr. in Phys.* **20**, 433 (1957).

tion electrons, or decay into electrons and ions until, when the exposure is completed, the grains contain aggregates of silver atoms, of which those containing four or more silver atoms are capable of initiating development. The two- and three-atom aggregates are stable, but will not, under ordinary conditions, confer developability on the grain.

DETAILED STUDY

The first step in the study of the behavior of the photographic grain is the study of the development centers. Microscopic examination of exposed, partially developed, grains shows that the grain starts developing at one or more points, and these points were originally called sensitivity specks.⁶ The empirical facts about their behavior are simple. If one such center exists in a grain, the grain is developable; the centers are distributed randomly throughout the grain population. These two facts indicate that in any study of the photographic behavior of silver halide grains, this sensitivity center is a more fundamental unit than the grain itself. The probability of grain development may be determined by statistical means from a knowledge of the number of sensitivity centers in the grain population. These centers will be assumed to be aggregates of silver atoms, built up to a size of four or more by alternate trapping of photoelectrons and interstitial ions.

The electronic and ionic details of the formation of the silver aggregates determine, for the purposes of this article, the developability of a grain, or, in a qualitative way, the optical density of the developed film. The basic processes which must be quantitatively considered are the following:

(1) The absorption of energy by the grain, resulting in the production of an exciton, or one or more electron-hole pairs.

(2) Decomposition of the exciton into a hole and a conduction band electron.

(3) Migration of the electron to a final trap. This trap may be a positive hole, resulting in recombination.

(4) Neutralization of the trapped electron by an interstitial silver ion, forming a "silver atom."

(5) Decay of the silver atom by thermal loss of an electron.

(6) Capture by the silver atom of a second electron, which is produced either by the exposure, or by decay of another atom.

(7) Neutralization of the trapped electron by a second silver ion, producing a stable configuration.

(8), Continuation of (4) and (5) until all radiation-produced electrons fall into one of three categories;

Recombined with a hole,

Immobilized in a stable but not developable aggregate,

Immobilized in a stable, developable aggregate.

To treat all of these effects at once would lead to mathematical difficulties so great as to obscure the physical picture. For this reason certain simplifications have been introduced. They will be discussed in more detail in a later section of the article.

First, the details of steps (1)–(3) have been neglected, and it is assumed that the exposure-produced photoelectrons are immediately trapped. Although theoretically and experimentally it seems very likely that excitons are sometimes formed, their effect on the photographic process is assumed to be negligible because they disappear in a time which is short compared with the ionic neutralization time.^{7–9} The same approximation is applied to the finite lifetime of the electron in the conduction band.

The dominant feature of this part of the photographic process is assumed to be the ionic neutralization time. This is most clearly shown in studies of high-intensity reciprocity law failure. Theoretical work by Berg and by Katz, and experimental work by Webb and by Khartuzhanskii show that high intensity failure is connected with ionic conductivity.^{10–13}

Proceeding to step (5), the decay of the silver atom by loss of an electron is involved in low-intensity reciprocity law failure, and the existence of short exposures. Work by Webb and by Maerker indicates that the average life of a single silver atom in an emulsion is between 2 and 10 sec.^{14,15} Thus, for optimum or short exposures there will be no appreciable amount or decay during the exposure. For long exposures, this decay of silver atoms is the presumed cause of low-intensity reciprocity law failure. For exposures shorter than the ionic neutralization time, the decay furnishes electrons after the exposure is over to build up developable silver aggregates.

The low-intensity effects are not due solely to the decay; but to the possibility that the electron may recombine with a hole. If the electron does not recombine with a hole the result will be a redistribution of silver atoms. The fact that the decay-neutralization-decay cycle may recur means that there may be a high probability of eventual recombination, even though the chance is small in each successive electron excursion. The recombination probability will also depend upon the number of holes present, which means that the loss is apt to be greater for heavy exposures, resulting in a loss of contrast.

The capture and neutralization of successive electrons, as assumed in steps (7) and (8), is based pri-

⁷ N. F. Mott, *Nature* **175**, 234 (1955).

⁸ R. Woods, thesis, Cornell University (1949).

⁹ M. Blitz, *J. Opt. Soc. Am.* **42**, 898 (1952).

¹⁰ W. F. Berg, *Proc. Roy. Soc. (London)* **A174**, 559 (1940).

¹¹ E. Katz, thesis, University of Utrecht (1941).

¹² J. H. Webb, *J. Opt. Soc. Am.* **28**, 249 (1938).

¹³ A. L. Khartuzhanskii, *J. Exptl. and Theoret. Phys.* **26**, 763 (1954), in Russian.

¹⁴ J. H. Webb, *J. Opt. Soc. Am.* **40**, 3 (1950).

¹⁵ R. E. Maerker, *J. Opt. Soc. Am.* **44**, 625 (1954).

⁶ T. Svedberg, *Phot. J.* **62**, 186 (1922).

marily on the existence of print-out silver, although there are other relevant facts. The existence of print-out silver is definite proof that silver aggregates can act as electron traps. This is different from metallic silver behavior because there is an upper limit to the size of the aggregates. It is here assumed that there is no lower limit.

The physical results of the processes described in steps (1)–(8) are to be converted to mathematical terms and examined more quantitatively. The principle is to set up equations for the growth of various sizes of silver atom aggregates, including the processes described. The developability of a grain is determined by the statistical probability of having one or more four-atom aggregates in it. The equations of change for the average trap (site of aggregate) may be written

$$dN_i/dt = \alpha N_{i-1} - \gamma_i N_i \quad (1)$$

$$dN_i^-/dt = -\alpha N_i^- + I N_i/T \quad (2)$$

N_i is the number of traps per grain which have accumulated i silver atoms (neutralized electrons), while N_i^- is the number of traps with i atoms and an extra electron. α is the neutralization frequency. If no other processes were operating, $1/\alpha$ would be the average lifetime of a negatively charged trap, related by a constant to the ionic relaxation time. γ_i is the decay frequency of the i -atom aggregate, and will generally be assumed to be zero except for one atom traps. I represents the number of electrons trapped (produced) per grain per second. This number is a function of time, since it contains the exposure interval as well as the generation of electrons from decay of single aggregates. T is the number of electron traps per grain, and N_i/T is the probability that an electron will reach an N_i trap.

If the aggregates are distributed throughout the grains according to a Poisson distribution, the fraction of developable grains is

$$F = 1 - e^{-A}; \quad A = \sum_{i=4}^{\infty} N_i(t \rightarrow \infty), \quad (3)$$

it being assumed that the grain has reached an equilibrium state before it is developed.

The Poisson distribution is a special case of the binomial, being applicable when the probability of a single traps' becoming developable is small. In modern fast emulsions this is no longer true, and the binomial probability distribution is required. The Poisson formulas will still be used here, since much of the data used will refer to older emulsions.

All the difficulties in the system of equations arise from the intensity term, which may be time dependent, and contains the contribution of electrons from the decaying single atoms, making the equations nonlinear. It is practical to treat the nonlinearity and the time dependence separately, because most of the single atom

decay occurs after the exposure is over. This will be referred to as the post exposure case and treated first.

It will be assumed that the only source of electrons is the decay of single atoms. Thus the atoms decay and new atoms, or multi-atom aggregates are formed. For this study no account of the electronic details is needed, and the equations for the aggregate growth become

$$dN_i/dt = (N_{i-1} - N_i) N_1 \gamma / T;$$

$$i > 1: dN_1/dt = -N_1 \gamma \sum_{i=2}^{\infty} N_i / T, \quad (4)$$

where $N_1 \gamma$ is the rate of electron supply, and N_i/T is the probability that an electron goes to an i -type trap, or, equivalently, the probability that an i -type aggregate increases in size. Each size of aggregate is increased from below, and loses by advancing to a higher state of aggregation. The nonlinearity is confined to the equation for N_1 , and can be removed by replacing

$$\sum_{i=2}^{\infty} N_i$$

by $N_1(0)/\delta$, where δ is the average size of an aggregate. δ will be assumed to be a constant, although it actually must start equal to 1 and increase to about 2.5. The time variation will not be correct, but the final state will not be so bad.

The solutions for the modified equations are

$$N_1(t) = N_1(0) e^{-\beta t}; \quad \beta = \gamma N_1(0) / T \delta;$$

$$N_i(t) = N_i(0) \exp[-\delta(1 - e^{-\beta t})] + \beta \delta \exp \delta e^{-\beta t}$$

$$\times \int_0^t N_{i-1} \exp[-\beta x - e^{-\beta x}] dx. \quad (5)$$

For the present purposes there is no need to determine any higher members of the solution than N_3 . The number of aggregates of more than three atoms can most easily be determined by comparing the lower aggregates with the total amount of silver in the grain. As an illustrative example, some data taken by Webb will be used.¹⁶ (See Table II.) The fourth line of the table will be used, which refers to a case where the average grain received 84 quanta, and, according to the Poisson distribution would have 80 single-atom aggregates after the end of the exposure, and two double-atom aggregates. With $e^{\delta} = 10$, the equilibrium values of the two and three atom aggregates which build up from the repeated decay of the single atoms are shown in the first two lines of Table I. T , the number of electron traps per grain, was set equal to 1500, for reasons which will be explained in connection with Table II. γ was set equal to $1/10$, a convenient number taken from the data of Webb and Maerker referred to earlier.

¹⁶ J. H. Webb, J. Opt. Soc. Am. **38**, 312 (1948).

TABLE I. Aggregate distribution.

Aggregate number	from $N_1(0)$	from $N_2(0)$	Total
N_2	12	0.2	12
N_3	16	0.5	17
N_4	0.1	2.0	2.1

The values of N_4 were determined from the requirement that the total silver should add up to 84 quanta, so it automatically contains the higher aggregates also, although there are not apt to be many.

There are two important features of Table II, which are seldom stressed in photographic theory. The first is that the total number of developable aggregates after the exposure and rearrangement have reached equilibrium is about the same as the number of initial two atom aggregates. This is not coincidence, as is shown by the relative contributions of the initial single- and double-atom aggregates. This fact leads to an apparent importance of two atom aggregates.

The other feature is the mechanism of high-intensity reciprocity law failure. The amount of failure is determined by the disparity between the contributions from the initial single and double atom traps, which is, in turn, dependent upon the number of available traps (or aggregates) available in the original grain. In particular, the amount of high-intensity failure can be reduced by reducing the number of electron traps in the original grain.

The purpose behind treating the post-exposure approximation first was to make it reasonable to concentrate attention on the two-atom aggregates. There are many pieces of experimental evidence which indicate that the two-atom aggregate is a critical point in the photographic process, aside from the estimates shown in Table I. In the following sections, therefore, the post-exposure behavior of the grain will be neglected, and the emphasis will be placed upon the growth of two-atom aggregates during the exposure. When the equations have been studied, the experimental evidence will be examined.

Assuming that the two-atom aggregates formed by an exposure are distributed among the grain population according to a Poisson distribution, and that any grain with such an aggregate is developable, the fraction of developable grains is given by

$$f = 1 - e^{-N_2}, \quad (6)$$

where N_2 is the average number of two-atom aggregates per grain at the end of the exposure. The equations for the formation of the various relevant complexes are (1) and (2), except that it is assumed that γ_2 is zero, implying that two-atom aggregates are stable. N_0 is the total number of unoccupied traps, and equals the total T minus charged and uncharged traps of other kinds.

The exposure is given by I , standing for intensity,

TABLE II.

N	F	A	$T(R=2)$	$T(R=3)$	N_2	N_3
10	0.03	0.03	1600	75	0.03	0.000006
20	0.12	0.12	1900	110	0.12	0.00002
40	0.50	0.50	1100	120	0.5	0.00008
84	0.90	2.30	1500	210	2.3	0.0004
128	0.99	4.61	1800	280	4.61	0.0008

and measured in terms of absorbed photons, (produced conduction band electrons) per grain per second. The contribution from decaying single atoms will be neglected.

The equations are now reduced to four simultaneous first-order differential equations in four unknowns. They can be solved in terms of La Place transforms.¹⁷ Denoting the transforms by L , the fundamental relations are

$$L_0^-(x) = \int_0^\infty N_0^-(x) \exp(-tx) dt;$$

$$xN(0) - L(x) = \int_0^\infty [dN(x)/dx] e^{-xt} dt. \quad (7)$$

Multiplying the equations by e^{-tx} and integrating from zero to infinity, the simultaneous equations for the transforms become

$$\begin{aligned} -L_0^- &= -\alpha L_0^- + i/x - (i/T)(L_0^- + L_1^- + L_2^-) \\ -L_1^- &= \alpha L_0^- - \gamma L_1^- \\ -L_1^- &= -\alpha L_1^- + (i/T)L_1^- \\ -L_2^- &= \alpha L_1^-. \end{aligned} \quad (8)$$

These equations can be solved for L_2 by means of determinants, giving,

$$L_2 = (i^2/Tx) [x(x + \alpha + iT + 1)(x, \alpha + 1)(x + \gamma + i/T) + x\{i^2/\alpha T^2 + i^2/T^2 + (i/T)(x/\alpha + 1)\}]^{-1}. \quad (9)$$

This transform can be inverted in closed form, but the result is not enlightening. It is more instructive to study the various limiting cases of large, medium, or small intensity i , which correspond to the various kinds of reciprocity failure. (The exposure has been assumed to be of constant intensity. The case of intermittent exposures can be studied the same way, but the mathematics become considerably more complex.)

OPTIMUM CONDITIONS

If the causes of reciprocity failure were removed, the so-called optimum speed would result. This can be accomplished in the mathematical problem by setting $\alpha = \infty$ (immediate neutralization) and $\gamma = 0$ (no decay and loss of electrons). The transform then becomes

$$L_2 = (i^2/T) [x(x + i/T)^2]^{-1}. \quad (10)$$

¹⁷ G. Doetsch, *Theorie und Anwendung der La Place Transformation* (Dover Publications, New York, 1943).

This is easily inverted, giving

$$N_2(t) = T[1 - e^{-it/T}(1 + it/T)]. \quad (11)$$

This expression will be discussed further later, but two things should be noticed. The first is that the intensity only occurs multiplied by the exposure time, meaning no reciprocity failure. The second is that the expression in the brackets is the Poisson probability of achieving a two-atom aggregate, when the exposure per trap is it/T .

LOW-INTENSITY CONDITIONS

Neglecting high-intensity troubles as before, by setting $\alpha=0$, and assuming that the exposing intensity is sufficiently small to be negligible compared with any constants, the transform becomes

$$L_2 = (i^2/x^2)(x + \gamma)^{-1}, \quad (12)$$

and the low-intensity solution is

$$N_2(t) = (i^2/T)[t/\gamma - (1 - e^{-\gamma t})/\gamma^2]. \quad (13)$$

For very long exposures, the exponential term will vanish, and the approximate form of the expression is

$$N_2 \approx i^2 t / \gamma T. \quad (14)$$

Both (13) and (14) show reciprocity law failure; that is, the value of the number of two-atom aggregates per grain is not dependent simply on some function of the product of the intensity and the exposure.

HIGH-INTENSITY CONDITIONS

An intermediate high-intensity expression can be obtained, covering the region between the extremely short exposure covered in the post-exposure approximation, and the optimum region covered above. γ is set equal to zero and it is assumed that the intensity is high enough to permit the neglect of constants compared to the intensity terms. Then

$$L_2 = (\alpha^2 t/x)(x + \alpha)^{-2} \quad (15)$$

and

$$N_2(t) = T[1 - (1 + \alpha t)e^{-\alpha t}]. \quad (16)$$

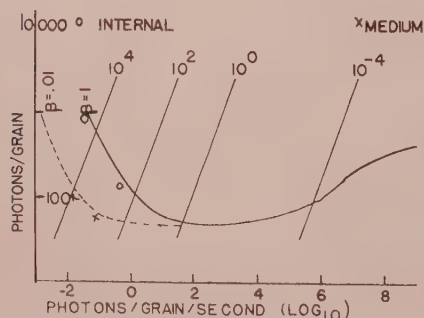


FIG. 1. Reciprocity failure.

The results of these calculations are plotted in Fig. 1. T was set equal to 1600; $\alpha=10^5$; $\gamma=\beta/10$, where β is the probability of recombination with a hole. This was not included in Eqs. (1) and (2), and was not included in the study of the post exposure effect, since in that case silver was removed from the picture by forming stable aggregates. It is necessary to introduce it here because the exposure term no longer contains the non linear term. The graphs are shown for two values of β , the maximum value of 1, and a desirable value of 0.01.

DISCUSSION

At this point it seems appropriate to discuss more fully the reasons behind the use of the equations which have just been solved, especially with regard to the importance which has been attached to the four-atom aggregate, and transferred to the two-atom aggregate. First of all, it will be valuable to examine two pieces of experimental data bearing on the question.

From the experimental facts that an emulsion grain is developable if there is one development center in it, and that the centers are distributed according to a Poisson distribution, it is possible to write out expressions for the fraction of developable grains, and the average number of centers per grain. These expressions are given in Eq. (3), assuming that the critical number is four. However, this critical number can be determined from experimental data taken by Webb.¹⁶ These data consist of the determination of the fraction of grains which become developable as a function of the number of absorbed photons per grain. Several values of the fraction (f) and the number of absorbed photons (N) are listed in the first two columns of Table II. The third column shows (A) as calculated from Eq. (3). (A) is actually the number of developable traps per grain, on the average. This can be calculated from the Poisson distribution, when the average number of absorbed photons (=silver atoms) per trap is known and when the critical size is known. The expression is

$$A = T \left[\sum_{i=R}^{\infty} (N/T)^i / i! \right] e^{-N/T}, \quad (17)$$

where R is the critical number for developability, and T is the unknown number of electron traps in the grain. The fourth column of Table II shows the value of T calculated for each value of N and A , for $R=2$, while the fifth column shows T for $R=3$. The sixth and seventh columns show the expected number of two and three atom aggregates when the average number of photons per trap is $N/1600$.

Since the number of traps in an emulsion grain is an inherent property of the grain, not of the exposure, the correct value of R is the one which gives a constant value of T , or $R=2$. The fluctuations are ascribable to the random nature of the process, but in spite of them it is clear that the calculated number of traps is dependent on the exposure when it is assumed that $R=3$.

Equation (17) and Eq. (11) are identical, if N_2 is identified with A , and the number of photons with the product of the intensity and the time. It is a property of the Poisson distribution that

$$1 = \sum_{i=0}^{\infty} [(N/T)^i / i!] e^{-N/T}. \quad (18)$$

If no other evidence were available, it would be permissible to assume that a two-atom aggregate would make a grain developable; but other evidence is available. A more accurate statement is that developability will result when a grain has a two-atom aggregate, and some single atoms, at the end of the exposure.

Another evidence of the importance of the two-atom aggregate is furnished by the theoretical and experimental work on low-intensity reciprocity law failure.^{18,19} It is a property of theories which postulate an important place for a two-atom aggregate, or a two-hit sublatent image, that the low intensity reciprocity law curves approach a limiting slope of minus one. This is shown for the present method in Eq. (14) and in Fig. 1. Experimental emulsions seem to show the same limiting slope, unless other effects are present.

Both of the foregoing effects are of great importance to any theory of the photographic effect, since they are largely independent of the model used, depending solely on statistical laws. Any theory with a proper statistical basis will therefore agree with these experiments, and such agreement must not be overemphasized.

The distinction between a two-atom aggregate, which is assumed to be stable, and a four-atom aggregate which is assumed to be stable and developable, is made necessary by the existence of the Herschel and Becquerel effects. In the latter effect, a silver halide emulsion is made sensitive to green light by giving a blue previous exposure. This implies, and experiments²⁰ confirm, that there are present, in the pre-exposed grain, silver aggregates of stable, but not developable size, which, incidentally, absorb farther into the green than the original silver halide grain. The Becquerel effect thus constitutes evidence for the presence of stable, but not developable, silver aggregates.

The Herschel effect²¹ consists of bleaching or destroying the developable aggregates by means of exposure to red light. The different spectral regions involved in these two effects indicate that the developable aggregate, which is destroyed, is different from the undevelopable aggregate of the Becquerel effect. (It should be mentioned here that the proper interpretation of the two effects is that it is in the red region that the absorptions of the two types of aggregate are different.

The experimental evidence is not clear on the short wavelength limits of either effect.)

It is here assumed that the differing absorptions are related to different states of aggregation, rather than to different positions in the grain, or some other easily realizable difference. With this assumption, the question of the necessary size can be rapidly answered.

First it is necessary to test the hypothesis that the three-atom aggregate is developable, and the two-atom one is stable, and the basis of the Becquerel effect. Under this hypothesis, an exposed, developable grain would contain a mixture of two- and three-atom aggregates. The action of a Herschel exposure would be to eject an electron from a three-atom aggregate, and, presumably, the ion would migrate away. However, the electron would go to a two-atom aggregate, attract another ion, and restore the original condition. The smallest size aggregate, subject to the assumptions of the model being studied here, which will permit Herschel effects, is the four-atom aggregate. To decide decisively against a five-atom aggregate being the smallest developable one, it would be necessary to make a more accurate study of the solutions of Eq. (4).

There are two further experimental and theoretical features of this aggregate model which deserve consideration and explanation. The outstanding facts have already been mentioned, consisting of the fact that the larger aggregates have a smaller electron affinity for the last electron than the smaller ones. This tendency is carried to its logical extreme in the print-out effect, in which extremely heavy exposures built up visible amounts of silver in the grains. Microscopic examination of these grains shows that a very large number of small separate aggregates are present in a printed-out grain, rather than a few very large ones, such as result from the partial development studies. This indicates that when the aggregates reach a certain size they no longer capture electrons. This is substantiated by the Haynes-Shockley type experiments on large silver halide crystals.²² In these latter, visible amounts of silver are formed in the crystals by exposures to light, but the silver does not affect the electron range, since the Hall mobility and the ordinary mobility agree. Since the Herschel effect occurs, to some degree, in many, if not all emulsions, and the Haynes Shockley experiments show reasonable electron mobilities in many varieties of silver halide-with-additive crystals, this phenomenon of decreasing electron affinity must be rather general and not due to any detailed feature of the silver halide. It can only be true of small aggregates, in the sense that when the aggregate becomes large enough, it will have metallic properties, and will always attract electric charges of either sign. The limiting size for metallic attraction is probably related to the size where the electrostatic potential energy of an electronic charge on a metal sphere is equal to KT , the thermal energy. This

¹⁸ J. H. Webb, *J. Opt. Soc. Am.*, **40**, 3 (1950).

¹⁹ W. J. Albersheim, *J. Soc. Motion Picture Engrs.*, **32**, 79 (1939).

²⁰ F. Weigert, *Sitzber. preuss. Akad. Wiss., Physik. math. Kl.* **641** (1921).

²¹ J. H. Webb and C. H. Evans, *J. Opt. Soc. Am.*, **28**, 249 (1938).

²² J. Haynes and W. Shockley, *Phys. Rev.*, **82**, 935 (1951).

is roughly a 100-Å sphere. Below this the aggregate may apparently be nonmetallic, and an attempt has been made to calculate the electron affinity directly.

Since the exact nature of the original trapping center is not known, and since a multi-electron problem is involved, an exact calculation is out of the question. The statistical atom treatment will be used, using the variational form as outlined by Gombas.²² The basic result is that if the initial trap involves a limited region of the lattice and the interstitial ion can only reach the outer part of this region, then the binding energy for successive electrons decreases due to the rapid increase of the Fermi repulsion. The limitation on the motion of the ions prevents the large contribution to the binding energy which is supplied by the nucleus in the atomic case. The positive charges are spread throughout a region, rather than concentrated in one point.

The energy integral to be minimized is²³

$$E = x_K \int \varphi^{10/3} d\tau - x_a \int \varphi^8 d\tau - \int V e \varphi^2 d\tau. \quad (19)$$

The x 's are constants and $\int \varphi^2 d\tau = N$, the number of atoms in the aggregate. The units to be used will be electron volts. The first integral represents the Fermi energy, arising from the Fermi statistics of the electrons; the second represents an exchange correction, and the third is the classical electrostatic energy. Other terms are discussed by Gombas, but are not important here and are omitted for simplicity. To minimize (19) it is necessary to select an analytic form for the function φ , evaluate the integrals, and minimize the resulting expression with respect to the parameters of the trial function. The work is not interesting, and the results will be presented without detailed calculations. For mathematical reasons the trial function was chosen to be Ae^{-ar} . For the various integrals $d\tau = 4\pi r^2 dr$. The electrostatic term should be determined by solving Poisson's differential equation, but a different method was used.

The electrical configuration consists of the original trap, characterized as a coulomb trap containing half a positive charge in a medium of dielectric coefficient 4.5; the attracted interstitial ions which are considered to occupy a sphere half a lattice spacing away from the trap center; and the electrons which are assumed to be distributed throughout the region. In evaluating the electrostatic energy, these electrons were assumed to lie on a shell coincident with the ions, which would be the final configuration in the macroscopic case. The energy is then easy to compute. The result is

$$E = 13.6 (0.3 V^{1/2} Q - 0.5 N \epsilon F - 0.1 N Q - 0.2 N^{1/2} Q) \quad Q = A_0 \alpha, \quad (20)$$

²² P. Gombas, *Die Statistische Theorie des Atoms* (Interscience Publishers, Inc., New York, 1950), p. 115.

where A_0 is the Bohr radius. This expression must be minimized with respect to Q for each N , and a value of the binding energy of the last electron determined. Values of the change of energy with N for two values are given below. For smaller

N	dE/dN
8	0.5
125	0

values of N the value of the energy increase levels off, and even drops for $N=1$. This could be changed by changing some of the parameters, but the main result remains—namely that the binding energy decreases with increasing N (due to the Fermi term), and that the amount is dependent, but not simply, on keeping the positive charges from concentrating at the center of the trap. This result is in agreement with the print-out data, and the trend is right for the Herschel and Becquerel effects, but the statistical model is not valid for such small numbers.

Aside from the growth and importance of various aggregates, the fundamental model of the photographic process used here is based upon the electron trapping and neutralization by interstitial ions. This point will not be discussed further here, since it seems established best by the work of Hamilton and Brady²⁴ in their work on the location of the aggregates as a function of the applied electric field.

APPLICATIONS

The results obtained can be used to study various photographic effects, and, in principle, to calculate them quantitatively, but this last is only true in the case where grain count data are available. Semiquantitative conclusions can be drawn by assuming photographic results are proportional to the number of developed grains. On this basis it is possible to gain an insight into reciprocity failure, and sensitization mechanisms, and high-energy exposing agents, which depend upon the grain parameters introduced in the aggregate equations. These parameters are

(A) γ , the fractional probability that a single silver atom will decay in one second. It has been assumed to be 1/10 in the numerical examples used here.

(B) α , the fractional probability that a trapped electron will be neutralized in one second. It has been set equal to 10^{+3} in the numerical examples.

(C) T , the number of electron traps per grain. According to the example studied, this number is about 1600 for some emulsions.

(D) β , the recombination probability for an electron. This is a derived constant, used in plotting the solutions of Eqs. (7). The γ used there differs from that used in Eq. 1, because it must include the effects of the neglected nonlinear term. The decay of a silver atom does

²⁴ J. F. Hamilton and L. E. Brady, *J. Appl. Phys.* **30**, 1893 (1959).

not lead to a loss of silver in the grain unless the electron recombines with a hole. Otherwise, the electron is retrapped and reneutralized, and the grain is unchanged.

This is equivalent to saying, in the model of Eqs. (7), that the effective decay rate is the actual one, γ , multiplied by the recombination fraction β . The curves of figure one are labelled with different values of β .

Low-intensity reciprocity law failure is due to the combined action of single atom decay, and eventual loss of electrons by recombination. Figure 1 shows that for a recombination coefficient of one, which is the theoretical maximum, the limiting slope of minus one would be attained in about a hundred seconds, whereas with a more reasonable value of 0.01, several hours would be required. Representative points for two types of emulsion are plotted in correct relative positions. The internal image was chosen because it is expected to have a high recombination rate. Low-intensity failure will be reduced by removing holes, by removing electron traps, and by lowering the rate of decay of single atoms. This last process will be temperature sensitive, and will contribute to the shift of the entire reciprocity curve to the left at reduced temperatures.

High-intensity reciprocity law failure is attributed to the time lag between electron capture and neutralization. The magnitude of the failure, as distinguished from the cause, is determined by the number of traps again, since a large number of traps means a large number of potential sites for undevelopable silver. In principle, a grain with only one trapping site would show no reciprocity failure at high intensity, since the electrons would remain free until neutralization occurred, and would then go to the only available aggregate, one by one. This condition is approached by some modern fast emulsions.

According to the model being discussed here, the neutralization time should be the ionic conductivity relaxation time,¹⁰⁻¹³ but the work of Hamilton and Brady²⁴ indicates that things are not so simple. Grimley²⁵ and Grimley and Mott²⁶ have done some theoretical work on the interaction between the silver ion concentration of the gelatin and the silver ion concentration in the grain, and their work shows that the conductivity might change by a factor of 10^4 . The neutralization time could be reduced by altering the silver ion concentration away from the neutral point, but other effects intervene, especially fogging, and the ability of the emulsion to accept holes from the grains. At present it is not clear how to relate the bulk conductivity of silver halide crystals to the effective relaxation time of photographic grains.

The speed of an emulsion at the optimum exposure level is determined by the number of traps in the grain. This idea of competitive action between different parts

of a single grain was first advanced by Sheppard,²⁷ and seems to still be applicable. Ideally, a photographic grain should have only one trap, preferably pre-exposed to contain three silver atoms, but this condition is not yet attained. (See section on sensitization.)

The discussion so far has tacitly assumed that the exposure is to visible light, so that one photon produces one electron. The extension to high-energy radiations or particles is not difficult, and contains some interesting features. It is convenient to adopt the terminology that an exposing agent which ultimately produces more than one electron per absorption is a high energy exposure. The simultaneous production of two or more electrons in a photographic grain automatically produces high-intensity reciprocity law failure conditions. The emulsion of figure one and table two has grains that are essentially certain to be developed upon absorbing 100 photons in the visible region, or 1000 photons under high-intensity conditions. Assuming that 7.4 ev are required to produce an electron-hole pair, a 10 000-v exposure should produce certain development of a grain. This is in agreement with experiment. Minimum ionization electrons, encountered in nuclear emulsion work, may produce only 300 electrons in their passage through an emulsion grain, and when high-intensity failure is taken into account, only a small percentage of the grains which are traversed will become developable.

Soft x rays, which will here refer to those whose wavelength is greater than 40 Å, or, in more appropriate units, photons which produce less than 350 electrons, are not able to produce developability in every grain which absorbs a photon. According to the work of Tomboulou and Hartmann,²⁸ the emulsion is energy dependent in this range, showing negligible reciprocity failure even for exposures which last several hours. Charlesby²⁹ discusses evidence which shows that even 30-ev electrons do not show reciprocity failure. Apparently the redistribution of the electrons, primary and secondary, produced by the high-energy exposure, is fast enough and complete enough to permit the formation of the stable two-atom aggregates. Theoretical calculations by Tewordt³⁰ predict that the conversion of a single high-energy electron into a number of low-energy secondaries is quite efficient once the energy requirements are met, which is borne out by the results just cited. In particular, it seems that if an exposing agent can create two or more conduction electrons, reciprocity failure will not occur. For photons this means at least 15 ev, or wavelengths less than 800 Å.

A detailed study of the quantitative problem posed by intermittent exposures, even at lower intensities, has not been attempted here. It seems unlikely that such a study would be profitable except in a specific case

²⁷ F. E. Sheppard, *Phot. J.* **66**, 399 (1926).

²⁸ D. H. Tomboulou and P. Hartmann, *Phys. Rev.* **102**, 1423 (1956).

²⁹ A. Charlesby, *Proc. Phys. Soc.* **52**, 657 (1940).

³⁰ I. Tewordt, *Z. Physik* **138**, 499 (1954).

²⁵ T. B. Grimley, *Proc. Roy. Soc. (London)* **A201**, 49 (1950).
²⁶ T. B. Grimley and N. F. Mott, *Discussions Faraday Soc.* **1**, 3 (1947).

where the various physical parameters were known. The La Place transform method is still applicable, but the solution becomes even less intelligible until approximations are introduced.

SENSITIZATION

It is hard to imagine a process involving free electrons which is not strongly dependent upon the number and distribution of traps, and the photographic process is certainly no exception to the general rule. The expressions for optimum speed and degree of reciprocity law failure all involve the constant T , the number of electron traps per grain. In this section some of the possible effects of sensitization on electron trapping are discussed, with the realization that the complexities of the process of making a practical photographic emulsion are so great that most of the important features will not even be mentioned. (Two such features are the removal of holes, presumably by the gelatine, and the concentration of developable aggregates at the grain surface where the developer can reach them.)

One kind of sensitization of silver halide grains for photographic purposes is called sulfur sensitization. Sulfur compounds naturally present in gelatine led to its early pre-eminence as a vehicle for the silver halide grains, although the compounds responsible for its success were not identified for a long while. The work of Sheppard indicated that sulfur compounds were present, and for convenience it will be assumed that silver sulfide is formed on the surface of the photographic grains. The main function is to reduce recombination, as can be seen by the effect on the reciprocity failure curves.³¹ Unsensitized emulsions reach the limiting slope of -1 for low-intensity exposures much more rapidly than sensitized ones. The recombination of an electron and a hole may occur in many ways, the exact method depending upon the environment. In most materials, the main mode of recombination involves an intermediate step—the trapping of one or the other of the constituents at a trapping center. The direct recombination of the free carriers is much less likely, because of the stringency of the energy and momentum conditions. However, the commercial desirability of low recombination rates has resulted in photographic grains in which, according to quantum yield studies, recombination is effectively absent.

The elimination of recombination at trapping centers is conceivably possible, but the direct recombination cannot be avoided, and it is of interest to know how important it is in the photographic process. This can be calculated with relative accuracy by means of the principle of detailed balance,³² using the experimentally determined absorption coefficient. This same method has been used to calculate the recombination rate and

the amount of recombination radiation from electron-hole recombination in germanium by van Roosbroek and Shockley.³³ For the details of the calculation reference should be made to Fowler. The theory gives an expression for the direct recombination coefficient which involves the measured absorption coefficient. A numerical integration, using values measured by Moser of Eastman Kodak Research Laboratory, gives

$$\sigma = 10^{-28} \text{ cm}^2/\text{sec.}$$

The number of electrons lost by recombination in a time T , when the concentration of electrons and holes is N , is roughly

$$\text{loss} = \sigma N^2 T.$$

In a grain such as was studied in Table II, with dimensions of about $\frac{1}{10}$ by $\frac{1}{10}$ by 1μ , using such a high-intensity exposure that the electron lifetime is the limiting factor, the loss can be calculated. 1000 photons would, at high-intensity conditions, be required to produce the degree of developability shown in Fig. 1. N , therefore, is $1000/10^{-14}$. For an electron lifetime of ten microseconds, the loss would be

$$\text{loss} = 10 \text{ electrons.}$$

This is negligible compared to the 1000 electron exposure. If the grain volume were less by a factor of 10, however, the loss would be complete. Since any emulsion must contain some small grains, even though they do not make an important contribution to the photographic image, there will be some direct recombination loss under high intensity exposure conditions. Since the loss is proportional to the square of the exposure, the practical effect will be a loss of contrast in developed negatives. This is observed, but not important with more sensitive emulsions, or less intense exposures. To eliminate the other recombination, whose presence is evidenced by the reciprocity curves already referred to, it would be necessary to remove all possible trapping sites, or remove the holes. Haynes-Shockley type experiments, carried out on silver halide crystals with sulfide additions by Castle, indicate that the action of the sulfide is in the direction of removing the holes, although it simultaneously reduces the electron lifetime.

The sensitizing sulfur is probably on the surface of the grains, along with the traps it creates. This statement is based on the position of the sensitizing steps in emulsion making, and on experiments with emulsion grains which indicate that aggregates are formed wherever photoelectrons reach the surface. The addition of sulfur to the surface of the silver halide lattice will result in the presence of an effective negative ion vacancy, due to the affinity of the sulfur for two electrons. Thus, on the surface of the grain there will be regions whose charge distributions are respectively more positive and more negative than the normal lattice.

³¹ M. Biltz, *J. Opt. Soc. Am.* **42**, 898 (1952).

³² R. Fowler, *Statistical Mechanics* (Cambridge University Press, New York, 1936), p. 476.

³³ W. Van Roosbroek and W. Shockley, *Phys. Rev.* **94**, 1558 (1954).

(The negative ion vacancy and the bivalent sulfur.) The relative positions of these two entities are not known, although experiments on large crystals suggest that they are close together. However, to estimate the effectiveness of these traps in eliminating recombination it will be assumed that it, the effectiveness, is determined by the percentage of the grain surface protected by the hole traps, and that a single trap will protect an area determined by the relative sizes of the electrostatic potential energy of the trap and the thermal energy of the hole. At about 100 Å, the potential energy of an electronic charge in a medium of dielectric coefficient of about 4 has dropped to $1/40$ eV, the room temperature average thermal energy. The surface protected by a single sulfur atom (through its hole trap) is thus about 3×10^{-12} cm². The fraction of the grain surface which is protected, which is assumed to be the efficiency of protection, is

$$\text{Efficiency} = 3 \times 10^{-12} (S/A), \quad (21)$$

where A is the grain area in cm², and S is the number of sulfur atoms per grain. An efficiency of unity could be obtained, if there were no objection to large amounts of sulfur in each grain, but there are at least two. Too much sulfur will cause fogging (development of unexposed grains), and an actual loss of sensitivity. The fogging is a complicated process, probably partly due to the formation of silver sulfide crystals on the surface of the grains. The loss, according to the model being studied here, is due to the introduction of electron traps which is necessary when a divalent atom is introduced into a monovalent lattice. An increase in the number of traps causes a reduction of efficiency in all types of exposure, by leading to dispersal of silver atoms in undevelopable aggregates.

The speed of a photographic emulsion is usually defined to be inversely proportional to the exposure required to produce a fixed density of developed negative. An analogous measure, based upon Eqs. (11) and (21) is

$$\begin{aligned} \text{Speed} &= K(S/A)S^{-1/2} \quad S \text{ less than } A \\ &KS^{-1/2} \quad S \text{ greater than } A. \end{aligned} \quad (22)$$

The efficiency is proportional to S/A from Eq. (21) until the efficiency reaches unity. The $S^{-1/2}$ factor comes from assuming, according to Table II, that the number of absorbed photons is less than the number of traps, leading to the approximate result that, for a fixed number of N_2 aggregates per grain,

$$N_2 = (1/2)(\text{exposure})^2/T. \quad (23)$$

If each sulfur atom introduces an electron trap, and no other traps are present, Eq. (22) follows. This expression is plotted for two different sizes of grain in Figure 2, along with some of Sheppard's experimental data. The latter are plotted on two arbitrary scales. The necessary number of sulfur atoms per grain is not susceptible to test, being below the level of chemical detection, in

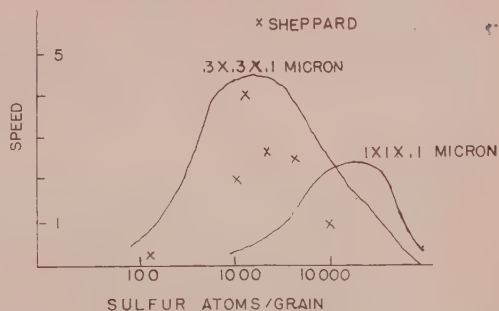


FIG. 2. Sulfur sensitizing.

theory and in fact. The peak speed, according to these simplified estimates, is proportional to $A^{-1/2}$, and so small grains should be more sensitive, in terms of absorbed photons. This is intrinsic sensitivity, and agrees with some work on older emulsions. In practical work, the large grain will be more sensitive because with its greater area it will absorb more photons per exposure than a small one, and, according to the present model, will be faster by a term proportional to $A^{1/2}$.

An unsensitized grain will develop, indicating that it contains some "natural" electron traps, which is not surprising. Their nature is not known, but a possible candidate is the interstitial silver ion itself. Although calculations have indicated that its trapping ability is small, there is general agreement that interstitial silver is present. An experiment carried out by Biltz is of interest in this connection.³⁴ He shows a case where an internal image showed no signs of high-intensity reciprocity law failure. According to the present model, this implies a very high neutralization rate, or else the trap is an interstitial ion, in which case neutralization is instantaneous.

If the interstitial ions are traps, it is advantageous to reduce their number, and this can be done by introducing some multivalent positive ion into the lattice. This is a feature of reduction sensitizing, tin being generally used. (It is interesting to note that tin has a chemical tendency to change its valence by two units, which could contribute to its effectiveness in a process where two is such an important number.) The number of ions removed can be calculated by using the physical equivalent of the common ion effect. The product of the number of interstitial ions and ion vacancies should be a constant. The number of vacancies should be equal to the number of interstitials (T) plus the number of multivalent ions (M) assuming they are divalent.

$$(M+T)(T) = T_0^2, \quad (24)$$

or

$$2t = -M + (M^2 + 4T_0^2)^{1/2}. \quad (25)$$

Assuming, as in the case of sulfur sensitization, that the speed is inversely proportional to the exposure needed to attain some fixed number of two atom aggre-

³⁴ M. Biltz, J. Opt. Soc. Am. **39**, 994 (1949).

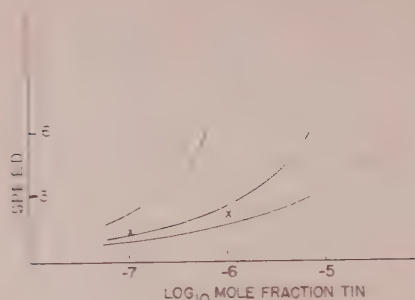


FIG. 3. Reduction sensitizing.

gates, makes the speed proportional to T^{-1} . In Figure 3 is shown a graph of this hypothetical speed for two values of the equilibrium concentration, T_0 . This function has no maximum, due partly to simplifying assumptions. Experimental work by Lowe, Jones, and Roberts indicates that if the trap reduction action of reduction sensitizing has any validity, it is confined to the region near equilibrium.³⁵ In practice, any attempt to get the factors of three shown in Fig. 3 would lead to heavy fogging of the grains.

Sulfur and reduction sensitizing might almost be described as classical methods of sensitizing. The number of traps per grain is of the order of a part per million, at the limit of chemical purity. For a reproducible emulsion this number must be controlled, and has been, for several decades. To get a material free of electron traps would seem extremely difficult, yet the example of germanium shows that it is possible. The modern high-speed emulsions have done it also, but the mechanism is not known to the author. Figure 4 shows the results of a study of the distribution of the developable aggregates in one of these rapid (ASA greater than 200) grains. The solid line shows the theoretical relation

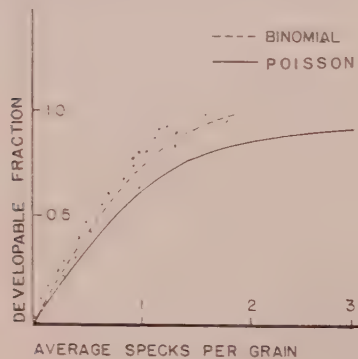


FIG. 4. Trap distribution.

between the average number of aggregates per grain, and the fraction of developable grains. This is the Poisson probability which has always been found to be valid for the old emulsions. The Poisson expression is applicable because the probability that any given trap will be developed is small—the number of quanta absorbed is a factor of ten smaller than the number of traps. The dashed line shows the relation which would hold if there were two traps per grain. It is obtained from the binomial distribution. The dots are experimental points for an emulsion similar to Kodak Royal Pan. They diverge noticeably from the Poisson case. Modern emulsion makers have succeeded in producing a reproducible material with less than a part in 10^6 of impurities. This conclusion is not dependent on the details of the theoretical explanation of the photographic process.

SUMMARY

The foregoing article has discussed the photographic process in emulsion grains up to the initiation of development. The primary interest has centered on the behavior of the silver in the grains and its growth and distribution during and after the exposure itself. It appears reasonable to assume that an aggregate of four silver atoms will produce developability in a grain, and that under most conditions, the production of a two-atom aggregate during the exposure will ensure the presence of the four-atom aggregate before development. The efficiency of the various steps in the photographic process is dominated by the number of traps in each grain. These traps cause the dispersion of silver in undevelopable aggregates, by immobilizing photoelectrons, or electrons from thermally decaying silver atoms. From a physical point of view, the removal of electron traps is the most important feature of photographic sensitization. (But this assumes that recombination is negligible, and that the gelatine environment is ideal.)

Although the work and terminology are based upon a slight extension of the Gurney-Mott theory, no direct proof of its validity is presented here. It is plausible, but not, on the basis of this work, unique. However, it seems likely that any future, more successful theory, will use the mathematical apparatus developed here, even though the constants may have different names.

ACKNOWLEDGMENTS

Most of the work described above was carried out at the Research Laboratory of Eastman Kodak. The encouragement and advice received there have greatly increased the value of the present work, and eliminated many of the errors. The author is especially indebted to J. Castle, J. Hamilton, and L. Brady for discussions, and experimental information on other types of photographic experiments.

³⁵ W. G. Lowe, J. E. Jones, and H. E. Roberts, *Fundamental Mechanisms Photo. Sensitivity*. Proc. Symposium Univ. Bristol, Engl., 1950, 112 (1951).

Transparency of Glass and Certain Plastics under Shock Attack

H. DEAN MALLORY AND WILLIAM S. McEWAN

Chemistry Division, Research Department, U. S. Naval Ordnance Test Station, China Lake, California

(Received April 3, 1961)

It is considered common knowledge by many workers in the field of detonation phenomena that transparent plastics quickly go opaque under strong shock wave attack. In this paper high-speed photographs are shown, and it is seen that Lucite and Plexiglas do not go opaque until shattered by tension waves. The behavior of plate glass is somewhat similar. By adjustment of dimensions and lighting, events can be observed with good photographic quality through the shock front for an undetermined length of time.

I. INTRODUCTION

DURING the course of an investigation of the shock initiation of propellants and explosives, it became apparent that the impact plane in the receptor explosive was a critical area. It was necessary to observe this area in detail. An obvious method, which greatly limited the application, was the use of transparent explosives. An alternative solution, which gave rise to the present paper, was the use of thin specimens enclosed in a massive block of clear plastic through which strongly shocked test materials could be seen.

Initially, it was believed that such observation through a window might be unfeasible, since it is a commonly held belief among workers in the field of detonation that clear plastics quickly go opaque under strong shock attack. Reference to this opaquing phenomenon in Lucite has been made in the literature.^{1,2} However, in agreement with the present work, an earlier report³ indicated the region behind the shock front in glass and Plexiglas to be transparent although no attempt was made to observe fine detail. A useful technique, which is closely related to present experiments, employs a piece of clear plastic, covering a thin argon or an air gap at the boundary of an explosive charge. Arrival of the detonation wave at the gap is clearly marked by an intense light flash, the duration of which is related to gap thickness. Sudden quenching of the light flash was previously attributed to opaquing of the plastic cover, but the present experiments show that such is not necessarily the case, and indeed the plastic may retain its optical clarity long after the gap has closed. These experiments indicate that duration of the light flash is due not only to gap width but also to rate of gas cooling and the thickness of plastic. It is suggested that, with thick plastic, extinction of the light flash is due only to cooling of trapped gas as the thickness of the gap approaches zero. In this investigation we have used Lucite, Plexiglas, and plate glass as observation windows with the impact surface either treated or untreated. Conclusions are based on a num-

ber of different experiments using various shock strengths, gases, and gap widths.

II. EXPERIMENTAL DETAILS

The basic experiment consisted of a plane wave initiated block of explosive which drove an aluminum plate onto a thick section of clear plastic or plate glass. A plane gap as thick as $\frac{3}{8}$ in. between the metal plate and the transparent receiver was enclosed so that the space could be flushed with a given gas prior to and during the test. The transparent block was usually $6 \times 6 \times 1$ in. with inked or painted characters on the impact side. A mirror just under the assembly permitted observation of the characters during the experiment. In many experiments the edges of the transparent piece were polished to allow direct observation of the shock front position. The lower face of the glass or plastic test piece was arranged nearly to coincide with the optical axis of the Cordin high-speed framing camera so that events seen in the mirror could be correlated with the position of the shock front. The results showed quite clearly that, with the plastics used, good optical clarity was maintained throughout the shock event, and this clarity was lost only when the transparent free surface spalled in tension.

Another series of experiments was performed wherein designs cut from aluminum foil were laminated between sheets of $\frac{1}{4}$ in. Plexiglas to a final thickness of 1 in. Air was excluded between the sheets by the use of silicone oil, the excess being squeezed out when the sheets were bolted together. The purpose of this series was to determine if the foil designs disappeared sequentially, as they would if opaquing occurred due to shock events on the impact side or simultaneously as would occur if the opacity were caused by front surface spall. No sequential disappearance was observed indicating, in conformity with experiments incorporating direct observation of the shock front position, that opacity would not occur during shock attack per se.

Prior to the first tests it was believed that rarefactions following the initial shock set up by metal plate impact on the test piece might cause opacity. In this way transparency would be maintained for a length of time depending on the thickness of the impacting metal plate without regard to thickness of the transparent piece. Several metal thicknesses up to $\frac{1}{2}$ in. were used

¹ J. M. Walsh and R. H. Christian, *Phys. Rev.* **97**, 1544 (1955).

² D. B. Moore and G. M. Muller, "Electrical initiation of insensitive explosives," Poulter Laboratories Tech. Rept. No. 016-59 (November 14, 1959), p. 30, Stanford Research Institute, Menlo Park, California.

³ E. M. Pugh, *J. Appl. Phys.* **22**, 487 (1951).

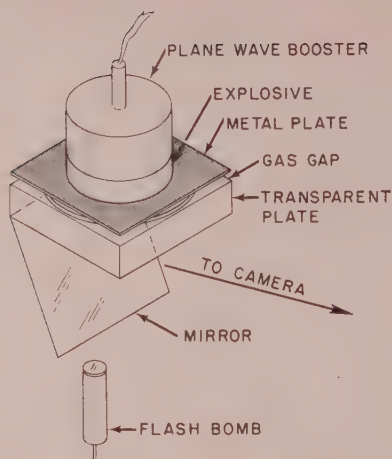


FIG. 1. Experimental arrangement.

with no detectable qualitative difference in the results. Gas gaps from 0.02 in. to 0.38 in., allowing differing lengths of free run, were also without qualitative effect.

For part of the work an argon flash bomb was detonated simultaneously with the main charge and the resulting light directed on the under side of the transparent plate (Fig. 1). Both white and black lettering was used in some tests so that the origin of the light in a particular frame in the film sequence could easily be determined. The flash bomb came on before the start of plate collapse, and the black and white lettering was first seen in its proper contrast with the white characters being more intense. As the metal plate moved, intensity of light emitted by the gas gap increased. Since the white paint was translucent, the intense back light produced a reversal of contrast showing black characters in silhouette while white ones were less easily visible against the background. Near the time of contact between the metal and the transparent surface, gas cooling occurred, and the back light was largely extinguished. At that time the original black and white contrast was restored due to continuing incident light from the flash bomb. This particular experiment was repeated several times using plate glass, Lucite, and Plexiglas as the transparent piece with qualitatively similar results regarding persistence of transparency. However, the breakup of glass appeared to proceed differently. This will be described later.

III. EXPERIMENTAL RESULTS

Results with Plastic

Differences between Lucite and Plexiglas were neither expected nor found. However, shock-produced opacity has been mentioned specifically for Lucite in the literature,¹ and it was, therefore, most desirable to include it in the present tests. A number of different

gases were used as gap material in an investigation of cooling rates in contact with various surfaces. The gases included air, hydrogen, helium, and argon. The surfaces included Lucite, Plexiglas, Saran, polyethylene, Mylar, silicone oil, hydrocarbon oil, and glass. Cooling rate results will be reported elsewhere. Subsequent transparency of the plastic block was not greatly affected by these surface changes. Four frames from a sequence are shown in Fig. 2 where the contrast reversal previously mentioned can be seen. The transparent piece was a 1-in. thick block of Lucite with a $\frac{3}{8}$ -in. air gap above it. The impact surface was cleaned and lettered but otherwise untreated. The metal plate was aluminum, $\frac{1}{4}$ in. thick, and powered by a 4-in.-diam plane wave booster. The second frame shown occurred about 1 μ sec after maximum brightness where the effect of gas cooling already can be seen in the granular structure of the background. Just above the white painted line, USNOTS, the inked letters, "1-in. Lucite- $\frac{1}{4}$ -in. Al" can be seen faintly. In subsequent frames letters inked directly onto the plastic surface always disappeared from view. However, if they were covered by a strip of paper tape they remained clearly visible until front spall of the plastic occurred to produce opacity. With dimensions as stated above, spall occurred about 8 μ sec after appearance of first background light. The marked background granularity as seen in the third frame probably was due to two effects: (1) radiating gas pockets and (2) light reflected from the main charge off the shock front proceeding through the Lucite block. The raised surface of the paper tape, seen above the lettered lines, shows outlines produced by trapped gas which continued to glow after the metal plate contacted the Lucite.

Figure 3 is a sequence showing four surfaces for comparison: (1) untreated Lucite, (2) hydrocarbon oil,

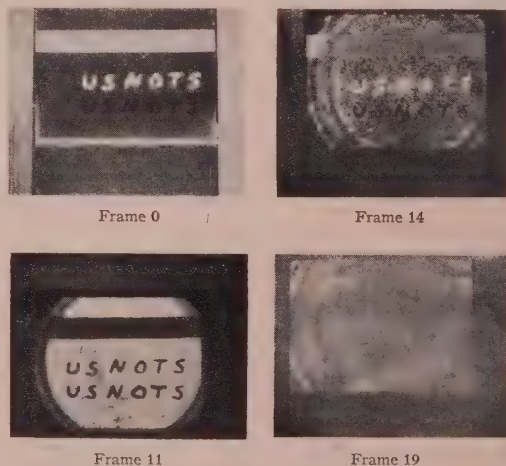


FIG. 2. Frames 0, 11, 14, and 19 from a sequence of 25 showing contrast reversal. Exposure time $\frac{1}{4}$ μ sec, framing interval $\frac{1}{2}$ μ sec.

(3) silicone oil of viscosity 800 cps, and (4) silicone vacuum grease. The separate areas were marked out by paper tape. Conditions were the same as those for Fig. 2 except that the aluminum shock driver was $\frac{1}{8}$ in. thick and no auxiliary flash bomb was used. The third frame shown was of particular interest in that the paper tape and inked letters were made visible by light from the explosion reflected upward from the shock front in the plastic. The shock front itself can be seen in profile through the polished edge of the Lucite plate and has not quite reached the free surface. In the last frame the free surface of the plastic has spalled so that the mirror image shows no view of the upper-loaded surface; however, looking into the polished edge of the plastic plate one sees a curved band of diffused light scattered from the reflected shock wave and behind it what appears to be a reflected image or a shadow of the tape grid on the upper surface. In any event, it seems probable that the tape is still intact at this time.

Figure 4 is a single frame which occurred about $5\frac{1}{2}$ μ sec after maximum light and shows differences in gas cooling rate on Lucite and glass. The position of the shock front and the two detonator leads behind the assembly can be seen through the polished edges of the 1-in. thick Lucite. The faint lighting used to show the shock front was produced by partially blacking out the two unpolished edges so that scattered light reflected from the shock front would not appreciably illuminate the impact surface. The two rightmost squares are aluminum foils on the impact surface, one with the bright side and the other with the dull side facing the camera. By reflection these foils served as sensitive detectors of front light which might otherwise be attributed to glowing gas on the impact surface. The leftmost square is aluminum foil on the free surface of

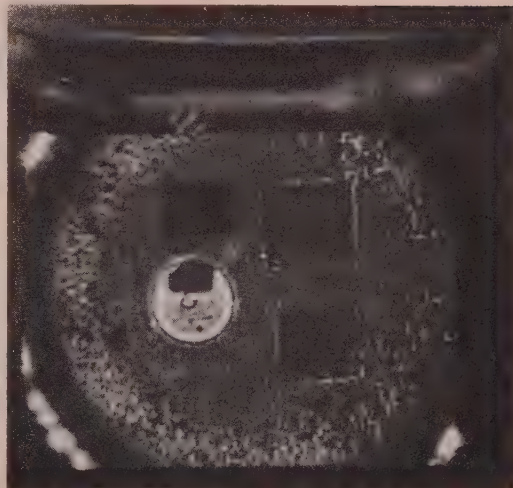


FIG. 4. Detail seen through shocked glass and Lucite. Cooling rate differences are apparent. Exposure time $\frac{1}{4}$ μ sec.

the plastic on which was painted both white and black characters. It serves to detect the amount of "spin on" image produced by camera mirror rotation while the shutter is open both before and after the shot. The edges are not outlined since this foil is not in contact with compressed gas. The absence of printed detail on the outside foil shows that printed characters on and under the circular microscope cover glass are seen by the aid of light coming from behind the glass alone. The thin cover glass was floated on a layer of silicone oil, both to cushion it and to exclude air between it and the plastic surface. Along the upper edge on the impact side was printed "TOP" which was covered by paper tape. That word is not visible since front lighting was not used. In the center the letter "G" was printed on the Lucite surface. On the lower edge the letters "Tg" were printed on the impact side of the cover glass. The strong and persistent light over a glass surface is apparently a real effect which cannot be due to scattered light, since the aluminum foils are quite dark. It cannot be due to gas trapped between the glass-plastic surfaces, since that space is filled by silicone oil visibly free from bubbles; moreover, the letters G and Tg are on opposite sides of the glass wafer so that glowing gas under the glass would show the G on the Lucite surface in silhouette but would completely obscure the Tg. It is evident that glowing gas was trapped above the glass surface and that both the plastic plate and the glass wafer remained transparent during the event. Bridgman and Simon have shown⁴ that glass wafers can retain their transparency after having been subjected to pressures near 100 katm where plastic flow and an increase in density have occurred.

The granular structure in the remainder of the circular field appears to be due to stagnant pools of radiating

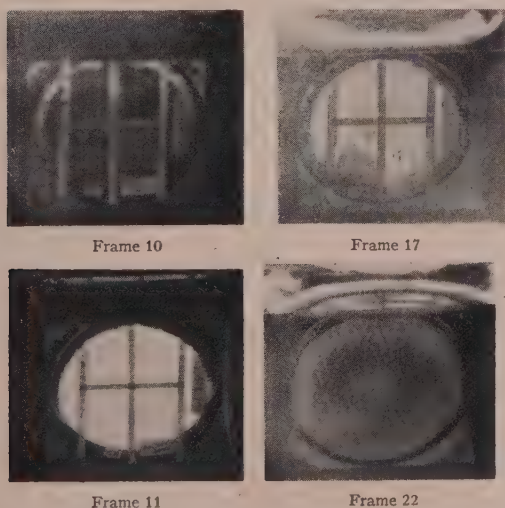


FIG. 3. Frames 10, 11, 17, and 22 from a sequence of 25 showing detail through the shock in Lucite. Exposure time $\frac{1}{2}$ μ sec, framing interval $\frac{1}{8}$ μ sec.

⁴ P. W. Bridgman and I. Simon, J. Appl. Phys. 24, 405 (1953).

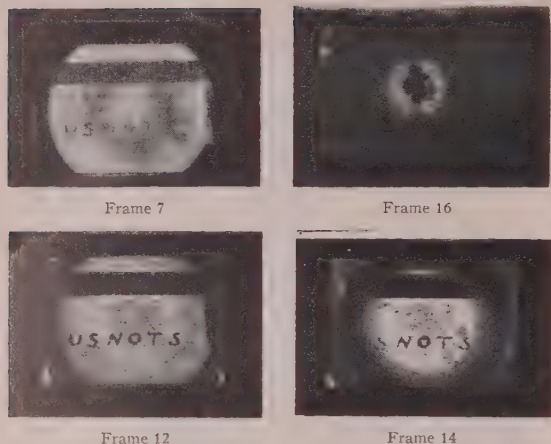


FIG. 5. Detail seen through shocked plate glass. Frames 7, 12, 14, and 16 from a sequence of 25. Exposure time $\frac{1}{2}$ μ sec, framing interval $\frac{1}{5}$ μ sec.

gas, which do not cool quickly even though the aluminum plate is in "good" contact with the impact surface. The granular structure persists, though growing ever fainter, until the free surface of the plastic moves out. Under these experimental conditions the free surface nearly always spalls, although small areas may remain clear for an undetermined length of time. In general, the profile view shows a "fog" moving out, but this may be partially due to image blur. At the same time the mirror shows detail on the impact plane which gradually fades as though one were watching through an ever thickening snow storm. In this event a persistent spot of light, such as occurs over the microscope cover glass, is at first made diffuse then gradually fades from view. This observation would lead to the conclusion that spall in Lucite and Plexiglas occurs quite readily over the range of shock strengths encountered here. This effect may be due to the short, sharp pressure pulse put into the plastic from the impact of the thin metal plate. This follows from the well known fact that spall in metal targets may be varied over a desired thickness range down to zero by adjustment of the thicknesses of the impacting plate with that of the target. In confirmation, a shot using $\frac{3}{4}$ -in. Plexiglas and a $\frac{1}{4}$ -in. aluminum shock driver was fired where, in this case, the bulging free surface appeared to be transparent.

Results with Glass

Two features which distinguish glass from plastic in these tests are long-light persistence time and ease of radial fracture. Figure 5 is from a sequence showing typical features. Lighting was from the $\frac{3}{16}$ -in. air gap. The explosive was a 4-in.-diam plane wave booster. The legend, " $\frac{3}{4}$ in. glass- $\frac{1}{4}$ in. Al, no light bomb," was lettered on the impact surface with pen and writing ink while USNOTS was white enamel. The strip of drafting tape above the lettering was added to aid in estimating shock distortion and impact time. In the first frame shown, impact has not occurred; the edges of the tape are parallel and the tape transmits back-light. In the next frame, impact has occurred and the upper edge of the tape is distorted, being viewed through the curved edge of the shock in glass. The granular structure produced by gas pockets is evident. The last two frames show the filigree network of cracks which work in radially from the impact boundary and opaque the area before free surface motion occurs. Parts of the letters "NOT" can be faintly seen in the last frame, and the compressed gas is still strongly luminous. This is in agreement with the previously mentioned result using a microscope cover glass on plastic. At the paper tape edge in Fig. 2 and at the edges of the right-most foils in Fig. 4, gas has been trapped and continues to glow long after impact. A similar raised surface on plate glass also traps gas, but the adjacent area cools more slowly than on plastic and the brightness difference is not great.

IV. CONCLUSIONS

Lucite and Plexiglas, in addition to plate glass, retain their transparency under strong shock wave attack. Their optical quality under such conditions and before rupture by tension waves is a function primarily of the regularity of the advancing shock front through which observation is made. The photographs shown indicate that light emitted from a compressed gas is transmitted through transparent materials until the gas cools.

ACKNOWLEDGMENTS

The authors would like to express their appreciation to Rolland Gallup, Madison Haas, and Charles Arnold for their assistance in the experimental work.

Determination of Field Strength for Field Evaporation and Ionization in the Field Ion Microscope*

ERWIN W. MÜLLER AND RUSSELL D. YOUNG†

Department of Physics, The Pennsylvania State University, University Park, Pennsylvania

(Received June 16, 1961)

The field strength required for field evaporation of tungsten and for best image conditions in the field ion microscope is measured by comparison with field electron emission of the same emitter. The evaporation field is independent of emitter radius except for radii below 150 Å where the influence of free surface energy becomes noticeable. The field for the best conditions of a helium ion image of a typical emitter of 1000 Å radius is 440 Mv/cm. This field increases gradually with decreasing tip radius, so that the ratio of evaporation field to best image field for tungsten decreases from 1.27 at 1000 Å radius to 1.0 at about 40 Å radius. The radius dependence of this ratio can be calculated by assuming that the time a hopping atom spends in the critical ionization zone is a constant fraction of the ionization time. Practical implications are that large tip radii are preferable for easily evaporating emitter materials, and small radii may be useful when field evaporation is to be studied under best image conditions.

I. INTRODUCTION

THE field ion microscope employs the process of field evaporation to prepare atomically perfect surfaces of refractory metal specimens and then images these surfaces in atomic detail by field ionization of an ambient gas. Both field evaporation and field ionization have been described in detail elsewhere.¹⁻³ However, no attempts have been made to determine experimentally the field strengths required. Certain features of these effects are pertinent to the present discussion and will be considered briefly.

II. FIELD EVAPORATION

The almost hemispherical tip of the emitter as produced by chemical etching, sometimes followed by annealing in vacuum, contains small protrusions and irregularities. If the average field above such a surface is raised sufficiently, the locally enhanced field above these protrusions is high enough to permit spontaneous evaporation of these atoms in the form of ions over an energy hump which is formed by the image force and the external field. The field to overcome this Schottky saddle has been shown⁴ to be

$$F_D = e^{-3}[\Lambda + V_I - \phi - kT \ln(\tau/\tau_0)]^2, \quad (1)$$

where F_D = evaporation field strength, e = charge of the ion, Λ = evaporation energy of atom, V_I = ionization energy of atom, ϕ = work function of substrate, k = Boltzmann constant, T = absolute temperature, τ = time allowed for evaporation, and τ_0 = vibration time of the bound atom.

When all irregular protrusions have disappeared field evaporation can be continued by slowly raising the applied voltage. This results in a gradual and perfectly

controllable removal of surface atoms at any desired rate, and is used in field ion microscopy to investigate the interior of the specimen by exposing it to the surface layer by layer.

III. FIELD IONIZATION AND IMAGE FORMATION

The hemispherical emitter surface is depicted by radial projection of its atomic protrusions onto a screen by ions formed closely above the surface where a suitable gas, usually He, is ionized. The important features of the ionization process are tunneling of an electron from the gas atom in the locally enhanced field above a surface protrusion, and the fact that the gas atoms are supplied to these regions by surface diffusion in the form of a hopping motion. The ionization by tunneling through a triangular potential barrier which is formed when the square well of the atom is brought into a field can be described by the life time of the electron inside the gas atoms

$$\tau = \frac{1}{\nu} \exp \frac{6.8 \times 10^7 V_I^{1/2}}{F}, \quad (2)$$

where ν is the frequency with which the electron strikes the barrier.

If the square well approximation for the atom is improved by a funnel shape, and if further the lowering of the potential near the surface due to the image force is taken into consideration, the exponential in (2) becomes smaller and assumes a more complicated form. For practical purposes in this paper it suffices to divide the exponent by 1.4 in order to explain the observed ionization at a field of about 440 Mv/cm for helium at a typical tip radius of 1000 Å. If for He atoms ν is assumed to be $2.4 \times 10^{16} \text{ sec}^{-1}$, the life time before ionization can be numerically expressed by

$$\tau_{\text{He}} = 4.16 \times 10^{-17} \exp(59/F), \quad (3)$$

where this time F is measured in volts/angstrom. Tunneling can only occur beyond a critical distance

$$x_c = (V_I - \phi)/F \quad (4)$$

* This work was supported in part by the Office of Scientific Research of the Air Research and Development Command.

† Now at the National Bureau of Standards, Washington, D. C.

¹ E. W. Müller, Phys. Rev. **102**, 618 (1956).

² E. W. Müller and K. Bahadur, Phys. Rev. **102**, 624 (1956).

³ E. W. Müller in *Advances in Electronics and Electron Physics*, edited by L. Marton (Academic Press, Inc., New York, 1960), Vol. 13, pp. 83-179.

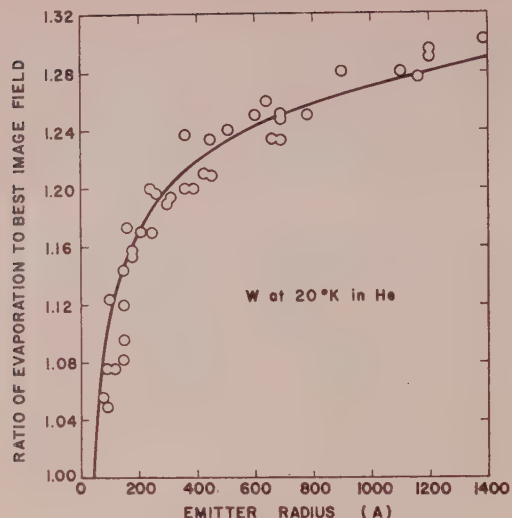


FIG. 1. Ratio of field for evaporation at 20°K to best image field in helium, measured for a number of tungsten tips of different radius. The solid curve has been calculated using the parameters given in the text.

above the surface so that the electron can enter the metal above the Fermi level.

Under best image conditions the ionization probability of gas atoms when arriving from outside at the tip is extremely small because of their high velocity due to dipole attraction. After accommodation to the low tip temperature the atoms perform a slow hopping motion as they are pulled back to the surface by dipole attraction $P = \alpha F dF/dr$ (α = polarizability) in the inhomogeneous field near the emitter. Setting the energy in the vertical direction of the hopping gas atom equal to $\frac{1}{2}kT_{\text{tip}}$ and assuming a relation

$$F = F_0(r_0/r)^{\frac{1}{2}} \quad (5)$$

for the field as a function of field strength at the surface (F_0) and distance from the surface $r - r_0$, one obtains an average hopping height

$$h = 3kT_{\text{tip}}/8\alpha F^2. \quad (6)$$

The experimental dependence of ionization probability upon field strength and the observed resolution even of adjacent surface atoms suggest that under best image conditions practically all the ionization takes place a very short distance above the critical distance x_0 , probably within a zone of less than one angstrom width.

IV. EXPERIMENTAL OBSERVATIONS

Steady images of a surface can only be obtained when the field for evaporation is larger than the field necessary for ionization. This is a particularly critical condition for microscopy with helium. Its high ionization potential and the consequently high image field provide best reso-

lution and prevent any contaminating gas molecules which always have a lower V_I from reaching the specimen surface. For a typical tungsten tip of 1000 Å radius the ratio of field evaporation voltage at 20°K to best image voltage is 1:27, while for platinum the two voltages or the corresponding fields are closer together, the ratio being about 1.13. This ratio was found to decrease with the radius and approaches 1.00 at a tip radius of 40 Å for tungsten, and 100 Å for platinum. A plot of the ratio of evaporation field to best image field as a function of tip radius for tungsten is shown in Fig. 1. The data were obtained by stepwise raising the field evaporation voltage until the evaporation rate had slowed down to about one atom per second from the entire tip area. After each evaporation step the voltage was lowered and adjusted to best image conditions in the region of a circular area about 10° to 30° off the central 011 plane. The definition of "best image" appears to be somewhat arbitrary, but it turns out that different observers will always adjust the best image voltage (BIV) for a given tip to within about $\pm 1\%$.

The description of an emitter by one radius of curvature is only a crude approximation, as the shape of the field evaporation end form is quite complex.⁴ With the work function ϕ varying with crystallographic orientation of a surface element, and the field evaporation depending upon ϕ , the dynamic field evaporation end form is such that low work function regions assume a small local radius. Thereby the local field strength adjusts itself everywhere so that a uniform evaporation rate maintains the dynamic end form. Perfect imaging conditions can be achieved only at a distinct field strength, and the "best image voltage" is then a compromise over the various crystallographic areas of the emitter. Local radii of curvature are measured in field ion microscope images by counting the number of net plane steps of known atomic height between two nearby net planes^{2,5}. For the data in Fig. 1 the number of ring shaped steps between the central 011 plane and one of the four adjacent {123} planes was multiplied by 30 in order to give an average tip radius. As only voltages but not fields, can be measured directly, it appears from Fig. 1 that either field evaporation or best image field, or both are a function of emitter radius.

One way to determine the field strength is to compare the field evaporation or field ionization voltage of a given emitter with the voltage necessary to cause a certain field electron emission current density when the tip is made negative. The validity of the Fowler-Nordheim theory has been established experimentally within about $\pm 15\%$ of field strength,⁶ and more recent measurements of the energy distribution of field emitted

⁴ E. W. Müller, *Acta Met.* 6, 620 (1958).

⁵ E. W. Müller, *IV Int. Kongr. Elektronenmikroskopie, Berlin, 1958* (Springer-Verlag, Berlin, Germany, 1960), Vol. 1, p. 820.

⁶ W. P. Dyke and W. W. Dolan in *Advances in Electronics and Electron Physics*, edited by L. Marton (Academic Press, Inc., New York, 1956), Vol. 8, p. 89.

electrons⁷ strengthen the confidence in this theory. We have therefore measured with a given emitter the voltage for field evaporation (which can be precisely defined), the best image voltage, (which is somewhat subjective) photographed the image for later determination of tip radius, and then after evacuation the voltage V_0 necessary for field electron emission at two or more different current densities. The microscope tube was baked to obtain a good high vacuum, and pure helium was filled in by diffusion through a heated Vycor tube. The field electron current density j was determined from the measured current divided by the emitting tip area $2r_0^2$. Tabulated data for field strength vs current density⁸ were then used to obtain the ratio β between field and applied voltage. Multiplying the field evaporation voltage by β gives then the field strength for field evaporation. Results are shown in Fig. 2 for an emitter whose radius was increased in seven steps to cover a range from 83 to 800 Å. Contrary to the gradual slope of the ratio of evaporation field and best image field as shown in Fig. 1 the evaporation field turns out to be essentially independent of emitter radius except for very small radii.

V. INTERPRETATION OF EXPERIMENTAL RESULTS

Looking at Eq. (1) one can expect only the energy of vaporization Δ of a surface atom to be radius dependent. The thermodynamic increase of vapor pressure of a small sphere of radius r results in a reduction of Δ by

$$\Delta\Delta = (2\gamma/r) \cdot (3M/2\rho N), \quad (7)$$

where γ =free surface energy, M =molecular weight, N =Avagadro's number, and ρ =density).

If the surface is not spherical, one can replace the first factor in (7) by $\gamma(1/r_1 + 1/r_2)$ with r_1 and r_2 as the main radii of curvature. For a field evaporating tip the smallest local radii are significant, and they occur not only at the low work function areas, but also, and more prominently at the regions producing the rim of the image. Neglecting the variation of work function the shape of a field evaporated emitter must be such that the local curvature increases with the distance from the apex, so that the field strength is essentially constant over the entire area that appears in the ion image. Then there is a sudden drop of curvature towards the shank. The main radii of curvature near the rim can be estimated from counting net plane rings near the margin and from shadow pictures of tips in an electron microscope to be about $\frac{1}{2}r_0$ for the azimuthal radius and about $\frac{1}{3}r_0$ for the meridional radius, when r_0 is the average tip radius near the apex. In Eq. (7) r is then to be replaced by $\frac{2}{3}r_0$. With $\gamma=2900$ ergs/cm² according to Barbour

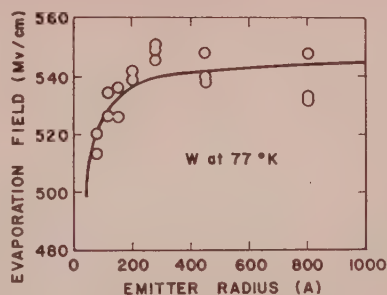


FIG. 2. Field strength for evaporating tungsten at 77°K as measured by comparison with field electron emission of the same tips. Solid curve has been calculated using a field enhancement factor of 1.8 at the site of the evaporating metal ion.

et al.⁹ one obtains numerically

$$\Delta\Delta = 21.5/r_0 \text{ ev} \quad (8)$$

(r_0 measured in Å). For comparison with the measured data in Fig. 2 the evaporation field has been calculated using Eq. (1) with $\phi=4.54$ eV, $T=77^\circ\text{K}$, $\tau=10$ sec, $\tau_0=10^{-13}$ sec. These data give the field effective at the site of the evaporating atom, that is at a kink of the lattice step. At such a position the field is enhanced compared to the over all field as measured in a 10-Å wide potential barrier in field electron emission. The geometrical field enhancement factor at the crest of a hemisphere on a plane is 3, and on the crest of a hemicylinder it is 2. For the evaporation site this factor is estimated to be 1.8, and this figure could be checked by model measurements in an electrolytic trough. The result of the calculation is shown as the solid line in Fig. 2, which matches the measured data satisfactorily.

The gradual increase with radius of the ratio of evaporation field to best image field as presented in Fig. 1 must be due to a radius dependence of best image field, probably as a result of the varying hopping height according to Eq. (6). We postulate tentatively that comparable ionizing conditions, for instance for best image field, are effective when the time t a hopping helium atom spends in the ionization zone above x_c is a certain constant fraction $1/n$ of its ionization life time as given by Eq. (2) or (3). The hopping time can be obtained by noting that with Eq. (5) the force that attracts the hopping atom from its crest h is

$$P = \alpha F dF/dr (4\alpha F_0^2/3r_0) \quad (9)$$

and hence the total time spent above the critical distance is

$$t = [6(h-x)mr_0/\alpha F^2]^{1/2} \quad (10)$$

Numerically one obtains for a one angstrom unit wide ionization zone and for helium

$$t = 4.2 \times 10^{-13} (\sqrt{r}/F) \text{ sec}, \quad (11)$$

⁷ R. D. Young and E. W. Müller, Phys. Rev. **113**, 115 (1959).

⁸ R. H. Good, Jr., and E. W. Müller, *Handbuch der Physik*, edited by S. Flüge (Springer-Verlag, Berlin, Germany, 1956), Vol. 21, pp. 173-231.

⁹ J. P. Barbour, F. M. Charbonnier, W. W. Dolan, W. P. Dyke, E. E. Martin, and J. K. Trolan, Phys. Rev. **117**, 1452 (1960).

where r is measured in Å and F in volts/Å. A reasonable number of hops before ionization may be $n=10$. By equating τ_{He} of Eq. (3) with $10t$ of Eq. (11) we obtain a relation between best image field and emitter radius which is more conveniently expressed as follows:

$$\log r = 2 \log F + (51.5/F) - 10. \quad (12)$$

From this equation a number of emitter radii have been computed. The evaporation field was also calculated for $T=20^\circ\text{K}$ using Eq. (1), including the free surface energy correction of Eq. (8) and the local field enhancement factor 1.8. The solid line drawn in Fig. 1 represents the results of this computation and it appears that the presented explanation describes the experimental situation very well. The parameters that have been used for adjustment are the factor of $1/1.4$ in the exponential leading to Eq. (3), which serves to provide the experimental image field (known only within the same accuracy as in field electron emission, that is $\pm 15\%$), and the number $n=10$ hops before ionization. Any other reasonable assumption for n , between 2 and 50, will only

shift the absolute image field strength well within the limit of experimental uncertainty but will not alter the character of the radius dependence.

VI. CONCLUSION

The field strength for field evaporation is independent of emitter radius except for a correction due to the free surface energy which becomes noticeable below ≈ 150 Å. The best image field strength for a typical tungsten emitter of 1000 Å radius is 440 Mv/cm for H ions. It increases for smaller radii so that the margin between evaporation field and image field is getting narrower until at 40 Å evaporation occurs at the best image field. These results suggest (1) that very large tip radii are more useful in studying non refractory metals which field evaporate easily, (2) that small emitter radii are useful if desorption and evaporation processes are to be observed near best image conditions while they are taking place, and (3) that the previously introduced concepts of field ion image formation are further supported experimentally.

X-Ray Measurement of Stacking Fault Widths in fcc Metals*

B. E. WARREN

Massachusetts Institute of Technology, Cambridge, Massachusetts

(Received June 19, 1961)

A generalized derivation of the broadening of powder pattern lines by stacking faults has been carried through allowing for fault planes of arbitrary dimensions. A minimum dimension for the fault plane T_{\min} is obtained from the measurable effective particle sizes $D_e(111)$ and $D_e(200)$. Values of T_{\min} of the order of 200 Å are obtained for samples of filings of copper, α brass, and silver. The results suggest that, in the drastic cold work involved in filings, the stacking faults tend to extend over rather large distances comparable to the coherent domain dimensions.

I. INTRODUCTION

IN a face-centered cubic metal, faulting takes place on the 111 planes. Deformation stacking faults produce peak shifts, twin faults produce peak asymmetries, and both types of faulting contribute to the peak broadening. Equations for obtaining these quantities from the x-ray powder patterns have been given in a review article which will be designated as (PMP).¹ The derivation was based on the assumption that the fault plane extends right across the coherent domain, rather than being confined to a narrow ribbon between two half dislocations. A section of the reciprocal lattice in terms of the hexagonal reciprocal axes B_1 and B_2 parallel to the 111 planes and B_3 normal to the 111 planes, is shown schematically by Fig. 1. The assumption that the fault plane exists over wide areas requires that the

intensity be sharply confined to vertical rods in reciprocal space. If the fault planes are narrow, the intensity spreads out laterally from the vertical rods. By carrying through the derivation assigning arbitrary dimensions to the fault plane, and allowing for the lateral spreading of the intensity, we obtain more general equations which allow the calculation of a minimum value for the fault plane dimension.

II. GENERALIZED DERIVATION

Since narrow faulting areas mean narrow coherent diffracting domains, it is sufficient to consider that the faulting extends across the coherent domains, and then formulate the problem so as to allow for coherent domains of arbitrary dimensions. At the point HKL of Fig. 1, we introduce orthogonal axes uvw , where w is parallel to B_3 , u is in the plane of B_3 and the diffraction vector, and v is normal to the plane of Fig. 1. We assume

* Research sponsored by the U. S. Atomic Energy Commission.

¹ B. E. Warren, Progr. in Metal Phys. 8, 147 (1959).

that the coherent domains have average dimensions T and S along the directions u and v .

Since we are interested only in the peak broadening, the small peak shifts and asymmetries can be neglected. For this case (PMP), Eq. (36) reduces to

$$I(h_1h_2h_3) = \psi^2 \sum_{m=-\infty}^{+\infty} N_m Z^{|m|} \cos 2\pi m \left(\frac{h_3 - L_0}{3} \right), \quad (1)$$

where $I(h_1h_2h_3)$ is the intensity at the position $h_1h_2h_3$ in reciprocal space; ψ^2 is the intensity per layer; N_m is the number of layers having an m th neighbor; $Z = 1 - 1.5\alpha - \beta$, where α and β are the probabilities of deformation faulting and twin faulting; L_0 is the hexagonal index corresponding to the hexagonal axes \mathbf{A}_1 and \mathbf{A}_2 in the 111 plane and \mathbf{A}_3 normal to the 111 plane. The intensity per layer is given by

$$I_e = I_e f^2 \sum_{m_1} \sum_{m_2} \exp \left[2\pi i \left(\frac{\mathbf{s} - \mathbf{s}_0}{\lambda} \right) \cdot (m_1 \mathbf{A}_1 + m_2 \mathbf{A}_2) \right] \sum_{m_1'}^* \sum_{m_2'}^*.$$

The diffraction vector can be represented in terms of the continuous variables $h_1h_2h_3$. However, we are interested in the intensity only in the vicinity of the HK line, and hence it is convenient to introduce the small quantities h_1' and h_2' where $h_1 = H + h_1'$ and $h_2 = K + h_2'$.

$$(\mathbf{s} - \mathbf{s}_0)/\lambda = (H + h_1')\mathbf{B}_1 + (K + h_2')\mathbf{B}_2 + h_3\mathbf{B}_3.$$

The sum over m_1 and m_2 becomes

$$\sum_{m_2} \exp \left[2\pi i \left(\frac{\mathbf{s} - \mathbf{s}_0}{\lambda} \right) \cdot (m_1 \mathbf{A}_1 + m_2 \mathbf{A}_2) \right] = \sum_{m_1} \sum_{m_2} \exp [2\pi i (h_1' \mathbf{B}_1 + h_2' \mathbf{B}_2) \cdot (m_1 \mathbf{A}_1 + m_2 \mathbf{A}_2)].$$

In terms of unit vectors \mathbf{i} and \mathbf{j} parallel to the u and v axes, let $h_1' \mathbf{B}_1 + h_2' \mathbf{B}_2 = \mathbf{i}u + \mathbf{j}v$ and $m_1 \mathbf{A}_1 + m_2 \mathbf{A}_2 = \mathbf{i}X + \mathbf{j}Y$. Since we are interested only in small values of u and v , the sum can be replaced by an integral

$$\sum_{m_2} = \int_{-T/2}^{T/2} \int_{-S/2}^{S/2} \exp [2\pi i (uX + vY)] \times \frac{dXdY}{|\mathbf{A}_1 \times \mathbf{A}_2|} = \frac{ST}{|\mathbf{A}_1 \times \mathbf{A}_2|} \frac{\sin \pi Tu}{\pi Tu} \frac{\sin \pi Sv}{\pi Sv}.$$

But $ST/|\mathbf{A}_1 \times \mathbf{A}_2|$ is the number of atoms per layer, and this quantity can be expressed by N/N_3 , where N is the number of atoms in a domain and N_3 is the average number of 111 layers per domain. The intensity per layer is given by

$$\psi^2 = I_e f^2 (N/N_3)^2 \left(\frac{\sin \pi Tu}{\pi Tu} \right)^2 \left(\frac{\sin \pi Sv}{\pi Sv} \right)^2. \quad (2)$$

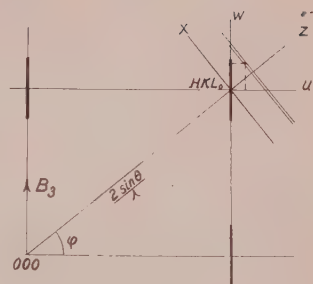


FIG. 1. A section in reciprocal space showing the relation between the different sets of axes at the lattice point HKL_0 .

Making the change $(h_3 - L_0)|\mathbf{B}_3| = w$, where $|\mathbf{B}_3| = \frac{1}{3}d_{111}$, and combining Eqs. (1) and (2), we express the intensity in terms of the variables uwv .

$$I(uvw) = I_e f^2 (N/N_3)^2 \left(\frac{\sin \pi Tu}{\pi Tu} \right)^2 \left(\frac{\sin \pi Sv}{\pi Sv} \right)^2 \times \sum_{m=-\infty}^{+\infty} N_m Z^{|m|} \cos 2\pi m d_{111} w. \quad (3)$$

The diffracted power is given by the powder pattern power theorem (PMP) Eq. (86).

$$P = \frac{MR^2 \lambda^3}{4} \iiint \frac{I(uvw)}{\sin \theta} dV_{RS},$$

where M is the number of domains, $I(uvw)$ is the intensity per domain, and dV_{RS} is a volume element in reciprocal space. It is now convenient to change to the orthogonal axes xvz shown in Fig. 1. The z axis is an extension of the line from the origin of reciprocal space to the point HKL_0 . The x axis is perpendicular to z and in the plane of the paper. As before, the v axis is perpendicular to the paper. A convenient element of volume is given by $dV_{RS} = dx dv dz$. Using the relations $dz = d(2 \sin \theta / \lambda) = (\cos \theta / \lambda) d(2\theta)$, $P = \int P_{2\theta} d(2\theta)$, and $P_{2\theta} = P_{2\theta} / 2\pi R \sin 2\theta$, the power per unit length of a powder pattern line is given by

$$P_{2\theta}' = MR \lambda^2 / 16\pi \sin^2 \theta \iint I(uvw) dx dv. \quad (4)$$

The integral with respect to v is readily evaluated;

$$\int_{-\infty}^{+\infty} \left(\frac{\sin \pi Sv}{\pi Sv} \right)^2 dv = 1/S.$$

With the abbreviation

$$G = I_e f^2 MR \lambda^2 N^2 / 16\pi S \sin^2 \theta N_3^2,$$

the power per unit length of diffraction line is expressed by

$$P_{2\theta}' = G \sum_{m=-\infty}^{+\infty} N_m Z^{|m|} \times \int_{x=-\infty}^{+\infty} \left(\frac{\sin \pi Tu}{\pi Tu} \right)^2 \cos 2\pi m d_{111} w dx. \quad (5)$$

From the geometry of Fig. 1,

$$w = z \sin\phi + x \sin\phi,$$

$$u = z \cos\phi - x \sin\phi.$$

To evaluate $P_{2\theta}'$ we hold z constant, and let u be the new variable

$$w = z/\sin\phi - u/\tan\phi,$$

$$du = -\sin\phi dx.$$

The integral in Eq. (5) becomes

$$\begin{aligned} \int_{-\infty}^{+\infty} \left(\frac{\sin\pi T u}{\pi T u} \right)^2 \cos 2\pi m d_{111} w dx \\ = \frac{1}{|\sin\phi|} \cos \left(\frac{2\pi m d_{111} z}{\sin\phi} \right) \\ \times \int_{-\infty}^{+\infty} \left(\frac{\sin\pi T u}{\pi T u} \right)^2 \cos \left(\frac{2\pi m d_{111} u}{\tan\phi} \right) du. \end{aligned}$$

This integral is tabulated,² and Eq. (5) becomes

$$\begin{aligned} P_{2\theta}' = \frac{G}{T|\sin\phi|} \sum_{m=-\infty}^{+\infty} N_m Z^{|m|} \left(1 - \frac{|m| d_{111}}{T|\tan\phi|} \right) \\ \times \cos \left(\frac{2\pi m d_{111} z}{\sin\phi} \right). \quad (6) \end{aligned}$$

For expressing the shape of a powder pattern peak in terms of its Fourier coefficients, it is convenient to treat the peak as a 00 l' reflection in terms of orthorhombic axes \mathbf{a}_1' and \mathbf{b}_1' . The connecting relation is $z = (h_3' - l')|\mathbf{b}_3'|$, and with this substitution $\cos(2\pi m d_{111} z/\sin\phi) = \cos 2\pi m q (h_3' - l')$, where $q = d_{111} \times |\mathbf{b}_3'|/\sin\phi$. The coefficients of the Fourier series represented by Eq. (6) are slowly varying, and we can make the replacement

$$\sum_m A(m) \cos 2\pi m q x \rightarrow \frac{1}{|q|} \sum_n A(n/|q|) \cos 2\pi n x.$$

With these changes, Eq. (6) can be written

$$\begin{aligned} P_{2\theta}' = \frac{G}{T d_{111} |\mathbf{b}_3'|} \sum_{n=-\infty}^{+\infty} N(n/|q|) Z^{|n/q|} \\ \times \left(1 - \frac{|n| |\cos\phi|}{|\mathbf{b}_3'| T} \right) \cos 2\pi n (h_3' - l'). \quad (7) \end{aligned}$$

Each powder pattern peak contains contributions from several components; those which are broadened by faulting we designate by b , and those which are unbroadened by faulting are designated by u . The contri-

bution by all the components with the same $h_0^2 = h^2 + k^2 + l^2$ is given by the Fourier series.

$$P_{2\theta}'(h_0) = \frac{G N_3(u+b)}{T d_{111} |\mathbf{b}_3'|} \sum_{n=-\infty}^{+\infty} A_n \cos 2\pi n (h_3' - l'), \quad (8)$$

where

$$\begin{aligned} A_n = \frac{1}{u+b} \left\{ \sum_b \frac{N(n/|q|)}{N_3} Z^{|n/q|} \left(1 - \frac{|n| |\cos\phi|}{|\mathbf{b}_3'| T} \right) \right. \\ \left. + \sum_u \frac{N(n/|q|)}{N_3} \left(1 - \frac{|n| |\cos\phi|}{|\mathbf{b}_3'| T} \right) \right\}. \quad (9) \end{aligned}$$

We are only interested in the low-order Fourier coefficients, and hence approximations appropriate for small n can be made

$$\frac{N(n/|q|)}{N_3} = 1 - \frac{|n|}{|q| N_3} = 1 - \frac{|n| |\sin\phi|}{|\mathbf{b}_3'| d_{111} N_3} = 1 - \frac{L}{D},$$

where $L = n|\mathbf{a}_3'| = n/|\mathbf{b}_3'|$ is a column length normal to the reflecting planes, and $1/D = |\sin\phi|/N_3 d_{111}$ taken as an average coherent domain dimension determined by the number of layers N_3 . With approximations suitable for small L ,

$$\begin{aligned} \frac{N(n/|q|)}{N_3} \left[1 - \frac{|n| |\cos\phi|}{|\mathbf{b}_3'| T} \right] &= \left(1 - \frac{L}{D} \right) \\ &\times \left(1 - \frac{L |\cos\phi|}{T} \right) = 1 - L \left(\frac{1}{D} + \frac{|\cos\phi|}{T} \right), \quad (10) \end{aligned}$$

$$Z^{|n/q|} = (1 - 1.5\alpha - \beta)^{|n/q|} = 1 - L(1.5\alpha + \beta)$$

$$\times |\sin\phi|/d_{111} = 1 - L(1.5\alpha + \beta) |L_0|/ah_0.$$

Incorporating these expressions in Eq. (9), we obtain the Fourier coefficient A_L

$$\begin{aligned} A_L = 1 - L \left\{ \frac{1}{D} + \left(\frac{1}{u+b} \right) \sum_{\mu+b} \frac{|\cos\phi|}{T} \right. \\ \left. + \frac{(1.5\alpha + \beta)}{ah_0} \frac{1}{(u+b)} \sum_b |L_0| \right\} \end{aligned}$$

An effective particle size dimension D_e , which includes the effect of coherent domain size, faulting, and stacking fault width, is given by the initial slope of the coefficient A_L

$$\begin{aligned} - \left(\frac{dA_L}{dL} \right)_{L=0} &= \frac{1}{D_e} = \frac{1}{D} + \left(\frac{1}{u+b} \right) \\ &\times \sum_{\mu+b} \frac{|\cos\phi|}{T} + \frac{(1.5\alpha + \beta)}{ah_0(u+b)} \sum_b |L_0|. \quad (11) \end{aligned}$$

² D. Bierens de Haan, *Nouvelles Tables d'Integrals Definies*, Table 157, No. 5.

For the first two fcc powder pattern lines,

$$\frac{1}{D_e(111)} = \frac{1}{D} + \frac{(1.5\alpha + \beta)\sqrt{3}}{a4} + \frac{1}{T\sqrt{2}}, \quad (12)$$

$$\frac{1}{D_e(200)} = \frac{1}{D} + \frac{(1.5\alpha + \beta)}{a} + \frac{1}{T\sqrt{1.5}}.$$

To obtain the stacking fault width T from the measured values of $D_e(111)$ and $D_e(200)$, we might use the values of α and β obtained from the peak shifts and peak asymmetries, and then eliminate the coherent domain size D from the two equations. However, this procedure is not practical, since it involves very small differences, and the values of α and β are not known with sufficient accuracy. It is more practical to eliminate $(1.5\alpha + \beta)$ from the two equations, and then solve for T .

$$\frac{0.82}{T} = \frac{2.31}{D_e(111)} - \frac{1}{D_e(200)} - \frac{1.31}{D}. \quad (13)$$

By dropping the term $1.31/D$, we obtain a minimum value for T

$$T_{\min} = 0.82 / \left(\frac{2.31}{D_e(111)} - \frac{1}{D_e(200)} \right). \quad (14)$$

III. APPLICATION TO SAMPLES OF FILINGS

Measured values for $D_e(111)$ and $D_e(200)$ are available for several samples where the particle size broadening is largely due to faulting. The cold work was produced by filing, either at room temperature or under liquid nitrogen. The resulting values of T_{\min} computed from Eq. (14) are given in Table I.

Although the values of T_{\min} are not very accurate, they are of the order of 200 Å, and it should be emphasized that these are minimum values. It does not appear possible to estimate rigorously how much greater the real values of T may be. If the assumption is made that $D = T$, the values of T are given by Eq. (14) with the factor 0.82 replaced by 2.13. This would result in values of T which are 2.6 times the T_{\min} values listed in Table I. It is customary to picture the stacking fault ribbon as very long in one direction, and having a narrow width W between two half-dislocations. Since the dimension T obtained in this analysis is an average dimension for all directions in the ribbon, it might be thought that the surprisingly large values of T_{\min}

TABLE I. Values of T_{\min} for samples of filings.

Sample	Ref.	Temp of filing	Temp of meas.	$D_e(111)$	$D_e(200)$	T_{\min}
90 Cu-10 Zn	(3)	20°C	20°C	235 Å	145 Å	283 Å
80 Cu-20 Zn	(3)	20°C	20°C	170 Å	100 Å	228 Å
70 Cu-30 Zn	(3)	20°C	20°C	153 Å	89 Å	210 Å
65 Cu-35 Zn	(3)	20°C	20°C	127 Å	62 Å	390 Å
Copper	(4)	liquid N ₂	-160°C	155 Å	95 Å	186 Å
90 Cu-10 Zn	(4)	liquid N ₂	20°C	125 Å	75 Å	158 Å
80 Cu-20 Zn	(4)	liquid N ₂	20°C	90 Å	50 Å	146 Å
70 Cu-30 Zn	(4)	liquid N ₂	20°C	70 Å	38 Å	123 Å
65 Cu-35 Zn	(4)	liquid N ₂	20°C	65 Å	32 Å	190 Å
Silver	(5)	liquid N ₂	-160°C	160 Å	94 Å	216 Å

which we have obtained result from the averaging over both the short and the long dimension. However even for an infinitely long ribbon of width W , the average dimension T is given by

$$\left\langle \frac{1}{T} \right\rangle = \frac{2}{\pi} \int_0^{\pi/2} \frac{\sin \gamma}{W} d\gamma = \frac{2}{\pi W}.$$

For this extreme case, the minimum ribbon width W is about two-thirds of the listed T_{\min} values. In filed samples such as Al and W where there is no evidence for faulting, it is possible to obtain rather accurate values of the coherent domain sizes. The values obtained are of the order 300 Å, and hence our fault plane dimensions T_{\min} are close to the coherent domain sizes.

Picturing a stacking fault plane as a narrow ribbon existing between two half dislocations, an approximate expression for the width W is given by dislocation theory.⁶

$$W = \mu a^2 / (24\pi\epsilon).$$

If the values for copper are taken as $\mu = 4 \times 10^{11}$ dynes/cm², $a = 3.6 \times 10^{-8}$ cm, and $\epsilon = 20$ ergs/cm², we obtain $W = 35$ Å. The minimum value in Table I for copper, $T_{\min} = 186$ Å is about five times larger.

It appears that, in the drastic cold work represented in filings, the stacking fault planes exist over dimensions considerably greater than the values given by the formulas of dislocation theory. For this type of severe distortion, there is presumably no question of equilibrium, and the faults tend to extend right across the small coherent domains.

³ B. E. Warren and E. P. Warekiois, *Acta Met.* **3**, 473 (1955).

⁴ C. N. J. Wagner, *Acta Met.* **5**, 427 (1957).

⁵ C. N. J. Wagner, *Acta Met.* **5**, 477 (1957).

⁶ A. H. Cottrell, *Dislocations and Plastic Flow in Crystals* (Clarendon Press, Oxford, England, 1953), p. 74.

(110) Nickel Surface

L. H. GERMER, A. U. MACRAE, AND C. D. HARTMAN
Bell Telephone Laboratories, Murray Hill, New Jersey

(Received May 19, 1961)

Nickel (110) surfaces, in clean and nearly clean conditions, have been studied by low-energy electron diffraction. When free from foreign atoms, the surface (110) plane of atoms has the normal arrangement expected for such a plane. Very slight contamination by oxygen (and perhaps other atoms) results, in some cases, in an arrangement of the topmost layer of atoms in which nickel and oxygen (or another atom) alternate along each $[100]$ line and also along each $[110]$ line. Study of such a surface has shown that the superficial half-layer of nickel atoms is displaced toward the bulk of the crystal by about 0.10 Å.

THE diffraction of slow electrons from a (110) surface of a nickel crystal has revealed three different arrangements of the topmost layer of nickel atoms. Two of these arrangements are shown in the

sketches of Figs. 1(a) and 1(b), while the third arrangement is just the normal planar array in a (110) plane. This is in marked contrast to earlier work upon (100) and (111) planes of a nickel crystal in which it was found that the atoms at these surfaces always take up the third of these arrangements, by which we mean just the arrangement of atoms appropriate to mathematical (100) and (111) planes of a face-centered cubic structure.^{1,2} The striking difference between a (110) surface and these more dense surfaces is related to its more open character and to the consequent firmness of the bonding of foreign atoms to it.

It is shown below that a (110) surface which is free from foreign atoms has the planar structure, and the two arrangements of nickel atoms illustrated in Figs. 1(a) and 1(b) are conditioned by the presence of other atoms firmly held on the surface. It is presumed that the other atoms fit between the nickel atoms of the topmost layer to make a "complete" (110) plane in which nickel atoms and foreign atoms take alternate positions. This arrangement is inferred from the fact that the foreign atoms give no diffraction pattern in addition to that which is attributed to the nickel atoms in the arrangements of Figs. 1(a) and 1(b).

A (110) face of a nickel crystal which has been electropolished and etched by the method we have used is always found after heating to high temperature in a good vacuum to have the surface structure shown in Fig. 1(a). This structure is very stable, being quite unchanged when the crystal is cooled after heating in very high vacuum to temperatures close to the melting point. The structure of Fig. 1(b) and the "planar structure" are attained after treatments at elevated temperatures in oxygen and/or in hydrogen. This paper is concerned solely with the structure of Fig. 1(a). Calculations regarding this structure are carried out as if no foreign atoms were present. Intensity changes, which must be introduced by these atoms, seem to be unimportant. The planar structure and the structure of Fig. 1(b) are taken up only to the extent that is necessary in order to understand the structure of Fig. 1(a). A later publication will be devoted to the other structures and to

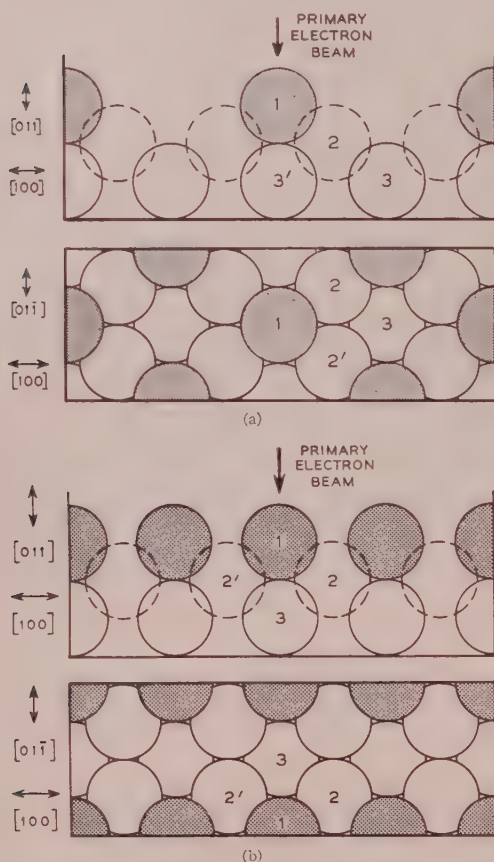


FIG. 1. Sketches of nickel atoms at a (110) crystal surface, looking at the cross section in the upper sketches, and directly down on the surface in the lower sketches. Each atom is represented by a sphere of diameter equal to its nearest neighbor distance. Atoms of the superficial half-filled layer are shaded and designated by the numeral 1, atoms of the first complete layer are designated by 2 and 2', and atoms of the second complete layer by 3 and 3'. (a) The structure with which paper is concerned, which we have called the C2 structure. (b) Another structure which is sometimes found, the B2 structure.

¹ L. H. Germer, E. J. Scheibner, and C. D. Hartman, *Phil. Mag.* **5**, 222 (1960).

² L. H. Germer and C. D. Hartman, *J. Appl. Phys.* **31**, 2085 (1960).

periments in which the crystal is heated in oxygen and in hydrogen.

The structure of Fig. 1(a) consists of half a plane of nickel atoms resting upon the topmost complete (110) plane. Expressed differently, every alternate nickel atom is missing from the surface (110) plane of atoms. The structure of this half-layer of nickel atoms is that which has been appropriately named the "2-structure" when referring to foreign atoms adsorbed upon a cube face (reference 2, p. 2088). That designation appears now to be ambiguous because the ratio of the number of nickel atoms in the topmost complete layer to the number in the superficial half-layer is 2 for both of the structures of Figs. 1(a) and 1(b), and so both can be called the "2-structure." They are referred to here, respectively, as the *C2* structure and the *B2* structure. We are concerned in this paper only with the *C2* structure.

Representative diffraction patterns from which the *C2* structure of Fig. 1(a) is deduced are reproduced in Fig. 2. These diffraction patterns are composed of two sets of spots, one set attributable to a mathematical (110) nickel surface and the other corresponding to a double spacing between atoms of the superficial half-layer. The fact that the latter diffraction spots cannot be eliminated by cleaning the crystal by vaporization and that they are just as intense as those due to the first complete layer of nickel atoms indicates that the superficial layer is composed of nickel atoms and is an intrinsic part of the (110) nickel surface prepared in this manner.

THREE SURFACE STRUCTURES

Although this paper is concerned solely with the *C2* structure of Fig. 1(a), the other two must be considered briefly because of the interrelations of the three structures. The *C2* structure is the one which has always been found first.

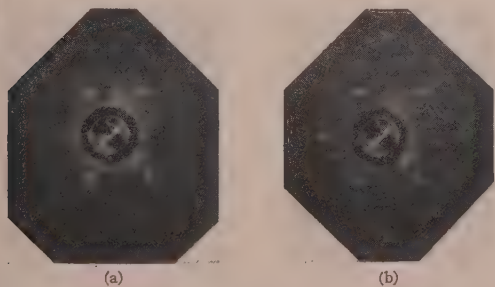


FIG. 2. Typical diffraction patterns showing beams in the *A*, *B*, and *C* azimuths. The *A* azimuth is horizontal, the *B* azimuth vertical, and the *C* azimuth inclined by 55° to the horizontal—the same orientation as in the sketch of Figs. 1 and 3. (a) 80 v. First-order diffraction beams in *A* and *B* azimuths, and beams representing double spacing in the *C* azimuth. (b) 90 v. Beams of double spacing in the *C* azimuth. The *A* and *B* azimuth beams of Fig. 2(a) are not present at this voltage.

The planar surface structure with surface atoms forming a complete (110) plane has been obtained only after heating the crystal for long periods at very high temperatures in vacuum, after it had been heated in oxygen and in hydrogen. The conditions which are required to produce the planar surface structure are still under investigation and are not yet understood. The *B2* structure of Fig. 1(b) has been produced by transformation from the *C2* structure by heating in oxygen and then in vacuum, which is less drastic than that which produces the planar structure. What is strictly required to give this structure has also not yet been well worked out.

The key to the conclusion that only the planar structure is free from foreign atoms is furnished by the observation that the sticking probability of oxygen upon the planar structure is of the order of unity and is of the order of 0.01 on each of the other surfaces. To this must be added the observation that the added oxygen is readily removed from the *C2* and the *B2* structures by low temperature heating ($\sim 200^\circ\text{C}$) but is not so easily removed from the planar structure.

These deductions are made from observations of diffraction patterns. When a nickel surface having the planar structure is exposed to oxygen at room temperature, weak diffraction beams characteristic of the *C2* and of the *B2* structures develop very rapidly. They can be seen by the time the oxygen exposure has reached 0.5×10^{-6} mm sec and reach maximum intensity at an exposure of about 1.5×10^{-6} mm sec. This means a sticking probability of oxygen molecules of about unity. Further exposure leaves the diffraction spots (representing both the *C2* structure and the *B2* structure present on different parts of the surface) still quite weak and not sharp. This is interpreted to mean that the superficial half-layers of these structures are predominantly oxygen rather than nickel.

When such a surface is heated slightly, which may be to only 200°C , the diffraction spots representing the double spacings of these superficial structures are remarkably strengthened. This strengthening occurs even in very high vacuum when the total previous oxygen exposure has been no more than 1×10^{-6} mm Hg sec, and is not greater when following very much larger oxygen exposure. We conclude that heating produces diffusion of nickel atoms outward from the crystal to make up a composite surface plane in which the nickel atoms have now the arrangements sketched in Fig. 1(a). It is presumed that oxygen atoms which were already on the surface take up the intermediate positions to make a composite (110) plane in which all positions are filled. This is inferred from the fact that no additional diffraction beams are found which are not accounted for by the arrangements of nickel atoms in the structures of Figs. 1(a) and 1(b). If the oxygen atoms were displaced to have a different symmetry, such additional diffraction spots would be seen.

All of the work reported in this paper was carried out

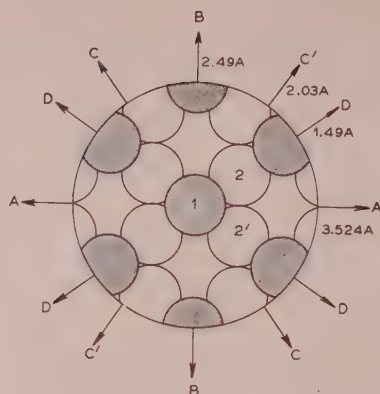


FIG. 3. Sketch of the C2 type of surface showing the superficial half-layer of atoms (marked 1) and atoms of the first complete layer (marked 2) with designation of the A, B, C, and D azimuths.

upon a surface in which the *nickel* atoms had the structure shown in Fig. 1(a). In some tests, it was known that other atoms on the surface were oxygen. In other tests, when the surface had never been brought to the planar structure after mounting the crystal, the additional atoms were of unknown kind. Positions of intensity maxima, for example of the (00) diffraction beam, were found to be identical in the two cases as far as our observations went. And in no case was any direct contribution to the diffraction pattern from oxygen or other foreign atoms detected.

EXPERIMENTAL TECHNIQUE

The diffraction patterns of this investigation were produced by electrons of speeds corresponding to potential differences of the order of 100 v, incident normally upon the nickel crystal and at inclinations of 6° and 13° to the surface normal. The diffracted elec-

trons were accelerated by potentials of the order of 4 k before striking a fluorescent screen.³ The patterns were then observed visually or photographed. The half-angle of 40°, subtended by the screen at the crystal, was sufficiently large to observe the essential diffracted beams.

The nickel target was cut from a single crystal said to contain no single element other than nickel in an amount exceeding 50 parts per million.⁴ Prior to mounting, and again after mounting, the nickel was electrochemically polished in a glacial acetic acid (75%) and perchloric acid (25%) solution; then chemically etched in a solution of hydrochloric acid and bromine in methyl alcohol, and finally washed in methyl alcohol and then in acetone. A crystal etched in this way has, on four separate occasions, given patterns characteristic of the C2 structure after only mild heating in vacuum (~500°C). Subsequently, heating to approximately 100°C of the melting point did not change the surface structure. It is clear that even this heating was insufficient to remove the material responsible for holding the surface nickel atoms in the C2 structure. During this heating the pressure in the system was maintained at about 4×10^{-10} mm Hg.

AZIMUTHS OF DIFFRACTION BEAMS

For convenience, the azimuths in which diffraction beams appear have been designated by letters of the alphabet with A denoting the azimuth of largest spacing between rows of surface atoms, B the azimuth of second largest spacing, etc. These spacings are $a_0/N^{\frac{1}{2}}$, where $N = h^2 + k^2$, h and k being two-dimensional Miller indices defining atoms in the (110) surface plane.

The azimuths having the four largest spacings are indicated in Fig. 3. All the azimuths in which diffraction beams have been observed from the surface containing,

TABLE I. Azimuths of observed diffraction beams.

Designation of azimuths	2-Dimensional Miller indices ($h\bar{k}$)	N ($h^2 + k^2$)	Angle with A azimuth	Orders in which reflections are found	
				Integral	Fractional
A	(10)	1	0°	1,2,3,4	
B	(01)	2	90°	1,2	
C	(11)	3	55°	1,2	$\frac{1}{2}, \frac{3}{2}$
D	(21)	6	35°	1	
E	(12)	9	70°	1	
F	(31)	11	25°	1	$\frac{1}{2}$
GH	mixed				
I	(13)	19	77°		$\frac{1}{2}$
J	mixed				
K	(51)	27	16°		$\frac{1}{2}$
LMNOP	mixed				
Q	(53)	43	40°		$\frac{1}{2}, \frac{3}{2}, \frac{5}{2}$
R	(15)	51	82°		$\frac{1}{2}, \frac{3}{2}, \frac{5}{2}$
S	(71)	51	11°		$\frac{1}{2}, \frac{3}{2}, \frac{5}{2}$
TUV	mixed				
W	(35)	59	67°		$\frac{1}{2}$

off screen for voltages below 500

³ L. H. Germer and C. D. Hartman, Rev. Sci. Instr. 31, 784 (1960).

⁴ K. M. Olsen, Metal Progress 72, 105 (1957).

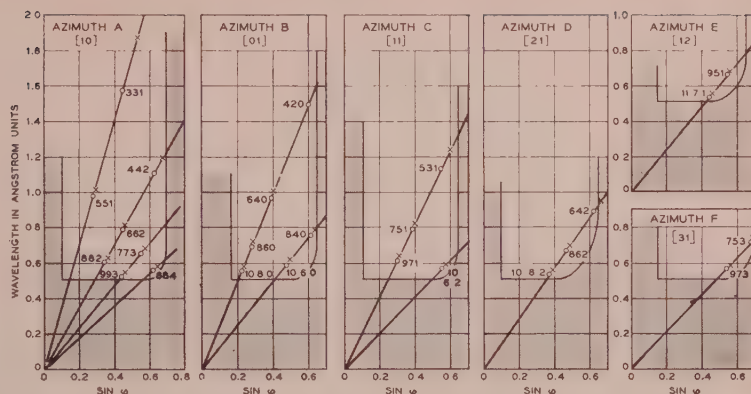


Fig. 4. Calculated positions of all possible Laue diffraction beams within the angular and voltage range of the measurements are plotted as open circles. Observed Laue beams at their maximum intensities are plotted as crosses.

the C2 structure are listed in Table I. Beams in the first order of the grating spacing are observed in the A azimuth, in the first two orders in the B and C azimuths, and in the first order in the D, E, and F azimuths. In addition, diffraction beams in the $\frac{1}{2}$ and $\frac{3}{2}$ orders are observed in the C azimuth, and in the $\frac{1}{2}$ order in all other azimuths designated by two odd Miller indices h and k as far as azimuth W. Stated differently, the spacing between lines of surface atoms is double the normal value in those azimuths for which the Miller indices are both odd. This observation establishes the fact that the topmost layer of surface atoms is that attached in Figs. 1(a) and 3. Although it has been inferred from experiments described above that there are other atoms filling in the intermediate positions in this superficial half-layer, these must have lower scattering power than nickel and they have not been directly observed. The designation "C2 structure" is based on the fact that C is the first azimuth in which a double spacing occurs. Correspondingly, for the B2 structure the B azimuth is the first in which a double spacing occurs.

LAUE DIFFRACTION BEAMS

All diffraction beams, including those of fractional orders, reach their maximum intensities at rather well-defined voltages, corresponding to reinforcement by scattering from atoms in underlying planes. In the case of all normal Laue diffraction beams, the voltage giving the maximum intensity is less well defined for the low-voltage beams than for those of high voltage, because of lesser penetration by the former.

The plane grating lines of integral order for all of the azimuths in which diffraction beams of integral order are observed are plotted in Fig. 4. The open circles are calculated positions for all possible Laue diffraction beams within the wavelength and angle range of the experiments. The observed Laue beams at their maximum intensities are represented by crosses. All possible diffraction beams are observed and all of them are displaced by an inner potential of the order of 16 v. Deviations from this value are moderate and may not be greater than experimental errors in the observations.

In addition to the Laue diffraction beams of Fig. 4, other and weaker integral order diffraction beams are observed in the first 5 of these 6 azimuths, all of them falling accurately upon the straight line plots of Fig. 4. These other weak diffraction beams will be discussed later.

DIFFRACTION BEAMS FROM THE SUPERFICIAL HALF-LAYER OF NICKEL ATOMS

Plots like those of Fig. 4 have been made of the fractional-order diffraction beams for the azimuths C, F, I, K, Q, R, S, and W for which the two-dimensional Miller indices are both odd. These plots consist of lines having slopes $a_0/\mu N^{\frac{1}{2}}$, with μ equal to $\frac{1}{2}$ and $\frac{3}{2}$ for the C azimuth, and equal to $\frac{1}{2}$ for each of the other azimuths. The wavelengths (and angles) at which the fractional-order diffraction beams reach their maximum intensities are marked on these lines. The plots do not show the wavelength resolution of the diffraction beams, some of which are found over a wide wavelength range and others over quite a narrow range. Since the plots were not very meaningful they have not been reproduced here.

More useful information is presented by plots of the intensity of diffraction beams in different individual azimuths as a function of voltage (or wavelength). Such plots are reproduced in Fig. 5, for the diffraction beam corresponding to the double spacing in the C azimuth (designated $C_{\frac{1}{2}}$), for the beam of $\frac{3}{2}$ order in the C azimuth ($C_{\frac{3}{2}}$), and for the beam of one-half order in the F azimuth ($F_{\frac{1}{2}}$). In the plot of $C_{\frac{1}{2}}$ of Fig. 5(a), one notes that the diffraction beam is strong at 80 and 90 v, which are the voltages of Figs. 2(a) and 2(b).

VARIATION OF INTENSITY OF THE FRACTIONAL-ORDER BEAMS

One naturally attributes the intensity variations shown in Fig. 5 to interference between scattering from the superficial half-layer of atoms [marked 1 in Figs. 1(a) and 3] and underlying atoms. For the diffraction beam of the $C_{\frac{1}{2}}$ reflection, the scattering from atom 2 is exactly out of phase with that from atom 2'. The same

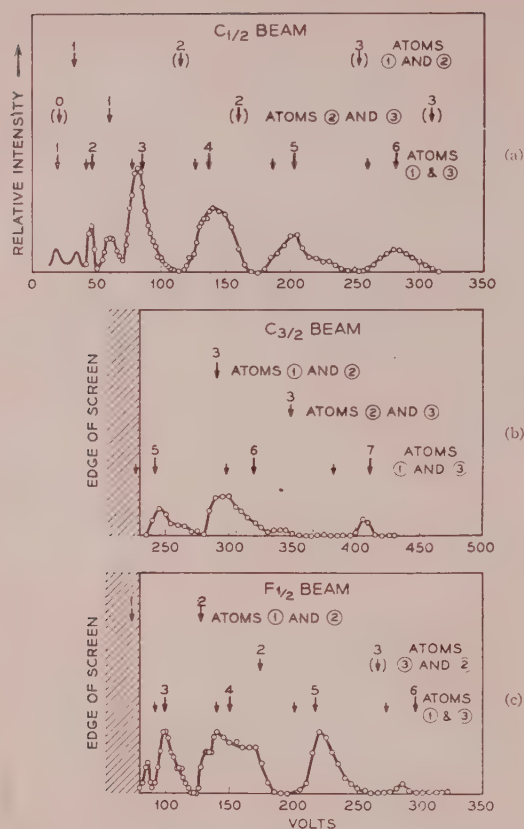


Fig. 5. Variations with voltage of the intensities of diffraction beams representing doubled spacings. Intensities estimated by eye on a series of photographs at closely spaced voltages. (a) The $C_{1/2}$ diffraction beam. (b) The $C_{3/2}$ beam. (c) The $F_{1/2}$ beam.

relation holds for atoms 3 and 3' with, however, an important difference, i.e., atom 3' is shielded by atom 1 and must scatter very much less than atom 3. Thus, we shall have variations of intensity due to interference between the scattering from atoms 1 and 3. The calculated voltages for which these atoms are in phase (for the $C_{1/2}$ diffraction beam) are marked on the plot of Fig. 5(a) by short arrows above the plot on the line marked "atoms 1 and 3." These arrows mark the observed positions of the intensity maxima quite well at low voltages (except for weak additional maxima at 33 and 61 v), but progressively more poorly at higher voltages.

The discrepancies between the voltages of the small arrows and of the experimental maxima are in the sense opposite to that which would be accounted for by a refractive index different from unity, but are of the sort to be accounted for by a slightly decreased spacing between the plane of the 1 atoms and the plane of the 3 atoms. If this spacing is assumed to be smaller than the normal value of $a_0/2^{1/2} = 2.49$ Å by just 0.10 Å, then one calculates for the voltages of the intensity maxima the values marked by the long arrows on the line "atoms 1

and 3." The agreement is now quite excellent, except for the very weak maxima at 33 and 61 v. Justification for assuming a spacing smaller than the usual value is found in the fact that the 1 atoms have only 5 nearest neighbors rather than the 12 neighbors possessed by atoms within the crystal.

It is suggested that the unexplained maxima at 33 and 61 v are due to interference of the scattering by atoms 1 and 3 with scattering from atoms 2 and 2'. Although it is true that the scattering from atom 2 is exactly out of phase with that from atom 2', and these atoms are exposed exactly equally to the primary electron beam, in many azimuths the electrons scattered from these atoms do not have equal opportunities to escape. The shielding afforded by the 1 atoms is different in different azimuths. The scattering from the 2 atoms which actually escapes can, in this way, interfere with scattering from the 1 atoms (and also with scattering from the 3 atoms) to produce new weak intensity maxima. Looking now at Fig. 3, it is obvious that in those two C azimuths which are marked C' , the scattering from the 2' atom will be stronger than from the 2 atom, and vice versa. From this, one calculates that interference between 1 and 2 atoms will give maxima at 32, 115, and 254 v, which are indicated by small arrows on the line marked "atoms 1 and 2." Correspondingly, interference between 3 and 2 atoms will give maxima at 12, 61, 161, and 310 v, which are indicated by small arrows on the line marked "atoms 1 and 3." The calculated voltages of 32 and 61 agree well with the very weak additional observed maxima which are otherwise not explained. The calculated maximum at 12 v is in a region where it could not be observed, and the calculated maxima at higher voltages cannot be expected because, at these higher voltages, the diffracted beam makes such a small angle with the surface normal that scattered electrons can escape almost equally well from atoms 2 and 2'.

In these calculations, the voltages of intensity maxima are obtained from wavelengths given by the formula $\lambda_{\text{max}} = 2Kl/[K^2 + \mu^2 N(l/a_0)^2]$. These values of λ are the wavelengths for which the diffraction beam from any plane of atoms is in phase with the scattering from any atom lying below the plane. The quantity l is the depth in the crystal of this atom below the plane considered [that is, the distance measured normal to the (110) surface plane], μ is the order of the surface grating line for the diffraction beam considered (that is, $\frac{1}{2}$, $\frac{3}{2}$, or an integer), $N = h^2 + k^2$, where h and k are two-dimensional Miller indices determining the azimuth under consideration, and K is in some cases equal to any integer n and in other cases equal to $n + \frac{1}{2}$. The rule whether K shall be equal to n or to $n + \frac{1}{2}$ is complex although easily determined, involving μ , the Miller indices, and the coordinates of the atom considered.

⁵ For the present case, the rule can be written: For $l = 2.39$ Å, $K = \mu + n$. For $l = 1.165$ Å, $K = n$; except $K = n + \frac{1}{2}$ for $(h+k)$ odd and μ odd. For $l = 1.225$ Å, $K = n$; except $K = n + \frac{1}{2}$ for $(h+k)$ odd and μ odd, and for $(h+k)$ even and μ fractional.

the values of l which are used are:

3 atoms below the plane of the 1 atoms,

$$l_{13} = a_0/2^{\frac{1}{2}} - 0.10 = 2.39 \text{ \AA}$$

2 atoms below the plane of the 1 atoms,

$$l_{12} = a_0/2^{\frac{1}{2}} - 0.08 = 1.165 \text{ \AA}$$

3 atoms below the plane of the 2 atoms,

$$l_{32} = a_0/2^{\frac{1}{2}} - 0.02 = 1.225 \text{ \AA}.$$

In choosing l_{12} and l_{32} it has been assumed that the 2 atoms, the first complete (110) plane of nickel atoms, depressed by 0.02 Å with respect to the bulk of the crystal—one-fifth of the distance by which the superficial half-layer of atoms is depressed. Justification for this will appear later. One should note, however, that the results of the present calculations would be only slightly altered if this displacement of the 2 atoms were omitted. The probable errors of these values of l we estimate to be about $\pm 0.01 \text{ \AA}$.

For the fractional-order diffraction beams $C_{\frac{1}{2}}$ and $F_{\frac{1}{2}}$ in Figs. 5(b) and 5(c), the calculated locations of the intensity maxima are marked on the plots in just the same way as in Fig. 5(a). One notes that the agreement with the observed peaks is fairly good but it seems clear that some factor has not been taken into account. This is the situation for the other azimuths also, I , K , Q , R , and W . The agreement between observed and calculated voltages of the maxima is too good to be attributed to chance but always not quite perfect. The interpretation of the disagreements is not known.

EXTRA INTEGRAL-ORDER DIFFRACTION BEAMS

It has just been pointed out that the intensity variation with voltage of the diffraction beams representing the double spacing of the superficial half-layer of nickel atoms is fairly well accounted for by constructive interference between scattering from the half-layer and scattering from other nickel atoms which are completely exposed on the surface. Constructive interference between these same atoms must quite obviously account for maxima in diffraction beams of *integral* orders as well. If the superficial layer were not slightly depressed, and if the electron wavelength over the interference in path were altered to correspond to the inner potential of the metal, these maxima would be just the normal Laue beams of the crystal. But, because of this superficial change of spacing and because the path difference is in a region outside the crystal, they are not true Laue beams. They are displaced from the normal Laue beam positions and wavelengths.

These beams must be the additional weak beams of integral orders observed in various azimuths which are mentioned above. Yet the voltages at which these additional weak beams reach maximum intensities are not those which are calculated. At present, we are unable to account for the discrepancies, which are large. As a pure speculation, we are suggesting that these beams are perturbed by their proximity in wave-

length to true Laue beams. Each Laue diffraction beam can be thought of as split up into a number of components by the absence of any inner potential over the path difference between certain atoms and by the small change in position of the topmost atoms. It is the various components of these beams which should be represented by the weak additional integral order beams.

P. M. Morse⁶ has shown that the electron beams reflected from differently spaced planes interact with one another. Ordinarily, only one set of planes at a time satisfies the condition for a diffraction maximum, and this interaction is negligible. However, when two or more sets of planes satisfy the condition for a diffraction maximum at approximately the same wavelength, the interaction can be considerable. A change in the wavelength of the diffraction maximum occurs in this instance, producing what could ordinarily be interpreted as anomalous values of the inner potential. In the present case, every one of the expected extra integral-order beams is near in wavelength to a true Laue beam and perhaps this "Morse effect" gives disturbances so severe that we can no longer identify the disturbed beams. The effect should be quite complicated and it is possible that it will not be amenable to exact interpretation.

In the case of the diffraction beams representing the double spacing from the superficial half-layer of nickel atoms, one should note that these are never in the wavelength neighborhood of Laue beams. Therefore, they should not be significantly disturbed and it is observed that they are not.

VARIATION OF INTENSITY OF THE (00) REFLECTED BEAM

One expects that crystal spacings in the direction of the surface normal will be most easily obtained from measurements upon the (00) diffraction beam. In order to make such measurements, the crystal was turned slightly so that the (00) beam can be seen on the fluorescent screen. Observations have been made at angles of 6° and 13° between the incident beam and the surface normal. Diffraction patterns showing the (00) beam are reproduced in Fig. 6, where the beam is marked by an arrow. Intensities of this beam have been measured at various voltages by a photometer [Spectra Brightness Spot Meter manufactured by Photo Research Corporation, Hollywood, California], and the results plotted as Fig. 7. The photographs of Fig. 6 show the (00) diffraction beam at one of the minima and three of the maxima of this trace.

Some of the peaks of Fig. 7 are to be interpreted as normal Laue beams from the crystal with a reasonable value of inner potential. These peaks are marked on the trace by arrows with the accompanying values of the inner potential Δ which give the best fit. These experi-

⁶ P. M. Morse, Phys. Rev. **35**, 1310 (1930).

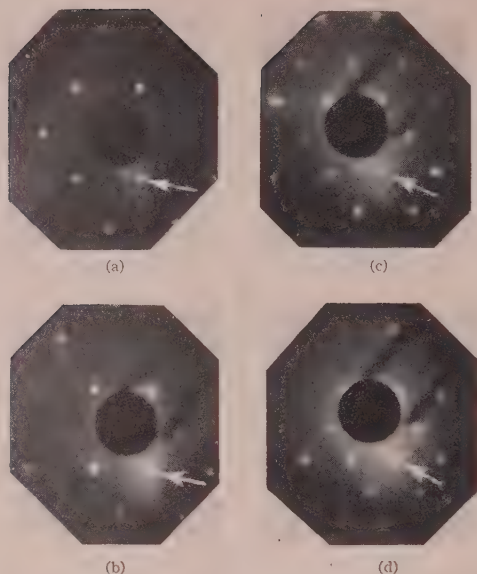


FIG. 6. Diffraction patterns showing different intensities of the regularly reflected (00) beam marked by white arrows. Primary beam inclined by 13° to surface normal. (a) 90 v, the (00) beam at an intensity maximum. (b) 120 v, the (00) beam at another intensity maximum. (c) 150 v, the (00) beam at an intensity minimum. (d) 200 v, the (00) beam at an intensity maximum.

mental values of Δ are, respectively, 12, 13, 16, and 16 v for the first four orders.

Some other peaks of Fig. 7 fit moderately well for constructive interference between atoms 1 and 2, and between atoms 2 and 3, of course without an inner potential. The agreement is best for a depression of the 2 atoms by 0.02 Å, which is the best experimental evidence for this assumed displacement of these atoms. Some such displacement is expected to accompany the depression of the superficial half-layer by 0.10 Å, which seems now to be experimentally well established.

The over-all agreement of the data of Fig. 7 with theory is still only moderately good, and there are some completely uninterpreted maxima. One of these is the strong peak around 125 v. Again we are led to invoke the Morse effect and make no further attempt to understand the anomalous voltages of some of the intensity maxima. Evidence that anomalies of great magnitude should be expected is afforded by Figs. 3 and 4 of an old paper by Davisson and Germer.⁷

An unexpected feature of Fig. 7 is the fact that the strong intensity maximum at 13 v corresponds to one wavelength path difference between the scattering from adjacent atomic planes *with the incident wavelength decreased from the value outside the crystal by the amount corresponding to a reasonable value of the inner potential*. This we interpret to mean that 13-v electrons penetrate the crystal considerably, which seems surprising.

⁷ C. J. Davisson and L. H. Germer, Proc. Natl. Acad. Sci. U. S. A., 619 (1928).

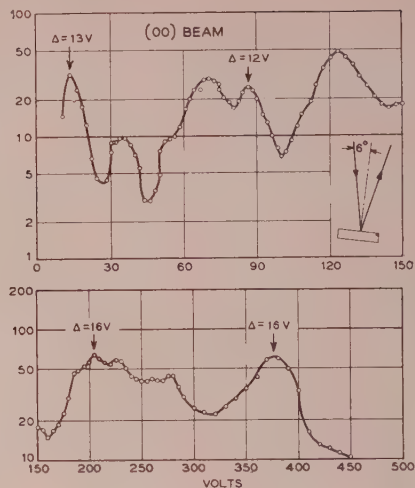


FIG. 7. Photometer record of the intensity of the regularly reflected (00) beam from the crystal surface (with the crystal turned to make the incident beam inclined by 6° to the surface normal).

DISCUSSION

We have concluded from experiments reported here that the nickel atoms of the superficial half-layer of the C2 structure owe their stability to foreign atoms located between them. In those cases in which a clean (111) surface having the planar structure was exposed to oxygen, these foreign atoms are certainly oxygen. But there is no presumption that they were oxygen when the C2 structure was observed before the surface had been completely cleaned after etching. Some evidence that these original foreign atoms were not oxygen is furnished by the extreme difficulty of cleaning the surface completely for the *first* time; subsequent cleaning after admitting oxygen was always easier.

The oxygen, or other atoms of the C2 structure might be expected to introduce an inner potential in the path difference between scattering from the 1 atom and the 3 atoms. That no inner potential is found means that the inner potential of oxygen is small when tested in this way.

The superficial half-layer of nickel atoms is observed to be compressed toward the bulk of the crystal by 0.10 Å. No such compression has been observed for atoms at a (100) face or at a (111) face,^{1,2} but the amount of the compression should certainly be smaller. Furthermore, even a large displacement would be difficult to observe. It would be manifested by broadening of the normal Laue beams on the high-voltage side of their peaks. In the case of the (111) surface, beams due to the double spacing of the top half-layer of atoms show this compression directly in the locations of the peaks.

While it has been possible to calculate the equilibrium

sition of surface atoms for inert gas⁸ and ionic crystals,⁹ a similar type of calculation is difficult to carry through for metals, and especially difficult for transition metals. Quantitative calculations of the cohesive forces of transition metals are unusually difficult due to the contributions from the $3d$ electrons. However, this compression can be thought of as arising from the image force of the surface ions which are floating in a sea of electrons. This compression of the nickel lattice is in contrast to the expansion of the surface layers predicted for inert gas and ionic crystals.

H. H. Schmidt and G. Jura, *J. Phys. Chem. Solids* **16**, 60 (1960).

R. Shuttleworth, *Proc. Phys. Soc. (London)* **A62**, 167 (1949).

Such a compression should be noticed only on materials whose interatomic forces are central and additive, a situation that does not apply for metals.

The atomic spacing in nickel is principally determined by the s electrons but the d electrons also contribute to the binding and cause the lattice spacing to be smaller than that due to the s electrons alone.¹⁰ The compression of the superficial half-layer of atoms is probably accompanied by an increase in the d character of the bands at the surface. If this is so, the magnetic properties of the (110) nickel surface should be perturbed from its ordinarily expected value.

¹⁰ E. P. Wigner and F. Seitz, *Solid State Phys.* **1**, 118 (1955).

Production of High Ion Densities in Helium by Means of High Explosives*

G. E. SEAY AND L. B. SEELY, JR.

Los Alamos Scientific Laboratory, Los Alamos, New Mexico

AND

R. G. FOWLER

University of Oklahoma, Norman, Oklahoma

(Received May 15, 1961)

Temperatures of about 20 000°K with ion densities ranging from 10^{17} to 10^{18} cm⁻³ have been produced in helium by means of explosive-driven shocks. Helium was used because of its relatively simple structure, but this choice eliminated usual shock methods because of the high sound speed and high ionization potential. Shock waves having sufficient strength and planarity were obtained by reflecting against a glass plate initially strong shock waves produced by high explosives. Equilibrium calculations based on smear camera velocities of accurately plane shocks were used to determine the state of the gas behind the reflected shock wave.

The light emitted consisted of a continuum on which were superimposed shifted and broadened lines of the normal helium spectrum and forbidden lines as well. Time-resolved spectrograms showed evidence of a measurable relaxation time at the shock front but no evidence of significant radiative cooling of the gas behind the shock.

Under the conditions of these experiments, it was demonstrated that a quantitative prediction of the behavior of the helium states with principal quantum numbers 2, 3, and 4 requires consideration of the effects of electrons as well as ions.

INTRODUCTION

In 1955, Kivel, Bloom, and Margenau¹ proposed a quantum mechanical theory of electron broadening, and later that same year Kivel² extended the theory to include line shift and applied it to helium. It was suggested that the theory might be checked quantitatively if a sample of helium could be produced in which the electron and ion densities were about 10^{18} cm⁻³, and the temperature was 1 or 2 electron volts. Helium was desirable for experiment since it has the

simplest atomic structure of any gas which is not subject to first order Stark broadening by ions. The theory of the hydrogen atom is, of course, simpler and better known, but the first order Stark effect of the ions is so great as to make the measurement of additional effects due to electrons difficult.³ Studies by Kantrowitz *et al.*,⁴ had shown that electrons were important in perturbing the energy levels of neutral argon in a partially ionized gas, but, because of the complexity of the argon atom, Kivel could check his theory only to an order of magnitude.

* Work performed under the auspices of the U. S. Atomic Energy Commission and submitted by G. E. Seay in partial fulfillment of the requirements for the degree of Doctor of Philosophy at the University of Oklahoma.

¹ G. E. Seay, S. Bloom, and H. Margenau, *Phys. Rev.* **98**, 495 (1955).

² B. Kivel, *Phys. Rev.* **98**, 1055 (1955).

³ E. B. Turner, "The production of very high temperatures in the shock tube with an application to the study of spectral line broadening," AFOSR TN-56-150, ASTIA Document No. AD 86309 (1956).

⁴ H. Petschek, P. Rose, H. Glick, A. Kane, and A. Kantrowitz, *J. Appl. Phys.* **26**, 83 (1955).

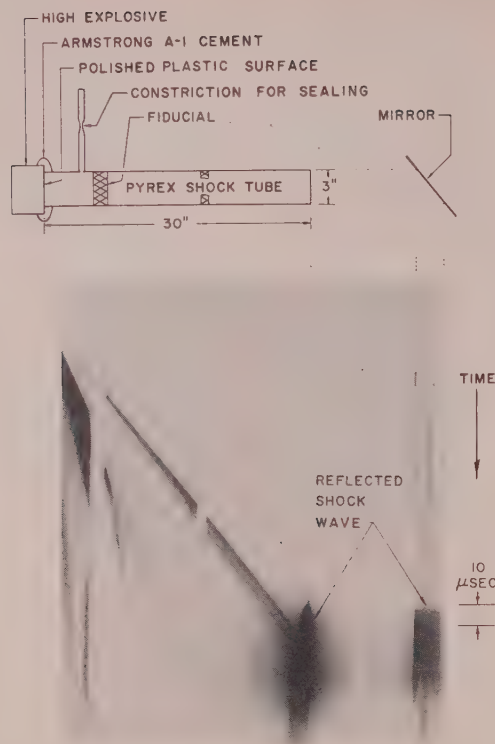


FIG. 1. Explosive-driven shock tube and smear camera record. Positions along the sketch of the shock tube may be projected directly to the photograph.

In order to obtain a sample of pure helium equilibrated under the conditions suggested by Kivel,² it was necessary to modify conventional shock tube techniques for heating a gas. Kantrowitz and his co-workers had obtained a temperature of about 1.5 eV in a hydrogen-driven argon shock tube. This technique, however, is limited by the ratio of the sound speed in the driver gas to that in the driven gas. Thus, helium could be shocked only about one-third as strongly as argon by the same driver gas. Since helium has a much higher ionization potential than argon, and since higher maximum electron densities than those obtained with argon were desired, the conventional shock tube would not suffice. Other methods, each having its own complications, which might have provided the desired electron densities, are high current arcs and electromagnetically driven shock tubes.

It was possible to produce the desired temperatures and electron densities in helium by replacing the driver gas and diaphragm in a conventional shock tube by a block of high explosive. A plane shock from the explosive was allowed to travel in a tube containing helium until it reached the end plate and was reflected. The thermodynamic state of the gas behind the reflected shock front was calculated from the initial con-

ditions in the shock tube and the measured velocity of the primary shock wave. Light from the gas compressed behind the reflected shock front was observed with time-resolving spectrograph. Line shapes and positions were measured and compared with theoretical predictions for the calculated state of the gas.

EXPERIMENTAL APPARATUS AND PROCEDURES

A sketch of the explosive shock tube is shown at the top of Fig. 1. One end of a cylindrical Pyrex tube was closed with a flat Pyrex plate, and the other end was cemented to a high explosive charge. An $\frac{1}{8}$ -in. i.d. glass tube was sealed into the wall for pumping and filling. The high explosive was about 4 in. long by 4 in. diameter, with one end coated with a hard black plastic. This coating provided a reasonably vacuum-tight surface and an opaque layer in front of the explosive. The other end of the explosive was initiated by an explosive plane wave generator. Since it was found that a plane shock wave was essential to the experiments, the plastic coating on the explosive was ground flat before the tube and explosive were cemented together.

The assembly was then evacuated to a pressure about 10^{-6} mm Hg, while being baked at about 300°C in the regions remote from the explosive. The tube was flushed with helium and evacuated again, filled to the desired pressure with spectroscopically pure helium, and finally sealed off at the constriction in the pumping tube (see Fig. 1).

It was found that an acceptable shock tube should fulfill the following requirements:

- (1) The assembly must hold a vacuum of 10^{-5} mm Hg; otherwise easily excited impurity lines contribute significantly to the observed spectrum. This is qualitatively reasonable when it is recalled that the first excited state of helium is at about 19.8 eV, whereas sodium and calcium are ionized at about 6 eV.
- (2) The shock waves must be plane, primarily because plane shock theory was used to calculate the thermodynamic state of the gas behind the reflected shock wave. Nonplanar waves were always accompanied by seriously contaminated spectra, probably due to mixing of the explosive products with the helium.

When a shock tube had been filled to the desired pressure (5, 20, or 35 mm Hg) with helium, it was placed outside a bombproof building in firing position where it could be observed by either a smear camera or a time-resolving spectrograph. Each of these instruments employed a rotating mirror which could work for only a fraction of each revolution, and, thus, it was necessary to synchronize the detonation time of the high explosive with the position of the mirror in the instrument being used. Because of this required synchronization only one of the two instruments could be used to observe any given shot. It was necessary

establish the reproducibility of the phenomena in apparently identical shock tubes so that shock velocity data obtained from the smear camera could be applied to shots in which the spectrum was observed. In this manner the spectrum obtained with a given set of initial conditions was identified with a thermodynamic state which was calculated in terms of the initial conditions and shock velocity.

A sample smear camera record is shown in Fig. 1, where positions along the sketch of the shock tube may be projected directly to the photograph as shown. If the primary shock front had been sharp and luminous, its slope could have been used to determine the shock velocity. However, as shown in Fig. 1, no distinct line representing the shock front was apparent. Experiments with shock tubes of various lengths showed that the shock velocity did not change appreciably during the 30-in. run. Thus, the velocity could be obtained from a measurement of the transit time recorded on the edge of the film by means of a mirror placed at the end of the shock tube as shown in Fig. 1. This portion of the photograph also demonstrated that the shock was plane when it was reflected at the end plate. After the primary shock was reflected from the end of the tube, there followed a period of about $10 \mu\text{sec}$ of bright light. Spectrographic interest lies in this light, emitted by helium gas which is presumably at equilibrium behind the reflected shock front.

Figure 2 shows the way in which time-resolved spectra were obtained by sweeping the image of a small region near the end of the shock tube along the slit of a Hilger medium quartz spectrograph by means of a rotating mirror. With the rotating mirror in the position shown, an image of the shock tube slit was formed on and crossed with the spectrograph slit (Sec. CC). The spectrograph was stigmatic; thus, a spectrum whose height was equal to the width of the image of the shock tube slit was formed in the film plane of the spectrograph. As the rotating mirror turned (Sec. BB), the position of the image moved down the spectrograph slit, and changes in the light source at the shock tube slit could be recorded on the spectrogram as a function of time. The synchronizer on the rotating mirror was adjusted so that the spectrograph would begin recording shortly before the primary shock wave reached the end of the tube. The speed of the mirror was chosen so that the spectrograph could record for about $15 \mu\text{sec}$, whereas, the lifetime of the reflected shock wave was about $10 \mu\text{sec}$. Nevertheless, because of jitter in the synchronizer mechanism, some of the shots fired in this way did not give a full time-history of the reflected shock wave. The region to be viewed by the spectrograph (intersection of *projected spectrograph slit* and *shock tube slit* in Fig. 2, Sec. AA) was located as near to the end of the shock tube as seemed practical. A small aperture was necessary to exclude light which might have been emitted by material from the Pyrex end plate.

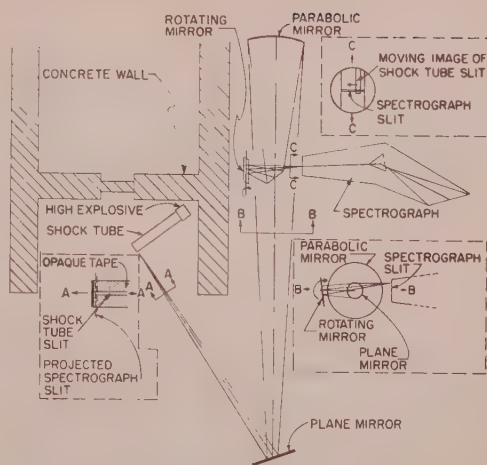


FIG. 2. Experimental arrangement for obtaining time-resolved spectra.

The total response time of this system will be defined as the time required for the intensity at the spectrogram to rise to full value if a step-function light source moves down the tube. This time response may be conveniently divided into two parts: (1) that due to the shock tube slit width and rotating mirror speed, and (2) that due to the spectrograph slit width and the speed with which the step-function moves.

First, assume that the shock tube slit area becomes suddenly illuminated uniformly. The length of time t_1 during which light falls on any point on the photographic plate is equal to the length of time required for the image to sweep its own width. This can be expressed by

$$t_1 = W_s / S = W / (M2\omega a),$$

where

W = width of shock tube slit,

$M = \frac{\text{parabolic mirror to shock tube distance}}{\text{parabolic mirror to spectrograph slit distance}},$

ω = angular velocity of rotating mirror,

$W_s = W/M$ = width of image of shock tube slit,

a = writing arm (rotating mirror to spectrograph slit distance), and

$S = 2\omega a$ = writing speed.

For a typical set of numbers $t_1 \approx 1.0 \mu\text{sec}$.

Now consider the case in which the mirror is not moving, but a step-function light source travels down the shock tube. Here the intensity at the spectrogram will rise during the time t_2 required for the step-function to travel across the image of the spectrograph slit projected into the shock tube. There is also a correction for the effective spreading of the slit due to the depth

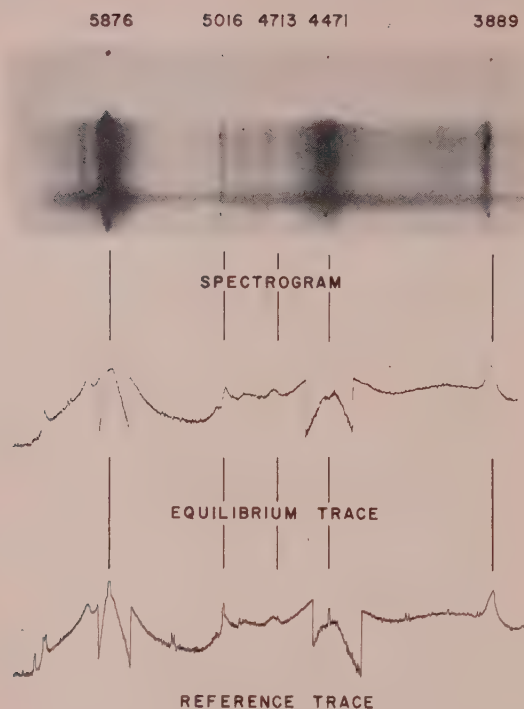


Fig. 3. Time-resolved spectrogram and microphotometer traces. Wavelengths are given in angstrom units at the top of the figure. Time increases from top to bottom on the spectrogram, the time between the upper and lower helium reference spectra being about 13 μ sec. The response time in this spectrogram is about 1 μ sec. The reference trace was made at the center reference spectrum and the equilibrium trace was made just below the center reference spectrum. The actual length of the spectrogram between 3889 and 5876 Å was 3.3 mm, whereas, the corresponding distance on the microphotometer traces was about 125 cm. From the traces it is apparent that the granularity of the photographic emulsion limited resolution, but in most cases the reduced speed of a less granular emulsion would not have produced a measurable film density.

of the light source in the shock tube. For this case

$$t_2 = \frac{0.07 \text{ mm} + W_s}{U_R/M},$$

where W_s = spectrograph slit width, U_R = velocity of the step-function (reflected shock velocity), and 0.07 = effective spreading of slit (mm). A typical set of numbers yields $t_2 \approx 0.2 \mu$ sec. The total response time of the system is $t_1 + t_2 = t$.

Prior to each shot, helium reference spectra were placed at the top, center, and bottom of the spectrogram. These were about $\frac{1}{2}$ mm high, corresponding to about $\frac{1}{2}$ μ sec in writing time. This caused at least one reference spectrum to be superimposed on a small portion of the spectrum from the helium in the reflected shock wave. A time-resolved spectrogram on which the helium reference spectra can be seen is presented in Fig. 3.

Measurements of the shape (intensity vs wavelength) of a spectral line from a spectrogram required that the photographic emulsion (Kodak Tri-X, 1955 type) be calibrated with respect to relative light intensity in the spectral vicinity of the line. This required a light source which emitted continuous radiation in the vicinity of the interesting helium lines. The calibration plates which were used for all of the quantitative measurements were obtained with a 7-step neutral density filter and an Edgerton, Germeshausen, and Grier XP-xenon flash lamp.

EXPERIMENTAL RESULTS

The purpose of these experiments was to study the shape and shift of spectral lines of helium in a thermodynamic state where perturbations of the energy level by electrons were expected to be important. Calculated values of the thermodynamic state of the gas behind the reflected shock depended on the initial pressure in the shock tube and the velocity of the primary shock. The shock velocity was found to be the same, to within the precision of the measurements, for initial helium pressures of 5, 20, and 35 mm Hg. Therefore, the average of velocities from tubes with all these pressures was used for the calculations. The mean primary shock velocity measured from 6 shock tubes was 12.47 mm/ μ sec with a standard deviation of 0.13 mm/ μ sec.

In Fig. 3 is shown a time-resolved spectrogram of the light from the reflected shock in a tube with an initial helium pressure of 20 mm Hg. Other tubes were fired at this pressure and at 5 and 35 mm Hg. The existence of a steady state behind the reflected shock was quantitatively confirmed on several spectrograms by making microphotometer traces at three times all of which preceded the collision of the explosion products with the reflected shock. No changes in line broadening, shift, or intensity were detected, implying either negligible change in ion and electron density or balance between losses by recombination and a long-term relaxation phenomenon leading to ionization. The latter is considered unlikely because of the rapidity with which a steady radiation state is reached near the shock front.

In spectrograms where time response was about μ sec, the apparent times to reach a steady radiation state were about as given below.

Initial pressure (mm Hg)	5	20	35
Relaxation time (μ sec)	1	1/2	<1/2

This indication that relaxation time is dependent of initial pressure is reasonable, but the time resolution of the equipment was not good enough to permit an exact quantitative study of the kinetic phenomena.

Measurements of the spectra were made on traces from a recording microphotometer. At least two traces from each spectrogram were necessary for its analysis. One record was made along what appeared to be the center of the equilibrium region. Another was made

TABLE I. Data from time-resolved spectra.

Initial pressure (mm Hg)	Final temperature (ev)	Electron and ion density (10^{17} cm^{-3})	Shift (Å)						Width at half-intensity (Å)	
	Wavelength of line (Å)		3889	4470 ^a	4471	4713	5016	6069 ^a	3889	5876
5 ^b	1.70±0.01	1.8±0.1	2±1	14±2	12±2	9±2		6±2	12±2	40±10
20 ^c	1.82±0.02	5.8±0.3	4±1	20±2	19±2	26±3	7±2	9±2	18±2	140±20
35 ^c	1.87±0.02	9.3±0.6	7±1	25±2	26±2		13±2	11±2	29±2	280±30

^a Forbidden transition.^b One spectrogram.^c Two spectrograms.

along a reference spectrum which lay in the equilibrium region. The second trace provided a spectrograph dispersion curve and a direct wavelength reference for the shock spectrum. The microphotometer traces used in the analysis of the spectrogram are shown at the bottom of Fig. 3. Without changing the sensitivity or focus of the microphotometer, traces were also made at various wavelengths on the step-wedge calibration plate. This provided a direct relationship between microphotometer chart reading and relative exposure on the plate. The calibration procedure used here gave only relative values; absolute measurements of source intensities were not made.

The helium lines at 3889, 4471, 4713, 5016, and 5876 Å appear on the shock spectrum in Fig. 3. Also, two forbidden lines are seen: $4^3\text{F}-2^3\text{P}$ at 4470 Å and $3^3\text{P}-2^3\text{P}$ at 6069 Å. Measurements of both width and shift could not be made in every case because the lines were often too weak or too broad to obtain a position or width. Under the conditions of our experiments, shift measurements could usually be made on the lines at 3889, 4470, 4471, 4713, 5016, and 6069 Å. The lines at 3889 and 5876 Å were analyzed for shape. The line at 6687 Å was not studied because the sensitivity of the photographic emulsion changes rapidly with wavelength in this region of the spectrum.

Line shifts were measured by superposing the reference trace on the equilibrium trace and converting chart shift to wavelength shift with a dispersion curve. The major uncertainty in the line shift measurements from a given plate was the location of the center (wavelength of maximum intensity) of the shifted line, particularly if the line were broadened asymmetrically.

The shape (relative intensity vs wavelength) of a spectral line was obtained as follows: The chart reading was transformed to a function which was proportional to the light intensity at the spectrogram by using the emulsion calibration curve for the wavelength region of the line in question. The spectral response of the emulsion changed sufficiently slowly with wavelength that it could be assumed constant over the width of the line and equal to its value at the center of the line. Since the transmissivities of the quartz spectrograph and the Pyrex shock tube were essentially constant from 3600 to 6500 Å, a function which is proportional to light incident on the spectrogram is also proportional to the light emitted at the helium source within the

shock tube. Call this function I_x , where x is an index representing a linear measure along the spectrogram or microphotometer trace. If I_λ is proportional to the intensity per angstrom unit incident on the spectrogram, then $I_\lambda = I_x/S$, where S is the slope of the dispersion curve, i.e., $S = d\lambda/dx$. In order to study a particular line it was necessary to subtract the background radiation from I_λ . (By "background" radiation is meant all radiation which is not due to the line itself.) Usually this merely involved subtracting a constant equal to the I_λ at the two minima bounding a line, but in cases where the edges of two lines overlapped the shape of one of the lines had to be estimated before the shape of the other could be deduced.

Broadening and shift data are presented in Table I. The error ranges in the shifts and half-widths in this table were estimated, respectively, according to the difficulty of determining the center of the shifted lines and the intensity of background radiation. The absence of values for certain lines at certain pressures implies that the lines were not measurable because of low intensity or excessive broadening. Two experimentally determined line shapes are presented in Fig. 4.

THERMODYNAMIC STATE OF THE SHOCKED HELIUM

Plane wave shock hydrodynamic theory predicts the state of an equilibrated gas behind a shock wave as a function of initial conditions and shock velocity.^{3,5} The following assumptions were made in the calculation of the thermodynamic state of the emitting gas.

(1) It was assumed that the flow phenomena in the shock tube could be described by the equations for a one-dimensional shock wave with heat conduction, radiative cooling, and viscosity neglected.

The observed planarity of the shock waves tended to justify the one-dimensional assumption.

(2) Thermodynamic equilibrium was assumed to exist in finite regions behind the shock fronts.

The steady radiation state on the time-resolved spectrograms was believed to indicate that all relaxation phenomena had been completed and that radiative

⁵ E. Resler, S. Lin, and A. Kantrowitz, J. Appl. Phys. **23**, 1390 (1952).

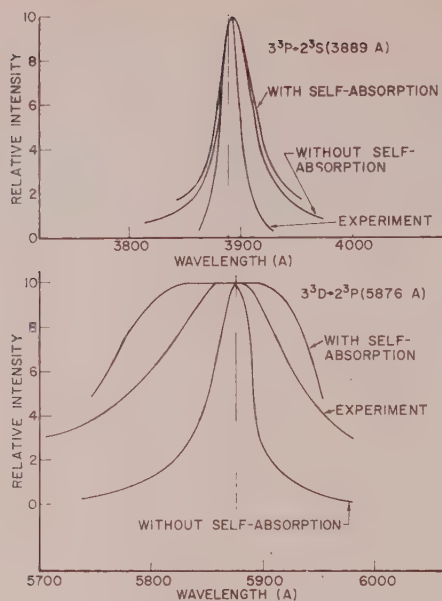


FIG. 4. Comparison of theory and experiment for two spectral lines emitted by helium at a temperature of 1.82 eV with ion and electron density of $5.8 \times 10^{17} \text{ cm}^{-3}$.

losses caused negligible changes in the thermodynamic state. A calculation of losses by bremsstrahlung, recombination, and line radiation for the conditions encountered in the experiments suggested that radiation losses amounted to less than 4% of the energy of the gas in the reflected shock wave during the 10 μsec observation period.

(3) Reflection of the shock wave was assumed to occur at a perfectly rigid wall.

No motion of the end plate on the shock tube was observed on the camera records during the first 10 μsec following reflection, and a calculation showed that this motion should have been less than 0.02 mm.

(4) It was assumed that helium atoms, helium ions, and electrons formed an ideal gas.

(5) The Saha equation was assumed to give the correct degree of ionization. Electronic excitations and pressure ionization were neglected because they are both small effects for the conditions of the experiments and tend to cancel each other in a calculation of the degree of ionization. (Here "pressure ionization" refers to the effective lowering of the ionization potential when the density of particles is not vanishingly small).

Calculated values for the electron and ion density and temperature behind a reflected shock as a function of initial helium pressure are shown in Fig. 5. The way in which the standard deviation of the velocity measurements influences the calculated thermodynamic state is shown by the dashed lines.

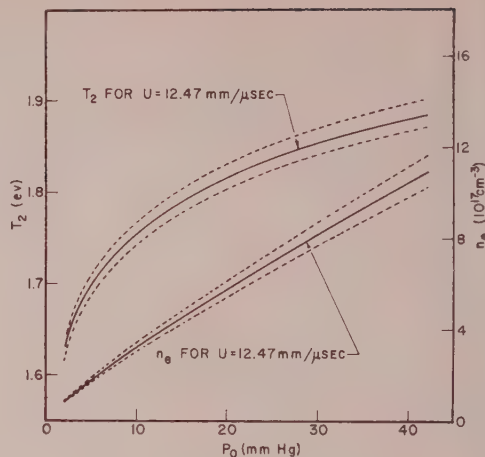


FIG. 5. Temperature and ion and electron density vs initial pressure of helium in the shock tube. Dashed lines indicate the spread in calculated values caused by the standard deviation in the measurement of shock velocity ($12.47 \pm 0.13 \text{ mm}/\mu\text{sec}$).

COMPARISON WITH THEORY

Line broadening and shift. The broadening and shift of spectral lines stem from several causes; the relative importance of these depends on the conditions within the emitting gas. In the experiments considered here the effect of interactions with charged particles was so great that other sources of broadening and shift were negligible. Among those neglected effects are dipole and quadrupole interactions, radiation damping, van der Waals interactions, and Doppler broadening.

The interaction of charged particles with a radiating atom has been treated for two limiting cases, that in which the emitting atom is disturbed by discrete encounters, and that in which the emitting atom is assumed to be in a slowly varying field produced by the surrounding particles. Kivel² has applied his theory of broadening and shift by electron impact to the particular case of helium, and that treatment has been used here for a comparison with the experimental results. Holtsmark's⁶ theory has been used to calculate the slowly varying fields due to the helium ions.

The prediction of the shape and position of a spectral line required a method of combining the effects of the ions and electrons. This was done in the following manner:

(1) The splitting of the line due to a quadratic Stark effect was calculated as a function of the electric field due only to the ions. According to Bethe,⁷ the energy shift of a Stark component is given by

$$\Delta E_{n,l,m} = e^2 F^2 \left(\frac{z_{n,l+1,m}^2}{E_{n,l} - E_{n,l+1}} + \frac{z_{n,l,m}^2}{E_{n,l} - E_{n,l-1}} \right),$$

⁶ J. Holtsmark, *Ann. Physik* **58**, 577 (1919).

⁷ H. Bethe, *Handbuch der Physik* (Verlag Julius Springer, Berlin, 1933), 2nd ed., Vol. 24, Part I.

where the shift of the lower state of the transition is neglected. The notation is as follows:

$\Delta E_{n,l,m}$ = energy shift of state with quantum numbers n, l , and m ,

e = electronic charge,

F = electric field,

$E_{n,l}$ = energy of unperturbed level with quantum numbers n and l ,

$$z_{n,l,m}^2 = (z_{n,l,m}; n, l-1, m)^2 \\ = \left| \int \psi_{n,l,m}^* \mathbf{r} \cos\theta \psi_{n,l-1,m} d\tau \right|^2, \text{ where}$$

$\psi_{n,l,m}$ = hydrogen wave function for state with quantum numbers n, l , and m .

The matrix elements $z_{n,l,m}^2$ are evaluated by Bethe,⁷ and helium energy levels were taken from Moore.⁸

(2) An electron-broadened line shape of the form $I(\omega) \propto [\gamma^2 + (\omega - \omega_0)^2]^{-1}$ was assumed for each Stark component where $I(\omega)$ is the radiated intensity per unit frequency at an angular frequency ω , and γ is the half width at half intensity of the line. Use was made of Kivel's² expression for the half width due to electron broadening

$$\gamma_{n,l} = \frac{2n_e v_\lambda \sigma_\lambda}{3} \sum_{l'=l+1} \left(\frac{r_{n,l}^{n,l-1}}{a} \right)^2 2 \ln \left| \frac{4\epsilon_\lambda}{E_{n,l} - E_{n,l-1}} \right|,$$

where

$\gamma_{n,l}$ = half-width at half-intensity of an emission line originating at state n, l (independent of m , and neglecting smearing of lower state) in units of $2\pi\nu$;

n_e = electron particle density;

v_λ = electron velocity;

$\sigma_\lambda = \pi/k_\lambda^2$, where k_λ = electron propagation number;

$$(r_{n,l}^{n',l'})^2 = \sum_{m'} |r_{n,l,m}^{n',l',m'}|^2 = \frac{l}{2l+1} |R_{n,l}^{n',l'}|^2$$

a = first Bohr radius;

ϵ_λ = electron kinetic energy; and

$E_{n,l}$ = energy of level with quantum numbers n and l .

Values for $|R_{n,l}^{n',l'}|^2$ are tabulated in reference 7, and v_λ , σ_λ , and ϵ_λ were taken to be the most probable values for a temperature T when a Maxwellian distribution is assumed.

⁸ Charlotte E. Moore, "Atomic Energy Levels," National Bureau of Standards Circular 467 (1948).

(3) Each electron-broadened Stark component was numerically integrated over a probability distribution function for the electric field F due to the ions. Breene's⁹ corrected form of the Holtsmark⁶ distribution function is

$$W(\beta) d\beta = \frac{4\beta^2 d\beta}{3\pi} (1 - 0.462\beta^2 + 0.1227\beta^4 - 0.02325\beta^6 + \dots)$$

for small β , and

$$W(\beta) d\beta = \frac{d\beta}{\beta^{\frac{1}{2}}} 1.496 \left(1 + \frac{2.555}{\beta^{\frac{1}{2}}} + \frac{14.43}{\beta^{\frac{3}{2}}} + \frac{0}{\beta^{\frac{5}{2}}} + \dots \right)$$

for large β , where $\beta = F/F_n$, and F_n is given by $2.61 en_e^{\frac{1}{2}}$ for an ion density n_e . The integral

$$I(\nu) = \int_0^\infty I[\nu, \nu_0(F)] W(F) dF,$$

where $I[\nu, \nu_0(F=0)]$ is the electron-broadened Stark component, was assumed to give the shape of the component when broadened by both electrons and ions.

(4) The Stark components were added graphically to give a total line shape. The area, or strength, of each component is proportional to the sum of the intensities of the transitions originating in state n, l, m . Values for these strengths were taken from Condon and Shortley.¹⁰

(5) The total line shape was shifted by an amount depending on the electron density and temperature. The shift of the level n, l is given by Kivel² as

$$\delta_{n,l} = -\frac{2n_e v_\lambda \sigma_\lambda \pi}{3} \sum_{n',l'} \left(\frac{r_{n,l}^{n',l'}}{a} \right)^2 \frac{\omega_{n,l}^{n',l'} - \delta_{n,l}}{|\omega_{n,l}^{n',l'} - \delta_{n,l}|},$$

where the sum over n and l includes all states that can be excited by a free electron with velocity v_λ . The energy shift of level n, l is $\delta_{n,l}$ in units of $2\pi\nu$, and $\omega_{n,l}^{n',l'}$ is the energy difference between levels n, l and n', l' in units of $2\pi\nu$. Algebraic subtraction of the shifts of the upper and lower states of a transition gives the shift of a spectral line due to electrons.

The results of such a treatment on lines at 3889 and 5876 Å for a temperature of 1.82 eV and ion density of $5.8 \times 10^{17} \text{ cm}^{-3}$ are compared with experimentally measured shapes in Fig. 4. The discrepancy in the width of the strong 5876 Å line is thought to be partly due to self-absorption and is discussed in the next section. No such explanation can be applied to the disagreement between theory and experiment in the case of the line at 3889 Å, since the experimental width is less than (slightly more than one-half) the predicted width.

Here it is noteworthy that the neglect of the effect of

⁹ R. G. Breene, Jr., Revs. Modern Phys. **29**, 94 (1957).

¹⁰ E. U. Condon and G. H. Shortley, *The Theory of Atomic Spectra* (Cambridge University Press, Cambridge, England, 1953), p. 411.

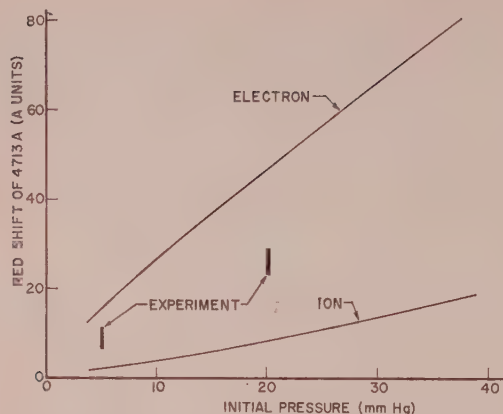


FIG. 6. Shift of the line at 4713 Å. Predicted shifts due to ions and electrons are compared with experimentally measured values.

the electrons would have resulted in half-width predictions of less than 1 Å and less than 4 Å for the lines at 3889 and 5876 Å, respectively. These values are clearly too small by an order of magnitude and show the necessity of considering electron effects. The question as to whether Kivel's treatment is adequate or whether more elaborate methods¹¹ are necessary is not answered by these experiments.

Wavelength shifts have been calculated for the lines at 4713 and 5016 Å and are compared with experiment in Figs. 6 and 7. Note that the predicted ion effects alone are again insufficient to account for the observed shifts, whereas, inclusion of the electron effects yields a somewhat greater shift than that which was observed.

Self-absorption. When a spectral line is emitted by a gas sample having a finite thickness, the line will appear broader as the sample thickness is increased. Consider the simple case of a column of gas of unit cross section

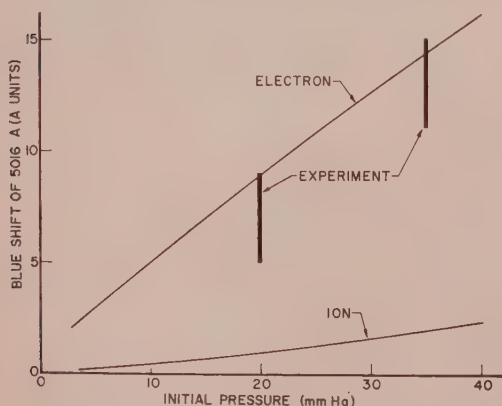


FIG. 7. Shift of the line at 5016 Å. Predicted shifts due to ions and electrons are compared with experimentally measured values.

which emits collimated light uniformly in the positive x direction. The observed shape of the line at x is

$$I(\nu, x) = I_B(\nu, T) \{1 - \exp[-\mu(\nu)x]\},$$

where $I_B(\nu, T)$ denotes the radiation from the surface of a blackbody at temperature T , and $\mu(\nu)$ is the absorption coefficient of the line. In order to predict $I(\nu, x)$ the self-absorbed line shape, it is necessary to know $\mu(\nu)$. The shape of $\mu(\nu)$ was taken to be the predicted broadened shape shown in Fig. 4, and a magnitude was obtained by using published transition probabilities.

This approximate method for predicting self-absorption has been applied to the calculated line shapes at 3889 and 5876 Å. Resulting self-absorbed line profiles are shown in Fig. 4 where they are compared with the calculated profiles without self-absorption and with the experimentally determined profiles.

Depression of the series limits. The helium lines at 4471 Å (4^3D-2^3P) and 4713 Å (4^3S-2^3P) were observed experimentally, although they were very broad, whereas, the normally strong line at 4026 Å (5^3D-2^3P) was never observed. This implies that the energy levels with principal quantum numbers 5 and greater are smeared together.

Inglis and Teller¹² have treated the depression of the series limits in one-electron spectra by determining the ion density necessary to cause Stark broadened levels with different principal quantum numbers to overlap into a continuum. A similar calculation can be made to obtain an approximate value for the ion density necessary to cause merging by second order Stark broadening^{6,7} of helium lines with different principal quantum numbers.

For the minimum ion density obtained in the experiments, about $2 \times 10^{17} \text{ cm}^{-3}$, this calculation predicted, as was observed, that the series limits would be somewhere between levels with principal quantum numbers 4 and 5.

Forbidden lines. Lines were observed experimentally which corresponded to the normally forbidden transitions 3^3P-2^3P and 4^3F-2^3P . The wavelengths and relative intensities of these forbidden transitions can be predicted as a function of the electric field at the emitting atom.

These two lines were treated by separate methods. The line originating at the 3^3P level is subjected to a treatment in which it is assumed that all ionic effects are proportional to the square of the electric field.^{6,7} This assumption is valid only as long as the perturbation of the energy level is small compared to the initial separation of the level from others with the same principal quantum number. Theoretically predicted values for the line shift of 3^3P-2^3P line at 6069 Å are compared with experimental values in Fig. 8. The predicted shifts were obtained in the same way as

¹¹ H. R. Griem, M. Baranger, A. C. Kolb, and K. Y. Shen (to be published).

¹² D. R. Inglis and E. Teller, *Astrophys. J.* **90**, 439 (1939).

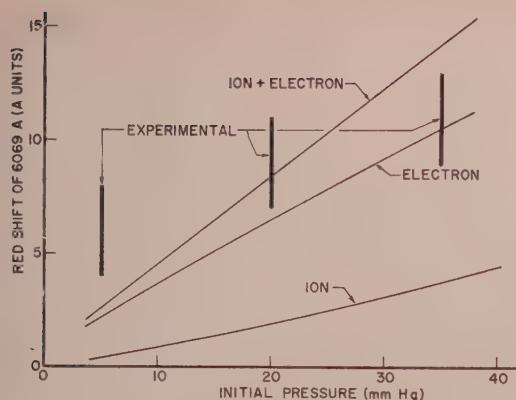


FIG. 8. Shift of the forbidden line at 6069 Å. Predicted shifts due to ions and electrons are compared with experimentally measured values.

were those plotted in Figs. 6 and 7. A rough calculation of the intensity of the forbidden line to that of the allowed line at 5876 Å yields 0.03, which agrees to within an order of magnitude with the experimental results.

In the case of the allowed-forbidden pair 4^3D-2^3P and 4^3F-2^3P at about 4470 and 4471 Å, respectively, the perturbations of the levels 4^3D and 4^3F were greater than the normal energy separation. For this reason, it was necessary to extend Foster's¹³ treatment of the effect of the helium ions to higher field strengths. Predicted shifts are compared with experimental results in Fig. 9. Foster's method for determining the ratio of the intensity of the forbidden line 4^3F-2^3P to that of the allowed line 4^3D-2^3P predicts that the forbidden line is actually slightly stronger for the ion densities obtained in the experiments. This was observed to be the case.

CONCLUSIONS

A method has been devised for driving shocks in gases by means of high explosive charges. The sample of compressed gas after reflection of such a shock can be maintained without much contamination under equilibrium conditions for times of the order of 10 μ sec. In the particular case of helium, the technique has produced temperatures near 20 000°K with ion densities near 10^{18} cm⁻³. These conditions can be evaluated by hydrodynamic calculation from shock

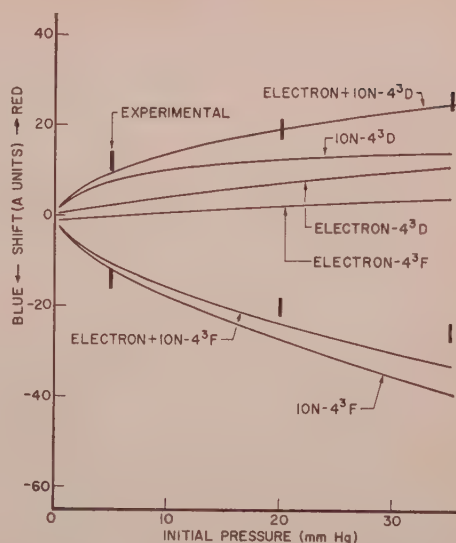


FIG. 9. Shifts of the allowed-forbidden pair at 4470 and 4471 Å. Predicted shifts due to ions and electrons are compared with experimentally measured values.

measurements and are roughly confirmed by the spectroscopic measurements.

Time-resolved spectra of helium in such reflected shocks showed that a steady radiation state was reached in 1 μ sec or less, the relaxation time varying in some inverse fashion with the initial pressure in the shock tube. This steady state persisted without change in continuum intensity, line intensity, or line shape until the reflected shock collided with the driver explosive products. All observable lines were broadened and shifted. The ion effect was not sufficient to explain the magnitude of the broadening and shift for most of the lines, but inclusion of the free electron effect provided better agreement between theory and experiment. Self absorption corrections were necessary for the strong line at 5876 Å.

Depression of series limits and the wavelengths and intensities of two forbidden transitions (3^3P-2^3P and 4^3F-2^3P) also confirmed the hydrodynamic calculation of the conditions in the compressed gas.

ACKNOWLEDGMENTS

The authors wish to thank Bennett Kivel for his theoretical contributions, J. O. Johnson for technical assistance, and R. E. Duff for the thermohydrodynamic calculations.

¹³ J. S. Foster, Proc. Roy. Soc. (London) **A117**, 137 (1927).

Magnetization Curve of an Infinite Cylinder

M. W. MULLER AND A. WEHLAU
Varian Associates, Palo Alto, California

(Received May 15, 1961)

We have calculated the magnetization curves of an infinite ferromagnetic cylinder with negative uniaxial anisotropy. The cylinder axis is a hard magnetocrystalline direction and the basal plane is an easy plane. The applied field lies along the cylinder axis. The distribution of the magnetization corresponds to the azimuthally symmetric mode denoted as "magnetization curling." With the present choice of anisotropy, stable solutions for the distribution can be obtained through partial reversal of the magnetization.

I. INTRODUCTION

THE magnetization curve of an infinite isotropic ferromagnetic cylinder has been discussed by Brown¹⁻³ and by the group of workers at the Weizmann Institute of Technology.^{4,5} These authors conclude that such a cylinder has a rectangular hysteresis loop, and they give expressions for the coercive force as a function of the exchange constant and saturation magnetization of the material, and of the radius of the cylinder.

The theory of the rectangular hysteresis loop may be briefly summarized as follows: For a sufficiently large applied field, the (nonlinear) equation for the distribution of the magnetization admits only the trivial solution, which describes uniform saturation. As the applied field is reduced (and reversed), a value of the field (called the nucleation field) is reached which allows infinitesimal deviations from saturation to occur. The form of these deviations is determined by solving a linear approximation of the distribution equation. It can be shown that this solution of the linearized equation is not a stable solution of the full nonlinear problem; in fact, the only stable solution of the nonlinear problem is again the trivial saturated solution with the magnetization reversed. Thus, the magnetization curve is rectangular, and the coercive force is given by the nucleation field.

It has been recently shown⁶ that for certain geometries of *anisotropic* ferromagnetic samples it is possible to predict stable finite deviations from saturation. The work of reference 6 was primarily concerned with demonstrating incipient domain formation by means of an approximate treatment. In the present note it will be shown that the theory can be used rigorously to predict the magnetization curve of an infinite cylinder with a particular form of the magnetocrystalline anisotropy. The anisotropy is uniaxial, with a hard axis of magnetization along the cylinder axis, and an easy plane of magnetization in the basal plane (this form of anisotropy is characteristic, for example, of the group of ferrites known as "ferroxplana").

II. THEORY

The energy of first-order uniaxial magnetocrystalline anisotropy is given by

$$E_k = K \sin^2 \omega, \quad (1)$$

where K is the first-order anisotropy constant and ω is the angle between the magnetization I_s and the principal (hexagonal) axis, here taken as the z axis. If $K > 0$, the z axis is an easy axis; if $K < 0$, it is a hard axis and the basal plane is an easy plane. We will deal with $K < 0$.

The nonlinear differential equations for the transverse components of the magnetization α, β are:

$$-\frac{2A}{I_s}(\gamma \nabla^2 \alpha - \alpha \nabla^2 \gamma) + \frac{2K}{I_s} \alpha \gamma + \left(\gamma \frac{\partial U}{\partial x} - \alpha \frac{\partial U}{\partial z} + \alpha H \right) = 0, \quad (2)$$

$$\frac{2A}{I_s}(\beta \nabla^2 \gamma - \gamma \nabla^2 \beta) + \frac{2K}{I_s} \beta \gamma - \left(\beta \frac{\partial U}{\partial x} - \gamma \frac{\partial U}{\partial y} - \beta H \right) = 0,$$

where $\gamma = \cos \omega$, A is the exchange constant, U is the magnetostatic potential, and $\mathbf{H} = H_z$ in the applied field. If these equations are linearized by dropping terms of second or higher order in small quantities, we obtain the linear equations given in reference 5, with E replaced by $H + 2K/I_s$. Thus the linear theory of reference 5 is completely applicable to the problem treated here. In particular, we conclude that the nucleation mode is the "curling" mode for $S > 1.1$, and that the reduced nucleation field is given by

$$\pi S^2 h_n = -\pi S^2 2k - 3.39, \quad (3)$$

where we have adopted the notation

$$h = H / (2\pi I_s), \quad k = K / (2\pi I_s^2), \quad R_0 = A^{1/2} / I_s, \quad S = R / R_0$$

and where R is the radius of the cylindrical sample.

Thus, if we restrict ourselves to $S > 1.1$, we need to consider only the curling mode in the nonlinear problem. This is not a very serious restriction, since for typical magnetic materials R_0 is of the order of 100 Å.

¹ W. F. Brown, Jr., Phys. Rev. **105**, 1479 (1957).

² W. F. Brown, Jr., J. Appl. Phys. **30**, 62S (1959).

³ W. F. Brown, Jr., J. Appl. Phys. **29**, 470 (1958).

⁴ E. H. Frei, S. Shtrikman, and D. Treves, Phys. Rev. **106**, 446 (1957).

⁵ A. Aharoni and S. Shtrikman, Phys. Rev. **109**, 1522 (1958).

⁶ M. W. Muller, Phys. Rev. **122**, 1485 (1961).

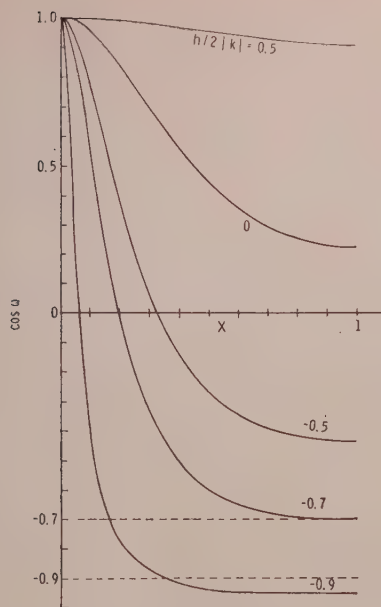


FIG. 1. Radial distribution of the axial component of magnetization for various values of applied field; $S^2|k| = 1.21$.

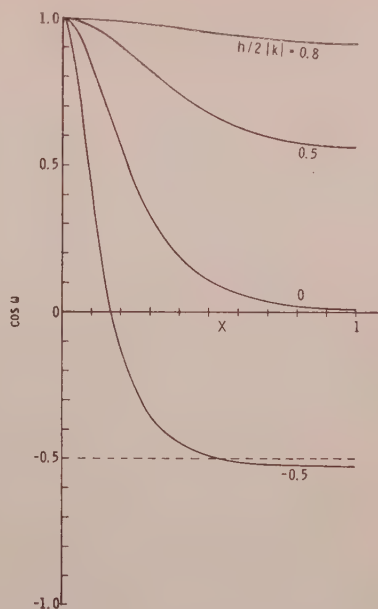


FIG. 2. Radial distribution of the axial component of magnetization for various values of applied field; $S^2|k| = 4$.

The nonlinear equation for the curling mode is⁷

$$\frac{d^2\omega}{dx^2} + \frac{1}{x} \frac{d\omega}{dx} - \left[2\pi S^2|k| \left(\frac{h}{2|k|} - \cos\omega \right) + \frac{\cos\omega}{x^2} \right] \sin\omega = 0, \quad (4)$$

where $x = r/R$. The boundary conditions are

$$\omega(0) = 0, \quad \omega'(1) = 0. \quad (5)$$

If S is very large, Eqs. (4) and (5) are solved by

$$\omega = 0, \quad x = 0, \\ \cos\omega = h/2|k|, \quad x \neq 0, \quad (6)$$

and the magnetization curve is given by

$$I_z = I_s \cos\omega = I_s H/H_a,$$

where $H_a = -2K/I_s$ is the "anisotropy field."

For finite values of the cylinder radius, Eq. (4) can be integrated numerically. This was done on Stanford University's Burroughs 220 computer using a Runge-Kutta method. The two-point boundary value problem was solved by trial and error. The procedure was to choose a value of $\omega'(0)$, and to adjust this value until the first null of $\omega'(x)$ came at $x=1$.

It should be noted that while this condition probably ensures uniqueness of the solution, it does not necessarily lead to the minimum energy configuration. Indeed, for

sufficiently negative values of $h/2|k|$, and large enough values of $2\pi S^2|k|$, no solution exists meeting the stated conditions. With these values of the parameters, it appears plausible that the minimum energy configuration corresponds to a solution in which the second (or higher) zero of $\omega'(x)$ coincides with $x=1$. It is also possible that under these conditions the distribution of the magnetization may be unstable to perturbations of lower symmetry than the curling mode.⁸ We have made no attempt to obtain such solutions, but we will discuss the regions in which they might be applicable in the next section.

Once a solution $\omega(x)$ has been obtained, the magneti-

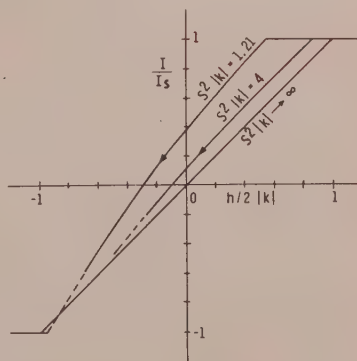


FIG. 3. Magnetization curves of the infinite cylinder for several values of the cylinder radius.

⁷ Note that Eq. (4) is identical with Eq. (1) of reference 3, except for the sign of the anisotropy constant. It is because of the negative anisotropy assumed here that the solutions of Eq. (4) are stable.

⁸ A. Aharoni, E. H. Frei, and S. Shtrikman, J. Appl. Phys. **30**, 1956 (1959).

zation curve is computed from

$$I_z/I_0 = 2 \int_0^1 x \cos \omega x. \quad (7)$$

This procedure produces results valid for an infinite cylinder. An approximate extension to finite cylinders can be obtained by the use of demagnetizing factors as suggested by Brown.³

III. RESULTS

Computed curves of $\cos \omega(x)$ versus x for various values of $h/2|k|$ and for $S^2|k| = 1.21$ and $S^2|k| = 4$ are given in Figs. 1 and 2. All the curves displayed in these figures satisfy the condition that the first zero of $\omega'(x)$ comes at $x=1$. It was determined by direct compu-

tation that no such solution exists if $S^2|k|=4$ and $h/2|k| < -0.7$. Note also that for sufficiently negative values of $h/2|k|$ it is found that $\cos \omega < h/2|k|$ in the outer portion of the cylinder. In this region, the magnetization has reversed further than one would predict on the basis of the Zeeman and anisotropy energies alone. Since it is plausible that exchange forces would tend to reduce the amount of magnetization reversal, one can tentatively conclude that these states are physically inaccessible. In accordance with this consideration, the magnetization curves shown in Fig. 3 have been drawn dashed in the corresponding regions. It appears likely that in the region the magnetization may assume distributions in which $\omega'(x)$ has more than one zero. It is not obvious, however, how such distributions are reached from the nucleation mode.

Effects of Transition Metal Solutes on the Electrical Resistivity of Copper and Gold Between 4° and 1200°K

C. A. DOMENICALI AND E. L. CHRISTENSON
Honeywell Research Center, Hopkins, Minnesota

(Received May 17, 1961)

We have determined the solute contribution $\rho_i(T, c)$ of the solutes Cr, Mn, Fe, Co, and Ni in copper and of the solutes Mn, Fe, and Co in gold over the temperature range 4° to 1200°K and over a wide range of solute concentrations. The parameter $\rho_i(T, c)$ for a given solute is defined here as the difference $\rho_i(T, c) = \rho_{\text{alloy}}(T, c) - \rho_{\text{solvent}}(T)$. The temperature dependence of ρ_i is quite complicated for several of the solutes, in particular, Fe and Co. For example, in an alloy containing 0.05 at. % Fe in copper this quantity ρ_{Fe} exhibits a minimum at 25°K and a maximum at 65°K. Alloys of Fe in gold exhibit a broad maximum in ρ_{Fe} at temperatures between 70° and 200°K, depending upon the iron concentration. In all the alloys investigated, except for Ni in copper, ρ_i decreases with increasing temperature in the region of high temperatures (above about 500°K).

I. INTRODUCTION

The electrical transport properties of the noble metals, copper, silver, and gold are considerably altered by the presence of transition metal atoms in solid solution. In general, the electrical resistivity of a given alloy depends upon the temperature and solute concentration in a rather complicated way¹ and often exhibits a minimum as well as a maximum in the temperature region below 10° or 20°K. This behavior of the resistivity is usually accompanied by surprisingly large values of thermoelectric power and by various peculiarities in the magnetic properties, electronic specific heat, and in other parameters. In this paper we shall be concerned with the temperature dependence of electrical resistivity of noble metal binary alloys containing relatively large concentrations of certain transition metal solutes.

Most if not all of the specific theoretical models which have been proposed²⁻⁶ for treating the electrical resistivity have involved the assumption that the impurity or solute component of this resistivity is simply additive to the phonon component, and that this latter part is just the resistivity of the pure solvent at the same temperature. Now if this assumption is correct, it is clear that attention should be given to the experimentally determinable quantity

$$\rho_i(T, c) \equiv \rho(T, c) - \rho_T(T). \quad (1)$$

Here $\rho_i(T, c)$ is the temperature and concentration dependent *impurity* or solute resistivity, $\rho(T, c)$ is the measured resistivity of the given alloy, and $\rho_T(T)$ is the resistivity ("thermal" component) of the solvent metal itself. However, except for a few of the results presented

¹ A. N. Gerritsen, *Physica* **25**, 489 (1959). This paper contains a very useful table which summarizes the electrical and magnetic properties of noble metal alloys; it also contains an extensive list of references.

² J. Korrington and A. N. Gerritsen, *Physica* **19**, 457 (1953).

³ R. W. Schmitt, *Phys. Rev.* **103**, 83 (1956).

⁴ K. Yosida, *Phys. Rev.* **107**, 396 (1957).

⁵ A. D. Brailsford and A. W. Overhauser, *Phys. Rev. Letters* **3**, 331 (1959). See also A. J. Dekker, *Physica* **25**, 1244 (1959).

⁶ C. A. Domenicali, *Phys. Rev.* **117**, 984 (1960).

by Gerritsen and Linde⁷ and by Pearson,⁸ it seems that no one has seriously attempted to "separate out" the impurity scattering ρ_i from the thermal scattering ρ_T over large ranges of temperature and of solute concentration.

Our purpose is to describe what we find for this functional relation $\rho_i(T, c)$ in the case of the solutes Mn, Fe, and Co in both copper and gold solvents and in the case of the solutes Cr and Ni in copper over the temperature range between 4.2° and 1200°K and for a rather wide range of solute concentrations. Reference to the accompanying figures shows that this relationship can be quite complicated. In an earlier publication⁶ we tried to show how a rather simple mathematical model of electron scattering from an individual solute atom can correlate a considerable portion of the known electrical behavior of noble metal alloys. However, while this model seems to be in accord with many of the experimental facts, it cannot explain the simultaneous presence of a minimum and a maximum in the impurity component ρ_i for a single solute such as we find for chromium, iron, and cobalt in copper, and for iron in gold.

II. EXPERIMENTAL METHODS

All the alloys used in this work were prepared by melting the components (accompanied by mechanical shaking) in sealed quartz tubes and with appropriate precautions described in an earlier publication.⁹ The ingots were homogenized at temperatures near the melting point of the alloy for several hours, after which treatment they were rolled into square cross-section wires. In most cases the wires were given an intermediate anneal during the rolling stages, at about 500°C for several hours *in vacuo*, and all wires were given such an anneal before installation into the resistance apparatus. The copper used in this work was from American Smelting and Refining Company, and all the solute metals were from Johnson-Matthey. Before making the manganese alloys, we melted the J-M manganese in hydrogen to remove the oxide; this treatment was found necessary for obtaining good ingots. The gold was either from Johnson-Matthey or Baker Platinum Division, Englehard Industries (mint gold). In all cases the $\rho_T(T)$ used in Eq. (1) was the resistivity corresponding to the appropriate gold (J-M or Baker) used in the corresponding alloy.

The standard potentiometric method was used for determining the resistance of a given wire specimen between two probes, each of which consisted of an 0.010-in.-diam wire twisted around the specimen at a position marked by a small circumferential groove. In

the first stages of our work we measured one alloy specimen at a time, using thermocouples to indicate temperature, and the resistivity of pure copper (or pure gold) was determined separately with the same apparatus (and with the same thermocouples). Later on we used a "companion wire" technique in which a pure copper (or gold) specimen was measured at the same time as the alloy specimen in an "isothermal" holder with the two wires side by side. Also, in the earlier work we used a Rubicon type B potentiometer while in the later work we used a Rubicon six-dial thermofree potentiometer. The results for a given alloy were identical for these two methods.

The cross-section area of the wires was determined by weighing the wire and making use of published or calculated values of density; the calculated values were obtained from published data on crystal lattice parameters. In all cases we were careful to see that the density vs composition curve extrapolated to the value for pure copper (8.92 g/cm³) or pure gold (19.3 g/cm³). It can be seen that to a very good approximation the value of ρ_i obtained from Eq. (1) in this way depends only upon the difference between the densities of the alloy and of the pure solvent, and that the precise value used for the density of the pure solvent is not especially important. The thermal expansion or contraction of the alloy and of the pure solvent likewise has only a minor effect on the difference in Eq. (1).

The measurements made below 77°K were carried out with a wire specimen holder in the form of a thick-walled copper cylinder which also served as a helium-gas thermometer. The outer surface of this cylinder had six axial pairs of grooves lined with paper, and a set of six hairpin-shaped specimens were placed in these groove pairs. As before, the potential probes were small wires wrapped carefully around the wire specimen at well-defined points. The accuracy of the temperature readings with our helium thermometer is better than 1%.

III. DISCUSSION OF RESULTS

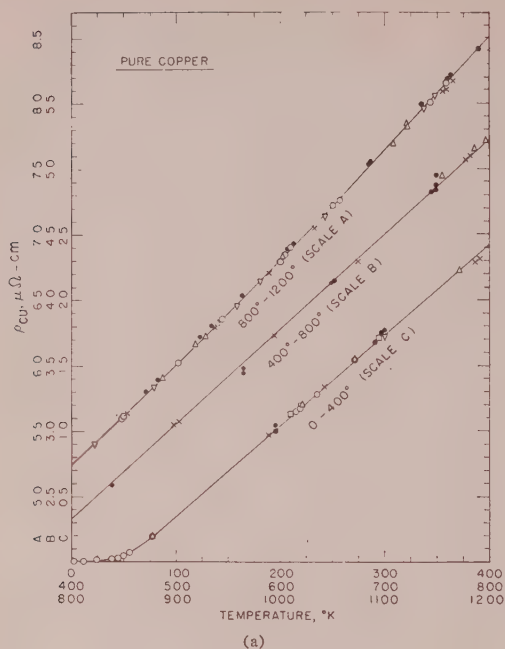
Pure Copper and Pure Gold

In determining $\rho_i(T, c)$ for a given alloy from Eq. (1), we have taken for $\rho_T(T)$ the resistivity of the corresponding solvent metal that was actually used in making this particular alloy. The resistivities of our copper and gold are shown in Figs. 1(a) and (b). The solvent metals we have used contain perhaps 10⁻⁴ to 10⁻³% of various "unintentional" impurities, including (probably) iron, and we are forced to assume here that these unwanted impurities in the *finished alloy* wire are the same in kind and amount as in the original solvent metal. If this is not so, but if the minute additional impurities picked up during wire fabrication contribute essentially a temperature independent component of resistivity to the alloy, then our ρ_i vs T curves need merely to be shifted slightly and parallel to their

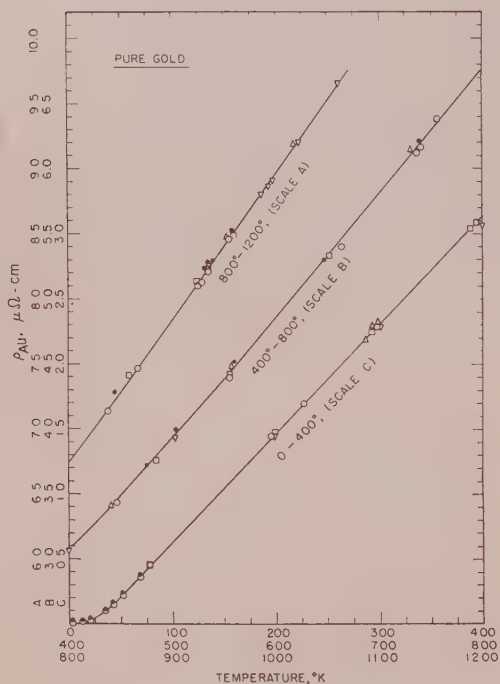
⁷ A. N. Gerritsen and J. O. Linde, *Physica* **18**, 877 (1952).

⁸ W. B. Pearson, quoted by D. K. C. MacDonald in *Handbuch der Physik* (Springer-Verlag, Berlin, Germany, 1956), Vol. XIV, Part 1, p. 189, Fig. 40(a) and (b).

⁹ C. A. Domenicali and E. L. Christenson, *J. Appl. Phys.* **31**, 1730 (1960).



(a)



(b)

FIG. 1. (a) Electrical resistivity of pure copper (American Smelting and Refining Company) over range 4° to 1200°K found in numerous series of resistivity determinations. The heavy dots represent one run, the crosses another, etc. (b) Resistivity of pure gold between 4° and 1050°K. The heavy dots are for mint gold (see text); all other points (circles, triangles, etc.) represent various runs on Johnson-Matthey gold.

present positions. It does not seem reasonable to us to suppose that our alloys have picked up enough extraneous impurities to alter the shape of our ρ_i vs T curves, particularly with those containing the highest concentrations of solute. Some of the minor irregularities that are found on several of the curves may be attributed to such trace impurities, such as for the copper cobalt alloys in the range of 4° to 10°K.

Chromium in Copper

The contribution ρ_i of the solute chromium in copper, which we now denote by ρ_{Cr} , is shown in Fig. 2 for 0.09 at. % Cr. The unusually large change in total resistivity between 4° and 25°K has already been reported by Linde¹⁰ for an 0.17 at. % Cr alloy. But we see in addition that ρ_{Cr} has a maximum at about 65°K which is also relatively large; that is, ρ_{Cr} is about 4% higher at 65°K than at 25°K for 0.09 at. % Cr in copper. This behavior, previously found in gold-chromium alloys by Gerritsen and Linde,⁷ adds further complications to an already difficult problem. We are not able to explain these effects with our model described in reference 6.

Manganese in Copper

Extensive work has been done on the electric and magnetic properties of copper manganese alloys at low temperatures.^{7,11,12} In fact the original discovery of the low temperature "resistance maximum" by Gerritsen and Linde^{7,13} in 1951-52 was made on alloys of copper, silver, and gold containing small concentrations of manganese. It is interesting that the high temperature resistance maximum in copper manganese alloys has been known¹⁴ since 1895 and has long been exploited in the commercial uses of manganin wire.

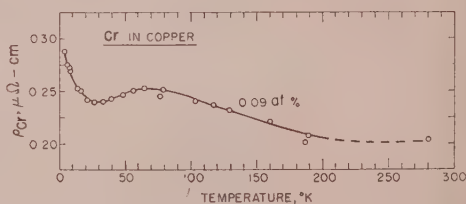


FIG. 2. Temperature dependence of the solute contribution ρ_{Cr} to the resistivity of a copper+0.09 at. % Cr alloy in the range 4° to 300°K.

¹⁰ J. O. Linde in *Proceedings of the Fifth International Conference on Low Temperature Physics and Chemistry, August 26-31, 1957*, edited by J. R. Dillinger (University of Wisconsin Press, Madison, Wisconsin), p. 402. See also N. Bäcklund, *J. Phys. Chem. Solids* **7**, 94 (1958).

¹¹ R. W. Schmitt and I. S. Jacobs, *J. Phys. Chem. Solids* **3**, 324 (1957).

¹² O. S. Lutes and J. L. Schmit, *Magnetic Remanence in Cu(Mn) Alloys* (to be published).

¹³ A. N. Gerritsen and J. O. Linde, *Physica* **17**, 573 (1951).

¹⁴ K. Feussner and St. Lindeck, *Wiss. Abhandl. physik-techn. Reichsanstalt*, **2**, 501 (1895).

Figure 3 shows the temperature dependence of ρ_{Mn} for various concentrations of manganese in copper. These curves, together with the results found by other workers¹¹ using still lower manganese concentrations, indicate that the maximum in ρ_{Mn} is characteristic of a very wide range of manganese concentrations, and that as one adds more and more manganese the maximum in ρ_{Mn} simply moves toward higher temperatures. The same can be said for manganese in gold, as we shall see, and this behavior is essentially in accord with our mathematical model described in reference 6.

Manganese in Gold

We have investigated only one alloy of AuMn containing 10 at.% Mn, and our results for ρ_{Mn} in gold shown in Fig. 4 fit in with those of Gerritsen and Linde⁷ on their alloys containing 5.95 and 11.4 at.% Mn in gold. However, we consider their presentation of atomic resistivity (impurity resistivity per atomic percent) vs temperature to be misleading in the case of very dilute alloys for the following reason. Suppose that the original solvent metal contains traces of an "unintentional" impurity *A* which causes a very small "hump" in the ρ_B vs *T* curve for an intentionally added solute *B*. If the amount of this trace *A* and also the size of the hump are reasonably independent of the concentration of solute *B*, then the apparent effect of this hump on the ρ_B vs *T* curve will be greatly exaggerated in the alloys containing small amounts of solute *B*.

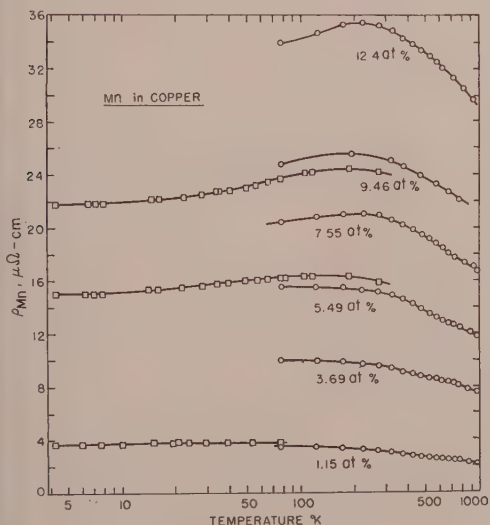


FIG. 3. Temperature dependence of the solute contribution ρ_{Mn} to the resistivity of copper manganese alloys; temperature scale is logarithmic 4° to 1000°K. The separation of the low temperature curves from the high temperature curves comes from our using two separate sections of the same piece of wire in the low and high temperature apparatus. The wires with 3.69, 5.55, and 12.4 at.% Mn were not investigated in the low temperature region.

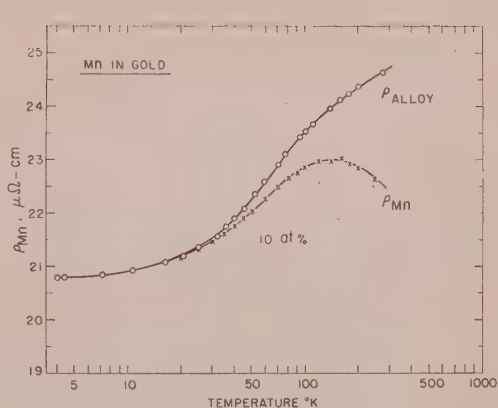


FIG. 4. Temperature dependence of the solute contribution ρ_{Mn} to the resistivity of a gold+10 at.% Mn alloy. Also shown is the variation of total resistivity ρ_{alloy} of this alloy over the temperature range 4° to 300°K.

Iron in Copper

The behavior of iron in copper is indeed complicated, as may be seen from Figs. 5 and 6. In the first of these figures we have used a logarithmic scale for the temperature in order to show the entire region from 4.2° to about 1000°K, while in the second of these figures we have shown the details in the range 4° to 80°K on a linear temperature scale. In this system we must, of course, contend with limited solubility of the iron. However, except for the portions of the curves shown by wavy lines in Fig. 5, we are confident that we have determined the true temperature dependence of the resistivity of the alloy. We have measured the resistance of the CuFe wires with temperature increasing as well as decreasing; we have allowed the wires to remain at certain appropriate temperatures for long times while

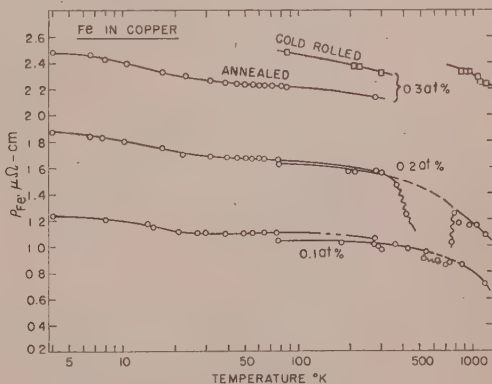


FIG. 5. Temperature dependence of the solute contribution ρ_{Fe} to the resistivity of copper iron alloys in the range 4° to 1000°K. The wavy lines in the region between 300° and 700°K indicate the precipitation of iron. Above 700°K the solubility is sufficient for stability of the iron concentrations shown, while below 300°K the precipitation is too slow to affect the resistivity of the wires quenched from high temperatures. See text for discussion of the 0.3 at.% Fe alloy.

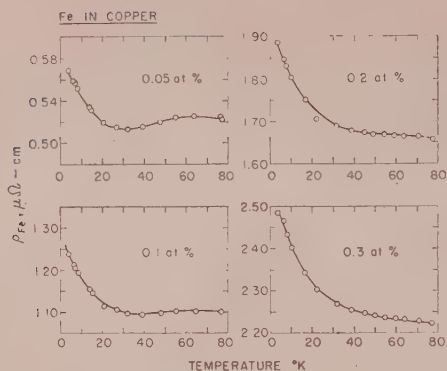


FIG. 6. Temperature dependence of the solute contribution ρ_{Fe} to the resistivity of copper-iron alloys in the range 4° to 80°K.

the resistance was "monitored," and we have performed numerous experiments involving quenching of the wires. All of these experiments substantiate the correctness of these curves.

The rapid decrease of ρ_{Fe} between 4° and 50°K is rather remarkable, as is also the fact that ρ_{Fe} at the highest temperatures shown here is only about six-tenths of its value in the liquid helium range. Furthermore, there is a persistent hump in ρ_{Fe} in the 50–100°K

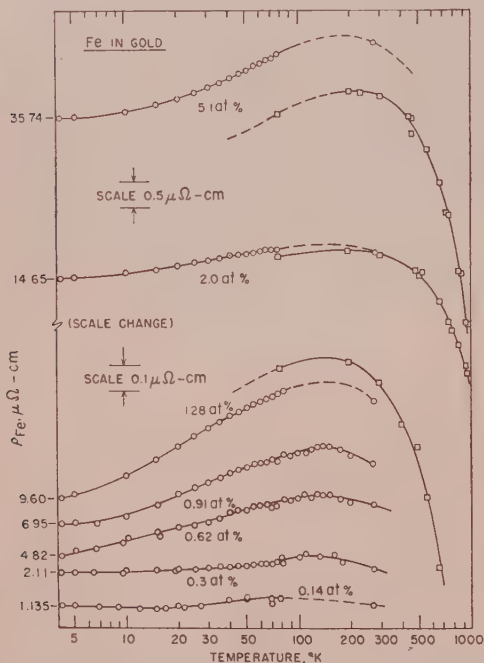


FIG. 7. Temperature dependence of the solute contribution ρ_{Fe} to the resistivity of gold-iron alloys in the range 4° to 1000°K. The separation of the low-temperature curves from the high-temperature curves comes from our using two separate sections of the same piece of wire in the low- and high-temperature apparatus. See text for discussion of the 0.62 at.% Fe alloy (this figure), and the 0.59% alloy of Fig. 8.

region for the two CuFe alloys with the lowest iron concentrations. These humps do not stand out very clearly on the large scale of ρ_{Fe} used in Fig. 5 but are obvious in Fig. 6. The beginnings of such a hump can also be seen on the "anomalous resistance component" of Pearson's alloys of Cu+0.005 at.% Fe and Cu+0.044 at.% Fe shown in reference 8. The temperatures at which the minima in ρ_{Fe} occur for the combined set of Pearson's and our alloys are as follows: 0.005% Fe, 23°K; 0.044% Fe, 30°K; 0.05% Fe, 32°K; 0.103% Fe, 42°K; 0.20% Fe, no minimum, but flattening out in the region around 60°K; 0.30% Fe, a nearly flat region between 50° and 100°K.

Those portions of the curves at the highest temperatures (above 800°K, say) in Fig. 5 are subject to an error of at most $\pm 0.05 \mu\text{ohm-cm}$. However, we are quite certain that ρ_{Fe} continues to decrease as the tem-

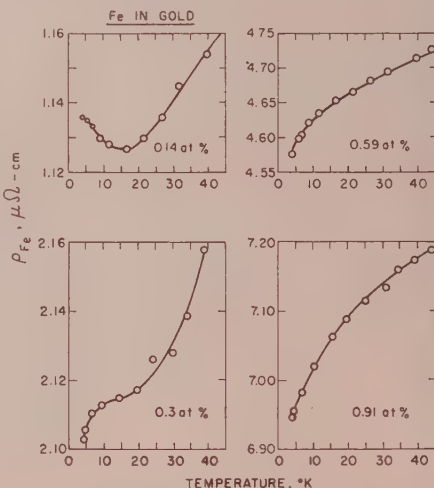


FIG. 8. Temperature dependence of the solute contribution ρ_{Fe} to the resistivity of gold-iron alloys in the range 4° to 40°K.

perature increases even above 800°K in the manner shown in Fig. 5.

In the 0.3 at.% Fe alloy, the lower over-all level of resistivity below room temperature, as compared with that above about 800°K, shows that not all the iron present was actually kept in solution upon quenching.

Iron in Gold

Iron dissolved in gold gives rise to a broad hump in ρ_{Fe} which moves gradually from the region of 75°K for 0.14 at.% Fe to approximately 200°K for 5.1 at.% Fe, as may be seen in Fig. 7. If the iron concentration is less than 0.2 or 0.3%, the curve of ρ_{Fe} vs T shows a minimum, as we see in Fig. 8. Linde and Bäcklund¹⁰ find that at still lower concentrations (specifically for 0.12% Fe) the resistivity passes through a narrow (in temperature) maximum which is located at 3° or 4°K. In our Fig. 7 there are two curves each for the 1.28, the 2.0

and the 5.1% Fe alloy. This situation comes about because our low temperature apparatus accommodates shorter wires than does our high temperature apparatus. It is seen that our wires are not entirely uniform along their length. This, however, has no appreciable effect on the temperature dependence. The AuFe alloys with 0.62 at. % Fe (Fig. 7) and with 0.59% Fe (Fig. 8) were intentionally prepared with slightly different iron concentrations as "checks" on our over-all techniques of alloy fabrication and resistivity measurements. Their behavior was found to be identical except, of course, for the slightly higher resistivity of the 0.62% alloy.

Cobalt in Copper

Copper cobalt alloys behave in the manner shown in Figs. 9 and 10. Here, too, we have difficulties with solute precipitation; but as with iron solute, we feel that these curves represent the true effects of cobalt on the resistivity of copper. Jacobs and Schmitt¹⁵ have

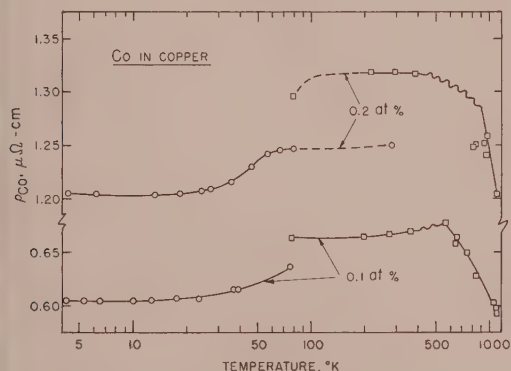


FIG. 9. Temperature dependence of the solute contribution ρ_{Co} to the resistivity of copper-cobalt alloys in the range 4° to 1000°K. The separation of the low-temperature curves from the high-temperature curves comes from our using two separate sections of the same piece of wire in the low- and high-temperature apparatus. The wavy lines indicate uncertainty because of cobalt precipitation.

found a decreasing (total) resistivity of copper-cobalt alloys with increasing temperature in the range 2° to 20°K. Linde and Bäcklund¹⁰ also find this behavior in the region between 1° and 5°K. Linde gives results for cold-drawn wires, whereas Bäcklund's data is for annealed wires. Our CuCo curves at the low-temperature end in Fig. 9 are for cold-rolled specimens. It is seen from Fig. 10 that the general behavior of these alloys at low temperatures is essentially the same for cold-rolled as for annealed, then quenched, wires.

A spectrographic analysis was made to determine the iron contamination in the copper cobalt wires. This analysis indicated less than 0.0005% Fe in the 0.1% Co wires, both annealed and cold rolled, less than 0.005% Fe in the 0.2 and 0.3% Co wires, and less than 0.01%

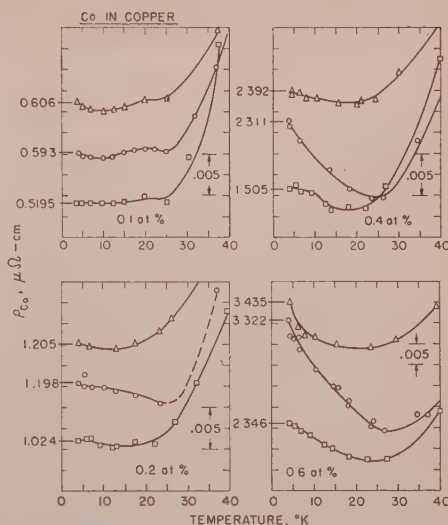


FIG. 10. Temperature dependence of the solute contribution ρ_{Co} to the resistivity of copper-cobalt alloys in the range 4° to 40°K. In these figures the triangles represent cold-worked (rolled) wires; the circles represent these same wires after vacuum anneal, and the squares represent internally oxidized wires as explained in the text.

Fe in 0.4% Co wires. In an attempt to remove effectively any iron impurities from our copper cobalt alloys, we heat-treated a set of these latter wires at 990°C for 2 hr in an atmosphere of pure oxygen at approximately 0.09-μ pressure. The "critical" pressures of oxygen necessary for internal oxidation of cobalt on the one hand, and iron on the other, are not very different⁹; in our attempt to internally oxidize the

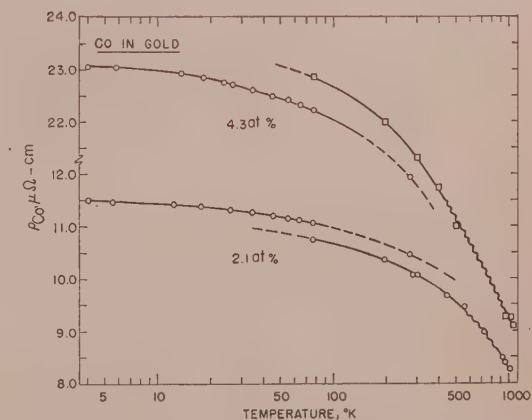


FIG. 11. Temperature dependence of the solute contribution ρ_{Co} to the resistivity of gold-cobalt alloys in the range 4° to 1000°K. The separation of the curves comes from our using two separate sections of the same piece of wire in the low- and high-temperature apparatus. The wavy lines in the high-temperature regions indicate uncertainty resulting from possible precipitation of cobalt. However, the sets of data in the vicinity of 1000°K represent the effects of the fully dissolved solute, so that the wavy curves give a good idea of the actual behavior of these alloys.

¹⁵ I. S. Jacobs and R. W. Schmitt, Phys. Rev. **113**, 459 (1959).

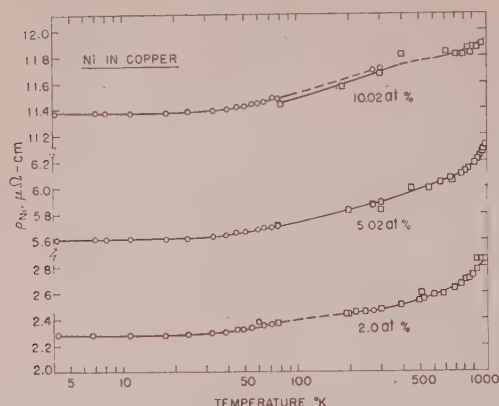


FIG. 12. Temperature dependence of the solute contribution ρ_{Ni} to the resistivity of copper-nickel alloys in the range 4° to 1200°K.

iron we also oxidized a considerable fraction of the cobalt. While this "overshooting" was unintentional, it is actually fortunate that we oxidized some of the cobalt as well (we hope) as the iron, because we now know that the behavior of cold-worked, vacuum-annealed, and partially oxidized copper cobalt alloys is essentially the same. It is interesting that the resistivity minima for the "vacuum-anneal" curves all lie at significantly higher temperatures than the minima for the corresponding "oxygen anneal" curves. In view of the rapid drop-off of resistivity ρ_{Fe} with increasing temperature, shown in Fig. 6, it may be reasonable to suppose that this shift in temperature of the minima of ρ_{Co} is caused by the removal (by internal oxidation) of the iron traces contained in the original copper-cobalt alloys. On the other hand, this would require considerable amounts of iron, and we would expect this iron also to be in solid solution in the cold-worked specimens of CuCo wire, so that the minima for the "cold-work" curves in Fig. 10 should then be located at about the same temperatures as those for the "vacuum-anneal" curves. However, this is obviously not so.

As with the dilute copper-iron alloys we can state here, too, that, despite the relatively large errors involved in determining ρ_{Co} at the high-temperature regions in Fig. 7, there is little doubt that ρ_{Co} continues to fall with increasing temperature in the region above 600°K approximately.

Cobalt in Gold

Gerritsen¹ has studied the low-temperature resistivity of AuCo alloys containing between 0.1 and 0.44 at.% Co. Linde and Bäcklund¹⁰ have investigated this system in the temperature range 1° to 5°K with alloys containing 0.12, 1.0, and 7.0 at.% Co. Figure 11 shows

our results for ρ_{Co} for two alloys with 2.1 and 4.3 at.% Co over the temperature range 4° to 1000°K. These two alloys show a clear-cut minimum in their total resistivity vs temperature curves: for Au+2.1 at.% Co the total resistivity is 11.50 $\mu\text{ohm cm}$ at 4.2°K and is 11.36 $\mu\text{ohm cm}$ at the minimum located at 30°K; for Au+4.3 at.% Co the total resistivity is 23.06 $\mu\text{ohm cm}$ at 4.2° and is 22.67 $\mu\text{ohm cm}$ at the minimum located at 60°K. The two separate pieces of wire used in the high- and low-temperature apparatus and the displacements of the curves give a measure of the nonuniformity of our wires. It is remarkable that the solute contribution ρ_{Co} is about 25% less at 1000°K than at 4°K.

Nickel in Copper

Nickel atoms affect the resistivity of copper in quite a different way from that of the other transition metals just described. Figure 12 shows how ρ_{Ni} increases monotonically with temperature over the entire range from 4° to nearly 1200°K. The ratio of ρ_{Ni} at 1200°K to ρ_{Ni} at 4.2°K has the value 1.26 for 2.0% Ni, 1.12 for 5.02% Ni, and 1.05 for 10.02% Ni. This trend must continue, of course, since commercial constantan, (containing 38% nickel) has a *negative* temperature coefficient of resistivity in the region around room temperature.

IV. CONCLUSIONS

We have described the effects of various transition-metal solutes on the electrical resistivity of pure copper and pure gold over a wide range of temperature and of solute concentration. The parameter $\rho_i(T, c)$ displayed in our various figures represents the *excess* resistivity of the particular alloy over that of the pure solvent at the same temperature. Unfortunately, the behavior of most of these alloys is even more complicated than would be expected from our previously described model.⁶ It may be that at least in some of these alloys there is a characteristically low temperature effect on the resistivity which depends on the solute concentration. Such a low temperature effect is best illustrated by the gold iron system (Fig. 8). In addition, in some alloys there appears to be a specifically high temperature effect which shows up as a very broad hump in ρ_i and which seems to be relatively insensitive to concentration. This latter behavior may be associated with changes in the extent of lattice scattering of the conduction electrons.

ACKNOWLEDGMENTS

We wish to acknowledge the valuable help given to us by Paul Lund, who did a considerable amount of the earlier work on this project. We also wish to thank Martin Stanquist for his assistance in some of this work.

Interrelation of Electronic Properties and Defect Equilibria in PbTe

E. MILLER, K. KOMAREK, AND I. CADOFF

Department of Metallurgy and Materials Sciences, New York University, University Heights, New York

(Received December 12, 1960)

The resistivity, Hall coefficient, and Seebeck coefficient of single crystals of PbTe were investigated in the range from 77° to 900°K using a capsuling arrangement which prevented tellurium loss from the specimens at elevated temperatures. The low temperature properties obtained agree with the data reported in the literature. The thermal energy gap obtained from the high temperature measurements cannot, however, be brought into agreement with the energy gap determined from room temperature absorption measurements by considering solely the excitation of electron-hole pairs across the energy gap at elevated temperatures. Rather, it is necessary to include the carriers generated by defect formation at elevated temperatures. Both Schottky-Wagner and Frenkel defects are present, the activation energies for formation of the two types of defects being related by the equation $E_F = \frac{1}{2}E_S + 0.55 \text{ ev} \approx 0.7 \text{ ev}$.

INTRODUCTION

THE electronic properties of the intermetallic compound PbTe, of interest for use in thermoelectric generators, have been investigated frequently. Putley¹ obtained an energy gap of 0.62 ev (for 0°K) for PbTe from elevated temperature resistivity data. However, infrared absorption data yielded a significantly lower value of 0.3 ev.² Similar discrepancies also exist for PbS and PbSe, and it was shown by Scanlon³ that this could be attributed at least partly to vaporization of the chalcogenide from the compounds at elevated temperatures. He showed that for PbS the thermally obtained value could be reduced if measurements were performed below about 500°K where vaporization is quite limited.

Recent measurements on PbTe in this lower temperature range⁴ have given an energy gap at 0°K of 0.35 ev. In a careful redetermination of the infrared absorption spectrum of PbTe, Scanlon⁵ computed the energy gap for indirect transitions to be 0.29 ev at room temperature. Using the temperature dependence of the energy gap determined by Gibson⁶ this would correspond to 0.17 ev at 0°K. This is still decidedly below the value of 0.35 ev determined by Shoenji.

The possible occurrence of such discrepancies has been discussed by Smith,⁷ who concluded that they can be attributed either to unusual changes in the band structure of the compound with temperature, to vaporization of tellurium, and/or to the formation of defects at elevated temperatures.

Since the discrepancy between optical and thermal energy gap values has not yet been completely resolved, the purpose of the present investigation was to redetermine the electronic properties of the compound using a capsulating technique which would completely eliminate

tellurium losses at elevated temperatures during measurements and to compare these data with room temperature optical data.

The results obtained show that the energy gap calculated from measurements of resistivity as a function of temperature is indeed considerably greater than that obtained from optical absorption experiments, even when tellurium vaporization is completely suppressed. The experimental results show that marked variation of the basic electronic parameters with temperature is unlikely, and that this mechanism cannot be used to explain the discrepancy. However, quenching experiments indicate that defects present at elevated temperatures create additional carriers in PbTe, and that such carrier generation can satisfactorily explain the disparity between the optical and thermal energy gaps. While Smith considered that defects were produced at elevated temperatures primarily as a result of vaporization of tellurium from the specimens, our data indicate that the lattice defects that predominantly affect the electronic properties are lead interstitial ions. The energy of formation of the interstitials can be calculated from the electronic data, and the analysis is presented in the discussion.

EXPERIMENTAL PROCEDURE

Specimen Preparation

Starting materials were lead and tellurium obtained from the American Smelting and Refining Company. The lead was zone-refined and the tellurium vacuum distilled. Spectroscopic analysis showed an impurity concentration of the order of $5 \times 10^{16} \text{ cm}^{-3}$.

Two single crystals, $\frac{5}{8}$ in. in diameter and 4 in. long of over-all compositions 49.7 at% Te (ingot 1) and 50.2 at% Te (ingot 2), were grown by a modified Bridgman technique, the specimens being segregated along the direction of growth. The composition at each point of ingot 1 was determined by the lead-rich solidus line, and since the maximum melting point occurs at 50.002 at% Te,⁸ the seed end was tellurium rich and

¹ E. H. Putley, Proc. Phys. Soc. (London) **B65**, 993 (1952); R. P. Chasmar and E. H. Putley, *Semiconducting Materials* Butterworth's Scientific Publications, Ltd., London, 1951, p. 208.

² D. G. Avery, Proc. Phys. Soc. (London) **67**, 2 (1954).

³ W. W. Scanlon, Phys. Rev. **92**, 1573 (1953).

⁴ K. Shoenji and S. Uchiyama, J. Phys. Soc. Japan **12**, 431 (1957).

⁵ W. W. Scanlon, J. Phys. Chem. Solids **8**, 423 (1958).

⁶ A. F. Gibson, Proc. Phys. Soc. (London) **B65**, 378 (1952).

⁷ R. A. Smith, Physica **20**, 910 (1954).

⁸ E. Miller, K. Komarek, and I. Cadoff, Trans. Am. Inst. Mining, Met., Petrol. Engrs. **215**, 882 (1959).

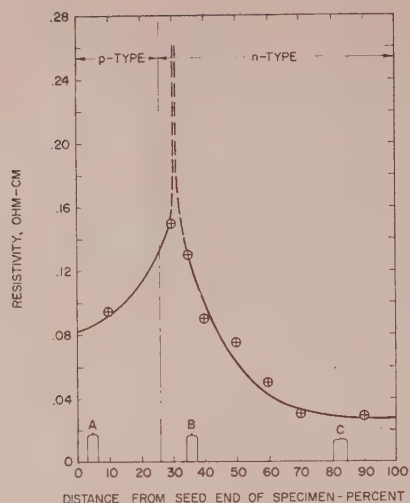


FIG. 1. Resistivity scan of ingot 1.

the tail end lead rich (Fig. 1). The specimen was cut into sections $\frac{1}{8}$ in. thick perpendicular to the growth axis to obtain samples of different compositions. The sections were sealed into evacuated quartz capsules and homogenized at 800°C for 48 hr. The resistivities of the two faces of the slices were determined after annealing and were found to be the same within the limit of measuring error (1×10^{-4} ohm-cm). Three sections were chosen for study. Sample A (*p* type) was cut from the seed end of the ingot; sample B was the slice with the highest resistivity after homogenization, sample C (*n* type) was cut from the tail end of the specimen. The slices were then cut into rectangles with length-to-width ratios of about 5:1 for measurement. The region of the ingot from which each specimen was cut is shown in Fig. 1.

Ingot 2, containing excess tellurium, was segregated according to the tellurium-rich solidus line, being *p* type in carrier sign along its entire length, with only a slight decrease in resistivity from the seed to tail end. The ingot was annealed at 600°C for 192 hr.

Resistivity and Hall Coefficient

All measurements were made using direct current, the voltages produced being measured with a Rubicon type B potentiometer sensitive to 1 μ v. Current and potential leads of 5-mil tungsten wire were welded to the samples by touching the surface of the specimen with the probe wires and impressing 5 v across the specimen.

Two experimental arrangements were employed to prevent vaporization of tellurium from the surface of the samples during experiments at elevated temperatures. Samples A, B, and C had Hall and resistivity leads welded on and were placed in 25-ml Pyrex beakers, the beakers filled with Sauereisen cement #10 (a low-

temperature-hardening liquefied porcelain), and the porcelain hardened by baking at 80°C for 24 hr. After the completion of resistivity and Hall measurements the Sauereisen was removed by careful sawing, and the specimen's surface polished on 2/0 paper preparatory to determination of the Seebeck coefficient.

Ingot 2 was sealed in an evacuated Pyrex capsule (Fig. 2) with tungsten lead wires passing through Pyrex-metal seals. The probes were first welded to the specimen and then sealed to the Pyrex capsule.

To reduce emf's generated by thermoelectric effects the current was passed through the specimens for as short a time as possible. Any emf observed immediately after the current was interrupted was assumed to be due to spurious thermoelectric effects and was subtracted from the emf readings taken while the current was flowing. Measurements were made with all possible combinations of current and field directions.

Seebeck Coefficient

The samples were clamped between two copper blocks in which thermocouples were embedded and the assembly completely coated with Sauereisen cement. A temperature gradient of 10°C was established across the samples by placing the assembly in a furnace or Dewar flask.

Infrared Absorption

The infrared absorption spectrum was determined for a *p*-type section of ingot 1 with room temperature resistivity 0.035 ohm-cm using a Beckman model IR-2 spectrophotometer with an associated micro attachment which permits examination of specimen areas $\frac{1}{8}$ in. in diameter. The resolution in the region of the absorption edge was approximately 0.007 ev. The specimens were ground to the desired thickness on a low speed polishing wheel with 600 \times alundum powder and a final polish with alpha alumina #2 on silk velveteen cloth was used to eliminate surface scratches.

EXPERIMENTAL RESULTS

Electrical Properties

The resistivity, Hall coefficient and Seebeck coefficient data for samples A, B, and C, are summarized in Figs. 3-5. The Hall coefficient in the exhaustion



FIG. 2. Ingot 2 capsuled for resistivity vs temperature measurements.

ange can be written as

$$R = r/ne, \quad (1)$$

where r is a factor depending on the statistics obeyed and the ratio of impurity to lattice scattering in the sample. Since the Hall coefficient does not increase with decreasing temperature for specimens A and C, the impurity centers are completely ionized. Although some uncertainty exists in the value of r , the value of $3\pi/8$ was used for the calculation of carrier concentration at room temperature.

The resistivities for the samples in the intrinsic range are shown in Fig. 6. The plots are virtually straight lines, but as will be shown in the discussion, the slope does not give the energy gap of the compound.

The reproducibility of the resistivity curves in the intrinsic range on repeated heating and cooling indicates that significant composition change by vaporization was avoided by encapsulation. The room temperature resistivity of samples A, B, and C, however, were changed permanently by about 0.5% with each cycle. Ingot 2, encapsulated in Pyrex, showed no change in room temperature resistivity after repeated cycling and 16 hr holds at temperature, indicating no composition change. The very small change in room temperature resistivity of the coated samples A, B, and C, the agreement of the values for these samples and ingot 2 in the intrinsic region indicates that any reaction that may have

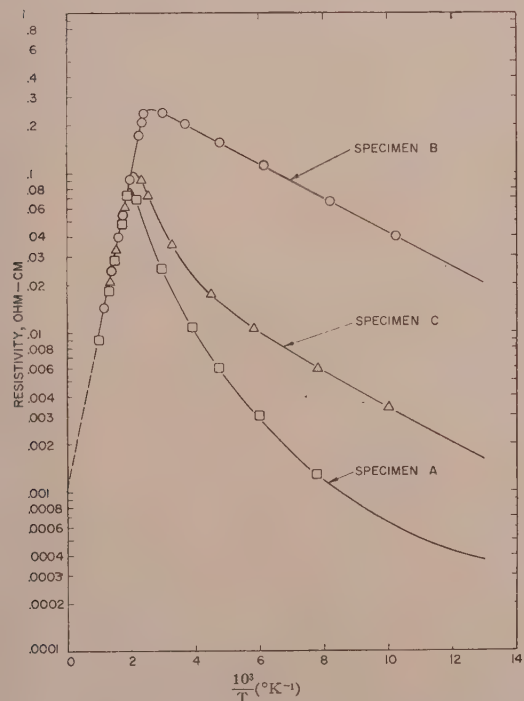


FIG. 3. Resistivity vs temperature data of specimens A, B, and C.

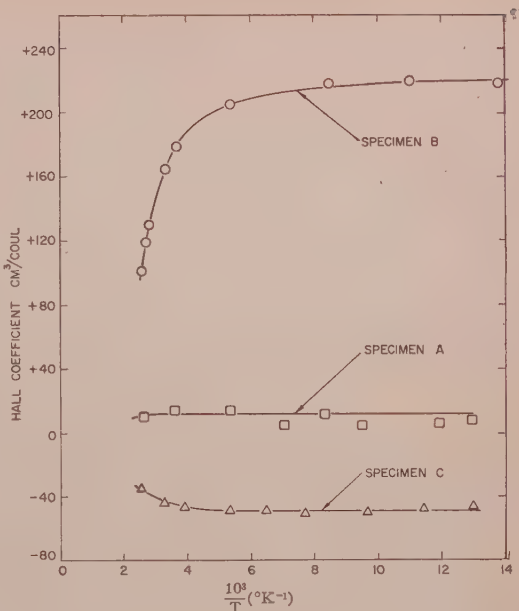


FIG. 4. Hall coefficient vs temperature data of specimens A, B, and C.

occurred between the Sauereisen and the specimen does not affect the results significantly.

The carrier mobilities were determined from the Hall coefficient and conductivity data from the relation

$$\mu = 8\sigma R/3\pi. \quad (2)$$

Figure 7 shows the majority carrier mobility as a function of temperature for the three samples investigated. At approximately room temperature the mobilities of the two p -type samples approach each other, and the mobility of the n -type sample approaches a value of $2.1\mu_p$, indicating that above 200°K lattice scattering is predominant, while below this temperature the scattering is sample dependent. The low temperature mobility of the purest sample B is lower than the mobility of the other p -type sample A, and therefore the major source of low temperature scattering cannot be impurity centers, but are probably imperfections formed during growth. At room temperature and above the mobility of all three samples varies as $T^{-2.5}$.

The effective masses of the charge carriers can be obtained from the Seebeck coefficient data in the extrinsic range. In this region the Seebeck coefficient is given by

$$S = \pm \frac{k}{e} \left[\left(\frac{5}{2} - s \right) - \ln \left\{ \frac{n h^3}{2(2\pi m^* k T)^{3/2}} \right\} \right], \quad (3)$$

where s is the exponent determining the variation of the relaxation time with energy $\tau = aE^{-s}$. Since the mobility data indicate that lattice scattering is predominant above 200°K , the most reasonable value of s is

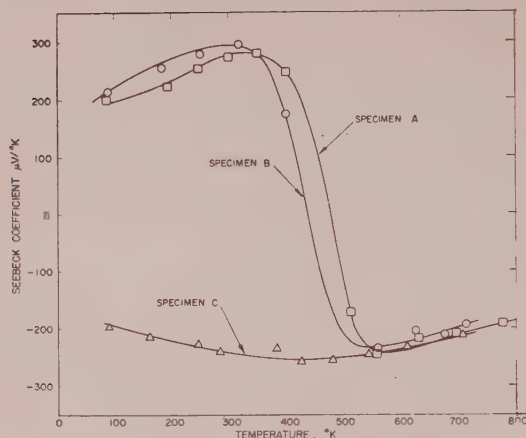


FIG. 5. Seebeck coefficient vs temperature data of specimens A, B, and C.

$\frac{1}{2}$, and the effective masses obtained are

$$m_e = 0.22m_0,$$

$$m_h = 0.29m_0.$$

Despite the existence of impurity scattering at low temperatures, the effective mass values calculated are constant for the entire extrinsic range, from 77°K to 300°K, and agree with the values previously reported in the literature.¹

Infrared Absorption

Electrons can be excited from the valence band to the conduction band by absorption of infrared radiation. Absorption can occur as a result of direct transitions in which the wave number remains constant or indirect transitions in which the wave number changes due to the violation of the selection rules by means of electron-phonon interactions. Since, during resistivity and Hall coefficient measurements as a function of temperature, the electron-phonon interactions generate the charge carriers, the energy gap obtained from such measurements therefore should correspond to the infrared indirect transition threshold energy.

The threshold energy for indirect transitions can be obtained by a straight line extrapolation on a plot of the square root of the absorption coefficient vs the photon energy.⁵ The extrapolation is shown in Fig. 8. From this figure the energy gap for indirect transitions at 300°K is 0.296 eV, in agreement with the optical data of Scanlon.⁵

The energy gap at 0°K can be calculated if the variation with temperature is known. This variation has been reported in the literature⁶ from the shift of the absorption edge as a function of temperature to be 4×10^{-4} eV/°K.

When this value is used, the value of the optical energy gap extrapolated to 0°K is 0.17 eV.

Quenching Experiments

Specimens A and C were capsuled in quartz, heated to selected temperatures, held at temperature for 4 min, and cooled to room temperature at different rates without breaking the capsule. Quenching the specimen at a more rapid rate by breaking the capsule under water caused the samples to crack, presumably due to the large thermal stresses generated.

A plot of the carrier concentration at room temperature determined from Hall coefficient measurements as a function of holding temperature for furnace cooling, air cooling, and water quenching is shown in Fig. 9. The retained carrier concentration increases in both the *p*-type and *n*-type samples with increasing cooling rate and holding temperature in the range from 500–800°K. The average slope of the resistivity-annealing temperature curve for the fastest quenching rate in the range 500–800°K is 0.45 eV, but it is doubtful if the cooling rate was rapid enough to retain at room temperature all the excess carriers produced at the holding temperature.

DISCUSSION

The energy gap of a semiconductor is generally obtained by one of the following three methods:

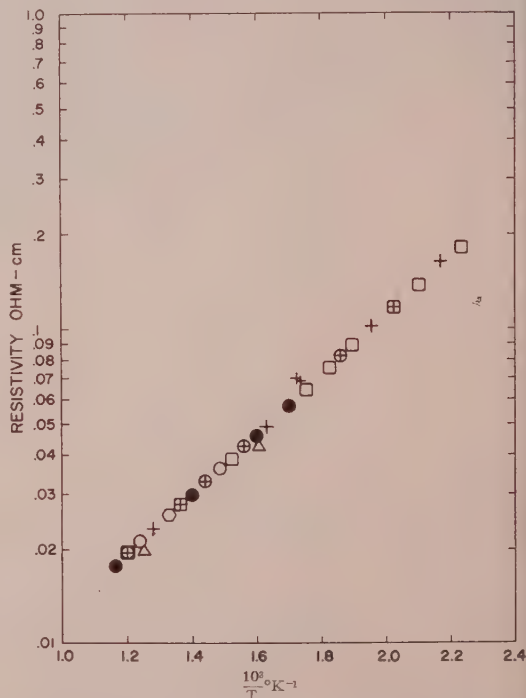


FIG. 6. Resistivity in the intrinsic range for specimens A, B, C, and ingot 2. Δ specimen A heating; \square specimen B heating; \circ specimen C heating; \bullet specimen C cooling; hexagon, specimen C heating; $+$ ingot 2 heating; \oplus ingot 2 held 16 hr at 830°K, measured cooling; \boxtimes ingot 2 reheated to 830°K, held 16 hr, measured cooling.

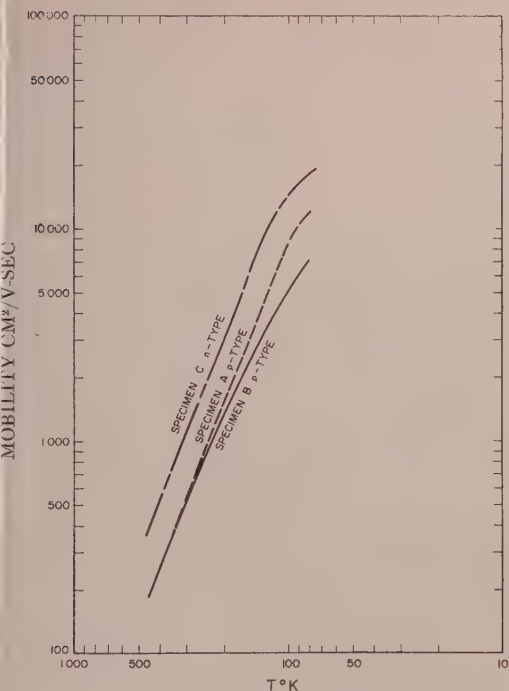


FIG. 7. Majority carrier mobility vs temperature for specimens A, B, and C.

(1) Determination of the absorption edge; that is, the minimum value of photon energy which is absorbed after correction for free carrier absorption.

(2) From conductivity vs temperature measurements. If the specimens can be assumed to be intrinsic, then

$$\sigma = 2(2\pi kT)^{3/2} (m_e m_h)^{1/2} (\mu_n + \mu_p) \exp(-E/kT)$$

$$\sigma = AT^{3/2} (\mu_n + \mu_p) \exp(-E_0/kT), \quad (4)$$

where A is a constant depending on the shape of the energy contours, effective masses and temperature variation of the energy gap. If $\mu = cT^{-3/2}$, then the slope of a $\ln \sigma$ vs $1/T$ plot should yield the energy gap at 0°K.

(3) From Hall coefficient vs temperature measurements. If the specimen is either in the transition or intrinsic region, the Hall coefficient can be given by

$$R = r(nb^2 - p)/(nb + p)^2 e, \quad (5)$$

where r depends on the shape of the energy contours and the statistics obeyed by the charge carriers, and b is the mobility ratio.

The usual analysis is to set $n - p = N_D$ in the transition region and $n = p$ in the intrinsic region, where N_D is the impurity concentration. Then, since

$$npT^{-3} = B \exp(-E_0/kT), \quad (6)$$

the slope of a $\ln npT^{-3}$ vs $1/T$ plot should give the energy gap at 0°K.

However, direct application of these standard equations to the data has resulted in definite discrepancies. The optical value of the energy gap extrapolated to 0°K is 0.17 eV, while the best slope of the $\ln \sigma$ vs $1/T$ curve is 0.35 eV. As stated previously, similar discrepancies have been observed in the homologous compounds PbS and PbSe. The optical and thermal energy gaps for PbS are 0.22⁵ and 0.32 eV,³ and for PbSe 0.15⁵ and 0.48 eV.⁹ In addition, it is quite surprising that a straight line can be drawn through the elevated temperature conductivity data since from Fig. 7 it is seen that above 300°K the mobility dependence on temperature is $T^{-3/2}$. If this region is the true intrinsic region, the conductivity line should definitely curve concave upward. It is shown later that the conductivity in this region is controlled by defects.

Although such differences have been mainly discounted in previous work as the result of composition change at elevated temperatures,³ the reproducibility of the data after extended heating times shown in Fig. 6 indicates that no significant composition change occurred, and therefore the discrepancies observed are real effects.

As has been stated by Smith,⁷ the thermally determined value of the energy gap will yield the true energy gap at 0°K only if the energy gap varies linearly with temperature, and the factors A in Eq. (4) and B in Eq. (6) are constant (implying m^* and b are independent of temperature).

If the bandgap is quadratically dependent on T , then

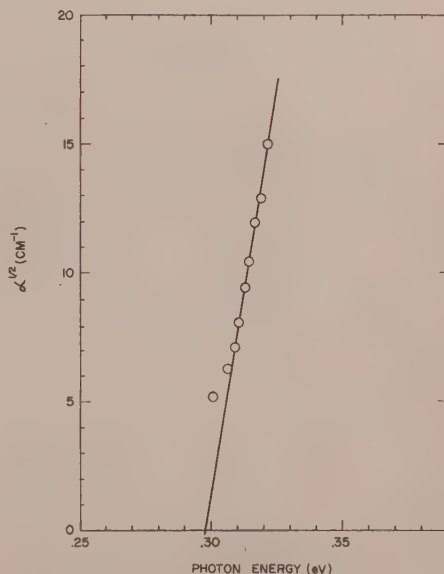


FIG. 8. Absorption coefficient for PbTe.

⁹ E. Hirahara and M. Murakami, J. Phys. Soc. Japan 9, 671 (1954).

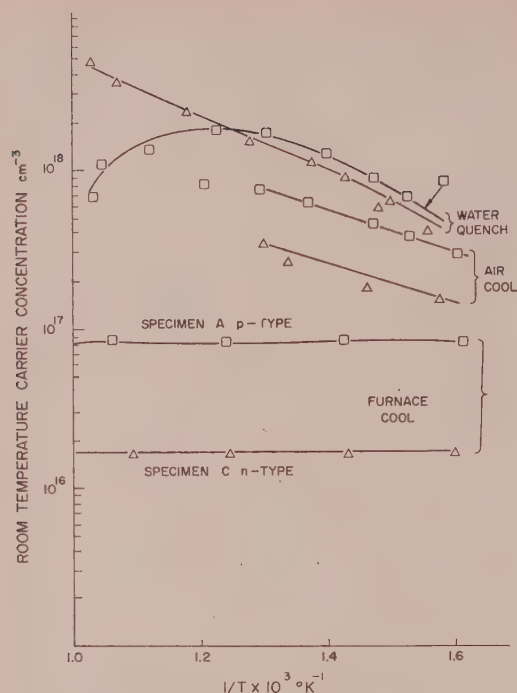


Fig. 9. Effect of quenching on room temperature resistivity of samples A and C.

the energy gap can be written as

$$E = E_0 + \beta T - \gamma T^2, \quad (7)$$

and the energy gap calculated from the slope of the $\ln \sigma$ vs $1/T$ curve will actually be⁷

$$E = E_0 + \gamma T^2. \quad (8)$$

The energy gap of PbTe as a function of temperature has been plotted by Smith⁷ from the infrared absorption data of Gibson.⁶ Although there is some curvature to the graph, the effect on the measured bandgap due to the curvature as calculated by Eq. (8) is only about 0.07 eV.

With regard to the possible variation of the factor A in Eq. (4), the Seebeck coefficient data of Fig. 5 gives a constant effective mass from 77° to 300°K. Even more conclusive proof of the constancy of the effective mass is the thermoelectric data of Kolomoets et al.,¹⁰ who observed no change in the effective mass over the wide temperature range from 0° to 450°C. This temperature interval includes most of the region over which the intrinsic resistivity data of Fig. 6 was taken, and variation of the pre-exponential factor therefore can be considered negligible. Therefore, the other possibility suggested by Smith must be considered, that is, the generation of defects at elevated temperatures.

¹⁰ N. Kolomoets, T. Stavitskaya, and L. Stil'bans, Zhur. Tekh. Fiz. **27**, 73 (1957).

Measurements taken as a function of temperature will, in this case, detect carriers generated by two distinct mechanisms: (1) the excitation of electron-hole pairs and (2) the formation of structural defects at elevated temperatures and the ionization of their isolated energy levels. Optical measurements at room temperature, on the other hand, will only generate carriers by mechanism 1.

The data obtained from quenching experiments indicate that carriers are generated due to defect formation at elevated temperatures. Two temperature ranges can be observed in the data of Fig. 9. In the temperature interval from 500–800°K, the carrier concentration of both the n - and p -type samples increases while above the upper temperature the carrier concentration of the n -type sample continues to rise, while that of the p -type sample begins to fall.

The lower temperature range has been studied previously. Koval'chick and Maslakovets¹¹ obtained an activation energy for the production of carriers of 0.62 eV in p -type material assuming a bimolecular reaction (0.31-eV slope). They stated that the production of carriers during annealing is caused by the solution of excess quiescent impurity atoms. Fritts¹² obtained a slope of 0.55 eV in both n - and p -type material. He concluded that both lead and tellurium show retrograde solubility in PbTe. Such retrograde solubility has been reported for PbTe.¹³

However, in the temperature range above 800°K, the concentration of electrons in both n - and p -type samples after quenching begins to increase. The carriers therefore apparently come from the generation of structural defects, which is independent of the small composition difference of the two samples.

If, as will be proposed later, the structural defects produced at elevated temperatures which cause significant changes in the electronic properties are lead interstitial atoms, then migration and recombination of the interstitials with lead vacancies would be expected to be fairly rapid, even at relatively low temperatures.¹⁴ Only on quenching from elevated temperatures, where their concentrations are relatively high, would a measurable concentration of interstitials be expected to be trapped. In the lower temperature range the excess lead or tellurium atoms dissolved in the lattice due to retrograde solubility, which are substitutional and therefore cannot migrate as rapidly as the interstitials, would be quenched in and would control the room temperature electronic properties.

If the increase in carrier concentration due to retrograde solubility were the only source of additional carriers, then in p -type material the conductivity would

¹¹ T. Koval'chick and Y. Maslakovets, Zhur. Tekh. Fiz. **26**, 2417 (1956).

¹² R. Fritts, *Thermoelectric Materials and Devices* (Reinhold Publishing Corporation, New York, 1960), p. 143.

¹³ R. Brebrich and R. Allgaier, J. Chem. Phys. **32**, 1826 (1960).

¹⁴ A. H. Cottrell, *Vacancies and Other Point Defects in Metals and Alloys* (Institute of Metals, London, 1958), p. 1.

be given at elevated temperatures by

$$\sigma = (n + p_{re})e\mu_p + ne\mu_n = (n[b+1] + p_{re})e\mu_p,$$

where p_{re} = No. of carriers/cm³ due to increasing solubility with increasing temperature and n = number of electrons excited across the energy gap. At any temperature

$$(n + p_{re})n = n_i^2.$$

If we take the mobility as being given by

$$\mu_p = dT^{-\frac{1}{2}} \quad \text{and} \quad b = \mu_n/\mu_p = 2.1,$$

then solving for the number of excess carriers gives

$$\sigma = [-0.55p_{re} + 1.55(p_{re}^2 + 4n_i^2)^{\frac{1}{2}}]ecT^{-\frac{1}{2}}$$

$$p_{re} = \frac{0.71\sigma cT^{\frac{1}{2}} + (4\sigma^2 T^5 c^2 - 14n_i^2)^{\frac{1}{2}}}{1.75}, \quad (9)$$

where $c = 0.645/ed$. While the value of n_i^2 is unknown, its temperature dependence must be $CT^3 \exp(-0.17/kT)$ (using the energy gap obtained from the infrared absorption measurements). After substituting the values for σ and c from Figs. 3 and 7, then, regardless of what reasonable value of C is chosen (to make $n_i = 10^{15}$ to 10^{18} at room temperature), solution of Eq. (9) shows that the concentration of additional carriers at 600°K and above must be significantly greater than that generated by intrinsic electron-hole pair excitation, and the latter may be neglected with little error.

Considering retrograde solubility only, since the concentration of additional carriers is greater than that from electron-hole excitation, the Seebeck coefficient of p -type material should remain positive in sign for all temperatures. Since the Seebeck coefficient is negative above 500°K for all samples, the number of carriers introduced by retrograde solubility must be fairly small compared to that produced by lattice defects and need not be considered at elevated temperatures, contradicting the suggestion by Fritts and Karrer.¹⁶

DEFECT FORMATION ENERGY

The calculation based on Eq. (9) and the fact that the Seebeck coefficient is n -type for all samples at elevated temperatures indicate that above 600°K thermally generated n -type defect centers become controlling. The conductivity-temperature curves at these temperatures can be used to determine the activation energy for defect formation. For n -type carriers predominating, we have

$$\sigma = n'e\mu_n,$$

where n' is the number of carriers due to defect formation. Since above room temperature the mobility

can be written as

$$\mu_n = c'T^{-\frac{1}{2}},$$

then σ can be written as

$$\sigma = DT^{-\frac{1}{2}} \exp(-E_T/kT).$$

This equation can be fitted to the conductivity data in Fig. 6 for $E_T = 0.31$ eV over the entire intrinsic temperature range studied. Therefore,

$$n' = F \exp(-0.31/kT). \quad (10)$$

There is relatively little data on the types of defects present in PbTe and their energies of formation. The activation energy for diffusion of Pb and Te in PbTe was obtained by Boltaks and Makhov¹⁶ as 0.6 and 0.75 eV, respectively. The low value of the activation energy suggests an interstitial diffusion mechanism, but since the activation energy for diffusion of both Pb and Te are close, and the radius of the Te⁼ ion is too large to permit interstitial migration, they concluded that the mechanism must be one of vacancy migration.

Defects that will result in energy levels in the forbidden band can either be Frenkel defects, Schottky-Wagner defects, or antistructure disorder.¹⁷ Although antistructure disorder is possible, such defects are extremely unlikely to occur in polar compounds, and this type of defect can be ignored. If both Schottky-Wagner and Frenkel defects exist in PbTe, then Te vacancies, Pb vacancies, and Pb interstitials will be present. Because of the large ionic radius of the Te ion, the concentration of Te interstitials will be very small and can be neglected. The Hall effect data indicate that the ionization energy of the defects is quite small, and we can conclude that the first ionizations of the defects occur with an extremely low activation energy, while second ionizations do not occur.

The interactions involving the various defects consist of the formation of the lead vacancies and interstitials, the tellurium vacancies, the ionization of these defects, and the generation of electrons and holes by excitation across the forbidden band. The charge on the various components is written below with respect to the lattice, so that the ordered lattice is designated by the neutral symbol PbTe. The charge of the vacancies is therefore opposite that of the lattice site occupied by its normal ion. In this convention a lead ion sitting on a lead site is uncharged with respect to the lattice, while a lead interstitial will be double positively charged, and a lead vacancy doubly negatively charged. The equations denoting the first ionizations of the various defects follow directly from the apparent charges on the defects. In setting up these equations it is important to note that as a result of the encapsulation, the com-

¹⁶ S. B. Boltaks and Y. Makhov, Zhur. Tekh. Fiz. 28, 1046 (1958).

¹⁷ F. A. Kroger and H. J. Vink, *Solid State Physics* (Academic Press, Inc., New York, 1955), Vol. 3, p. 260.

¹⁶ R. W. Fritts and S. Karrer, Bull. Am. Phys. Soc. 1, 226 (1956).

position of the crystal is constant and does not vary as a function of temperature. This requirement is specified in Eqs. (17) and (18).

The various equilibria involving the different defects and the charge carriers can therefore be written as

$$\text{ground state} = n^- + p^+, \quad K_1 = [n^-][p^+] = n_i^2, \quad (11)$$

$$\text{PbTe} = V_P^{\equiv} + V_T^{++}, \quad K_2 = [V_P^{\equiv}][V_T^{++}], \quad (12)$$

$$\text{Pb} = I_P^{++} + V_P, \quad K_3 = [I_P^{++}][V_P], \quad (13)$$

$$I_P^{++} = I_P^+ + p^+, \quad K_4 = \frac{[p^+][I_P^+]}{[I_P^{++}]}, \quad (14)$$

$$V_P^{\equiv} = V_P^- + n^-, \quad K_5 = \frac{[V_P^-][n^-]}{[V_P^{\equiv}]}, \quad (15)$$

$$V_T^{++} = V_T^+ + p^+, \quad K_6 = \frac{[p^+][V_T^+]}{[V_T^{++}]}. \quad (16)$$

The electroneutrality condition is

$$[n^-] - [p^+] + [V_P^-] - [V_T^+] - [I_P^+] - 2[I_P^{++}] - 2[V_T^{++}] + 2[V_P^{\equiv}] = 0, \quad (17a)$$

and the requirement that the composition remains unchanged by defect formation is

$$[I_P^{++}] + [I_P^+] = [V_P] + [V_P^{\equiv}] - [V_T^{++}] - [V_T^+]. \quad (18a)$$

These equations can be solved using the approach suggested by Brouwer¹⁸ by obtaining simplified electroneutrality and composition equations.

It was shown from Eq. (9) that $n \gg p$, and therefore the hole concentration can be neglected in Eq. (17a), as can the concentration of doubly charged vacancies in Eq. (18a) as well as Eq. (17a). Then,

$$[n^-] = 2[I_P^{++}] + [I_P^+] - [V_P^-] + [V_T^+]. \quad (17b)$$

If $[I_P^{++}] = 0$, complete compensation of the various defects occurs, and $[n^-] = 0$. This limiting case is therefore impossible. The other limit is to let $[I_P^+] = 0$, that is, to consider the case where the interstitial lead atoms have a large ionization energy.

If $[I_P^+] = 0$, then from Eq. (18a)

$$[I_P^{++}] = [V_P^-] - [V_T^+].$$

The simplified electroneutrality condition is

$$[n^-] = [I_P^{++}]. \quad (17c)$$

Equation (18a), also can be simplified. From the diffusion experiments of Boltaks and Makhov we can conclude that $[I_P^{++}] + [I_P^+] \ll [V_P^+]$ and can be neglected.

Equation (18a) simplifies to

$$[V_P^-] - [V_T^+] = 0. \quad (18b)$$

The equations governing the equilibria are, therefore Eqs. (11)–(16) and Eq. (17c) and (18b). Solution of these eight simultaneous equations for the concentration of electrons yields

$$[n^-] = F \exp(-E_0 + E_S + E_{IT} - 2E_F - E_{IP})/4kT. \quad (19)$$

E_{IT} and E_{IP} are very small, $E_0 = 0.17$ eV and, from Eq. (10), $[n^-]$ varies experimentally as $\exp(-0.31/kT)$. Substitution of these quantities into Eq. (19) yields

$$E_F = 0.55 + \frac{1}{2}E_S. \quad (20)$$

The energies of formation of Frenkel and Schottky defects are therefore related. The small energy of formation of both these defects is probably due to the high polarizability of the Pb^{++} and Te^{\equiv} ions, which permits coulombic relaxation to reduce the energy of the defects once formed.

E_S can be estimated to be approximately one-half the activation energy of diffusion (0.6 eV) so that

$$E_F \approx 0.7 \text{ eV}.$$

The activation energy for movement of a Frenkel defect can be taken to be very roughly one-half that of movement of a Schottky defect¹⁴ so that the activation energy for diffusion of a Frenkel defect is

$$D_F \approx 0.8 - 0.9 \text{ eV}.$$

The larger energy of formation of Frenkel defects indicates that the concentration of these defects is significantly less than that of the Schottky defects. This therefore corroborates the assumption of Boltaks and Makhov that diffusion is essentially controlled by a vacancy mechanism.

ACKNOWLEDGMENTS

The work presented in this paper is based on research supported by Aeronautical Research Laboratories, Wright Air Development Division, U. S. Air Force, J. W. Poynter, Project Engineer. Permission to publish the results is gratefully acknowledged. The authors also wish to acknowledge the assistance of Mr. Irwin Kudman who determined the absorption spectrum of the samples.

LIST OF SYMBOLS

A, B, C, D, F	Constants
b	Mobility ratio μ_n/μ_p
e	Electronic charge
E_0	Energy gap at 0°K
E_S	Activation energy for formation of Schottky-Wagner defects
E_F	Activation energy for formation of Frenkel defects
E_{IT}	Ionization energy of Te vacancies

¹⁸ G. Brouwer, Philips Research Rept. 9, 336 (1954).

ϵ_{IP}	Ionization energy of Pb vacancies	$p, [p^+]$	Concentration of holes
$[I_p^{++}], [I_p^+]$	Concentration of doubly and singly charged Pb interstitials	p_{re}	Carrier concentration resulting from retrograde solubility
$K_1 \cdots K_6$	Equilibrium products	$[V_T^{++}], [V_T^+]$	Concentration of doubly and singly charged Te vacancies
m_e^*	Effective mass	$[V_P^-], [V_P^-]$	Concentration of doubly and single charged Pb vacancies
m_e	Effective electron mass	R	Hall coefficient
m_h	Effective hole mass	S	Seebeck coefficient
m_0	Free electron mass	σ	Electrical conductivity
$n, [n^-]$	Concentration of electrons	μ	Mobility
N_D	Impurity concentrations		
n_0^2	Electron-hole equilibrium product		

Determination of Certain Spectral Distributions of Soft X Rays by Theoretical Analysis of Absorption Experiments*

NANCY A. KERR

Lawrence Radiation Laboratory, University of California, Livermore, California

(Received February 17, 1961)

The temperature of a blackbody source which emits continuous radiation with a spectral peak in the range 0.6 to 8 kev in photon energy (soft x rays) may be determined by analyzing an absorption experiment. The technique employed here may be useful for the analysis of other continuous radiation distributions of soft x rays (e.g., free-free continuum radiation from plasma discharges and deceleration radiation from thick targets). Use is made of the approximation that over a limited energy region the absorption coefficient varies inversely with the cube of the spectral energy. The following equation,

$$I(x) = I_0(1 + C_1x \log_{10}x + C_2x + C_3x^3),$$

neglecting terms of magnitude $C_4x^{6/3}$ or less for thin absorbers, describes the relative dependence of the transmitted x-ray intensity $I(x)$ on the absorber thickness x for a blackbody spectrum of incident intensity I_0 . The constants C_1 through C_3 are related in a known manner to the temperature of the blackbody source for a given absorber material. Similarly, the equation,

$$I(x) = I_0 D_1 x^{7/8} (1 + D_2 x^{-1/4}) \exp(-D_3 x^{1/4}),$$

neglecting terms of magnitude $D_4 x^{-1/2}$ or less for thick absorbers, describes the transmission of a blackbody spectrum characterized by a source temperature which may be determined from the constants D_1 through D_3 .

INTRODUCTION

ABSORPTION experiments, though less precise than standard methods of crystal spectrometry, afford some advantages for investigating the energy distribution of a continuous x-ray spectrum. Namely, total, integrated intensity measurements are useful for weak sources of x rays which would be so attenuated by x-ray diffraction as to be undetectable. Furthermore, the experimental geometry is simple, time-consuming crystal calibrations are unnecessary, and experimental costs can be kept to a minimum. Methods of analyzing spectral distributions from sources emitting soft x rays are currently of interest to experimental physicists concerned with a variety of specialized fields.

Previous work on the analysis of continuous x-ray spectra from x-ray tubes with potentials at and below 100 kv has been conducted by Silberstein,¹ Emigh and

Megill² (100 kv and below), Jones³ (150 to 300 kv), and Greening⁴ (50 to 270 kv). Silberstein¹ represented the transmission data by the equation,

$$I(x) = I_0 \exp\{-Ax - Bx^{1/2}\},$$

where A and B are constants, I_0 is the incident intensity, and $I(x)$ is the transmitted x-ray intensity after absorption through a thickness x of absorber material. Jones³ found that a modification of the above equation, namely,

$$I(x) = I_0 \exp\{-Ax - B[(x+d)^{1/2} - d^{1/2}]\},$$

provided a better fit to the experimental data. The new constant d , he suggested, was dependent on the thickness of a primary filter which transmits an intensity I_0 . Greening⁴ extended the method for distri-

* C. R. Emigh and L. R. Megill, J. Soc. Non-Destructive Testing **11**, 30 (1953).

³ D. E. A. Jones, Brit. J. Radiol. **13**, 95 (1940).

⁴ J. R. Greening, Brit. J. Radiol. **20**, 71 (1947).

* This work was done under the auspices of the U. S. Atomic Energy Commission.

¹ L. Silberstein, Phil. Mag. **15**, 375 (1933).

butions including characteristic radiation. Emigh and Megill² found that Laplace transformations could be used to fit the filtration data more easily and accurately than was previously thought.

The above equations are not applicable to the transmission analysis for Planck radiation distributions, since the blackbody spectrum differs in shape from that of an x-ray tube. Furthermore, special considerations must be made for soft x-ray absorption due to *K* edge singularities in the absorption coefficients which occur for many materials at spectral energies of a few kev.

In general, x-ray transmission is described by the equation,

$$I(x) = I_0 \exp\{-\langle\mu(E)\rangle_{av}x\}.$$

The mean linear absorption coefficient $\langle\mu(E)\rangle_{av}$ is the average of the linear absorption coefficient over the transmitted energy distribution (which hardens as *x* increases due to the preferential absorption of soft x rays). Consequently, $\langle\mu(E)\rangle_{av}$ decreases with increasing absorption. For the initial stages of soft x-ray transmission the slope of the intensity versus absorber thickness curve decreases in magnitude in a complex manner. A specific analysis for different energy distributions is necessary to explain the behavior of the curve.

The author introduces two equations in the following sections to describe soft x-ray absorption of Planck radiation distributions for a wide range of absorber thicknesses. Both matrix inversion and Laplace transform representation methods showed no promise. It is relatively easy to calculate x-ray intensity versus absorber thickness curves for a given spectral energy distribution. The inverse problem, namely, using transmission data to determine the spectral distribution, is much more complicated. An analysis of intensity versus absorber thickness curves (subject to reasonable experimental errors) is required in order to unfold the incident distribution. Details of the analysis are given for Planck radiation. The resulting thin and thick absorber equations for soft x-ray transmission are compared with hypothetical data obtained using a 7090 IBM computer.

Two other radiations distributions are considered in brief, namely, the continuous spectrum of deceleration radiation from a thick target x-ray tube and the free-free continuum radiation from plasma discharges present in a "Sherwood" experiment. The leading terms describing thin absorber transmission of the above spectra are given. The author suggests that thick absorber transmission of bremsstrahlung from plasma discharges may be evaluated in a manner analogous to that used for a Planck distribution of soft x rays.

I. ABSORPTION OF PLANCK RADIATION DISTRIBUTION

For a given x-ray energy spectrum $F(E)$, the functional dependence of the intensity $I(x)$ transmitted by

an absorber of thickness *x* is given by the equation

$$I(x) = I_0 \int_0^\infty F(E) e^{-\mu(E)x} dE, \quad (1)$$

where I_0 is the incident intensity per unit detector area on the absorber, $\mu(E)$ is the linear absorption coefficient and

$$\int_0^\infty F(E) dE = 1.$$

A blackbody source emits radiation with the energy distribution

$$F(E) = [15(\pi kT)^{-4}] E^3 (e^{E/kT} - 1)^{-1} \quad (2)$$

for

$$(k = 1.38 \times 10^{-16} \text{ erg deg}^{-1})$$

which is derived from Planck's radiation law.⁵ The incident intensity per unit detector area I_0 is defined as

$$I_0 = G\sigma T^4, \quad (3)$$

where *G* is a dimensionless constant dependent on the source geometry and distance from the detector. The Stefan-Boltzmann constant σ has the value 5.672×10^{-5} erg cm⁻² deg⁻⁴ sec⁻¹. The absolute temperature of the blackbody source is represented by *T*. Hence, absorption of blackbody radiation may be expressed by the relation

$$I(x) = G\sigma T^4 \int_0^\infty \frac{15}{\pi^4} \frac{n^3}{e^n - 1} e^{-\mu(nkT)x} dn, \quad (4)$$

where we have defined a new variable *n* such that $E = nkT$ and $\mu(E) = \mu(nkT)$.

The purpose of the paper is to solve Eq. (4) and obtain approximate analytic representations for $I(x)$ with appropriate simplifying assumptions. These representations must be valid for a wide range of absorber thicknesses. The validity is tested using values for the integral calculated with a 7090 IBM digital computer.

Approximate functions representing Eq. (4) for small and large values of *x* may be derived under the following conditions. First, thin (or thick) absorbers are used ("thin" and "thick" to be defined by the region of validity of the representation). Second, it will be assumed that the linear absorption coefficient can be represented by the relationship, $\mu(E) = A/E^3$, where *A* is a constant characteristic of the absorber material (to be explained later).

The function, to be derived in Sec. IV, for thin absorbers is

$$I(x) = I_0(1 + C_1x \log_e x + C_2x + C_3x^{4/3}), \quad (5)$$

where C_1 through C_3 are constants dependent upon the

⁵ F. K. Richtmyer and E. H. Kennard, *Introduction to Modern Physics* (McGraw-Hill Book Company, Inc., New York, 1947), 4th ed., p. 178.

absorber material and the temperature of the blackbody source.

The representation valid for thick absorbers (to be derived in Sec. V) is

$$I(x) = I_0 D_1 x^{7/8} (1 + D_2 x^{-1/4}) \exp(-D_3 x^{1/4}), \quad (6)$$

where the constants D_1 through D_3 are related to the temperature of the blackbody source and to the absorber material.

Equations (5) and (6) are extended and modified in Sec. VI to explain transmission of blackbody radiation over the range ($I_0 \geq I \geq 0.00005 I_0$) as a function of the absorber, its thickness, and the temperature of the radiating source.

II. INADEQUACY OF MATRIX INVERSION SOLUTIONS

Equation (1) may be expressed in the matrix representation

$$I_j = \sum_{i=1}^N \alpha_{ji} F(E_i) \Delta E_i, \quad (7)$$

where the matrix elements α_{ji} are defined by

$$\alpha_{ji} = \exp\{-x_{ji} \mu(E_i)\},$$

and $F(E_i)$ represents the fractional intensity of the true spectrum within the energy interval ΔE_i . Matrices of high orders are necessary to minimize the error of taking $\mu(E_i)$ as the mean linear absorption coefficient over a finite energy interval (where E_i is the mean energy of the interval ΔE_i). Equation (7) can in principle be unfolded to yield a derived spectrum, namely,

$$F'(E_i) \Delta E_i = \sum_{j=1}^N (\alpha_{ji})^{-1} I_j. \quad (8)$$

Now $F'(E_i)$ should be identical (in the ideal case) with $F(E_i)$. However, in practice this is not always true. A discrepancy exists which is found to be critically dependent on the accuracy retained for input values of I_j . A tenth-order matrix inversion problem was studied in detail, using an IBM 650 computer to unfold 1- and 2-keV blackbody distributions. Intensity values I_j calculated to eight significant figures from Eq. (7) (to represent transmission through beryllium) were used as input for Eq. (8). The values of $F'(E_i)$ and $F(E_i)$ agreed to four significant figures. However, random errors in the fourth significant figure of I_j [i.e., the input values for Eq. (8)] furnished a derived spectrum $F'(E_i)$ bearing no resemblance to the original spectrum $F(E_i)$ when elements α_{ji} differed greatly in magnitude. The author believes that the use of higher-order matrices and larger computers will not help in reproducing the original spectrum since experimental errors invalidate the usefulness of the matrix inversion method for unfolding blackbody distributions of soft x-rays from transmission data.

III. THE LAPLACE INTEGRAL FORM

Equation (4) may be transformed into the form of a Laplace integral, namely,

$$I(\xi) = \int_0^\infty G(\nu) e^{-\nu \xi} d\nu, \quad (9)$$

by approximating the energy dependence of the linear absorption coefficient as follows: $\mu(nkT) = A/(nkT)^3$ for $(E = nkT)$, and defining two new variables: $\nu = A/n^3$ and $\xi = x/(kT)^3$, where the constant A is dependent on the absorber material. Consequently,

$$\mu(nkT)x = \nu \xi. \quad (10)$$

We determine the function $G(\nu) = -I_0 F(E) dE/d\nu$ using Eqs. (2) and (3) with the substitution

$$E = (A/\nu)^{1/3} kT.$$

Hence,

$$G(\nu) = (5/\pi^4) I_0 A^{4/3} \nu^{-7/3} [\exp(A/\nu)^{1/3} - 1]^{-1}. \quad (11)$$

Equations (9) and (11) represent Eq. (4) in the form of a Laplace transform which has not been evaluated anywhere, to the author's knowledge, but which is interesting in itself.

IV. A USEFUL REPRESENTATION FOR TRANSMISSION OF BLACKBODY, FREE-FREE CONTINUUM AND THICK TARGET DECELERATION RADIATION THROUGH THIN ABSORBERS

The procedure used to determine representations for thin absorber transmission of certain radiation distributions is outlined in Table I.

We restate Eq. (4) for blackbody radiation in terms of a new variable $z = Ax/(kT)^3$ and approximate the linear absorption coefficient $\mu(nkT)$ by $A/(nkT)^3$. Hence,

$$I(z) = -I_0 \int_0^\infty \frac{n^3}{\pi^4} \frac{1}{e^n - 1} \exp\left(-\frac{z}{n^3}\right) dn, \quad (12)$$

where $n = E/kT$ assumes all possible values of the spectral energy scaled by the factor kT . Using the methods outlined in Table I we obtain

$$I(z) = I_0 \{ 1 + (15/\pi^4) [(z/3)(\log_e z) - 0.14093z - 0.50780z^{4/3} + 0.066974z^{5/3} - 0.007769z^2 + 0.00060453z^{7/3} + 0(10^{-5}z^3)] \}, \quad (13)$$

which is useful when $(0 \leq z \leq 40)$. The first four terms of Eq. (13) are used as an approximate representation for Eq. (4) under the assumptions that: $\mu(E) = A/E^3$, and terms in z^α where $\alpha \geq 5/3$ are negligible for $(0 \leq z \leq 1)$, and $z = Ax/(kT)^3$.

Thus, the intensity can be represented by Eq. (5), namely,

$$I(x) = I_0 (1 + C_1 x \log_e x + C_2 x + C_3 x^{4/3}) \quad (5)$$

for

$$[0 \leq Ax/(kT)^3 \leq 1],$$

$$C_1 = (5/\pi^4)A/(kT)^3;$$

$$C_2 = C_1 \{ \log_e [A/(kT)^3] - 0.42279 \};$$

$$C_3 = -1.5234 C_1 A^{1/3}/(kT),$$

where A is a constant, characteristic of the absorber, and (kT) is the energy of the blackbody source.

A representation for thin absorber transmission of blackbody radiation may be obtained when the absorption coefficient is approximated by $\mu(E) = A/E^\beta$ (e.g.,

$\beta = 2.857$). The evaluation of

$$I(z') = -I_0 \int_0^\infty \frac{n^3}{e^n - 1} \exp\left(\frac{-z'}{n^\beta}\right) dn \quad (14)$$

for $z' = Ax/(kT)^\beta$ and $\beta = 2.857$ is similar to that given above for Eq. (12) (in which $\beta = 3$ and $z' = z$) with the result using the above arbitrary β for $(2 < \beta \leq 3)$

$$I(z') = I_0 \{ 1 + (15/\pi^4) [-7.0914(z') + 6.8693(z')^{1.05} - 0.4654(z')^{1.40} + 0.0806(z')^{1.75} \pm O((z')^2)] \}, \quad (15)$$

TABLE I. Methods of evaluating useful integrals for transmission of radiation.*

Source emission	Blackbody Planck radiation	Plasma discharge free-free continuum radiation	Thick target x-ray tube deceleration radiation
Normalized energy distribution	$\frac{15}{\pi^4} \frac{n^3}{e^n - 1}$ for $(0 \leq n = E/kT \leq \infty)$	e^{-n} for $(0 \leq n = E/kT_e \leq \infty)$	$\frac{2(1+K-n)}{(1+2K)}$ for $(0 \leq n = E/E_0 \leq 1)$
Attenuation $e^{-\mu z}$	$\exp\left(\frac{-z'}{n^\beta}\right), z' = Ax/(kT)^\beta$ for $(2 < \beta \leq 3)$	$\exp\left(\frac{-z'}{n^\beta}\right), z' = Ax/(kT_e)^\beta$ for $(2 < \beta \leq 3)$	$\exp\left(\frac{-z'}{n^\beta}\right), z' = Ax/E_0^\beta$ for $(2 < \beta \leq 3)$
Transmitted intensity	$I(z') = -I_0 \int_0^\infty \frac{n^3}{e^n - 1} \exp\left(\frac{-z'}{n^\beta}\right) dn$ $= I_1 + I_2$ $I_1 = -I_0 \int_0^1 \frac{n^3}{e^n - 1} \exp\left(\frac{-z'}{n^\beta}\right) dn$ $= -I_0 \int_0^1 \sum_{m=0}^\infty \frac{B_m}{m!} n^{m+2} \times \exp\left(\frac{-z'}{n^\beta}\right) dn$	$H(z') = N(kT_e)^{1/2} \int_0^\infty e^{-n} \exp\left(\frac{-z'}{n^\beta}\right) dn$ $= H_1 + H_2$ $H_1 = H_0 \int_0^1 e^{-n} \exp\left(\frac{-z'}{n^\beta}\right) dn$ $= H_0 \int_0^1 \sum_{p=0}^\infty \frac{(-1)^p}{p!} n^p \times \exp\left(\frac{-z'}{n^\beta}\right) dn$ $= H_0 \sum_{p=0}^\infty \frac{(-1)^p}{p!} \frac{1}{\beta} \int_1^\infty \frac{e^{-z'\rho} d\rho}{\rho^{1+(p+1)/\beta}}$	$J(z') = CZE_0^2 \int_0^1 (1+K-n) \times \exp\left(\frac{-z'}{n^\beta}\right) dn$ $= J_1 - J_2$ $J_1 = \frac{2}{1+2K} J_0 \int_0^1 (1+K) \times \exp\left(\frac{-z'}{n^\beta}\right) dn$ $= \frac{2(1+K)J_0}{(1+2K)\beta} \int_1^\infty \frac{e^{-z'\rho} d\rho}{\rho^{1+1/\beta}}$
<p>where the Bernoulli numbers, B_m, are $B_0 = 1, B_1 = -1/2, B_2 = 1/6,$ $B_4 = -1/30, B_6 = 1/42, B_8 = B_5,$ $= B_7, \dots = 0$ (see reference 6)</p>			
$= -I_0 \sum_{m=0}^\infty \frac{B_m}{m!} \frac{1}{\beta} \int_1^\infty \frac{e^{-z'\rho} d\rho}{\rho^{1+(3+m)/\beta}}$			
for $I_0 = G\sigma T^4$			
Integrate I_1 by parts:			
$I_1 = -I_0 \sum_{m=0}^\infty \frac{B_m}{m!} \left\{ \frac{e^{-z'}}{3+m} - \frac{z'}{3+m} \int_1^\infty \frac{e^{-z'\rho} d\rho}{\rho^{(3+m)/\beta}} \right\}$			
Integrate H_1 by parts:			
$H_1 = H_0 \sum_{p=0}^\infty \frac{(-1)^p}{p!} \left\{ \frac{e^{-z'}}{p+1} - \frac{z'}{p+1} \int_1^\infty \frac{e^{-z'\rho} d\rho}{\rho^{(p+1)/\beta}} \right\}$			
Integrate J_1 by parts:			
$J_1 = \frac{2(1+K)}{(1+2K)} J_0 \left\{ e^{-z'} - z' \int_1^\infty \frac{e^{-z'\rho} d\rho}{\rho^{1/\beta}} \right\}$			

* H. Margenau and G. M. Murphy, *Mathematics of Physics and Chemistry*, (D. Van Nostrand Company, Inc., Princeton, New Jersey, 1956), 2nd ed., p. 474.

TABLE I (continued)

Source emission	Blackbody Planck radiation	Plasma discharge free-free continuum radiation	Thick target x-ray tube deceleration radiation
Transmitted intensity	Continue integrating by parts until the power of ρ in the integrand of the remaining integral is positive. Approximate this integral by a gamma function and estimate the magnitude of the error. Expand terms containing $e^{-z'}$ in a power series for $(0 \leq z' \leq 1)$.	Continue integrating by parts until the power of ρ in the integrand of the remaining integral is positive. Approximate this integral by a gamma function and estimate the magnitude of the error. Expand terms containing $e^{-z'}$ in a power series for $(0 \leq z' \leq 1)$.	Continue integrating by parts until the power of ρ in the integrand of the remaining integral is positive. Approximate this integral by a gamma function and estimate the magnitude of the error. Expand terms containing $e^{-z'}$ in a power series for $(0 \leq z' \leq 1)$.
	$I_2 = -\frac{15}{\pi^4} \int_1^\infty \frac{n^3}{e^n - 1} \exp\left(\frac{-z'}{n^\beta}\right) dn$ $= -\frac{15}{\pi^4} \sum_{p=0}^\infty \frac{(-1)^p (z')^p}{p!} \int_1^\infty \frac{n^{3-\beta p}}{e^n - 1} dn$ $= -\frac{15}{\pi^4} \sum_{p=0}^\infty \frac{(-1)^p (z')^p}{p!} S_p$	$H_2 = H_0 \int_1^\infty e^{-n} \exp\left(\frac{-z'}{n^\beta}\right) dn$ $= H_0 \sum_{p=0}^\infty \frac{(-1)^p (z')^p}{p!} \int_1^\infty n^{-\beta p} e^{-n} dn$ $= H_0 \sum_{p=0}^\infty \frac{(-1)^p (z')^p}{p!} U_p$	$J_2 = \frac{2}{1+2K} J_0 \int_0^1 n \exp\left(\frac{-z'}{n^\beta}\right) dn$ $= \frac{2J_0}{(1+2K)\beta} \int_1^\infty \frac{e^{-z'\rho} d\rho}{\rho^{1+2/\beta}}$
	for $(0 < S_p \leq S_0 < \pi^4/15)$	for $(0 < U_p \leq U_0 < 1)$	
	An estimate for S_p can be made quite simply by determining the area under the curve $T_p(\eta)$ vs η for	An estimate for U_p can be made quite simply by determining the area under the curve $V_p(\eta)$ vs η for	Integrate J_2 by parts:
	$S_p = \int_1^\infty \frac{n^{3-\beta p} dn}{e^n - 1}$ $= \int_0^1 T_p(\eta) d\eta,$	$U_p = \int_1^\infty n^{-\beta p} e^{-n} dn$ $= \int_0^1 V_p(\eta) d\eta,$	$J_2 = J_0/(1+2K)$ $\times \left\{ e^{-z'} - z' \int_1^\infty \frac{e^{-z'\rho} d\rho}{\rho^{2/\beta}} \right\}.$
	where $T_p(\eta) = \eta^{\beta p - 5}/(e^{1/\eta} - 1)$ ($0 \leq \eta \leq 1$).	where $V_p(\eta) = \eta^{\beta p - 2} e^{-1/\eta}$ ($0 \leq \eta \leq 1$).	Continue integrating by parts until the power of ρ in the integrand of the remaining integral is positive. Approximate this integral by a gamma function and estimate the magnitude of the error. Expand terms containing $e^{-z'}$ in a power series for $(0 \leq z' \leq 1)$.
	Combine terms $I = I_1 + I_2$ to obtain the thin absorber representation for transmission of Planck radiation from a black-body source.	Combine terms $H = H_1 + H_2$ to obtain the thin absorber representation for transmission of free-free continuum radiation from a plasma discharge.	Combine terms $J = J_1 - J_2$ to obtain the thin absorber representation for transmission of deceleration radiation from the continuous spectrum of an x-ray tube.

Thin absorber representation ($0 \leq z' \leq 1$).

neglecting terms in $(z')^\alpha$ where $\alpha \geq 2$ for $(0 \leq z' \leq 1)$. The term $(1/3)(z' \log z')$ is noticeably absent for $\beta \neq 3$. The method used to evaluate Eq. (12) may be applied to represent thin absorber transmission of continuous spectral distributions differing from that of a blackbody. Two examples of this will be given briefly below.

We use Kulenkampff's empirical formula as cited by Compton and Allison⁷ for the continuous spectrum of deceleration radiation from a thick target x-ray tube: $(E) = CZ(E_0 - E) + BZ^2$ for $E = h\nu \leq E_0$, with B , C , E_0 , and Z constant, and $F(E) = 0$ for $E > E_0 = h\nu_0$. Thin absorber transmission (neglecting geometrical effects) may be expressed by

⁷ A. H. Compton and S. K. Allison, *X Rays in Theory and Experiment* (D. Van Nostrand Company, Inc., Princeton, New Jersey, 1957), 2nd ed., p. 106.

$$J(z') = CZE_0^2 \int_0^1 (1 + K - n) \exp\left(\frac{-z'}{n^\beta}\right) dn, \quad (16)$$

where $z' = Ax/E_0^\beta$, $\mu(E) = A/E^\beta$, $n = E/E_0$, and $K = BZ/CE_0 < 1$. The integral of Eq. (16) may be evaluated for small z' (i.e., $0 \leq z' \leq 1$) with the result

$$J(z') = \frac{CZE_0^2}{2} \left\{ (1+2K) - \frac{2\beta}{\beta-1} (1+K) \Gamma\left(2 - \frac{1}{\beta}\right) (z')^{1/\beta} \right. \\ + \frac{\beta}{\beta-2} \Gamma\left(2 - \frac{2}{\beta}\right) (z')^{2/\beta} - \frac{2}{\beta-1} \left(\frac{1}{\beta-2} - K\right) (z') \\ \left. + \frac{1}{2(2\beta-1)} \left(\frac{1}{\beta-1} - 2K\right) (z')^2 \pm O((z')^3) \right\}, \quad (17)$$

for $\beta > 2$ neglecting terms in $(z')^\alpha$ where $\alpha \geq 3$. Equation (17) reduces to

$$J(z) = (CZE_0^3/2) \{ (1+2K) - 2.7083(1+K)z^{1/3} + 2.6790z^{2/3} - (1-K)z + 0.05(1-4K)z^2 \pm O(z^3) \} \quad (18)$$

for $\beta = 3$ [i.e., $\mu(E) = A/E^3$].

One further application of the above method concerns the analysis of free-free continuum radiation resulting from the acceleration of electrons in the Coulomb field of the ions in a magnetically compressed plasma. The energy dependence of the radiation as cited by Jahoda *et al.*⁸ is $F(E) = N(kT_e)^{-1/2} \exp\{-E/kT_e\}$, where N is a constant dependent upon the density of electrons at a "temperature" T_e and the effective nuclear charge and density of the plasma. (In this case, "temperature" refers to a dynamical quantity and not to the thermodynamical quantity defined for conditions of equilibrium.) We evaluate the equation representing thin absorber transmission,

$$H(z') = N(kT_e)^{1/2} \int_0^\infty e^{-n} \exp\left(-\frac{z'}{n^\beta}\right) dn, \quad (19)$$

(neglecting geometrical aspects) for $z' = Ax/(kT_e)^\beta$, $\mu(E) = A/E^\beta$, and $n = E/kT_e$ in a manner similar to that used for Eq. (12). The resulting expression giving the leading terms for small z' (i.e., $0 \leq z' \leq 1$) when $\beta = 3$ and $z' = z$ is

$$H(z) = N(kT_e)^{1/2} \{ 1 - 1.3541z^{1/3} + 1.3395z^{2/3} + (1/6)(z \log_e z) - 0.5331z - 0.1693z^{4/3} + 0.0335z^{5/3} \pm O(z^2) \}, \quad (20)$$

(neglecting terms in z^α where $\alpha \geq 2$). A similar analysis may be used to solve Eq. (19) for nonintegral values of $\beta > 2$ for which terms occur in orders of z' which are positive integers and multiples of $(1/\beta)$. The term $z' \log_e z'$ will not occur for $\beta \neq 3$ but appears as $(z')^2 \log_e z'$ for $\beta = 5/2, 7/2, 9/2, \dots$ and as $(z')^p \log_e z'$ for $\beta = (2p+1)/p, (3p+1)/p, (4p+1)/p, \dots$, when $p = 1, 2, 3, \dots$.

The methods used to evaluate Eqs. (14), (16), and (19) are summarized in Table I.

V. AN APPROXIMATE REPRESENTATION FOR THICK ABSORBER TRANSMISSION OF BLACKBODY RADIATION

We will now determine a representation for transmission of blackbody radiation through thick absorbers by solving Eq. (12) of the previous section for large values of z .

It is possible to obtain an asymptotic representation for Eq. (12) using the saddle point method as suggested by Dr. Walter A. Aron and Dr. Harvey Hall of the Lawrence Radiation Laboratory. The condition $[1/(3z)^{1/4} \ll 1]$ is imposed in order to arrive at a representa-

⁸ F. C. Jahoda, E. M. Little, W. E. Quinn, G. A. Sawyer, and T. F. Stratton, *Phys. Rev.* **119**, 843 (1960).

tion for $I(z)$ valid when z is large. The expansion $(e^n - 1)^{-1} = e^{-n} + e^{-2n} + \dots + e^{-pn}$ is used giving

$$I(z) = \left(\frac{15}{\pi^4}\right) I_0 \sum_{p=1}^{\infty} \int_0^\infty \exp[-F_p(n, z)] dn, \quad (21)$$

where $F_p(n, z) = pn + z/n^3 - 3 \log_e n$ (for $p = 1, 2, 3, \dots$). For large z (e.g., $z \geq 100$) only the first term in the expansion need be considered (i.e., $p = 1$). The function $F_1(n, z)$ is expanded in a Taylor series about its maximum point n_0 such that $F_1'(n, z)$ vanishes at $n = n_0$. Equation (21) becomes

$$I(z) = \left(\frac{15}{\pi^4}\right) I_0 \int_0^\infty \prod_{m=1}^6 \left\{ \exp\left[-\left(\frac{d^m}{dz^m}\right) F_1(n_0, z)\right] \times \frac{(n-n_0)^m}{m!} \right\} dn. \quad (22)$$

The number of terms retained in the integrand is limited for practical reasons. The value of n_0 determined by expanding $n_0 = (3z)^{1/4} (1 - 3/n_0)^{-1/4}$ in negative powers of $(3z)^{1/4}$ is

$$n_0 = (3z)^{1/4} \left[1 + (3/4)(3z)^{-1/4} + (27/32)(3z)^{-1/2} + (27/32)(3z)^{-3/4} + (1215/2048)(3z)^{-1} \right], \quad (23)$$

neglecting terms in $(3z)^{-\alpha}$ where $\alpha > 1$ for large values of z . We let $F_1''(n_0)/2! = C^2$ and define $v_0^2 = C^2 n_0^2$ with the expansion

$$v_0^2 = 2(3z)^{1/4} \left[1 - (3/2)(3z)^{-1/4} + (27/32)(3z)^{-1/2} + (27/32)(3z)^{-3/4} + (1215/2048)(3z)^{-1} \right]. \quad (24)$$

The higher order derivatives of Eq. (22) are expanded in powers of $1/v_0$ which gives (for $v = Cn$)

$$I(z) = \left(\frac{15}{\pi^4}\right) I_0 \{ \exp[-F_1(n_0, z)] \} \int_{-v_0}^\infty \frac{\exp(-v^2)}{C} \times \left[1 + v_0^{-1} \left(\frac{5v^3}{3} \right) + v_0^{-2} \left(\frac{25v^6}{18} - \frac{5v^4}{2} \right) + v_0^{-3} \left(\frac{125v^9}{162} - \frac{25v^7}{6} + \frac{7v^5}{2} \right) + v_0^{-4} \left(\frac{625v^{12}}{1944} - \frac{125v^{10}}{36} + \frac{215v^8}{24} - \frac{14v^6}{3} \right) \right] dv. \quad (25)$$

We obtain by performing the integration

$$I(z) = (15/\pi^4) I_0 \{ \exp[-(z/n_0^3 + n_0)] \} (n_0^4/v_0) \times [(\pi)^{1/2} (1 + 1.80661/v_0^2 + 0.013931/v_0^3 - 0.73595/v_0^4) + [5v_0 \exp(-v_0^2/6) \times (1 + 1.91111/v_0^2 - 2.29167/v_0^3 - 0.44815/v_0^4)]]]. \quad (26)$$

Equations (23), (24), and (26) are used to determine

approximate representation for Eq. (12) valid for $z \geq 100$,

$$I(z) = (15/\pi^4) I_0 (\pi/2)^{1/2} (3z)^{7/8} \{1 + 4.6533(3z)^{-1/4} + 13.980(3z)^{-1/2}\} \{\exp[-4(3z)^{1/4}/3] \times [1 + (27/32)(3z)^{-1/2} + (27/32)(3z)^{-3/4} + (1215/2048)(3z)^{-1}]\}, \quad (27)$$

neglecting small terms [i.e., $0.014/v_0^3$ and $5v_0 \exp(-v_0^2)/v_0^3$]. The successive terms in the expansion of Eq. (21) for $p=2, 3, 4, \dots$ furnish solutions similar to that of Eq. (27) but reduced by the factor $p^{-11/8} \exp[-\frac{4}{3}(p^{3/4}/1)(3z)^{1/4}]$, which for $z \geq 100$ is small (i.e., ≤ 0.022 when $p=2$).

Hence, the equation

$$I(x) = I_0 D_1 x^{7/8} (1 + D_2 x^{-1/4}) \exp(-D_3 x^{1/4}), \quad (6)$$

neglecting terms in $z^{-\alpha}$ where $\alpha \geq \frac{1}{2}$ for thick absorbers (i.e., $z = Ax/(kT)^3 \geq 500$) describes the transmission of a blackbody spectrum, characterized by a source temperature which may be determined from the constants

$$D_1 = 0.1930(3A)^{7/8}(kT)^{-21/8}; \quad D_2 = 4.653(3A)^{-1/4}(kT)^{3/4}; \\ D_3 = 1.333(3A)^{1/4}(kT)^{-3/4}.$$

The constant A [for the approximation $\mu(E) = A/E^3$ over a limited energy region] must be chosen so that Eq. (2) is consistent with known absorption coefficients for a given material. The approximation $\mu(E) = A/E^3$ where $(2 < \beta \leq 3)$ is sometimes more consistent with experimental values of $\mu(E)$ depending on the absorber and photon energy spread.

The saddle point method may be used to determine a representation for Eq. (14) which represents the transmission of blackbody radiation through materials with absorption coefficients that vary with energy as E^β [e.g., for nonintegral values of β between 2 and 3 when $(\beta z')^{1/(\beta+1)} \gg 3$]. The value of n_0 (i.e., the maximum point) differs from that given by Eq. (23) and may be determined by expanding $n_0 = (\beta z')^{1/(\beta+1)} (1 - 3/n_0)^{-1/(\beta+1)}$ in negative powers of $(\beta z')^{1/(\beta+1)}$. Comparable modifications are necessary for Eqs. (24) through (27).

The integral of Eq. (14) has an interesting property which may apply to other continuous x-ray distributions. The ratio of the integrand evaluated at n_0 to the integral remains nearly constant (i.e., 0.22 ± 0.03 when $\beta=3$), for $(0 \leq z' \leq 10^4)$. This is useful when a simple approximation for n_0 in terms of z' is valid. This property will not be pursued for the blackbody problem since, for a wide range of absorber thicknesses, the expression for n_0 is a complicated function of $z' = Ax/(kT)^3$. It is cumbersome to compute the integral under this condition. The corresponding integral for the transmission of bremsstrahlung from a plasma discharge, Eq. (19), can be evaluated more easily using the saddle point method since

$$n_0 = (\beta z')^{1/(\beta+1)}.$$

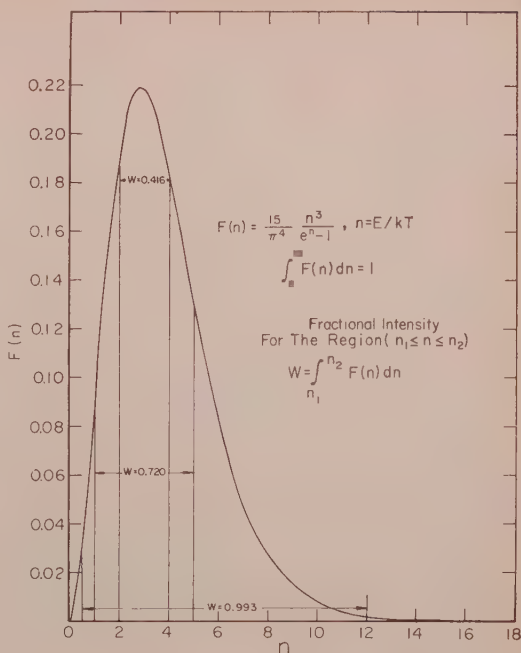


FIG. 1. Incident energy spectrum for blackbody radiation.

VI. DETERMINATION OF BLACKBODY TEMPERATURES THROUGH ANALYSIS OF A HYPOTHETICAL ABSORPTION EXPERIMENT

Beryllium is used to absorb the radiation from blackbody sources at temperatures between 0.2 and 3 keV. The validity of the approximation $\mu(E) = A/E^3$ is considered. The accuracy of the "thin" and "thick" absorber representations is estimated and a modified representation is determined to be used in the "intermediate thickness" region.

Hypothetical data is furnished by a 7090 IBM computer program originated by Dr. Lee W. Parker of the Lawrence Radiation Laboratory. He integrates Eq. (4) by quadrature in steps of one hundred intervals on either side of the blackbody peak (see Fig. 1). The results using $\mu(E) = A/E^3$ are compared with those obtained with the semiempirical formula for $\mu(E)$ given by Victoreen.⁹

Figure 1 is a plot of the energy distribution of a blackbody spectrum. The abscissa is equal to E/kT where kT represents the blackbody temperature. The area under the curve is normalized to unity.

The energy region where the beryllium absorption coefficient may be approximated by $\mu(E) = A/E^3$ (e.g., $A = 1220 \text{ keV}^3 \text{ cm}^{-1}$) is shown in Fig. 2 and extends over the range $0.2 \text{ keV} \leq E \leq 15 \text{ keV}$.⁹⁻¹⁰ Referring again to

⁹ J. A. Victoreen, J. Appl. Phys. **20**, 1141 (1949).

¹⁰ R. T. McGinnies, X-Ray Attenuation Coefficients from 10 keV to 100 MeV (U. S. Dept. of Commerce, National Bureau of Standards, Washington 25, D. C., 1959), Natl. Bur. Standards Suppl. to Circ. No. 583, p. 6.

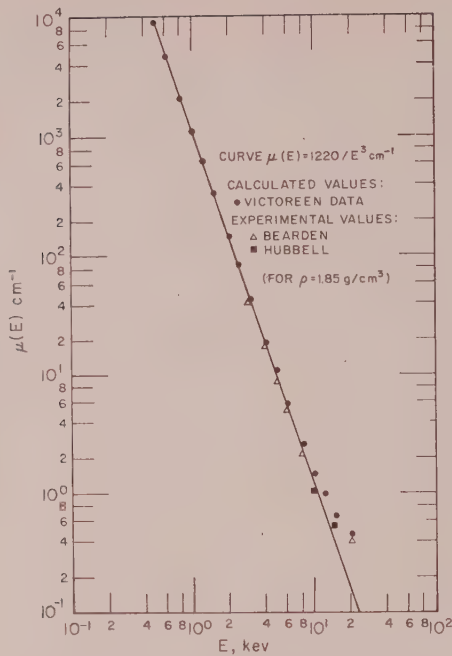


Fig. 2. Energy dependence of the absorption coefficient for beryllium.

Fig. 1, 72% of the incident intensity occurs with spectral energies between kT and $5kT$. We expect the analysis of the preceding two sections to be applicable for source temperatures between 0.2 and 3 keV, for which the radiation has maximum intensity at energies between 0.56 and 8.5 keV. The limitation of the approximation $\mu(E) = A/E^3$ on the low-energy side is due to the beryllium K edge which occurs at 0.112 keV.¹¹ The high-energy limitation occurs when the scattering coefficient per electron, given by the Klein-Nishina formula, becomes appreciable.

Figure 3 shows the results of Dr. Parker's code which integrates Eq. (12) for the range of values $[0 \leq z = Ax/(kT)^3 \leq 10^4]$. Equation (13), the "thin" absorber expansion, agrees with the results of the 7090 IBM code to 1% of $I(z)/I_0$ for transmissions greater than 40% of the incident spectrum. Equation (5), which neglects terms of order $5/3$ and greater in $Ax/(kT)^3$, may be used to 1% accuracy for transmissions greater than 90% of I_0 . Similarly, Eq. (27), the "thick" absorber expansion, is accurate to 4% of $I(z)/I_0$ for transmissions less than 25% of the incident intensity. Equation (6), which retains the first few terms of the above expansion, is valid to 6% of $I(z)/I_0$ for transmissions less than 5% of I_0 .

Intermediate transmission values between 25% and

90% agree to 0.04% of $I(z)/I_0$ with the equation

$$I(z) = (15/\pi^4)I_0(\frac{1}{2}\pi)^{1/2}(3z)^{7/8}\{1 + 2.9204(3z)^{-1/4} + 5.6393(3z)^{-1/2} + 8.2599(3z)^{-3/4} + 0.95845(3z)^{-1}\} \exp[-\frac{4}{3}(3z)^{1/4}], \quad (28)$$

where $z = Ax/(kT)^3$. Equation (28) represents a modification of Eq. (27) for $(1 \leq z \leq 100)$. This was determined by using the results of the code at $z = 1, 5, 20$, and 100 and testing intermediate values of z with the resulting equation (since thin and thick absorber expansions were less accurate in this region).

Figure 4 shows the dependence of the transmitted intensity (normalized to unit incident intensity) on temperature for a given absorber thickness. The curve is nearly linear on a logarithmic scale for intensities less than 0.004 I_0 , which indicates the dependence of transmitted intensities I/I_0 on some high power (between 7 and 10) of the temperature.

We consider the following gedanken experiment to determine the temperature of an unknown blackbody source. We measure the relative transmission I_1/I_0 for two thick absorbers x_1 and x_2 of a substance which has negligible K -edge effects over the energy region in question. If we limit both transmission measurements to intensities less than 0.4% of the incident intensity, the equation

$$kT = \left\{ \frac{4(3A)^{1/4}(x_2^{1/4} - x_1^{1/4})}{3[\log_e I_1/I_2 + \frac{7}{8}(\log_e x_2/x_1)]} \right\}^{1/3} \quad (29)$$

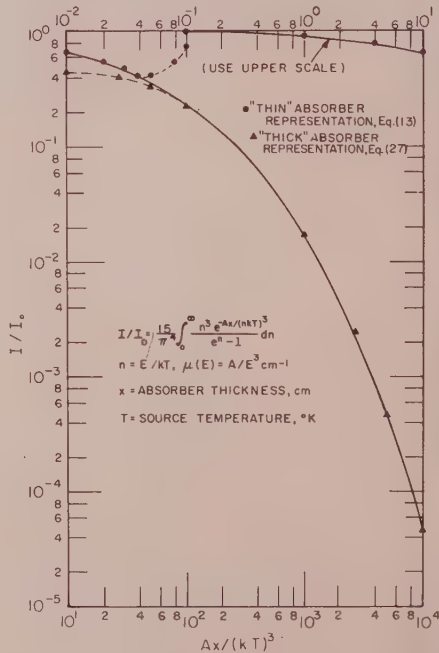


Fig. 3. X-ray transmission versus absorber thickness for blackbody radiation.

¹¹ *Handbook of Chemistry and Physics* (Chemical Rubber Publishing Company, Cleveland, Ohio, 1957), 39th ed., p. 2462.

valid. This relationship is obtained using the first term of Eq. (6), the thick absorbers representation for soft x-ray transmission of blackbody radiation.

We see from Fig. 2 that the constant $A=1220 \text{ kev}^3 \text{ cm}^{-1}$ is a good choice for beryllium absorbers. The thicknesses x_1 and x_2 should be chosen much greater than the quantity $[625(kT)^3/3A] \text{ cm}$ to justify neglecting the second term of Eq. (6) in the above analysis. For beryllium this means choosing both thicknesses greater than or equal to $2(kT)^3 \text{ cm/kev}^3$. Using Fig. 3 we determine the ratio I_1/I_2 for $(kT)=1 \text{ kev}$ and two thicknesses 2 and 4 cm, respectively. Equation (29) reproduces the temperature (i.e., $kT=1 \text{ kev}$) to an accuracy of 2.5%. If the source intensity is high and the backgrounds are insignificant, the above hypothetical experiment furnishes a convenient and fairly accurate determination of the source temperature. An advantage of this method, as pointed out by Dr. Parker, is that less weight is placed on the fact that the incident radiation obeys the Stefan-Boltzmann law for a blackbody emitter (i.e., the analysis depends solely on relative intensity measurement). In addition (from an experimental point of view) a relative intensity measurement can be made more easily and with greater accuracy.

Beryllium absorption coefficients for the curves of Fig. 5 were obtained using Victoreen's semiempirical formula,⁹

$$\mu(E) = \rho[C\lambda^3 - D\lambda^4 + \sigma_e N_0 Z/A],$$

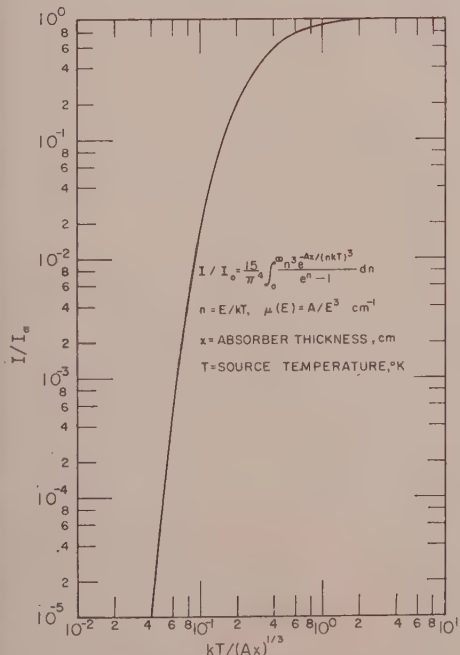


FIG. 4. X-ray transmission versus temperature for blackbody radiation.

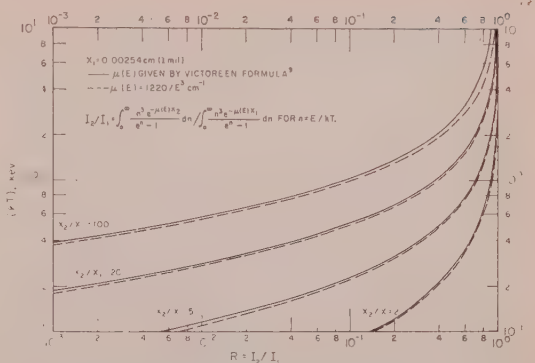


FIG. 5. Determination of blackbody temperatures from the transmitted intensity ratio R for different pairs of beryllium absorbers with and without a simple approximation for the absorption coefficient.

which takes into account the contributions due to photoelectric ($\rho[C\lambda^3 - D\lambda^4]$) and scattering ($\rho\sigma_e N_0 Z/A$) processes. The constants C , D , ρ (the density), and $N_0 Z/A$ (the number of electrons per gram) were determined for beryllium. The cross section σ_e represents the Klein-Nishina value for the scattering by free electrons and depends on the wavelength λ of the incident photons. The absorption coefficient was reduced by a factor of 9.143 (computed from experimental measurements given by Tomboulou and Bedo)¹² at the beryllium K -edge which occurs at 0.112 kev.¹¹ The first term of Victoreen's formula (reduced by a constant) was used to approximate the coefficients at energies below the K edge. Corrections were not made for the L edge which occurs at a much lower energy (i.e., 9.324 ev).¹³

Figure 5 shows the transmitted intensity ratios $R = I_2/I_1 < 1$ for different pairs of beryllium absorbers (with thicknesses $x_2 > x_1$) determined for blackbody temperatures between 1/10 and 10 kev. A comparison is made between the results obtained using the Victoreen formula for $\mu(E)$ and the comparable results using the approximation $\mu(E) = (1220/E^3) \text{ kev}^3 \text{ cm}^{-1}$. The temperatures computed by the two methods differ at most by 11% for $0.2 \text{ kev} \leq kT \leq 3 \text{ kev}$.

CONCLUSION

A determination of blackbody temperatures between 0.2 and 3 kev is possible using the "thin" absorber expansion

$$I(z) = I_0 \{ 1 + (15/\pi^4) [(z/3)(\log_e z) - 0.14093z - 0.50780z^{4/3} + 0.66974z^{5/3} - 0.007769z^2 + 0.00060453z^{7/3}] \},$$

for $z = Ax/(kT)^3$ which is useful when $(0 \leq z \leq 40)$ (i.e., for $I(z)/I_0 \geq 0.40$) and the "thick" absorber

¹² D. H. Tomboulou and D. E. Bedo, Rev. Sci. Instr. 26, 747 (1955).

¹³ See reference 7, p. 792.

expansion

$$I(z) = (15/\pi^4) I_0 (\pi/2)^{1/2} (3z)^{7/8} \{ 1 + 4.6533 (3z)^{-1/4} \\ + 13.980 (3z)^{-1/2} \} \{ \exp[-(4/3)(3z)^{1/4}] \\ \times [1 + (27/32)(3z)^{-1/2} + (27/32)(3z)^{-3/4} \\ + (1215/2048)(3z)^{-1}] \},$$

when $(100 \leq z \leq 10,000)$ (i.e., for $I(z)/I_0 \leq 0.25$). The accuracies of the two expansions are respectively 1% and 4% of $I(z)$ for the regions given, as shown in Fig. 3. The determination of (kT) based on the assumption $\mu(E) = A/E^3$ (where A is a constant equal to $1220 \text{ kev}^3 \text{ cm}^{-1}$ for beryllium) differs by 11% (at most) with the results using the Victoreen formula⁹ for $\mu(E)$ when kT is between 0.2 and 3 kev as shown by Fig. 5.

It is likely that the method used to develop the thin absorber representation will be useful in the analysis of other continuous distributions of soft x rays (e.g., deceleration radiation from thick targets and bremsstrahlung from plasma discharges). The saddle point method (used to determine a thick absorber representa-

tion for the transmission of Planck radiation) may be useful in the evaluation of plasma discharges present in a "Sherwood" experiment.

ACKNOWLEDGMENTS

The author is indebted to a number of physicists from the Lawrence Radiation Laboratory. Dr. Arnold Clark, Dr. Jack Shearer, Wayne Woodruff, and Robert Olson suggested the problem and made many constructive criticisms. The assistance of Dr. Lee Parker, who devised a program for the 7090 IBM computer which integrates Eq. (4), was invaluable. His many suggestions were equally helpful. Further appreciation extended to Dr. Gordon Latta (Department of Mathematics, Stanford University) whose ingenious idea led to "thin absorber" representation, to Dr. I. Bancroft and Dr. A. Skumanich (Los Alamos Scientific Laboratory), and their colleagues at LASL who realize that "thick absorber" transmission varied rapidly with blackbody temperatures, and to Mrs. Edward Ellison for her valuable assistance with the manuscript.

Forbidden Reflections in Electron Diffraction Patterns of Evaporated Tin Films

RICHARD W. VOOK

International Business Machines Corporation, Yorktown Heights, New York

(Received May 26, 1961)

Previous work has shown the existence of some structurally forbidden reflections in the electron diffraction patterns of (100) oriented polycrystalline films. These films were deposited under ultra-high vacuum conditions. A continuation of this work has resulted in the observation of these and other forbidden reflections in the diffraction patterns of two other kinds of films: (001) oriented single crystals containing deformation twins and (100) oriented single crystals. The existence of these strong reflections is probably due to strong dynamic interactions between the electron beam and the crystal lattice.

PREVIOUS work¹ on ultra-high vacuum evaporated tin films has shown that the concept of simultaneous diffraction² can be used to explain the structurally forbidden reflections appearing in (100) oriented polycrystalline films. The reflections observed were the (002), (022), and (042).

Further work has resulted in the film shown in Fig. 1. This photograph was taken with a Phillips EM-100 electron microscope operating at 100 kv. The tin film was deposited at liquid nitrogen temperature on an NaCl substrate at pressures less than 3×10^{-9} torr. It was then warmed to room temperature, removed from the vacuum system, and prepared for electron optical examination. The large white regions in Fig. 1 are holes in the film, the origin of which is presently not clear.

Around the holes are large (100) oriented single crystals. Selected area diffraction of these (100) single crystals gave the pattern shown in Fig. 2. Careful examination of this pattern permitted the determination of the k and l axes in reciprocal space. One can immediately see from the symmetry that many structurally forbidden reflections have occurred. Indeed all reflections of the type $(0kl)$ where $(k+l)=0$ or an even integer are present. This includes the (002), (022), and (042) reflections observed in the (100) oriented polycrystalline films.

Other structurally forbidden reflections have been obtained from the diffraction pattern of deformation twins³ (see Fig. 3). Deformation twinning in tin results in an effective lattice rotation of $63^\circ 10'$ about a $[100]$

¹ Richard W. Vook, *J. Appl. Phys.* **32**, 1557 (1961).

² J. A. Darbyshire and E. R. Cooper, *Proc. Roy. Soc. (London)* **A152**, 104 (1935).

³ J. T. Fourie, F. Weinberg, and F. W. C. Boswell, *Acta Metall.* **8**, 851 (1960).



FIG. 1. Electron micrograph of an ultra-high vacuum evaporated tin film. The large white areas are holes. They are surrounded by large (100) oriented single crystals. The matrix is (100) oriented and polycrystalline.



FIG. 2. Selected area diffraction of large (100) oriented single crystals in Fig. 1.



FIG. 3. Selected area diffraction of a deformation twin in an (001) oriented single-crystal matrix.

axis. Such a rotation orients the electron beam into a position almost parallel to the (011) planes. The twin reflections are superimposed on the pattern due to the untwinned (001) oriented matrix. The structurally forbidden reflections that appear in this case are of the type $(h22)$, $(h\bar{2}2)$, $(h66)$, $(h\bar{6}6)$, etc., where $h=0, \pm 2, \pm 4, \dots$. Note here that the forbidden (022) reflection observed earlier appears again.

A qualitative explanation in terms of simultaneous diffraction events showing how these forbidden reflections may arise has been given earlier.¹ Finch and Wilman⁴ have also used essentially the same approach. They suggested that an (hkl) diffracted beam may act as a primary beam giving rise to $(h_1k_1l_1)$ reflections. It is thus possible to get, not only the (hkl) reflections, but also $(h+h_1, k+k_1, l+l_1)$ reflections. For example, the forbidden (022) reflection in tin may arise from an (031) reflection acting as a primary beam, thereby producing an (011) reflection (among others). Consequently the (022) reflection appears in the resulting

diffraction pattern. Similar considerations can be used to explain the existence of the other forbidden reflections.

ACKNOWLEDGMENTS

The author gratefully acknowledges the assistance of Mr. R. H. Jeppesen in the preparation of the films and to Mr. C. Fisher for the glassblowing. Thanks are also due Dr. R. DeMars and Mr. C. Aliotta for the use of the electron microscope.

⁴ G. I. Finch and H. Wilman, *Ergeb. exakt. Naturwiss.* **16**, 406 (1937).

Analysis of a Nonlinear First-Order System with a White Noise Input

T. K. CAUGHEY AND J. K. DIENES
California Institute of Technology, Pasadena, California
 (Received June 19, 1961)

A general technique for computing the power spectrum of nonlinear systems is presented, and the method is applied to the Brownian motion of a particle with idealized Coulomb damping. In this method the transition probability is obtained by solving the appropriate Fokker-Planck equation. Then the autocorrelation function is calculated by an appropriate integration, and finally the power spectrum is found by means of the Wiener-Khinchine relation. Comparison is made with the method of equivalent linearization, which is applicable to a wide class of nonlinear problems.

OUTLINE OF THE TRANSITION PROBABILITY METHOD

SYSTEMS which can be described by an ordinary differential equation and which are subject to random forces can be treated by the theory of continuous Markoff processes. Such processes are completely described if the transition probability, $T(q_i^0|q_i, t)$, is known, where $i=1, 2, \dots, n$ and n is the order of the system. The q_i are the coordinates of the process and are frequently taken to be the system displacement and its first $n-1$ derivatives. The q_i^0 are the initial values of these coordinates.

It is convenient to think of the transition probability as a density function in a space whose axes are the coordinates q_i . Then

$$T(q_i^0|q_i, t) \prod_{i=1}^n \Delta q_i$$

is the probability that a system, which initially has coordinates q_i^0 , at a later time, t , has coordinates which lie in a volume element containing the point with coordinates q_i and with sides of length Δq_i . The system coordinates must lie somewhere in this space, with probability one. Therefore,

$$\int_{-\infty}^{\infty} \cdots \int_{-\infty}^{\infty} T(q_i^0|q_i, t) \prod_{i=1}^n dq_i = 1. \quad (1)$$

Furthermore, the system must have initially the coordinates q_i^0 . The transition probability must therefore satisfy the initial condition

$$\lim_{t \rightarrow 0} T(q_i^0|q_i, t) = \delta(q_1 - q_1^0) \delta(q_2 - q_2^0) \cdots \delta(q_n - q_n^0). \quad (2)$$

The transition probability is the fundamental solution to the Fokker-Planck equation

$$\dot{T} = - \sum_i \frac{\partial (A_i T)}{\partial q_i} + \frac{1}{2} \sum_{i,j} \frac{\partial^2 (B_{ij} T)}{\partial q_i \partial q_j}. \quad (3)$$

The coefficients A_i and B_{ij} are to be determined from the differential equations of the process, and are defined

as follows:

$$\lim_{\Delta t \rightarrow 0} \left\langle \frac{\Delta q_i}{\Delta t} \right\rangle = A_i, \quad (4)$$

$$\lim_{\Delta t \rightarrow 0} \left\langle \frac{\Delta q_i \Delta q_j}{\Delta t} \right\rangle = B_{ij}. \quad (5)$$

The derivation of the Fokker-Planck equation and the justification of the formulas for A_i and B_{ij} are given by Wang and Uhlenbeck.¹

As the time t goes to infinity, the dependence of the process on the initial conditions will disappear if the system approaches stationarity. The transition probability then approaches the first probability density, $W_1(q_i)$. This function satisfies the stationary Fokker-Planck equation.

$$- \sum_i \frac{\partial (A_i W_1)}{\partial q_i} + \frac{1}{2} \sum_{i,j} \frac{\partial^2 (B_{ij} W_1)}{\partial q_i \partial q_j} = 0. \quad (6)$$

The second joint probability density, $W_2(q_i, q_i^0, t)$, is the probability that the system has coordinates in the range $(q_i^0, q_i^0 + \Delta q_i^0)$ at time t_0 and in the range $(q_i, q_i + \Delta q_i)$ at time t . If the system is in a stationary state at time t_0 the second joint probability is the product of the first probability density at time t_0 , $W_1(q_i^0)$, and the transition probability density at a later time t , $T(q_i^0|q_i, t)$. Then

$$W_2(q_i^0, q_i, t) = W_1(q_i^0) T(q_i^0|q_i, t) = f_1^n(t - t_0). \quad (7)$$

By means of the second probability density it is possible to calculate ensemble averages of functions which depend on the state of the system at two different times. The autocorrelation is such a function, and is a useful statistic in the analysis of random processes. It is defined as follows:

$$R_j(\tau) = \int_{-\infty}^{\infty} \cdots \int_{-\infty}^{\infty} W_2(q_i, q_i^0, t) q_j q_j^0 \prod_{m=1}^n dq_m^0 \prod_{k=1}^n dq_k, \quad (8)$$

$\tau = (t - t_0)$

It is convenient to define the mean value of the system

¹ M. C. Wang and G. E. Uhlenbeck, *Revs. Modern Phys.* **17**, 323 (1945).

displacement $\langle q_j(\dot{q}_i^0, t) \rangle$ by the equation

$$\langle q_j(q_i^0, t) \rangle = \int_{-\infty}^{\infty} \cdots \int_{-\infty}^{\infty} q_j T(q_i^0 q_i, t) \prod_{k=1}^n dq_k = f' n(\tau). \quad (9)$$

Then the autocorrelation can be written

$$R_j(\tau) = \int_{-\infty}^{\infty} \int_{-\infty}^{\infty} q_j^0 \langle q_j(q_i^0, t) \rangle W_1(q_i^0) \prod_{m=1}^n dq_m^0. \quad (10)$$

It is sometimes useful to deal with the Laplace transform of the time dependent variables rather than with their explicit values. The Laplace transform will be denoted by a bar, that is

$$f(s) = \int_0^{\infty} e^{-s\tau} f(\tau) d\tau.$$

Then (9) becomes

$$\langle \bar{q}_j(q_i^0, s) \rangle = \int_{-\infty}^{\infty} \cdots \int_{-\infty}^{\infty} q_j \bar{T}(q_i^0 q_i, s) \prod_{k=1}^n dq_k, \quad (11)$$

and (10) can be written

$$\bar{R}_j(s) = \int_{-\infty}^{\infty} \cdots \int_{-\infty}^{\infty} q_j W_1(q_i^0) \langle \bar{q}_j(q_i^0, s) \rangle \prod_{m=1}^n dq_m. \quad (12)$$

The power spectrum and the autocorrelation are connected by the Wiener-Khinchine relation,

$$\Phi_j(\omega) = \frac{2}{\pi} \int_0^{\infty} R_j(\tau) \cos \omega \tau d\tau. \quad (13)$$

Then the power spectrum can be obtained directly from the Laplace transform of the autocorrelation function by the formula below.

$$\Phi_j(\omega) = (2/\pi) \operatorname{Re} \bar{R}(i\omega), \quad (14)$$

where Re means the "real part of." These relations demonstrate the connection between the theory of Markoff processes and the theory of power spectra and can, in principle, be used to determine the power spectrum of nonlinear systems.

APPLICATION TO LINEAR SYSTEMS

In order to illustrate the relations discussed above, the application to a linear first-order system is given. The governing equation of the process is

$$\dot{y} + \beta y = N(t), \quad (15)$$

where $N(t)$ is Gaussian and has a white power spectrum. This may be thought of as an equation for the velocity, y , of a mass with linear damping subject to a random

force, $N(t)$. The appropriate Fokker-Planck equation is given in reference 1.

$$\dot{T} = \partial(\beta y T) / \partial y + D T_{yy}. \quad (16)$$

Its fundamental solution is also given there, and is

$$T = (2\pi\sigma^2)^{-1} \exp[-(y - y_0^*)^2 / 2\sigma^2], \quad (17)$$

where

$$y_0^* = \langle y \rangle = y_0 \exp(-\beta t), \quad \sigma^2 = D/\beta [1 - \exp(-2\beta t)]. \quad (18)$$

The mean value, $\langle y \rangle$, of y can be found as indicated in (9) by carrying out the integration, and is given above. The first probability density may be obtained by letting the time t go to infinity.

$$W_1(y) = (2\pi D/\beta)^{-1} \exp(-\beta y^2 / 2D). \quad (19)$$

The autocorrelation of the velocity, y , is then found by substituting these results into (10).

$$R(\tau) = D/\beta \exp(-\beta\tau). \quad (20)$$

Its Laplace transform is given by

$$\bar{R}(s) = D/\beta(\beta + s). \quad (21)$$

Finally, the power spectrum is obtained using (14)

$$\Phi(\omega) = (D/\pi(\beta^2 + \omega^2)) - \infty < \omega < \infty. \quad (22)$$

This result is well known and is usually derived by the method of spectral analysis. However, the transition probability method is somewhat more general since it applies to nonlinear systems.

APPLICATION TO A NONLINEAR SYSTEM

If, in the problem discussed above, the linear damping βy is replaced by a nonlinear one $f(y)$, the governing equation becomes

$$\dot{y} + f(y) = N(t), \quad (23)$$

and the appropriate Fokker-Planck equation is

$$\dot{T} = \partial/\partial y [f(y)T] + D T_{yy}. \quad (24)$$

This problem has been considered by Dienes² in his doctoral thesis along with some higher order processes. MacDonald³ has also made some preliminary studies of the behavior of such systems.

The first probability density $W_1(y)$ is the solution to the stationary equation

$$\frac{\partial}{\partial y} [f(y)W_1] + D \frac{\partial^2 W_1}{\partial y^2} = 0.$$

It is easily shown that the only solution of this equation

² J. K. Dienes, Ph.D. thesis, 1961, California Institute of Technology, Pasadena, California.

³ D. K. C. MacDonald, Phys. Rev. **108**, 541 (1957).

satisfying the condition (1) is

$$W_1 = \frac{\exp[-F(y)/D]}{\int_{-\infty}^{\infty} \exp\left[-\frac{F(y)}{D}\right] dy} \quad (26)$$

where $F(y) = \int f(y) dy$.

Although the first probability density can be determined for arbitrary damping, the transition probability cannot be so easily obtained. However, if the damping is of the idealized Coulomb type, the calculations outlined in the first section can be carried through explicitly. In this case $f(y)$ is of the form

$$f(y) = k \operatorname{sgny}, \quad (27)$$

where sgny means the sign of y . Then the appropriate Fokker-Planck equation is

$$\dot{T} = k \operatorname{sgny} T_y + D T_{yy} \quad (28)$$

Taking the Laplace transform and using the initial condition (2) an ordinary differential equation is obtained.

$$D \bar{T}_{yy} + a \bar{T}_y - s \bar{T} = -\delta(y - y_0), \quad (29)$$

where

$$a = k \operatorname{sgny} \quad (30)$$

and is constant in the regions $y > 0$ and $y < 0$. With this notation, the general solution of (29) is

$$\bar{T} = A \exp\left\{[-a + (a^2 + 4Ds)^{\frac{1}{2}}]y/2D\right\} + B \exp\left\{[-a - (a^2 + 4Ds)^{\frac{1}{2}}]y/2D\right\} \quad (31)$$

The probability must vanish at $y = \pm \infty$. Furthermore, the effect of the delta function in (29) is the same as requiring a jump in T_y at $y = y_0$; that is,

$$\bar{T}_y(y_0+, s) - \bar{T}_y(y_0-, s) = 1/D. \quad (32)$$

Therefore $\bar{T}(y)$ requires three different representations over the y axis.

$$\left. \begin{aligned} \bar{T} &= A \exp(\alpha_1 y) & y \leq 0 \\ \bar{T} &= B \exp(\alpha_2 y) + C \exp(-\alpha_1 y) & 0 \leq y \leq y_0 \\ \bar{T} &= E \exp(-\alpha_1 y) & y > y_0 \end{aligned} \right\} \quad (33)$$

where

$$\alpha_1 = \frac{(\lambda^2 + s)^{\frac{1}{2}} + \lambda}{D^{\frac{1}{2}}}, \quad \alpha_2 = \frac{(\lambda^2 + s)^{\frac{1}{2}} - \lambda}{D^{\frac{1}{2}}}, \quad \lambda = \frac{k}{2D^{\frac{1}{2}}} \quad (34)$$

There are four quantities, A , B , C , and E to be determined, which are functions of y_0 and s , and these can be found from the four conditions: (a) the jump condition, (32); (b) continuity at $y = 0$; (c) continuity at $y = y_0$; and (d) the transformed version of the normalization condition, (1)

$$\int_{-\infty}^{\infty} \bar{T}(y, y_0, s) dy = 1/s.$$

The result of solving the four simultaneous equations

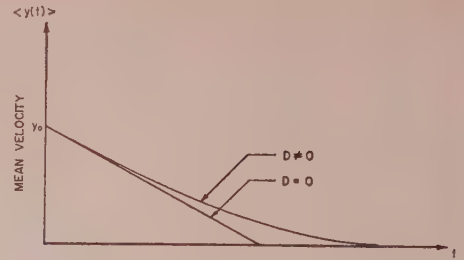


FIG. 1. The mean velocity of a mass with Coulomb damping subject to a random force with spectral density $2D$.

arising from these conditions is given below.

$$\left. \begin{aligned} A &= \frac{\exp(-\alpha_2 y_0)}{2\alpha_2 D} & B &= \frac{\exp(-\alpha_2 y_0)}{D(\alpha_1 + \alpha_2)} \\ C &= \frac{\alpha_1 - \alpha_2 \exp(-\alpha_2 y_0)}{\alpha_1 + \alpha_2} & & 2D\alpha_2 \\ E &= \frac{\alpha_1 - \alpha_2 \exp(-\alpha_2 y_0)}{\alpha_1 + \alpha_2} & & \frac{\exp(\alpha_1 y_0)}{D(\alpha_1 + \alpha_2)} \end{aligned} \right\} \quad (35)$$

Equations (33), (34), and (35) together determine the Laplace transform of the transition probability explicitly. The inverse transform is given by

$$T = \frac{k \exp(-k|y|/D)}{2\pi^{\frac{1}{2}} D} \int_{-\infty}^{\infty} \exp(-u^2) du + \frac{\exp[k(y - |y|)/2D - (y - y_0 + kt)^2/4Dt]}{(4\pi Dt)^{\frac{1}{2}}}, \quad (36)$$

where

$$w = \frac{y_0 + |y|}{2(Dt)^{\frac{1}{2}}}. \quad (37)$$

The mean value of the velocity, given its initial value y_0 , is difficult to evaluate explicitly, but its Laplace transform can be calculated from (11) by means of a straightforward, but lengthy, integration.

$$\langle \bar{y}(y_0, s) \rangle = \frac{y_0}{s} + \frac{k}{s^2} [1 - \exp(-\alpha_2 y_0)]. \quad (38)$$

In the limit as D goes to zero the solution to the deterministic initial value problem is recovered.

$$\bar{y}(s) = y_0/s - k/s^2; \quad y(t) = y_0 - kt, \quad t \leq y_0/k. \quad (39)$$

In the absence of any imposed force, the velocity decreases linearly to zero, which is to be expected from elementary mechanics. The effect of the random force $N(t)$ is to make the decrease to zero velocity asymptotic as the time becomes infinite. This is illustrated in Fig. 1.

The Laplace transform of the autocorrelation $\bar{R}(s)$, can now be obtained by substitution of (38) into (12) and computing the first probability density $W_1(y)$ by

combining (26) and (27).

$$W_1(y) = (k/2D) \exp(-k|y|/D). \quad (40)$$

Then, upon carrying out the integration,

$$\bar{R}(s) = \frac{D}{2\lambda^2 s} - \frac{D}{s^2} + \frac{4\lambda^2 D}{s^4} [\lambda - (\lambda^2 + s)^{\frac{1}{2}}]^2. \quad (41)$$

It may be noted here that the mean-squared displacement can be obtained from the above result by means of the Tauberian theorem

$$\lim_{t \rightarrow 0} R(t) = \langle y^2 \rangle = \lim_{s \rightarrow \infty} s \bar{R}(s) = \frac{2D^2}{k^2}. \quad (42)$$

Finally, the power spectrum is found by carrying out the algebra indicated in (14).

$$\Phi(\omega) = \frac{D}{\pi \lambda^4} \left\{ \frac{\lambda^4}{\omega^2} + \frac{8\lambda^8}{\omega^4} \left[1 - \left(\frac{1 + (1 + \omega^2/\lambda^4)^{\frac{1}{2}}}{2} \right)^{\frac{1}{2}} \right] \right\}. \quad (43)$$

An ambiguity in the algebra arises because of the square root appearing in (41). The sign of the radical in (43) is chosen so that the power spectrum is finite at $\omega = 0$, and its value there is $5D^3/\pi k^4$.

It is convenient to deal with nondimensional power spectra. In order to accomplish this here, one can define a nondimensional frequency, $\eta = \omega/\lambda^2$, and a nondimensional spectrum $\phi(\eta)$ which is normalized to have a unit area.

$$\phi(\eta) = 2\Phi(\omega)\lambda^2/\langle y^2 \rangle, \quad 0 < \eta < \infty. \quad (44)$$

Then it follows that

$$\int_0^\infty \phi(\eta) d\eta = 1,$$

and the detailed expression for the normalized power spectrum is

$$\phi(\eta) = \frac{4}{\pi} \left\{ \frac{1}{\eta^2} + \frac{8}{\eta^4} \left[1 - \left(\frac{1 + (1 + \eta^2)^{\frac{1}{2}}}{2} \right)^{\frac{1}{2}} \right] \right\}. \quad (45)$$

This function is plotted in Fig. 2, and is seen to be monotonically decreasing.

THE EQUIVALENT LINEAR SYSTEM

One motivation for the above analysis is that it provides a standard for evaluating the accuracy of the method of equivalent linearization, which provides a convenient approximation in many problems. Some applications are given in references 4 and 5. For first-order problems the linear system equivalent to (23) is found by determining the value of β which minimizes the expected mean-squared "deficiency" $\epsilon(y)$ in the equation

$$\dot{y} + \beta y + \epsilon(y) = N(t), \quad (46)$$

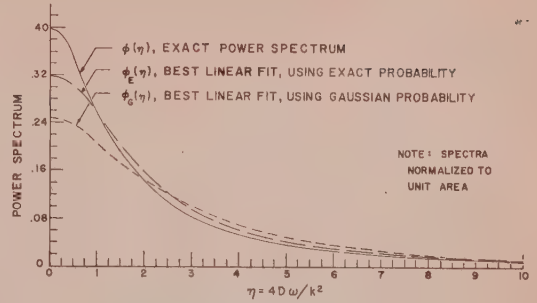


FIG. 2. Comparison of the exact and approximate power spectra of y , where $y + k \operatorname{sgn} y = N(t)$.

where

$$\epsilon(y) = f(y) - \beta y. \quad (47)$$

The expected value of the mean-squared deficiency is

$$\langle \epsilon^2(y) \rangle = \int_{-\infty}^{\infty} [\beta y - f(y)]^2 W_1(y) dy, \quad (48)$$

and the value of β which minimizes the expression above is

$$\beta = \frac{\int_{-\infty}^{\infty} y f(y) W_1(y) dy}{\int_{-\infty}^{\infty} y^2 W_1(y) dy}. \quad (49)$$

The value of β depends upon the choice of the first probability density. If the exact distribution (26) is used, the resultant value of β will be called β_E . However, in many problems the exact first probability density is not known. In these cases it is frequently convenient to prescribe a Gaussian distribution. In this example, if a Gaussian distribution is chosen for $W_1(y)$ the equivalent damping is written β_G . Carrying out the integration above, the equivalent damping in the two cases is

$$\beta_E = k^2/2D, \quad \beta_G = 2k^2/\pi D. \quad (50)$$

Then the equivalent linear system is found by dropping the deficiency term $\epsilon(y)$ in (46)

$$\dot{y} + \beta y = N(t). \quad (51)$$

Using the formula (22) the nondimensional power spectra of the equivalent systems are found.

$$\phi_E = [\pi(1 + \eta^2/4)]^{-1}; \quad \phi_G = [8(1 + \pi^2 \eta^2/64)]^{-1}. \quad (52)$$

The comparison of these two approximate spectra with the exact result is given in Fig. 2. It may be noted that for large η the exact power spectrum $\phi(\eta)$ and the equivalent one $\phi_E(\eta)$ are both asymptotically equal to $4/\pi\eta^2$, whereas the spectrum $\phi_G(\eta)$ is equal to $8/\pi^2\eta^2$. The general agreement is somewhat better when the exact first probability density is used to minimize the deficiency than when the Gaussian distribution is used.

⁴ T. K. Caughey, J. Appl. Mech. 26, 345 (1959).

⁵ R. C. Booten, Jr., in *Proceedings of the Symposium on Non-linear Circuit Analysis* (Polytechnic Institute, Brooklyn, New York, 1953), Vol. 2, pp. 369-391.

Study of Impact Cratering in Sand

F. L. CULP AND H. L. HOOPER
Tennessee Polytechnic Institute, Cookeville, Tennessee
 (Received February 17, 1961)

An investigation of cratering in dry sand using 22-caliber long rifle bullets was carried out. Measurements of craters formed by bullets moving at velocities of 50 to 550 m/sec showed crater volume to vary directly with the square of the bullet velocity at the low end of this range and to approach a linear dependence on bullet velocity at the high end. An equation relating the crater volume to the bullet velocity was developed from a model which assumed hydrodynamic-like flow behind the induced shock wave and was found to provide an excellent fit to the experimental data. It was further found that for velocities below 245 m/sec bullet deformation is small and increases rather slowly with increase in velocity. At 245 m/sec, however, an abrupt transition occurs, and the deformation increases very rapidly. Above 245 m/sec the deformation appears to become constant. This transition velocity is believed to be related to the appropriate velocity of sound in sand.

I. INTRODUCTION

A SURVEY of the literature reveals that numerous studies of cratering under conditions which result in craters of much larger dimensions than those of the impacting pellets have been made. Most of these studies have been made with metal pellets and metal targets. Consequently, rather high velocities have been required to achieve the type of cratering described. In unconsolidated materials, however, no such requirement is involved, and therefore a study of such materials is quite simple. Partly for this reason it was decided to use dry sand as a target material in making a further investigation of impact cratering. Twenty-two-caliber long rifle bullets served as the pellets in this investigation and were fired at normal incidence into the sand at velocities ranging from 50 m/sec to 550 m/sec. Of principal interest in this study was the crater volume-pellet velocity relation and its possible dependence on the velocity of sound in the target material. Previous studies by other investigators¹ have suggested that the target sound velocity may be an important parameter in describing this relation. At velocities well below sonic most observers have reported volume to be

directly proportional to the square of the pellet velocity—i.e., to the kinetic energy of the pellet.² In a study with lead targets and steel pellets at velocities in excess of 1200 m/sec (approximate velocity of sound in lead), one of the present authors³ found that crater volume per unit incident energy of the pellet monotonically decreases with increase in pellet velocity, while crater volume per unit incident momentum increases monotonically. It was therefore concluded that over the velocity range covered (2000 to 5000 m/sec) crater volume varies as some power of velocity between 1 and 2. In this paper evidence is presented which shows that the crater volume-pellet velocity relation for lead bullets fired into sand is consistent with the observations referred to above. Further, an analysis applied to a model based on the assumption of hydrodynamic-like flow behind a shock front is presented and is shown to yield a volume-velocity relation which is in excellent agreement with the observed facts. The results of other observations will also be given, the most significant being those obtained from measurements of bullet deformation.

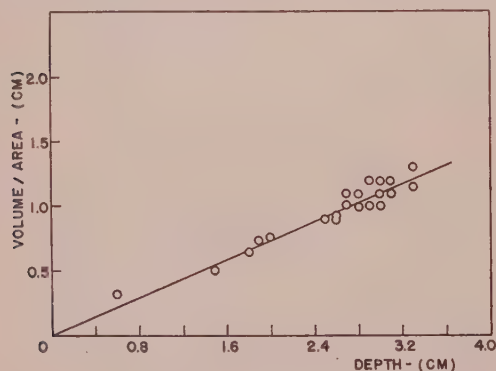


FIG. 1. Crater volume per cross-sectional area at the undisturbed surface level vs crater depth.

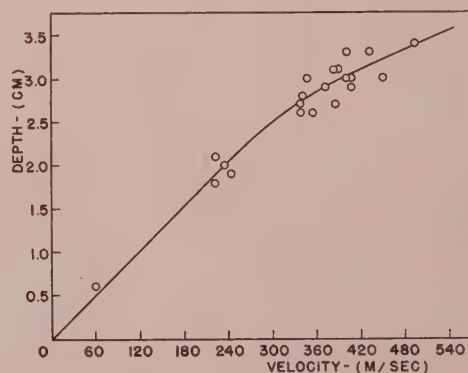


FIG. 2. Crater depth vs pellet velocity.

² M. E. Van Valkenburg, W. G. Clay, and J. H. Huth, *J. Appl. Phys.* **27**, 1123 (1956).

³ F. L. Culp, *Proceedings of Third Hypervelocity Symposium 1958* (unpublished).

¹ W. S. Partridge and W. G. Clay, *J. Appl. Phys.* **29**, 939 (1958).

II. EXPERIMENTAL

A. Experimental Procedure

A 22-caliber rifle was mounted vertically above a $4 \times 4 \times 1$ -ft box filled with dry sand. Between the rifle and the box was mounted a 1-m long tube, on both ends of which aluminum foil strips were placed. These strips served as shorting elements in an electric circuit containing a capacitor which was allowed to discharge when the top strip was severed by a bullet. When the bottom strip was severed the charge remaining on the capacitor was sent through a ballistic galvanometer. In this way the velocity of each bullet used in the experiment was measured. Reduction in bullet velocity was achieved by removing powder from the casing, making it possible to vary the velocity from about 50 m/sec to approximately 550 m/sec. Measurements of crater volume were made by filling the crater with sand to the level of the undisturbed surface and determining the volume required. Measurements were also made of crater depth and crater diameter.

B. Experimental Results

It was observed that a cylindrical-like crater exists during crater formation, but the final shape of the crater is always found to be nearly conical. This is so because the wall of the crater collapses after the bullet comes to rest. That the resultant crater approximates a cone is shown in Fig. 1, where the slope of the straight line obtained by plotting crater volume per unit area of opening at the mouth versus crater depth is seen to be approximately one-third.

The dependence of crater geometry on bullet velocity is illustrated in Figs. 2-4. Figures 2 and 3 show that crater depth and crater diameter both increase more rapidly at low velocities than at high velocities. The explanation for this behavior is, of course, intimately related to the basic mechanism controlling the crater volume, whose dependence on bullet velocity is shown in Fig. 4. A curve which varies directly with the square of the velocity in the low range and linearly with the

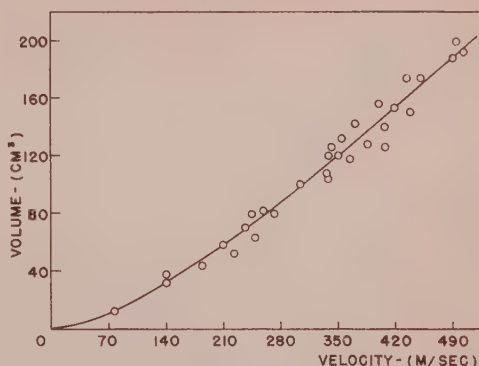


Fig. 4. Crater volume vs pellet velocity.

first power of the velocity in the high range is seen to provide an excellent fit to the data presented. The equation for this curve will be seen to follow from an analysis given in the theory section of this paper.

Finally, the effect of velocity on bullet deformation is shown in Fig. 5, where it is seen that the deformation increases slowly at velocities below 245 m/sec and remains essentially constant at higher velocities. The deformation increases very rapidly at 245 m/sec. It is believed that this velocity corresponds to a penetration rate equal to the velocity of sound in sand under the condition of compaction present during the experiment. A calculation based on a rough determination of the density and bulk modulus of the sand revealed the sound velocity to be approximately 140 m/sec, a velocity about 25% below the calculated penetration rate. The basis for this comparison will be made clear later.

III. THEORY

Proposed Mechanism of Cratering

It is proposed that what happens when a high-speed bullet strikes the sand is the following. The bullet immediately undergoes hydrodynamic-like flow and begins to deform. Simultaneously an anisotropic shock wave is generated which travels radially outward along the surface from the point of impact and also into the

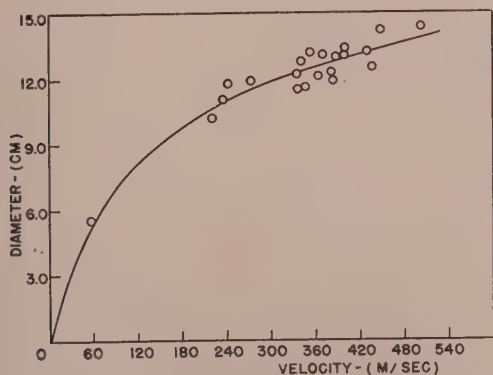


Fig. 3. Crater diameter vs pellet velocity.

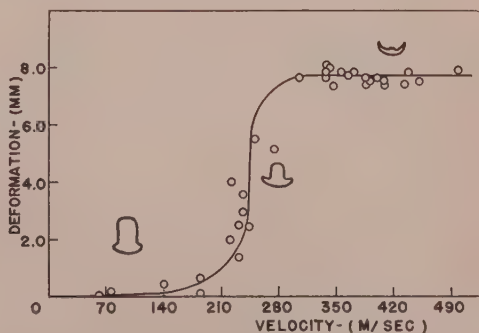


Fig. 5. Pellet deformation vs pellet velocity.

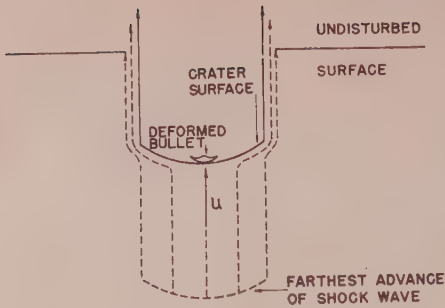


FIG. 6. Formation of the crater as viewed from a reference frame moving with the crater surface.

sand normal to the surface. The radial component of the shock travels very much faster than the normal component although the normal component is by far the more intense. The shock is sustained until the bullet is completely deformed. This is assumed to take place in a time interval which can be considered infinitesimal compared to the total time of crater formation. At the completion of the bullet deformation no more energy is delivered to the shock, and consequently the shock, advancing into the sand with very little radial expansion, dies out. All the sand that was behind the shock front is now in a state of flow. The pattern of this flow at some subsequent time is depicted in Fig. 6. From the description of the way in which this flow pattern was established it is clear that the sand near the crater surface has a greater flow velocity than the sand ahead of it. Consequently, the crater surface overtakes the sand in its path. Considerable compaction of this sand would take place except for the fact that it is able to escape by flowing around the advancing crater surface. Figure 6 views this flow from a frame of reference which moves with the crater surface. The flow is assumed to be both laminar and viscous and as a result must eventually cease. When this happens, a cylindrical-shaped crater momentarily exists. The crater does not continue to exist in this form, however, since the crater collapses under the action of gravity, and a conical shaped crater results. Inasmuch as this collapse leaves the volume unchanged, it plays no role in the determination of the volume-velocity relation. It is to be noted that the role of the bullet in this mechanism is simply to generate the shock wave, after which it becomes part of the mass flow which creates the crater. An analysis based on this mechanism proceeds as follows:

Analysis. The equation of motion for one-dimensional fluid flow may be written

$$\rho du/dt = -(\partial P/\partial x) + \sigma_x, \quad (1)$$

where ρ = the density of the fluid, du/dt = the acceleration of a particle in the fluid at the point (x) , $\partial P/\partial x$ = the conservative component of the pressure gradient, and

σ_x = the nonconservative component of the pressure gradient.

Assuming the density constant, the equation of continuity can be written as

$$Au = dV/dt, \quad (2)$$

where A = the area of a cross section normal to the flow at the point (x) and dV/dt = the volume discharge rate through A , or the rate at which the crater volume increases. In order that Eqs. (1) and (2) be compatible with Fig. 6, u must be interpreted as a mean velocity obtained by averaging over the area A in such a way that the actual volume discharge is properly accounted for. Differentiating Eq. (2),

$$Adu/dt = d^2V/dt^2, \quad (3)$$

Incorporating the cross section A into the Reynolds number and using the expression appropriate for nonturbulent flow for the friction factor, the non-conservative component of the pressure gradient due to viscosity can be written

$$\sigma_x = -8\pi\eta u/A, \quad (4)$$

where η = the viscosity. If it is assumed that P is a linear function of x ,

$$\partial P/\partial x = \text{a constant} = \rho\beta/A. \quad (5)$$

To simplify the impending differential equation governing the rate of formation of the crater, ρ and A were incorporated into the constant. Making use of Eqs. (3) to (5), Eq. (1) becomes

$$\frac{d^2V}{dt^2} + \alpha \frac{dV}{dt} + \beta = 0, \quad (6)$$

where $\alpha = 8\pi\eta/\rho A$. The general solution to Eq. (6) is

$$V = \frac{\beta}{\alpha^2} + \frac{c_1}{\alpha} - \frac{\beta t}{\alpha} + c_2 \exp(-\alpha t), \quad (7)$$

where c_1 and c_2 are constants of integration. If u_0 represents the initial flow velocity, the initial conditions may be expressed as

$$V = 0 \quad \left. \vphantom{\begin{matrix} V \\ dV/dt \end{matrix}} \right\} \text{ at } t = 0. \quad (8a)$$

$$dV/dt = Au_0 \quad \left. \vphantom{\begin{matrix} V \\ dV/dt \end{matrix}} \right\} \text{ at } t = 0. \quad (8b)$$

Imposing these conditions on Eq. (7), the constants c_1 and c_2 are found to be

$$c_1 = Au_0, \quad (9a)$$

$$c_2 = -\left(\frac{Au_0}{\alpha} + \frac{\beta}{\alpha^2}\right). \quad (9b)$$

If V_c represents the final crater volume and τ the time

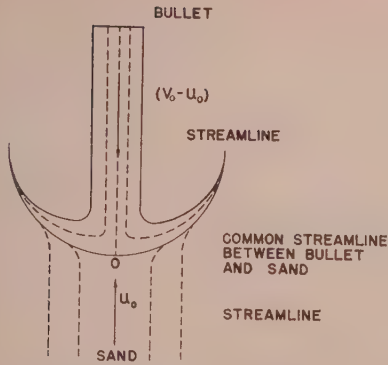


Fig. 7. Pellet deformation as viewed from a frame of reference moving with the common streamline.

for flow to cease, the terminal conditions become

$$V = V_c \quad (10a)$$

$$dV/dt = 0 \quad \text{at } t = \tau. \quad (10b)$$

Imposing these conditions on Eq. (7) and its first derivative yields

$$\alpha\tau = \ln \left[\frac{\alpha A u_0 + \beta}{\beta} \right], \quad (11)$$

$$V_c = \frac{A u_0}{\alpha} - \frac{\beta}{\alpha^2} \ln \left[1 + \frac{\alpha A u_0}{\beta} \right]. \quad (12)$$

To relate u_0 , the initial flow velocity, and v_0 , the velocity of the impacting bullet, the assumption is made that the bullet undergoes streamline hydrodynamic flow during the initial stage of its deformation. Referring to Fig. 7, where the assumed pattern of flow is depicted, and applying Bernoulli's equation for the steady state at the common streamline,

$$\rho' (v_0 - u_0)^2 = \rho u_0^2, \quad (13)$$

where ρ' = the density of the bullet. Solving for u_0 and substituting into Eq. (12),

$$V_c = \frac{A v_0}{\alpha [1 + (\rho/\rho')^{\frac{1}{2}}]} - \frac{\beta}{\alpha^2} \ln \left[1 + \frac{\alpha A v_0}{\beta [1 + (\rho/\rho')^{\frac{1}{2}}]} \right]. \quad (14)$$

Equation (14) gives the desired relation between crater volume and bullet velocity.

When

$$\frac{\alpha A v_0}{\beta [1 + (\rho/\rho')^{\frac{1}{2}}]} \ll 1,$$

which corresponds to low velocity impact, the logarithm can be expanded, and, if only two terms in the expansion are kept,

$$V_c \approx \frac{A^2 v_0^2}{2\beta [1 + (\rho/\rho')^{\frac{1}{2}}]^2}. \quad (15)$$

Thus it is seen that at low velocities the crater volume varies directly with the square of the bullet velocity, in agreement with the finding of most observers.

When

$$\frac{\alpha A v_0}{\beta [1 + (\rho/\rho')^{\frac{1}{2}}]} \gg 1,$$

which corresponds to high velocity impact, Eq. (14) can be simplified to

$$V_c \approx \frac{A v_0}{\alpha [1 + (\rho/\rho')^{\frac{1}{2}}]} - \frac{\beta}{\alpha^2} \ln \left[\frac{\alpha^2}{\beta} \right]. \quad (16)$$

Hence, at high velocities the crater volume approaches a linear dependence on bullet velocity.

If $A/\alpha [1 + (\rho/\rho')^{\frac{1}{2}}]$ is given the value 0.6 and β/α^2 the value 60, Eq. (14) is found to fit the data presented in Fig. 4 quite well. It is to be observed that the data shown in this figure does not extend into the range where complete linearity is predicted, and hence the need for higher velocities is strongly indicated. A program involving higher velocities will be undertaken shortly. Preliminary data, acquired with a specially made 22-caliber rifle and self-loaded bullets of slightly different mass from those used in this experiment, show very close agreement with that predicted by Eq. (14) after correction for the mass difference is made. This correction is made on the assumption that crater volume varies directly with bullet mass, an assumption well verified by previous investigators.⁴ This data was taken at 1250 m/sec, and the agreement between predicted and measured volume was within 5%. Two things of significance were noted at this higher velocity. The bullets were completely pulverized, and the craters tended toward hemispherical shape with no evidence of collapse.

To complete a point referred to earlier in this paper, it should be mentioned that Eq. (13) was used to calculate the initial flow rate u_0 presumed to be identical with the initial penetration rate for a bullet velocity of 245 m/sec. A value of 175 m/sec was obtained for u_0 , using the values 1.5 gm/cm³ and 11 gm/cm³ for ρ and ρ' , respectively. While this value is about 25% higher than the calculated velocity of sound in the sand, it is felt that better definition of the appropriate sonic value would give closer agreement.

CONCLUSION

It is believed that the mechanism of cratering used in this paper in interpreting the crater volume-pellet velocity relation is also involved in cratering in metals at high velocities. If this is true, it would be expected that crater volume would vary linearly with pellet

⁴ R. J. Eichelberger, *Proceedings of First Hypervelocity Symposium 1956* (unpublished).

momentum for sufficiently high pellet velocities, as also proposed by Bjork.⁵ The range of velocities covered in work reported in the literature does not appear to be great enough to test this conclusion. It would also seem that the volume-velocity curve should be continuous through the target sound velocity, in contrast with observations made by Partridge and Clay.¹ These contrary findings, if indeed they are

⁵ R. L. Bjork, *Proceedings of the Tenth International Astronautical Congress 1959* (unpublished).

contrary, may be because these latter investigators attempted a quadratic fit to their data both above and below the target sonic velocity, in which case it is quite understandable that their curves would not join smoothly at this point if the true relation were similar to that found for sand. Finally, it is concluded that whatever significance may be associated with the target sound velocity lies in its connection with the target penetration rate rather than with its relation to the pellet velocity per se.

Radiation from a Modulated Electron Beam with a Plasma Background

PHILIP PARZEN

Republic Aviation Corporation, Farmingdale, New York

(Received June 1, 1961)

Expressions are derived for the electromagnetic radiation of current modulated electron beams which emerge from a plasma. Simple expressions are derived in the case where the dielectric constant of the plasma is zero or infinity.

I. FORMULATION OF THE PROBLEM

WE consider the radiation from a current modulated electron beam with a plasma background (Fig. 1). Using cylindrical coordinates ρ , ϕ , and z , the modulated current density J is assumed to be in the z direction only and

$$J = \phi(\rho)e^{-jhz}e^{j\omega t}; \quad 0 < \rho < a \\ = 0; \quad \rho > a. \quad (1)$$

Also

$$h > k_0; \quad k_0 = \omega(\epsilon_0\mu_0)^{1/2}. \quad (2)$$

Here ω is the applied angular frequency and, ϵ_0 and μ_0 are the dielectric constant and magnetic permeability of free space in the mks system of units. By symmetry considerations, the nonvanishing field components are E_z , E_ρ , and H_ϕ , which are independent of ϕ . The Maxwell's equations in mks units reduce to

$$\nabla^2 E_z + k^2 E_z = (j/\omega\epsilon)(k^2 - h^2)J_z \quad (2)$$

$$j\omega E_z + J_z = (1/\rho)[\partial(\rho H_\phi)/\partial\rho] \quad (3)$$

$$j\omega E_\rho = -(\partial H_\phi/\partial z) \quad (4)$$

$$k^2 = \omega^2\epsilon\mu_0. \quad (5)$$

ϵ is the dielectric constant of the region under consideration. We seek a solution of Eqs. (1)–(4) which behaves in the free space half plane as $(1/r)\exp(-jk_0r)$ for large r (distance from the origin). We give k and h a small negative imaginary part to guarantee the convergence of subsequent mathematical operations. We obtain the solution to our problem by letting the small imaginary part approach zero. We observe that in the

plasma region,

$$\epsilon = \epsilon_0\{1 + \omega_p^2/[j\omega(j\omega + Z)]\} \quad (6)$$

where ω_p = angular plasma frequency and Z = the collisional frequency of the electrons in the plasma.

II. TRANSFORMED MAXWELL'S EQUATIONS

We solve Eqs. (2)–(4) with the boundary conditions of outgoing waves with the aid of Hankel-Fourier sine or cosine transforms with respect to ρ and z , respectively.¹ We define the following transforms

$$J_z = - \int_0^\infty \int_0^\infty \tilde{j}(q, p) q J_0(q\rho) \sin pzdqdp \quad (7)$$

$$E_z = - \int_0^\infty \int_0^\infty \tilde{e}_z(q, p) q J_0(q\rho) \sin pzdqdp \quad (8)$$

$$H_\phi = - \int_0^\infty \int_0^\infty \tilde{h}(q, p) q J_1(q\rho) \sin pzdqdp \quad (9)$$

$$E_\rho = - \int_0^\infty \int_0^\infty \tilde{e}_\rho(q, p) q J_1(q\rho) \cos pzdqdp. \quad (10)$$

The use of the corresponding lower case letter and the bar denote the Hankel [J_0 or J_1] and Fourier [sine or cosine] transforms, respectively. J_0 and J_1 are the Bessel functions of zeroth and first order, respectively.

¹ C. J. Tranter, *Integral Transforms in Mathematical Physics* (John Wiley & Sons, Inc., New York, 1951).

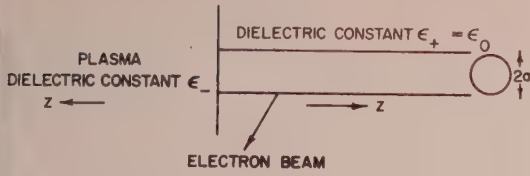


FIG. 1. Modulated electron beam.

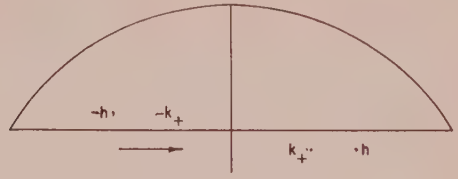


FIG. 2. Path of integration.

Also

$$\bar{J}_z(p) = \phi(p) [p / (p^2 - h^2)] \quad (11)$$

$$\bar{J}_z(q, p) = \psi(q) p / p^2 - h^2 \quad (12)$$

$$\psi(q) = \int_0^\infty \phi(\rho) \rho J_0(q\rho) d\rho. \quad (13)$$

The transformed equations are

$$(k^2 - p^2 - q^2) \bar{e}_z = -pL(q) + \frac{j}{\omega\epsilon} (k^2 - h^2) \frac{p}{p^2 - h^2} \psi(q) \quad (2a)$$

$$L(q) = e_z \text{ at } z=0$$

$$j\omega\epsilon\bar{e}_z + \bar{J}_z = q\bar{h}_\phi \quad (3a)$$

$$j\omega\epsilon\bar{e}_\rho = -p\bar{h}_\phi. \quad (4a)$$

Solving these equations, we obtain

$$\bar{e}_z = \frac{P}{k^2 - p^2 - q^2}, \quad (15)$$

$$P = -pL + (j/\omega\epsilon) [(k^2 - h^2)/(p^2 - h^2)] p\psi, \quad (15)$$

$$\bar{h}_\phi = (1/q) [j\omega\epsilon P / (k^2 - p^2 - q^2) + \psi p / (p^2 - h^2)], \quad (16)$$

$$\bar{e}_\rho = -(1/j\omega\epsilon q) \times [j\omega\epsilon p P / (k^2 - p^2 - q^2) + \psi p^2 / (p^2 - h^2)]. \quad (17)$$

$$h_\phi = \frac{1}{q} \left[j\omega\epsilon L + \frac{k^2 - h^2}{k^2 - q^2 - h^2} \psi \right] \exp[-j(k^2 - q^2)^{1/2} z] - \frac{\psi}{q} \frac{q^2}{k^2 - h^2 - q^2} \exp(-jhz), \quad (21)$$

$$e_\rho = -\frac{1}{j\omega\epsilon q} \left[-j\omega\epsilon (k^2 - q^2)^{1/2} L - \frac{(k^2 - h^2)(k^2 - q^2)^{1/2}}{k^2 - q^2 - h^2} \psi \right] \exp[-j(k^2 - q^2)^{1/2} z] - \frac{1}{j\omega\epsilon q} \frac{q^2 h}{k^2 - h^2 - q^2} \psi \exp(-jhz). \quad (22)$$

Matching h_ϕ and e_ρ at $z=0$, we obtain

$$j\omega\epsilon_+ L_+ + j\omega\epsilon_- L_- = -\psi \quad (23)$$

$$(k_+^2 - q^2)^{1/2} L_+ - (k_-^2 - q^2)^{1/2} L_- = -\psi \frac{(k_+^2 - q^2)^{1/2}}{j\omega\epsilon_+} \left[\frac{k_+^2 - h^2}{k_+^2 - q^2 - h^2} - \frac{q^2 h}{(k_+^2 - q^2 - h^2)(k_+^2 - q^2)^{1/2}} \right]. \quad (24)$$

Solving these equations,

$$L_+ = \frac{\psi \left[- (k_-^2 - q^2)^{1/2} - \frac{\epsilon_-}{\epsilon_+} (k_+^2 - q^2)^{1/2} \left(\frac{k_+^2 - h^2}{k_+^2 - q^2 - h^2} - \frac{q^2 h}{(k_+^2 - q^2 - h^2)(k_+^2 - q^2)^{1/2}} \right) \right]}{j\omega\epsilon_- (k_+^2 - q^2)^{1/2} + j\omega\epsilon_+ (k_-^2 - q^2)^{1/2}}. \quad (25)$$

To match the tangential fields in the plasma and free-space regions at their interface $z=0$, we write corresponding expressions for the fields in their respective regions with the provisions that the positive z directions are oppositely directed. We will denote, when necessary, corresponding parameters in the plasma and free-space regions with the subscripts $-$ and $+$, respectively. L_+ and L_- in Eq. (15) are determined by matching e_ρ and h_ϕ . Now h_ϕ is given by

$$h_\phi = - \int_0^\infty \frac{2}{\pi} \bar{h}_\phi \sin pz d p \quad (18)$$

which equals

$$\frac{1}{j\pi} \int_{-\infty}^\infty \bar{h}_\phi \exp(jpz) dp, \quad (19)$$

since \bar{h}_ϕ is an odd function of p . The path of integration in the p plane is shown in Fig. 2. The integrand in Eq. (16) has simple poles at $p = \pm (k^2 - q^2)^{1/2}$ and $\pm h$. Completing the path with the semicircle at infinity, only those poles whose imaginary part is greater than zero will contribute. These are

$$p_1 = -(k^2 - q^2)^{1/2}; \quad \text{Im}(p_1) > 0 \quad (20)$$

$$p_2 = -h.$$

Hence,

III. COMPUTATION OF THE RADIATION FIELDS

We now have to invert the transforms. However, since we desire only the radiation fields, the inverses at large ρ suffice. Now,

$$\bar{H}_{\phi+} = \int_0^{\infty} \bar{h}_{\phi+} q J_1(q\rho) dq. \quad (26)$$

Hence,

$$\begin{aligned} \frac{1}{\rho} \frac{\partial}{\partial \rho} \left(\rho \frac{\partial \bar{H}_{\phi+}}{\partial \rho} \right) + \left(k_+^2 - p^2 - \frac{1}{\rho^2} \right) \bar{H}_{\phi+} \\ = \int_0^{\infty} (k_+^2 - p^2 - q^2) \bar{h}_{\phi+} q J_1(q\rho) dq = T(\rho). \end{aligned} \quad (27)$$

The asymptotic solution $H_{\phi+}'$ for large ρ is

$$\begin{aligned} \bar{H}_{\phi+}' = \left(\frac{\pi}{2} \right)^{\frac{1}{2}} j \exp \left(j \frac{3\pi}{4} \right) \\ \times \exp \left[\frac{-j\gamma_+ \rho}{(\gamma_+ \rho)^{\frac{1}{2}}} \right] \int_0^{\infty} T(\rho') \rho' J_1(\gamma_+ \rho') d\rho' \end{aligned} \quad (28)$$

$$\gamma_+ = (k_+^2 - p^2)^{\frac{1}{2}}; \quad \text{Im}(\gamma_+) < 0. \quad (29)$$

Now, using the fact that

$$\delta(q - \gamma_+) = \int_0^{\infty} q \rho' J_1(q\rho') J_1(\gamma_+ \rho') d\rho', \quad (30)$$

we have

$$\bar{H}_{\phi+}' = \left(\frac{\pi}{2} \right)^{\frac{1}{2}} \frac{\omega \epsilon_+}{\gamma_+} \exp(j3\pi/4) \frac{\exp(-j\gamma_+ \rho)}{(\gamma_+ \rho)^{\frac{1}{2}}} P(\gamma_+); \quad (31)$$

$$\begin{aligned} H_{\phi+}' = \frac{\omega \epsilon_+}{2j\gamma_+} \exp(j3\pi/4) \left(\frac{2}{-} \right)^{\frac{1}{2}} \\ \times \int_{-\infty}^{\infty} \exp[j(pz - \gamma_+ \rho)] \frac{P_+(\gamma_+)}{(\gamma_+ \rho)^{\frac{1}{2}}} d\dot{p}, \end{aligned} \quad (32)$$

since \bar{H}_{ϕ} is an odd function of \dot{p} . Also, here we let the imaginary part of k_+ approach zero. Thus,

$$\begin{aligned} \gamma_+ = (k_+^2 - p^2)^{\frac{1}{2}} \quad \text{Re}(\gamma_+) \text{ is positive for } |p| < k_+ \\ \text{Im}(\gamma_+) \text{ is negative for } |p| > k_+. \end{aligned} \quad (33)$$

The path of integration is shown in Fig. 3.

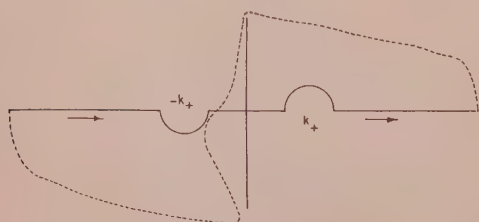


FIG. 3. Path of integration.

It is fairly simple to show that the integrals around the small semicircles of radius δ vanish as $\delta^{\frac{1}{2}}$. We evaluate the integral in Eq. (32) by the method of steepest descent.² Introducing spherical coordinates r, θ, ϕ such that

$$\begin{aligned} z = r \cos \theta \\ \rho = r \sin \theta \end{aligned} \quad \left. \begin{aligned} 0 < \theta < \frac{\pi}{2} \end{aligned} \right\} \quad (34)$$

$$\begin{aligned} H_{\phi+}' = \frac{\omega \epsilon_+}{2j} \left(\frac{2}{\pi} \right)^{\frac{1}{2}} \int \exp[jr(p \cos \theta - \gamma_+ \sin \theta)] \\ \times \frac{P_+(\gamma_+)}{(\gamma_+ \rho)^{\frac{1}{2}}} \frac{1}{\gamma_+} d\dot{p}. \end{aligned} \quad (35)$$

Let

$$f(p) = j(p \cos \theta - (k_+^2 - p^2)^{\frac{1}{2}} \sin \theta); \quad (36a)$$

then

$$f'(p) = j \left(\cos \theta + \frac{p}{(k_+^2 - p^2)^{\frac{1}{2}}} \sin \theta \right), \quad (36b)$$

$$f''(p) = j \left[\frac{1}{(k_+^2 - p^2)^{\frac{1}{2}}} + \frac{p^2}{(k_+^2 - p^2)^{\frac{3}{2}}} \right] \sin \theta. \quad (36c)$$

The saddle point

$$p = p_s = -k_+ \cos \theta \quad (37)$$

and

$$f(p) = -jk_+ + (j/k_+ \sin^2 \theta) [(p - p_s)^2/2] + \dots \quad (38)$$

The steepest descent curve, which is given by

$$\text{Im}[j(p \cos \theta - (k_+^2 - p^2)^{\frac{1}{2}} \sin \theta)] = -k_+, \quad (39)$$

reduces in the neighborhood of the point p_s to the straight line,

$$p - p_s = R e^{j\pi/4} \quad (40)$$

and

$$\text{Re} f(p) = -(R^2/2)(1/k_+ \sin^2 \theta). \quad (41)$$

The asymptotic behavior of the steepest descent curve is obtained by placing p equal to $R e^{j\pi/4}$ in Eq. (34), and solving for p in the case of large R , we get

$$\cos(x - \theta) = -(k_+/R)$$

or

$$x - \theta \sim \frac{1}{2}\pi + \delta \quad (\text{small}). \quad (42)$$

The deformed path of integration is shown in Fig. 3 for $\theta=0$, by the dashed line and circular arcs at infinity over which the integral vanishes. Hence, utilizing the steepest descent formula,

$$H_{\phi+}' = \frac{\omega \epsilon_+ \exp(-jk_+ r)}{j} \frac{P_+(k_+ \sin \theta)}{r k_+ \sin^2 \theta} \sin \theta, \quad (43)$$

which represents a spherical outgoing wave. The power

² V. M. Papadopoulos, Quart. Appl. Math. XVII, 423 (1960).

flow $S(\theta, \phi)$ per unit solid angle is³

$$S(\theta, \phi) = \frac{120\pi}{2} (\omega\epsilon_+)^2 \frac{|P_+(k_+ \sin\theta)|^2}{k_+^2 \sin^4\theta} \sin^2\theta \quad (44)$$

$$P_+ = \frac{\psi(q_s)}{j\omega\epsilon_+} \left[\frac{(k_-^2 - q_s^2)^{\frac{1}{2}}}{Q} + \frac{\epsilon_-}{\epsilon_+} \left(\frac{k_+^2 - h^2}{k_+^2 - q_s^2 - h^2} - \frac{q_s^2 h}{(k_+^2 - q_s^2 - h^2)(k_+^2 - q_s^2)^{\frac{1}{2}}} \right) \times \frac{(k_+^2 - q_s^2)^{\frac{1}{2}}}{Q} - \frac{k_+^2 - h^2}{p_s^2 - h^2} \right] p_s, \quad (45)$$

where

$$\begin{aligned} p_s &= -k_+ \cos\theta \\ q_s &= k_+ \sin\theta \\ Q &= (\epsilon_-/\epsilon_+)(k_+^2 - q_s^2)^{\frac{1}{2}} + (k_-^2 - q_s^2)^{\frac{1}{2}} \end{aligned} \quad (46)$$

This formula simplifies considerably in the case $|\epsilon_-| = 0$ or ∞ . We discuss these cases now

$|\epsilon_-| = 0$:

$$S = \frac{120\pi}{2} k_+^4 \frac{\cos^2\theta \sin^2\theta}{(k_+^2 \cos^2\theta - h^2)^2} \times \left| \int_0^a \phi \rho J_0(k_+ \sin\theta \rho) d\rho \right|^2; \quad (47)$$

$$L_- = \frac{\psi \left\{ - (k_+^2 - q_s^2)^{\frac{1}{2}} + (k_+^2 - q_s^2)^{\frac{1}{2}} \left[\frac{(k_+^2 - h^2)}{(k_+^2 - q_s^2 - h^2)} - \frac{q_s^2 h}{(k_+^2 - q_s^2 - h^2)(k_+^2 - q_s^2)^{\frac{1}{2}}} \right] \right\}}{[(k_+^2 - q_s^2)^{\frac{1}{2}} j\omega\epsilon_- + j\omega\epsilon_+(k_-^2 - q_s^2)^{\frac{1}{2}}]}. \quad (52)$$

Hence the power flow per unit solid angle $S(\theta, \phi)$ is

$$S(\theta, \phi) = \frac{120\pi}{2} (\omega\epsilon_+)^2 \frac{P_\infty}{k_+^2 \sin^4\theta} \sin^2\theta, \quad (53)$$

where $P_\infty = P_+ + Q_+$. P is given by Eq. (45).

$$Q_+ = \frac{\left[\frac{\psi(q_s)}{j\omega\epsilon_+} \right] p_s (k_-^2 - q_s^2)^{\frac{1}{2}} \left[-1 + \frac{(k_-^2 - h^2)}{(k_-^2 - q_s^2 - h^2)} + \frac{q_s^2 h}{(k_-^2 - q_s^2 - h^2)(k_-^2 - q_s^2)^{\frac{1}{2}}} \right]}{(\epsilon_-/\epsilon_+)(k_+^2 - q_s^2)^{\frac{1}{2}} + (k_-^2 - q_s^2)^{\frac{1}{2}}}. \quad (54)$$

It is noted that ψ , k_+ , and h have been replaced by $-\psi$, k_- , and $-h$ in Eq. (52). P_∞ is zero in the case $\epsilon_+ = \epsilon_-$, which is to be expected since an infinite electron beam

³ The contribution due to the pole at $p = k_+[\epsilon_+/(\epsilon_- + \epsilon_+)]^{\frac{1}{2}}$ vanishes since ϵ_- is complex.

$|\epsilon_-| = \infty$:

$$S(\theta, \phi) = \frac{120\pi}{2} \frac{\beta^2 \sin^2\theta}{(\beta^2 \cos^2\theta - 1)^2} \times \left| \int_0^a \phi \rho J_0(k_+ \sin\theta \rho) d\rho \right|^2, \quad (48)$$

$$\beta = k_+/h,$$

which agrees with others.⁴ In the case of $k_+ a \ll 1$,

$$S(\theta, \phi) = \frac{120\pi}{2} \frac{\beta^2 \sin^2\theta}{(\beta^2 \cos^2\theta - 1)^2} \frac{|I|^2}{4\pi^2}, \quad (49)$$

where I = total modulated current. The radiation resistance

$$R = (120\pi) \frac{2\pi}{4\pi^2} \beta^2 \int_0^{\pi/2} \frac{\sin^3\theta d\theta}{(\beta^2 \cos^2\theta - 1)^2}, \quad (50)$$

which in the case of small β reduces to

$$R = 40\beta^2 \text{ ohms}. \quad (51)$$

IV. INFINITE ELECTRON BEAM

Previously we have discussed the case of a semi-infinite electron beam in the free space region only. We discuss now the case of an infinite electron beam which permeates both media with the current density varying as $\exp(-jkz)$. This case is treated as a superposition of two semi-infinite electron beams in their respective media. Now it follows from Eq. (24) that

does not radiate. The case where the current density is an arbitrary function of z may be handled similarly.

⁴ Yu. N. Dnestrovskii and D. P. Kostomarov, Soviet Phys.—Doklady 4, 132 (1959).

Letters to the Editor

Damping Effects of Thin Surface Films*

R. J. HUBER, G. S. BAKER, AND P. GIBBS

University of Utah, Salt Lake City, Utah

(Received May 8, 1961)

THE temperature dependence of the viscoelastic properties of thin films may be conveniently studied by use of the piezoelectrically driven composite oscillator. The method is based on the fact that the internal friction of undeformed aluminum oxide single crystals is less than 10^{-6} at 50 kc, at all temperatures between room temperature and 1400°C .¹ If a thin film of some material is coated on an aluminum oxide sample and the damping is observed in the usual manner for studying high-temperature internal friction by the composite oscillator method,^{1,2} the observed damping changes are due to the surface film.

During a study of internal friction of Al_2O_3 single crystals it was observed that approximately 4 mg of NaNO_3 , which formed a layer of material about 2.5μ thick on the surface of the crystal, caused a damping peak, maximum log decrement 5×10^{-6} centered on the melting temperature of the salt. (See Fig. 1.) The damping was attributed to a second phase layer, a viscous fluid, on the Al_2O_3 crystal surface. The decrease in damping at temperatures above the peak temperature was due to decreased viscosity and evaporation of the layer.

As an approach to this problem consider an infinite plane layer of solid material forced to vibrate in a viscous fluid. The motion of the viscous fluid is described by the boundary value problem for the velocity v of the fluid

$$\partial v(x,t)/\partial t = c \partial^2 v(x,t)/\partial x^2 \quad (1)$$

$$v(0,t) = v_0 \exp(i\omega t) \quad (2)$$

$$v(x,t) \rightarrow 0 \quad \text{as} \quad x \rightarrow \infty. \quad (3)$$

In these equations $x=0$ is the plane of the solid-liquid interface and the viscous liquid extends to $x=+\infty$. Here $c=\eta/\rho$, where η is the viscosity in poises, and ρ is the fluid density. The solution of this problem is

$$v(x,t) = v_0 \cos(\omega t - \alpha x) \exp(-\alpha x) \quad (4)$$

$$\alpha = (\omega/2c)^{1/2}. \quad (5)$$

Substitution of the room temperature values of constants for water gives $\alpha = 4 \times 10^{13} \text{ cm}^{-1}$. The corresponding attenuation length of the shear wave is $2.5 \times 10^{-4} \text{ cm}$. This value is very small compared to the thickness of the crystals. Therefore, this boundary value problem describes approximately the physical situation of the thin film on the vibrating solid.

The power flowing into the liquid per unit area p at the solid-liquid interface is given by

$$p = v(0,t) \eta (\partial v / \partial x) |_{x=0}. \quad (6)$$

The surface velocity of a cylindrical rod vibrating in longitudinal resonance is

$$v(0,t) = A_m \cos(2\pi y/L) \sin \omega t, \quad (7)$$

where A_m is the maximum amplitude of the standing vibrations, and L is the wavelength. By integrating p over the surface of the rod and over one cycle of vibration, one gets for the energy transfer from the rod to the viscous fluid per cycle

$$\Delta w = (\frac{1}{2} \pi^2 r L) \eta A_m^2 \omega \alpha, \quad (8)$$

where r is radius of the rod. The maximum elastic energy w , stored in a rod of length $L/2$ vibrating in its fundamental longitudinal mode, is

$$w = \pi^2 A_m^2 f^2 m, \quad (9)$$

where f is the frequency of vibration and m the mass of the rod. The log decrement is equal to the ratio of the energy lost per cycle

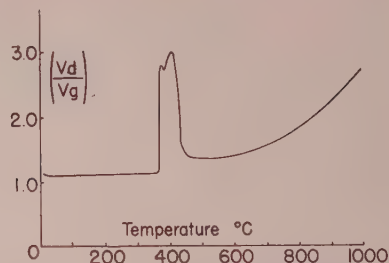


FIG. 1. Log decrement vs temperatures for Al_2O_3 with NaNO_3 surface contamination.

to twice the maximum elastic energy. Thus

$$\delta = \Delta w / 2w = \pi r L \eta \alpha / (2 f m). \quad (10)$$

By substituting the definition of α , this may be written to show the dependence of δ upon η and f .

$$\delta = \rho^{1/2} / (2 \pi^2 r L / m) \eta^{1/2} \omega. \quad (11)$$

Substitution of the values of the constants appropriate to a layer of water on the vibrating crystal gives $\delta = 6.4 \times 10^{-4}$ when $r = 0.127 \text{ cm}$, $L = 8 \text{ cm}$, $\eta = 10^{-2} \text{ g cm}^{-1} \text{ sec}^{-1}$, $\alpha = 4 \times 10^{13} \text{ cm}^{-1}$, $f = 5 \times 10^4 \text{ sec}^{-1}$, and $m = 2 \text{ g}$. This calculated log decrement is of the same order of magnitude as the losses caused by moistening the surface of the sample.

* This work was sponsored by the Office of Naval Research.
¹ R. J. Huber, G. S. Baker, and P. Gibbs, Technical Report No. XIV, University of Utah, Salt Lake City, Utah (1960).
² J. Marx and J. Sivertsen, J. Appl. Phys. **24**, 81-87 (1953).

Electrical Control of the Critical Angle of Total Reflection

H. NASSENSTEIN

Department of Applied Physics, Farbenfabriken Bayer AG, Leverkusen, Germany

(Received June 5, 1961)

THE critical angle of total reflection at the boundary between two media (refractive indices n_1 and n_2 , respectively) merely depends upon the ratio n_1/n_2 . If it is intended to change the critical angle by some degrees by electrical means (current, voltage), an electro-optical effect is required which allows changes of the refractive index of the order 0.01 to 0.1. This has hitherto not been possible for visible light; the most important electro-optical effect, the Kerr effect, allows maximum changes of the refractive index of the order 0.001 in the visible region. A new electro-optical method¹ allowing changes of the refractive index 10 to 100 times greater than the Kerr effect, provides the possibility of obtaining such changes of the critical angle of total reflection as it is shown in the following experiment.

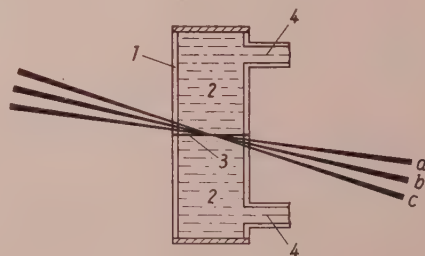


FIG. 1. Scheme of the experimental arrangement. (1) glass cuvette, (2) solution, (3) membrane, (4) connecting tubes to the electrodes a, b, c: light beams. The refraction of the light beams by the walls of the cuvette is not shown.

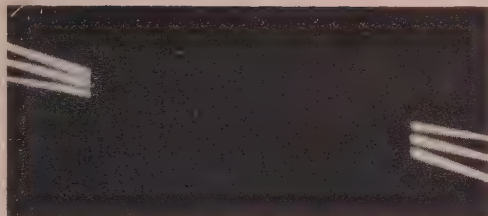


FIG. 2. Control of the critical angle by the electric current initial state.



FIG. 3. Control of the critical angle by the electric current. Total reflection of the beam a.

A glass cuvette 1 (see Fig. 1) is filled with an aqueous solution 2. This solution contains a high concentration of electrically charged particles (micelles and ions); the refractive index of the solution amounts to 1.407. The glass cuvette is divided into two sections by a cellophane membrane 3 which is impermeable to the micelles. In the upper and lower sections of the cuvette are two connecting tubes to the electrodes 4. Three light beams a, b, and c coming from the right below pass through the membrane at different angles of incidence. Since the refractive indices of the membrane and the solution are nearly equal, the light beams pass through the membrane without appreciable refraction and reflection losses and leave the cuvette on the left side of the upper section. In the experiment the light beams are optically indicated by a grazing incidence on two white screens on the left and right sides of the cuvette, as shown in Fig. 2. When electrical current is passed through the cell, a depletion layer with a lower refractive index is formed on one side of the membrane and an enrichment layer with a higher refractive index on the other side. These changes of the refractive index amount to a high value and are concentrated to a very thin layer ($1\text{--}100\ \mu$), just as it is desired for the total reflection because of the small penetration depth of the light into the optically thinner medium. Figures 3, 4, and 5 show the changes of



FIG. 4. Control of the critical angle by the electric current. Total reflection of the beams a and b.



FIG. 5. Control of the critical angle by the electric current. Total reflection of the beams a, b, and c.

the critical angle of total reflection on the passage of electrical current. First the light beam a, then beam b, and finally beam c are totally reflected. The maximum reduction of the refractive index which is obtainable with the solution used amounts to 0.07, corresponding to a critical angle of total reflection of about 72° . With other solutions refractive index changes >0.1 have been obtained. The total intensity of light reflected by the membrane can also be measured by means of a photoelectrical cell and an oscillograph. Figure 6 illustrates by way of example such an oscillogram. In the upper part of the oscillogram is shown the current density, and in the lower part the reflected light intensity as a function of time. Details and further results of this method are reported elsewhere.²

The electrical control of the reflection coefficient of a boundary offers interesting possibilities for applications in practice. If the current density distribution at the boundary is controlled via the conductivity changes of a photoconductive layer by electromagnetic (visible, ultraviolet light, x rays, γ rays) or corpuscular radiation (electrons, ions, nuclear radiation), there is obtained a

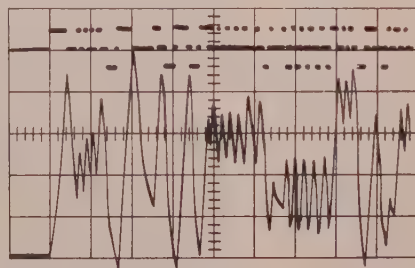


FIG. 6. Oscillogram of the current density and the reflected light intensity. Angle of incidence: $78\text{--}79^\circ$; current density: 5 ma/cm^2 ; time scale: 1 sec per scale division.

new type of image converter and image intensifier, the boundary layer image converter and intensifier, respectively. Its principal advantage resides in the fact that the light source, the light flux of which is controlled by the refractive index distribution at the boundary, may be chosen arbitrarily in respect of intensity and spectral distribution so that a projection of the image is also possible. Laboratory models of such a boundary layer light amplifier have been built and are now being tested.

¹ H. Nassenstein, *Naturwissenschaften* **48**, 214 (1961).

² H. Nassenstein, *Z. angew. Phys.* (to be published).

Preparation of Silicon Ribbons

E. S. GREINER, J. A. GUTOWSKI, AND W. C. ELLIS

Bell Telephone Laboratories, Incorporated, Murray Hill, New Jersey
(Received June 26, 1961)

SILICON ribbons have been made by reacting silicon pellets with iodine and hydrogen in a closed tube in a temperature gradient. Arsenic-doped silicon pellets with resistivities from 0.001 to 0.005 ohm-cm have produced ribbons. Source silicon of 0.002 ohm-cm resistivity has given optimum yields. The arsenic content of this source material is estimated to be 4×10^{19} atoms/cc.

For the preparation of ribbons, reagent grade iodine and purified hydrogen were introduced into a quartz tube with silicon pellets ($\frac{1}{8}$ -in. cubes) to give partial pressures at 950°C of 2.3 atmospheres of I_2 and from 0.5 to 1.1 atm of H_2 . The occurrence of ribbons is related also to small amounts of impurities in the iodine. As an example, when nickel in amounts of 0.01 or 0.02% of the iodine was added as NiI_2 ribbon formation was greatly enhanced. The quartz tube after sealing was approximately 10 in. long and 0.8 in. in diameter. The tube with the silicon at one end was placed in an electric resistance furnace constructed to permit independent temperature control of each half of the cylindrical

core. The closed quartz tube was located so that the silicon pellets at one end were at 1100°C and the other end of the tube was at 800°C. The temperature gradient over the length of the tube, with the exception of about two inches where the silicon pellets were located, was about 40°C/in. In most experiments the time of heating was three hours, but ribbons have been produced in as short a time as ten minutes. In all but a few experiments, the furnace tube was inclined about 1.8 in./ft with the silicon source at the lowest point. It is not believed, however, that the inclination of the tube is a necessary condition for ribbon production.

Silicon ribbons and, to a variable extent, needle-like crystals having a hexagonal cross section were formed in a loose mass (Fig. 1) in the tube where the temperature was approximately 950°C. Individual ribbons were uniform in thickness except for local overgrowths in some cases. A considerable range of thicknesses from about 0.1 to 15 μ was found. Some ribbons were as long as 20 mm and widths of as much as 0.15 mm were observed. The thinner ribbons, some of which are shown in Fig. 2, are semi-transparent. Where ribbons cross each other or a ribbon crosses a supporting copper wire, the underneath ribbon or the copper wire is dimly visible. With about 4×10^{19} atoms/cc of arsenic in the source silicon, an approximately one-to-one transfer of arsenic to the silicon ribbon was found in a few instances.¹

The morphology and structure of silicon ribbons are discussed by R. S. Wagner and R. G. Treuting² in this Journal. Briefly, they determined the silicon ribbons to be twinned crystals with {111} faces and a $\langle 112 \rangle$ long axis.

The chemical reactions, nucleation, and growth mechanisms in ribbon production are not clear. Some facts are known. When the source silicon was heated for three hours at 1000°C, transfer was not observed. An initial hydrogen atmosphere was necessary for ribbon production, but not for the transfer of silicon and its deposition as a film on the tube walls. In the absence of hydrogen the film formed at the lowest temperature in the tube, 800°C. When ribbons formed they grew in the region of the tube at about 950°C and only when arsenic was present in the source material.

The transfer process in the absence of hydrogen has been discussed by Schäfer and Morcher³ and later by Wajda, Kippenhan, and White⁴ and is considered essentially a disproportionation reaction: $2\text{SiI}_2 \rightleftharpoons \text{Si} + \text{SiI}_4$. When hydrogen is present the reaction may involve SiH_4 . A residual nearly white solid freezes in the tube on cooling. The melting temperature of this solid of between 122° and 128°C, depending on the details of the experiment, suggests that SiI_4 is involved in the reaction.

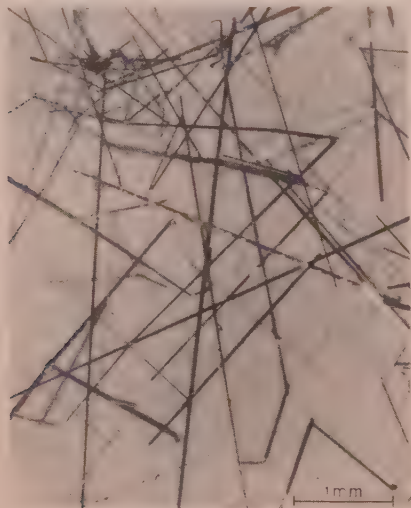


Fig. 1. Mass of silicon ribbons and whiskers after removal from reaction tube.

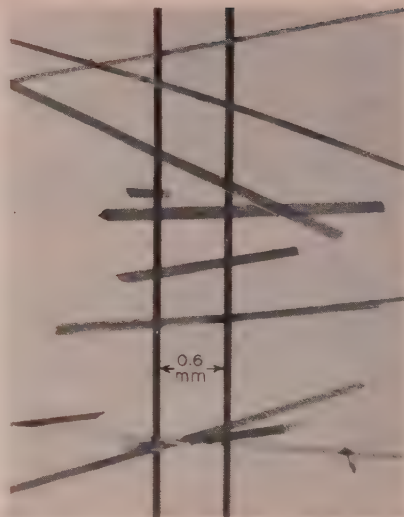


Fig. 2. Individual silicon ribbons supported on two parallel copper wires 75 microns in diameter and spaced 0.6 mm apart.

The authors are pleased to thank H. C. Theuerer and C. D. Thurmond for helpful discussions in the course of this investigation, and S. M. Arnold for the photographs.

¹ R. A. Logan (private communication).

² R. S. Wagner and R. G. Treuting, *J. Appl. Phys.* **32**, 2490 (1961).

³ H. Schäfer and B. Morcher, *Z. anorg. allgem. Chem.* **290**, 279 (1957).

⁴ E. S. Wajda, B. W. Kippenhan, and W. H. White, *I.B.M. J. Research Develop.* **4**, 288 (1960).

Morphology and Growth Mechanism of Silicon Ribbons

R. S. WAGNER and R. G. TREUTING

Bell Telephone Laboratories, Incorporated, Murray Hill, New Jersey
(Received June 26, 1961)

IN a concurrent paper¹ E. S. Greiner *et al.* describe the growth of silicon crystals of two distinct forms: acicular and ribbon-like. The acicular form is that of a whisker of hexagonal cross section and has a $\langle 111 \rangle$ growth direction as previously reported by Treuting and Arnold.² The present paper reports on the morphology and suggests a growth mechanism for the ribbon form.

A typical ribbon is shown in Fig. 1 taken by transmitted visible light. The ribbons are characteristically of uniform width (30 to 150 μ), varying length (1 to 20 mm), and of thickness 0.1 to 15 μ which varies stepwise along the ribbon length. The width is more or less controlled by the size of the nucleus from which the ribbon originates. The steps of different height revealed in Fig. 1 show a symmetry related to the crystallography. The threefold symmetry of the step boundaries indicates that the ribbon plane is {111}. The ribbons were found to cleave normal to the growth (axial) direction. Since silicon cleaves along {111}, this establishes the normal to the growth direction as $\langle 110 \rangle$ and the axis accordingly $\langle 112 \rangle$.

These observations were confirmed by x-ray diffraction photographs taken in oscillation about the ribbon axis giving the growth direction, and by Weissenberg photographs which, in conjunction with microscopic observations, gave the ribbon faces.

During cleavage experiments it was found that the cleaved surface was not a planar {111} face but consisted of two {111} faces in twin relationship, with the coherent twin plane parallel to the surface of the ribbon. This was observed in all of about 25 cleaved specimens, and the twin relationship was confirmed by upper-level normal inclination Weissenberg photographs. In Fig. 2 the growth axis of a ribbon is normal to the plane of the photo-

FIG. 1. Silicon ribbon face photographed by transmitted visible light.

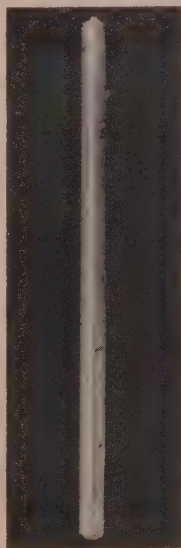


graph, and the unusual cleavage surfaces are shown. The crystallography of the cleavage surfaces with regard to the ribbon geometry is shown in Fig. 3. The coherent twin plane is shown by the central line of intersection. Symmetry considerations would require that the number of such coherent twin planes be odd; in each of the specimens studied only one was found (within the resolving power of an optical microscope).

The angle between the side faces bounding the ribbon has been measured on the optical goniometer as very close to 117° . The angle between $\{113\}$ planes in the $\langle 112 \rangle$ zone is 117.04° .

The importance of the role which coherent twin planes play in the dendritic growth process of germanium and silicon from supercooled melts has been reported previously.³⁻⁵ There are, however, striking differences between Si dendrites and Si ribbons with regard to their morphology. First, Si ribbons grown from the vapor phase exhibit on their surface stable crystallographic planes other than $\{111\}$. Most important are the $\{311\}$ side faces of the

FIG. 2. Cleavage surfaces of a silicon ribbon viewed along growth direction.



ribbons. Second, Si ribbons do not appear to branch in a direction coplanar to the twin plane.

It has been shown³⁻⁵ that a coherent $\{111\}$ twin plane creates favorable nucleation sites at the growth interface along $[10\bar{1}]$, $[\bar{1}10]$, and $[0\bar{1}1]$ crystallographic directions. According to this theory, atoms arriving from the vapor phase can be readily accommodated at the nucleation sites, which will result in a rapid net growth in the $[\bar{1}12]$, $[2\bar{1}\bar{1}]$, and $[\bar{1}2\bar{1}]$ directions. As shown in Fig. 3, the stable $\{311\}$ faces on the sides of a growing ribbon form a ridge configuration, which is unfavorable for nucleation and, therefore, constrains growth to one of the three possible $\langle 112 \rangle$ directions and also prevents the formation of side branches. The twin plane growth mechanism accounts for continuous growth in length; however, these ribbons also grow in thickness, presumably by surface and imperfection nucleation. The occasional occurrence of growth hillocks on the principal ribbon faces (Fig. 1) is evidence for imperfection nucleation.

Nucleation of the silicon ribbons and their relation to acicular growth forms are being investigated.

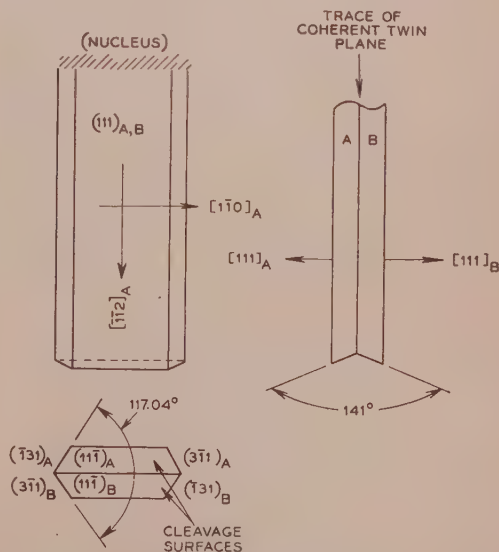


FIG. 3. Morphology of cleaved silicon ribbons.

The authors wish to acknowledge their indebtedness to S. M. Arnold for aid in handling and mounting the specimens, to E. S. Greiner for supplying them, and to W. C. Ellis and W. G. Pfann for their helpful discussions.

¹ E. S. Greiner, J. A. Gutowski, and W. C. Ellis, *J. Appl. Phys.* **32**, 2489 (1961).

² R. G. Treuting and S. M. Arnold, *Acta Met.* **5**, 598 (1957).

³ A. J. Bennett and R. L. Longini, *Phys. Rev.* **116**, 53 (1959).

⁴ R. S. Wagner, *Acta Met.* **1**, 57 (1960).

⁵ D. R. Hamilton and R. G. Seidensticker, *J. Appl. Phys.* **31**, 1165 (1960).

Backward Waves in Longitudinally Magnetized Ferrite Rods

G. H. B. THOMPSON

Standard Telecommunication Labs. Ltd., London Road,
Harlow, Essex, England

(Received June 12, 1961)

TRIVELPIECE, Ignatius, and Holscher¹ use an approximate magnetostatic method for investigating the behavior of backward waves propagating along a small diameter longitudinally magnetized ferrite rod; they confine their attention to the frequency range where the diagonal component of the ferrite permeability tensor μ_1 is negative. The modes they derive correspond to

the "volume" modes of Damon and Eshbach² and Joseph and Schlömann.³ Their experimental measurements do not, however, lie in this range and can be shown to apply to another set of backward modes (so-called "surface" modes) which propagate in the frequency range where μ_1 is positive, but $\mu_2 - \mu_1$ is negative (μ_2 is the off-diagonal component of the permeability tensor). An approximate characteristic equation for determining the conditions of propagation is derived in their paper [Eq. (16)] and is solved for negative μ_1 only. It is shown below, that additional solutions of the equation can be obtained outside this range.

The equation can be written as follows:

$$xJ_n'(x)/J_n(x) + n\mu_2/\mu_1 = 0,$$

where $x = \beta a / (-\mu_1)^{1/2}$.

Here a is the guide radius, n is the number of azimuthal variations of the mode (positive or negative, depending on the direction of circular polarization), and β is the propagation coefficient. As the authors state, there is an infinite number of both radial and azimuthal solutions of both polarizations when μ_1 is negative. There are also solutions for μ_1 positive, one for each negative value of n , provided $\mu_2/\mu_1 > 1$, which satisfy the magnetostatic conditions of the derivation of the approximate formula (i.e., $B^2/\mu \gg \delta$, when $a \ll 1/\beta_e$, where β_e is the propagation coefficient of a plane wave in a dielectric material of the same permittivity as the ferrite). These modes propagate up to a higher frequency for a given magnetic field than do the first set, the frequency range corresponding to

$$\gamma H_0 [1 + M_0/(\mu_0 H_0)]^{1/2} < \omega < \gamma (H_0 + M_0/\mu_0),$$

and they fit in well with the measured magnetic fields and phase characteristics presented in Fig. 9 of the above paper.

¹ A. W. Trivelpiece, A. Ignatius, and P. C. Holscher, *J. Appl. Phys.* **32**, 259 (1961).

² R. W. Damon and J. R. Eshbach, *J. Appl. Phys.* **31**, 104S (1960).

³ R. I. Joseph and E. Schlömann, *J. Appl. Phys.* **32**, 1001 (1961).

Dislocation Etching Solution for Potassium Chloride and Other Alkali Halides

J. S. COOK

Division of Electrotechnology, National Standards Laboratory, Commonwealth Scientific and Industrial Research Organization, Australia

(Received July 13, 1961)

IN connection with a study of the dielectric absorption of alkali halide crystals, doped with small quantities of divalent cation impurities, it was desired to assess the relative dislocation densities between certain crystals of potassium chloride by counting the etch pits developed on the surface of cleaved specimens after treatment with a suitable etching solution.

Several etching solutions for potassium chloride are mentioned in the literature. Among these are acetic acid, with and without the addition of zinc,¹ ethanol containing barium bromide,² and a mixture of methanol and ethanol containing barium bromide.³ These solutions were tried but were not entirely satisfactory. The solvents are difficult to dry and keep dry during use. Moreover, with the acetic acid etches, although the pits produced are quite

good, the etching times are inconveniently short. In view of this, propionic acid was tried and gave quite good results, with etching times ranging from 10 sec to 1 min.

It has been observed in other cases^{1,3,4} that the addition of certain multivalent cations to etching solutions improves the quality of the etch pits produced. The effect of the addition of iron, magnesium, zinc, calcium, strontium, barium, copper, and lead to propionic acid was therefore investigated. All were without much effect, except barium, which improved the contrast and sharpness of the pits, and zinc, which inhibited pit formation to such an extent that only small, rounded pits were produced. The optimum concentration of barium was found to be 1.75% by weight, and the etching solution finally used was made up by dissolving the appropriate quantity of reagent grade barium carbonate in freshly distilled propionic acid under reflux. This solution produces pits of excellent sharpness and contrast on the surface of freshly cleaved potassium chloride as shown in Fig. 1.

As Moran⁵ has pointed out, one of the problems of producing satisfactory etch pits is the tendency of the solvents commonly used as post-etching rinses to pick up water, which leads to water marking of the etched surface and sometimes to complete obliteration of the pits. Petroleum ether (bp 40–60°C) was found not to suffer from this disadvantage and to be an effective rinse for the above propionic acid/barium etching solution. The crystals were dried after rinsing in a blast of cool, dry air, a method which is preferable to the more usual technique of blotting dry with absorbent paper.

Gilman, Johnston, and Sears⁶ report that there is a difference between the pits formed at edge and screw and at fresh and aged dislocations when lithium fluoride is etched with a solution of ferric fluoride in water. No such difference was found in potassium chloride etched with the above propionic acid/barium solution, although pits produced in a crystal quenched from 300°C are slightly larger than in one cooled slowly.

The etching behavior of other alkali halides towards the propionic acid/barium solution was investigated. Good quality pits were produced in sodium chloride, potassium bromide, and sodium fluoride. A somewhat longer etching time was necessary for sodium fluoride, presumably due to its relative insolubility. No other alkali halide crystals were available, but it is suggested that the solution may be generally useful for etching the more soluble alkali halides. The use of petroleum ether as a rinse is strongly recommended.

¹ M. Sakamoto and S. Kobayashi, *J. Phys. Soc. Japan* **13**, 800–809 (1958).

² L. W. Barr, I. M. Hoodless, J. A. Morrison, and R. Rudham, *Trans. Faraday Soc.* **56**, 697–708 (1960).

³ P. R. Moran, *J. Appl. Phys.* **29**, 1768–9 (1958).

⁴ J. J. Gilman, W. G. Johnston, and G. W. Sears, *J. Appl. Phys.* **29**, 747–54 (1958).

Fission Fragment Damage to Platinum

E. RUDEL,* P. DELAVIGNETTE, and S. AMELINCKX

Centre d'Etudes de l'Energie Nucléaire, Mol, Belgium

(Received June 5, 1961)

FISSION tracks have been observed by means of electron microscopy in cleaved foils of mica¹ and in very thin evaporated films of uranium oxide.^{2–3} So far no evidence has been presented which is more or less representative of fission tracks in bulk metals. In insulators, ionization effects and local heating along the paths of the fission fragments are probably important factors in determining the nature of the damage left along the path. In the case of uranium dioxide films, for instance, Noggle² has shown that the visibility of the tracks is due to enhanced transmission, or as a consequence of the formation of a furrow on the surface, probably as a result of local heating and sublimation of the metal. In bulk metals a quite different behavior is to be expected.

In the course of an electron microscopic study of fission damages in relatively thick platinum foils (± 1000 Å) no evidence for tracks of the type referred to above was found. The result of neutron irradiation of platinum foils, sandwiched between two thin foils of natural uranium, was the formation of black dots and small



FIG. 1. Potassium chloride etched 30 sec in solution described in text. 48X.



FIG. 1. Platinum foil irradiated with fission fragments. Notice the linear arrangements of defects along the lines indicated by arrows. Some of the defects are clearly resolved as loops (L).

loops of the kind described by Silcox and Hirsch⁴ and by Barnes⁵ in the case of neutron-irradiated copper. From the proportionality of their concentration with dose and from their annealing behavior it could be concluded that the dots represent defect clusters formed during irradiation.⁶ A typical area of an irradiated foil is represented in Fig. 1. Some dots can clearly be resolved as loops, e.g., in L.

It was found that the dots are *not* arranged at random but, on the contrary, show a preference to be on straight lines in certain areas. This is shown in Fig. 1 where the linear arrangements are indicated by arrows.

As shown earlier⁶ spots line up along boundaries and more specifically along coherent twin boundaries. This effect is however completely different from the phenomenon discussed here, which takes place within the bulk of the grains.

In order to recognize the linear arrangement it is helpful to view the photograph under a grazing angle along the directions indicated by arrows. A statistical analysis shows that the probability of the linear arrangement being fortuitous is negligible. It is therefore suggested that they result from the passage of a fission fragment at a very small angle of incidence with the foil. The dots or loops are presumably formed at spots where primary knock-ons have taken place, resulting in displacement cascades as suggested by Silcox and Hirsch.⁴ The dots would then represent vacancy loops. In a second type of experiment a platinum foil was irradiated, only partly in contact with uranium, the geometry being as shown in Fig. 2. One has now a continuous transition between heavily-irradiated material in A, and material only reached by a few fission fragments impinging under a grazing angle at B. Figure 3 refers to a specimen taken from region B about 2 mm from the edge of the uranium foil. It is clear that the distribution of loops is certainly not at random, the general direction of the lines being along AB.

FIG. 2. Geometry of irradiation of platinum exposed to fission fragments of uranium.

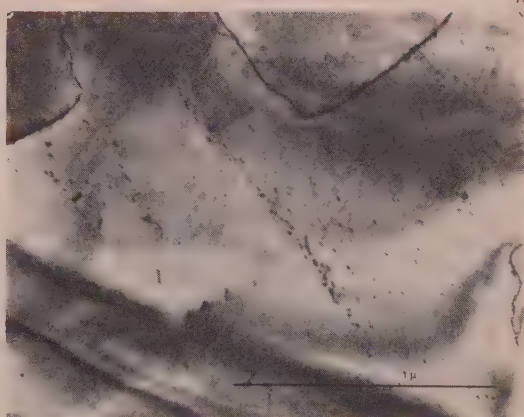


FIG. 3. Platinum foil irradiated with fission fragments coming in under grazing incidence from the right bottom part. Notice the more pronounced linear arrangements which are believed to be due to fission tracks.

It has been noted in the course of this investigation that some of the dots move by conservative climb under the influence of a nearby moving dislocation in the way described by Kroupa and Price for zinc.⁷ This proves convincingly that the dots are loops, and, for instance, not a surface effect. It has however been impossible to record this phenomenon because of the long exposure times involved (10 sec).

This work is part of a research program undertaken at CEN, Mol, Belgium, on behalf of the Joint Research and Development Program of the agreement for cooperation between Euratom and the United States of America.

* Permanent address: Euratom, Brussels, Belgium.

¹ E. C. H. Silk and R. S. Barnes, *Phil. Mag.* **4**, 970 (1959).

² T. S. Noggle and J. O. Stiegler, *J. Appl. Phys.* **31**, 2199 (1960).

³ T. K. Bierlein and B. Mastel, *J. Appl. Phys.* **31**, 2314, 2315 (1960).

⁴ J. Silcox and P. B. Hirsch, *Phil. Mag.* **4**, 1356 (1959).

⁵ R. S. Barnes, *Discussions of the Faraday Society on Radiation Effects in Inorganic Solids*, Paris, 1961 (to be published).

⁶ E. Ruedl, P. Delavignette, and S. Amelinckx, *Phys. Rev. Letters* (to be published).

⁷ F. Kroupa and P. B. Price, *Phil. Mag.* **6**, 243 (1961).

Transient Effects in Peltier Coolers

A. D. REICH, T. ARAI, AND J. R. MADIGAN

Roy C. Ingersoll Research Center, Borg-Warner Corporation,
Des Plaines, Illinois

(Received June 29, 1961)

IT has been suggested to us by Professor Paul E. Gray¹ of the Massachusetts Institute of Technology that we should explicitly point out those results of our two papers on transient effects in Peltier coolers^{2,3} which are consequences of the restrictive assumptions of our model. In particular, the assumption of a constant Peltier voltage gives results which, while qualitatively correct, differ in detail from those of a more exact analysis.

The treatment may be termed a modified hot junction analysis (i.e., an analysis for a constant hot junction temperature), in which the assumption of a constant Peltier voltage P makes the steady state ΔT versus time curve symmetrical about the optimum current I_{opt} (Fig. 2 of the first paper). For a hot junction in which P varies linearly with temperature the curve will be skewed in the direction $I < I_{opt}$.

The limitation on the size of the thermal cold spikes appears to be more general than one would expect from our model. In particular, it still holds when $P = \Delta S T_c(t)$, where ΔS is the difference in Seebeck coefficients for the two legs of the couple, and $T_c(t)$ is the temperature at the cold junction at time t .

The problem we solved in which the heat absorption term is represented by a constant heat sink localized by a spatial type delta function at the cold junction is exactly equivalent to the

problem in which one solves separately for the temperatures in the p and n legs of the couples. This requires continuity of the two temperatures at the cold junction and the sum of the heat flowing into the junction through both legs of the couple to be equal to the Peltier heat absorbed there. That is, our problem is equivalent to the following one:

$$\begin{aligned} 0 \leq x \leq a/2 & \quad a/2 \leq x \leq a \\ c_p \frac{\partial \theta_l(x,t)}{\partial t} = k \frac{\partial^2 \theta_l(x,t)}{\partial x^2} + j^2 \rho & \quad c_n \frac{\partial \theta_r(x,t)}{\partial t} = k \frac{\partial^2 \theta_r(x,t)}{\partial x^2} + j^2 \rho \\ \theta_l(x,0) = 0; \quad \theta_l(0,t) = 0 & \quad \theta_r(x,0) = 0; \quad \theta_r(a,t) = 0 \\ \theta_l(a/2,t) = \theta_r(a/2,t) - k \frac{\partial \theta_l(a/2,t)}{\partial x} + k \frac{\partial \theta_r(a/2,t)}{\partial x} = Pj, & \end{aligned}$$

where a is the total length of the thermocouple circuit, j is the current density, c_p , k , and ρ are the specific heat per unit volume, thermal conductivity, and resistivity, respectively, of the material in legs of the couple, P is the Peltier voltage at the cold junction, and the subscripts l and r refer to the left and right legs of the couple, respectively. The Laplace transform of the temperature at the cold junction then becomes

$$\bar{\theta}(a/2, s, j) = (\gamma/\alpha^2)(1 - \text{sech} \alpha a/2) - (\beta/2\alpha)(\tanh \alpha a/2)$$

where $\alpha^2 = c_p/k$, $\gamma = j^2 \rho/k$, and $\beta = Pj/k$ if $P \neq f(T)$ or $\beta = \Delta S j/k [T_h/s + \bar{\theta}(a/2, s, j)]$ if $P = f(T)$. In the first case the inverse transform of this expression gives Eq. (14) of our first paper. Inversion of the expression with the second form for β gives the equation obtained by Stilbans and Fedorovich⁴ and by Parrott.⁵ In fact their result reduces to ours if the same assumptions are used. Thus, when we set $g = \beta = 0$, $d = j^2 \rho/k$, $f = Pj/2k$, $l = a/2$, and $T_0(l) = \bar{\theta}(a/2, l, j)$ in Parrott's paper to be consistent with our notation and assumptions, the equation determining the ψ_i reduces to $\cot \psi_i = 0$ or $\psi_i = (2n+1)\pi/2$. Substituting these results into his Eq. (17) and normalizing the time and temperature with respect to $\tau = c_p a^2/\pi^2 k$ and $\theta_{\max} = -P^2/8k\rho$ gives Eq. (14) of our first paper.

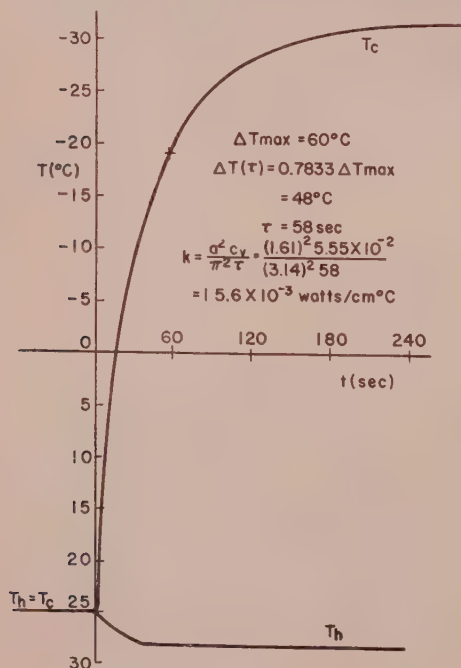


FIG. 1. Transient response of a couple.

To obtain information about the size of the thermal spikes, we must recognize that they occur closer to the turn on time, the larger the current. We are thus justified in considering the limiting behavior of the Laplace transform for small values of t or large values of s . The case of constant P then gives the results on page 298 of the first paper except for some errata in the equations which, however, do not affect the limiting value of $2/\pi$ for the size of the thermal spike. When $P = f(T)$ we find to same order of approximation that the size of the thermal spikes becomes

$$\frac{\theta(a/2, t, j)}{\theta_{\max}} = \frac{2}{\pi} \frac{(1 - \theta_{\max}/T_c)^2}{(1 - \theta_{\max}/T_c)^2 + (\theta_{\max}/T_c)^2}$$

The numerator of this expression is always smaller than the denominator so that for this case the size of the thermal spikes will be less than those when $P \neq f(T)$.

For higher order approximations when $P = \Delta S T_c$ we find that θ/θ_{\max} for small t is expressible as a power series in $l/(t/\tau)^{1/2}$. When this is maximized with respect to the current we find that, at the times corresponding to the maxima, $(t/\tau)^{1/2} \propto (1/l)$ so the size of the spikes is independent of the current. Unfortunately, the coefficients in the series which are functions of θ_{\max} and T_h or T_c are so complicated that it is difficult to say what limiting value the thermal spikes attain.

Professor Gray also suggests that the assumption $P \neq f(T)$ prevents us from making any quantitative statements about thermal conductivity as was suggested in the first paper. This would indeed seem to be true since the transient response should only be qualitatively correct. In Fig. 1 we show the transient response of a couple with cylindrical legs about 0.635 cm long and 0.50 cm in diameter made from Melcor p and n material and the thermal conductivity of the material in arms of couple as determined by the method suggested in the first paper. The average thermal conductivity of a series of p - and n -type $\frac{1}{2}$ -in.-diam Melcor samples was determined in this laboratory by an independent method to be 13.8 and 16.73×10^{-3} w/cm $^{\circ}\text{C}$, respectively.⁶ If we assume that the effective thermal conductivity of the thermocouple circuit is the average of that for the p and n legs, we obtain 15.3×10^{-3} w/cm $^{\circ}\text{C}$.

This is embarrassingly good agreement considering the crudeness of the model. A possible reason for its apparent success is that the variations with temperature in the individual parameters are such that they tend to cancel one another near room temperature.

In preparing this letter we found some errors in both the first and second articles. In the first article [J. Appl. Phys. 32, 294 (1961)] the equations defining the limiting value of the thermal spike should read

$$\begin{aligned} \frac{\bar{\theta}(a/2, s, j)}{\theta_{\max}} &= -\frac{8l^2}{\pi^2} \left\{ \frac{1}{s^3} - \frac{\text{sech} \pi/2(\tau s)}{s^2} \right\} + \frac{4l}{\pi \tau^{\frac{1}{2}}} \frac{\pi \tanh 2(\tau s)}{s^{\frac{1}{2}}} \\ \frac{\bar{\theta}(a/2, s, j)}{\theta_{\max}} &= -\frac{8l^2}{\pi^2 \tau} \frac{1}{s^2} + \frac{4l}{\pi \tau^{\frac{1}{2}}} \frac{1}{s^{\frac{1}{2}}} \quad \text{for } s \gg 1 \\ \frac{\theta(a/2, t, j)}{\theta_{\max}} &= -\frac{8l^2}{\pi^2 \tau} \frac{t}{\tau} + \frac{8l}{\pi} \left(\frac{t}{\tau} \right)^{\frac{1}{2}} \\ & \quad (t/\tau)^{\frac{1}{2}} = \pi^{\frac{1}{2}}/2l. \end{aligned}$$

Fortunately, these changes have no effect on the limiting value itself. The exponent in the expression for c_p at the bottom of page 300 should be -2 not -3 .

In the second paper [J. Appl. Phys. 32, 609 (1961)] the discussion of Fig. 4 at the top of the second column on page 613 should read "a current pulse whose amplitude is equal to one-half the optimum current superposed on a steady current one-half the optimum value." The sketch of j as a function of t in Fig. 4 should also show the pulse rising only to j_{opt} and not $(3/2)j_{\text{opt}}$.

¹ Paul E. Gray (private communication).

² A. D. Reich and J. R. Madigan, J. Appl. Phys. 32, 294 (1961).

³ T. Arai and J. R. Madigan, J. Appl. Phys. 32, 609 (1961).

⁴ L. S. Stilbans and N. A. Fedorovich, Zhur. Tekh. Fiz. 28, 489 (1958).

⁵ J. E. Parrott, Solid State Electronics 1, 135 (1960).

⁶ C. Rufer (private communication).

New Magnetic Ternary Compound with a High Crystalline Anisotropy

J. H. WERNICK, S. E. HASZKO, AND W. J. ROMANOW

Bell Telephone Laboratories, Incorporated, Murray Hill, New Jersey
(Received June 26, 1961)

A FERROMAGNETIC ternary compound MnAlGe, exhibiting a large crystalline anisotropy, was discovered during the course of a study of the structural and magnetic relationships in the Mn-Al-Ge system. The purpose of this letter is to report on the properties of this compound determined to date.

The crystal habit of MnAlGe grown from the melt is platelike. Chemical analysis of single crystals showed the stoichiometry to be MnAlGe. Differential thermal analysis of single crystals showed that the freezing point of MnAlGe is 786°C. Three other thermal arrests were noted, at 710°, 690°, and 584°C. They occur on heating as well as on cooling. The 786°C thermal arrest is the largest, characteristic of isothermal freezing, and the 690°C arrest is the smallest. Quenching experiments were performed in attempts to retain the elevated temperature phases. These experiments were not successful. Our experience to date, including metallographic and single-crystal pulling experiments, suggests that the 710°, 690°, and 584°C thermal arrests are due to solid-state transitions. However, in order to fully understand the nature of these transitions, the phase relations in the Mn-Al-Ge system, particularly in the vicinity of MnAlGe, must be investigated in detail. This investigation is in progress.

The crystal structure of MnAlGe was determined from powder and single-crystal precession photographs to be tetragonal, the most probable space group being $D_{4h}^n - P4/n$ mm. The lattice constants are $a = 3.910 \pm 0.005$ Å and $c = 5.943 \pm 0.005$ Å. The measured density of single crystals is in agreement with the calculated value 5.65 g/cc when two formula units per cell are assumed. The observed and calculated interplanar spacings and observed intensities are shown in Table I. A detailed structure analysis is necessary to locate precisely the atomic positions. The easy axis of magnetization is the c axis, and it is normal to the plate faces of our single crystals.

The magnetization per gram versus the applied field in oersteds obtained on an MnAlGe single crystal is shown in Fig. 1. From the approach to saturation in the hard direction, a crystalline anisotropy constant K_1 of 5.3×10^6 ergs/cm³ was computed from

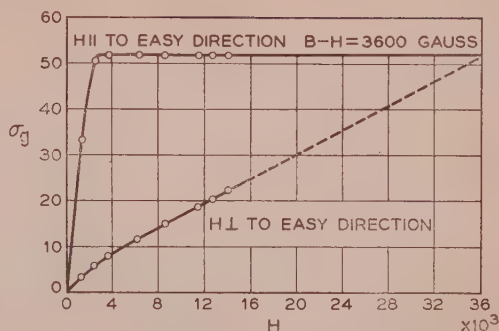


FIG. 1. Room temperature magnetization curves in the easy and hard directions for MnAlGe.

the relationship $H = 2K_1/M_s$, where M_s = saturation moment and H = anisotropy field. The anisotropy field of about 36 000 oe is estimated from the approach to saturation in the hard direction. This field is the upper limit of the attainable coercive force. Coercive forces varying between 1500 to 2200 oe were measured on unsieved powders of MnAlGe embedded in molten wax in a field and samples pressed in a field. Much larger values undoubtedly could be obtained by using sized samples aligned at higher field strengths.

The magnetic properties of MnAlGe are comparable at present to BaFe₁₂O₁₉, and therefore, fine particle permanent magnets with magnetic properties in the BaFe₁₂O₁₉ class¹ are possible with this material.

The magnetic measurements made by H. J. Williams and R. C. Sherwood are gratefully acknowledged. We wish also to thank E. A. Nesbitt for helpful discussions and D. Dorsi for the preparation of the alloys.

¹ J. Smit and H. P. Wijn, *Ferrites* (John Wiley & Sons, Inc., New York, 1959).

Books Reviewed

TABLE I. Observed and calculated interplanar spacings and observed powder intensities for MnAlGe. CrK α radiation.

hkl	d_{calc}	d_{obs}	I_{obs}
001	5.943	5.869	w-m ^a
101	3.267	3.245	m
002	2.972	2.953	w
110	2.765	2.749	w-m
111	2.507	2.495	s
102	2.366	N.O. ^b	
112	2.024	2.017	vs
003	1.981	1.976	m
200	1.955	1.949	s
201	1.857	1.855	w
103	1.767	1.764	w
211	1.678	1.675	w-m
202	1.633	1.631	w
113	1.610	N.O.	
212	1.507	N.O.	
004	1.4858	1.4844	m
203	1.3915	1.3913	m-s
104	1.3889	N.O.	
220	1.3824	1.3819	m-s
221	1.3465	1.3460	vw
213	1.3110	1.3104	w-m
114	1.3088	1.2986	vw
301	1.2731	1.2732	w
222	1.2534	1.2537	m
310	1.2365	1.2365	w-m
311	1.2105	1.2103	m
302	1.1936	N.O.	
005	1.1886	N.O.	
204 ^a	1.1829	1.1829	s

^a α_1 and α_2 averaged.

^b N.O. = not observed.

^c s = strong, m = medium, w = weak, v = very.

Prompt, noncritical reviews appear in this column. Critical reviews of many of the books described here will appear in Physics Today, The Review of Scientific Instruments, or American Journal of Physics.

Crossed-Field Microwave Devices, Vols. I and II. E. OKRESS, Editor, Pp. 648 and 520. Academic Press, Inc., New York and London, 1961. Price Vol. I \$22.00; Vol. II \$18.00.

These two volumes fill an important gap in the literature by summarizing the progress and state of the art of crossed-field microwave devices in theory and practice.

In order to indicate not only established uses but also possible future applications, the authors have included thorough surveys of the available literature and have added new material as warranted. Their primary objective has been to enable students and professional physicists and engineers to understand the fundamentals of all existing important types of crossed-field devices, to perceive the problems posed by each element of the devices in practice and in theory, to know the essentials of the means available for solving these problems, and to develop approaches to the design of other devices.

Boundary Layer and Flow Control—Its Principles and Application. Vol. I. G. V. LACHMANN, Editor. Pp. 600. Pergamon Press, New York and Oxford, 1961. Price \$35.00—Set of 2 Volumes.

Vol. I—Part 1—History of Boundary Layer and Flow Control Research in Various Countries.

Part 2—Boundary Layer and Flow Control to Prevent Separation and/or Increase Lift in Subsonic Flow.

Boundary Layer and Flow Control contains contributions by 38 international authorities and encompasses the entire field of the subject. The work, in two volumes, gives a complete historical review of boundary layer research. It reflects fully the present situation and indicates lines of future research.

Emphasis is on engineering applications. Included are related subjects, such as the influencing of boundary layer flow and character through geometric design, modern applications of the slot effect, the jet flap, and methods to prevent separation in transonic flow. The latest investigations into the nature of separation and transition, and the effects of roughness on the stability of a laminar boundary layer are discussed.

Contributions contain information either novel or additive to the work previously published on the subject. This applies particularly to methods dealing with the calculation of sucked boundary layers in two-dimensional and three-dimensional flow, research on suction surfaces, design aspects of low drag aircraft, and the control of boundary layer separation in the presence of shock waves.

Quantum Mechanics. EUGEN MERZBACHER. Pp. 544. John Wiley & Sons, Inc., New York, 1961. Price \$12.00.

The development of the discussion of quantum mechanics is presented in three stages which are clearly articulated and held together by a common thread. In the first stage, ordinary wave mechanics is developed, enabling the student to handle actual problems of atomic and nuclear physics as early as possible. Secondly, the matrix form of quantum mechanics is explicitly introduced as a useful tool in formulating one dimensional problems and is used again in the treatment of spin. In the third stage, the two versions of quantum mechanics (wave and matrix) are unified in the general and more abstract Dirac formulation, which is subsequently employed throughout the second-half of the book.

Plastic Flow and Fracture in Solids, Vol. 2. TRACY Y. THOMAS. Pp. 267. Academic Press, Inc., New York, 1961. Price \$8.50.

This book is devoted mainly to a study of the propagation, growth, and decay of discontinuities in solids, including the theory of characteristic surfaces and the spread of plastic into elastic regions. The material is based largely on articles published by the author in various mathematical journals during the preceding five years.

Progress in Biophysics and Biophysical Chemistry, Vol. II. J. A. V. BUTLER, B. KATZ, AND R. E. ZIRKLE, Editors. Pp. 277. Pergamon Press, New York and Oxford, 1961. Price \$12.50.

This is the eleventh volume to be published by Pergamon Press in the series *Progress in Biophysics and Biophysical Chemistry*. The series is designed to cover the ground between the physical and biological sciences. The papers in Vol. II include:

- The Natural Radioactivity of the Human Body
- The Engineering Approach to the Problem of Neutral Organization
- Effects of X-Rays on Nucleic Acid Biosynthesis and on Activity of Nucleases in Mammalian Cells
- The Effect of Ionizing Radiations and Tumour-chemotherapeutic Agents on the Bone Marrow
- Some Factors Influencing the Dispersion of Indicator Substances in the Mammalian Circulation
- The Buoyancy of Fish and Cephalods.

The Quantum Mechanics of Many-Body Systems. D. J. THOULESS. Pp. 175. Academic Press, Inc., New York and London, 1961. Price \$5.50.

This book is a unified introduction to many-body theory. It is concerned with problems common to nuclear physics, atomic physics, the electron theory of metals, and the theory of liquid helium three and four; it describes the methods which have recently been developed to solve such problems. Main emphasis is on the theories of atomic nuclei, electron gas, and liquid helium.

The reader is expected to be familiar with the principles of nonrelativistic quantum mechanics and statistical mechanics. A knowledge of field theory and a detailed knowledge of nuclear and solid-state physics are not assumed.

The Theory of Subsonic Plane Flow. L. C. WOODS. Pp. 594. Cambridge University Press, New York, 1961. Price \$22.50.

This book presents a concise and systematic treatment of two-dimensional subsonic, inviscid fluid motion and its aeronautical applications. Part I surveys the relevant fluid dynamics; it is assumed only that the reader has had an introductory course in it. In Part II, the methods of conformal mapping and Cauchy integrals are developed, on the assumption that the reader has only an elementary understanding of complex variable theory; this part should prove useful to a wide range of applied mathematicians and engineers (e.g., for the treatment of elasticity and diffusion problems, as well as aeronautical ones).

In Part III, the methods are applied to several important problems in fluid and aerodynamics. It is the first book to give an extensive account of mixed boundary-value problems and to treat such examples of these problems as occur in ventilated wind-tunnel theory, jet-flap theory, and unsteady Helmholtz motions.

Problems in Quantum Mechanics. I. I. GOL'DMAN, V. I. KRIVCHENKOV, V. I. KOGAN, AND V. M. GALITSKII. D. TER HAAR, Editor. Pp. 394. Academic Press, Inc., New York, 1961. Price \$12.00.

This collection contains all problems from the text by Gol'dman and Krivchenkov, as well as a selection from those by Kogan and Galitskii. The latter are arranged in the corresponding chapters of the Gol'dman and Krivchenkov collection and distinguished by asterisks.

Although these problems are used in the U. S. S. R. with Landau and Lifshits' *Quantum Mechanics*, they can be used equally well with any other textbook on quantum mechanics such as those by Schiff or Kramers, or as advanced reading by students familiar with the basic ideas of quantum mechanics e.g., acquired from Pauling and Wilson's text.

Physics of the Aurora and Airglow, Vol. 2. JOSEPH W. CHAMBERLAIN. Pp. 704. Academic Press, Inc., New York, 1961. Price \$16.50.

This monograph discusses completely the physics of the aurora and airglow, emphasizing those subjects not covered extensively elsewhere in the literature. The bibliography of more than 1500 entries is complete to January, 1960, and contains selected references to the literature published later. The book requires only a background in classical and atomic physics. It will be of great interest to all scientists active in the field, and will be suitable as a textbook in graduate courses for which both practical and theoretical problems are given at the ends of the chapters.

Introduction to Relativistic Quantum Field Theory. SILVAN S. SCHWEBER. Pp. 904. Row, Peterson and Company, Evanston, Illinois and Elmsford, New York, 1961.

This book is an outgrowth of *Mesons and Fields* written by the author in collaboration with Hans Bethe and Frederick J. Dyson in 1955. It is intended as a text for the graduate level.

The Physical Principles of Astronautics—Fundamentals of Dynamical Astronomy and Space Flight. ARTHUR I. BERMAN. Pp. 350. John Wiley & Sons, Inc., New York, 1961.

This book is designed to fill the important need for a clear and thorough exposition of the basic principles of astronautics at a level suitable for a wide technical audience. A general reader, or student with a background in introductory physics and calculus, can progress through the subject matter with little difficulty. Vector notation is used for exactness and clarity, and a concise introduction to vectors is included as an appendix so that readers unfamiliar with their use will be at no disadvantage.

The book is also valuable as an adjunct text in astronomy and mechanics at an intermediate level. The physics of the solar system is given a more advanced and succinct treatment than in elementary astronomy texts. Subjects in mechanics such as weight and weightlessness and Coriolis acceleration, which are often given only limited coverage in introductory physics courses, are treated in depth.

Noteworthy features of the book are the large number of original illustrative examples, which are worked out in detail within the body of the text, and the thought-provoking unsolved problems, many with answers given at the end of each chapter.

An Introduction to the Theory and Practice of Transistors. J. R. TILLMAN AND F. F. ROBERTS. Pp. 340. John Wiley & Sons, Inc., New York, 1961. Price \$8.00.

Part I presents the basic physical theory of semiconductors and of the transistor in terms that, without sacrificing precision, should be more than usually comprehensible to electronic engineers and experimental physicists; an analysis is made of a practical three-dimensional model of a transistor, which gives a realistic account of its electrical properties. Part II begins with a description of the preparation of the two key semiconductors; it continues with a critical survey of the electrical characteristics of semiconductor diodes and transistors before showing, with many examples, how circuits can be quantitatively designed around them in the fields of amplification, oscillation, switching, logic, and waveform generation.

Proceedings of the Third Symposium on Electron Beam Technology. R. BAKISH, Editor. Pp. 379. Alloyd Electronics Corporation, Cambridge, Massachusetts, 1961. Price \$15.00.

The third Alloyd Electron Beam Symposium Proceedings present the most up-to-date compilation of information on electron beam technology. There are 22 papers by scientists working in the forefront of electron beam technology and the areas covered are as follows:

- Physics of Electron Beams
- Electron Beam Welding
- On Less Known Electron Beam Applications
- Electron Beams in Microminiaturization.

Progress in Optics, Vol. I. EMIL WOLF, Editor. Pp. 342. North-Holland Publishing Company, Amsterdam, and Interscience Publishers, Inc., New York, 1961. Price \$12.00.

It is the aim of this new series to provide information in the form of review articles about current optical research, both

theoretical and applied. Articles dealing with progress in related fields, for example, in electron optics, x-ray structure analysis, microwave antenna design, and in radio astronomy may be included from time to time. All articles will be written in English, but the authorship will be international in order to insure broad and expert coverage.

Introduction to Elementary Particle Physics. R. E. MARSHAK AND E. C. G. SUDERSHAN. Pp. 231. Interscience Publishers, Inc., New York, 1961. Price \$4.50.

This tract is very limited in its objectives. It concentrates on those aspects of elementary particle physics which do not depend on detailed dynamical calculations. Except for the last section of the book, distinct fields are associated with the well-established particles, the usual distinction is made between the strong, electromagnetic, and weak interactions, and the only invariance principles and selection rules considered are those on a firm experimental footing. Even within this limited framework, no attempt is made to achieve rigor or completeness; instead, the physical meaning of the various concepts is emphasized and the experimental material is introduced chiefly for illustrative purposes. In a word, this book is a brief introduction to elementary particles intended for the nonexpert in theoretical high-energy physics.

Semiconducting III-V Compounds. C. HILSUM AND A. C. ROSE-INNES. Pp. 239. Pergamon Press, Oxford and New York, 1961. Price \$10.00.

This volume is a concise but comprehensive treatment of theoretical and experimental aspects. It deals with the band structure, crystal structure, preparatory techniques, transport processes, optical absorption, photoelectric effects, and galvanomagnetic properties, as well as with a number of device applications. Certain physical processes, which are absent or only of minor importance in element semiconductors, are very prominent in the III-V compounds. These matters receive detailed discussion.

Books Received

Response of Metals of High Velocity Deformation, Vol. 9. P. G. SHEWMON AND V. F. ZACKAY, Editors. Pp. 491. Interscience Publishers, Inc., New York and London, 1961. Price \$18.00.

Physical Chemistry in Aerodynamics and Space Flight. Proceedings of the Conference on Physical Chemistry in Aerodynamics and Space Flight sponsored by the Air Force Office of Scientific Research and the General Electric Company, Missile and Space Vehicle Department, University of Pennsylvania, Philadelphia, Pennsylvania, September 1 to 3, 1959. A. L. MYERSON AND A. C. HARRISON, Editors. Pp. 288. Pergamon Press, New York, 1961.

Combustion and Propulsion, Fourth AGARD Colloquium, High Mach Number Air-Breathing Engines. A. L. JAUMOTTE, A. M. ROTHROCK, AND A. H. LEFEBVRE, Editors. Pp. 396. Pergamon Press, New York and Oxford, 1961. Price \$15.00.

Dispersion Relations and the Abstract Approach to Field Theory. LEWIS KLEIN, Editor. Pp. 273. Gordon and Breach Publishers, Inc., New York, 1961. Price \$4.95.

The Science of Adhesive Joints. J. J. BIKERMAN. Pp. 258. Academic Press, Inc., New York and London, 1961. Price \$8.00.

Reactor Handbook, 2nd ed., Vol. II—Fuel Reprocessing. S. M. STOLLER AND R. B. RICHARDS, Editors. Pp. 665. Interscience Publishers, Inc., New York and London, 1961. Price \$21.40.

Modern Computing Methods, 2nd ed. Pp. 170. Philosophical Library, Inc., New York, 1961. Price \$6.00.

Proceedings of the 1961 Heat Transfer and Fluid Mechanics Institute. R. C. BINDER, M. EPSTEIN, R. L. MANNES, AND H. T. YANG, Editors. Pp. 236. Stanford University Press, Stanford, California, 1961. Price \$8.00.

Advances in Electron Tube Techniques, Proceedings of the Fifth U. S. National Conference. DAVID SLATER, Editor. Pp. 235. Pergamon Press, New York, 1961. Price \$15.00.

Vacuum Technology Transactions, Proceedings of the Seventh National Symposium. C. ROBERT MEISSNER, Editor. Pp. 427. Pergamon Press, New York, 1961. Price \$20.00.

Mechanical Measurements. T. G. BECKWITH AND N. LEWIS BUCK. Pp. 559. Addison-Wesley Publishing Company, Inc., Reading, Massachusetts, 1961. Price \$8.75.

Encyclopaedic Dictionary of Physics, Vol. 1. J. THEWLIS, Editor. Pp. 800. Pergamon Press, New York and London, 1961. Price \$240.00 per set.

A Fortran Program for Elastic Scattering Analyses with the Nuclear Optical Model. MICHEL A. MELKANOFF, JOHN S. NOVICK, DAVID S. SAXON, AND DAVID G. CANTOR, Editors. Pp. 116. University of California Press, Berkeley and Los Angeles, 1961. Price \$4.50.

Progress in Very High Pressure Research, Proceedings of an International Conference held at Bolton Landing, New York, June 13 to 14, 1960. F. P. BUNDY, W. R. HIBBARD, JR., AND H. M. STRONG, Editors. Pp. 314. John Wiley & Sons, Inc., New York, 1961.

Lectures in Theoretical Physics. Vol. III, Lectures delivered at the Summer Institute for Theoretical Physics, University of Colorado, Boulder, 1960. WESLEY E. BRITTIN, B. W. DOWNS, AND JOANNE DOWNS, Editors. Pp. 531. Interscience Publishers, Inc., New York and London, 1961.

Progress in Astronautics and Rocketry, Vol. 3: Energy Conversion for Space Power. NATHAN W. SNYDER, Editor. Pp. 779. Academic Press, Inc., New York, 1961. Price \$7.25.

Progress in Astronautics and Rocketry, Vol. 5: Electrostatic Propulsion. DAVID B. LANGMUIR, ERNST STUHLINGER, AND J. M. SELLEN, JR., Editors. Pp. 579. Academic Press, Inc., New York, 1961. Price \$5.75.

Biography of Physics. GEORGE GAMOW. Pp. 338. Harper & Brothers, New York, 1961. Price \$5.95.

Progress in Dielectrics, Vol. III. J. B. BIRKS AND J. HART, Editors. Pp. 292. John Wiley & Sons, Inc., New York, 1961. Price \$10.00.

Radioactive Substances. M. CURIE. Pp. 94. Philosophical Library, Inc., New York, 1961. Price \$2.75.

Progress in Solid Mechanics, Vol. II. I. N. SNEDDON AND R. HILL, Editors. J. E. Adkins, M. J. P. Musgrave, J. D. Eshelby, M. R. Horne, J. W. Craggs, K. W. Hillier, and R. Hill, Contributors. Pp. 331. North-Holland Publishing Company, Amsterdam, and Interscience Publishers, Inc., New York, 1961. Price \$11.75.

Powder Metallurgy—Proceedings of an International Conference held in New York, June 13 to 17, 1960, under the joint sponsorship of the Metal Powder Industries Federation and the Powder Metallurgy Committee of the Institute of Metals Division, The Metallurgical Society, American Institute of Mining, Metallurgical, and Petroleum Engineers. WERNER LESZYNSKI, Editor. Pp. 845. Interscience Publishers, Inc., New York and London, 1961. Price \$25.00.

Iterative Arrays of Logical Circuits. FREDERICK C. HENNIE, III. Pp. 242. The Massachusetts Institute of Technology Press, Cambridge, Massachusetts, and John Wiley & Sons, Inc., New York and London, 1961.

Dispersion Relations and Elementary Particles. C. DE WITT AND R. OMNES, Editors. Pp. 671. John Wiley & Sons, Inc., New York, 1961. Price \$20.00.

Elementary Fluid Mechanics, 4th ed. JOHN K. VENNARD. Pp. 570. John Wiley & Sons, Inc., New York, 1961.

Research Reports

This column will announce the availability of reports describing research in the fields of physics represented in the Journal of Applied Physics. The supply of copies of most reports are strictly limited and are rarely reprinted when the initial printing is exhausted.

An announcement for this column should be fewer than 150 words in length and should provide information on the content, length, price and address from which the report can be obtained. The announcement should be accompanied by a copy of the report, which will be reviewed to determine whether the report is of sufficient interest and relevance to warrant an announcement.

Energy Transfer in Polyacene Solid Solutions—II. A Bibliography for 1957-1960. F. R. LIPSETT, N.R.C. 6404. Pp. 63. National Research Council, Ottawa 2, Ontario, Canada, 1961. Price 50 cents.

When a small quantity (about 1 part in 10^5) of tetracene (the "impurity") is added to anthracene (the matrix) the fluorescence of the anthracene is suppressed and tetracene fluorescence of high efficiency appears. With increase of the concentration of the tetracene, the intensity of the tetracene fluorescence increases and that of the anthracene decreases. A similar process takes place when tetracene is added to naphthalene, or anthracene to naphthalene, etc. The emission of the impurity is said to take place by means of a transfer of the absorbed energy of radiation from the matrix molecule to the impurity molecules, and a necessary condition for this is that the fluorescence of the impurity molecules should lie at longer wavelengths than that of the matrix. The energy transfer process in solids has most often been studied in systems of the polyacenes and related molecules.

The Bibliography is a continuation of an earlier publication of the same title (F. R. Lipsett, N.R.C. 4320, 1957) in which references to the literature on energy transfer are collected under six main headings—books and reports of meetings; theories on spectra; experiments on spectra; energy transfer related subjects; and experimental techniques—and 21 subheadings. Many of the references deal with subjects related to energy transfer rather than with the transfer process itself, for example, molecular structure and photoconduction. 61-reference author index.

Announcements

International Conference on the Physics of Semiconductors

The Institute and Society on behalf of the International Union of Pure and Applied Physics, and the British National Committee for Physics are arranging an International Conference on the Physics of Semiconductors, which will be held at the University of Exeter from July 16 to 20, 1962. The Conference is planned to follow the previous sequence of conferences on the physics of semiconductors, which were held in Reading in 1950, Amsterdam in 1954, Garmisch in 1956, Rochester in 1958, and Prague in 1960.

Accommodation will be provided in Halls of Residence at the University. Further information regarding the Conference may be obtained from the Administration Assistant, The Institute of Physics and The Physical Society, 47 Belgrave Square, London S. W. 1.

Kodak reports on:

Ektaline, sweet Ektaline... $f/1$ lenses for 2μ to 14μ ... new personal monitoring film, very sensitive

IS paper

THIS oscillograph paper dries thoroughly at high speeds the automatic oscillogram processor *without creases*. *in./min. is not too fast.*

THIS paper gives trace lines that stand out as black as face of spades. *Background is nice and clean.*

THIS paper isn't fussy about how long it sits around before use. *O.K. to keep plenty on hand.*

THIS paper is rugged. *No cracking, no crumbling.*

THIS paper holds its dimensions. *Justifies careful measurement.*

THIS" won't do for a trademark. (The code name for the field was "Kind 1534.") Let's call it Kodak Ektaline Paper. It lies in the two usual speeds for oscillographs, Kodak Ektaline 16 Paper and Kodak Ektaline 18 Paper. Kodak Ektaline Chemicals are as liquids. The stabilization principle used in the automatic oscillogram processors came from Kodak, too. An inquiry to Eastman Kodak Company, Photorecording Methods Division, Rochester 4, N. Y., puts everything in place right up to the moment.

Sharp eye for infrared

The decision to announce off-the-shelf availability of $f/1$ Irtran-2 Aspheric Lenses in 2- and 3-inch focal lengths has been reached in struggle against deeply rooted inhibitions. The photographic film and paper trade we are habituated to longer silence before the first blast of the trumpets. Infrared technology hates to wait, however, and puts a heavy hand on the phone company's long lines.

These Irtran-2 lenses transmit usefully from 2μ to 14μ . Sharpness was the goal. For both lenses, the minimum circle of confusion computes at less than .001" for any wavelength in 4.25μ to 10μ .

Much care and a valuable ingenuity have been exercised in impressing our tenth-degree equation upon the concave side of these meniscus lenses, in grinding and polishing the spherical convex side, in placing the center of the spherical curvature on the axis of the asphere, in maintaining the proper thicknesses at the 9.1 mm and 10.4 mm values respectively that the calculations assume,

the optical homogeneity of the Irtran-2 material. More than we cannot claim. To the extent that the ingenuity we succeeded in making the calculations represent the accuracy, the circle of confusion is less than .001". The customer's willingness to take a chance that we have hit it will, in good sense, depend on how badly his project needs a 2μ - 14μ infrared image of high definition and high aperture.

In the lead sulfide region, the sharpness does not compute as good as farther out in the infrared. Yet we have customers who use the lenses there and are happy with con-circle minima as large as .008".

In comparison with reflective optics hitherto used, Irtran-2 lenses offer compactness and a wider field that doesn't show any appreciable deterioration as far as 2° off axis.

You do give up the perfect achromatism of reflective optics. In the 2-inch lens the minimum circle of confusion for 10μ radiation is located 2 mm beyond the minimum circle of confusion for 4.25μ radiation; in the 3-inch lens the separation is 3 mm.

We have said enough to establish our frankness and to indicate whether there is any need for you to burden the long lines to Rochester, N. Y., LOCust 2-6000, Extension 5166, which is one way to reach Eastman Kodak Company, Special Products Division. Bear in mind that Irtran-2 material has a hardness of 354 Knoop, is not at all brittle, withstands thermal shock and the solvent action of water, and can get very hot without losing transparency or giving off toxic fumes.

Down with the administrative dose

Two little packets of film are extracted from a factory-fresh carton. One is locked away in a clean safe. The other is worn by a worker in the vicinity of ionizing radiation. After a month the two are processed together. Both turn out equally blank. A good densitometer discloses no difference in their optical densities. What can be inferred about the quantity of ionizing radiation the worker has absorbed?

Anybody who draws the obvious conclusion has failed fully to engage his brain cells in thought. The answer to the question depends on the sensitivity of the film. Once that is known, one can say how much of a dose the worker has probably had less than.

Social ethics in advanced countries require the assumption that the worker has actually had that much radiation. This is known as the "administrative" dose. Records are kept as in a bank. When administrative and physical doses add up to a critical figure, the worker is shifted to a different job. He may habitually spend every Saturday night cruising the center line of a busy highway at 80 m.p.h. Nevertheless, the critical figure assumes that he wants to live forever and become the progenitor of an infinite line of biologically perfect descendants. Pressure to squeeze it down will never let up, we hope.

Without relaxation of solicitude, we have taken steps to cut down the waste of his job experience. By reducing the administrative dose (which is the only kind of radiation dose he really ought ever to get on the job), we can keep him in his slot longer. It is within our power. All we have to do is make more sensitive film. This we have now done. It is called Kodak Personal Monitoring Film, Type 3.

The packet it comes in also includes a piece of low-sensitivity film. Its sensitivity is so low that it can measure 1800 roentgens, a horrible thought. The lower limit of dose measurement for the high-sensitivity film in the packet runs somewhere below 10 milliroentgens. The vague phrasing of that statement doesn't mean that the exact value is unimportant. The main point of this discussion is the importance of the figure. It's just that its precise determination depends on such a complexity of factors that we won't try to explain it here.

If interested, prepare yourself by studying pp. 10-53 to 10-75 of Radiation Hygiene Handbook (McGraw-Hill Book Company, Inc., 1959). Then bring your knowledge up to date by requesting a data sheet on Kodak Personal Monitoring Film, Type 3 from Eastman Kodak Company, Special Sensitized Products Division, Rochester 4, N. Y. Be impressed with the fact that the boys who built this film have just finished measuring the dose to which a recent Discoverer satellite exposed itself in its travels. It's no administrative dose.



The concave side is trickier.

Kodak
TRADE MARK



ADVANCED SOLID STATE RESEARCH & DEVELOPMENT

Senior scientists and engineers are needed to fill new positions in our rapidly expanding research and development laboratories near San Francisco. Our broadening interests have created challenging positions for individuals with significant backgrounds in the following fields:

SURFACE PHYSICS AND CHEMISTRY
ELECTROCHEMISTRY
ELECTRON MICROSCOPY
MAGNETIC THIN FILMS
EVAPORATED CIRCUITRY
SEMICONDUCTOR MATERIALS
ELECTRO-OPTICS
ADVANCED CIRCUIT DEVELOPMENT
MICROWAVE PHYSICS

A Ph.D. Degree or commensurate experience is especially desirable.

Applicants are invited to send detailed resumes, including salary history and requirements, to Mr. Donald Palmer, Palo Alto interviews for qualified applicants will be arranged from anywhere in the United States. All inquiries strictly confidential and acknowledged promptly. All qualified applicants will be considered regardless of race, creed, color or national origin.

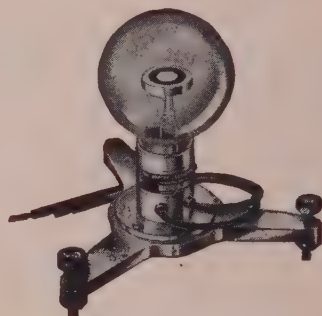
FAIRCHILD

SEMICONDUCTOR

844 CHARLESTON ROAD • PALO ALTO, CALIFORNIA

EPLAB

PYRHELIOMETER For the Measurement of SOLAR RADIATION



Eppley Pyrheliometers are used for solar radiation measurements at ninety-eight weather stations in the continental United States, Canada, Alaska, Greenland, Iceland, Caribbean Sea, and the Pacific Ocean. Sixty-two of these stations are under the direction of the United States Weather Bureau.

The Eppley Pyrheliometer was adopted as standard equipment by the Weather Bureau after considerable experimentation. It was found to be the best instrument so far tested by the Bureau.

Used in conjunction with a suitable recorder, the Eppley Pyrheliometer will provide an accurate and reliable record of total solar and sky radiation on a horizontal surface.

Bulletin No. 2 On Request

THE EPPLEY LABORATORY, INC.

Scientific Instruments

6 Sheffield Ave.

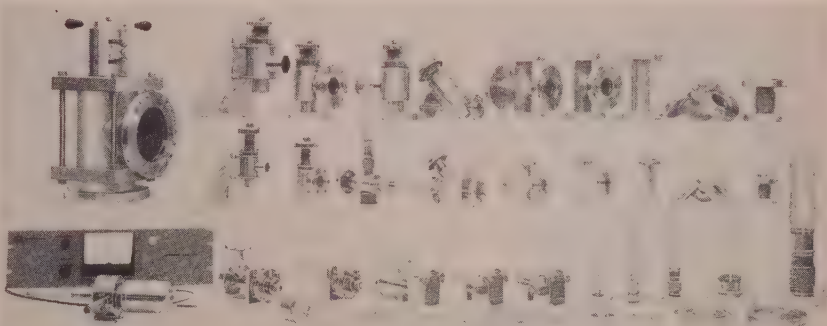
Newport, Rhode Island, U.S.A.

For ULTRA-HIGH VACUUM or ULTRA-CLEAN SYSTEMS

All-metal bakeable valves • Elbows, tees, crosses, nipples • Variable leaks
Flanged metal to glass seals • Bakeable capacitance manometers • Flanged bellows assemblies

AVAILABLE FROM STOCK

At right are some of the standard Granville-Phillips components available from stock. None contain organic materials. All are bakeable to 450°C. and useful at 10^{-10} mm Hg or lower. Right-angle valves presently available in $\frac{1}{2}$ ", 1", 2", 4", and 6" sizes, straight-through valves in $\frac{1}{2}$ ", 1", 2½", and 4" sizes. Complete line of demountable plumbing. Custom designs on request.



WRITE OR TELEPHONE FOR COMPLETE CATALOG



Granville-Phillips Company

P. O. Box J-198 Pullman, Washington • telephone LOgan 4-1130

ILFORD

industrial "G" X-ray film for crystallography

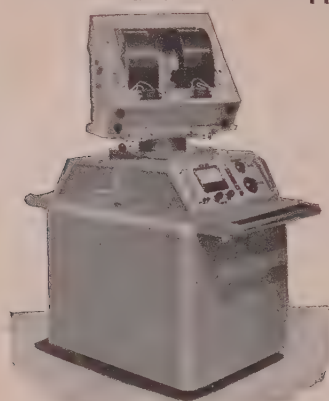
If you are seeking a superior film for X-ray diffraction studies, Ilford Industrial "G" X-ray Film will meet your requirements. This film combines the advantages of maximum speed and medium grain with extremely low background fog and relatively high contrast. It is manufactured to close tolerances to simplify standardization of X-ray reflection intensities.

Industrial "G" and other Ilford X-ray films are available from General Electric, Keleket, Picker, Westinghouse and their authorized dealers.

For further details write to:

ILFORD INC. 37 WEST 65th STREET, NEW YORK 23, N.Y.

High Performance ELECTROMAGNETS and Power Supplies



ECONOMY

7" Electromagnet
Type E
(7" pole diameter).
Fields up to 8,000
gauss.
Homogeneity of at
least 4 parts in 10^5
in $\frac{1}{2}$ cc.

ROTATION

Rotating Base
Type AE.
360° scale.
Positive friction
lock.

STABILITY

Current-Stabilized
Power Supply Unit
Type B.

Also available:—

- 1½" Electromagnet Type C—for Teaching purposes.
- 4" Electromagnet Type A—for all purposes.
- 3" Electromagnet Type D—for Electron Resonance and Nuclear Magnetic Resonance work.
- Direct Reading Magnetometer Type G.
- Proton Resonance Magnetometer Type P.

NEWPORT INSTRUMENTS (Scientific & Mobile) Ltd

10 CRAWLEY ROAD, NEWPORT PAGNELL, BUCKS
Telephone: NEWPORT PAGNELL 401/2

PHYSICIST

The Engineering Department of Chandler Evans Corporation, designers and manufacturers of precision aircraft and space vehicle sub-systems, desires to employ a Physicist, preferably Ph.D. level, to serve as a staff consultant in science and physics. A broad general knowledge and interest in the fields of science coupled with more intensive knowledge in astro and/or acoustic or nuclear physics is desired to enable consultation on problems encountered in the application of pneumatic and hydraulic control devices to space, nuclear and underwater applications.

For further details write in confidence to Mr. S. C. Mason, Personnel Department.

CHANDLER EVANS CORPORATION
WEST HARTFORD 1, CONN.

An equal opportunity employer

TRANSLATIONS OF SOVIET JOURNALS

Published by the American Institute of Physics with the cooperation of the National Science Foundation.

SOVIET PHYSICS—JETP

Monthly. Translation of *Zhurnal Eksperimental'noi i Teoreticheskoi Fiziki*.

SOVIET PHYSICS—SOLID STATE

Monthly. Translation of *Fizika Tverdogo Tela*.

SOVIET PHYSICS—TECHNICAL PHYSICS

Monthly. Translation of *Zhurnal Tekhnicheskoi Fiziki*.

SOVIET PHYSICS—DOKLADY

Bimonthly. Translation of the Physics Sections of Proceedings of Academy of Sciences, USSR.

SOVIET PHYSICS—ACOUSTICS

Quarterly. Translation of *Akusticheskii Zhurnal*.

SOVIET PHYSICS—CRYSTALLOGRAPHY

Bimonthly. Translation of *Kristallografiya*.

SOVIET PHYSICS—USPEKHI

Bimonthly. Translation of *Uspekhi Fizicheskikh Nauk*.

SOVIET ASTRONOMY—AJ

Bimonthly. Translation of *Astronomicheskii Zhurnal*.

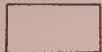
Send orders and inquiries to:

American Institute of Physics

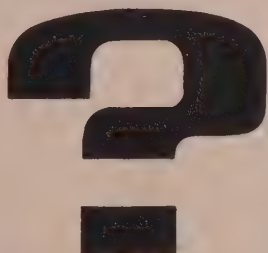
335 East 45 Street, New York 17, N. Y.



What do you need to know about



PURE FERRIC OXIDES MAGNETIC IRON OXIDES



Since the final quality of your production of ferrites and magnetic recording media depends on the proper use of specialized iron oxides—you'll find it mighty helpful to have the latest, authoritative technical data describing the physical and chemical characteristics of these materials. This information is available to you just for the asking. Meanwhile, here are the highlights.

PURE FERRIC OXIDES—For the production of ferrites, both hard and soft, we manufacture a complete range of iron oxides having the required chemical and physical properties. They are produced in both the spheroidal and acicular shapes with average particle diameters from 0.2 to 0.8 microns. Impurities such as soluble salts, silica, alumina, and calcium are at a minimum while Fe_2O_3 assay is 99.5+%. A Tech Report tabulating complete chemical analysis, particle shape, particle size distribution, surface area, etc., of several types of ferric oxides, hydrated ferric oxide, and ferrous-ferric oxide is available.

MAGNETIC IRON OXIDES—For magnetic recording—audio, video, computer, and instrumentation tapes; memory drums; cinema film stripping; magnetic inks; carbon transfers; etc.—we produce special magnetic iron oxides with a range of controlled magnetic properties. Both the black ferrous-ferric and brown gamma ferric oxides are described in a Data Sheet listing magnetic properties of six grades.

If you have problems involving any of these materials, please let us go to work for you. We maintain fully equipped laboratories for the development of new and better inorganic materials. Write, stating your problem, to C. K. Williams & Co., Dept. 38, 640 N. 13th St., Easton, Penna.

WILLIAMS
COLORS & PIGMENTS

*Pigment
Technology
at its
best*

E. ST. LOUIS, ILLINOIS • EASTON, PENNSYLVANIA • EMERYVILLE, CALIFORNIA

THE JOURNAL OF APPLIED PHYSICS NOVEMBER, 1961

TECH NEWS

FOR SCIENTISTS,
MATHEMATICIANS
**OPERATIONS
EVALUATION
GROUP, M.I.T.**

In its research and analysis for the Chief of Naval Operations and Fleet Commanders, the Operations Evaluation Group, M.I.T., pursues knowledge in virtually every sphere of naval interest.



Consider OEG study 644, for example, entitled "Echo Variability and the Formulation of a Radar Theory." OEG's analysts found that blaming radar operators and poor radar maintenance for variability of signal presentation on radar scopes (all other things supposedly being equal) was convenient but erroneous. New culprits will have to be isolated and bested. OEG thinks it has found some

of them for the Navy.

When is a sea not a sea? When it's a swell. Seriously. Seas and swells, ramp-to-touchdown distances, vertical velocities, wave-to-wave amplitude variations, and similarly specialized factors enter into "The Effect of Ship Motion and Flight Deck Geometry upon Carrier Air Operations." This is Naval Warfare Analysis Group Study No. 20 (NAVWAG being the long-range studies division of OEG). One interesting conclusion: Position of the touchdown point has a greater effect on precluded flying time than does ship length. And on the subject of ship length, the minimum recommended (for an angled-deck carrier) is 800 feet.



Would you like to have a hand in similar research, knowing that you would be contributing importantly to the national defense? Well paid career appointments in Washington, D.C., and Cambridge are available to scientists, mathematicians and engineers with advanced degrees. Direct your inquiry to the Director, Dr. Jacinto Steinhardt, either in Washington or in Cambridge.

OEG

OPERATIONS EVALUATION GROUP

Box 6196, Apex Station, Washington 4, D. C.
or 292 Main St., Cambridge, Mass.

An equal opportunity employer.

INDEX TO ADVERTISERS

<i>Name</i>	<i>Page</i>	<i>Name</i>	<i>Page</i>
AEROSPACE CORPORATION	xx	HARSHAW CHEMICAL CO. ...	Cover 2
ASARCO, AMERICAN SMELTING & REFINING COMPANY	xxi	HUGHES AIRCRAFT CO.	iv
AMPEREX ELECTRONIC CORP. ..	xi	ILFORD INC.	xxv
BELL TELEPHONE LABORA- TORIES	ix	ILIKON CORPORATION	xiv, xv
CENTRAL RESEARCH LABS., INC.	xvii	KEITHLEY INSTRUMENTS, INC.	vi
CENTRAL SCIENTIFIC CO.	xv	LINK DIVISION GENERAL PRECISION, INC. ...	xii
Manufacturers of Cenco physical ap- paratus and instruments to meet all re- quirements of University, College and High School Physics Laboratories. Specializing in high vacuum pumps and development of instruments and appa- ratus for various sciences.		LOS ALAMOS SCIENTIFIC LAB. ..	vii
CHANDLER EVANS CORP.	xxvi	MATERIALS RESEARCH CORP. .	xxix
CONSOLIDATED ELECTRO- DYNAMICS	x	NRC EQUIPMENT CORP	xxix
EASTMAN KODAK COMPANY ..	xxiii	Manufacturers of standard and special high vacuum components, equipment, and systems including mechanical booster, and diffusion pumps; gauges; valves; seals; connectors; melting and heat-treating furnaces; coaters; im- pregnators; gas in metal analyzers; driers and freeze driers; altitude cham- bers and leak detectors.	
THE EPPLEY LABORATORY, INC.	xxiv	NEWPORT INSTRUMENTS LTD.	xxvi
FAIRCHILD SEMICONDUCTOR CORP.	xxiv	OPERATIONS EVALUATION GROUP, M.I.T.	xxvii
GENERAL RADIO CO.	Cover 4	PHILIPS ELECTRONIC INSTRU- MENTS	xviii
Manufacturers of electronic measuring instruments; vacuum-tube voltmeters, amplifiers, and oscillators; wave ana- lyzers, noise meters and analyzers, stroboscopes, laboratory standards of capacitance; inductance and frequency; impedance bridges, decade resistors and condensers, air condenser and variable inductors; rheostats, variacs, transform- ers; other laboratory accessories.		RADIO CORP. OF AMERICA ..	Cover 3
GRANVILLE-PHILLIPS CO.	xxv	S. A. M. E. S.	viii
		SPERRY RAND RESEARCH CENTER	xxx
		SYLVANIA ELECTRONIC SYS- TEMS, AMHERST LABORA- TORIES	xix

INDEX—Continued

Company	Page
TECHNICAL MEASUREMENT CORP.	iii
Nuclear instrumentation—single and multichannel pulse height analyzers, liquid scintillation beta spectrometers, reactor flux plotting systems, sealers, precision high voltage power supplies, ratemeters, linear amplifiers and custom nuclear system design.	
ELECTRONIC LAB., EQUIPMENT	xiii
ARIAN ASSOCIATES	
VACUUM DIVISION	v
VELCH SCIENTIFIC CO., W. M.	xxii
Manufacturers of high-vacuum pumps, both mechanical and diffusion; vacuum gauges; electrical measuring instruments; physics equipment; and other items for the physical and chemical laboratories.	
JOHN WILEY & SONS, INC.	xvi
J. K. WILLIAMS & CO.	xxvii

POSITION OPEN

PHYSICS DEPARTMENT OKLAHOMA STATE UNIVERSITY

Has openings for persons interested in combining teaching and academic research. Especially urgent is the need for staff to guide and supervise the research of both M.S. and Ph.D. candidates. Appointments effective immediately or as convenient. Rank Associate Professor or Professor. Salary dependent upon experience but competitive.

If interested, write to:

H. E. Harrington, Head
Stillwater, Oklahoma

TUBULAR SLIDE CONTACT RHEOSTATS
Toroidal RESISTORS
Winding Machines
REX RHEOSTAT CO.
49-a Babylon Tpke, Roosevelt, L.I., N.Y.

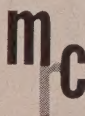
MRC announces a new specimen preparation service:

- electron beam refining
- single crystal growth
- crystal seeding
- single crystal tensile specimens
- foils and wires prepared from high purity single crystals
- crystals with specific interstitial content

99.996% pure iron

is the newest addition to MRC's stock of very high purity materials, which includes nickel, tungsten, molybdenum, niobium and tantalum. In every case interstitial impurity levels can be held to less than 25 ppm.

Our experience in controlling impurity content and the equipment developed for this processing can be put to work for you. Write us.



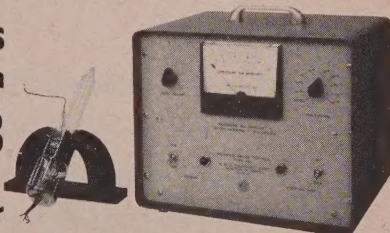
Advanced Materials Division
MATERIALS RESEARCH CORP.
47 Buena Vista Ave., Yonkers, N.Y.

**DIRECT
VACUUM
READINGS**
to less than

10⁻¹³
torr

**with NRC'S
REDHEAD
MAGNETRON
GAUGE**

The NRC Model 752 ultra-high vacuum gauge is a cold cathode linear output ionization tube which measures pressure several decades lower than any other commercially available gauge.



The Model 752 has several unique advantages — High Sensitivity of 4.5 amperes per millimeter of mercury — 50 times that of hot wire ionization gauges — Cold Cathode Operation which keeps the vapor pressure of gauge elements below operation pressures — eliminates contamination by metallic vapors ... No Outgassing Circuit required which simplifies operation ... Self Regulating Emission which keeps X-ray background current always much lower than the ionization current.

Write today for data sheet and prices for the Model 752.



A Subsidiary of National Research Corp.

160 Charlemont Street, Dept. 20K
Newton 61, Massachusetts

MANUFACTURING PLANTS IN NEWTON, MASS., AND PALO ALTO, CALIF.

PHYSICS AND CHEMISTRY OF SOLIDS

The new Sperry Rand Research Center in Sudbury, Massachusetts, is seeking scientists at the Ph.D. level with an interest in doing publishable basic work in the fields of:

CRYSTAL GROWTH
OPTICAL STUDIES
MAGNETIC RESONANCE
DEFECT STUDIES
ENERGY CONVERSION
ELECTRICAL TRANSPORT
STUDIES

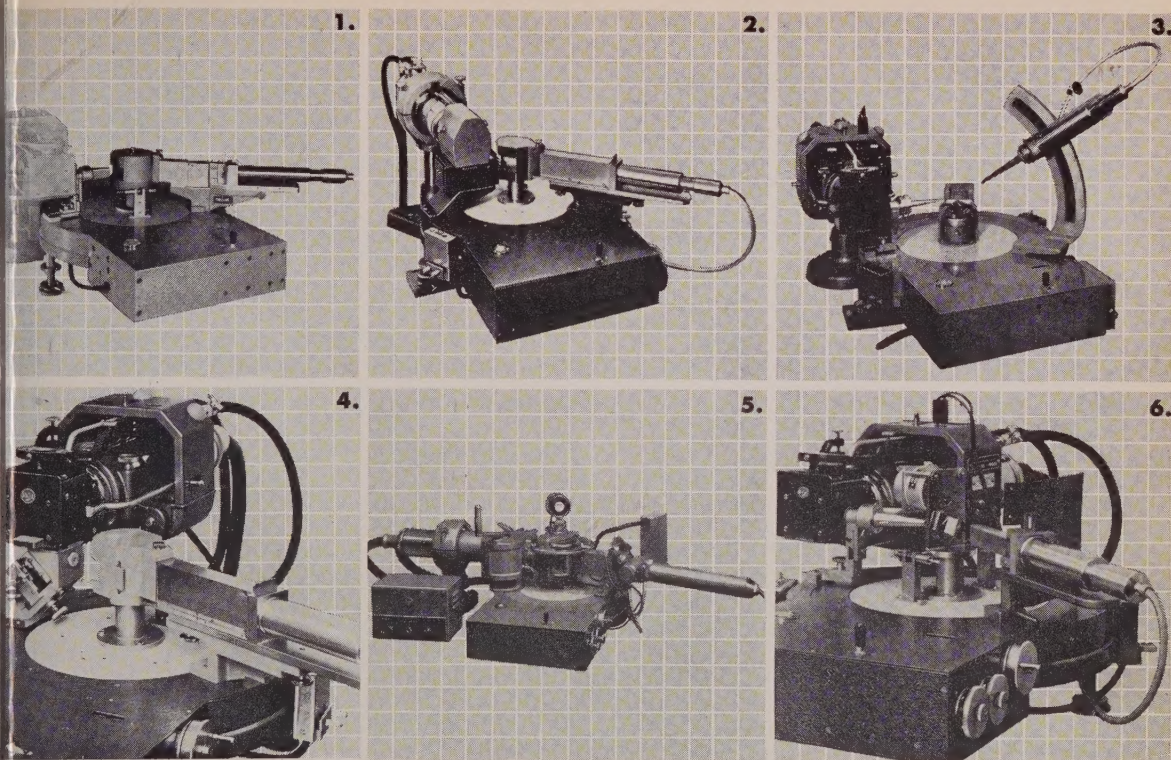
Our new laboratory located 25 miles west of Boston offers a basic research environment with maximum freedom to pursue fundamental ideas.

Please contact our representative Dr. Roger Newman at the headquarters hotel of the Magnetism and Magnetic Materials Conference, November 13-16 in Phoenix, Arizona.

If unable to visit with us at this time, please direct your resume to Mr. Frederick M. Swope, Jr.

SPERRY RAND RESEARCH CENTER

Box 400, Sudbury, Massachusetts
'An equal opportunity employer'



1. Counter Tube Diffractometry. 2. Spectroscopy. 3. Single Crystal Studies. 4. Spectroscopy of Small Areas. 5. Vacuum Spectroscopy of Light and Heavy Elements. 6. Studies of Orientation.

VERSATILITY!

RCA's horizontal goniometer performs 6 functions

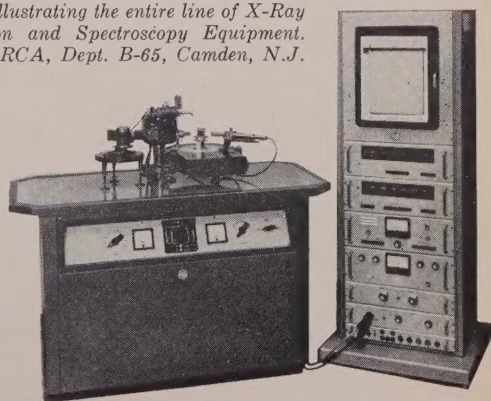
usual versatility is an important distinguishing characteristic of RCA's X-Ray Diffraction and Spectroscopy Equipment. This versatility is graphically demonstrated by the horizontal goniometer which performs six different functions merely by adding accessories, as illustrated above.

A X-Ray Diffraction and Spectroscopy Equipment offers many other outstanding features which make it one of today's most specified lines. For example, the DC regulated and filtered power supply, the option of mounting two tube stands on the Crystalloflex IV; a kit which permits conversion from diffraction to spectroscopy in minutes; and the vacuum spectrometer for analysis of light and heavy elements. For those engaged in film studies of crystals, the RCA Table Model Crystalloflex II can

be bought, complete with cameras, for as little as \$4000.

A NEW LEASING PLAN now makes it possible to obtain all RCA scientific instruments, including the Electron Microscope, with no down payment, low monthly terms, and a favorable option to buy.

Send for comprehensive new catalog, describing and illustrating the entire line of X-Ray Diffraction and Spectroscopy Equipment. Write to RCA, Dept. B-65, Camden, N.J.



Crystalloflex IV and Electronic Circuit Panel with Diffractometer



The Most Trusted Name in Electronics
RADIO CORPORATION OF AMERICA

PHOTOGRAPHING LIGHTNING... IN THE SKY

Using G-R's Pulse, Sweep, and Time-Delay Generator

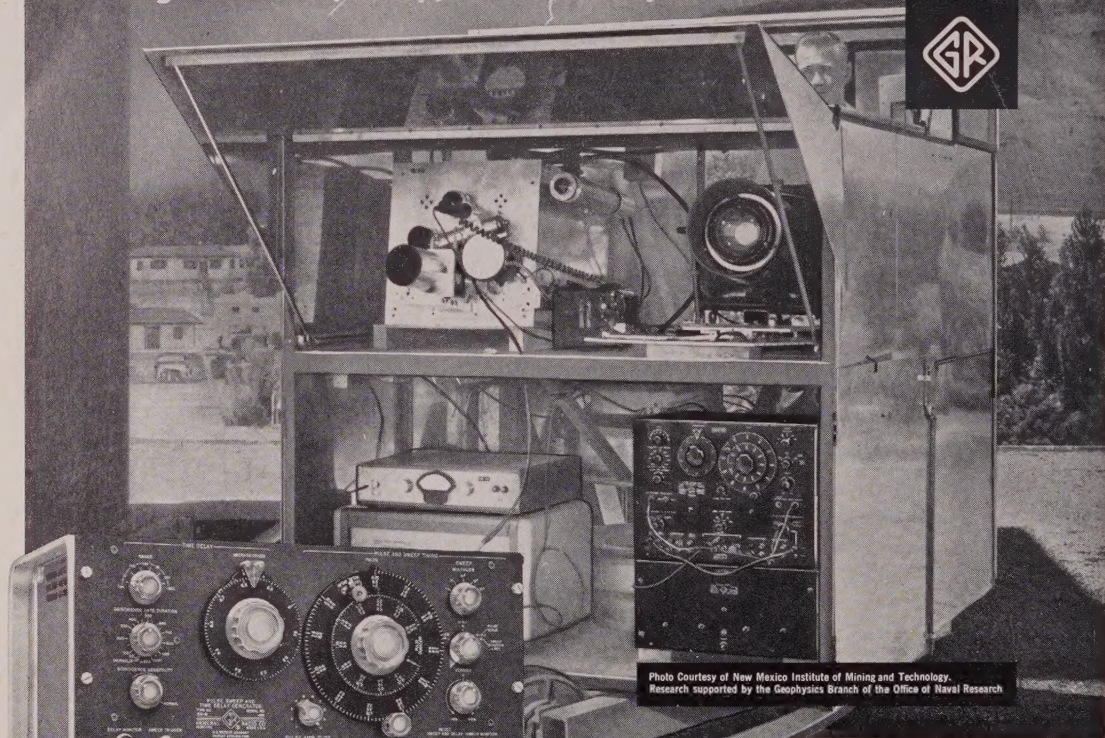


Photo Courtesy of New Mexico Institute of Mining and Technology.
Research supported by the Geophysics Branch of the Office of Naval Research

Type 1391-B

Pulse, Sweep, and Time-Delay Generator
The Complete, Wide Range Pulse Source

- ★ Fast Rise and Decay Times — better than 15 ns.
- ★ Push-Pull Pulses with Durations from 25 ns to 1.1 sec.
- ★ Time Delays from 1 μ sec to 1.1 sec.
- ★ No Duty Ratio Restrictions.
- ★ High Accuracy and High Resolution Throughout.
- ★ Coincidence Circuitry for Multiple Pulsing and Time Selection.
- ★ Variable Output Impedance — 50 to 600 ohms.
- ★ Versatility Unmatched — Variety of Outputs Conveniently Accessible on Panel.
- ★ Linear Sweep Voltage from 3 μ sec to 0.12 sec.

PRICE . . . \$2025.

Atop the Research Building of the New Mexico Institute of Mining and Technology stands a shelter containing complete apparatus for photographing lightning phenomena as the bolts streak across the sky. An integral part of this apparatus is the versatile General Radio Type 1391-B Pulse, Sweep, and Time-Delay Generator. Increased luminosity caused by the lightning stroke is detected by a photomultiplier tube, which delivers a negative pulse to the Type 1391-B. Using the time-delay function of the Generator, an accurate delay is inserted. This delayed output pulse is then delivered to a Kerr Cell modulator which supplies the necessary 0.1 μ sec, 50-kilovolt pulse for triggering the Kerr Cell shutter.

The sweep feature of the Type 1391-B is used to avoid exceeding the duty-ratio restrictions of the modulator. The initial trigger pulse starts the sequence with a pulse to the Kerr Cell, but no new pulses result until the predetermined sweep is over. Disarming the Generator in this manner allows a maximum of one pulse per 3 milliseconds to the Kerr Cell.

GENERAL RADIO COMPANY

WEST CONCORD, MASSACHUSETTS

NEW YORK, Worth 4-2722
District Office in Ridgfield, N. J.
Whitney 3-3140

CHICAGO
Oak Park
Village 9-3400

PHILADELPHIA
Abington
HAncock 4-7419

WASHINGTON, D. C.
Silver Spring
JUniper 5-1088

SYRACUSE
Syracuse
Glenview 4-9323

SAN FRANCISCO
Los Altos
WHitecliff 8-8233

LOS ANGELES
Los Angeles
HOLLYWOOD 9-6201

ORLANDO, FLA.
Orlando
GArden 5-4671

IN CANADA
Toronto
CHerry 6-2171